Origin and geodynamic significance of ultramafic-mafic complexes in the North Atlantic and Kaapvaal Cratons

George L. Guice

School of Earth and Ocean Sciences

Cardiff University

Submitted in fulfilment of the requirements for the degree of:

Doctor of Philosophy (PhD)

January 2019

Declaration

This work has not been submitted in substance for any other degree or award at this or any other university or place of learning, nor is being submitted concurrently in candidature for any degree or other award.

Signed…… (candidate) Date:……

Statement 1

This thesis is being submitted in partial fulfilment of the requirements for the degree of PhD.

Signed…… (candidate) Date:……

Statement 2

This thesis is the result of my own independent work/investigation, except where otherwise stated, and the thesis has not been edited by a third party beyond what is permitted by Cardiff University's Policy on the Use of Third Party Editors by Research Degree Students. Other sources are acknowledged by explicit references. The views expressed are my own.

Signed…… (candidate) Date:……

Statement 3

I hereby give consent for my thesis, if accepted, to be available online in the University's Open Access repository and for inter-library loan, and for the title and summary to be made available to outside organisations.

Signed…… (candidate) Date:……

Statement 4: previously approved bar on access

I hereby give consent for my thesis, if accepted, to be available for photocopying and for inter-library loans after expiry of a bar on access previously approved by the Academic Standards & Quality Committee.

Signed…… (candidate) Date:……

Acknowledgments

First and foremost, I would like to thank Iain McDonald and Hannah Hughes. Iain, you have provided tireless guidance and advice (on both academic and personal levels) throughout this process. I never felt discouraged by my mistakes in the lab or rubbish paper drafts, and I am grateful for the freedom and confidence that you have given me. Your commitment, enthusiasm and talent for teaching has been a source of inspiration as I take the first steps in my own career, and I hope to one day emulate you. Hannah, you have been a source of unrelenting encouragement and have an uncanny talent for making me feel good about a manuscript draft covered in red pen. No question was too stupid (even the stupid ones…) and I am extremely grateful for your perpetual patience. Perhaps more importantly, I would not have been introduced to the one and only Shady Prawn without you, which is a world not worth imagining. Remarkably, between you both, you have managed to mould me into a scientist, and I hope to continue working with you in the future. Thanks for everything, I have a feeling that the beer might be on me…

I have been fortunate to have worked with some other outstanding people (and fantastic scientists) during the last 3.5 years. In particular, I would like to thank John MacDonald, John Faithful, Kathryn Goodenough, Carl Anhaeusser, Denis Schlatter, Tom Blenkinsop and Bob Gooday. John (Mac), thanks for introducing me to the NW Highlands and holding your tongue in the presence of Ron (a “friendly” B&B owner). John (F), on top of your infectious enthusiasm for all things geology, thanks to you and Cath for your generous hospitality (on numerous occasions) and I am privileged to have spent a day in the field with the legendary Spud. Carl, I was honoured to receive your Johannesburg Dome masterclass tour, and am extremely grateful for access to your sample collection and kind words of encouragement. All, it has been a pleasure.

I would also like to thanks several individuals in the department here in Cardiff, without whom, this work would not have been possible. They are: Tony Oldroyd (for tireless production of high-quality thin sections), Duncan “architect of the Bute Park Bobble” Muir (for SEM-related training/assistance) and Katie Dobbie (without whom, the department would collapse, I’m sure). Thanks also to the PhD community (past and present) in the school, who have helped to make my time in Cardiff so enjoyable. There are too many to name individually (sorry to disappoint), but in particular, I am grateful for the support and friendship of Bethan, Kate and Bob. Diolch/thanks/cheers.

Life outside of university has helped to maintain a sense of perspective, and I would like to thank those responsible for keeping me grounded and, fundamentally, sane. The game of T-ball – a 3-player racquet sport invented by my imaginative colleagues Nick, Bob, Micky and Michael – deserves acknowledgment. Similarly, thanks to the Bute Park Bobble, its architect (and leader) Duncan and everybody that turns up on sweltering summer days to have a laugh kicking a football around. Thanks to everybody involved with Cardiff Dragons Football Club. Playing Sunday League football has allowed me to forget about work for several hours per week, because nothing says "forget your PhD" like being hacked to the turf on a cold February morning. I would also like to pay tribute to Rhodri, who is the undisputed glue of 66. Cheers for the laughs, golf, bike rides, coffees, rodent trapping activities and pool etc. etc. etc. Grandad, thanks for the chats and New Scientist magazines that started all of this science malarkey.

Also, thank you to Coventry City Football Club for being perpetually rubbish and preparing me emotionally for the inevitable failures that accompany the PhD process. That said, Jordan Shipley's goal at Wembley was perhaps the best single moment of my life and demonstrates the value of sticking at something, even if it does involve standing in the rain and watching your team concede 3 first half goals away at Bristol Rovers. PUSB.

And, of course, I would like to thank Amy. You are alright.

And finally, last but certainly not least, thank you to Mum, Dad and Will. The geology may have been taught by others, but this thesis wouldn't have been possible without everything I learnt from you. Enjoy this page-turner, and thanks for everything.

Abstract

The physical manifestations of plate tectonics on the modern Earth are relatively well-understood, but the nature and timing of its onset remains enigmatic, with the geodynamic regime(s) that operated during the Archaean hotly debated. This absence of a consistent geodynamic framework within which regional-scale observations can be placed limits our understanding of Archaean assemblages and associated mineral deposits. To engage with the Archaean geodynamics discussion, this thesis focuses on ultramafic-mafic complexes in the Lewisian Gneiss Complex (LGC) of the North Atlantic Craton and Johannesburg Dome of the Kaapvaal Craton. Globally, such complexes have been the subject of wide-ranging interpretations that have disparate implications for Archaean geodynamic regimes.

Throughout this thesis, it is demonstrated that confidently constraining element mobility is of paramount importance when aiming to constrain the origin of Archaean ultramafic rocks, with a variety of geochemical proxies shown to be susceptible to element mobility. Notably, high field strength element anomalies – a geochemical proxy commonly used to fingerprint subduction-related magmatism – are here shown to be highly susceptible to element mobility, with the role of subduction as an Archaean geodynamic process potentially overestimated as a result. Such mobility can, however, be constrained and a primary geochemistry obtained using the integrated approach utilised here, whereby detailed petrography, bulk-rock geochemistry and mineral chemistry are examined using the context provided by rigorous field geology.

Using this approach, the ultramafic-mafic complexes in the LGC are here interpreted as recording two temporally and petrogenetically distinct phases of Archaean magmatism. One group of complexes likely represents an early ultramafic-mafic crust that pre-dates the tonalite-trondhjemite-granodiorite (TTG) magmas, while a second group of complexes are interpreted as representing several layered intrusions that were emplaced *into* TTG. The ultramafic-mafic complexes in the Johannesburg Dome are considered to represent intrusive and extrusive remnants of an Archaean greenstone belt, contradicting a recently proposed hypothesis whereby the complexes are interpreted as fragments of an Archaean ophiolite. When combined with similar opposition to other proposed Archaean ophiolite occurrences in other cratons, this contradiction is potentially significant to the Archaean geodynamics debate, raising questions as to the validity of a > 3.6 Ga onset for modern-style plate tectonics.

Author note and status of publications

Chapters 3 to 4 present two papers published in international, peer-reviewed journals. While the text, figures and tables presented here are largely the same as those published in the journals, the content of the papers has been re-formatted and edited so as to be suitable for the thesis layout and avoid repetition. Moreover, Chapters 7 to 9 contain the text, figures and tables included in one additional paper, with the contents of this paper distributed throughout these chapters.

The status of the following papers, including co-author contributions, are as follows (correct as of thesis submission):

- **(Chapter 3)** George L. Guice, Iain McDonald, Hannah S. R. Hughes, John M. MacDonald, Thomas G. Blenkinsop, Kathryn M. Goodenough, John W. Faithfull, Robert J. Gooday. (2018) Re-evaluating ambiguous age relationships in Archean cratons: implications for the origin of ultramafic-mafic complexes in the Lewisian Gneiss Complex. *Precambrian Research,* **311,** 136-156.

  Author contributions and declarations: G.L.G. conducted field mapping, structural assessments, petrographic assessments and quantitative mineral chemical analyses. G.L.G. also conceived of the ideas presented, and wrote the entire chapter. I.McD., H.S.R.H., J.M.M., T.G.B., K.M.G. and J.W.F. were involved in discussions during the writing of the chapter, and J.M.M. and R.J.G. provided field assistance for a combined total of 5 days. Jochen Kolb and Tim Johnson provided constructive peer-reviews of the published paper, and Hugh Rollinson provided a constructive review of a previous version of the manuscript.

- **(Chapter 4)** George L. Guice, Iain McDonald, Hannah S. R. Hughes, Denis M. Schlatter, Kathryn M. Goodenough, John M. MacDonald, John W. Faithfull. (2018) Assessing the Validity of Negative High Field Strength-Element Anomalies as a Proxy for Archaean Subduction: Evidence from the Ben Strome Complex, NW Scotland. *Geosciences*, **8** (9), 338.

  Author contributions and declarations: G.L.G. conceived of and conceptualised the contents of the chapter, wrote the chapter, carried out sampling of the Ben Strome Complex, and conducted all A-SEM work, petrographic assessments, sample preparation for bulk-rock geochemistry and LA-ICP-MS data collection. I.McD., H.S.R.H.,

D.M.S., K.M.G., J.M.M. and J.W.F. were all involved in discussions during the writing of the manuscript, and contributed to developing the hypothesis for the origin of the HFSE anomalies in the Ben Strome Complex. I.McD. was responsible for bulk-rock analysis by ICP-OES and ICP-MS, and for supervision during LA-ICP-MS data collection. J.M.M., H.S.R.H. and J.W.F. contributed to fieldwork prior to and during G.L.G.'s fieldwork in 2016 and 2017.

- **(Chapters 7 to 9)** George L. Guice, Iain McDonald, Hannah S. R. Hughes, Carl R. Anhaeusser. (2019) An evaluation of element mobility in the Modderfontein ultramafic complex, Johannesburg: origin as an Archaean ophiolite fragment or greenstone belt remnant? *Lithos*, **332-333,** 99-119,

  Author contributions and declarations: G.L.G conducted fieldwork, sampling, petrographic assessments, A-SEM work, LA-ICP-MS data collection and sample preparation for bulk-rock geochemistry. I.McD., H.S.R.H. and C.R.A. were all involved in discussions during the writing of the manuscript. I.McD. was responsible for bulk-rock analysis by ICP-OES and ICP-MS, and supervised LA-ICP-MS data collection. H.S.R.H and C.R.A contributed to fieldwork during G.L.G.'s fieldwork in 2016, and C.R.A. also provided some of the samples utilised.

Tables of contents

List of figures

Page Number

List of tables

Abbreviations

A-SEM	Analytical scanning electron microscope
BMS	Base metal sulphides
BSE	Back-scattered electron
HFSE	High field strength elements
HREE	Heavy rare earth elements
ICP-MS	Inductively coupled plasma mass spectrometry
ICP-OES	Inductively coupled plasma optical emission spectrometry
IPGE	Ir-group platinum-group elements
LA-ICP-MS	Laser ablation inductively coupled plasma mass spectrometry
LGC	Lewisian Gneiss Complex
LILE	Large ion lithophile element
LOI	Loss-on-ignition
LREE	Light rare earth elements
MORB	Mid-ocean ridge basalt
MREE	Medium rare earth elements
NAC	North Atlantic Craton
OIB	Ocean island basalt
PGE	Platinum-group elements
PGM	Platinum-group minerals
PPGE	Pd-group platinum-group elements
PPL	Plane-polarised light
REE	Rare earth elements
SCLM	Sub-continental lithospheric mantle
SE	Secondary electron
SEM	Scanning electron microscope
SSZ	Suprasubduction zone
TTG	Tonalite-trondhjemite-granodiorite
XPL	Crossed-polarised light

Chapter 1

Introduction

Plate tectonics is the keystone theory of modern geological knowledge, representing a framework within which any portion of Earth's Phanerozoic crust can be interpreted. According to this theory (summarised in Figure 1.1), the Earth's lithosphere comprises an interlocking network of internally rigid plates that are mechanically decoupled from one another, with deformation largely focused at plate boundaries (e.g., Isacks et al. 1968, Forsyth and Uyeda 1975, Kearey et al. 2009, Cawood et al. 2018). Such boundaries are classified as either divergent (i.e., mid-ocean ridges), convergent (i.e., subduction zones and continent-continent collision) or strike-slip (Fig. 1.1), with plates comprising chemically and physically distinct oceanic and continental lithospheres that currently occur in a roughly 60:40 ratio (Isacks et al. 1968, Chen 1992, Philpotts and Ague 2009, Cawood et al. 2018).

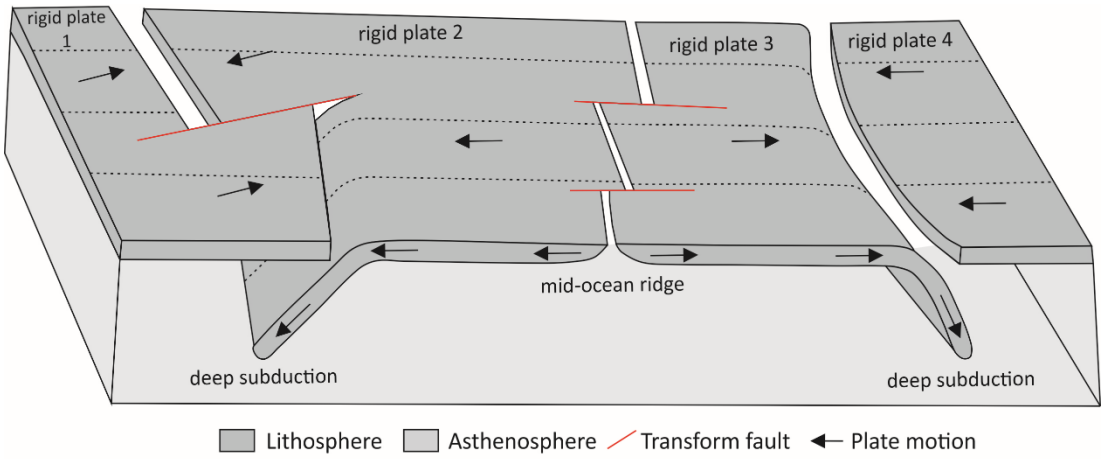

Figure 1.1: *Block diagram detailing the principle features of modern-style plate tectonics (redrawn after: Isacks et al. 1968, Kearey et al. 2009). Note: for simplicity, oceanic and continental crust are not distinguished.*

The physical manifestations of plate tectonics on the modern Earth (e.g., mid-ocean ridges, magmatic arcs, subduction zones, mountain ranges, and back-arc basins) are relatively well-constrained (e.g., Saunders and Tarney 1991, Condie 1993, Kearey et al. 2009, Searle 2013, Ducea et al. 2015), but the nature and timing of its onset remains enigmatic, with the geodynamic regime(s) that operated during the Archaean – which spans > 1.5 billion years – hotly debated (see Section 1.1; see Cawood et al. 2018 and references therein). The absence of a consistent geodynamic framework within which regional-scale observations can be placed has implications for interpreting Archaean assemblages and associated mineral

deposits. This is particularly pertinent when considering that Archaean crust is richly endowed in some types of mineral deposit (e.g., hosting > 25 % of Au resources globally) despite occupying < 6 % of the current continental crust volume (Cawood and Hawkesworth 2015). A greater understanding of the geodynamic regime(s) that operated during the Archaean would therefore provide a vital framework within which rocks and mineral deposits of this age may be interpreted.

This chapter first explores the Archaean geodynamics debate according to the previously published literature (Section 1.1), before outlining the scope (Section 1.2), research aims (Section 1.2) and structure (Section 1.3) of this thesis.

1.1 Archaean geodynamic regimes

The Archaean geodynamics debate is primarily articulated around when and how plate tectonics began on Earth, with age predictions for its onset (Fig. 1.2) ranging from the Hadaean/early Archaean (Hopkins et al. 2008, 2010, Arndt 2013, Turner et al. 2014, Hastie et al. 2016, Keller and Schoene 2018) to Neoproterozoic (Hamilton 1998, 2003, McCall 2003, Stern 2005, 2008, Hamilton 2011). For simplicity, the range of Archaean geodynamic models are here subdivided into the following broad groups, based on the predicted age for the onset of plate tectonics:

1. Hadaean to Palaeoarchaean (> 3.6 Ga) onset for plate tectonics, whereby (almost) all Archaean rocks are the product of plate tectonic processes (see: De Wit et al. 1987, 1992, De Wit 1998, Komiya et al. 1999, Nutman et al. 2002, Friend et al. 2002, Furnes et al. 2007a, Dilek and Polat 2008, Hopkins et al. 2008, Shirey et al. 2008, Furnes et al. 2009, Hopkins et al. 2010, Hastie et al. 2010, Friend et al. 2010, Korenaga 2013, Arndt 2013, Nutman et al. 2013, Turner et al. 2014, Hastie et al. 2016, Keller and Schoene 2018, Khanna et al. 2018).
2. Palaeoarchaean to early Palaeoproterozoic (3.6–2.2 Ga) onset of plate tectonics, whereby a pre-plate tectonic regime dominated before ca. 3.2 Ga, and after which a transition (over several hundred million years) into plate tectonics occurred (see: Smithies et al. 2003, Van Kranendonk et al. 2004, Brown 2006, Cawood et al. 2006, Van Kranendonk et al. 2007, Condie and Kröner 2008, Brown 2008, Bédard et al. 2013, Bédard 2013, Debaille et al. 2013, Van Kranendonk et al. 2014, Kamber 2015, Reimink et al. 2016, Smart et al. 2016, Johnson et al. 2017, Brown and Johnson 2018, Cawood et al. 2018, Halla 2018, Bédard 2018, Smithies et al. 2018, Moyen and Laurent 2018, Dhuime et al. 2018, Saji et al. 2018).

3. Neoproterozoic (1.0–0.7 Ga) onset for plate tectonics, whereby a pre-tectonic regime predominated during the entire Archaean Eon and much of the Proterozoic (see: Hamilton 1998, 2003, McCall 2003, Stern 2005, Hamilton 2007, Stern 2008, Hamilton 2011).

The succeeding sections summarise the evidence cited in favour of each broad hypothesis, with the main points of contention highlighted where necessary. Although not exhaustive, these sections aim to highlight the range of proposed models, alongside the variety of supporting evidence. Moreover, it should be noted that this discussion is complicated significantly by individual authors' definition of plate tectonics. While some authors define plate tectonics exactly as the modern-style outlined in Figure 1.1, others use the term move loosely. This is reflected in the succeeding sections, which attempt to capture some of this ambiguity.

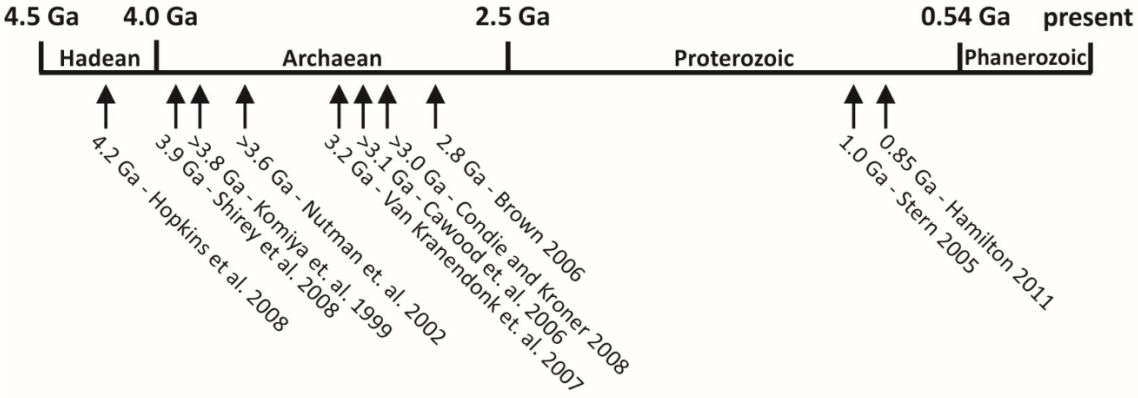

Figure 1.2: *Geological timescale detailing the range of suggested timings for the onset of plate tectonics, as suggested in a small subset of papers from the peer-reviewed literature (redrawn after: Korenaga 2013, Stern 2016).*

1.1.1 Hadaean to Eoarchaean (> 3.6 Ga) onset of plate tectonics

Many authors maintain that plate tectonics (broadly as outlined in the introduction to this chapter; Fig. 1.1) has operated since ~4 Ga, with the rocks and structures preserved in Archaean Cratons formed by processes akin to those observed on the modern Earth. Arndt (2013) argues that Archaean granitoids formed in subduction zones (like those produced today), with alternative mechanisms for generating voluminous granitic melt implausible as these scenarios lack the necessary H_2O. This is supported by high *P-T* experiments conducted by Hastie et al. (2016), who demonstrate that partial melting of Eoarchaean oceanic crust (and mixing with slab-derived fluids) is capable of generating melts that have compositions comparable to Eoarchaean continental crust. The average composition of continental basalts is also used to support a plate tectonic geodynamic regime for the Archaean Earth, with the

near-continuous trajectory of geochemical trends interpreted as the product of a single geodynamic regime throughout Earth history (Keller and Schoene 2018).

In addition to the geochemical evidence, Turner et al. (2014) present a lithostratigraphic succession from the 4.4–3.8 Ga Nuvvuagittuq Greenstone Belt (Canada) that is geochemically and stratigraphically comparable to the Palaeogene Izu-Bonin-Mariana forearc (Fig. 1.3). These authors argue that the similarity between these successions indicates that modern-style subduction (and therefore plate tectonics) operated throughout the Archaean (Turner et al. 2014). However, it is important to note that plate tectonics is not defined by subduction, with isolated subduction possible in other geodynamic regimes, as suggested on Venus (Pronin and Stofan 1990, Stofan et al. 1991, Fowler 1996, Piskorz et al. 2014, Davaille et al. 2017). Moreover, Pearce (2014) urged caution, stating that Turner et al. (2014) "may not yet have definitively fingerprinted the Earth's oldest rocks", but accepted that a subduction origin for the Nuvvuagittuq Greenstone Belt is a strong possibility.

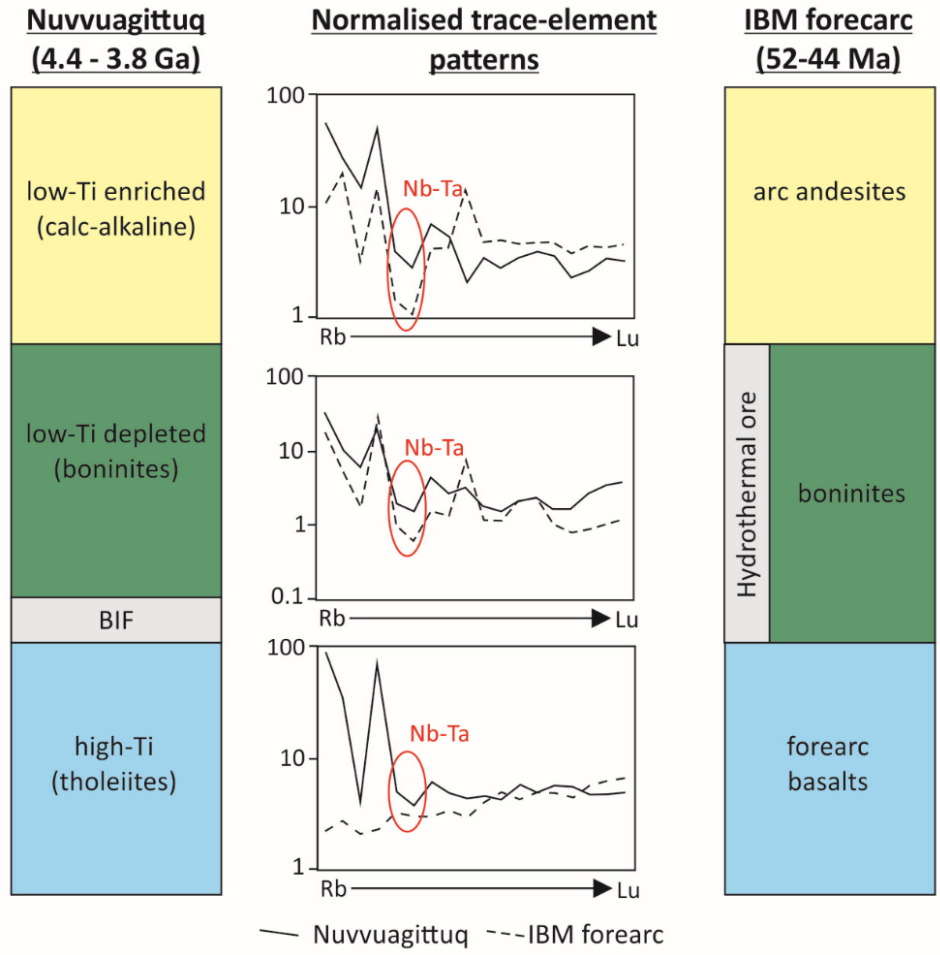

Figure 1.3: *Lithostraigraphic columns for the 4.4–3.8 Ga Nuvvuagittuq supracrustal belt (O'Neil et al. 2011) and 0.044-0.052 Ga Izu-Bonin-Mariana (IBM) arc (Reagan et al. 2010), with accompanying normalised trace element plots (redrawn after: Turner et al. 2014). Nb-Ta anomalies are highlighted.*

The most controversial evidence cited in favour of a modern-style plate tectonic regime having operated throughout the Archaean is the proposed existence of Archaean ophiolites (e.g., Harper 1986, De Wit et al. 1987, Hart et al. 1990, Kusky et al. 2001, Furnes et al. 2007a, Kusky and Li 2008, Dilek and Polat 2008, Furnes et al. 2009, Kusky 2012, Grosch and Slama 2017). As summarised in Table 1.1, the proposed examples of Archaean ophiolites range from 3.8 to 2.5 Ga, cover areas of between 18 and 350 km^2, and comprise a variety of ultramafic to felsic and metasedimentary lithologies that have generally been metamorphosed to amphibolite and/or granulite-facies. Interpretations of ancient ophiolites are generally based upon a lithological assemblage that is comparable to Phanerozoic ophiolites (albeit fragmented and incomplete; Furnes et al. 2009), and occasionally trace element geochemistry (e.g., HFSE anomalies for suprasubduction zone ophiolites; Yellappa et al. 2012). However, these interpretations are hotly disputed by a number of authors (e.g., Stern 2005, Hamilton 2007, 2011, Bédard et al. 2013, Kamber 2015). Moreover, there are no confirmed occurrences of residual mantle rocks, with none of those proposed withstanding detailed geochemical and petrographic investigation (Szilas et al. 2015, 2018).

1.1.2 Palaeoarchaean to early Palaeoproterozoic (3.6–2.2 Ga) onset of plate tectonics

In opposition to the broad hypothesis outlined in Section 1.1.1, several authors argue that the lithological assemblages, metamorphic imprints, structures and geochemical signatures recorded by Archaean cratons are inconsistent with a plate tectonic geodynamic regime having operated during the majority of the Archaean Eon (Bleeker 2002, Bédard et al. 2003, Van Kranendonk et al. 2004, Bédard et al. 2013, Van Kranendonk et al. 2014, Kamber 2015, Johnson et al. 2017, Bédard 2018). For example, in a regional study of the 3.45 Ga East Pilbara granite-greenstone terrane, Van Kranendonk et al. (2004) stated that there are a series of problems with horizontal tectonic models, including: the lack of evidence for large-scale tectonic duplications; the inferred directions of maximum compression, which vary with the orientation of individual greenstone belts; the contact-style of metamorphism; and the absence of high-*P* rocks. Instead, secular changes displayed by various geological and geochemical proxies are interpreted as evidence of a significant evolution in the Earth's geodynamic regime between 3.2 and 2.2 Ga (e.g., Cawood et al. 2018 and references therein; Fig. 1.4). In this scenario, the Earth transitioned from a non-plate tectonic mode (e.g., stagnant-lid or squishy-lid tectonics; Van Kranendonk et al. 2004, Bédard et al. 2013, Debaille et al. 2013, Rozel et al. 2017, Bédard 2018) to a modern-style plate tectonic geodynamic regime over a period of several hundred million years (Abbott et al. 1994, Condie and O'Neill 2010, Tang et al. 2016, Johnson et al. 2017, Condie 2018, Cawood et al. 2018).

Table 1.1: *Summary of proposed Archaean ophiolites from the North Atlantic, North China and Dharwar Cratons. Abbreviations: SSZ=suprasubduction zone.*

Name	Age (Ga)	Size (km^2)	Lithological assemblage	Metamorphic grade	Interpret-ation	Key evidence cited	Key references
North Atlantic Craton - Greenland							
Ivissartoq-Ujarassuit	3.08	~22	Pillow lava, volcanic breccia, picritic clinopyroxene cumulate, gabbro-diorite dyke, serpentinite, actinolite schist, anorthosite/leucogabbro, calc-silicate rocks, felsic schists	Amphibolite-facies	SSZ ophiolite	• Lithological assemblage similar to Phanerozoic (forearc) ophiolites • Trace element characteristics of the least altered samples, including negative HFSE anomalies and LILE enrichment	(Polat et al. 2008, Ordóñez-calderón et al. 2009)
Tartoq	3.19	~50	Pillow lava, gabbro, serpentinite, talc-schist, greenschist, amphibolite	Greenschist- to granulite-facies	SSZ ophiolite	• Trace element characteristics , including similarity to Phanerozoic arc-related rocks and negative HFSE anomalies. • Lithological assemblage comparable to oceanic crust • Structural studies suggesting that Tartoq was accreted in a convergent margin	(Kisters and Szilas 2012, Szilas et al. 2013, 2014)
Isua	3.80 - 3.70	87	Metabasalt, metagabbro, ultramafic rocks.	Amphibolite-facies	SSZ ophiolite	• It "contains all the major lithological units of a typical Penrose type complete ophiolite sequence" (Furnes et al. 2009). • O isotopes and petrographic features consistent with sea-floor hydrothermal alteration.	(Furnes et al. 2007a, 2007b, Friend and Nutman 2010, Hoffmann et al. 2010)
North China Craton							
Dongwanzi-Zunhua	2.51	~350	Banded Iron Formation, pillow lava, picritic amphibolites, gabbro, pyroxenite, cumulate ultramafic rocks (serpentinised dunite, pryoxenite, wehrlite and harzburgite), podiform chromitite	Amphibolite-facies	SSZ ophiolite	• Lithological assemblage comparable to Phanerozoic ophiolites. • Geochemistry of chromitites.	(Kusky et al. 2001, 2007, Zhao et al. 2007, 2008, Kusky and Jianghai 2010)
Dharwar Craton							
Devanur	2.53	80	Websterite, gabbro, mafic dykes, amphibolite, trondhjemite and pegmatite	Granulite-facies	SSZ ophiolite	• Trace element geochemistry, including negative HFSE anomalies and associated LILE enrichment.	(Yellappa et al. 2012)

For example, Cawood et al. (2018) interpreted the appearance of passive margins at ~2.75 Ga as evidence for this transition (Fig. 1.5a). Similarly, Brown and Johnson (2018) use plots of *dT, dP* and *dT/dP* versus age to demonstrate this secular variation, with metamorphic rocks subdivided into 3 natural groups based on *dT/dP* (thermal gradient) values (Fig. 1.5b). These authors interpret the appearance of paired metamorphic belts in the Neoarchaean (2.8–2.5 Ga) as the product of a form of plate tectonics during the Era (Fig. 1.5b). Similarly, studies of bulk-rock geochemical data from Archaean granitoid rocks globally have highlighted significant changes between 3.2 and 2.5 Ga (Halla 2018, Johnson et al. 2019), as shown by various element ratios (e.g., K_2O, Na_2O, Sr/Y and Rb Sr). Broader geochemical studies (e.g., Smithies et al. 2018, Moyen and Laurent 2018) also support a secular geochemical evolution, with Condie (2018) suggesting that the increasing proportion of basalts with "arc-like" geochemical signatures is evidence for a transitional geodynamic regime between 3.0 and 2.2 Ga. Furthermore, Dhuime et al. (2015) noted a marked increase in the Rb/Sr ratios of juvenile continental crust at ~3.0 Ga (Fig. 1.5c), with these authors interpreting this inflection as representing the generation of relatively thick and Si-rich crust as a result of the onset of plate tectonics.

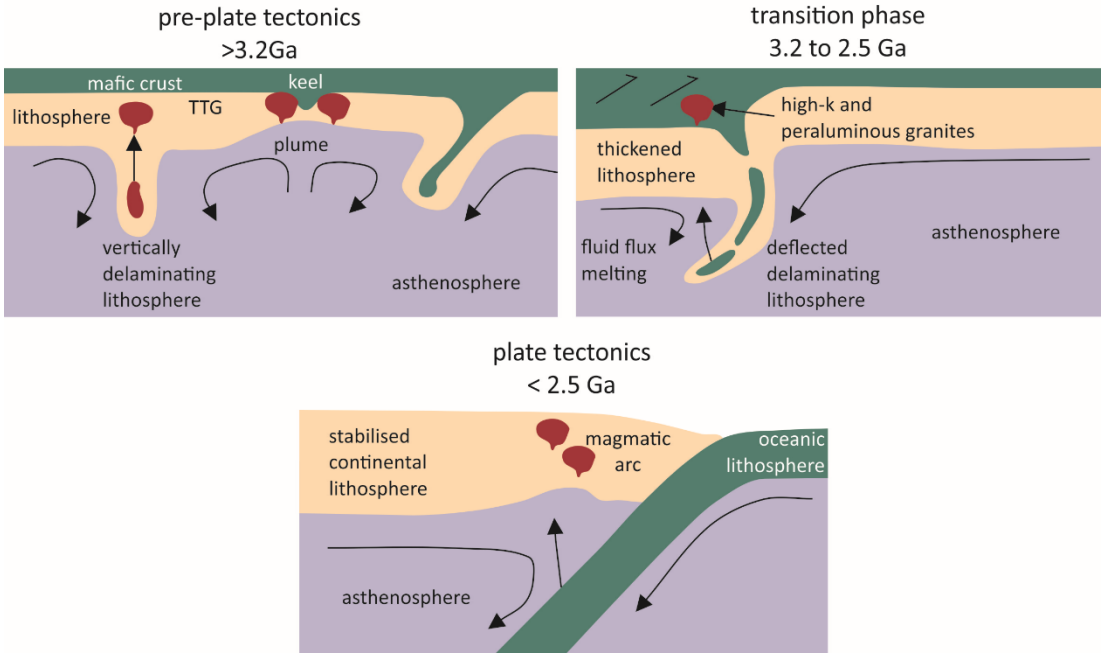

Figure 1.4: *Schematic model detailing the proposed temporal evolution of the Earth. Redrawn after: Cawood et al. (2018).*

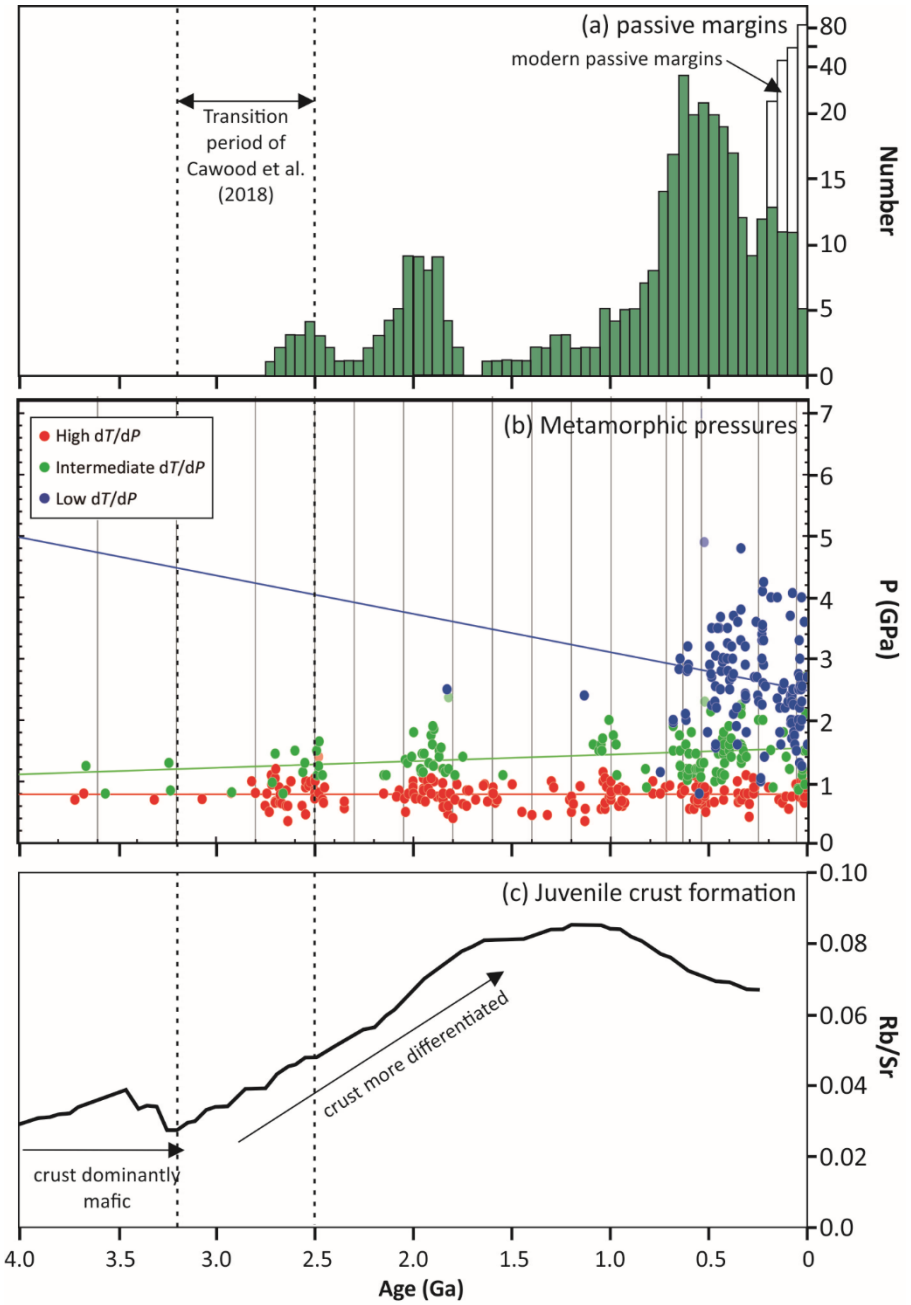

Figure 1.5: *Selected plots detailing the secular evolution of the Earth.* ***(a)*** *Histogram showing the age of ancient (green) and modern (white) passive margins (redrawn after: Bradley 2008, Cawood et al. 2018).* ***(b)*** *Summary of the metamorphic pressures of 456 localities (adapted after: Brown and Johnson 2018). The solid lines indicate linear regressions of the data by type, as defined by Brown and Johnson, 2018.* ***(c)*** *Variation of Rb/Sr ratios in juvenile crust as function of formation age (redrawn after: Dhuime et al. 2015).*

1.1.3 Neoproterozoic (1.0–0.7 Ga) onset of plate tectonics

Championed by a relatively small number of authors (Hamilton 1998, McCall 2003, Hamilton 2003, 2007, Stern 2008, Hamilton 2011), a Neoproterozoic onset for modern-style plate tectonics is a hypothesis based on the assertion that Archaean, Palaeoproterozoic and Mesoproterozoic rocks and structures differ greatly from both each other and Phanerozoic

rocks (Hamilton 2011). In such models, all tonalite-trondhjemite-granodiorite (TTG) – a dominant component of Archaean terranes globally – are considered to be the product of partial melting of a mafic proto-crust, with modern-style tectonics not commencing until 1.0–0.85 Ga (Stern 2005, Hamilton 2011). These authors also maintain that there are no preserved ophiolites older than 1.0 Ga (Stern 2005, Hamilton 2007, 2011), with the possible exception of a 2.0–1.9 Ga example in Finland (Jormua; Kontinen 1987, Peltonen et al. 1996). Moreover, an absence of blueschist-facies and ultra-high pressure metamorphic rocks in the geological record prior to the Neoproterozic is considered to support this hypothesis (Stern 2005). However, it should be noted that many authors dispute these assertions, with Van Kranendonk and Cassidy (2004) stating that Hamilton (2003) "ignores a wealth of compelling multidisciplinary geological evidence in support of [Neo-]Archaean plate tectonics".

1.2 Scope and research aims

To engage with the Archaean geodynamics debate outlined above, this thesis focuses on ultramafic-mafic complexes in the Lewisian Gneiss Complex (of the North Atlantic Craton; NAC) and Johannesburg Dome (of the Kaapvaal Craton; Fig. 1.6). Globally, such complexes are volumetrically minor components of Archaean cratons, with individual occurrences generally occupying less than 100 km^2 (Table 1.2). Despite their size, the range of lithologies present in ultramafic-mafic complexes may be diverse. For example, in the Greenlandic portion of the NAC, the Seqi Complex is interpreted to contain only intrusive ultramafic rocks (Szilas et al. 2018), while the Fiskenæsset Complex is suggested to comprise a variety of intrusive and extrusive ultramafic-mafic rocks (Polat et al. 2009). This range of lithologies is often further complicated by serpentinisation, alteration and/or polyphase, greenschist- to granulite-facies metamorphism (Table 1.2).

Notwithstanding these complexities, studies of ultramafic-mafic complexes have provided important and often contentious contributions to the Archaean geodynamics debate (as outlined in Table 1.2), with individual occurrences attributed to wide-ranging geological and geodynamic environments, including: Archaean ophiolites/fragments of ophiolites that may represent Archaean suture zone(s) (see Section 1.1.1; Table 1.1); layered intrusions associated with a range of potential geodynamic environments (Hoatson and Sun 2002, Ivanic et al. 2010, Wang et al. 2015, Bagas et al. 2016, Ivanic et al. 2017); subduction-related sills emplaced into oceanic crust (Polat et al. 2009); fragments of arc-related oceanic crust (Szilas et al. 2014); the sagducted remnants of greenstone belts (Johnson et al. 2016); and mantle residues following high degrees of partial melting (Szilas et al. 2018). Some interpretations (e.g., the Archaean ophiolite hypothesis) are suggestive of modern-style plate

tectonic regimes, while others (e.g., the sagudction hypothesis) are compatible with alternative (e.g., stagnant-lid) geodynamic regimes for the Archaean Earth.

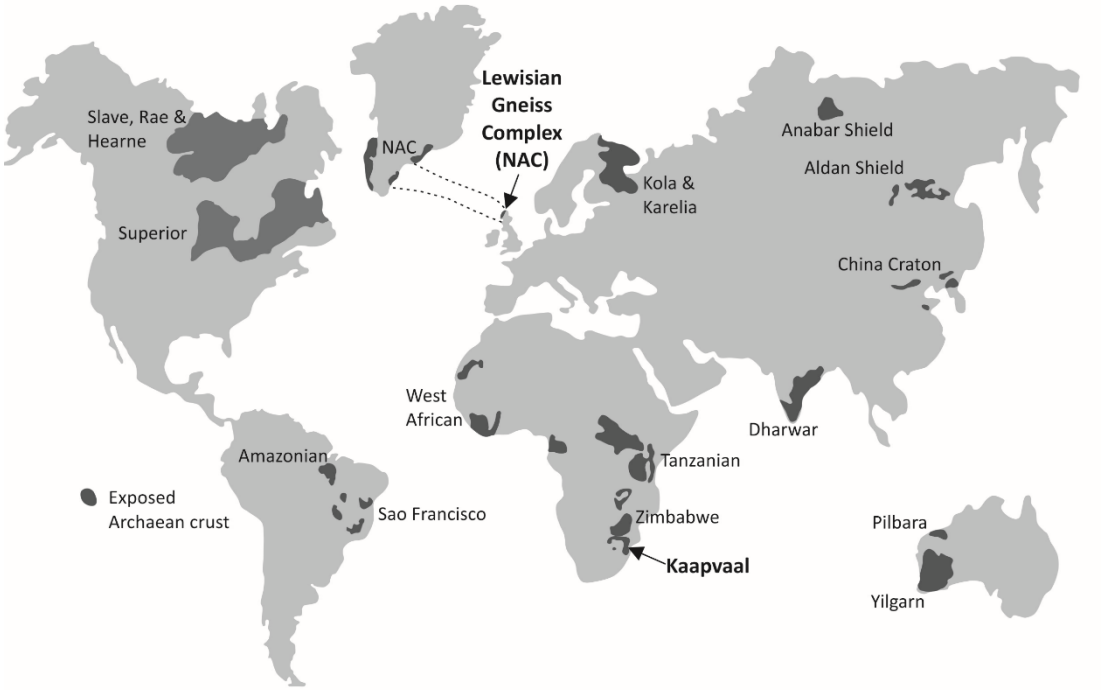

Figure 1.6: *Simplified world map detailing the location of exposed Archaean crust, including the location of the North Atlantic (NAC) and Kaapvaal Cratons (redrawn after: Bédard 2013, Anhaeusser 2014).*

The research presented in this thesis combines thorough field investigations (e.g., mapping, logging and structural assessment) with detailed petrography, bulk-rock geochemistry (lithophile elements and platinum-group elements (PGE)), major element mineral chemistry and trace element mineral chemistry. Further to several location-specific objectives, which are detailed in the appropriate sections of the thesis, this research project engages with the broad Archaean geodynamics debate by aiming to:

a) Critically evaluate geochemical proxies that may be used to interpret ultramafic rocks in Archaean cratons.
b) Investigate the origin of the ultramafic-mafic complexes in the North Atlantic and Kaapvaal Cratons.
c) Assess the implications for Archaean geodynamic regimes.
d) Evaluate the possibility that ultramafic-mafic complexes represent a primary source of placer PGM.

Table 1.2: *Summary of the basic characteristics of selected Archaean ultramafic-mafic complexes in the North Atlantic, Kaapvaal, Yilgarn and North China Cratons.*

Ultramafic-mafic complex	Age (Ga)	Size (km^2)	Lithological assemblage	Age relationship with host rocks	Metamorphic grade	Interpretation(s)	Key references
North Atlantic Craton – Greenland							
Thrym	2.85-2.75	> 70	Mafic and intrusive ultramafic	Invaded by orthogneiss	Granulite-facies	Ultramafic intrusions into a pre-existing mafic crust	(Kolb et al. 2013, Bagas et al. 2016)
Fiskenæsset	2.97	~100	Intrusive and extrusive mafic and ultramafic	Invaded by orthogneiss	Amphibolite- to granulite-facies	Arc-related sills emplaced into oceanic crust comprising basalt & gabbro	(Myers 1985, Polat et al. 2009)
Seqi	> 2.97	< 0.5	Intrusive ultramafic	Invaded by orthogneiss	Granulite-facies	Mantle residues following high degrees of partial melting	(Szilas et al. 2018)
Tartoq	3.19	50	Intrusive ultramafic	Invaded by orthogneiss	Greenschist- to granulite-facies	Remnants of oceanic crust that formed in a suprasubduction zone setting	(Szilas et al. 2013, 2014)
Akilia	?	< 0.5	Ultramafic-mafic rocks	Unknown: surrounded by orthogneiss	Granulite-facies	?	(Whitehouse and Fedo 2003)
Kaapvaal Craton							
Stolzburg	> 3.25	~15	Intrusive ultramafic-mafic rocks	Debated: intrusive into schist belt or tectonically juxtaposed?	Amphibolite-facies	Layered intrusion; accreted oceanic crust	(De Wit et al. 1987, Anhaeusser 2001)
Koedoe	3.5-3.2	~15	Intrusive ultramafic	Intruded Barberton greenstone belt	Greenschist-facies	Layered intrusion; accreted oceanic crust	(Anhaeusser 2006a)
Zandspruit	> 3.11	0.5	Intrusive ultramafic-mafic and greenstone	Invaded by TTG	Amphibolite-facies	Layered intrusion emplaced into a greenstone remnant; accreted oceanic crust	(Anhaeusser 1992, 2015)
Yilgarn Craton							
Windimurra	2.7-2.8	2500	Intrusive	Intrusion into greenstone belt	Greenschist-facies	Plume-related layered Intrusion	(Ivanic et al. 2010, 2017)
Munni Munni	2.93	> 100	Intrusive ultramafic-mafic	Intruded granite-supracrustal sequence contact	Greenschist-facies	Layered intrusion; magmatism generated by melting oceanic crust	(Hoatson and Sun 2002)
North China Craton							
Yinshan	2.6	10	Intrusive ultramafic - mafic rocks	Invaded by TTG	Amphibolite- to granulite-facies	Subduction-related, multi-phase intrusion	(Wang et al. 2015)

1.3 Thesis structure

The work presented in this thesis is subdivided into two parts, with Part 1 (Chapters 2–5) focusing on the ultramafic-mafic complexes in the Lewisian Gneiss Complex (LGC) and Part 2 (Chapters 6–9) centring on the ultramafic-mafic complexes in the Johannesburg Dome. Details of the employed analytical instrumentation and methodology are included in Appendix A, with information specific to individual chapters provided at the appropriate points in the thesis.

In Part 1, Chapter 2 reviews literature specific to the LGC, including a summary of the hypotheses previously proposed for the origin of the ultramafic-mafic complexes. Chapters 3–5, which comprise results chapters that combine multiple field-based and analytical techniques, are self-contained and can be read in isolation, with each chapter containing introduction and discussion sections that investigate specific research questions relevant to both the regional-scale objectives and broad aims of this thesis (Section 1.2). Chapter 3 (adapted from Guice et al. 2018a) utilises field mapping, petrography and spinel mineral chemistry to evaluate ambiguous age relationships in the mainland LGC, with the origin of the ultramafic-mafic complexes critically dependent upon such age relationships. Chapter 4 (adapted from Guice et al. 2018b) expands on the work presented in Chapter 3, employing detailed petrography, bulk-rock geochemistry and mineral chemistry to assess the validity of HFSE anomalies as a proxy for Archaean subduction. Chapter 5 combines field observations, petrography, bulk-rock geochemistry and spinel mineral chemistry to evaluate a series of research questions specific to the origin of the ultramafic-mafic complexes in the LGC.

The style of Part 2 is different to that of part 1, with individual chapters following on from one another, rather than being self-contained. Chapter 6 reviews literature specific to the Kaapvaal Craton, including a summary of the hypotheses previously proposed for the origin of its ultramafic-mafic complexes. Chapter 7 details field relationships, petrography and spinel mineral chemistry for three ultramafic-mafic complexes in the Johannesburg Dome, with Chapter 8 presenting the accompanying bulk-rock geochemistry for the three complexes. Chapter 9 discusses the implications for the origin of the ultramafic-mafic complexes in the Johannesburg Dome, establishes the specific petrogenetic environments represented by the individual complexes, and provides an assessment of element mobility. It should be noted that in Chapters 7-9, information pertaining to the Modderfontein Complex is adapted from (Guice et al. 2019). Chapter 10 – entitled “Synthesis” – addresses the research aims outlined in Section 1.2 by combining the findings presented in both parts of this thesis.

Part One:

The Lewisian Gneiss Complex

Chapter 2

Literature Review: The Lewisian Gneiss Complex

The LGC is a small, but intensely studied, fragment of the NAC that forms the basement to northern Scotland, northwest of the Great Glen Fault (Fig. 2.1; Bamford et al. 1978, Barton 1992). Exposed on the Outer Hebrides and NW Scottish mainland, the LGC is dominated by amphibolite- to granulite-facies TTG gneisses that represent metamorphosed felsic magmatic rocks (Peach et al. 1907, Sutton and Watson 1951, Park 1970, Wheeler et al. 2010, Mason 2016). These Mesoarchaean to Neoarchaean TTG gneisses, which occur in association with volumetrically subordinate ultramafic, mafic and metasedimentary lithologies, record a protracted and complex history of magmatism, metamorphism and deformation. In addition to polyphase, amphibolite- to granulite-facies metamorphism, the TTG gneiss and associated lithologies are cross-cut in places by Palaeoproterozoic mafic dykes and later granitic-pegmatitic sheets (e.g., Peach et al. 1907; Corfu 1998; Park et al. 2002; Wheeler et al. 2010; Crowley et al. 2015). This chapter focuses on the LGC of the NW Scottish mainland and summarises its geological evolution according to the previously published literature.

2.1 Stratigraphic subdivision of the mainland LGC

On the NW Scottish mainland, the LGC crops out as a 125 km long, 20 km wide coastal strip west of the Moine Thrust that is partially covered by Neoproterozoic sedimentary successions (Fig. 2.1; Peach et al. 1907; Sutton and Watson 1951; Wheeler et al. 2010). The mainland LGC has traditionally been subdivided into a granulite-facies Central Region bound by amphibolite-facies Northern and Southern Regions (Fig. 2.1; Peach et al. 1907; Sutton and Watson 1951; Park and Tarney 1987). Relative to the hornblende-bearing gneisses of the Northern and Southern Regions, the pyroxene-bearing gneisses of the Central Region are depleted in Cs, Rb, U, Th, K and Ta (Sheraton et al. 1973; Fig. 2.2). Thus, the Central Region has been interpreted as representing deeper crustal levels than the amphibolite-facies Northern and Southern Regions, with the mainland LGC collectively representing a faulted but once continuous crustal block (Park and Tarney 1987).

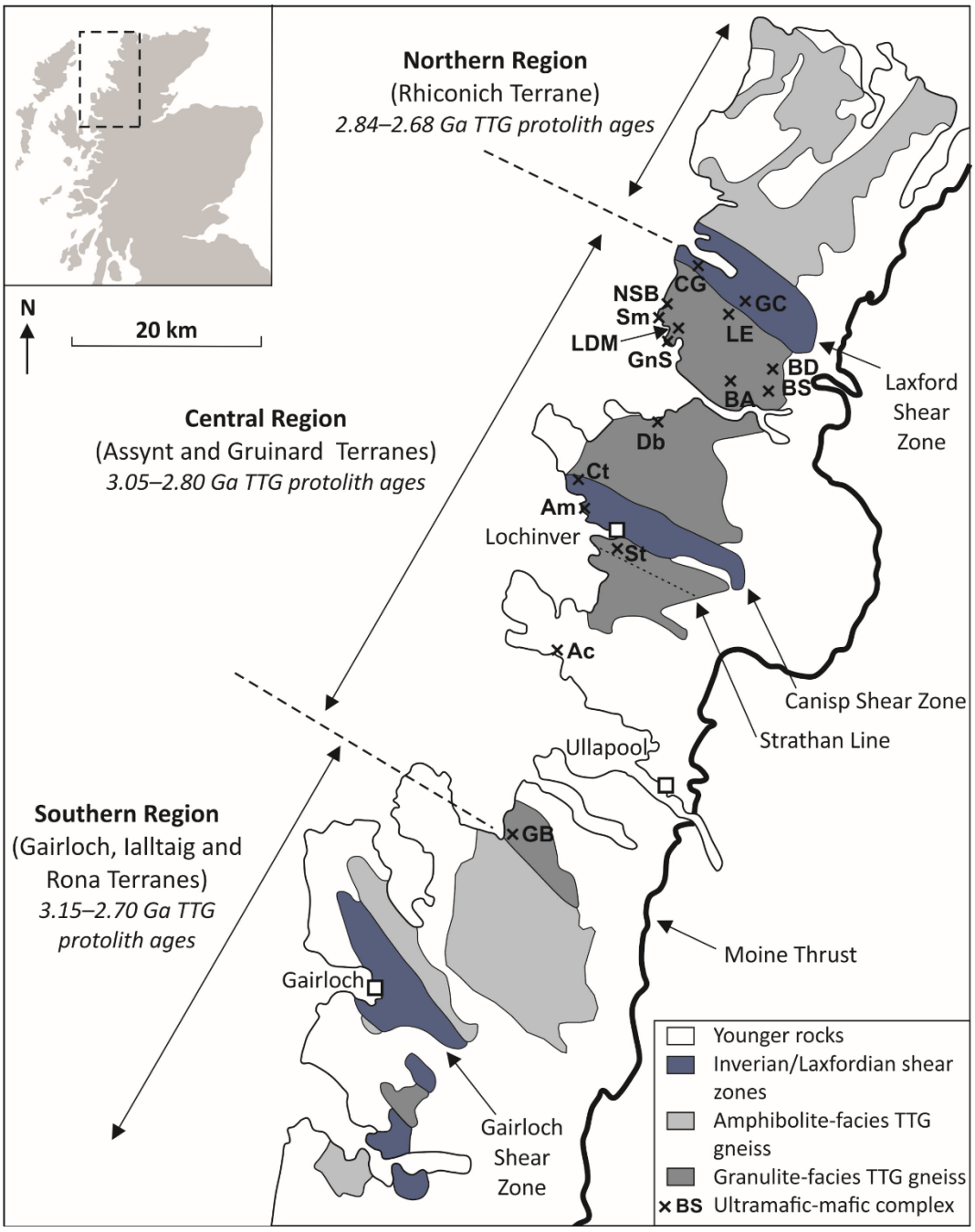

Figure 2.1: *Simplified geological map of the mainland LGC, detailing the traditional stratigraphic subdivision (Sutton and Watson 1951, Park and Tarney 1987), the terrane-model subdivision (Kinny et al. 2005, Love et al. 2010), and location of selected ultramafic-mafic complexes. Redrawn after: Wheeler et al. (2010) and Goodenough et al. (2010). Abbreviations: Ac=Achiltibuie; Am=Achmelvich; BA=Ben Auskaird; BD=Ben Dreavie; BS=Ben Strome; CG=Chnoc Gorm; Ct=Clachtoll; Db=Drumbeg; GB=Gruinard Bay; GC=Gorm Chnoc; GnS=Geodh' nan Sgadan; LDM=Loch an Daimh Mor; LE=Loch Eilean na Craoibhe Moire; NSB=North Scourie Bay; Sm=Scouriemore; St=Strathan.*

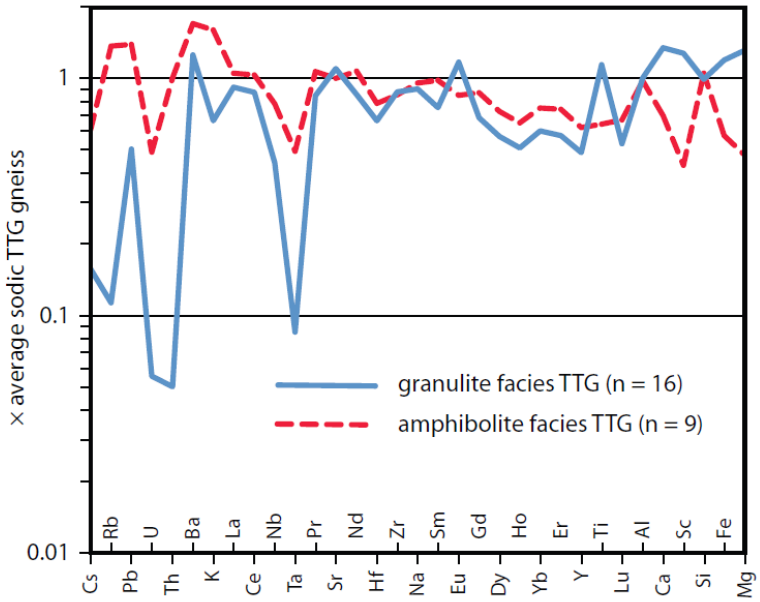

Figure 2.2: *Bulk-rock composition of the granulite-facies (Central Region) and amphibolite-facies (Northern and Southern Regions) TTG gneiss from the LGC, normalised to those of sodic Archaean TTGs globally (Moyen 2011). After: Johnson et al. (2013).*

More recently, geochronological-based studies, which utilise U-Pb dating of zircon in TTG gneiss, have shown that the mainland LGC records a wide range of protolith ages and metamorphic histories (Kinny and Friend 1997, Friend and Kinny 2001, Love et al. 2004, Kinny et al. 2005, Love et al. 2010). On this basis, the LGC has been subdivided into 6 terranes, named (from north to south): Rhiconich, Assynt, Gruinard, Gairloch, Ialltaig and Rona (Fig. 2.1; Kinny and Friend 1997; Friend and Kinny 2001; Love et al. 2004; Kinny et al. 2005; Love et al. 2010). The Rhiconich Terrane correlates directly with the Northern Region of the traditional subdivision, the Central Region is subdivided into the Assynt (north of the Strathan Line) and Gruinard Terranes (south of the Strathan Line), and the Southern Region is subdivided into Gairloch, Ialltaig and Rona Terranes (Fig. 2.1; Kinny et al. 2005 and references therein). This model has led to the suggestion that the mainland LGC comprises a series of disparate crustal blocks that record unique histories prior to their juxtaposition during the Proterozoic (Kinny and Friend 1997, Friend and Kinny 2001, Love et al. 2004, Kinny et al. 2005, Love et al. 2010). However, it is disputed by several authors (e.g., Park 2005, Feisel et al. 2018), with the variable protolith ages plausibly a function of multiple episodes of igneous activity in a single crustal block, rather than disparate blocks (Rollinson 2012). Moreover, phase equilibria modelling demonstrates that the Assynt and Gruinard terranes **both** record peak metamorphic conditions of 0.8–1.2 GPa and 900–1000°C (Feisel et al. 2018), contradicting the interpretation that they represent different terranes. Although the specific number of terranes remains controversial (e.g., Park 2005; Feisel et al. 2018), the Laxford

Shear Zone, which is a ductile shear zone that separates the Northern and Central Regions (or Assynt and Rhiconich Terranes; Fig. 2.1), is generally accepted as representing a major crustal boundary (Goodenough et al. 2010, 2013). For simplicity, this thesis utilises the traditional (Northern, Central and Southern Regions) subdivision of Park and Tarney (1987).

2.2 Chronology, stratigraphy and metamorphism

Although many aspects of the LGC's evolution remain controversial (Fig. 2.3; Wheeler et al. 2010 and references therein), the following broad stratigraphic and metamorphic history is generally accepted:

(i) Crystallisation of TTG magmas between 3.1 and 2.7 Ga (Friend and Kinny 2001, Kinny et al. 2005, Love et al. 2010, Whitehouse and Kemp 2010, MacDonald et al. 2015).

(ii) Granulite-facies tectonothermal event between 2.8 and 2.7 Ga, known locally as the Badcallian (Evans and Lambert 1974, Cartwright et al. 1985, Corfu et al. 1994, Andersen et al. 1997, Corfu 1998, Barooah and Bowes 2009, Crowley et al. 2015).

(iii) Amphibolite- to granulite-facies tectonothermal event between 2.5 and 2.4 Ga, known locally as the Inverian (Beach 1973, 1974, Corfu et al. 1994, Whitehouse and Kemp 2010).

(iv) Emplacement of a suite of mafic-ultramafic dykes between 2.42 and 2.38 Ga, known locally as the Scourie Dykes (Heaman and Tarney 1989, Davies and Heaman 2014).

(v) Greenschist- to amphibolite-facies tectonothermal event(s) between 1.9 and 1.6 Ga, known locally as the Laxfordian (Beach et al. 1974, Beach 1974, Goodenough et al. 2010, 2013).

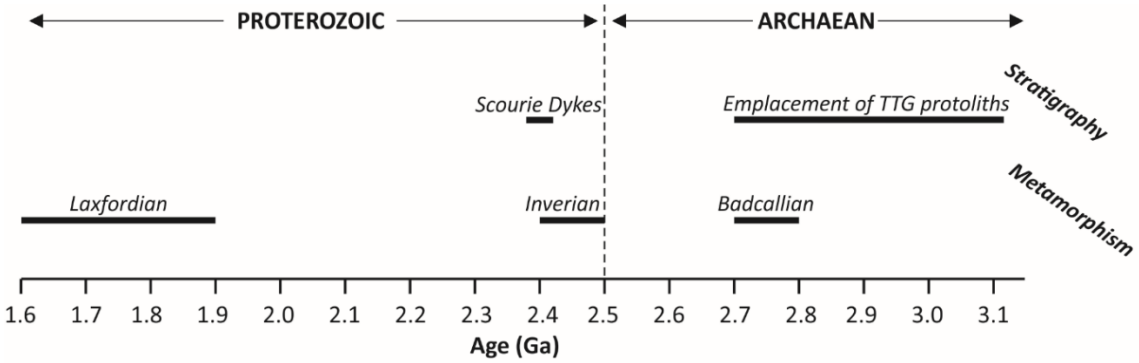

Figure 2.3: *Timeline detailing the established chronology of the mainland LGC. References as in text.*

2.2.1 TTG gneiss and associated rocks

The amphibolite-facies Northern Region predominantly comprises migmatitic, hornblende- and biotite-bearing granodiorite gneisses, with minor amphibolite inclusions and supracrustal rocks in places (Peach et al. 1907, Friend and Kinny 2001, Goodenough et al.

2010). Protolith ages generally range from 2.84 to 2.68 Ga, with rare inherited ages of ca. 3.5 to 3.0 Ga (Kinny and Friend 1997, Friend and Kinny 2001, Love et al. 2004, Kinny et al. 2005, Love et al. 2010). In this region, mafic enclaves rarely exceed 1 m in diameter and comprise less than 5 % of the exposure (Goodenough et al. 2010).

The granulite-facies Central Region predominantly comprises grey, pyroxene-bearing TTG gneisses, with volumetrically subordinate ultramafic, mafic and metasedimentary lithologies (O'Hara 1961, Bowes et al. 1964, 1966, Sills 1981, Cartwright et al. 1985, Park et al. 2002, Goodenough et al. 2010). Detailed descriptions of the ultramafic, mafic and metasedimentary lithologies, which together comprise ~10% of the outcrop in the Central Region and range from metre-scale pods to kilometre-scale complexes (O'Hara 1961, Bowes et al. 1964, Sills 1981, Sills et al. 1982, Johnson et al. 2016), can be found in Section 2.3. Protolith ages for the TTG gneiss, as determined using U-Pb geochronology, are ambiguous due to later granulite-facies metamorphism, with lattice distortion, Pb mobility and polyphase zircon growth contributing to a spread of data along Concordia between 3.1 and 2.5 Ga (Whitehouse and Kemp 2010, Zirkler et al. 2012, MacDonald et al. 2013, 2015). Despite this ambiguity, protolith ages for the Central Region TTG gneiss are generally interpreted as ranging from 3.05 to 2.80 Ga (Friend and Kinny 2001, Kinny et al. 2005, Love et al. 2010, Whitehouse and Kemp 2010, MacDonald et al. 2015).

The amphibolite-facies Southern Region predominantly comprises biotite-bearing granodiorite and trondhjemite gneisses (Rollinson 2012). Protolith ages for the TTG gneiss generally range from 3.15 to 2.70 Ga (Kinny et al. 2005, Love et al. 2010), with two separate magmatic events likely responsible for forming the felsic rocks in this region of the LGC (Rollinson 2012). In the Southern Region, mafic lithologies are rare, occurring as metre-scale pods (Park et al. 2002).

2.2.2 Badcallian metamorphic event

The granulite-facies Badcallian metamorphic event, for which peak *P-T* conditions have been estimated at 0.8–1.2 GPa and > 900° C (Barnicoat and O'Hara 1978, Barnicoat 1983, Corfu et al. 1994, Andersen et al. 1997, Zirkler et al. 2012, Feisel et al. 2018), is recorded only by the Central Region rocks (Fig. 2.1; Wheeler et al. 2010 and references therein). While some authors have suggested that this event occurred at ca. 2.49–2.48 Ga (Friend and Kinny 1995, Kinny and Friend 1997), it is generally accepted as occurring at ca. 2.76–2.71 Ga, with the 2.5 to 2.4 Ga dates attributed to the later Inverian metamorphic event (Cohen et al. 1991, Corfu 1998, Whitehouse and Kemp 2010, Crowley et al. 2015).

Away from later developed shear zones, the Badcallian metamorphic event is characterised by a pervasive, shallow- to moderate-dipping, centimetre-scale gneissosity that exhibits open to isoclinal folds (Goodenough et al. 2010). The granulite-facies mineral assemblage of plagioclase, clinopyroxene, orthopyroxene and quartz (in the TTG gneiss) is preserved in places, but retrogression is widespread (MacDonald et al. 2017). The aforementioned *P-T* conditions may have facilitated partial melting of felsic and some mafic lithologies throughout the Central Region (Johnson et al. 2012, 2013). Partial melting of mafic lithologies are believed to manifest as irregularly shaped patches and sheets of coarse-grained, plagioclase-rich leucosomes that may contain euhedral (peritetic) clinopyroxene, while partial melting of felsic lithologies manifest as quartz-rich leucosomes (Johnson et al. 2012, 2013).

2.2.3 Inverian metamorphic event

The Inverian metamorphic event, which is poorly constrained due to later reactivation during the Laxfordian metamorphic event, is defined as the retrogressive, amphibolite- to granulite-facies metamorphism and deformation that precedes Scourie Dyke emplacement (Evans 1965, Evans and Lambert 1974, Wheeler et al. 2010). This event, which occurred between 2.49 and 2.48 Ga (Cohen et al. 1991, Corfu et al. 1994, Corfu 1998, Whitehouse and Kemp 2010, Crowley et al. 2015), is confidently recognised in the Central Region (Corfu 1998, Park et al. 2002), with some attempts to correlate it with isolated features in the Southern Region (Park and Tarney 1987). Recent studies by Goodenough et al. (2010, 2013) have led to the suggestion that the Northern and Central Regions were accreted during the Inverian, with the Laxford Shear Zone (Fig. 2.1) representing a terrane boundary.

The Inverian metamorphic event manifests as locally-developed, steeply dipping, NW-SE to WNW-ESE-trending shear zones (Evans 1965, Evans and Lambert 1974), with the Canisp and Stoer shear zones representing kilometre-scale examples of Inverian ductile deformation (Attfield 1987, Goodenough et al. 2010). Pervasive retrogression of granulite-facies mineral assemblages (e.g., replacement of garnet by rims plagioclase in the mafic rocks) is a common relic of this metamorphic event throughout the Central Region (e.g., Johnson et al. 2012).

2.2.4 Scourie Dyke emplacement

First described by Teall (1885), the Palaeoproterozoic Scourie Dykes are most abundant in the Central Region, although several are also reported in the Northern and Southern Regions (Weaver and Tarney 1981, Heaman and Tarney 1989, Davies and Heaman 2014). Attempts to date the emplacement of these dykes have been numerous (Evans and Tarney 1964,

Chapman 1979, Heaman and Tarney 1989, Davies and Heaman 2014), with the majority of dykes intruding over a ~40 Ma period between 2.42 and 2.38 Ga (Davies and Heaman 2014). Individual dykes are steeply-dipping and up to 100 m wide, with the general NW-SE trend likely controlled by pre-existing shear zones (Weaver and Tarney 1981). The Scourie Dykes, which are part of a larger suite of Palaeoproterozoic dykes that extend throughout the Archaean portion of Labrador, Greenland and Baltica (Hughes et al. 2014, Nilsson and Hamilton 2016), are subdivided into four petrographic groups, namely: Mg-rich bronzite picrites; norites; olivine gabbros; and Fe-rich quartz dolerite (Tarney and Weaver 1987). Dykes in the northern and southern regions are altered to amphibolite (during the Laxfordian metamorphic event), while those in the Central Region are variably altered, with selected examples preserving igneous textures and minerals (Weaver and Tarney 1981).

2.2.5 Laxfordian metamorphic event

The Laxfordian metamorphic event, which occurred between 1.9 and 1.6 Ga, is recognised in all 3 regions of the mainland LGC, occurring after the proposed accretion of the Northern and Central Regions (Goodenough et al. 2010). It is commonly subdivided into an early phase (ca. 1.9–1.8 Ga) of amphibolite-facies metamorphism/deformation (D1/D2) and latter phase (ca. 1.75–1.65 Ga) of greenschist-facies metamorphism/deformation (D3/D4), with the latter associated with the emplacement of granites and pegmatites (Park et al. 2002, Goodenough et al. 2010). In the Northern Region, the granitic-pegmatitic sheets, which cross-cut the gneissose layering and were likely derived from partial melting of TTG gneiss, comprise up to 25 % of the total outcrop area and 50 % of the outcrop locally (Friend and Kinny 2001, Goodenough et al. 2010).

In the Central Region, the Laxfordian manifests as numerous discrete, broadly E-W-trending shear zones that are typically tens of metres wide (Goodenough et al. 2010, 2013). These shear zones, which increase in frequency towards the Laxford Shear Zone (Fig. 2.1), are marked by a steeply-dipping (50-70°) pervasive foliation, thinning of the gneissose layering and tight folding (Sutton and Watson 1951, Goodenough et al. 2010). It is generally considered that some of the larger shear zones in the Central Region (e.g., Canisp; Fig. 2.1) initially formed during the Inverian metamorphic event, before being reactivated during the Laxfordian (Attfield 1987, Goodenough et al. 2010).

In the Southern Region, Laxfordian structures exhibit greater complexity than elsewhere in the mainland LGC, with this complexity attributed to the presence of an intensely folded assemblage of supracrustal rocks known collectively as the Loch Maree Group (Wheeler et

al. 2010). Generally, however, the Southern Region displays a combination of low-strain lenses and anastomosing shear zones that decrease in frequency towards the southwest (Wheeler 2007, Wheeler et al. 2010).

2.3 Ultramafic-mafic complexes in the mainland LGC

Ultramafic-mafic complexes occur throughout the granulite-facies Central Region, ranging from centimetre-scale pods to kilometre-scale complexes (Peach et al. 1907, O'Hara 1961, Bowes et al. 1964, 1966, Davies 1974, Rollinson and Windley 1980, Sills 1981, Sills et al. 1982, Sills 1982, Rollinson 1987, Park et al. 2002, Rollinson and Gravestock 2012, Johnson et al. 2016). A group of large ultramafic-mafic complexes, which occur most commonly in the northern part of the Central Region and contain distinctly layered metapyroxenite and metaperidotite, cover areas up to 7 km^2 (Fig. 2.1; Bowes et al. 1964; Davies 1974; Sills et al. 1982; Johnson et al. 2016). Some of these occurrences – most notably in the Laxford Shear Zone (Figs. 2.1 and 2.4) – are spatially associated with quartz-feldspar-garnet-biotite gneiss (termed "brown gneiss" by Johnson et al. (2016)). These brown gneisses have previously been interpreted as representing metamorphosed sedimentary lithologies (Beach et al. 1974, Cartwright et al. 1985), although they could also plausibly be volcanogenic (Johnson et al. 2016). A series of smaller amphibolite blocks, which are surrounded by trondhjemite and occur on a scale of up to tens of metres, exist in the southern part of the Central Region, near Gruinard Bay (Fig. 2.1; Rollinson 1987; Burton et al. 1994).

Further to the large ultramafic-mafic complexes and amphibolite blocks, scarcely studied, centimetre- to metre-scale pods of pyroxenite, amphibolite and gabbro, are ubiquitous throughout the LGC (Park et al. 2002, Rollinson and Gravestock 2012). While these pods have traditionally been interpreted as representing smaller fragments of the larger layered complexes (e.g., Park et al. 2002), a recent mineral chemistry study focusing on the ultramafic-mafic rocks at Scouriemore (Fig. 2.1) demonstrates that they are likely un-related to one another (see Section 2.3.3 for full details; Rollinson and Gravestock 2012).

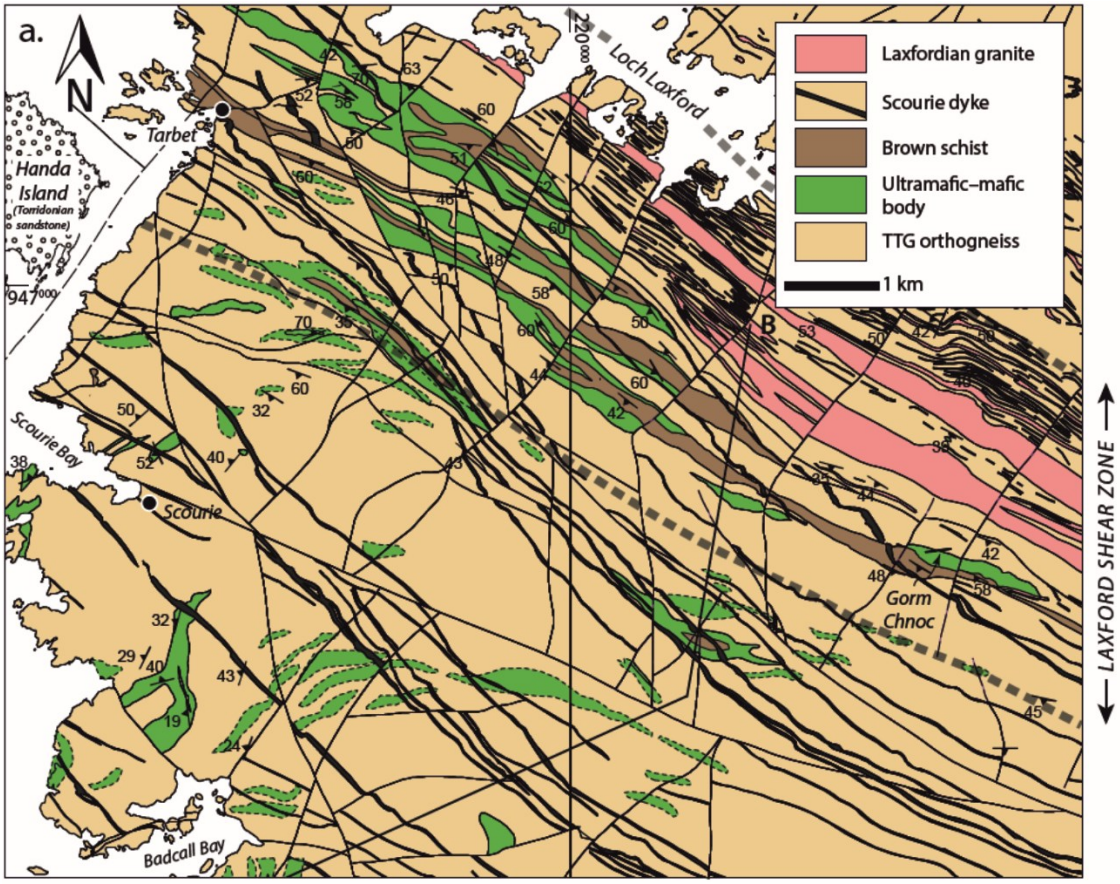

Figure 2.4: *Geological map of the northern Central Region (see Fig. 2.1), including the Laxford Shear Zone (Johnson et al. 2018).*

2.3.1 Age constraints

Attempts to constrain the age of the large, layered ultramafic-mafic complexes in the Central Region relative to the surrounding TTG gneiss using geochronological techniques have proved inconclusive. Re-Os dating of the complexes at Scouriemore and north of Scourie Bay (Fig. 2.1; Burton et al. 2000) yielded likely crystallisation ages of 2.68 ± 0.02 Ga and 3.26 ± 0.21 Ga, while Sm-Nd dating of the complexes at Achiltibuie, Drumbeg and Scouriemore (Whitehouse 1989) yielded dates of 2.85 ± 0.1 Ga, 2.91 ± 0.06 Ga and 2.67 ± 0.11 Ga. As these proposed ages show significant overlap with the 3.05 to 2.80 Ga protolith ages for the Central Region TTG gneisses (Fig. 2.1; Friend and Kinny 2001; Kinny et al. 2005; Love et al. 2010; Whitehouse and Kemp 2010; MacDonald et al. 2015), the age relationship between the ultramafic-mafic complexes and TTG gneiss have largely been informed by field relationships. Rollinson and Windley (1980) considered tonalitic gneiss at Geodh' nan Sgadan (Fig. 2.1) to cross-cut mafic rocks, with several authors subsequently suggesting that all of the ultramafic-mafic complexes likely pre-date the emplacement of the TTG magmas (Sills 1981, Park et al. 2002, Rollinson and Gravestock 2012). However, Johnson et al. (2016) found no evidence at

Geodh' nan Sgadan (or elsewhere in the northern part of the Central Region LGC) to support this assertion, and the relative age relationships remain ambiguous.

At Gruinard Bay, in the southern Central Region (Fig. 2.1), blocks of layered amphibolite are reportedly cross-cut by trondhjemite gneiss (Rollinson 1987), with this proposed age relationship supported by Pb-Pb and Sm-Nd geochronology (Burton et al. 1994). Both geochronological techniques yielded amphibole crystallisation ages of 3.3 Ga for the amphibolite, with these ages interpreted to represent an early metamorphic event not experienced by the Central Region TTG gneisses (Burton et al. 1994). However, as the genetic relationship between these amphibolite blocks and the larger complexes that are largely concentrated in the northern part of the Central Region is unclear (Rollinson 1987), this age relationship has never been extended to all ultramafic-mafic complexes in the LGC (Johnson et al. 2016).

2.3.2 Previous field descriptions and petrography

The ultramafic portions of the large layered ultramafic-mafic complexes (e.g., Scouriemore, Drumbeg and Achiltibuie; Fig. 2.1) generally comprise a combination of metapyroxenite and metaperidotite, while the mafic portions contain garnet-metagabbro, metagabbro and amphibolite (Johnson et al. 2016). On average, the ultramafic-mafic complexes have been reported to contain ultramafic and mafic rock types in a roughly 1:2 ratio, as observed at Scouriemore (Fig. 2.1; Bowes et al. 1964; Goodenough and Krabbendam 2011). However, the relative proportions of ultramafic and mafic rocks vary dramatically between individual complexes, with some containing no ultramafic rocks (e.g., Geodh' nan Sgadan; Rollinson and Windley 1980) and others that are almost exclusively ultramafic (e.g., Loch an Daimh Mor; Faithfull et al. 2018). The ultramafic rocks, which commonly display distinctive primary magmatic layering (Sills 1981, Sills et al. 1982), often form the structural bases of such complexes (O'Hara 1961, Johnson et al. 2012). These (sheet-like) ultramafic-mafic complexes commonly display isoclinal to open folds, with primary magmatic layering in the ultramafic portions generally concordant to both the complex margins and the gneissosity in the surrounding TTG gneisses (Bowes et al. 1964, Sills 1981). Moreover, the margins of individual complexes often display sheared or faulted contacts with the surrounding TTG gneiss that are commonly steeply dipping (Johnson et al. 2016). In addition to layering in the ultramafic rocks, the mafic portions of these complexes may preserve relict magmatic layering in places, alongside rare sulphide-rich layers (Sills et al. 1982).

Pre-dating the Badcallian (granulite-facies) metamorphic event, the ultramafic rocks in these large complexes exhibit a peak metamorphic assemblage of olivine, orthopyroxene, clinopyroxene, hornblende and spinel (Johnson and White 2011). The dominantly mesocratic- to melanocratic (and rarely leucocratic) mafic rocks comprise variable proportions of plagioclase, garnet, orthopyroxene, clinopyroxene and amphibole (Johnson et al. 2012, 2016). These minerals generally range from 0.5 to 2.0 mm in diameter, although garnet commonly forms porphyroblasts on the centimetre-scale (Bowes et al. 1964, Johnson et al. 2012).

The dominantly mafic occurrences located in the Laxford Shear Zone (Figs. 2.1 and 2.4), which show a spatial association with the aforementioned brown gneiss and are laterally continuous for several kilometres, range in thickness from a few metres to a several hundreds of metres (Goodenough et al. 2010). These occurrences display pronounced variation in strain, with complexes exhibiting relict igneous textures and layering in low strain zones, and fine-grained, strongly foliated and lineated assemblages in higher strain zones (Goodenough et al. 2010). Johnson et al. (2016) proposed a generalised stratigraphy for the ultramafic-mafic complexes (outlined in Figure 2.5) in the Central Region, whereby TTG gneiss is overlain by layered ultramafic rocks, garnet-rich metagabbro, garnet-poor (and plagioclase-rich) metagabbro and brown gneiss. In this model, individual ultramafic-mafic complexes preserve different portions of the proposed succession, with Johnson et al. (2016) attributing this to subsequent faulting/shearing.

The amphibolite occurrences in Gruinard Bay range from centimetre-scale, boudinaged pods to large blocks that occasionally show layering remnants and occur on a scale of tens of metres (Rollinson 1987). These blocks comprise 1–2 mm diameter plagioclase and hornblende, alongside variable proportions of secondary epidote, with layering reflecting the varying proportions of hornblende and plagioclase (Rollinson 1987).

2.3.3 Previous geochemical studies

Several bulk-rock geochemical studies have focused on the large layered ultramafic-mafic complexes in the northern Central Region (Fig. 2.1), with a large number concentrating on the occurrences at Scouriemore, Drumbeg and Achiltibuie (Sills et al. 1982, Burton et al. 2000, Rollinson and Gravestock 2012, Johnson et al. 2016). These studies reveal that the (anhydrous) ultramafic rocks contain between 19 and 37 wt. % MgO, 41 and 50 wt. % SiO_2, between 0.1 and 0.25 wt. % NiO and < 0.4 wt. % TiO_2, with most major elements showing broadly linear trends when plotted against MgO (Sills 1981, Sills et al. 1982, Johnson et al.

2016). In terms of their chondrite-normalised REE abundances, the ultramafic rocks display normalised values of less than 10 (Fig. 2.5; Johnson et al. 2016), with minor LREE enrichment ($[Ce/Yb]_N$= 0.8–5.0) described as comparable to layered intrusions (Sills et al. 1982).

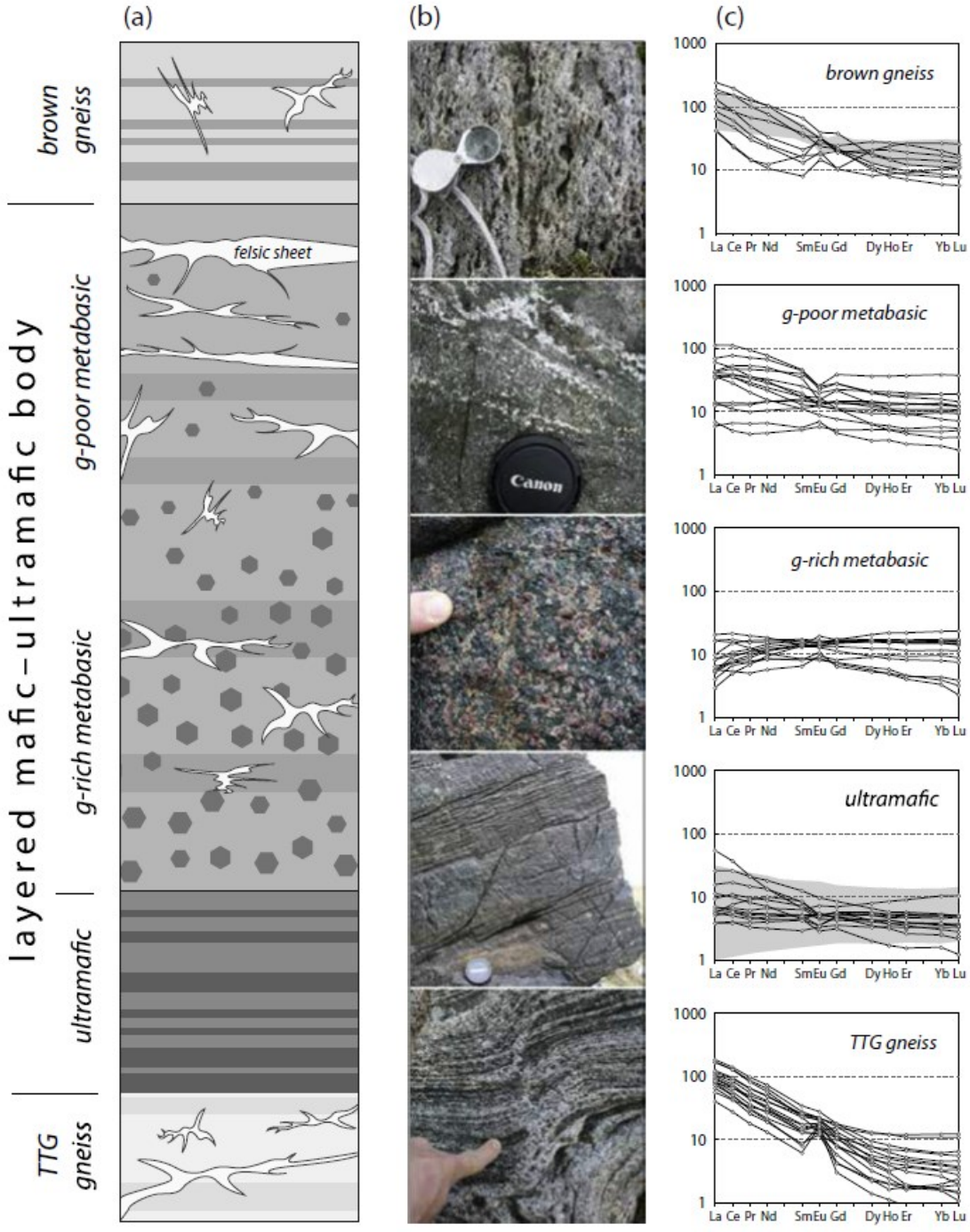

Figure 2.5: (a) *Generalised stratigraphy for the layered ultramafic-mafic complexes in the LGC, as proposed by Johnson et al. (2016).* ***(b)*** *Field photographs detailing the typical lithological characteristics of the units outlined in (a).* ***(c)*** *Chondrite-normalised (McDonough and Sun 1995) REE plots for the various lithological units outlined in (a). Abbreviations: g=garnet.*

The mafic portions of the ultramafic-mafic complexes typically contain between 6 and 14 wt. % MgO, with chondrite-normalised LREE abundances ranging from 8 to 30, and HREE abundances ranging from 6 to 15 ($[Ce/Yb]_N$= 0.6–4.8; Sills et al. 1982; Johnson et al. 2016). REE patterns for the mafic rocks are broadly parallel to those of the ultramafic rocks, with garnet-rich varieties generally displaying significantly lower LREE abundances than the garnet-poor varieties (Fig. 2.5; Johnson et al. 2016). The brown gneisses, which are sometimes spatially associated with the ultramafic-mafic complexes (Section 2.3.2), display major element compositions that are generally indistinguishable from those of retrogressed TTG gneisses and felsic sheets (Fig. 2.5; Johnson et al. 2016). Moreover, displaying moderately fractionated REE patterns ($[La/Lu]_N$= 2.0–42.0), the brown gneisses also exhibit trace element compositions comparable to the retrogressed TTG gneiss (Fig. 2.5; Johnson et al. 2016), although the former exhibit relative enrichment in the HREE.

Based on bulk-rock geochemical data from Scouriemore and Achiltibuie, and associated trace element modelling, Sills et al. (1982) suggested that the ultramafic-mafic complexes crystallised from a high-Mg, tholeiitic magma that contained between 15 and 20 wt. % MgO and was derived from 30–40 % partial melting of an undepleted mantle. In this scenario, these authors propose that the ultramafic rocks are the product of olivine and pyroxene crystallisation, and that the mafic rocks represent the fractionated products of this magma, while neither garnet nor hornblende were involved in fractionation (Sills 1981, Sills et al. 1982). Moreover, sampling traverses at Scouriemore (Fig. 2.1) reveal geochemical trends typical of un-metamorphosed layered complexes, with the ultramafic-mafic complexes showing upwards decreases in bulk-rock Mg numbers, and Ni and Cr contents, and upwards increases in the concentration of incompatible elements (Sills et al. 1982, Burton et al. 2000). Similarly, fractionating mineral chemical trends have been recorded at Achiltibuie (Fig. 2.1), with all minerals displaying upwards decreases in MgO contents within a single mafic unit (Fig. 2.6; Sills et al. 1982). These geochemical trends occur over extraordinarily small scales (< 40 m stratigraphically), suggesting that the ultramafic-mafic complexes experienced significant tectonic thinning during the protracted and polyphase metamorphism experienced by the LGC (Bowes et al. 1964, Sills 1981, Sills et al. 1982, Burton et al. 2000).

In a detailed mineral chemistry study of the ultramafic rocks at Scouriemore (Fig. 2.1), Rollinson and Gravestock (2012) demonstrated that clinopyroxene in layered pyroxenites (from a large ultramafic-mafic complex) exhibit trace element compositions distinct from those shown by small-scale pyroxenite pods, suggesting that the two have different origins. On chondrite-normalised REE plots (Fig. 2.7), clinopyroxenes from the latter show strong

LREE enrichment and pronounced negative Eu anomalies, while those from the layered pyroxenites are more variable (Rollinson and Gravestock, 2012; Fig. 2.7). Within the layered pyroxenites, 3 distinct groups were identified based on REE patterns (Fig. 2.7). Type A clinopyroxenes display flat REE patterns and small negative Eu anomalies, type B clinopyroxenes exhibit slightly steeper LREE patterns, and type C clinopyroxenes show strong LREE enrichment (Fig. 2.7). Rollinson and Gravestock (2012) concluded that such variability could not be attributed to primary magmatic processes, instead proposing that it resulted from variable LREE enrichment by interaction with a felsic melt produced during localised partial melting associated with the (granulite-facies) Badcallian metamorphic event (Section 2.2.2).

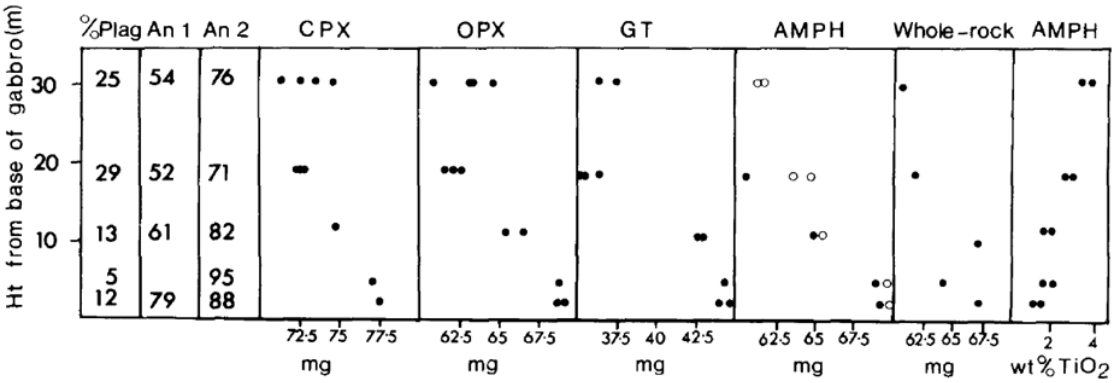

Figure 2.6: *Stratigraphic log detailing the chemistry of specific minerals within one mafic unit at Achiltibuie (Figure 2.1; Sills et al. 1982). CPX=clinopyroxene; OPX=orthopyroxene; GT=garnet; AMPH=amphibolite; An=anorthite number; Ht=height.*

2.3.4 Previous interpretations

There is no consensus regarding the genetic relationship between the various ultramafic and mafic rocks in the Central Region LGC, with it possible that there are multiple suites with different origins (e.g., Bowes et al. 1964). Despite this, single interpretations have generally been invoked to explain all of the ultramafic, mafic and associated rocks in the LGC, with these interpretations spanning a wide-range of geological and geodynamic environments, including:

(i) Remnants of a pre-TTG, possibly oceanic, mafic-ultramafic crust (Sills 1981, Sills et al. 1982);

(ii) Fragments of one or more layered intrusions (Bowes et al. 1964, Davies 1974);

(iii) Accreted oceanic crust (Park and Tarney 1987); or

(iv) The sagducted remnants of Archaean greenstone belts (Johnson et al. 2016).

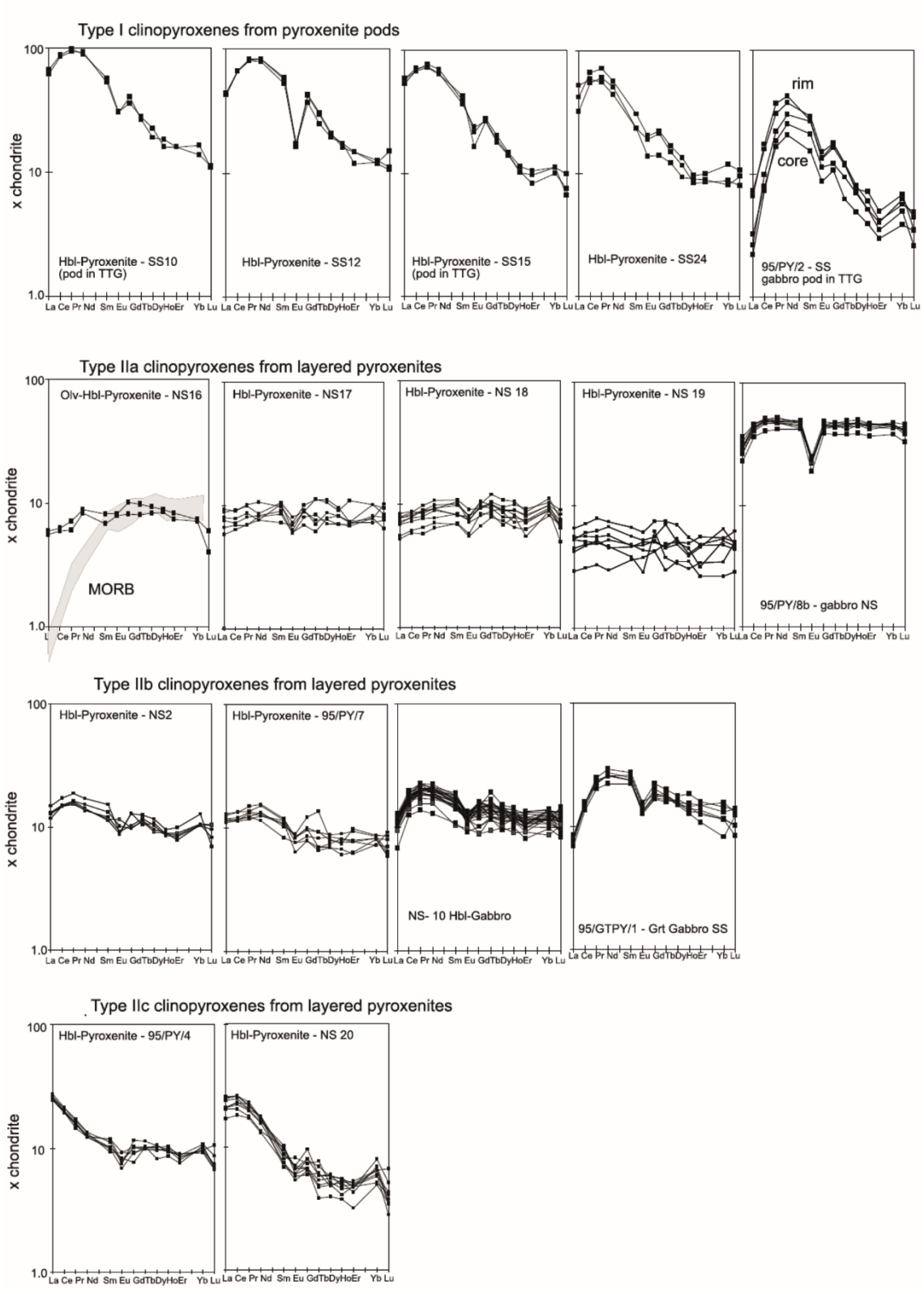

Figure 2.7: *Chondrite-normalised (Nakamura 1974) REE patterns for clinopyroxenes from metapyroxenites and metaperidotites from the Scouriemore area (Rollinson and Gravestock 2012). Grey shaded area=MORB.*

Several authors (e.g., Rollinson and Windley 1980; Sills 1981; Park et al. 2002) have argued that the seemingly chaotic map-scale distribution of the ultramafic-mafic rocks – including

both the larger complexes and smaller pods – is evidence supporting hypothesis (i). This hypothesis is also supported by the aforementioned cross-cutting relationship at Geodh' nan Sgadan (see Section 2.3.1), although this field evidence is contested by Johnson et al. (2016). Hypothesis (ii) is supported by the distinctive magmatic layering in the ultramafic portions of the larger complexes (Bowes et al. 1964), alongside the associated geochemistry conducted at Scouriemore (see Fig. 2.1; Section 2.3.3; Sills et al. 1982). However, if the ultramafic-mafic rocks are indeed older than the surrounding TTG gneiss, as proposed, it remains unclear what material such intrusions were emplaced into. The spatial association between metasedimentary, ultramafic and mafic rocks is used to support both hypotheses (iii) and (iv), with these interpretations in opposition due to a differing overarching view of the Archaean Earth (see Section 1.1). In the most basic terms, while hypothesis (iii) envisages a geodynamic regime comparable to modern-style plate tectonics (Park and Tarney 1987; see Fig. 1.1) – whereby horizontal thrusting led to the accretion of the ultramafic, mafic and metasedimentary rocks – hypothesis (iv) exists within a paradigm whereby vertical tectonics is predominant (Johnson et al. 2016).

Chapter 3

Re-evaluating ambiguous age relationships in Archaean cratons: Implications for the origin of ultramafic-mafic complexes in the LGC

This chapter is based upon the following published paper:

George L. Guice, Iain McDonald, Hannah S. R. Hughes, John M. MacDonald, Thomas G. Blenkinsop, Kathryn M. Goodenough, John W. Faithfull, Robert J. Gooday. (2018) Re-evaluating ambiguous age relationships in Archean cratons: Implications for the origin of ultramafic-mafic complexes in the Lewisian Gneiss Complex. *Precambrian Research,* ***311,*** *136-156.*

Author contributions and declarations:

G.L.G. conducted field mapping, structural assessments, petrographic assessments and quantitative mineral chemical analyses. G.L.G. also conceived of the ideas presented, and wrote the entire chapter. I.McD., H.S.R.H., J.M.M., T.G.B., K.M.G. and J.W.F. were involved in discussions during the writing of the chapter, and J.M.M. and R.J.G. provided field assistance for a combined total of 5 days. Jochen Kolb and Tim Johnson provided constructive peer-reviews of the published paper, and Hugh Rollinson provided a constructive review of a previous manuscript.

Abstract

Archaean ultramafic-mafic complexes have been the focus of important and often contentious geological and geodynamic interpretations. However, their age relative to the other components of Archaean cratons are often poorly-constrained, introducing significant ambiguity when interpreting their origin and geodynamic significance. The LGC of the northwest Scottish mainland contains a number of ultramafic-mafic complexes whose origin and geodynamic significance have remained enigmatic since they were first described. Previous studies have interpreted these complexes as representing a wide-range of geological environments, from oceanic crust, to the sagducted remnants of Archaean greenstone belts. These interpretations, which are often critically dependent upon the ages of the complexes relative to the surrounding rocks, have disparate implications for Archaean geodynamic regimes (in the NAC and globally). Most previous authors have inferred that the ultramafic-mafic complexes of the LGC pre-date the TTG magmas. This fundamental age relationship is re-evaluated in this investigation through re-mapping of the Geodh' nan Sgadan Complex (where tonalitic gneiss reportedly cross-cuts mafic rocks) and new mapping of the 7 km^2 Ben Strome Complex (the largest ultramafic-mafic complex in the LGC), alongside detailed petrography and spinel mineral chemistry. This new study reveals that, despite their close proximity in the LGC (12 km), the Ben Strome and Geodh' nan Sgadan Complexes are petrogenetically unrelated, indicating that the LGC (and thus NAC) records multiple temporally and/or petrogenetically distinct phases of ultramafic-mafic Archaean magmatism that has been masked by subsequent high-grade metamorphism. Moreover, field observations and spinel mineral chemistry demonstrate that the Ben Strome Complex represents a layered intrusion that was emplaced into a TTG-dominated crust. Further to representing a significant re-evaluation of the LGC's magmatic evolution, these findings have important implications for the methodologies utilised in deciphering the origin of Archaean ultramafic-mafic complexes globally, where material suitable for dating is often unavailable and field relationships are commonly ambiguous.

3.1 Introduction

As outlined in Section 1.2, ultramafic-mafic complexes are volumetrically minor components of Archaean cratons that have provided important and often contentious contributions to the Archaean geodynamics debate (Table 1.2). Individual occurrences have been attributed to wide-ranging geological and geodynamic environments, including: Archaean ophiolites/fragments of ophiolites that may represent Archaean suture zone(s) (De Wit et al. 1987, Anhaeusser 2006b); layered intrusions associated with a range of geodynamic environments (Hoatson and Sun 2002, Ivanic et al. 2010, Wang et al. 2015, Bagas et al. 2016); subduction-related sills emplaced into oceanic crust (Polat et al. 2009); fragments of arc-related oceanic crust (Szilas et al. 2014); the sagducted remnants of greenstone belts (Johnson et al. 2016); and mantle residues following high degrees of partial melting (Szilas et al. 2018).

Much of the debate in this field is a consequence of the inherent difficulty in dating ultramafic-mafic complexes, with their age relative to the other components of Archaean cratons often poorly constrained (Whitehouse and Fedo 2003, Kolb et al. 2013, Szilas et al. 2018). Such problems result from a scarcity or absence of suitable datable minerals (e.g., baddeleyite, zircon), commonly resulting in an overreliance on commonly ambiguous field relationships to decipher relative age relationships (Whitehouse and Fedo 2003, Ivanic et al. 2010, Johnson et al. 2016). Further, even if dateable minerals are present, the isotopic system of interest is often so disturbed by subsequent overprinting metamorphic events as to render isochron or regression analysis ambiguous and/or associated with unacceptably large errors (e.g., Timms et al. 2006). Some complexes, such as Zandspruit in the Johannesburg Dome (Kaapvaal Craton), are cross-cut by dateable rocks, providing straightforward field relationships and a quantitative minimum age for the formation of the ultramafic-mafic complex (Anhaeusser 2015; Chapters 6-7). However, ambiguous field relationships more commonly inhibit confident interpretation of relative ages. For example, the amphibolite-facies Stolzburg layered complex in the Barberton Greenstone Belt (Kaapvaal Craton) was originally believed to have been faulted against the host Nelshoogte Schist Belt (Anhaeusser 1985). Subsequent identification of a chilled contact at the margin of the complex led to a contrasting (and currently accepted) interpretation, whereby it was intrusive into the Nelshoogte Schist Belt (De Wit et al. 1987). The problem of ambiguous age relationships is exacerbated in high-grade cratonic regions, such as the NAC, where the field relationships may be complicated by long-lived, high-temperature metamorphism and partial melting, rather than primary (igneous) processes and relationships (Nutman et al. 2013, Johnson et

al. 2016). Such complications are exemplified by the ultramafic-mafic complexes of the Akilia terrane (western Greenland), where detailed field observations by Whitehouse and Fedo (2003) found no evidence to support the original assumption that they pre-date the volumetrically dominant 3.85–3.65 Ga tonalitic gneiss.

As a consequence of uncertain age relationships, the origin(s) of the ultramafic-mafic complexes in the LGC have been ascribed to a wide-range of geological and geodynamic environments (Chapter 2), including: one or more layered intrusion(s) (e.g., Bowes et al. 1964); fragments of a pre-TTG, possibly oceanic, mafic-ultramafic crust (e.g., Sills 1981); accreted oceanic crust (Park and Tarney 1987); or the sagducted remnants of Archaean greenstone belts (Johnson et al. 2016). This chapter presents new detailed geological maps, field descriptions, petrography and mineral chemistry for two ultramafic-mafic complexes in the LGC, namely the 7 km^2 Ben Strome Complex and 0.2 km^2 Geodh' nan Sgadan Complex (Fig. 2.1). Using these data and a critical review of the existing literature, the currently enigmatic origin of the ultramafic-mafic complexes is addressed, alongside the magmatic evolution of the LGC and its context within the wider NAC.

3.2 The Ben Strome Complex

The 7 km^2 Ben Strome Complex is located 13 km SE of Scourie (Fig. 2.1) and represents the largest ultramafic-mafic complex in the LGC (Fig. 3.1a). For comparison, the well-studied occurrences at Scouriemore (Sills 1981, Sills et al. 1982, Rollinson and Gravestock 2012), which exhibit many of the salient characteristics of the Ben Strome Complex, collectively cover an area less than 0.5 km^2. Despite this, the Ben Strome Complex has been little studied (Josey and Shaw 1974), with no detailed geological map or comprehensive description of the complex published prior to the research presented here. The Ben Strome Complex – one of the easternmost exposures of the LGC (Fig. 2.1) – is bordered by the summit of Ben Strome in the west, Loch an Leathaid Bhuain in the east and the Maldie River in the south (Fig. 3.1). It is surrounded by and interleaved with TTG gneiss typical of the Central Region LGC and is unconformably overlain by Cambrian quartzite in the east (Fig. 3.1a).

3.2.1 Field relationships

Approximately 70 % of the Ben Strome Complex is composed of mafic rocks predominantly comprising metagabbro, garnet-metagabbro, garnet-amphibolite and amphibolite. The remaining 30 % comprises layered ultramafic rocks (predominantly metapyroxenite, with subordinate metaperidotite) that are most commonly structurally underlain by TTG gneiss and structurally overlain by mafic rocks. However, this association is not ubiquitous, with

other associations observed, including: individual packages of ultramafic or mafic rocks surrounded by TTG gneiss (e.g., in the NW of the complex; Fig. 3.1a); and ultramafic rocks both underlain and overlain by mafic rocks (e.g., in the E of the complex; Fig. 3.1a). The exposed ultramafic-mafic contacts are gradational (typically over an interval of less than 30 cm) and irregular, with the clearest example occurring in the Maldie River (NC 25843401; Fig. 3.2a). Although the majority are obscured, the ultramafic-mafic contacts are consistently parallel to the layering in the ultramafic rocks (Fig. 3.1, Fig. 3.2b). Contacts between the Ben Strome Complex and surrounding TTG gneiss are sharp and commonly exhibit recrystallised quartz and slickensides, indicating that most are tectonic. On both the outcrop (Fig. 3.2c) and map scale (Fig. 3.1a-c), the centimetre-scale TTG gneissosity is concordant to both the layering in the ultramafic rocks and margins of the complex. Consequently, the age-relationship with surrounding TTG gneiss is not clear, with no cross-cutting relationships between TTG gneiss and ultramafic-mafic rocks of the Ben Strome Complex.

An E-W-trending, Laxfordian shear zone divides the Ben Strome Complex into the Leathaid (northern) and Maldie (southern) domains (Fig. 3.1). The shear zone exhibits a pervasive, millimetre to centimetre-scale foliation and dips of between 50 and 90°, which are generally towards the north (Fig. 3.1, Fig. 3.2d, Fig. 3.3a). Ten to ninety metre-thick, NW-SE-trending Scourie Dykes cross-cut both domains of the complex, with one strongly deformed dyke contained entirely within the Laxfordian shear zone (Fig. 3.1). A NE-SW-trending fault is best observed in the Maldie Domain, where it juxtaposes ultramafic and mafic rocks (Fig. 3.1). The fault is younger than the Ben Strome Complex and cross-cutting Scourie Dykes (Fig. 3.1), with the limited offset of dykes in the Maldie Domain indicating that they have sub-vertical dips. Occasional centimetre to metre-scale pods of ultramafic and mafic rocks are rare in the surrounding TTG gneiss and show no spatial correlation with the Ben Strome Complex (i.e., their density does not increase with decreasing distance to the edges of the complex).

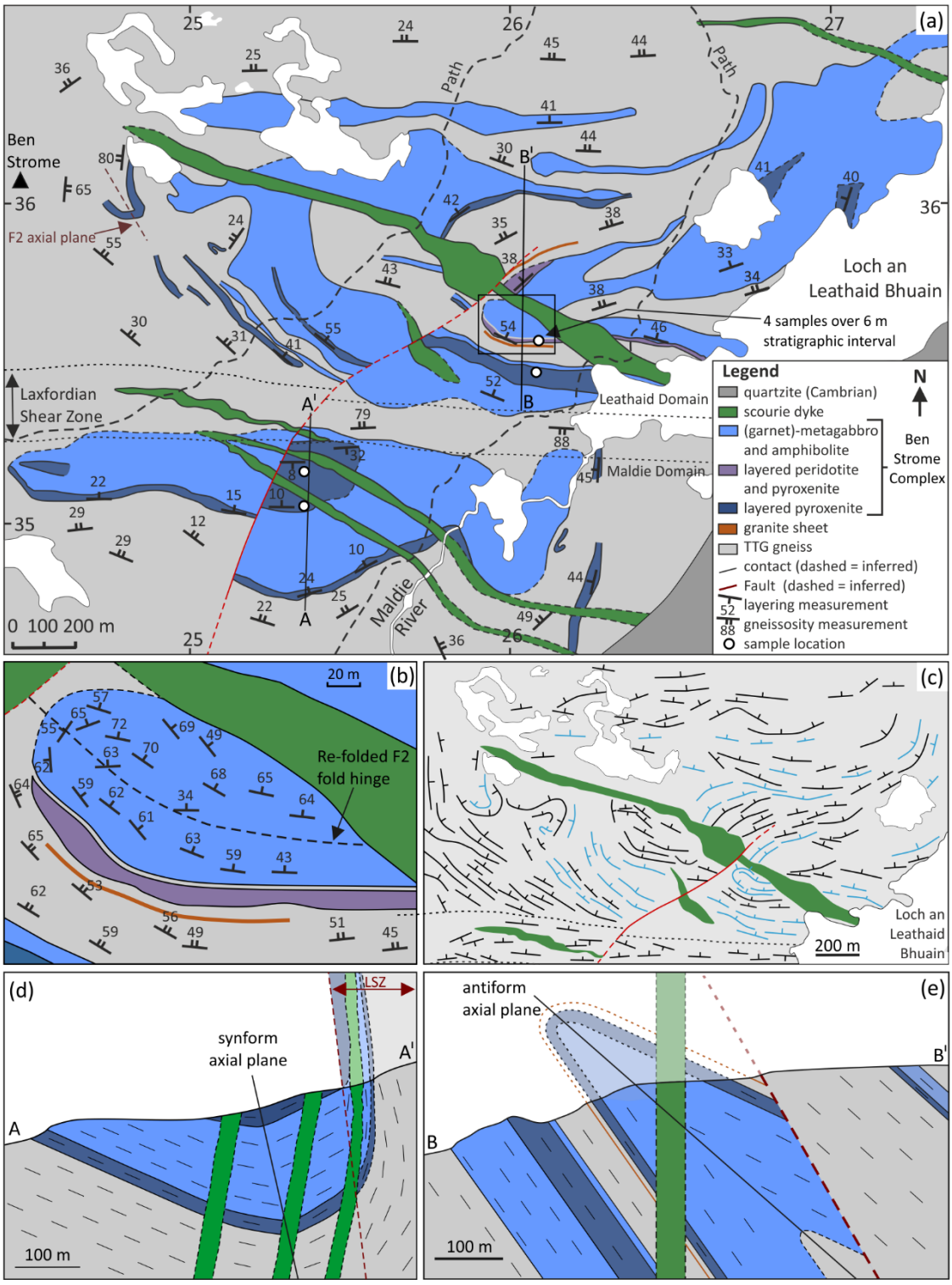

Figure 3.1: ***(a)*** *Simplified geological map of the Ben Strome Complex, including representative structural measurements.* ***(b)*** *Detailed geological map of a re-folded fold in the Leathaid Domain.* ***(c)*** *Form surface map of the Leathaid Domain and Laxfordian shear zone. Black lines represent TTG gneissosity. Blue lines represent igneous layering.* ***(d)*** *Cross-section from A-A^{I} detailing the structure of the Ben Strome Complex in the Maldie Domain and interaction with the Laxfordian shear zone (LSZ).* ***(e)*** *Cross-section from B-B^{I}, detailing the structure of the Ben Strome Complex in the Leathaid Domain.*

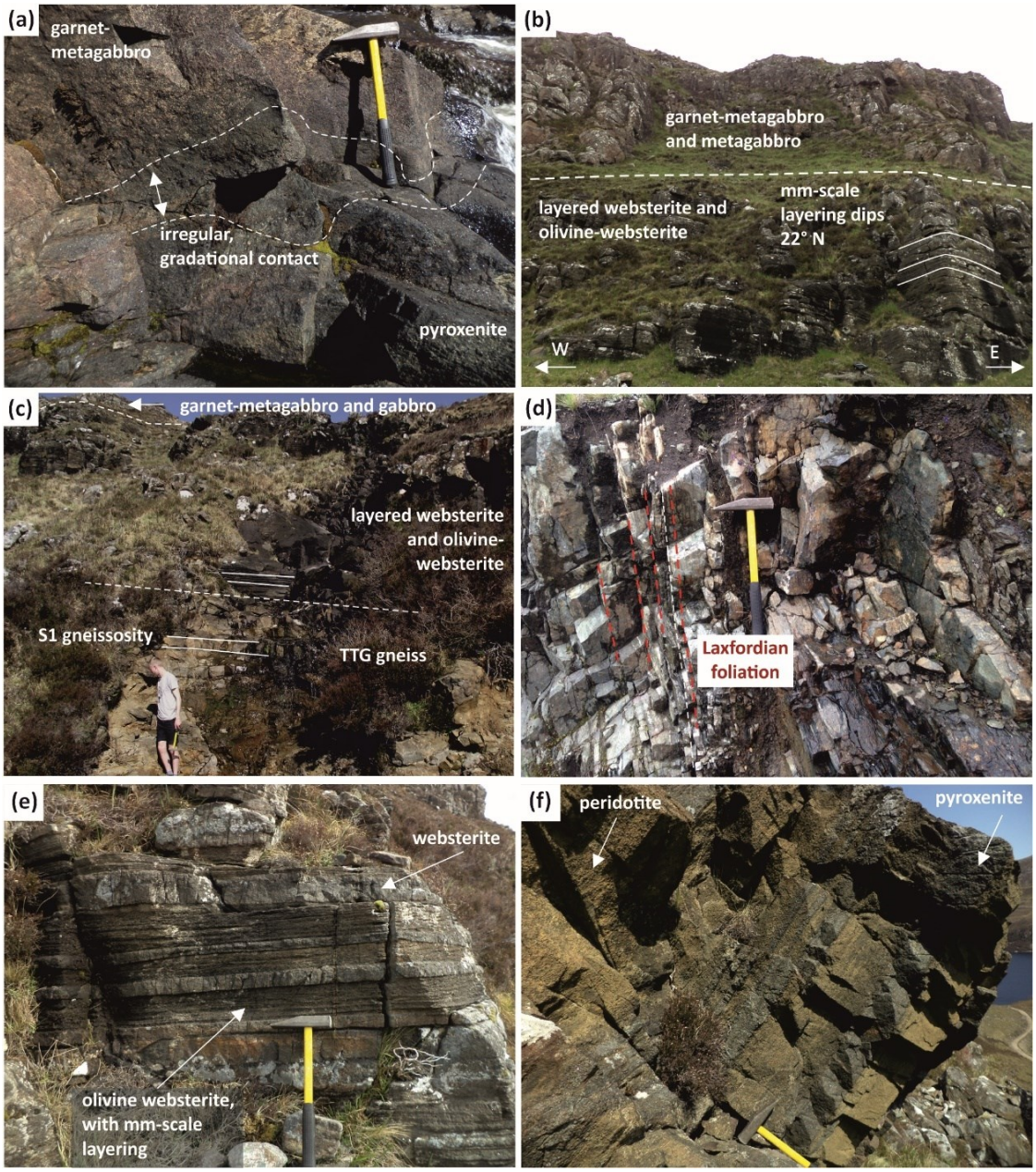

Figure 3.2: *Field photographs detailing representative rock types and field relationships in the Ben Strome Complex and surrounding TTG gneiss.* ***(a)*** *Gradational contact between layered metapyroxenite and garnet-metagabbro in the Maldie River, Maldie Domain.* ***(b)*** *Layered metawebsterite and metaolivine-websterite overlain by heterogeneous garnet-metagabbro and metagabbro, Maldie Domain.* ***(c)*** *Relationship between TTG gneiss and overlying Ben Strome Complex, Maldie Domain. Note: S1 gneissosity is parallel to layering of metawebsterite and metaolivine-websterite.* ***(d)*** *Steeply-dipping, centimetre-scale Laxfordian foliation.* ***(e)*** *Layered metaolivine-websterite (brown and internally layered on the millimetre-scale) and metawebsterite (grey and blocky), Maldie Domain.* ***(f)*** *Millimetre to metre-scale modal layering of metapyroxenite and metaperidotite, Leathaid Domain, with a combination of gradational and sharp contacts. Hammer length=40 cm; hammer head width=17 cm.*

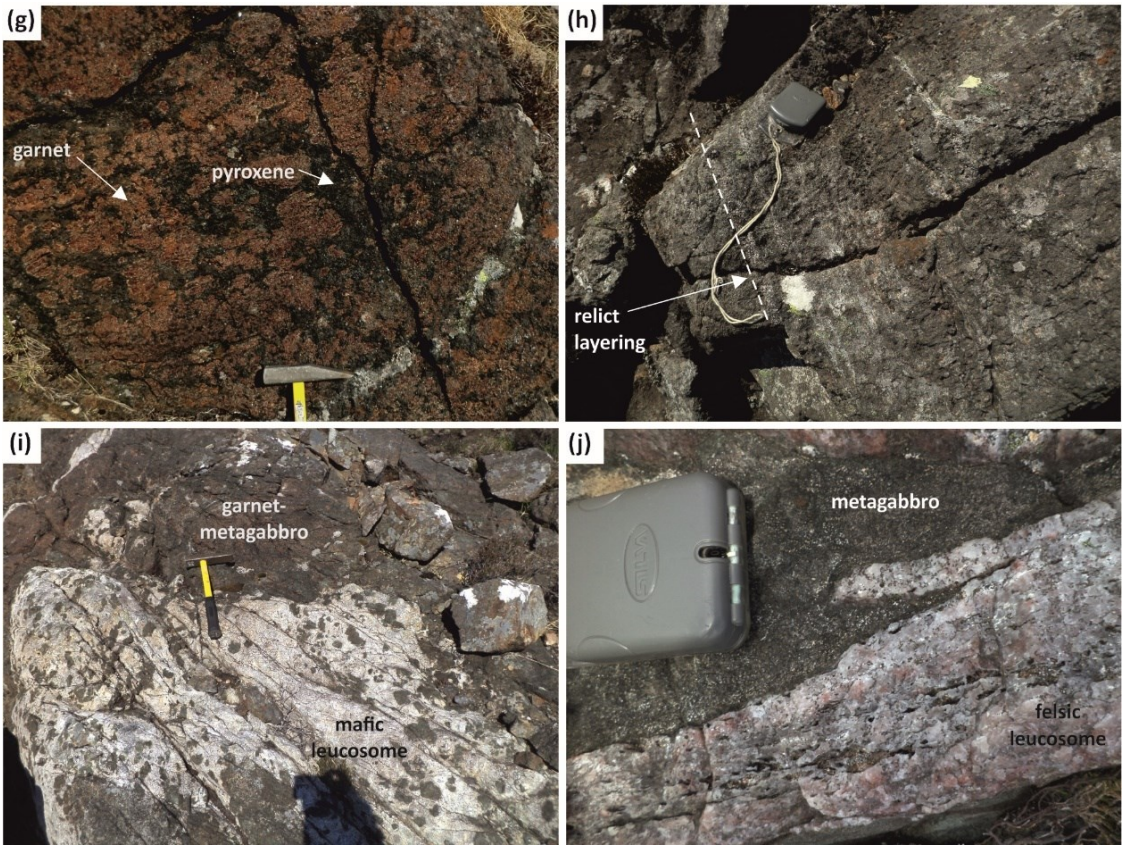

Figure 3.2 (cont.): (g) *Garnet-metagabbro, Leathaid Domain.* ***(h)*** *Metagabbro, with relict igneous layering preserved. Leathaid Domain.* ***(i)*** *Plagioclase and pyroxene-rich leucosome cross-cutting garnet-metagabbro, Maldie Domain.* ***(j)*** *TTG-derived quartz-rich leucosome cross-cutting Ben Strome Complex metagabbro, Leathaid Domain. Hammer length=40 cm; hammer head width=17 cm; compass clinometer length=10 cm.*

The numerous packages of layered ultramafic rocks are typically between 5 and 50 m in stratigraphic thickness, persist for hundreds of metres along strike, and form prominent, well-exposed ridges and small crags (Fig. 3.2b-c,e-f). Generally, these packages are dominated by metapyroxenite (metawebsterite and metaolivine-websterite), with rare peridotitic (metaharzburgite and/or metalherzolite) layers also present (Fig. 3.2e-f). Within these ultramafic portions, the contacts between the millimetre- to metre-scale layers of different lithologies are either sharp (Fig. 3.2e) or gradational, with both contact types present in a ~3 m thick package of ultramafic rocks in the Leathaid Domain (Fig. 3.2f). Gradational variation in modal mineralogy is also observed within individual layers of metapyroxenite and metaperidotite (Fig. 3.2f), which rarely are truncated. Ultramafic packages dominated by metaolivine-websterite commonly exhibit rhythmic, millimetre to centimetre-scale internal layering and sharp contacts with subordinate websterite layers, which are more massive and up to tens of centimetres thick (Fig. 3.2e). These metaolivine-websterite-dominated ultramafic packages predominate in the Maldie Domain, with the

small number of ultramafic packages that also contain volumetrically significant (> 10 vol. %) metaperidotite restricted to the Leathaid Domain (Fig. 3.1a).

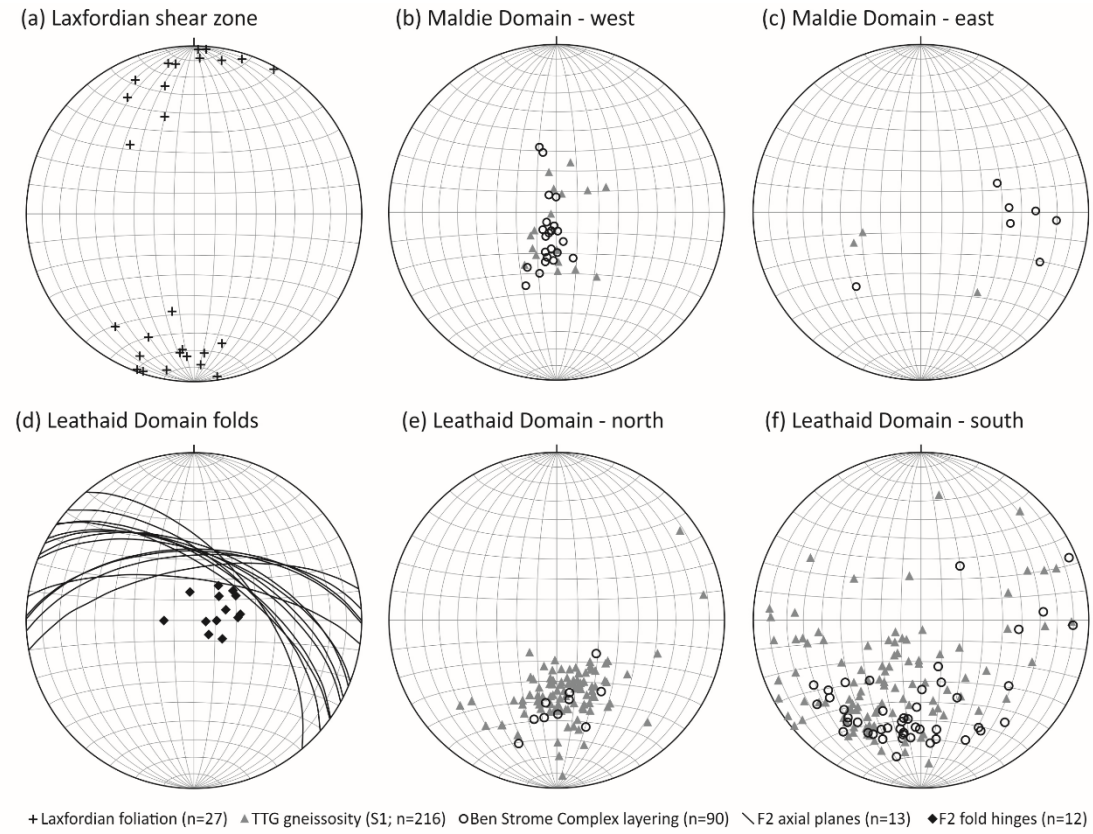

Figure 3.3: *Stereonet (lower hemisphere projection) of structures in and around the Ben Strome Complex.*

Rather than systematic layering, the mafic portions of the Ben Strome Complex are characterised by sporadic lithological heterogeneity on a scale of centimetres to tens of metres (Fig. 3.2g-h). Despite this, selected areas, such as the area outlined in Fig. 3.1b, retain remnants of primary layering that are defined by subtle variations in the modal proportion of plagioclase (Fig. 3.2h). Within the mafic portions of the complex, higher abundances of garnet-metagabbro (Fig. 3.2g) commonly exist close to ultramafic-mafic contacts, while plagioclase-rich metagabbro (Fig. 3.2h) is more common in the northwest of the Leathaid Domain (Fig. 3.1a). Oxide-rich (magnetite-dominated) horizons are sporadically distributed throughout these portions of the complex, which are cross-cut by plagioclase and pyroxene-rich leucosomes (as identified by Johnson et al. 2012, 2013). These leucosomes occur on a centimetre to metre-scale and generally exhibit irregular morphologies and sharp contacts with the surrounding mafic rocks (Fig. 3.2i). Rare quartz-rich veins, which likely represent leucosomes formed by partial melting of the surrounding TTG gneiss (c.f. Johnson et al. 2013), also occur in the mafic portions of the complex (Fig. 3.2j). Such TTG-derived

leucosomes are restricted to the peripheries of the complex (typically less than 5 m from TTG-mafic contacts) and are most abundant in the north of the Leathaid Domain.

3.2.2 Structure

The earliest recognised structure in the mapped area is the widespread, regional TTG gneissosity (S1), which comprises millimetre- to centimetre-scale layers of relatively mafic and felsic rocks. Individual layers comprise variable proportions of quartz, plagioclase, pyroxene and hornblende, with minor biotite and orthoclase. The S1 structure is consistently parallel to the layering in the Ben Strome Complex, as shown by outcrop-scale photographs (Fig. 3.2c), kilometre-scale mapping (Fig. 3.1c) and structural data (Fig. 3.3a-d), although it is not clear whether S1 pre- or post-dates the Ben Strome Complex.

Outcrop-scale, tight to isoclinal folds of the S1 structure (F2) in the Leathaid Domain (Fig. 3.4) reveal E-W to NW-SE-trending axial planes that dip moderately to steeply towards the N/NE and fold hinges that plunge steeply toward the E (Fig. 3.3d). Isoclinal F2 folds, which have axial planes dipping NW to NE, are also recognised on the map-scale, most notably in the west and southeast of the Leathaid Domain (Fig. 3.1a-c). In the Maldie Domain, the Ben Strome Complex comprises two distinct ultramafic packages separated by a thick package of mafic rocks (Fig. 3.1d). These ultramafic units can be distinguished based on their subtly different lithological components, with the upper unit containing a 2 m thick layer of serpentinised metaperidotite not observed in the lower unit. These ultramafic packages are conformable with the overlying/underlying mafic rocks, with no evidence for faulted contacts. Along with the underlying TTG gneisses, the Ben Strome Complex in the Maldie Domain forms an open synform (Fig. 3.1d). Given the E-W-trending hinge of this kilometre-scale structure (Fig. 3.3b), it likely correlates with the F2 structures identified in the Leathaid Domain.

As shown by Fig. 3.1b, S1 and F2 structures are re-folded by an open, N-S-trending structure (F3). The effect of the F3 fold can be observed on the kilometre-scale, where S1 and F2 structures trend NW-SE to W-E in the south of the Leathaid Domain (south of the large, central Scourie Dyke; Fig. 3.1a,c), but trend E-W to NE-SW in the north of the Leathaid Domain (Fig. 3.3e,f). S1, F2 and F3 structures are all cross-cut by (in chronological order): Scourie Dykes, the Laxfordian shear zone and a prominent NE-SW-trending fault (Fig. 3.1a). As these cross-cutting relationships constrain the S1, F2 and F3 structures as older than 2.38 Ga (the lowermost age of Scourie Dyke emplacement in the Central Region LGC; Davies and Heaman 2014), they can be attributed to the Badcallian and/or Inverian metamorphic events.

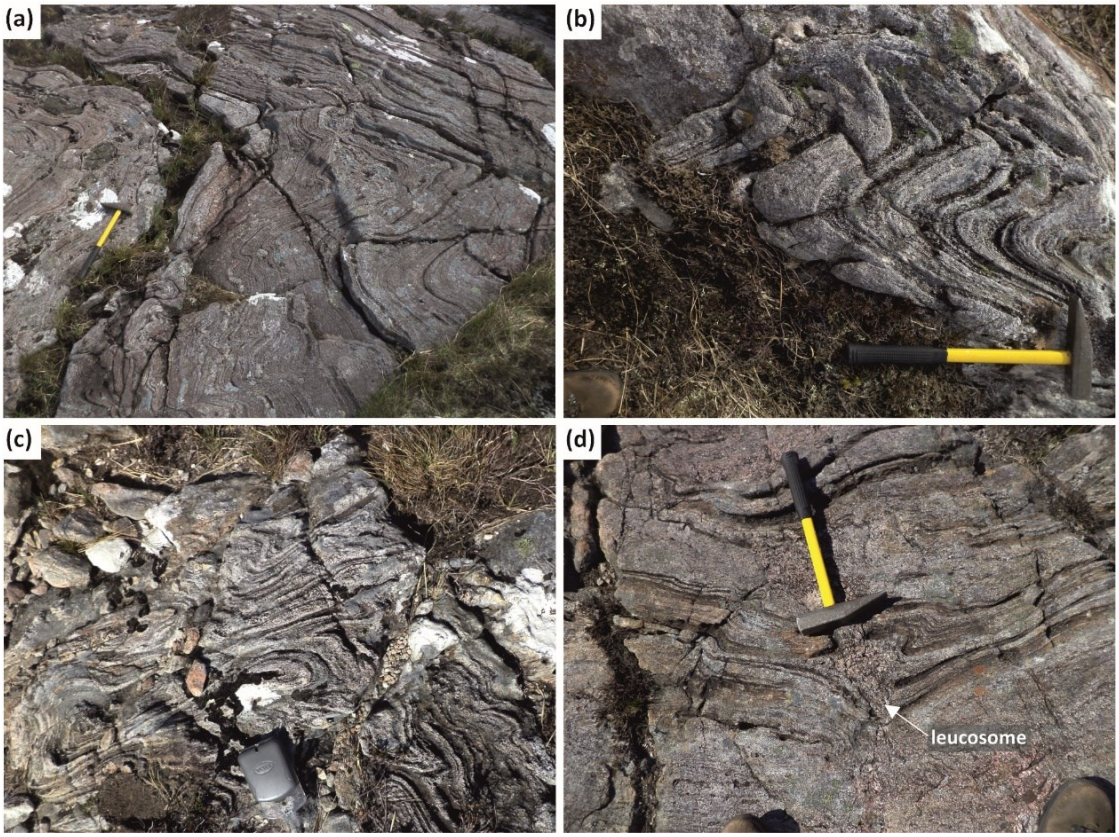

Figure 3.4: *Field photographs detailing the outcrop-scale folding of the S1 gneissosity in the Leathaid Domain. Hammer length=40 cm.*

3.2.3 Petrography

The majority of sampled ultramafic rocks may be classified as metaolivine-websterite or metawebsterite, with a small number of metalherzolite, metaorthopyroxenite and metaharzburgite (Fig. 3.5). Metaperidotites (Fig. 3.6a-b) comprise (in modal %): 50–95 % serpentinised olivine, < 20 % orthopyroxene, < 30 % clinopyroxene, < 10 % amphibole and < 5 % spinel. Serpentine is almost ubiquitous in its replacement of olivine, with small (< 0.5 mm diameter) olivine remnants preserved within large, millimetre to centimetre-scale, serpentine pseudomorphs (Fig. 3.6a-b). These areas of serpentinisation also contain fine-grained (< 0.1 mm diameter) magnetite. Pyroxene is 0.7 to 1.6 mm in diameter and subhedral to anhedral, with ortho- and clino-pyroxene generally occurring in equal proportions. The degree of replacement of clinopyroxene by fine-grained (< 0.3 mm diameter) amphibole varies between samples. Pargasite, which exhibits green-brown pleochroism and 120° triple junctions, is < 2 mm in diameter. Subhedral to anhedral spinel is 0.2 to 1.2 mm in diameter, while Fe-Ni-Cu sulphides occur as anhedral to subhedral < 0.15 mm in diameter.

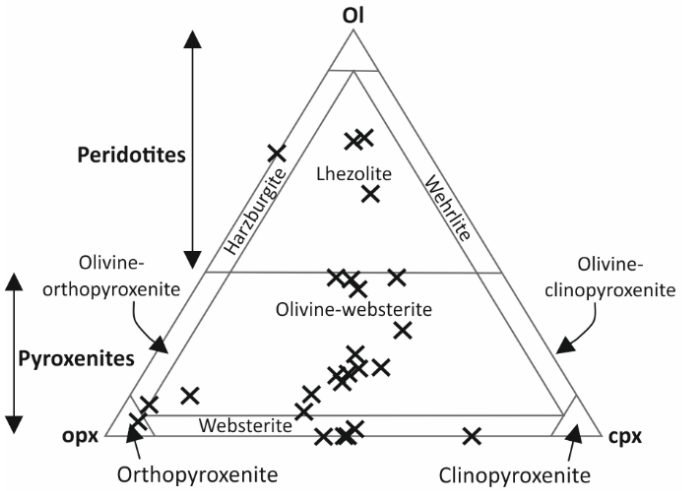

Figure 3.5: *Ternary plot detailing the modal mineral percentages of ultramafic rocks in the Ben Strome Complex.*

Metapyroxenites (Fig. 3.6c-f) comprise (in modal %): 25–90 % orthopyroxene, 3–65 % clinopyroxene, < 40 % serpentinised olivine, < 45 % pargasite and < 7 % spinel. A small number of thin sections exhibit the gradational variation in modal mineral proportions described within individual layers on the outcrop-scale, with serpentinised olivine contents grading from < 5 % to > 35 % over one 3 cm long thin section. Pyroxene is 0.3 to 3 mm in diameter and exhibits anhedral, subhedral and euhedral forms, with orthopyroxene – the only ubiquitous silicate phase – commonly dominant over clinopyroxene (Fig. 3.6c-f). Larger pyroxene grains, which are typically between 1.0 and 1.6 mm in diameter, are commonly anhedral to subhedral. By contrast, smaller pyroxene, which is typically < 0.8 mm in diameter, are commonly subhedral and exhibit 120° triple junctions (Fig. 3.6d). Pargasite, which is < 4 mm in diameter, exhibits green-brown pleochroism and 120° triple junctions. Olivine in the Leathaid Domain is almost entirely replaced by serpentine, but un-serpentinised olivine remnants may constitute < 5 modal % in the Maldie Domain. Spinel is < 2 mm in diameter and subhedral to anhedral, while sulphides are anhedral to subhedral and < 0.12 mm in diameter.

Mafic rocks (Fig. 3.6g-h), including metagabbro garnet-metagabbro, garnet-amphibolite and amphibolite, comprise (in modal %): 5–70 % clinopyroxene, 15–60 % amphibole, < 30 % plagioclase, < 40 % garnet, < 10 % orthopyroxene and < 10 % quartz, with accessory ilmenite, spinel, magnetite and sulphides also present. There is significant variation in the modal mineral percentages across the range of mafic rocks, with clinopyroxene and amphibole the only ubiquitous silicate phases (Fig. 3.6g-h). Moreover, the mafic rocks exhibit a large degree of textural variability. Clinopyroxene are commonly subhedral, range from 0.5 to 2.0 mm in

diameter and show varying degrees of retrograde metamorphism to amphibole. This green-brown, pleochroic amphibole ranges from 0.5 to 1.0 mm in diameter and commonly displays evidence for textural equilibrium. Finer-grained (< 0.3 mm diameter), subhedral amphibole co-exists with similarly-sized plagioclase, forming centimetre-scale interstitial patches that are intergrown with subhedral to anhedral quartz < 0.1 mm in diameter (Fig. 3.6h). Plagioclase is most commonly 0.4 to 0.9 mm in diameter and subhedral. Millimetre- to centimetre-scale, anhedral to subhedral garnet porphyroblasts are commonly surrounded by retrogressive plagioclase rims and may also be overgrown by fine-grained clinopyroxene and/or amphibole (Fig. 3.6g). Anhedral magnetite is the dominant oxide phase and is < 0.3 mm in diameter. Rare ilmenite is anhedral and < 0.7 mm in diameter, while fine-grained sulphides (< 0.2 mm in diameter) are typically anhedral and associated with the boundaries between silicate minerals.

3.2.4 Spinel Mineral Chemistry

Spinels are routinely used as petrogenetic indicators due to their occurrence in a variety of magmatic, tectonic and metamorphic environments (Barnes and Roeder 2001). Their suitability for these studies is enhanced by the wide-range of conditions at which they crystallise (in ultramafic and mafic magmas) and resistance to alteration relative to other high-temperature minerals (e.g., olivine; Barnes and Roeder 2001). The ultramafic rocks of the Ben Strome Complex contain both primary and secondary spinel, with primary spinels occurring as euhedral to subhedral, < 2 mm diameter grains that comprise < 3 modal % of samples (Fig. 3.7). These pale- to dark-green (in ppl) grains, which experienced the polyphase high-grade metamorphism outlined above (up to granulite-facies), are most abundant in metapyroxenite samples (Fig. 3.6c-f; Fig. 3.7). Secondary spinels, which are the product of serpentinisation and are therefore abundant in serpentine-rich samples, occur as generally elongate, anhedral and opaque (in ppl and xpl) grains < 0.8 mm in length. In order to assess the petrogenetic environment of the Ben Strome Complex, 314 analyses were conducted on the cores of primary spinel grains from 7 metapyroxenite samples, using the A-SEM and methodology described in Appendix A. Two samples are from the well-exposed package of ultramafic rocks in the north of the Maldie Domain, with 5 samples from the Leathaid Domain (see Fig. 3.1a and Appendix C for sample locations). Four of the samples from the Leathaid Domain were collected from the outstanding exposure detailed in Fig. 3.2f, with all the data are available in Appendix C.

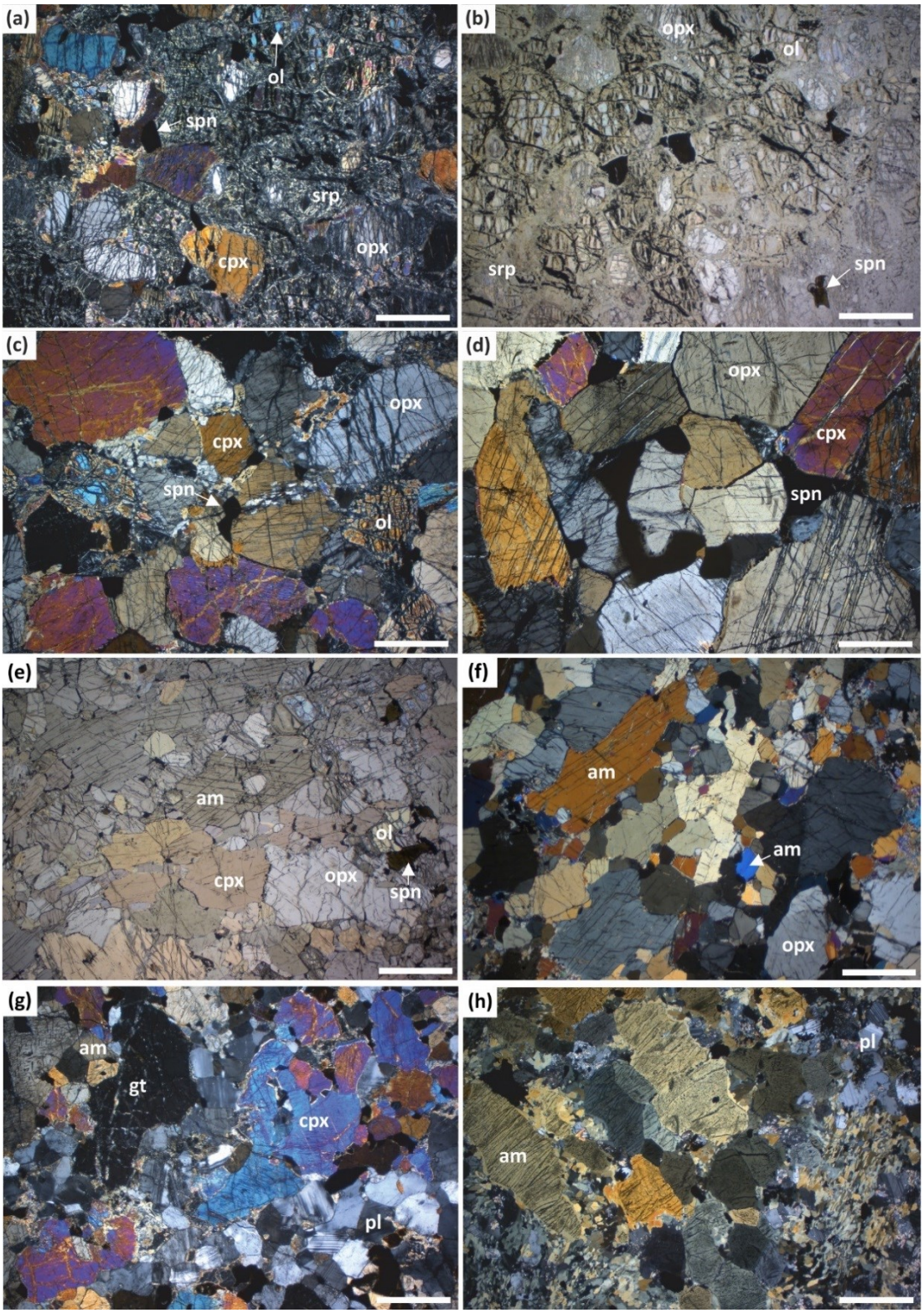

Figure 3.6: *Except (b) and (e), which are taken using PPL, photomicrographs are taken using XPL.* ***(a)*** *serpentinsed metalherzolite, including remnants of olivine.* ***(b)*** *Serpentinised metalherzolite, including remnants of olivine.* ***(c)*** *Metaolivine-websterite, including 120° triple junction grain boundaries.* ***(d)*** *Metawebsterite, including 120° triple junction grain boundaries.* ***(e)*** *Metaolivine-websterite.* ***(f)*** *Metaolivine-websterite.* ***(g)*** *Garnet-metagabbro.* ***(h)*** *Amphibolite, including finer-grained areas of plagioclase and amphibole. Abbreviations: srp=serpentine; am=amphibole; ol=olivine; cpx=clinopyroxene; opx=orthopyroxene; pl=plagioclase; spn=spinel; gt=garnet. White scale bar=1 mm.*

The chemistry of Ben Strome spinel has been assessed according to the key compositional parameters outlined by Barnes and Roeder (2001) and Warren (2016). Figure 3.8 compares the composition of Ben Strome spinels to those from layered intrusions, ophiolites and komatiites, alongside amphibolite-facies magnetite rims and those that nucleated during high-grade metamorphism. As with the Ben Strome spinels, which may have had their compositions altered slightly during high-grade metamorphism, the layered intrusion, ophiolite and komatiite fields of Barnes and Roeder (2001) contains spinels that have experienced metamorphism (of varying styles and grades). The Cr number (calculated as: molar Cr/[Cr+Al] x 100) of Ben Strome spinel range from 66.7 to 87.3, with Mg number (calculated as: molar Mg/[Mg+Fe^{2+}+Fe^{3+}] x 100) ranging from 0.8 to 3.4. The Fe^{2+} number (calculated as molar Fe^{2+}/[Fe^{2+}+Mg]) of Ben Strome spinel ranges from 0.9 to 1.0, the Fe^{3+} number (calculated as molar Fe^{3+}/[Cr+Al+Fe^{3+}]) ranges from 0.8 to 1.0 and all the TiO_2 contents are < 2.2 wt. % (Fig. 3.8).

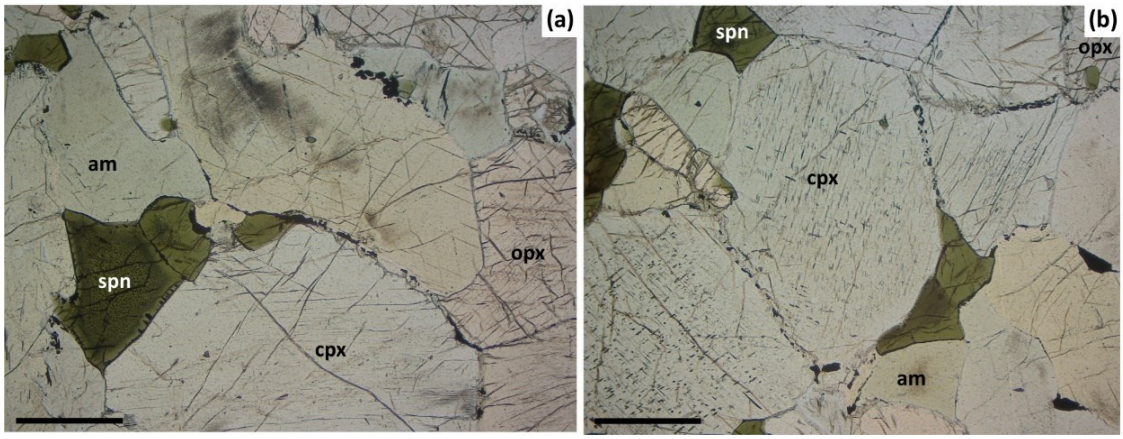

Figure 3.7: *Photomicrographs detailing representative spinel analysed in the metapyroxenites. Abbreviations: spn=spinel; cpx=clinopyroxene; opx=orthopyroxene; am=amphibole. Black scale bar=500 µm.*

The Ben Strome spinels are magnetites that show considerable overlap with the magnetite portions of the layered intrusion field on all plots detailed in Figure 3.8 (Barnes and Roeder 2001). By contrast, Ben Strome spinels are compositionally distinct from the ophiolites field (Barnes and Roeder 2001) on the Fe^{2+} number versus Fe^{3+} number plot, Fe^{3+} number versus TiO_2 plot and Fe^{3+}-Cr–Al ternary plot, although there is minor overlap with this field on the Fe^{2+} number versus Cr number plot (Fig. 3.8). Ben Strome spinels are compositionally distinct from the komatiite field on the Fe^{2+} number versus Fe^{3+} number plot, Fe^{3+} number versus TiO_2 plot and Fe^{3+}-Cr-Al ternary plot, although there is significant overlap on the Fe^{2+} number versus Cr number plot (Fig. 3.8). They are compositionally distinct from the high-grade metamorphic spinel field (Barnes and Roeder 2001) on Fe^{2+} number versus Fe^{3+} number plot

and Fe^{3+}-Cr-Al ternary plot, although there is significant overlap on the Fe^{2+} number versus Cr number plot (Fig. 3.8). Finally, Ben Strome spinel compositions are distinct from the amphibolite-facies magnetite rims field (Barnes and Roeder 2001) on the Fe^{2+} number versus Cr number plot and Fe^{3+}-Cr-Al ternary plot, with significant overlap on the Fe^{2+} number versus Fe^{3+}number plot (Fig. 3.8).

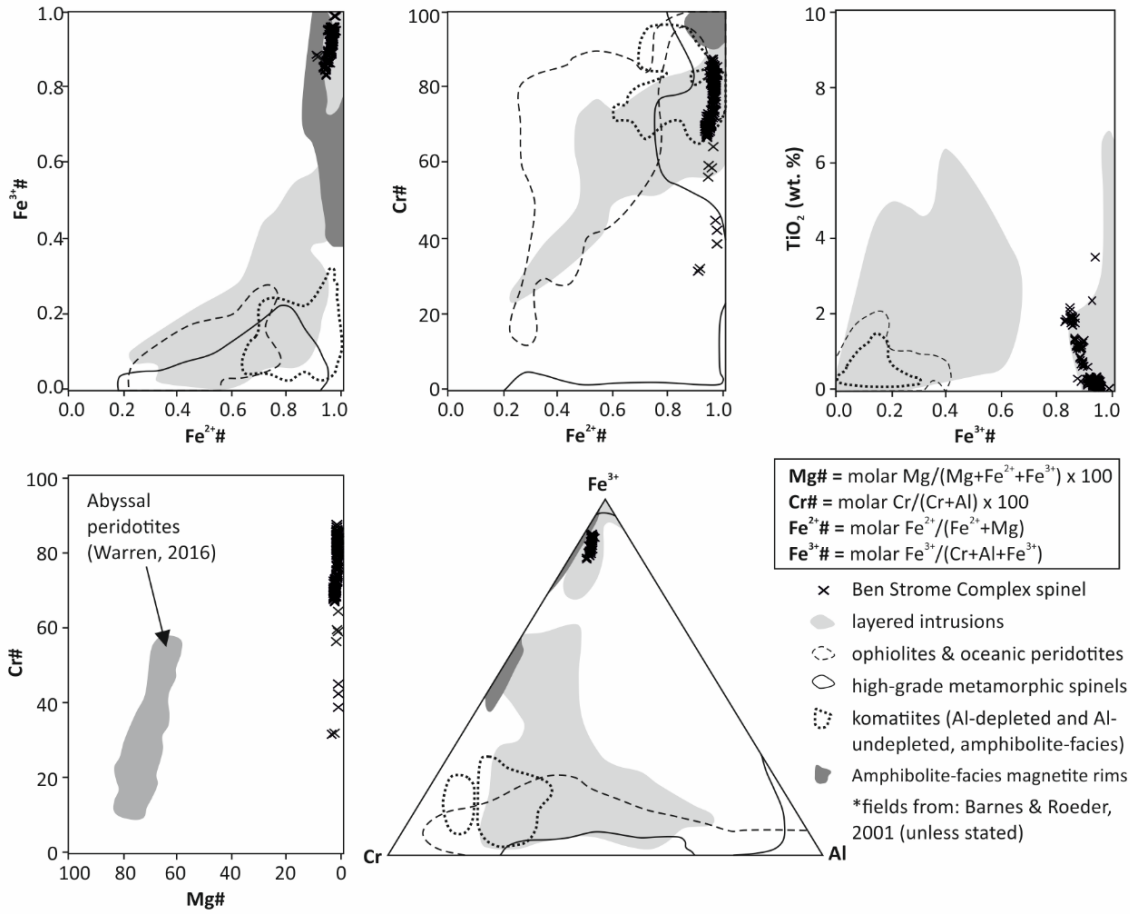

Figure 3.8: *Spinel compositions for the Ben Strome Complex. See Appendix C for the full dataset.*

3.3 The Geodh' nan Sgadan Complex

The 0.2 km^2 Geodh' nan Sgadan Complex represents the only reported occurrence of TTG gneiss cross-cutting mafic rocks in the LGC (Fig. 3.9; Rollinson and Windley 1980). Given its importance in informing the regional age relationships, this locality was re-mapped (Fig. 3.9a). Located 15 km NW of Ben Strome and ~1 km ESE of Badcall, Geodh' nan Sgadan is also located in the north of the Central Region (Fig. 2.3).

3.3.1 Field relationships

The Geodh' nan Sgadan Complex (Fig. 3.9a; Fig. 3.10) comprises a ~15 m thick package of layered mafic rocks structurally overlain and underlain by TTG gneiss. Layered ultramafic rocks like those observed in the Ben Strome Complex are notably absent (Fig. 3.9a). TTG

gneiss exhibits a well-defined gneissosity that is locally folded and contains centimetre to metre-scale pods of mafic and ultramafic rocks (Fig. 3.10a), which show elongation parallel to the gneissosity. Contacts between TTG gneiss and mafic rocks are sharp, with the layering in the mafic rocks parallel to TTG gneissosity (Fig. 3.9a). Both layering and gneissosity generally strike N-S to NE-SW and dip between 26 and 38° towards the W to NW (Fig. 3.9a). In the south of the mapped area, both felsic and mafic rocks are folded into NW-SE-striking orientations, where both units are truncated by a NE-SW-striking brittle fault (Fig. 3.9a; Fig. 3.10b).

Layering in the mafic rocks at Geodh' nan Sgadan is highlighted by a millimetre-scale variation in feldspar modal percentages and rare centimetre-scale layers of metapyroxenite (Fig. 3.10c). Relative to the Ben Strome Complex, mafic rocks are plagioclase-rich, with garnet-metagabbro restricted to rare, metre-scale horizons (Fig. 3.10d). Layering ranges from well-defined and laterally continuous to poorly-defined and chaotic, with common truncation of layers (Fig. 3.9e). Mafic rocks are extensively cross-cut by discordant felsic leucosomes (as identified by Johnson et al. 2013) that contain characteristic blue quartz and range from millimetre- to metre-scale (Fig. 3.9a-b; Fig. 3.10f-g). A metre-scale, layering-parallel sheet of massive trondhjemite is located towards the stratigraphic top of the package of mafic rocks (Fig. 3.9b; Fig. 3.10h).

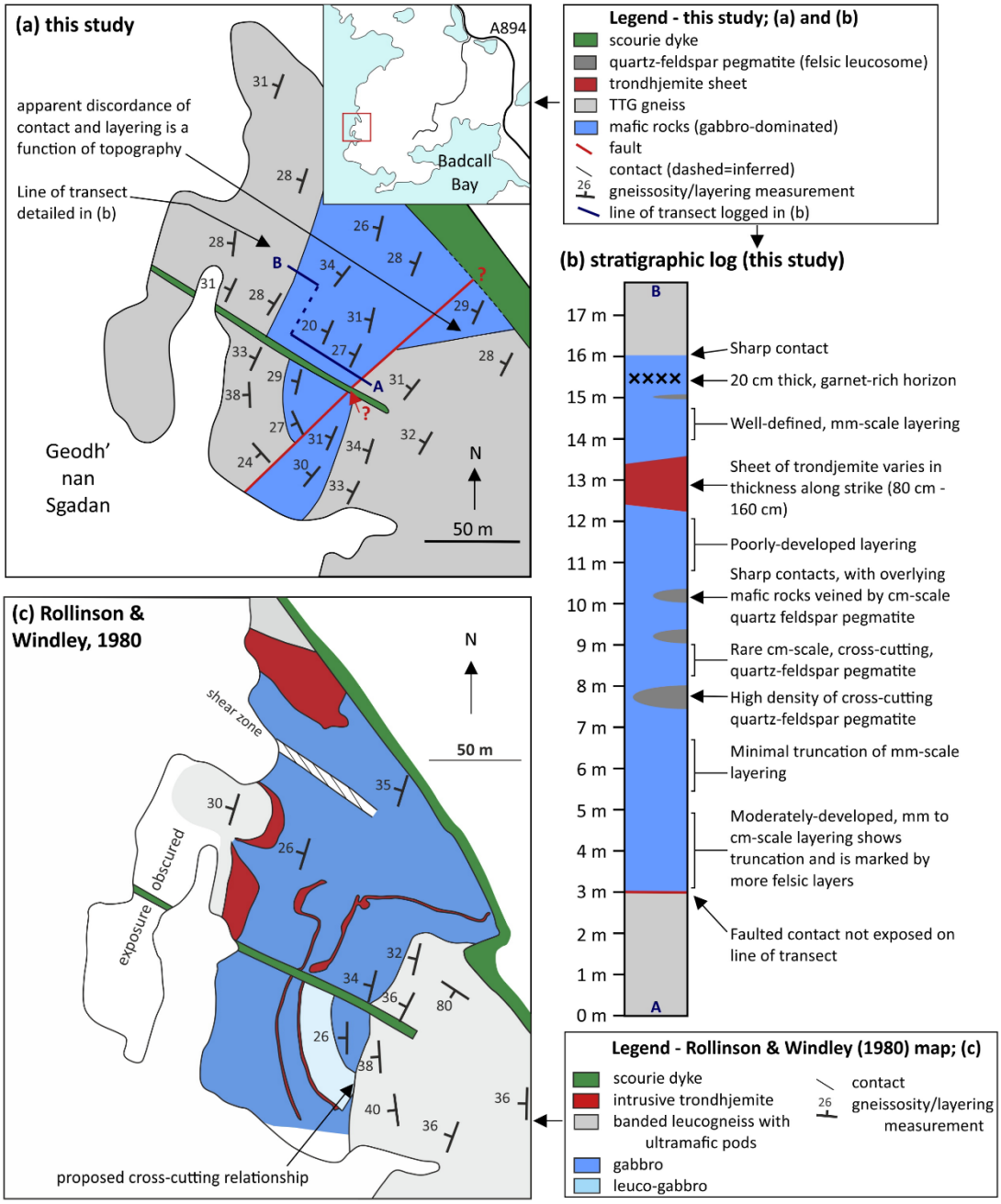

Figure 3.9: (a) *Simplified geological map of the Geodh' nan Sgadan locality (this study). Inset: location map, detailing the location relative to Badcall Bay and the A894 road.* ***(b)*** *Stratigraphic log from A to B (this study). Line of transect can be found on (a).* ***(c)*** *Geological map of the Geodh' nan Sgadan locality, redrawn after: Rollinson and Windley (1980).*

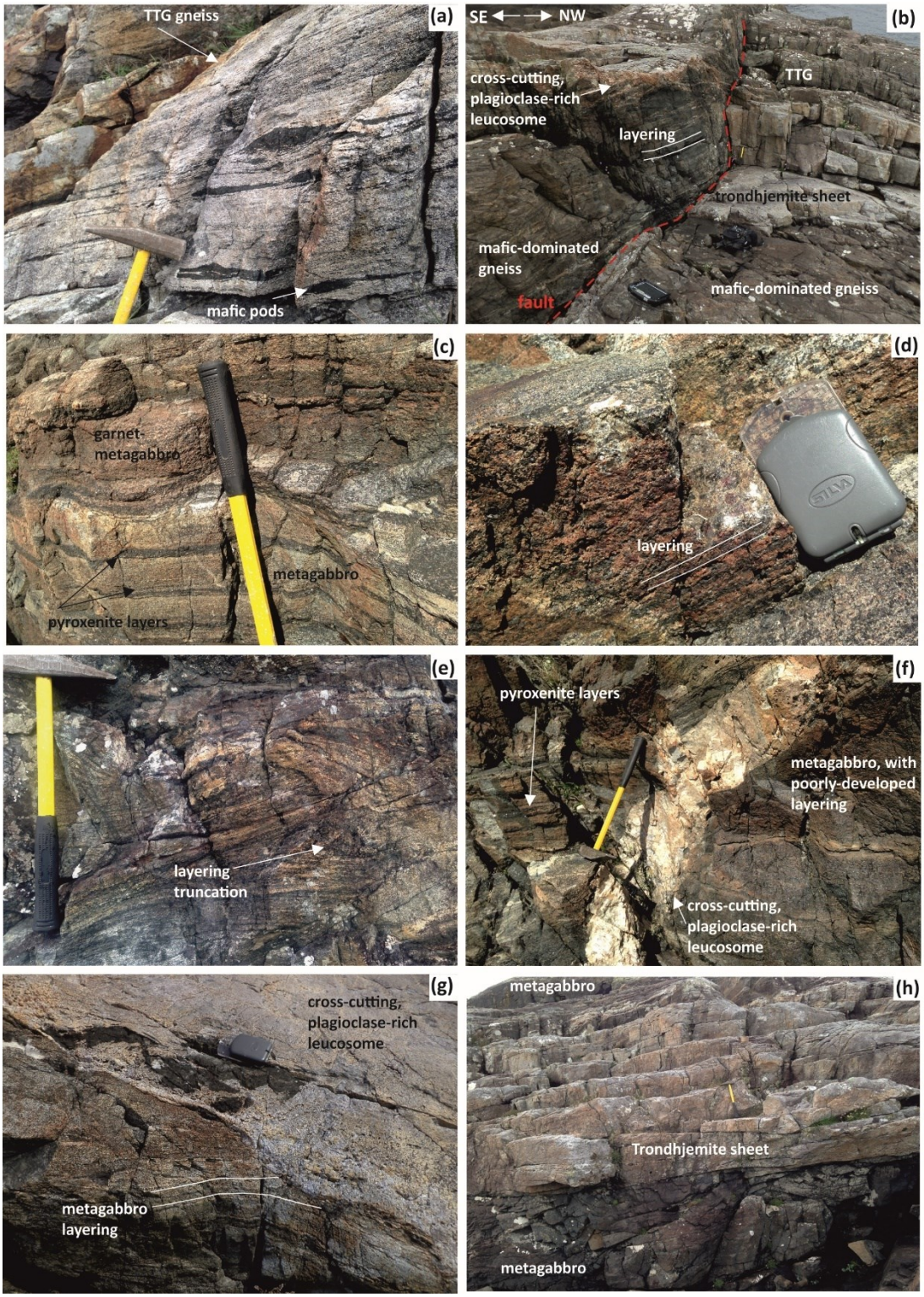

Figure 3.10: *Field photographs detailing the representative rock types and field relationships at the Geodh' nan Sgadan locality.* ***(a)*** *TTG gneiss containing mafic pods.* ***(b)*** *Juxtaposition of mafic rocks and TTG gneiss by fault.* ***(c)*** *Well-defined layering marked by centimetre-scale layers of metapyroxenite in metagabbro.* ***(d)*** *Centimetre-scale garnet-metagabbro layer.* ***(e)*** *Poorly-developed layering in metagabbro, with some truncation of layers.* ***(f)*** *Plagioclase-rich leucosome cross-cutting poorly-developed layering in metagabbro.* ***(g)*** *Plagioclase-rich leucosome cross-cutting subtly layered metagabbro.* ***(h)*** *1.5 m thick sheet of trondhjemite. Yellow hammer length=40 cm; yellow hammer head width=17 cm; compass clinometer length=10 cm.*

3.3.2 Comparison to the previously published map

The map and associated log presented in this study (Fig. 3.9a-b) display some key differences to the map published by Rollinson and Windley (1980; Fig. 3.9c). Although minor differences result from respective mapping styles, it is necessary to here clarify the major differences. First, Rollinson and Windley (1980; Fig. 3.9c) subdivided the mafic rocks into separate leucogabbro and gabbro units, whereas the map presented here groups all of these rocks into a unit of "mafic rocks" (Fig. 3.9a-b). The significant lithological variability within this unit is also recognised here, but no systematic spatial variability is identified, with the lithological variation therefore presented in log form (Fig. 3.9b). Second, the map presented in this study identifies a NE-SW-trending fault that truncates both the layering in the mafic rocks and gneissosity in the TTG gneiss (Fig. 3.9a). The presence of this fault, which exhibits a strike consistent with regional faulting patterns (BGS 2011), is not shown by the map of (Rollinson and Windley 1980; Fig. 3.9c), who reported that "layering in the gabbro is truncated by tonalitic gneiss indicating that the gabbro complexes…are older than the tonalitic gneisses". Third, the intrusive trondhjemite recorded by Rollinson and Windley (1980; Fig. 3.9c) is represented on the log presented in this study (Fig. 3.9b), instead of the map, as a result of it occupying less than 1 m in plan view and exhibiting variable thickness. (Fig. 3.9a). Finally, the scale of the log presented in this study (Fig. 3.9b) allows for the inclusion of the cross-cutting quartz-feldspar pegmatites omitted from the maps published both here and by Rollinson and Windley (1980).

3.3.3 Petrography

Although the samples exhibit a small degree of textural variability, all samples can be broadly classified as metagabbro (Fig. 3.11). Samples comprise (in modal %): 15 to 60 % amphibole, < 75 % feldspar, < 20 % clinopyroxene and < 5 % orthopyroxene, with rare < 0.3 mm diameter sulphides. It should also be noted that rare orthpyroxene-rich layers are present, but were not sampled. Clinopyroxene generally occurs as 0.2 to 0.6 mm diameter, subhedral to euhedral grains that exhibit some alteration to fine-grained amphibole (Fig. 3.11), with such alteration commonly forming thick (< 0.1 mm) rims (Fig. 3.11a). Amphibole also occur as subhedral grains that exhibit 120° triple junctions and range from 0.2 to 0.5 mm in diameter (Fig. 3.11a-b). Feldspar (dominantly plagioclase, with subordinate alkali-feldspar) are generally subhedral and 0.4 to 0.6 mm in diameter, with occasional triple junctions and variable replacement by amphibole (Fig. 3.11). Orthopyroxene is generally subhedral and < 0.3 mm in diameter (Fig. 3.11d). These plagioclase, orthopyroxene and clinopyroxene grains are surrounded by a fine-grained groundmass of amphibole (Fig. 3.11).

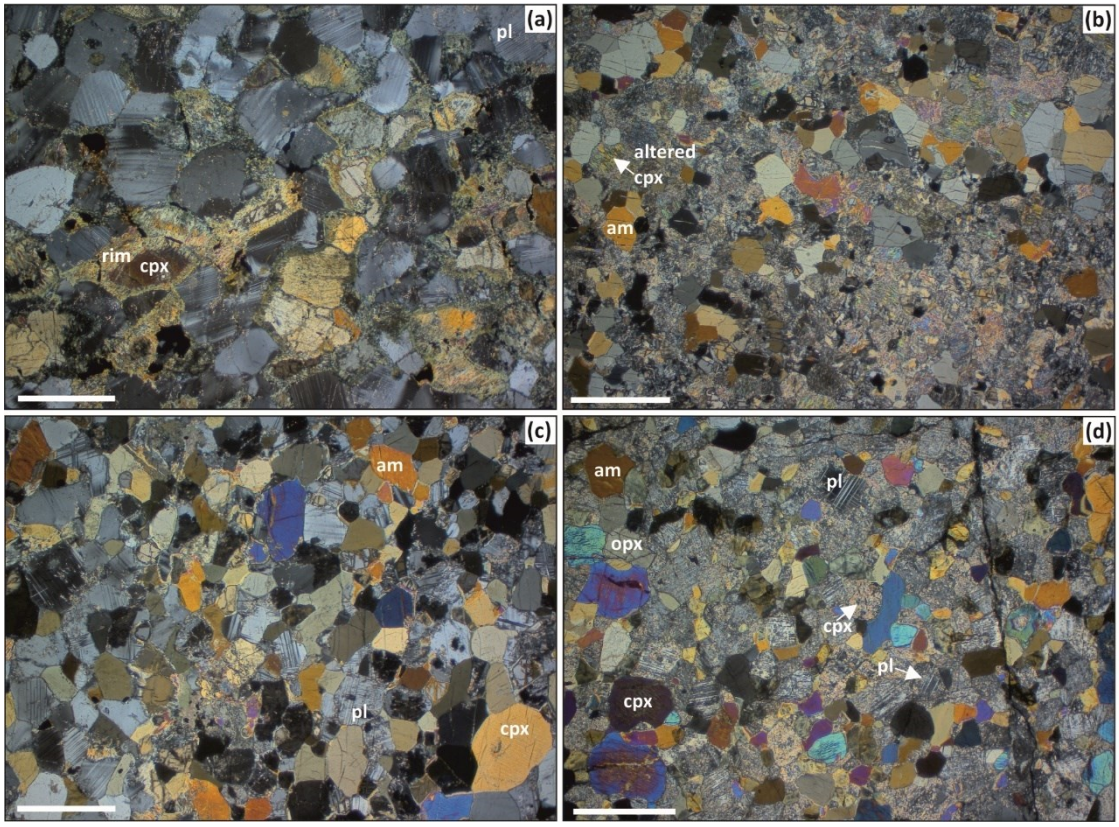

Figure 3.11: *Representative photomicrographs detailing the petrographic characteristics of the Geodh' nan Sgadan mafic rocks. All photomicrographs are taken using crossed-polarised light.* ***(a)*** *metagabbro, including thick rims of amphibole surrounding clinopyroxene.* ***(b)*** *metagabbro containing near-complete alteration of clinopyroxene to amphibole.* ***(c)*** *metagabbro containing relatively large, unaltered clinopyroxene and plagioclase.* ***(d)*** *metagabbro, including partial alteration of plagioclase. Abbreviations: cpx=clinopyroxene; opx=orthopyroxene; pl=plagioclase. White scale bar=1 mm.*

3.4 Discussion

3.4.1 Ben Strome and Geodh' nan Sgadan: evidence for multiple ultramafic-mafic suites in the LGC?

The Ben Strome Complex shares many of its salient features with ultramafic-mafic complexes described elsewhere in the LGC, such as those at Scouriemore, Drumbeg and Achiltibuie (Fig. 3.1; O'Hara 1961, Bowes et al. 1964, Sills 1981, Sills et al. 1982, Johnson et al. 2012):

1. Ultramafic and mafic rocks occur in a roughly 1:2 ratio, with the ultramafic portions generally found at the structural base of the complex, although this association is not ubiquitous (Fig. 3.1; e.g., O'Hara 1961, Bowes et al. 1964, Sills et al. 1982, Goodenough and Krabbendam 2011, Johnson et al. 2012, 2016).
2. The ultramafic portions of the complex exhibit distinctive millimetre to metre-scale layering with distinctive (often gradational) changes in modal silicate mineralogy and lithology. This layering, despite experiencing high-grade metamorphism, is very similar to that observed in layered intrusions globally, is laterally continuous across

entire ultramafic packages (Figs. 3.1-3.2; Bowes et al. 1964, Sills 1981, Sills et al. 1982, Johnson et al. 2012).

3. The mafic portions of the Ben Strome Complex are heterogeneous, garnet and clinopyroxene-rich, and exhibit garnet retrogression to plagioclase and orthopyroxene (± amphibole and magnetite; Sills 1981, Johnson and White 2011).
4. Despite being tightly folded (along with the adjacent TTG gneiss; Fig. 3.4; Bowes et al. 1964), magmatic layering in the Ben Strome Complex is consistently parallel with both the TTG gneissosity and margins of the complex (Fig. 3.1; Bowes et al. 1964, Sills 1981, Johnson et al. 2012, 2016). There is consistent parallelism between the TTG gneissosity, and magmatic layering in the ultramafic portions of the Ben Strome Complex. The presence of slickensides and, in some cases, recrystallised quartz at ultramafic-TTG gneiss contacts, indicate that these ultramafic slivers experienced polyphase shearing along the contacts of the Ben Strome Complex.

The Ben Strome Complex is considered to represent the largest (by an order of magnitude) example of a layered ultramafic-mafic complex in the Central Region LGC, displaying salient features directly comparable to the exposures at Scouriemore, Drumbeg and Achiltibuie (e.g., Sills 1981, Sills et al. 1982, Sills 1982, Rollinson and Gravestock 2012). Given its larger size and excellent exposure, the Ben Strome Complex provides crucial evidence pertaining to the genesis of such layered ultramafic-mafic complexes (see Section 3.4.2.1).

By contrast, the Geodh' nan Sgadan Complex represents a small occurrence of mafic rocks in the LGC that displays a number of characteristics notably distinct from those reported for the Ben Strome Complex:

1. Geodh' nan Sgadan does not contain the distinctly layered ultramafic rocks that characterise the ultramafic-mafic complexes at Ben Strome, Scouriemore, Achiltibuie and Drumbeg (this study; Sills 1981; Rollinson and Gravestock 2012).
2. The mafic rocks consistently exhibit prominent millimetre-scale layering defined by variation in plagioclase modal percentages (Fig. 3.10) that is not recorded at other ultramafic-mafic complexes in the LGC.
3. The garnet-rich mafic rocks that characterise the Ben Strome, Scouriemore, Drumbeg and Achiltibuie Complexes are restricted to rare, centimetre-scale horizons at Geodh' nan Sgadan (this study; Sills 1981).
4. The mafic rocks at Geodh' nan Sgadan are comparatively plagioclase-rich (< 75 modal %) and fine-grained, with clinopyroxene and plagioclase typically 200 to 400 µm in diameter. By contrast, plagioclase always comprises < 30 modal % of mafic rocks at

Ben Strome and clinopyroxene/plagioclase crystals range from 0.4 to 2.0 mm diameter. Moreover, alkali-feldspar occurs rarely at Geodh' nan Sgadan, but is completely absent in the Ben Strome mafic rocks.

Further to being truncated by multiple Scourie Dykes, the Geodh' nan Sgadan Complex displays multiple features characteristic of the Badcallian metamorphic event, including: a moderate-dipping gneissosity in the TTG gneisses surrounding the complex; granoblastic textures within the mafic rocks; and the presence of quartz-feldspar pegmatite (derived from partial melting; Johnson et al. 2013). The Geodh' nan Sgadan Complex therefore experienced the same broad metamorphic history as the Ben Strome Complex, with the contrasting features outlined above considered to be predominantly the result of primary processes. Although these differences may be explained by faulting exposing different stratigraphic levels in one ultramafic-mafic sequence (as proposed by Johnson et al. 2016), there exists the possibility that there may be more than one suite of ultramafic-mafic complexes in the LGC, as initially proposed by Rollinson and Gravestock (2012). The Geodh' nan Sgadan Complex may be petrogenetically unrelated to some of the other ultramafic-mafic complexes in the LGC, where layered ultramafic rocks are characteristically accompanied by garnet-rich mafic rocks (e.g., Ben Strome, Scouriemore, Drumbeg and Achiltibuie). Our field observations add to growing evidence (including the mineral chemistry of Rollinson and Gravestock 2012) for a scenario whereby the LGC records more than one phase of Archaean mafic and/or ultramafic-mafic magmatism prior to the Badcallian metamorphic event. This underlines the possibility that high-grade metamorphic events, such as the Badcallian in the LGC, may obscure temporally and/or petrogenetically distinct magmatic events, as may be typical in marginal cratonic regions (such as the LGC, within the wider NAC). This supports the study of Kolb et al. (2015), who identified multiple episodes of Archaean ultramafic-mafic magmatism in the Greenlandic portion of the NAC.

3.4.2 Origin of ultramafic-mafic complexes in the LGC

3.4.2.1 Ben Strome Complex

The observations reported in this study reveal that the Ben Strome Complex exhibits a range of features that are consistent with and characteristic of layered intrusions (Irvine 1982, Namur et al. 2015), such as: (i) laterally continuous igneous layering (Fig. 3.2a-c, e-f); (ii) gradational contacts between ultramafic and mafic units (Fig. 3.2a); (iii) gradational contacts between centimetre to metre-scale metaperidotite and metapyroxenite layers (Fig. 3.2f); (iv) existence of multiple ultramafic units within one continuous stratigraphic sequence (e.g., in the Maldie Domain; Fig. 3.1a,d), which may represent multiple megacyclic units; (v)

occasional truncation of layers within ultramafic units; and (vi) gradational variation in mineral composition within individual ultramafic layers on a scale of tens of centimetres. These field observations are consistent with the composition of spinel, which consistently correspond with the magnetite portion of the layered intrusion field (Fig. 3.8). By contrast, spinel compositions are distinct from both the komatiite and ophiolite/oceanic peridotite fields (Fig. 3.8). These data contradict the accreted oceanic crust hypothesis for the genesis of such ultramafic-mafic complexes in the LGC of Park and Tarney (1987). Johnson et al. (2016) invoked the sagduction hypothesis (whereby remnants of greenstone belts sank into partially molten TTG) to explain the spatial association between brown gneisses, which may represent metasedimentary rocks, and some of the layered ultramafic-mafic complexes (notably in the Laxford Shear Zone). The composition of spinel and distinct absence of metasedimentary rocks or demonstrably metamorphosed extrusive units (common components of Archaean greenstone belts (e.g., Brandl et al. 2006) within the Ben Strome Complex is contrary to this interpretation. Consequently, this paradigm, whereby the Ben Strome Complex (and associated layered ultramafic-mafic complexes in the LGC; e.g., Achiltibuie and Drumbeg) represents a layered intrusion, is considered to be more compatible with the data presented here.

Identification of the Ben Strome Complex as a layered intrusion does not, however, solve the crucial age relationship problem. Was the Ben Strome Complex emplaced into an early mafic-ultramafic crust that was subsequently invaded by TTG magmas – a model similar to the pre-TTG mafic-ultramafic crust hypothesis of Sills (1981) – or, alternatively, was it emplaced into TTG gneiss protoliths? Although the Ben Strome Complex demonstrably pre-dates the Badcallian metamorphic event, it is unclear whether the intrusion pre- or post-dates the development of the S1 gneissosity. One speculative possibility, which satisfies the consistent parallelism between S1 gneissosity and magmatic layering in the Ben Strome Complex, is that the S1 gneissosity was developed prior to the intrusion of Ben Strome. In this scenario, the S1 gneissosity may have facilitated the emplacement of the Ben Strome Complex as a sill-shaped intrusion in a manner similar to bedding-parallel sills. Alternatively, the rheology contrast between the ultramafic-mafic rocks of the Ben Strome Complex and surrounding TTG gneiss could have facilitated S1 development in the latter, but not the former. This could also have generated the consistent parallelism between the S1 gneissosity and magmatic layering, regardless of the relative age relationship.

Sills (1981) argued that the seemingly chaotic distribution of the ultramafic-mafic complexes amongst the TTG gneiss is evidence for the pre-TTG mafic-ultramafic crust model. Such a

distribution is evident in the west of the Leathaid Domain at Ben Strome, where slivers of ultramafic and mafic rocks are surrounded by TTG gneiss (Fig. 3.1a). In this area, individual slivers are up to 40 m thick, extend for up to 750 m along strike and occasionally exhibit tight F2 folds. However, this distribution may also be explained by polyphase shearing along lithological contacts, which is an interpretation supported by the observed field evidence involving slickensides and recrystallised quartz at exposed contacts between ultramafic rocks and TTG gneiss. Based on the F2 folding of ultramafic slivers in the NW of the Ben Strome Complex (Fig. 3.1), such shearing – if indeed responsible for the observed outcrop patterns – must have initially preceded the major folding events that affected the Ben Strome Complex, with the subsequent reactivation during the LGC's protracted and polyphase metamorphic history responsible for the preservation of slickensides.

If the Ben Strome Complex was not emplaced into TTG gneiss, what did it intrude and where is that material now? This question represents the biggest conceptual predicament associated with any interpretation that requires that the Ben Strome Complex preceded the TTG magmas. In the Johannesburg Dome, the Zandspruit ultramafic-mafic complex – an Archaean layered intrusion that was emplaced into a greenstone belt and subsequently invaded by TTG magmas – preserves evidence of the metavolcanic rocks that it intruded, despite the exposed intrusion and intruded greenstone belt covering a combined area of less than 1 km^2 (Anhaeusser 2015). Similarly, the granulite-facies Fiskenæsset Complex (Greenland, NAC), which comprises a series of arc-related, intrusive sills, preserves evidence for the extrusive units intruded by those sills (Polat et al. 2009). By contrast, the Ben Strome Complex and surrounding TTG gneiss preserve no evidence for any material that the magmas could have conceivably been emplaced into (other than the surrounding TTG gneiss). The small ultramafic-mafic pods that are distributed throughout the LGC represent the obvious candidates, but these pods are exceptionally rare in the TTG gneiss surrounding the Ben Strome Complex. By contrast, granulite-facies ultramafic-mafic complexes that have been unambiguously invaded by TTG magmas in the Greenlandic portion of the NAC, namely Seqi and Fiskenæsset, exhibit a high concentration of ultramafic-mafic pods at their margins (Polat et al. 2009, Bagas et al. 2016, Szilas et al. 2018). At Seqi, these pods occur as elongate lenses of amphibolite that are up to 40 m long and 25 m wide (Szilas et al. 2018). Consequently, it is considered extremely unlikely that the rare ultramafic-mafic pods found in TTG gneiss throughout the Central Region of the LGC represent small fragments of crust that the Ben Strome Complex intruded prior to being invaded by TTG magmas.

In summary, given the absence of unambiguous evidence supporting the interpretation whereby the Ben Strome Complex predates the surrounding TTG gneiss, a simple model is proposed, whereby the Complex was emplaced *into* the TTG gneiss that constitutes the bulk of the LGC.

3.4.2.2 Geodh' nan Sgadan Complex

In contrast to the Ben Strome Complex, the origin of the Geodh' nan Sgadan Complex remains harder to establish. The presence (albeit at a low abundance) of alkali-feldspar and high modal percentages of plagioclase in the Geodh' nan Sgadan rocks indicate that this occurrence crystallised from more felsic magmas than those of the Ben Strome Complex. However, the lack of primary spinel within these rocks prevents any quantitative petrogenetic comparison to the Ben Strome Complex. The previously reported, map-scale crossing cutting relationship of Rollinson and Windley (1980) is challenged by the evidence for a tectonic contact identified in this study (Fig. 3.9a; Fig. 3.10b) and it remains uncertain whether the complex pre- or post-dates the TTG magmas. This age relationship hinges on the genetic association between the trondhjemite sheets and surrounding TTG gneiss. Are these sheets, which intrude into the Geodh' nan Sgadan Complex (as originally suggested by Rollinson and Windley, 1980), associated with the initial emplacement of the TTG magmas or, alternatively, are they the product of Badcallian partial melting? While the field descriptions of the trondhjemite sheets hint at a partial melting origin (Johnson et al. 2013), the relatively high concentration of mafic pods located close to the margin of the complex may hint that these mafic rocks were invaded and fragmented by the TTG gneiss protoliths. In summary, in the case of Geodh' nan Sgadan, it is not possible to definitively comment on whether these mafic rocks pre- or post-date the TTG gneiss and consequently, the petrogenesis of this small complex remains enigmatic.

3.4.2.3 Wider context and future work

Largely as a consequence of uncertain age relationships, which commonly introduces significant ambiguity to Archaean geodynamic interpretations, the ultramafic-mafic complexes of the LGC have been subject to wide-ranging interpretations. As detailed in Figure 3.12, these hypotheses have disparate implications for interpretations of Archaean geodynamic regime(s), both in the wider NAC and Archaean cratons globally. The sagduction hypothesis of Johnson et al. (2016), which involves fragments of Archaean greenstone belts sinking into partially molten TTG (Fig. 3.12), supports the vertical tectonics view of the Archaean Earth. By contrast, the accreted oceanic crust hypothesis of Park and Tarney (1987),

which envisages the complexes as representing oceanic crust that was obducted during modern-style subduction processes (Fig. 3.12), supports the horizontal tectonics view of the Archaean Earth. The interpretation proposed in this study – whereby the layered ultramafic-mafic complexes in the LGC represent deformed layered intrusions (see Section 3.4.2.1) – may be applicable to a number of geodynamic environments (Fig. 3.12). Some of these environments are specific to horizontal tectonics (e.g., subduction and mid-ocean-related magmatism), while others can be applied to both horizontal and vertical tectonics (e.g., plume-related magmatism; Fig. 3.12). The present study of the Ben Strome Complex highlights how identification of relative age relationships can greatly enhance interpretations of ultramafic-mafic complexes in Archaean cratons. This is reinforced by the study of the Geodh' nan Sgadan Complex, where relative age relationships remain unclear and, consequently, the geological and geodynamic environments within which it formed remains enigmatic. Thus, only by a rigorous field campaign, through structural understanding and petrographic investigation may future geochemical studies be successful in investigating the geodynamic environments within which ultramafic-mafic complexes formed. Such studies may reveal the extent to which interpretations from the Ben Strome Complex can be extended to other ultramafic-mafic complexes in the LGC and wider NAC. Indeed, a thorough debate on the timing of the formation of such complexes, on a case-by-case basis, is crucial in order to apply geochemistry meaningfully to high-grade cratonic regions.

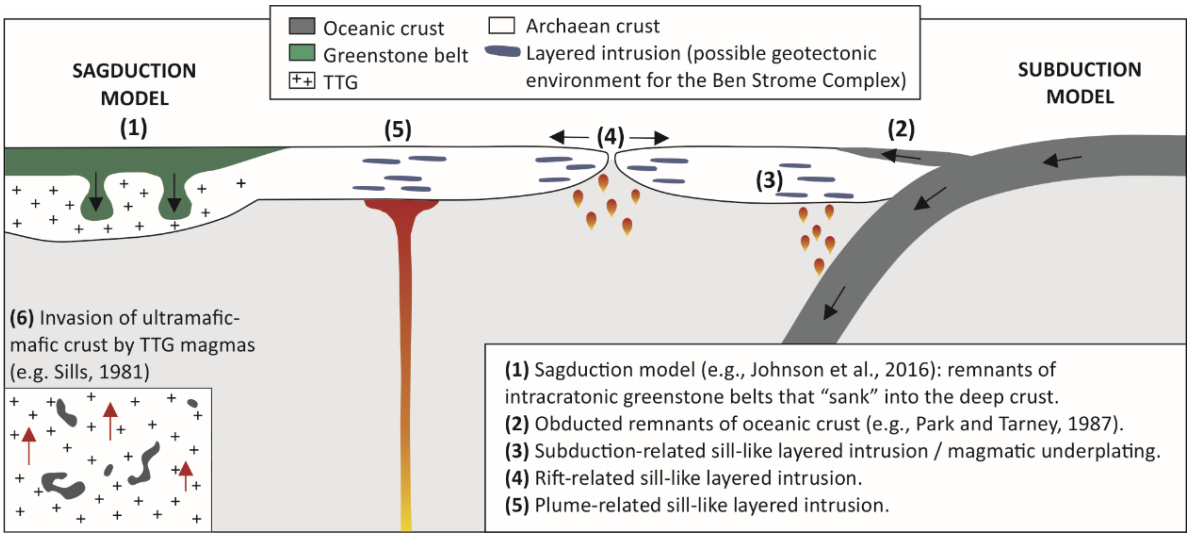

Figure 3.12: *Schematic diagram detailing the geotectonic environments potentially responsible for forming the various ultramafic-mafic components of the LGC.*

3.5 Conclusions

1. As a result of ambiguous field relationships and a scarcity of minerals suitable for geochronology, ultramafic-mafic complexes in Archaean cratons commonly exhibit unclear relative age relationships with the surrounding rocks. As a consequence, interpretations of ultramafic-mafic complexes are diverse and have disparate implications for Archaean geodynamic regimes. By applying an Ockham's Razor approach to the previously unstudied Ben Strome Complex, which represents the largest ultramafic-mafic complex in the LGC, it is concluded that it represents a layered intrusion emplaced *into* the surrounding TTG gneiss. Conversely, the origin of the Geodh' nan Sgadan Complex remains enigmatic as a consequence of its unclear age relationships with surrounding TTG gneiss.
2. The Ben Strome Complex shares salient features with the ultramafic-mafic complexes at Scouriemore, Drumbeg and Achiltibuie, which may represent genetically-related layered intrusions that were also emplaced into the TTG gneiss. This interpretation represents a significant re-evaluation of the magmatic evolution of the LGC, but is not specific to any particular geodynamic regime (e.g., horizontal or vertical tectonics) having operated during the Archaean.
3. High-grade metamorphic processes may mask temporally/petrogenetically distinct phases of crustal growth recorded by suites of ultramafic-mafic complexes in Archaean cratons. Rather than all ultramafic-mafic complexes in cratons representing singular events, it is highly likely that the portions of Archaean crust, such as that represented by the LGC, experienced multiple phases of ultramafic and/or mafic magmatism during the Meso- and Neo-Archaean – geological eras that, combined, span 700 Ma. In the LGC, this is exemplified by the disparate salient features of the Ben Strome and Geodh' nan Sgadan Complexes, which are here considered to be petrogenetically unrelated.

Chapter 4

Assessing the validity of negative high field strength element anomalies as a proxy for Archaean subduction: Evidence from the Ben Strome Complex, NW Scotland

This chapter is based upon the following published paper:

George L. Guice, Iain McDonald, Hannah S. R. Hughes, Denis M. Schlatter, Kathryn M. Goodenough, John M. MacDonald, John W. Faithfull. (2018) Assessing the Validity of Negative High Field Strength-Element Anomalies as a Proxy for Archaean Subduction: Evidence from the Ben Strome Complex, NW Scotland. *Geosciences,* **8** (9), 338.

Author contributions and declarations:

G.L.G. conceived of and conceptualised the contents of the chapter, wrote the chapter, carried out sampling of the Ben Strome Complex, and conducted all A-SEM work, petrographic assessments, sample preparation for bulk-rock geochemistry and LA-ICP-MS data collection. I.McD., H.S.R.H., D.M.S., K.M.G., J.M.M. and J.W.F. were all involved in discussions during the writing of the manuscript, and contributed to developing the hypothesis for the origin of the HFSE anomalies in the Ben Strome Complex. I.McD. was responsible for bulk-rock analysis by ICP-OES and ICP-MS, and for supervision during LA-ICP-MS data collection. J.M.M., H.S.R.H. and J.W.F. contributed to fieldwork prior to and during G.L.G.'s fieldwork in 2016 and 2017.

Abstract

The relative depletion of HFSE, such as Nb, Ta and Ti, on normalised trace element plots is a geochemical proxy routinely used to fingerprint magmatic processes linked to Phanerozoic subduction. This proxy has increasingly been applied to ultramafic-mafic units in Archaean cratons, but as these assemblages have commonly been affected by high-grade metamorphism and hydrothermal alteration/metasomatism, the likelihood of element mobility is high relative to Phanerozoic examples. To assess the validity of HFSE anomalies as a reliable proxy for Archaean subduction, their origin in ultramafic rocks from the Ben Strome Complex – a 7 km^2 ultramafic-mafic complex in the Lewisian Gneiss Complex of NW Scotland – is here investigated. Interpreted as a deformed layered intrusion, the Ben Strome Complex has been subject to multiple phases of high-grade metamorphism, including separate granulite- and amphibolite-facies deformation events. Additional to bulk-rock geochemistry, detailed petrography, and major and trace element mineral chemistry is presented for 35 ultramafic samples, of which 15 display negative HFSE anomalies. Our data indicate that the magnitude of HFSE anomalies in the Ben Strome Complex are correlated with LREE enrichment likely generated during interaction with H_2O and CO_2-rich hydrothermal fluids associated with amphibolitisation, rather than primary magmatic (subduction-related) processes. Consequently, bulk-rock HFSE anomalies alone are considered to be an unreliable proxy for Archaean subduction in Archaean terranes that have experienced multiple phases of high-grade metamorphism, with a comprehensive assessment of element mobility and petrography a minimum requirement prior to assigning geodynamic interpretations to bulk-rock geochemical data.

4.1 Introduction

Geochemical fingerprinting, which commonly involves plotting immobile element ratios on bivariate and ternary diagrams, can aid discrimination between Phanerozoic tectonic environments (Pearce and Cann 1973, Condie 2005, Pearce 2008). One such proxy, which involves the relative depletion of HFSE (e.g., Nb, Ta, Zr, Hf and Ti) on normalised trace element plots (Fig. 4.1; herein referred to as the 'HFSE anomaly'), is commonly used to identify Phanerozoic arc magmas (Klemme et al. 2005). Despite being widely used as evidence for subduction-related magmatism, application of the HFSE anomaly requires caution, as it can also be generated by alternative mechanisms, such as crustal contamination (Arndt 1999) or via interaction with the SCLM (Pearce 2014). Moreover, several authors have demonstrated that the HFSE and REE, which are crucial for geochemical fingerprinting (as they are commonly assumed to be immobile), can be mobilised during some types of hydrothermal alteration and metasomatism (Wood 1990, Lee and Byrne 1993, Rudnick et al. 1993, Lahaye et al. 1995, Smith et al. 2000, Rolland et al. 2003, Powell et al. 2004), leading to further scepticism of HFSE anomalies as a reliable subduction proxy.

Use of HFSE anomalies as supporting evidence for subduction-related magmatism has been extended to suites of mafic-ultramafic volcanic and/or plutonic rocks in several Archaean cratons over the last two decades (e.g., Manya 2004, Ordóñez-calderón et al. 2009, Manikyamba and Kerrich 2011, Yellappa et al. 2012, Szilas et al. 2013, Wang et al. 2015, Guo et al. 2017). Figure 4.1 details primitive mantle-normalised trace element patterns for selected Archaean assemblages attributed to subduction-related magmatism in several Cratons. When compared with those from the Phanerozoic Aeolian arc, these Archaean examples often display relatively flat trace element patterns and larger ranges in normalised abundances (as shown by Fig. 4.1a,b), although other examples are more comparable to Phanerozoic patterns (e.g., Fig. 4.1c). Given the implications that subduction-related interpretations have for Archaean geodynamic interpretations and the evolution of the early Earth (see Section 1.1 for a comprehensive summary), assessing the reliability of the HFSE anomaly as a viable fingerprint of Archaean subduction is of critical importance.

To assess the validity of HFSE anomalies as a reliable proxy for Archaean subduction, the origin of those displayed by well constrained and characterised ultramafic samples from the Ben Strome Complex of the LGC are here examined (see Chapter 3 for full details). Located on the northwest Scottish mainland, the Ben Strome Complex is an ultramafic-mafic complex that covers 7 km^2 and has been subject to multiple phases of high-grade metamorphism. Although the precise age of the Ben Strome Complex is ambiguous, it is interpreted as

representing a deformed layered intrusion that was emplaced into TTG gneiss between 3.0 and 2.7 Ga (Chapter 3), with the ultramafic and mafic rocks representing metamorphosed cumulates. Bulk-rock geochemistry, detailed petrography and mineral chemistry is presented for a suite of ultramafic rocks, which, unlike local mafic, intermediate and felsic lithologies, have not experienced partial melting (Johnson et al. 2012, 2013; Chapter 3). After discussing bulk-rock geochemical controls and the origin of the HFSE anomalies in the Ben Strome ultramafic rocks, the implications for geochemical fingerprinting of ultramafic-mafic units in Archaean cratons is outlined, alongside element mobility associated with high-grade metamorphism.

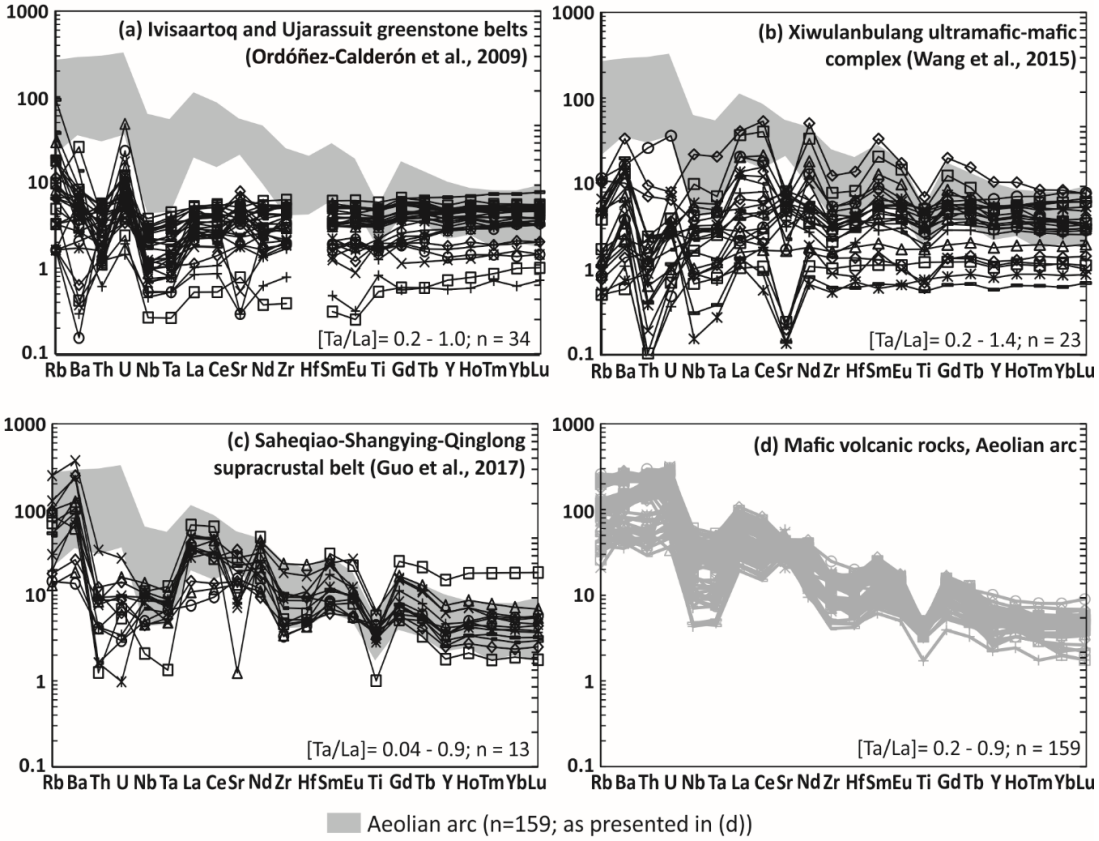

Figure 4.1: *Primitive mantle-normalised trace element plots comparing Archaean mafic rocks interpreted as the product(s) subduction-related magmatism (**a–c**) to mafic rocks from the Phanerozoic Aeolian arc (Metrich et al. 2001, 2005, Landi et al. 2006, Corazzato et al. 2008, Renzulli et al. 2009, Vezzoli et al. 2014), shown in (**d**).*

4.2 Materials and methods

Petrography and geochemical data for 35 ultramafic samples from the Ben Strome Complex is presented here. Of these samples, 18 are from north of the Laxfordian shear zone and 17 are from south of the shear zone (Fig. 4.2). Seven of the samples correspond to the spinel mineral chemistry samples reported in Chapter 3. The locations of the samples within the

Ben Strome Complex are detailed in Figure 4.2, with (British National Grid) GPS coordinates provided in Table 4.1. All 35 samples were analysed for bulk-rock major and trace element chemistry, and polished thin sections of 33 of these samples were made for further petrological analysis. Further to optical microscopy, thin sections were subject to detailed petrographic assessment by element mapping on an A-SEM at Cardiff University. Major element mineral chemistry was collected for 17 thin sections using an A-SEM at Cardiff University, with accompanying trace element mineral chemistry carried out on a subset of 8 thin sections by LA-ICP-MS at Cardiff University. For full details of the instrumentation and methodologies used for bulk-rock geochemistry, major and trace element mineral chemistry, and element mapping, see Appendix A.

4.3 Bulk-rock chemistry

Based on trace element geochemistry, the ultramafic rocks of the Ben Strome Complex are here subdivided into 3 groups, with distinctive patterns on chondrite-normalised REE and primitive mantle-normalised trace element plots (Fig. 4.3). These geochemical groups are best defined using chondrite-normalised Ce/Yb ratios, with group 1 samples (n=20) displaying values of between 0.6 and 1.4, group 2 samples (n=11) showing values of between 1.6 and 12.8, and group 3 samples (n=4) exhibiting values of between 15.6 and 34.9 (Fig. 4.3). On primitive mantle-normalised trace element plots (Fig. 4.3), the group 1 samples display largely flat patterns ($[La/Nb]_N$= 0.2–2.5), while group 2 samples show negative Nb-Ta anomalies ($[La/Nb]_N$= 0.8–34.8), and group 3 samples exhibit negative Nb-Ta-Zr-Hf-Ti anomalies ($[La/Nb]_N$= 13.1–43.1).

4.3.1 Spatial distribution of samples

Group 1 and 2 samples are numerous throughout the Ben Strome Complex, occurring to the north and south of the E–W-trending Laxfordian shear zone (Fig. 4.2a). Group 3 samples exclusively occur to the south of the large Laxfordian shear zone (Fig. 4.2a), with 3 of the samples present in one, 6 m thick package of ultramafic rocks on the southern edge of the Complex (Fig. 4.2b). Although stratigraphically thick (> 3 m) sequences of ultramafic rocks often contain several samples belonging to the same geochemical group (Fig. 4.2c), samples from different geochemical groups are often located less than 1 m (stratigraphically) from one another (Fig. 4.2b–f). In the case of Figure 4.2d, two group 1 samples (Y8a and Y8c), which exhibit flat REE patterns and no HFSE anomalies, are located less than 0.3 m (stratigraphically) above and below a group 2 sample (Y8b), which displays LREE enrichment and negative Nb-Ta anomalies (Fig. 4.3a–d). Similarly, in the case of Figure 4.2e–f, three

group 1 samples (Y10a–c) are located ~1 m (stratigraphically) below a group 2 sample (Y10d), which is located less than 0.5 m below a group 3 sample (Y10e).

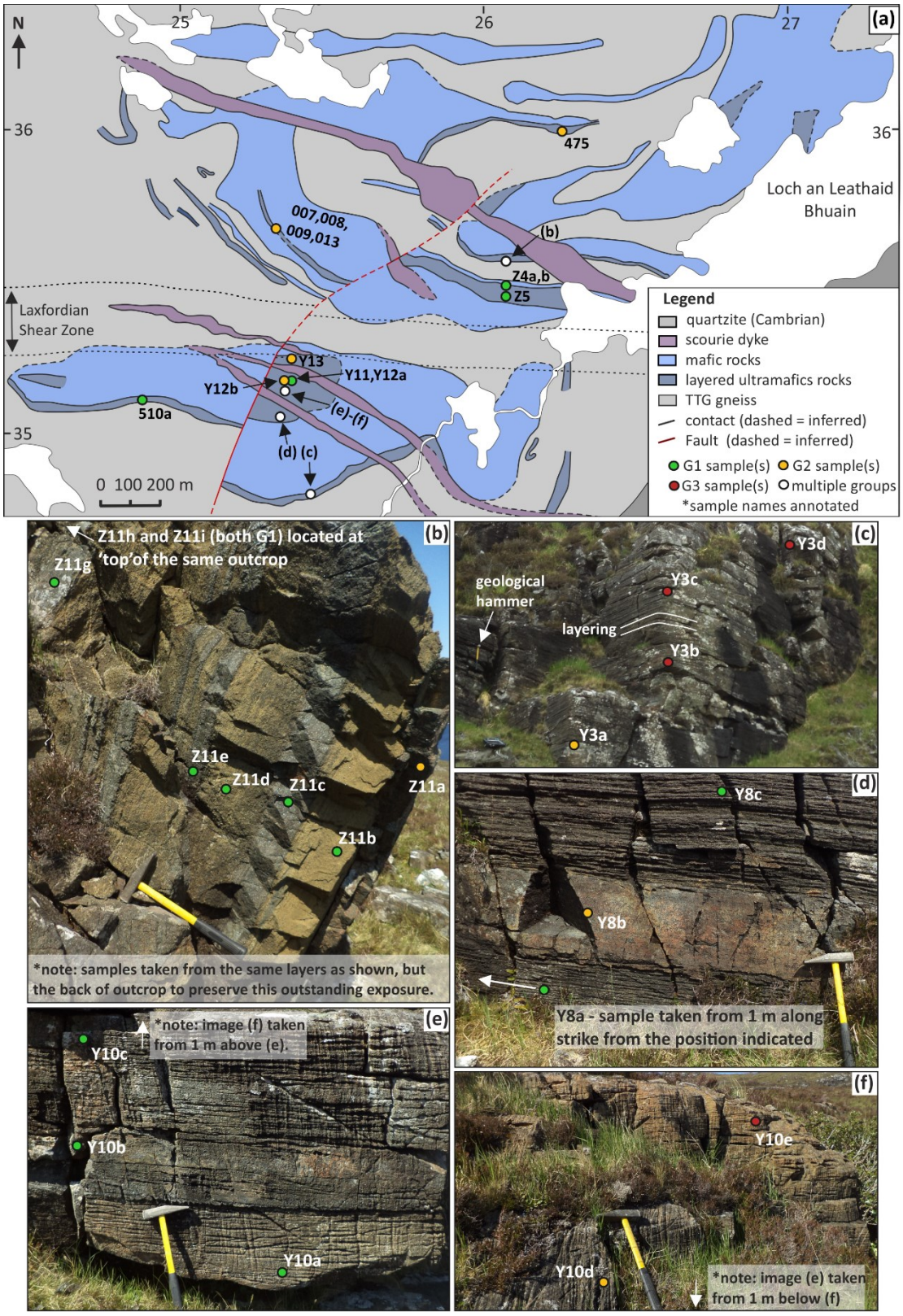

Figure 4.2: *(**a**) Simplified geological map of the Ben Strome Complex detailing the locations of samples used in this study (modified after Fig. 3.1). Structural measurements and stereonet plots are detailed in Chapter 3. (**b–f**) Field photographs detailing sample locations at specific outcrops marked on (a).*

Table 4.1: *Location and modal mineralogy for each sample. Abbreviations: ol=olivine; ser=serpentine; opx=orthopyroxene; cpx=clinopyroxene; amf=amphibole; spn=spinel; carb=carbonate; EM=element map; Y=yes.*

Thin Section	Grid Reference	Modal Mineralogy (%)							
		EM	ol	ser	opx	cpx	amf	spn	carb
Group 1 samples									
Lw16-Y8a	NC25333/35066	Y	0.0	0.0	58.1	23.5	16.4	2.0	
Lw16-Y8c	NC25333/35066	Y	0.9	16.5	29.0	44.8	8.2	0.7	
Lw16-Y10a	NC25340/35130	Y	0.0	44.1	28.3	18.6	9.1	0.0	Y
Lw16-Y10b	NC25340/35130	Y	0.0	0.0	49.9	19.1	29.2	1.8	
Lw16-Y10c	NC25340/35130	Y	5.0	2.0	57.0	12.8	22.5	0.8	
Lw16-Y11	NC25328/35174	Y	0.0	0.0	40.3	44.9	12.3	2.6	
Lw16-Y12a	NC25323/35182	Y	2.8	23.3	30.8	27.0	15.2	0.8	
Lw16-Z4a	NC26037/35434		0.0	0.0	46.0	3.0	48.0	3.0	
Lw16-Z4b	NC26041/35444	Y	0.4	54.8	12.9	5.3	26.7	0.0	Y
Lw16-Z5	NC26066/35466		3.0	55.0	4.0	8.0	28.5	1.5	
Lw16-Z11b	NC26072/35569		2.0	82.0	10.0	0.0	6.0	0.0	
Lw16-Z11c	NC26072/35569	Y	0.0	0.0	42.2	25.0	28.3	4.4	
Lw16-Z11d	NC26072/35569	Y	0.0	77.0	0.0	22.3	0.0	0.8	
Lw16-Z11e	NC26072/35569	Y	0.0	0.0	0.9	17.5	77.9	3.8	Y
Lw16-Z11g	NC26072/35569	Y	0.0	0.0	47.2	3.3	44.3	5.1	
Lw16-Z11h	NC26072/35569		0.0	0.0	58.0	10.0	28.0	4.0	
Lw16-Z11i	NC26072/35569	Y	0.0	70.0	0.0	24.6	2.7	2.7	
Lw16-510a	NC24879/35120	Y	0.0	2.7	38.2	0.0	57.8	1.4	
Group 2 samples									
Lw16-Y3a	NC25439/34795	Y	0.0	59.2	0.5	28.9	11.0	0.5	Y
Lw16-Y8b	NC25333/35066	Y	0.0	1.0	47.1	22.6	27.3	2.1	Y
Lw16-Y12b	NC25323/35182		0.0	0.0	36.0	4.0	59.0	1.0	
Lw16-Y13	NC25345/35234	Y	3.9	12.7	31.4	36.9	14.6	0.4	Y
Lw16-475	NC26263/35986	Y	1.7	36.6	10.0	9.1	41.6	0.4	Y
Lw16-Y10d	NC25340/35130	Y	0.0	78.8	8.8	9.0	0.1	3.4	Y
Lw16_Z11a	NC26072/35569	Y	0.0	30.7	0.0	20.1	49.2	0.0	Y
LEW007	NC25375/35591	Y	0.7	66.5	5.3	26.5	1.0	0.0	Y
LEW008	NC25375/35591		0.0	0.0	91.0	0.0	9.0	0.0	Y
LEW009	NC25375/35591	Y	3.0	51.0	4.0	35.0	5.0	0.0	Y
LEW013	NC25228/35666	Y	0.5	70.5	16.0	2.0	8.0	3.0	Y
Group 3 samples									
Lw16-Y3b	NC25439/34795	Y	5.2	9.1	45.6	0.0	39.7	0.4	Y
Lw16-Y3c	NC25439/34795	Y	0.0	2.4	37.6	4.6	54.8	0.0	Y
Lw16-Y3d	NC25439/34795	Y	0.0	45.8	5.6	43.1	4.3	1.1	Y
Lw16-Y10e	NC25328/35174	Y	0.0	100.0	0.0	0.0	0.0	0.0	Y
Group averages									
Group 1	n=18		1	24	31	17	26	2	
Group 2	n=11		1	37	23	18	21	1	
Group 3	n=4		1	39	22	12	25	0	

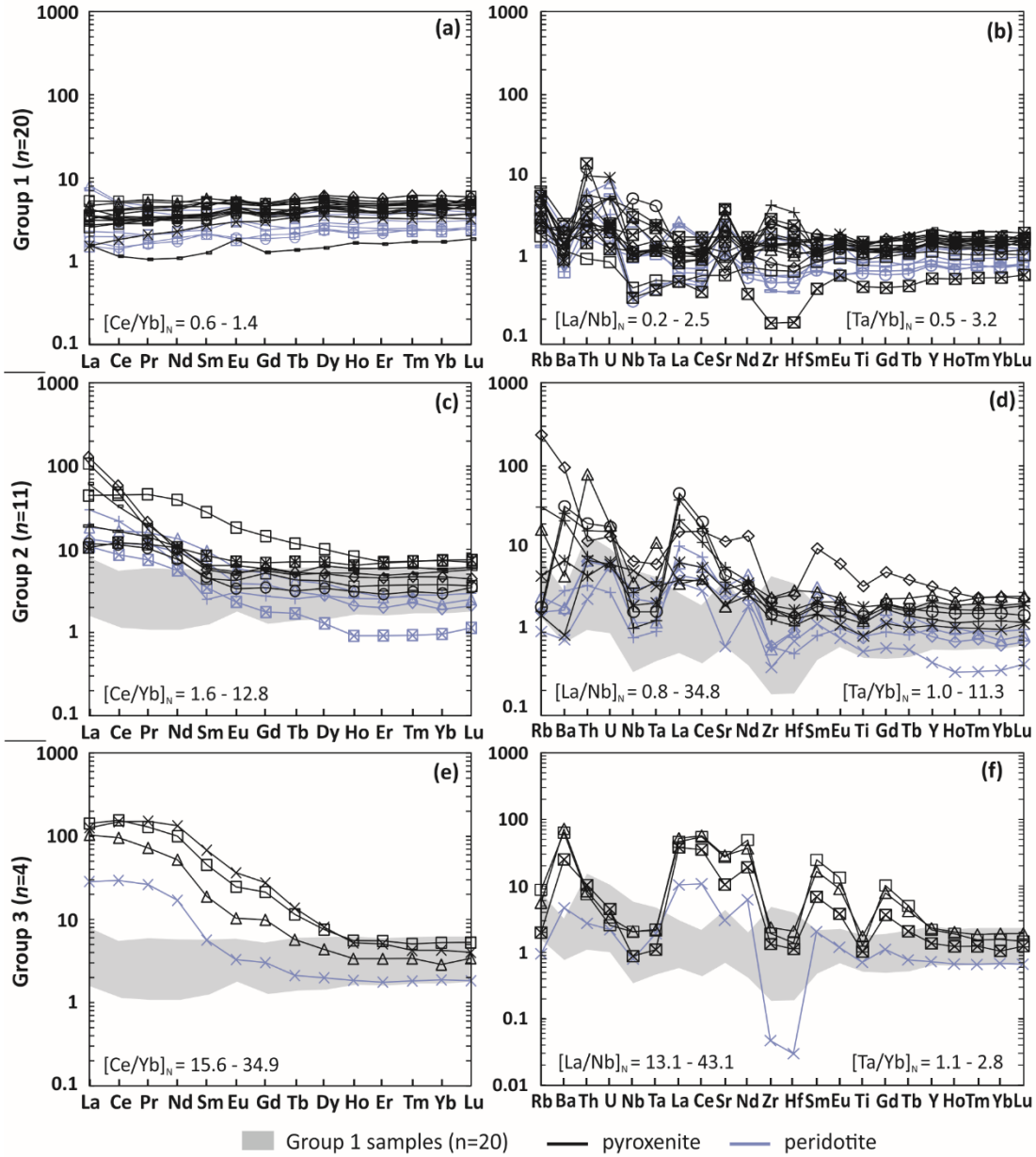

Figure 4.3: *Chondrite-normalised REE plots and primitive mantle-normalised trace element plots for the group 1 (a,b), group 2 (c,d) and group 3 (e,f) ultramafic rocks from the Ben Strome Complex. Normalised values from McDonough and Sun (1995). Note scale change on (f).*

4.3.2 Major elements

The three geochemical groups cannot be distinguished by major element geochemistry, with major element bivariate plots (Fig. 4.4) demonstrating that MgO in the Ben Strome ultramafic rocks displays moderate negative correlations with SiO_2, TiO_2, Al_2O_3, CaO and Na_2O, a moderate positive correlation with NiO (R^2= 0.5–0.6), and no correlation with Fe_2O_3 or Cr_2O_3 (R^2= < 0.1). These plots (Fig. 4.4) also include the compositional ranges of silicate minerals from the Ben Strome Complex, demonstrating that the bulk-rock major element compositions of the analysed rocks are essentially a function of modal mineral abundances.

The major element data are presented on a volatile-free basis in Figure 4.4, with summaries of each geochemical group included in Table 4.2 and the full dataset available in Appendix D.

4.3.3 Trace elements

The group 1 samples exhibit flat patterns ($[Ce/Yb]_N$= 0.6–1.4) on chondrite-normalised REE plots (Fig. 4.3a), with REE concentrations ranging from 1.1 to 8.1× chondrite. Peridotite samples show slightly lower absolute REE abundances than pyroxenite samples but display parallel patterns (Fig. 4.3a). On the primitive mantle-normalised trace element plot (Fig. 4.3b), the group 1 samples exhibit relatively flat patterns ($[Ta/Yb]_N$= 0.6–3.2) punctuated by positive Th, U and Rb anomalies. A key feature is that there are little or no negative HFSE anomalies ($[La/Nb]_N$= 0.2–2.4) on these trace element plots.

Group 2 samples exhibit moderate LREE enrichment ($[Ce/Yb]_N$= 1.6–12.8), negatively sloping LREE patterns ($[La/Nd]_N$= 1.0–13.5) and flat HREE on chondrite-normalised plots (Fig. 4.3c), with normalised REE values ranging from 0.9 to 128.1. Peridotite samples show slightly lower absolute REE abundances relative to pyroxenite samples, but the patterns are parallel (Fig. 4.3d). On the primitive mantle-normalised plot (Fig. 4.3d), the group 2 samples exhibit distinctive negative Nb-Ta anomalies ($[La/Nb]_N$= 0.8–34.8), LREE enrichment and positive Th-U anomalies. Notably, the $[Ta/Yb]_N$ ratios are generally comparable to those of the group 1 samples ($[Ta/Yb]_N$= 1.0–4.4), although one sample displays a ratio of 11.3.

On the chondrite-normalised REE plot (Fig. 4.3e), the group 3 samples exhibit strong LREE enrichment ($[Ce/Yb]_N$= 15.6–34.9) and REE values ranging from 1.8 to 155.2× chondrite, with the peridotite sample relatively depleted in all REE relative to pyroxenite samples. On the primitive mantle-normalised plot (Fig. 4.3f), the group 3 samples show distinctive negative Nb-Ta-Zr-Hf-Ti anomalies ($[La/Nb]_N$= 13.1–43.1), LREE enrichment, and positive Ba and Th anomalies. Notably, the normalised Ta/Yb ratios are comparable to both group 1 and 2 samples ($[Ta/Yb]_N$= 1.1–2.8).

As shown by trace element bivariate plots (Fig. 4.5), Yb (a relatively immobile trace element) displays strong positive correlations with Ho, Y and Ti (R^2= > 0.6), moderate positive correlations with Zr (R^2= 0.45), weak correlations with Nb, Th, Gd, Rb, Cs and Ba (R^2= 0.1–0.3) and no correlation with La and Sm (R^2= < 0.1) in the Ben Strome ultramafic rocks collectively. Although the relationship between Yb and other trace elements in the group 1 samples is generally comparable to the other geochemical groups (Fig. 4.5), these samples display a moderate to strong correlation between Yb and the LREE (Fig. 4.5; R^2= 0.5–0.8).

Table 4.2: *Representative bulk-rock analyses of ultramafic rocks from the Ben Strome Complex. Major element analyses conducted using inductively coupled plasma optical emission spectrometry (ICP-OES). Trace element analyses conducted using inductively coupled plasma mass spectrometry (ICP-MS). The full dataset is included in Appendix D. * SD=standard deviation.*

	Group 1 (n=20)				Group 2 (n=11)				Group 3 (n=4)			
	Min	**Max**	**Mean**	**SD**	**Min**	**Max**	**Mean**	**SD**	**Min**	**Max**	**Mean**	**SD**
Major elements (wt. %)												
SiO_2	35.8	44.8	41.6	2.3	41.0	48.0	43.9	2.2	39.4	47.1	44.1	2.9
TiO_2	0.1	0.4	0.3	0.1	0.2	0.7	0.3	0.1	0.2	0.3	0.2	0.1
Al_2O_3	3.1	9.3	6.1	1.6	2.4	12.8	5.9	2.9	3.0	6.8	5.1	1.5
Fe_2O_3	9.6	13.4	11.8	1.0	8.7	13.3	11.44	1.1	9.9	11.0	10.6	0.4
MnO	0.1	0.3	0.2	0.0	0.1	0.2	0.2	0.0	0.2	0.2	0.2	0.0
MgO	27.0	47.9	33.3	5.9	17.5	42.2	31.0	6.4	27.2	43.0	32.8	6.1
CaO	0.9	11.9	6.4	2.5	0.6	9.7	6.3	2.5	4.4	7.4	5.9	1.1
Na_2O	0.1	0.9	0.4	0.2	0.03	1.8	0.6	0.5	0.1	1.1	0.6	0.4
K_2O	0.01	0.1	0.06	0.0	0.01	1.35	0.2	0.4	0.01	0.4	0.2	0.2
P_2O_5	0.01	0.04	0.02	0.0	0.01	0.04	0.02	0.0	0.01	0.04	0.02	0.0
LOI	0.8	9.4	3.9	n/a	0.7	8.2	4.6	n/a	1.9	7.5	4.0	n/a
Trace elements (ppm)												
Sc	13.3	32.9	23.8	21.2	10.8	33.8	24.3	5.7	7.1	25.7	19.1	7.4
V	82.2	201.4	126.1	36.1	36.0	165.9	101.0	39.4	56.0	116.1	91.6	39.4
Cr	1577	3475	2697	446.8	1077	3165	2401	596.3	1787	2612	2161	344.7
Co	81.2	108.0	95.6	8.3	70.6	113.8	95.3	21.2	86.0	110.2	97.6	8.7
Ni	929	2350	1419	353.5	832	3236	1492	596.7	1079	2357	1532	515.9
Cu	3.5	445.2	67.4	93.8	4.8	118.3	42.1	31.6	4.9	393.8	133.5	157.0
Zn	56.5	1756	169	364.5	31.7	165.2	69.3	43.3	73.4	97.9	83.5	9.6
Ga	3.3	7.9	6.2	1.4	3.6	14.7	6.4	3.1	3.2	8.1	5.7	1.8
Rb	0.9	51.1	2.6	1.1	0.6	141.1	16.5	39.8	0.6	5.2	2.6	1.8
Sr	13.5	84.0	42.0	21.6	13.4	245.9	80.3	58.9	60.7	568.1	343.9	216.0
Y	2.7	10.5	6.7	2.0	1.9	15.3	80.6	3.7	3.1	9.9	7.1	2.8
Zr	1.9	49.4	17.5	11.4	4.0	27.4	15.7	8.0	0.5	24.9	14.9	9.2
Nb	0.2	3.7	1.2	0.9	0.6	4.7	1.9	1.2	0.5	1.4	1.0	0.4
Cs	0.1	1.4	0.7	0.4	0.2	4.4	0.8	1.2	0.2	0.3	0.3	0.0
Ba	4.9	20.8	11.4	4.4	5.4	634.4	119.0	176.3	31.0	474.2	271.5	181.2
La	0.4	1.9	0.8	0.4	2.5	30.4	9.8	6.8	6.7	33.6	23.7	10.3
Ce	0.7	3.2	2.0	0.8	5.3	35.7	15.7	8.1	18.0	95.1	18.0	31.0
Pr	0.1	0.5	0.3	0.1	0.7	4.4	1.6	0.9	2.4	14.0	8.8	4.5
Nd	0.5	2.4	1.5	0.5	2.5	18.0	5.5	4.1	7.8	61.0	34.6	20.4
Sm	0.2	0.8	0.5	0.2	0.4	4.1	1.2	1.0	0.8	10.0	5.1	3.5
Eu	0.1	0.3	0.2	0.1	0.1	1.0	0.3	0.2	0.2	2.1	1.1	0.7
Gd	0.3	1.0	0.7	0.2	0.4	2.9	1.1	0.6	0.6	5.5	3.1	1.9
Tb	0.1	0.2	0.1	0.0	0.1	0.4	0.2	0.1	0.1	0.5	0.3	0.2
Dy	0.4	1.5	1.0	0.3	0.3	2.5	1.2	0.6	0.5	2.0	1.4	0.6
Ho	0.1	0..3	0.2	0.1	0.1	0.5	0.2	0.1	0.1	0.3	0.2	0.1
Er	0.3	0.9	0.6	0.2	0.2	1.1	0.6	0.3	0.3	0.9	0.6	0.2
Tm	0.04	0.2	0.1	0.0	0.02	0.2	0.1	0.0	0.04	0.1	0.1	0.0
Yb	0.3	1.0	0.6	0.2	0.2	1.2	0.7	0.3	0.3	0.8	0.6	0.2
Lu	0.1	2.0	0.1	0.0	0.03	0.2	0.1	0.0	0.1	0.1	0.1	0.0
Hf	0.1	1.1	0.4	0.2	0.2	0.9	0.4	0.2	0.01	0.6	0.3	0.2
Ta	0.02	0.2	0.1	0.0	0.04	0.4	0.1	0.1	0.04	0.1	0.07	0.0
Pb	0.5	7.3	3.2	1.9	1.4	5.1	3.0	2.7	3.0	9.0	5.3	2.3
Th	0.1	1.2	0.3	0.3	0.2	6.3	1.2	1.7	0.2	0.8	0.6	0.2
U	0.02	0.2	0.1	0.1	0.1	0.4	0.2	0.1	0.04	0.1	0.06	0.0

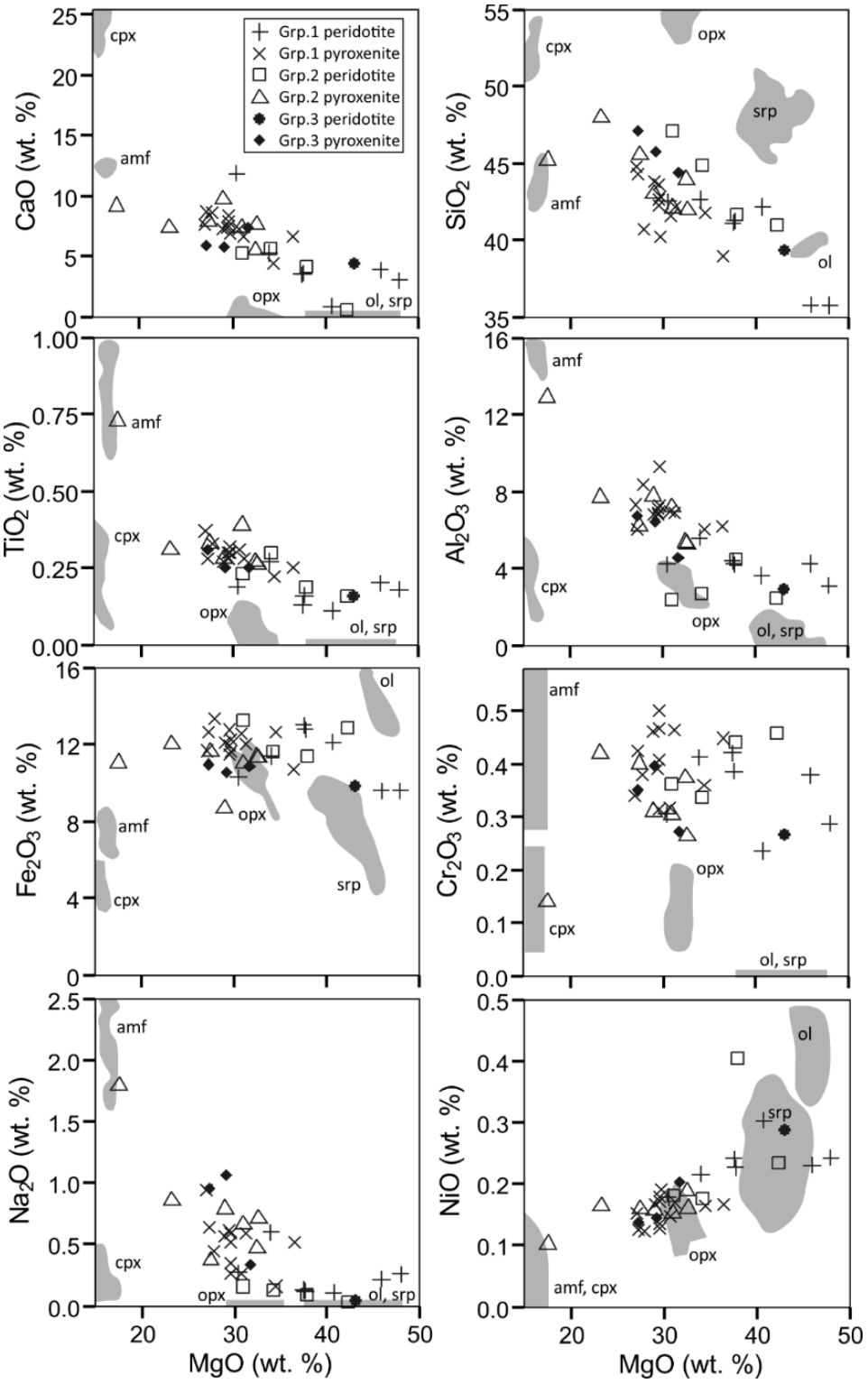

Figure 4.4: *Bivariate plots detailing the major and minor element compositions of the Ben Strome samples, with grey mineral chemistry field included for reference. Abbreviations: amf=amphibole; cpx=clinopyroxene; ol=olivine; opx=orthopyroxene; srp=serpentine.*

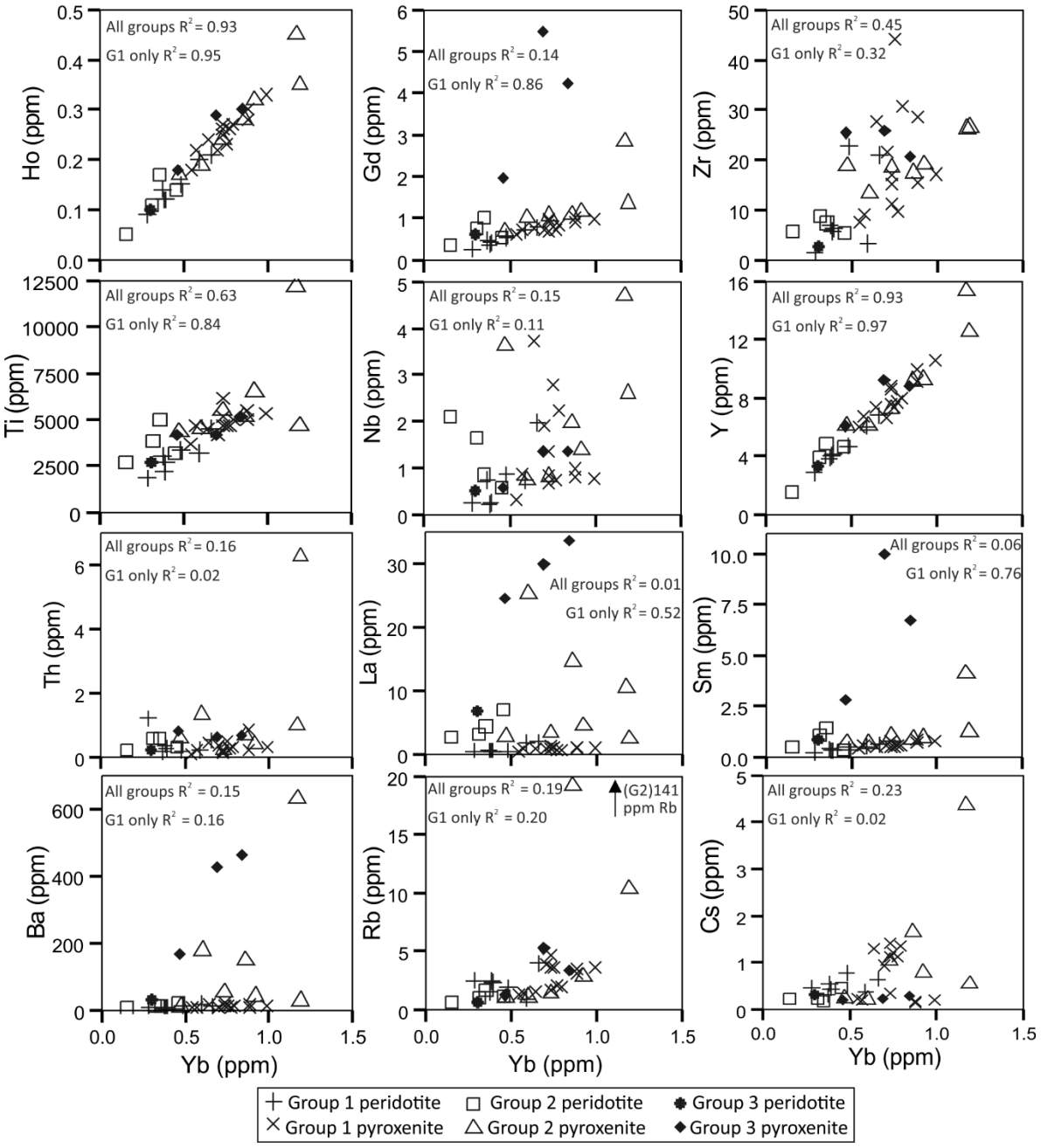

Figure 4.5: *Bivariate plots detailing the trace element compositions of the Ben Strome samples.*

4.4 Petrography

As described in Chapter 3, the ultramafic rocks of the Ben Strome Complex comprise serpentine, olivine, orthopyroxene, clinopyroxene and spinel in variable proportions (Fig. 4.6; Table 4.1), with rare sulphide minerals (pentlandite, pyrite, chalcopyrite and pyrrhotite) also present. All three geochemical groups contain a combination of metapyroxenite and metaperidotite lithologies, with each group displaying large ranges in the modal mineral abundances of silicate and oxide minerals. Table 4.1 details the modal mineral abundances of every thin section assessed in this study, alongside averages for each of the geochemical

groups. These data demonstrate that there is no systematic variation in the modal abundances of silicate/oxide mineral phases between the 3 geochemical groups.

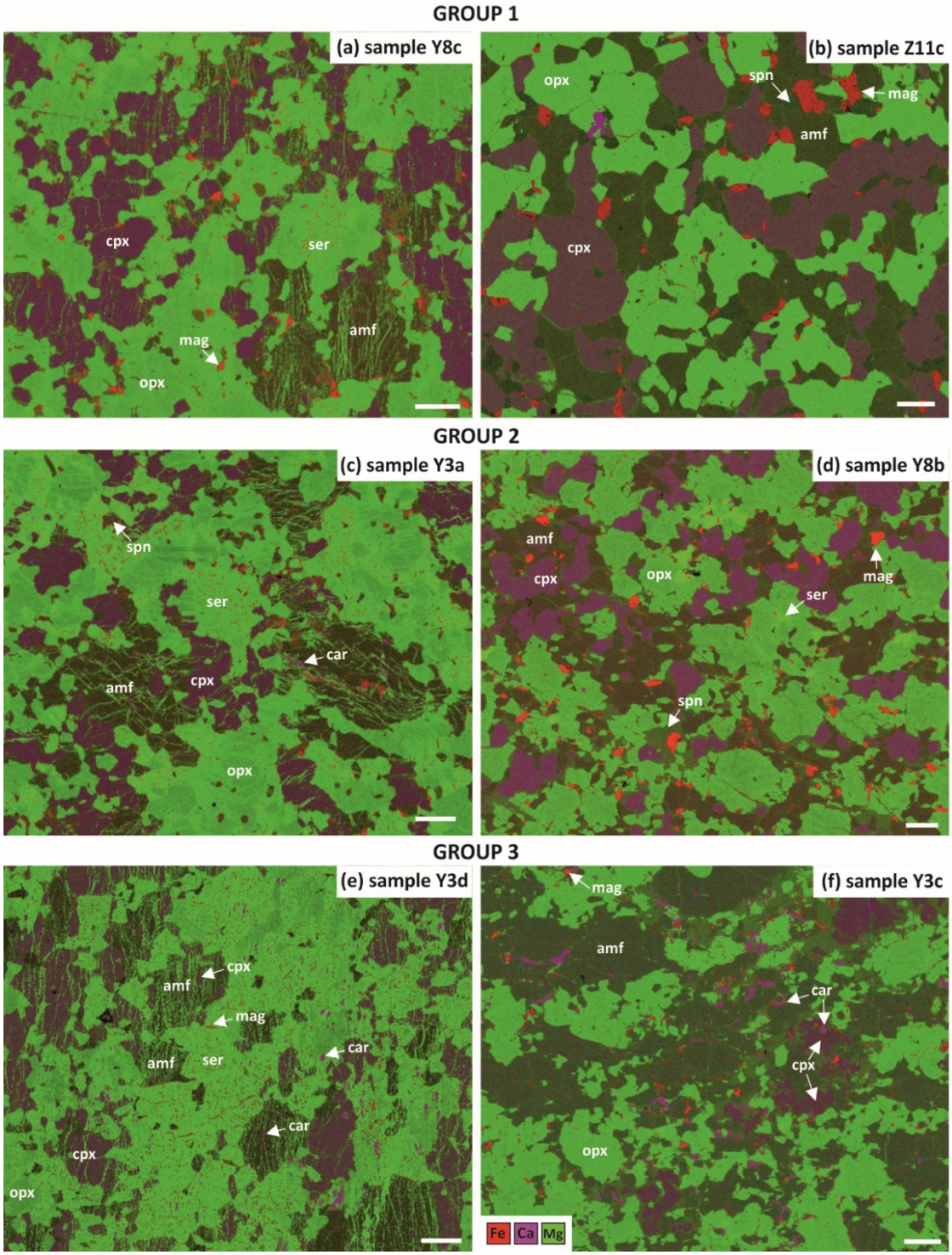

Figure 4.6: *Element maps detailing the petrographic and textural characteristics of the Ben Strome ultramafics. (**a**,**b**) group 1 samples. (**c**,**d**) group 2 samples. (**e**,**f**) group 3 samples. Note the comparable textures between the geochemical groups. White scale bar=1 mm. Abbreviations: amf=amphibole; car=carbonate phases; cpx=clinopyroxene; mag=magnetite; opx=orthopyroxene; ser=serpentine; spn=spinel.*

Olivine is almost entirely pseudomorphed by serpentine and minor magnetite, with olivine remnants only preserved in some thin sections (Table 4.1; Fig. 4.6). Clinopyroxene is variably rimmed, replaced and veined by secondary amphibole on all scales, with only anhedral clinopyroxene remnants preserved within amphibole in some thin sections (Fig. 4.6e,f). Such replacement can likely be attributed to polyphase amphibolitisation, with the Ben Strome Complex having experienced at least 2 distinct phases of amphibolite-facies metamorphism (during the ~2.5 Ga Inverian and 1.9–1.6 Ga Laxfordian events). Specific textures are not unique to individual geochemical groups, although clinopyroxene grains appear most intensely amphibolitised in group 2 and 3 samples, with amphibole veins commonly observed on the µm-scale (Figs. 7 and 8).

Further to silicate, oxide and sulphide mineral phases, selected samples contain carbonate mineral phases (dolomite and calcite) in trace amounts (< 0.2 modal %; Figure 4.7). Such carbonates display a range of mineralogical associations, occurring as: < 0.2 mm wide calcite veins that cross-cut all mineral phases in individual thin sections (Fig. 4.7a); < 0.1 mm wide calcite veins within amphibole (Fig. 4.7b); < 0.8 mm diameter calcite grains within amphibole (Fig. 4.7c); and < 1 mm dolomite 'clots' within a serpentinite (Fig. 4.7d). Carbonate minerals are extremely rare in the group 1 samples, with discontinuous veins (< 0.1 mm wide) occurring in 3 out of 19 samples. In contrast, carbonate mineral phases are identified in 10 out of 11 group 2 thin sections, occurring as: < 0.2 mm wide calcite veins through entire thin sections (Fig. 4.7a); and < 0.1 mm wide veins in amphibole (Fig. 4.7b). Similarly, such phases are identified in all group 3 samples (n=4), occurring, as: < 0.2 mm wide veins in amphibole (Fig. 4.7b); and µm-scale grains in amphibole and serpentine (Fig. 4.7c,d).

The sulphide mineral assemblage displayed by the Ben Strome ultramafic rocks shows systematic variation between the 3 geochemical groups. Group 1 samples contain extremely fine-grained (< 50 µm diameter) pentlandite that is distributed relatively evenly throughout the thin sections (Fig. 4.8a). Group 2 samples also contain fine-grained (<50 µm diameter) pentlandite, but also show rarer occurrences of coarser-grained (<150 µm diameter) pyrite (Fig. 4.8b). Additional to fine-grained (< 50 µm diameter) pentlandite, group 3 samples also contain frequent occurrences of coarse-grained (< 500 µm diameter) pyrite (Fig. 4.8c).

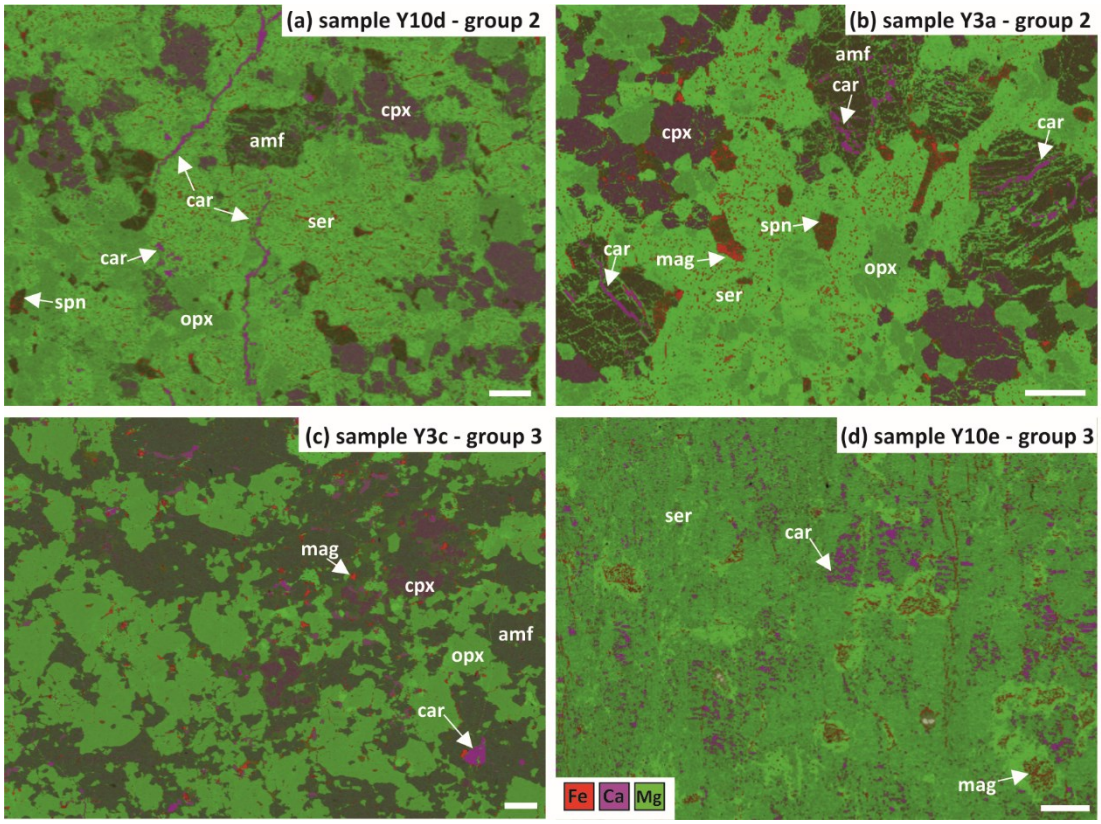

Figure 4.7: *Element maps detailing the mineralogical and textural associations of the carbonate minerals. White scale bar=1 mm. Abbreviations as in Figure 4.6.*

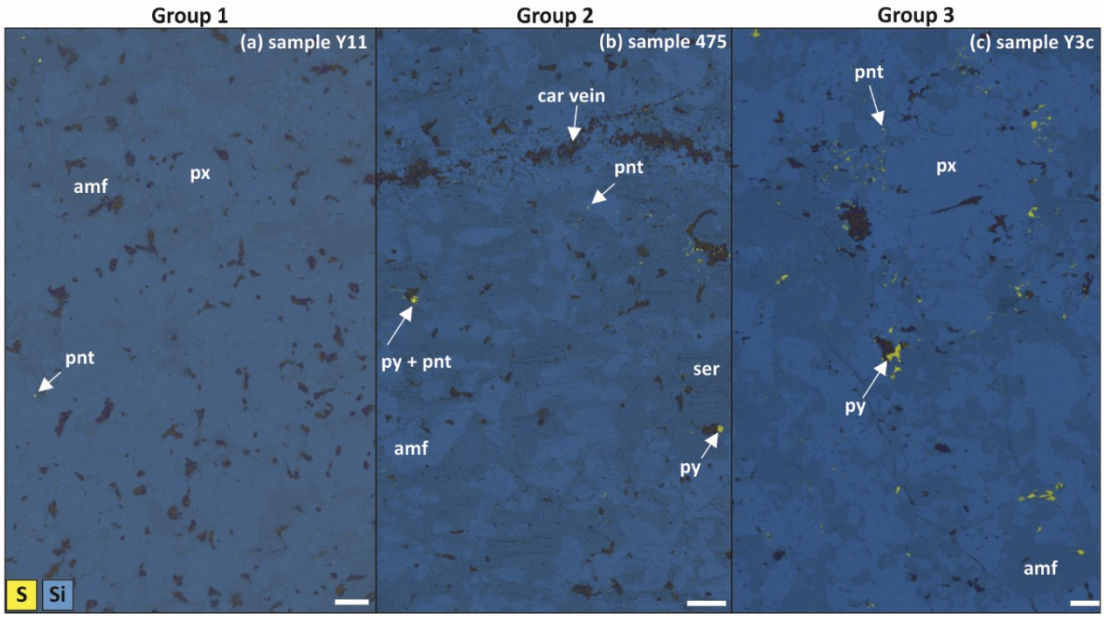

Figure 4.8: *Element maps detailing the mineralogical and textural associations of the sulphide minerals. Note: black areas represent both oxide and carbonate mineral phases. White scale bar=1 mm. Abbreviations: amf=amphibole; car=carbonate phase; pnt=pentlandite; px=pyroxene; py=pyrite; ser=serpentine.*

4.5 Mineral chemistry

Major element analysis of 366 orthopyroxene grains was conducted, alongside analyses of 152 clinopyroxene grains, 188 amphibole grains, 70 olivine grains, and 94 serpentine grains, with the Fe^{2+} and Fe^{3+} calculated stoichiometrically (Droop 1987). Trace element mineral chemistry was conducted on 46 orthopyroxene grains, alongside analyses of 40 clinopyroxene grains and 77 amphibole grains. In addition, 7 calcite grains were analysed, although some silicate material was included in the ablation process due to the small size (µm-scale) and morphology of these grains, which are often intergrown with silicate minerals. Individual analyses record SiO_2 values of between 2.5 and 15.1 wt. %, with this dilution of the pure carbonate signature taken into consideration in the discussion of the results. The complete mineral chemistry datasets are included in Appendix D.

4.5.1 Orthopyroxene

Orthopyroxenes classify as Al-rich hypersthene and exhibit the following compositional ranges: Wo= 0.2–5.0, En= 79.9–87.9; Fs= 11.9–18.8 and 1.7–4.2 wt. % Al_2O_3. On bivariate plots (Fig. 4.9), group 1 and 2 orthopyroxenes collectively form relatively tight clusters (Fig. 4.9), with restricted Si, Mg, Al, Ca and Fe ranges (Fig. 4.9). Group 3 orthopyroxene compositions are broadly comparable to groups 1 and 2, although they exhibit minor Si and Mg enrichment and minor Al depletion (Fig. 4.9).

On chondrite-normalised REE plots, group 1 orthopyroxenes exhibit concave upward patterns, negatively sloping LREE ($[La/Nd]_N$= 0.9–5.3) and positively sloping MREE to HREE ($[Pr/Yb]_N$= 0.04–0.17; Fig. 4.10a). Group 2 orthopyroxenes display similar concave upward patterns, negatively sloping LREE ($[La/Nd]_N$= 2.7–64.0) and positively sloping MREE–HREE ($[Pr/Yb]_N$= 0.03–1.97), although selected orthopyroxenes are slightly enriched in LREE relative to group 1 samples (Fig. 4.10b). Group 3 orthopyroxenes display negatively sloping LREE–MREE ($[La/Ho]_N$= 9.7–200.0) and positively sloping HREE ($[Ho/Yb]_N$= 0.05–0.5; Fig. 4.10), with LREE and MREE enrichment relative to the group 1 samples (Fig. 4.10c).

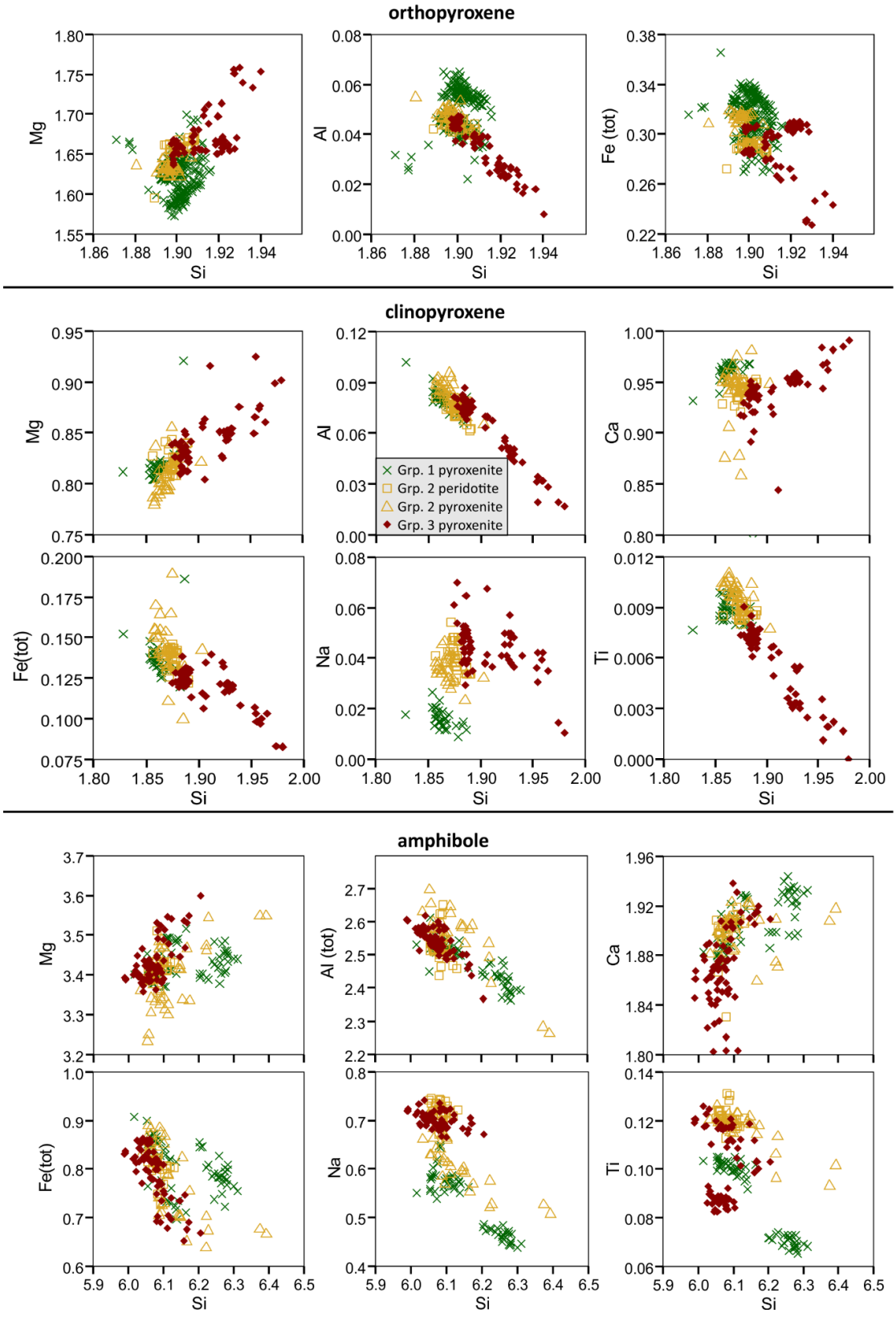

Figure 4.9: *Bivariate plots detailing the major and minor element compositions of orthopyroxene, clinopyroxene and amphibole. Axes are in atoms per formula unit (apfu).*

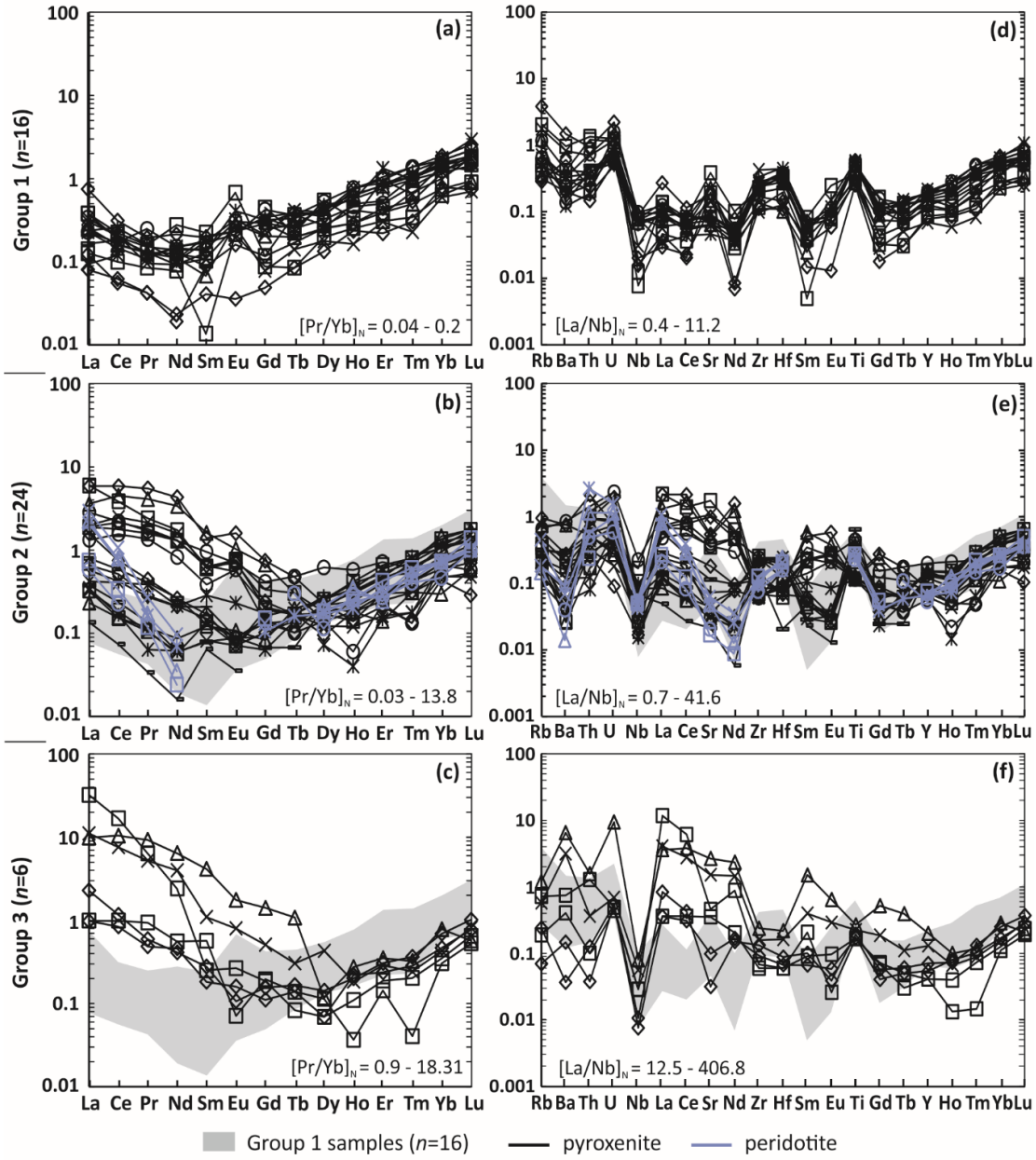

Figure 4.10: *Chondrite-normalised REE (**a–c**) and primitive mantle-normalised (McDonough and Sun 1995) trace element plots (**d–f**) for orthopyroxene grains.*

On primitive mantle-normalised trace element plots, group 1 orthopyroxenes show broadly concave upward patterns that are punctuated by positive Zr-Hf-Ti anomalies (Fig. 4.10d). The most compatible elements exhibit positive slopes ($[Gd/Yb]_N$= 0.1–0.3), the moderately compatible elements are relatively flat ($[Nb/Sm]_N$= 0.2–2.8), and there is consistent enrichment of the most incompatible elements (Rb-U; Fig. 4.10d). The normalised trace element patterns for group 2 orthopyroxenes also exhibit broadly concave upward patterns and positively sloping patterns for the most compatible elements ($[Gd/Yb]_N$= 0.1–0.5; Fig. 11e). However, unlike group 1, the group 2 orthopyroxenes display variable patterns for the moderately compatible elements, with some mild LREE enrichment and some mild

incompatible element depletion (Rb-U; Fig. 11e). Group 3 orthopyroxenes exhibit positively sloping patterns for the most compatible elements ($[Gd/Yb]_N$= 0.2–2.3) and normalised HFSE abundances comparable to the group 1 samples (Fig. 4.10f). However, unlike the group 1 samples, the group 3 orthopyroxenes exhibit apparent negative Nb anomalies and associated LREE enrichment (Fig. 4.10f).

4.5.2 Clinopyroxene

As described in Section 4.4 and detailed in Figure 4.6, clinopyroxene is variably rimmed and replaced by amphibole on all scales. It is, therefore, possible that clinopyroxene analyses incorporate some alteration to amphibole. All clinopyroxenes classify as Al-rich diopside and exhibit the following compositional ranges (Fig. 4.9): Wo= 41.7–51.3, En= 41.2–48.3, Fs= 4.3–10.1, and 0.9–6.4 wt. % Al_2O_3. On most major element bivariate plots, the group 1 and 2 clinopyroxenes together form relatively tight clusters, with comparable Si, Fe, Mg, Al, Ca and Ti concentrations (Fig. 4.9). However, group 2 clinopyroxenes are enriched in Na (0.16–0.37% Na_2O) relative to group 1 clinopyroxenes (< 0.18% Na_2O; Fig. 4.9). Group 3 clinopyroxenes show minor overlap with group 1 and 2 compositions, but exhibit significant Si and Na enrichment, significant Al and Ti depletion, minor Fe depletion, and minor Mg enrichment (Fig. 4.9).

On chondrite-normalised REE plots, group 1 clinopyroxenes exhibit relatively flat patterns ($[Pr/Yb]_N$= 0.3–1.9) and a relatively restricted range of normalised LREE abundances (Fig. 4.11a). Group 2 clinopyroxenes display flat MREE–HREE patterns and normalised abundances comparable to the group 1 samples (Fig. 4.11b). However, these clinopyroxenes display LREE enrichment ($[Pr/Yb]_N$= 0.5–38.3) relative to the group 1 samples, with such enrichment most prominent in peridotite samples (Fig. 4.11b). Group 3 clinopyroxenes exhibit relatively flat HREE patterns, with positively sloping LREE–MREE ($[Pr/Yb]_N$= 6.0–219.3; Fig. 4.11c) that are significantly enriched in LREE relative to the group 1 clinopyroxenes.

On primitive mantle-normalised trace element plots, group 1 clinopyroxenes display flat overall patterns that are punctuated by negative Sr-Nb-Ta-Ba-Rb anomalies ($[La/Nb]_N$= 2.0–19.9; Fig. 4.11d). The trace element patterns for the group 2 clinopyroxenes are comparable to the group 1 samples, but show relative LREE enrichment ($[La/Nb]_N$= 3.2–217.1; Fig. 4.11e). Similarly, group 3 clinopyroxenes display similar trace element patterns to the group 1 samples, with a more pronounced enrichment in the LREE ($[La/Nb]_N$= 28.9–873.4; Fig. 4.11f).

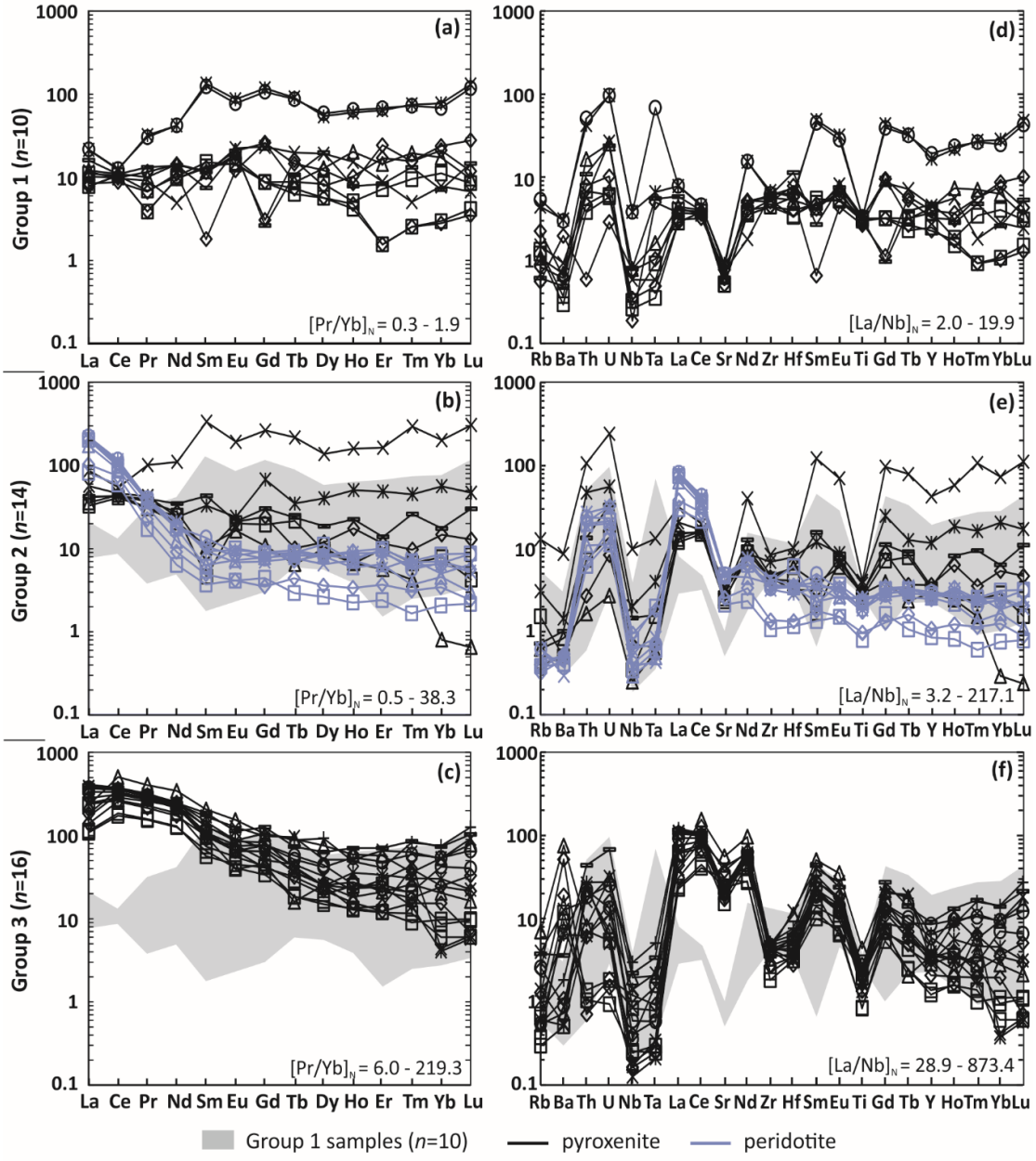

Figure 4.11: *Chondrite-normalised REE (**a–c**) and primitive mantle-normalised (McDonough and Sun 1995) trace element plots (**d–f**) for clinopyroxene grains.*

4.5.3 Amphibole

All amphiboles classify as pargasite and exhibit the following compositional ranges (in wt. %): 41.9–45.5% SiO_2, 13.7–16.2% Al_2O_3, 1.7–2.7% Na_2O, 15.4–17.1% MgO, 11.8–13.0% CaO, 0.6–1.2% TiO_2 and 5.9–8.6% Fe_2O_3 (Fig. 4.9). Group 1 amphiboles form two clusters on major element bivariate plots (Fig. 4.9), with one subgroup enriched in Si and Ca, and depleted in Na, Al and Ti relative to the other. Group 2 amphiboles are generally comparable to the Si-poor group 1 amphiboles in their Si, Mg, Al, Ca, Fe and Ti abundances, although group 2 amphiboles exhibit some Na depletion and Si enrichment relative to these group 1 amphiboles (Fig. 4.9). Group 3 amphiboles have similar Mg, Al, Ca and Fe abundances to the

Si-poor group 1 amphiboles, but are relatively enriched in Ti and Na, and relatively depleted in Ca (Fig. 4.9).

On chondrite-normalised REE plots, group 1 amphiboles exhibit flat patterns ($[Pr/Yb]_N$= 0.3–1.2) and a broad range of normalised REE abundances (2.1–119.2× chondrite; Fig. 4.12a). These group 1 amphiboles can be subdivided into high total REE and low total REE subgroups that have parallel REE patterns (Fig. 4.12a). Group 2 amphiboles display flat MREE–HREE ($[Eu/Lu]_N$= 0.3–1.5) and negatively sloping LREE patterns ($[La/Sm]_N$= 1.0–61.9), with peridotite samples significantly depleted in the REE relative to pyroxenite (Fig. 4.12b). Group 3 amphiboles exhibit flat HREE, negatively sloping MREE and flat LREE ($[Pr/Yb]_N$= 5.2–81.5), with significant LREE–MREE enrichment relative to the group 1 amphiboles (Fig. 4.12c).

On primitive mantle-normalised trace element plots, group 1 amphiboles generally display relatively flat patterns, with some negative Nb anomalies ($[La/Nb]_N$= 0.7–14.7; Fig. 4.12d). Group 2 amphiboles also exhibit flat trace element patterns, but are punctuated by positive LREE anomalies and some negative Nb-Ta-Rb-Ba anomalies ($[La/Nb]_N$= 3.8–201.0; Fig. 4.12e). Group 3 amphiboles have HREE abundances comparable to the group 1 samples, but display LREE, MREE and Ba enrichment, with prominent apparent negative anomalies ($[La/Nb]_N$= 15.8–293.9), although the Nb-Ta abundances are comparable to the group 1 samples (Fig. 4.12f).

4.5.4 Carbonate phases

As previously mentioned, the fine grain size of the carbonate phases relative to the laser beam diameter sometimes resulted in the incorporation of some silicate material into the analysis (Fig. 4.13). Consequently, the succeeding descriptions should be treated as an indication of the trace element budgets of the calcite in the Ben Strome ultramafic rocks, rather than absolute abundances.

On chondrite-normalised REE plots, carbonate analyses from group 2 samples display flat MREE–HREE patterns ($[Eu/Lu]_N$= 0.2–1.6) and negatively sloping LREE ($[La/Sm]_N$= 18.1–52.1; Fig. 4.13a). On primitive mantle-normalised trace element plots, these analyses display flat patterns for the most compatible elements (Gd-Lu), mild negative Zr-Hf anomalies and strong positive LREE anomalies ($[La/Nb]_N$= 39.3–71.5; Fig. 4.13b). Calcite analyses from group 3 samples display flat HREE and negatively sloping LREE–MREE ($[Pr/Yb]_N$= 140–160.3; Fig. 4.13c). On primitive mantle-normalised trace element plots, these analyses exhibit flat patterns for the most compatible elements (Tb-Lu), with negative Ti-Zr-Hf anomalies, and positive MREE and LREE anomalies ($[La/Nb]_N$= 343.8–408.8; Fig. 4.13d).

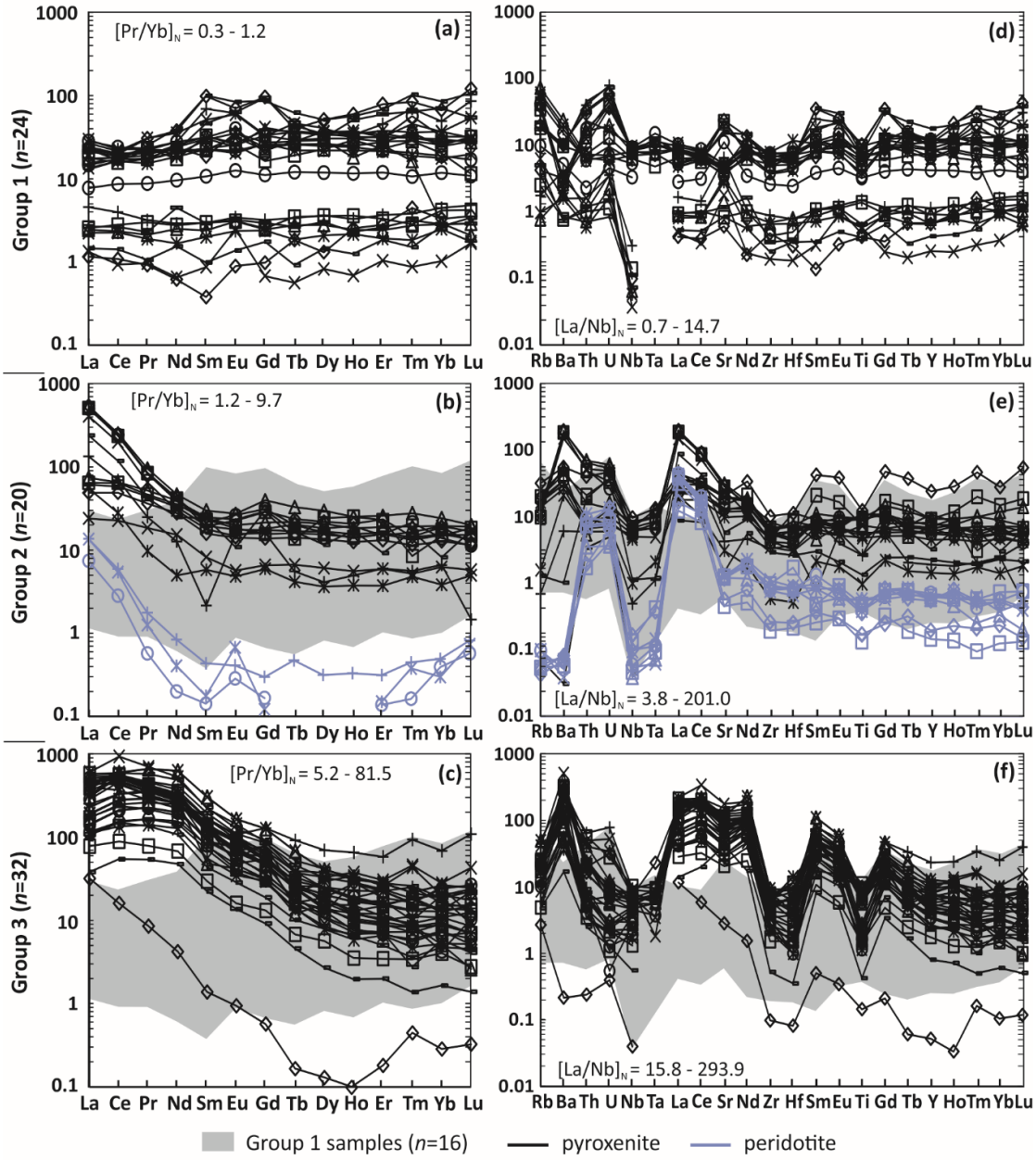

Figure 4.12: *Chondrite-normalised REE (**a–c**) and primitive mantle-normalised (McDonough and Sun 1995) trace element plots (**d–f**) for amphibole grains.*

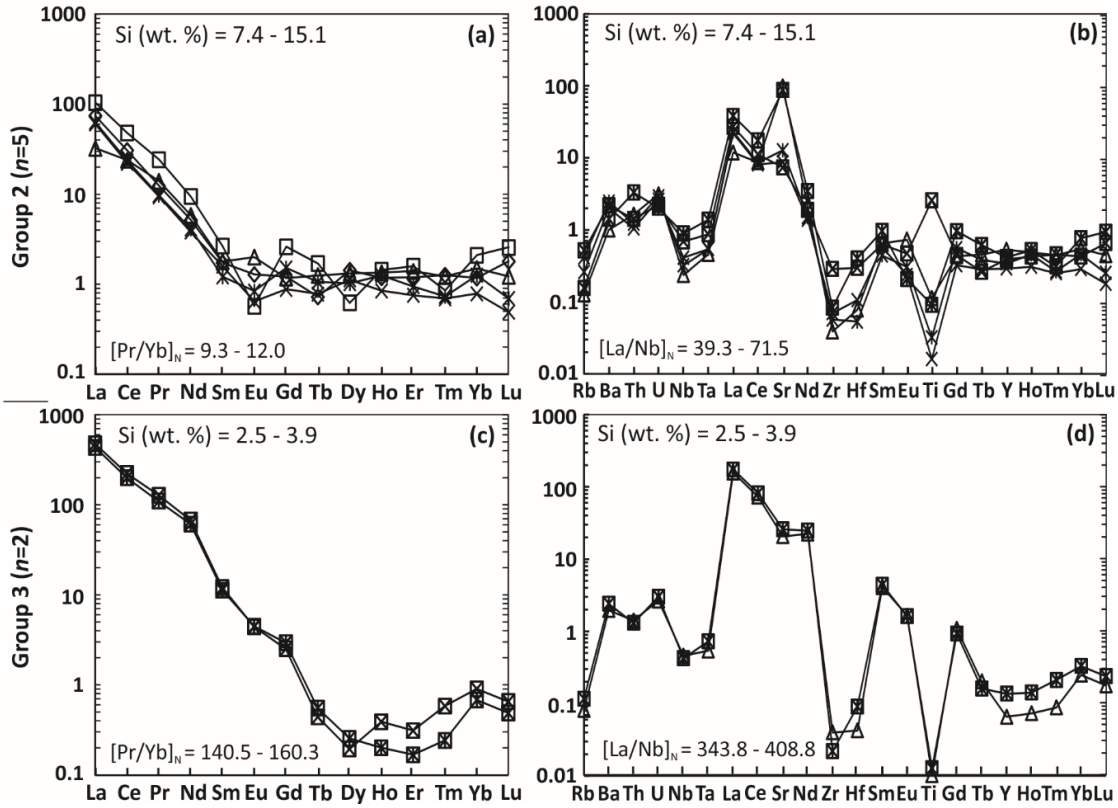

Figure 4.13: *Chondrite-normalised REE (a,c) and primitive mantle-normalised (McDonough and Sun 1995) trace element plots (b,d) for group 2 (**a**,**b**) and group 3 (**c**,**d**) carbonate grains. Note: due to the small size of carbonate grains, laser ablation (LA)-ICP-MS analyses include variable proportions of silicate material, as indicated.*

4.6 Discussion

4.6.1 Constraining the bulk-rock geochemical controls

Despite the fact that the outlined geochemical groups may be defined by the extent (or absence) of HFSE anomalies, the absolute abundances of the HFSE are remarkably consistent between the 3 groups of ultramafic rocks in the Ben Strome Complex (Fig. 4.3). Instead, the presence/absence of any HFSE anomalies is ultimately controlled by the degree of LREE enrichment (as demonstrated in Fig. 4.3d,f) and it is, therefore, necessary to examine the controls of the LREE budget within the Ben Strome ultramafic rocks. The simplest hypothesis is that it could be controlled by the modal mineral abundances of individual samples, with a greater proportion of LREE-bearing mineral phases present in group 2 and 3 samples. However, the data shown in Table 4.1 contradict this assertion, with each geochemical group displaying a wide-range of modal mineral abundances and no systematic variation between the groups. An alternative hypothesis is that the LREE budget of the Ben Strome ultramafic rocks could be controlled by variable trace element compositions of specific common minerals. This is supported by the normalised REE and trace element patterns for individual

silicate minerals, with clinopyroxene (Fig. 4.11) and, most prominently, amphibole (Fig. 4.12) showing significant enrichment of the LREE in groups 2 and 3 relative to group 1 samples. These patterns broadly mirror those of the bulk-rock geochemistry, with strong negative HFSE anomalies only associated with group 2 and 3 samples.

Mass balance calculations, as detailed in Figure 4.14, were carried out to test this hypothesis. Measured bulk-rock trace element patterns are compared to those calculated using the trace element compositions and modal mineral abundances of clinopyroxene and amphibole (Fig. 4.14). Although the analysed calcite grains also show the LREE enrichment, they are excluded from mass balance calculations due to the extremely low modal abundance (< 0.2 modal %) of these phases. Orthopyroxene is also excluded from mass balance calculations, as the trace element concentrations are 1–2 orders of magnitude lower than those of clinopyroxene and amphibole (Figs. 5.10-5.12), and they therefore have a limited contribution to the trace element budgets of the Ben Strome ultramafic rocks.

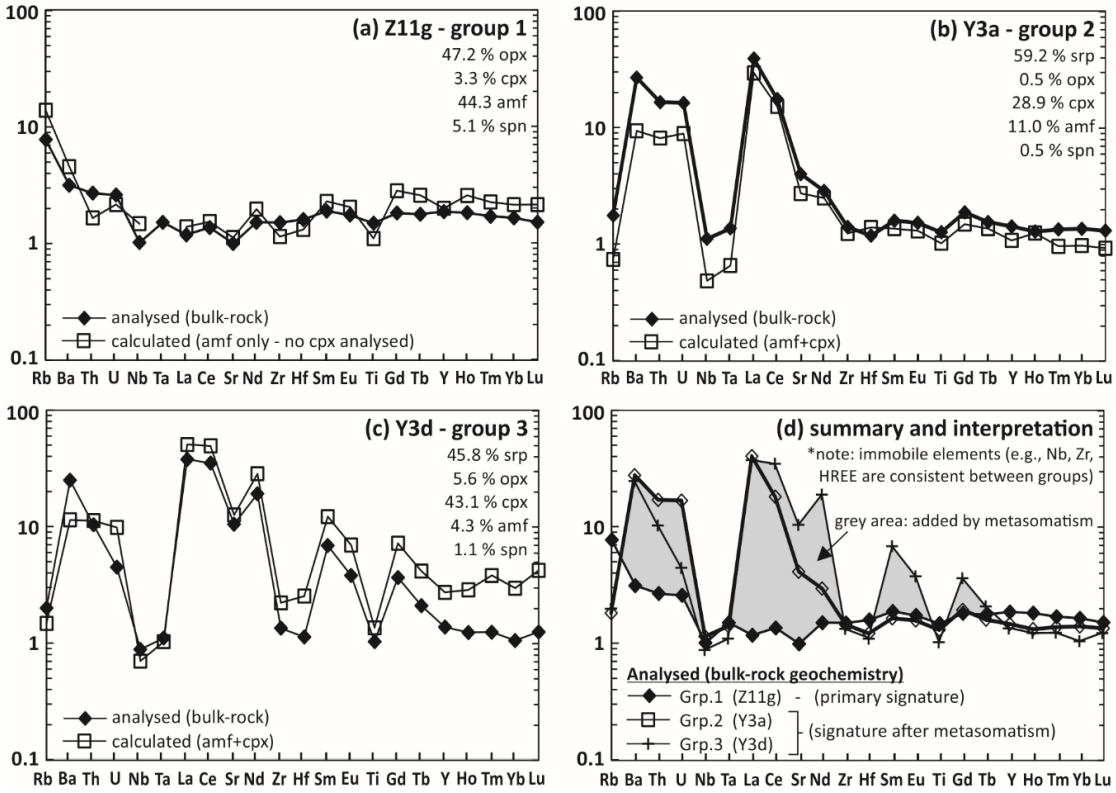

Figure 4.14: *(**a–c**) Primitive mantle-normalised (McDonough and Sun 1995) trace element plots displaying the mass balance calculations for the Ben Strome ultramafic rocks. (**d**) Primitive mantle-normalised trace element plot detailing an interpretation of the 3 patterns displayed in parts (**a–c**). Note: the data presented in parts (a)-(c) are representative examples of 5 mass balance calculation conducted using the collected data.*

For all three modelled samples, the calculated and measured trace element patterns are good matches (Fig. 4.14). For sample Z11g—a group 1 sample—the measured and calculated trace element compositions correspond well (Fig. 4.14a), with relatively flat patterns and enrichment of the most incompatible elements (Rb-U), although the calculated pattern is slightly enriched in the most compatible elements (the HREE) relative to the measured pattern (Gd-Lu; Fig. 4.14a). For sample Y3a—a group 2 sample—the measured and calculated trace element compositions also correspond well (Fig. 4.14b), displaying flat compatible element patterns (Hf-Lu), LREE enrichment, negative Nb-Ta anomalies and enrichment of the most incompatible elements (Ba-U), but the calculated composition is slightly depleted in Nb, Ta, Ba, Th and U (Fig. 4.14b). For sample Y3d—a group 3 sample—the measured and calculated trace element patterns (Fig. 4.14c) show LREE and MREE enrichment and associated negative Nb-Ta-Zr-Hf-Ti anomalies. Although the measured and calculated patterns are consistently parallel, the latter is enriched relative to the former (Fig. 4.14c), suggesting that the measured trace element compositions for clinopyroxene and amphibole in this sample are not wholly representative, or that modal mineral proportions are inaccurate.

The consistent correspondence between the calculated and measured trace element patterns indicates that the unique trace element compositions of the group 2 and 3 samples cannot be attributed to crystallisation of LREE-bearing mineral phases during fractionation. Rather, these data are in general agreement with a hypothesis whereby the trace element budgets of the Ben Strome ultramafic rocks are predominantly controlled by the composition of clinopyroxene and, predominantly, amphibole. In group 2 and 3 samples, the LREE contents in clinopyroxene and amphibole are 1–2 orders of magnitude greater than in the group 1 samples, with this LREE enrichment responsible for the presence of apparent HFSE anomalies in the bulk-rock data. The succeeding section therefore focuses on identifying the source of this LREE enrichment in the context of several hypotheses relating to the origin of HFSE anomalies.

4.6.2 Origin of the HFSE anomalies

4.6.2.1 Primary magmatic processes

Several authors have used HFSE anomalies present in intrusive and/or extrusive Archaean ultramafic-mafic suites as evidence that these rocks (interpreted as cumulates; Chapter 3) were produced by subduction-related magmatism (Manya 2004, Wang et al. 2015, Guo et al. 2017). Considering the bulk-rock geochemical data alone, a similar interpretation could be

offered for the Ben Strome ultramafic rocks. However, such an interpretation—whereby the LREE enrichment of clinopyroxene and amphibole, and associated bulk-rock HFSE anomalies shown by the group 2 and 3 ultramafic rocks result from fractional crystallisation of an initial magma inherently depleted in the HFSE—is contradicted by the evidence presented in this study. First, the group 2 and 3 ultramafic rocks do not represent the most fractionated portions of the layered complex, with bulk-rock MgO values for these samples (18–43 wt. % MgO) showing significant overlap with the group 1 samples (27–48 wt. % MgO). The bulk-rock data are supported by the composition of clinopyroxene, which shows no correlation between MgO and La (R^2= 0.01), indicating that the LREE-rich composition of this mineral phase in the group 2 and 3 samples cannot be attributed to fractional crystallisation. Second, group 2 and 3 samples exhibit a poor correlation between Yb and the LREE (R^2= 0.01–0.06; Fig. 4.5), suggesting that secondary processes have mobilised the LREE. This interpretation is supported by the moderate to strong correlation (R^2= 0.5–0.7) between Ba (a fluid mobile element) and the LREE, and by the strong correlation (R^2= > 0.9) between Sr (another fluid mobile element) and the LREE. In contrast, the group 1 samples display a good correlation between Yb and the LREE (R^2= 0.5–0.8; Fig. 4.5), implying that these rocks have not experienced the same mobility of these elements. Third, samples of different geochemical groups are often located less than a metre (stratigraphically) from one another, as detailed in Figure 4.2. Consequently, if the variable LREE contents of clinopyroxene and amphibole were to be achieved only by magmatic processes and thus using a common magma, it could only be accomplished through extreme (and implausible) variations in partition coefficients on a metre-scale. Thus, primary magmatic processes such as fractional crystallisation cannot explain the variation in composition between the geochemical groups.

4.6.2.2 Crustal contamination

Alternatively, several authors have attributed negative HFSE anomalies to crustal contamination (Sun and McDonough 1989, Arndt 1999), with this process potentially occurring during the emplacement of the Ben Strome Complex into the surrounding TTG gneiss (Chapter 3). This hypothesis was tested by performing simple mixing calculations to model the observed groups 2 and 3 compositions, as presented in Figure 4.15. Calculations involved mixing a group 1 sample (Z11g; Table 4.2) with the average composition of TTG gneiss analysed for the Central Region LGC (data from: Rollinson 2012). The calculated (chondrite-normalised) REE patterns indicate that some of the group 2 ultramafic rocks can be roughly re-created by mixing the group 1 ultramafic sample with 10–40% TTG gneiss (Fig. 4.15). However, this modelling predicts SiO_2 contents of between 44 and 51 wt. %, which

does not correlate with the 40 to 48 wt. % measured in the group 2 ultramafic samples. Moreover, the chondrite-normalised REE patterns displayed by the group 3 ultramafic rocks could not be re-created by any mixing scenario (Fig. 4.15). Consequently, the modelling presented in Figure 4.15 suggests that simple mixing between group 1 ultramafic rocks and local TTG gneiss offers a limited and inherently poor solution for the source of the LREE enrichment and HFSE anomalies displayed by the group 2 and 3 ultramafic rocks.

The crustal contamination hypothesis is also questioned by other evidence presented in this study. First, LREE enrichment and HFSE anomalies generated by crustal contamination are commonly associated with SiO_2 enrichment (Arndt 1999), but bulk-rock SiO_2 and La are poorly correlated (R^2= 0.02) in the Ben Strome ultramafic rocks. Second, the group 2 and 3 samples are randomly distributed throughout the Ben Strome Complex, rather than being preferentially concentrated towards the edges, where interactions with the surrounding TTG might be expected to be most intense. Moreover, group 2 samples may be located less than 30 cm (stratigraphically) from group 1 samples located both above and below, as shown in Figure 4.2d. Although this hypothesis cannot be completely ruled out without having conducted Hf and/or Nd isotopes on bulk-rock samples, the evidence presented here indicates that crustal contamination is unlikely the source of the HFSE anomalies in the Ben Strome ultramafic rocks.

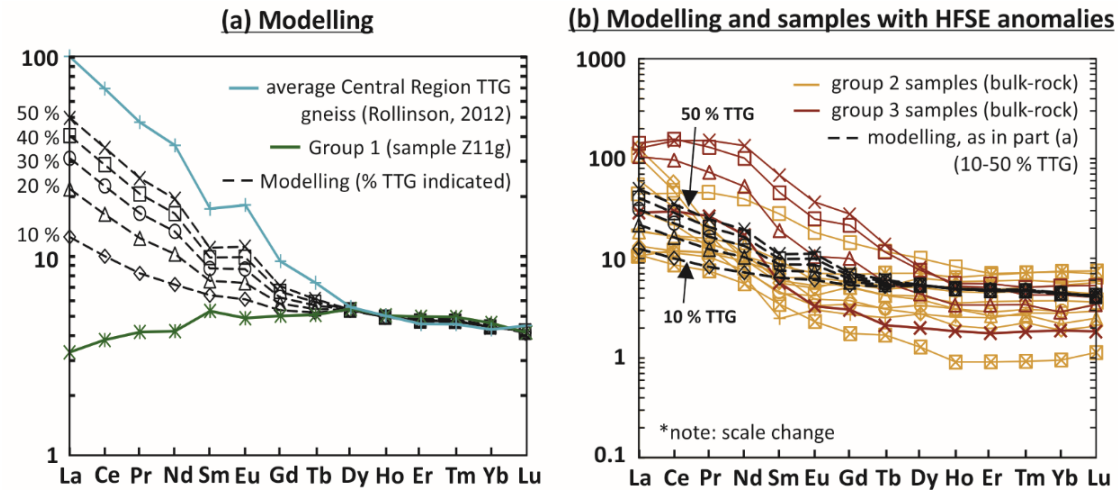

Figure 4.15: *Chondrite-normalised (McDonough and Sun 1995) REE plots detailing the mixing calculations used to test the crustal contamination hypothesis.* ***(a)*** *Modelling.* ***(b)*** *Modelling and bulk-rock analyses of samples HFSE anomalies.*

4.6.2.3 Secondary metasomatism

As outlined in Section 4.6.2.1, it is unlikely that the geochemical signatures displayed by the group 2 and 3 ultramafic rocks reflect primary magmatic processes involving a single magma. Rather, subsequent element mobility is likely responsible for the LREE enrichment and

associated HFSE anomalies displayed by the bulk-rock geochemistry for these samples (Fig. 4.5 and 15d). In contrast, the group 1 samples do not appear to have experienced the same LREE mobility, with the trace element compositions displayed by these samples interpreted to most closely resemble primary signatures (Fig. 4.14d). As stated above, this interpretation is supported by the moderate to strong positive correlation between Yb and the LREE (R^2= 0.5–0.9) in the group 1 samples, and the absence of any correlation between these elements in the groups 2 and 3 samples (Fig. 4.5). Moreover, the absolute abundances of elements considered to be immobile in the Ben Strome Complex (e.g., Nb, Ta, Zr, Hf, Ti, Y and the HREE) are comparable between all 3 geochemical groups (Fig. 4.3), demonstrating that the trace element budgets of the Ben Strome ultramafic rocks were likely comparable prior to metasomatism. This interpretation supports the mineral chemistry study of Rollinson and Gravestock (2012), who attributed similar LREE enrichment of clinopyroxene in layered ultramafic rocks from Camas nam Buth (located near Scourie, 13 km NW of Ben Strome; Fig. 2.1) to secondary, rather than primary, processes.

Although the relatively LREE-rich TTG gneiss that surrounds the Ben Strome Complex represents a potential local source of LREE, there is a limited number of processes capable of mobilising, transporting and depositing these elements (Williams-Jones et al. 2012). One possibility, as initially proposed by Rollinson and Gravestock (2012), is that the groups 2 and 3 Ben Strome ultramafic rocks interacted with LREE-rich, felsic melts produced during localised partial melting, which occurred during the 2.7 Ga Badcallian metamorphic event. This hypothesis is supported by the evidence for partial melting at Ben Strome (Chapter 3) and wider LGC (Johnson et al. 2012, 2013). However, it is questioned by the absence of any petrographic evidence for such melts at the macro or micro scale within the group 2 or 3 rocks. Moreover, there is no recorded field evidence for felsic partial melts cross-cutting ultramafic rocks, either at Ben Strome (Chapters 3 and 5) or elsewhere in the LGC (Johnson et al. 2012, 2013, 2016). This hypothesis is also hard to reconcile with the composition of felsic partial melts reported by Johnson et al. (2012), as all group 3 and some group 2 ultramafic rocks contain higher concentrations of LREE than these melts.

Alternatively, mobilisation, transport and deposition of the LREE (in the groups 2 and 3 ultramafic rocks) may have been facilitated by a CO_2 and H_2O-rich fluid associated with amphibolitisation. This is further to the work of Beach and Tarney (1978), who proposed that hydrothermal fluids were responsible for significant element mobility during the retrogression of the granulite-facies mineral assemblages in the LGC. The CO_2-rich, H_2O-rich fluid hypothesis is directly supported by the near-exclusive presence of LREE-rich carbonate

mineral phases (mixed analyses contain < 122 ppm La; Fig. 4.13) within the groups 2 and 3 samples (Fig. 4.7), which may represent the relics of fluid-rock interaction. This hypothesis is also consistent with the more intense amphibolitisation of clinopyroxene in the groups 2 and 3 samples relative to the group 1 samples (Fig. 4.6), and with the composition of amphibole and clinopyroxene, which reflect and ultimately control the bulk-rock trace element patterns (Figs. 5.11, 5.12 and 5.14). Moreover, the group 2 and 3 samples show evidence for introduction of S via hydrothermal fluids (as pyrite; Fig. 4.8) that is absent in the group 1 samples.

Amphibolitisation of the Ben Strome ultramafic rocks was probably polyphase (Fig. 4.6), occurring during both the Inverian and Laxfordian metamorphic events at ca. 2.48 and 1.9–1.6 Ga respectively (Goodenough et al. 2010, 2013, Crowley et al. 2015). Based on the cross-cutting carbonate veins present in group 2 and 3 ultramafic rocks, it is here suggested that the CO_2 and H_2O-rich fluids responsible for these rocks in the LREE were associated with the later stage, 1.9–1.6 Ga Laxfordian metamorphic event, when the rocks had already been amphibolitised. This interpretation is supported by the presence of the large, E–W-trending Laxfordian shear zone that cross-cuts the Ben Strome Complex, which plausibly provided a conduit for fluids that subsequently exploited a discrete fracture network in the Ben Strome Complex. Although CO_2 and H_2O-rich fluids are generally not considered the most efficient mechanism for transporting and concentrating the LREE (Williams-Jones et al. 2012), several authors report LREE mobility associated with CO_2-rich fluids, particularly in the upper mantle (Wood 1990, Yaxley et al. 1991, Lahaye et al. 1995, Yaxley et al. 1998, Powell et al. 2004, Williams-Jones et al. 2012). In these examples, the composition of clinopyroxene and amphibole often exhibit elevated Na and Si, and depleted Al and Ti concentrations relative to un-metasomatised samples, with these chemical effects reflected by the group 2 and 3 Ben Strome ultramafic rocks (Fig. 4.9; Yaxley et al. 1991, 1998, Powell et al. 2004).

Based on these combined characteristics, the HFSE anomalies displayed by the group 2 and 3 samples are most consistent with processes involving interaction with a CO_2 and H_2O-rich hydrothermal fluid associated with amphibolitisation and the Laxfordian metamorphic event, which represents the second phase of amphibolite-facies metamorphism experienced by the LGC. Therefore, only the trace element patterns displayed by the group 1 samples represent the original composition of the Ben Strome ultramafic rocks immediately after they crystallised (Figs. 4.3b and 4.14d).

4.6.3. Implications for geochemical fingerprinting in Archaean cratons

Although the role of modern-style plate tectonic processes (including Phanerozoic-style subduction) remains highly controversial, HFSE anomalies in extrusive/intrusive ultramafic-mafic Archaean assemblages have been widely cited as evidence for Archaean subduction-related magmatism (Fig. 4.1; Manya 2004, Ordóñez-calderón et al. 2009, Manikyamba and Kerrich 2011, Yellappa et al. 2012, 2014, Szilas et al. 2013, Wang et al. 2015, Guo et al. 2017). Such interpretations assume that, as with Phanerozoic subduction-related magmatism, the HFSE anomalies are generated by the enrichment of subduction-mobile elements (e.g., the alkali metals and LREE) relative to subduction-immobile elements (e.g., the HFSE; Klemme et al. 2005, Pearce 2014). However, the data presented in this study indicate that apparent negative HFSE anomalies can also be generated by discrete secondary processes that produce enrichment of LREE while the HFSE remain at (or close to) primary concentrations. This is further to previous research suggesting that the HFSE anomaly can also be generated by crustal contamination (Arndt 1999) and interaction with the SCLM (Pearce 2014). The HFSE anomaly is therefore considered to represent an unreliable proxy for Archaean subduction that should be treated with extreme caution, particularly in Archaean terranes such as the North Atlantic Craton that have experienced high-grade and polyphase metamorphism.

Some studies that invoke a subduction-related origin for HFSE anomalies in other Archaean intrusive/extrusive ultramafic-mafic assemblages offer several (and inconsistent) lines of evidence and argument to demonstrate that the rocks have not been subject to element mobility (Manya 2004, Ordóñez-calderón et al. 2009, Wang et al. 2015, Guo et al. 2017), with LOI values lower than 3.5 wt. % and the assumed immobility of the REE during hydrothermal alteration most commonly cited. The assertion that low LOI values can be used to 'screen' altered samples is contradicted by the data presented here, with the group 1 samples, which are here interpreted to have experienced limited element mobility, displaying values of < 9 wt. %. The groups 2 and 3 samples, which have experienced significant mobility of the LREE (and elements generally considered mobile), exhibit LOI values of < 8 wt. %, but some of these samples display values of less than 1 wt. % meaning they would appear 'fresh' under as simple LOI screening process. If the Ben Strome ultramafic samples had been screened based on this 3.5 wt. % LOI rule, 10 (out of 20) group 1 samples, 7 (out of 11) group 2 samples and 2 (out of 4) group 3 samples would have been discarded. This supports the work of Babechuk and Kamber (2011), who observed low (< 5% wt. %) LOI values in samples that had demonstrably experienced significant mobility of fluid mobile elements. With respect to the

assumed immobility of the REE during hydrothermal alteration, this paper is the latest of a plethora of studies demonstrating that the REE can be mobilised by hydrothermal alteration of varying styles (Wood 1990, Yaxley et al. 1991, Lahaye et al. 1995, Powell et al. 2004, Williams-Jones et al. 2012). It is, therefore, clear that such assumptions are frequently misplaced, particularly in high-grade cratonic regions that have experienced polyphase and high-grade metamorphism.

The findings presented here question some previous interpretations of Archaean ultramafic-mafic assemblages as associated with subduction-related magmatism, particularly where bulk-rock HFSE anomalies are cited as primary evidence. It is possible that the HFSE anomalies displayed by these examples may have been generated by discrete secondary processes akin to those described here, with the role of subduction during the Archaean potentially overestimated as a result. While it is entirely possible that subduction-related magmatism contributed to crustal growth during the Archaean, this finding must rest on reliable evidence. It is clear from the evidence presented here that a comprehensive assessment of element mobility and petrography (using well characterised and spatially constrained samples) is a minimum requirement prior to attaching a geodynamic interpretation, further demonstrating that geochemical fingering should be assessed on a location-specific basis (Collerson and Kamber 1999, Condie 2003, 2005, Babechuk and Kamber 2011). Given the effects of high-grade metamorphism and associated processes, which are unique on the terrane-scale, individual occurrences of ultramafic-mafic units should be placed within the regional framework to constrain primary geochemical signatures, with a 'one-size fits all' approach to bulk-rock trace element geochemical data inappropriate in such complex regions.

4.7 Conclusions

Negative HFSE anomalies, which are commonly used as evidence for subduction-related magmatism in the Archaean, can also be generated by secondary processes that may be petrographically discrete. In the case of the Ben Strome Complex, these anomalies were most likely generated by LREE enrichment during metasomatism by a CO_2 and H_2O-rich hydrothermal fluid associated with amphibolitisation, rather than reflecting a signature inherited from a subduction-related magma.

Our data demonstrate that the HFSE anomaly should be used (as a proxy for Archaean subduction) with extreme caution, particularly in Archaean terranes that have experienced multiple phases of high-grade metamorphism and where the rocks are likely to have

experienced differential element mobilities. Consequently, conducting a comprehensive assessment of element mobility and petrography (using well characterised and spatially constrained samples) is a minimum requirement prior to assigning any geodynamic interpretation to Archaean ultramafic-mafic units. In cases where such assessments have not been undertaken, it is possible that subduction-related interpretations have been erroneously invoked, with the role of subduction as an Archaean geodynamic process potentially overestimated as a result.

Chapter 5

Ultramafic-mafic complexes in the Lewisian Gneiss Complex: A record of multiple suites of Archaean magmatism

To investigate the origin and geodynamic significance of the ultramafic-mafic complexes in the LGC, this chapter aims to answer the following specific research questions:

(Q1) How many suites of temporally and/or petrogenetically distinct phases of ultramafic-mafic magmatism are recorded by the mainland LGC, and what is the relative age relationship between these suites and the TTG?

(Q2) How many of the ultramafic-mafic complexes share a common origin with the Ben Strome Complex (Chapters 3 and 4), and are the data for these complexes also consistent with a layered intrusion origin?

(Q3) What is the origin(s) of any ultramafic-mafic rocks that are not genetically related to the Ben Strome Complex?

In order to investigate these research questions, this chapter presents data from 12 ultramafic-mafic complexes in the Central Region LGC (for the location of individual occurrences, see Fig. 5.1). Further to the field and petrographic data for the Ben Strome and Geodh' nan Sgadan Complexes presented in Chapter 3, field constraints (including mapping of 4 occurrences) and petrographic investigations are detailed from 10 additional ultramafic-mafic complexes. Moreover, bulk-rock geochemistry (including: lithophile major, minor and trace elements, and PGE) is presented for all 12 ultramafic-mafic complexes studied, with spinel mineral chemistry conducted on samples from 10 occurrences.

5.1 Field relationships

Based on field relationships and associated mapping, the studied ultramafic-mafic complexes are here subdivided into Type A (n=9) and Type B (n=2) occurrences. The Type A complexes are a well-characterised group defined as sharing salient field features with the previously described Ben Strome Complex (see Chapter 3); while the Type B complexes, which exhibit limited shared characteristics, are defined as displaying contrasting field characteristics. Type A complexes include the occurrences at Achiltibuie, Achmelvich, Ben Auskaird, Ben Dreavie, Ben Strome (Chapters 3 and 4), Drumbeg, Loch Eilean na Craoibhe Moire, North Scourie Bay and Scouriemore, while Type B complexes include the occurrences at Geodh' nan Sgadan

(Chapter 3) and Loch an Diamh Mor (Fig. 5.1). An additional complex (Gorm Chnoc; Fig. 5.1) cannot be easily categorised based on field relationships and associated mapping, exhibiting a limited number of shared characteristics with the Type A complexes. Gorm Chnoc is therefore provisionally included in the group of Type B complexes throughout this chapter, with its genetic association evaluated (based on the data in the succeeding section) in Section 5.5.1.

Small-scale mapping – conducted in 2017 – of two Type A complexes (Loch Eilean na Craoibhe Moire and Drumbeg) and two Type B complexes (Gorm Chnoc and Loch an Daimh Mor) is included in Figure 5.2, with these localities chosen due to their good-excellent exposure. Detailed mapping of the Ben Strome Complex (the type locality for the Type A complexes) and Geodh' nan Sgadan Complex (classified here as a Type B complex), which are detailed in Chapter 3, are also referred to throughout this section.

5.1.1 Type A complexes

The Type A complexes are exposed across areas up to 7 km^2 and are composed of modally layered ultramafic rocks and cryptically layered mafic rocks. The ultramafic portions comprise up to 60 % of the exposed complexes and are dominated by metawebsterite and metaolivine-websterite (with volumetrically subordinate metaperidotite layers), while the mafic portions comprise up to 100 % of individual complexes and contain metagabbro, garnet-metagabbro, garnet-amphibolite and amphibolite in variable proportions. On average, the ultramafic and mafic rocks occur in a 1:2 ratio (e.g., Ben Strome and Scouriemore), although two Type A complexes mapped as part of this study (Drumbeg and Loch Eilean na Craoibhe Moire) each contain more than 50 % ultramafic rocks (Fig. 5.2a-b). Some complexes contain multiple ultramafic and mafic units (of varying character and thickness) within apparent individual successions, as is demonstrated in the Loch Eilean na Craoibhe Moire Complex (Fig. 5.2a). Although rocks interpreted as (possibly) metasedimentary occur at North Scourie Bay (Goodenough and Krabbendam 2011), the 3 largest Type A complexes – Ben Strome (Chapters 3 and 4), Loch Eilean na Craoibhe Moire (Fig. 5.2a) and Drumbeg (Fig. 5.2b) – record no spatial association with rocks that conceivably have a metasedimentary origin.

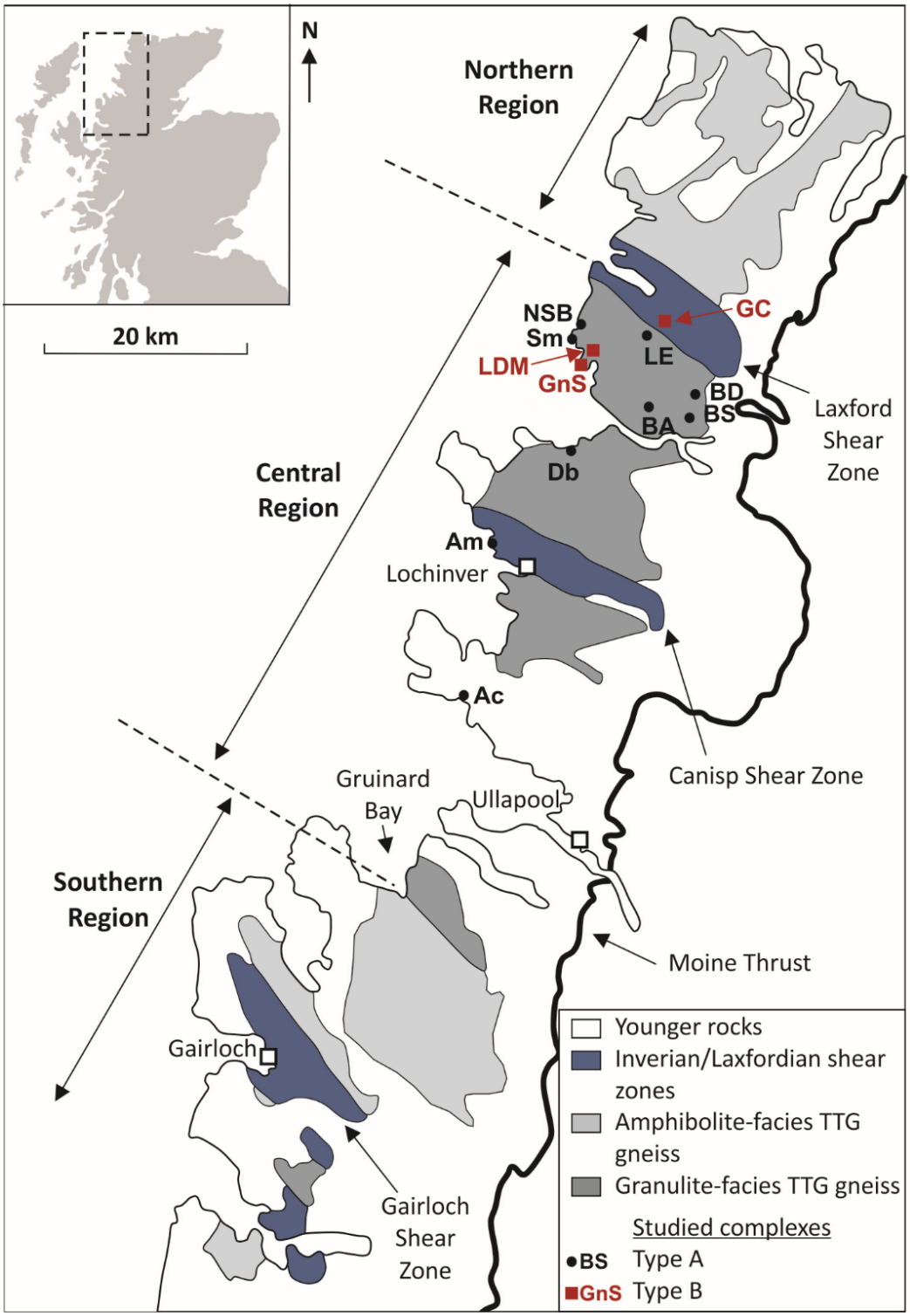

Figure 5.1: *Simplified geological map of the LGC detailing the locations of the ultramafic-mafic complexes investigated as part of this study (redrawn after: Kinny et al. 2005, Wheeler et al. 2010, Johnson et al. 2012). Abbreviations: Ac=Achiltibuie; Am=Achmelvich; BA=Ben Auskaird; BD=Ben Dreavie; BS=Ben Strome; Db=Drumbeg; GC=Gorm Chnoc; GnS=Geodh' nan Sgadan; LDM=Loch an Daimh Mor; LE=Loch Eilean na Craoibhe Moire; NSB=North Scourie Bay; Sm=Scouriemore.*

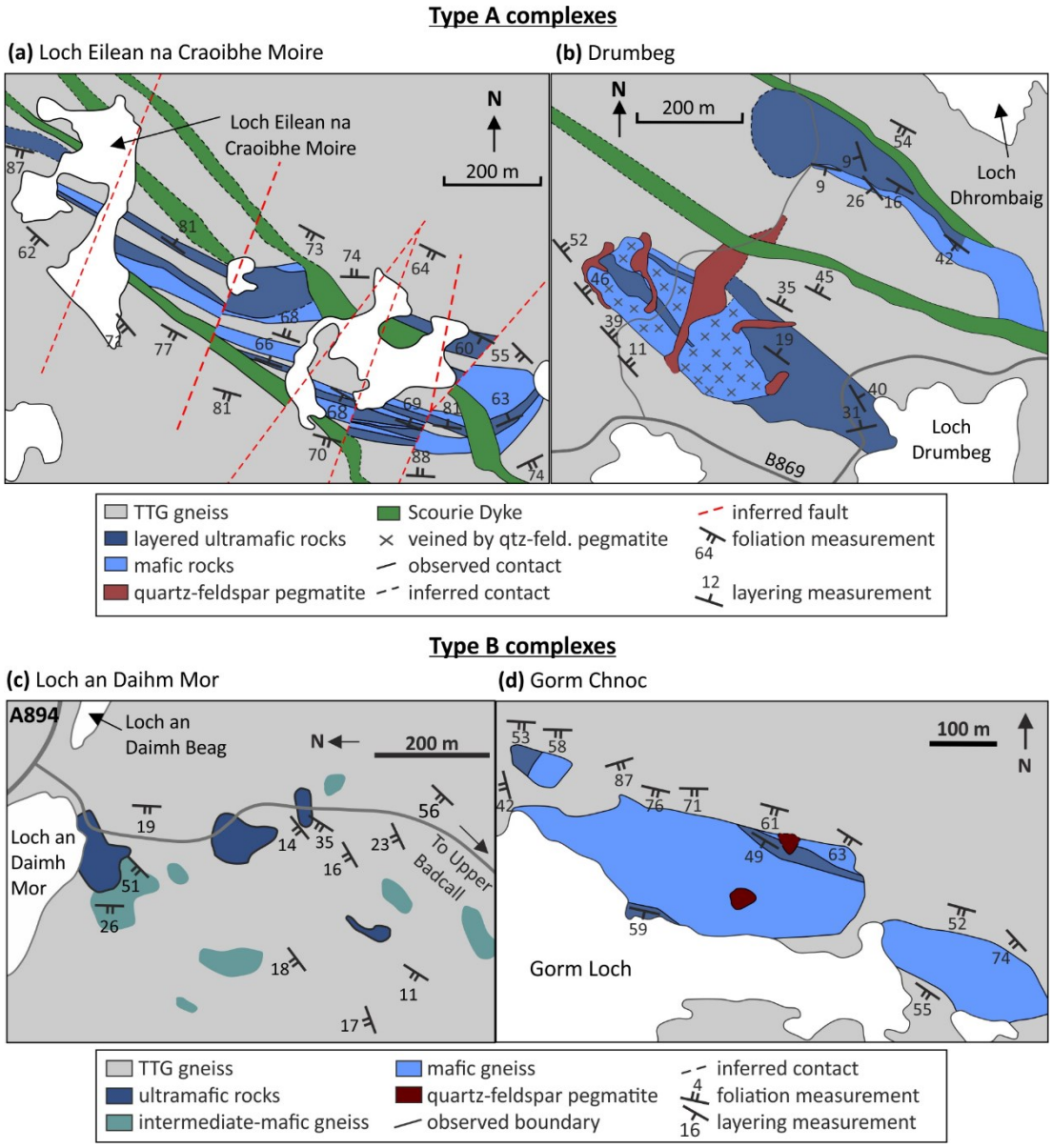

Figure 5.2: *Simplified geological maps of the Loch Eilean na Craoibhe Moire, Drumbeg, Loch an Daimh Mor and Gnoc Gorm Complexes. The location of each complex is detailed in Fig. 5.1.*

The contacts between the Type A complexes and surrounding TTG gneiss are almost always obscured by vegetation, although rare exposures at Ben Strome indicate that these contacts are often tectonic, as demonstrated by slickensides and recrystallised quartz (Chapter 3). Similarly, although many of the contacts between ultramafic and mafic units are obscured by vegetation, those observed are gradational on a scale of tens of centimetres (Chapter 3). Despite this, the Type A complexes exhibit a variety of structural architectures. The shallow- to moderate-dipping Ben Strome Complex (Fig. 3.1; Chapter 3) and Drumbeg Complex (Fig. 5.2b) both display Badcallian to Inverian folds (on all scales) that are cross-cut by Laxfordian shear zones and Scourie Dykes. In contrast, the steeply dipping (70–90°) Loch Eilean na Craoibhe Moire Complex exhibits a NW-SE Inverian/Laxfordian trend that is cross-cut by

Scourie Dykes and a suite of NE-SW-trending Phanerozoic faults. Although this group of complexes displays varying structural styles, there is a consistent parallelism between the gneissose foliation in the TTG, the layering in the ultramafic-mafic rocks, and all lithological contacts.

Individual ultramafic units can commonly be traced for hundreds of metres along strike (Fig. 5.2a-b) and are generally several metres to several tens of metres in apparent thickness. Generally, metaperidotite is restricted to rare, centimetre- to decimetre-scale layers within the ultramafic portions, although metaperidotitic rocks do comprise up to 50 % of individual ultramafic packages in the Ben Strome Complex (Chapter 3). The ultramafic rocks exhibit many features characteristic of layering in layered intrusions, such as: gradational and sharp contacts between individual layers; gradational variation in modal mineral abundances within individual layers; and truncation of layers on the centimetre-scale (Fig. 5.3a-c). The metawebsterites have distinctly grey weathered surfaces and generally show little-to-no internal layering (Fig. 5.3a-c), while the grey-brown metaolivine-websterites and brown metaperidotites exhibit prominent internal layering (Fig. 5.3b-c). Moreover, the more metaperidotitic layers are generally negatively weathered relative to the pyroxenitic layers (Fig. 5.3a) due to the serpentinisation of olivine. The Achmelvich Complex (Fig. 5.1) – unlike the other Type A complexes – exhibits centimetre- to decimetre-scale monomineralic layers of serpentinite and amphibolite (Fig. 5.3d).

The mafic portions of the Type A complexes comprise garnet-metagabbro, metagabbro, garnet-amphibolite and amphibolite in varying portions. In places, the mafic rocks show centimetre- to metre-scale layering that is more discrete than in the ultramafic rocks, with individual layers defined by the proportions of garnet, pyroxene and plagioclase (Fig. 5.3e). Garnet, which commonly occurs on the centimetre-scale and often exhibits retrogressive plagioclase rims, may form large clots up to 1 m in diameter (Fig. 5.3f). Millimetre- to centimetre-scale horizons containing high proportions of oxide minerals (dominantly magnetite and ilmenite) rarely occur.

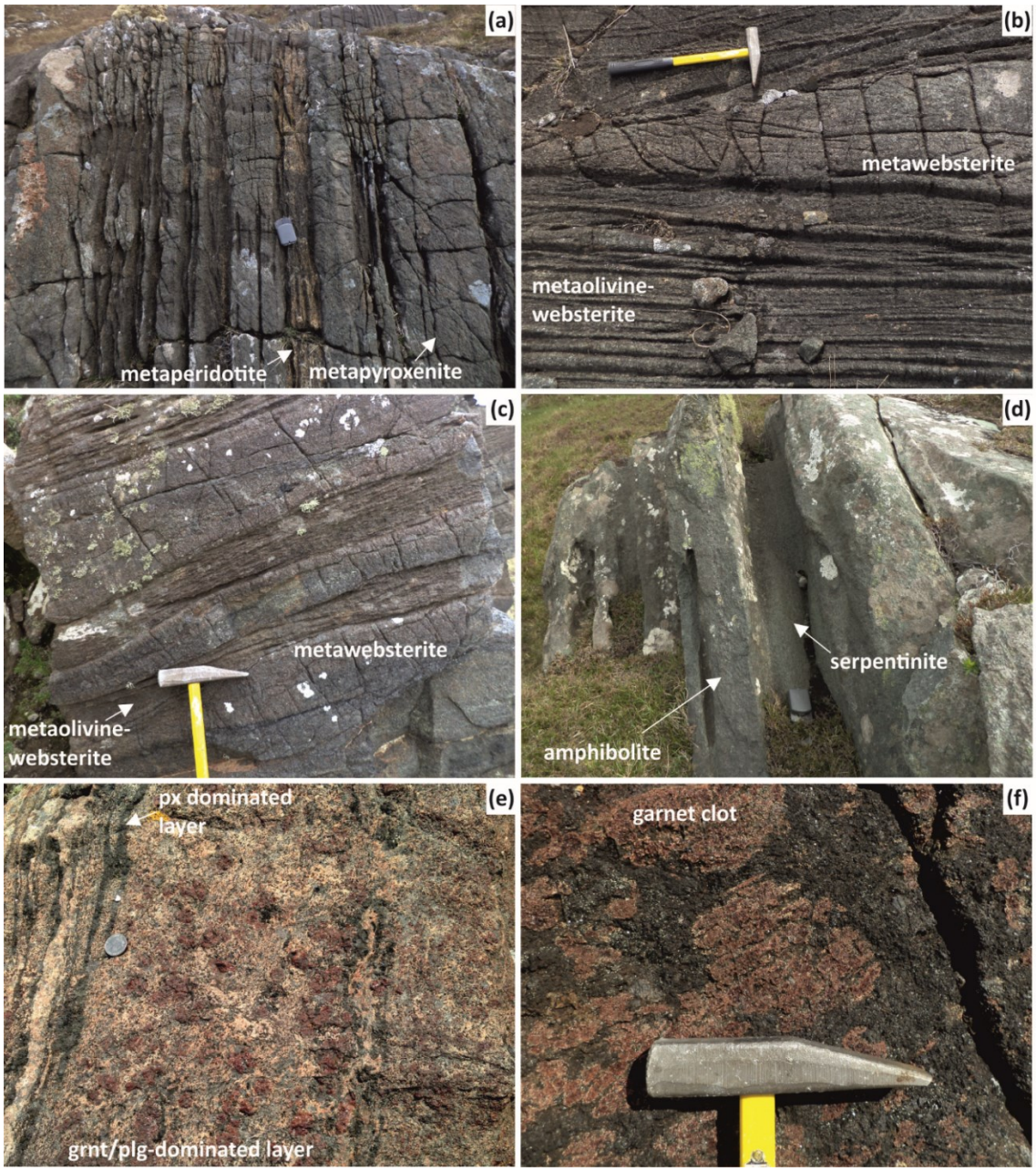

Figure 5.3: *Field photographs detailing the representative rocks types of the Type A complexes.* ***(a)*** *Negatively weathered (brown) metaperidotite and positively weathered (grey) metapyroxenite, Loch Eilean na Craoibhe Moire Complex.* ***(b)*** *Internally layered metaolivine-websterite and massive metawebsterite, with some evidence for truncation of layers, Loch Eilean na Craoibhe Moire Complex.* ***(c)*** *Modally layered metawebsterite and metaolivine-websterite, Scouriemore Complex.* ***(d)*** *Layered serpentine and amphibolite, Achmelvich Complex.* ***(e)*** *Layering in mafic rocks, Scouriemore Complex, as defined by the proportions of garnet (grnt), pyroxene (px) and plagioclase (plg).* ***(f)*** *Garnet clots within pyroxene-rich mafic rocks, Ben Strome Complex. Hammer length=40 cm. Hammer head width=17cm. Compass-clinometer length=10 cm.*

5.1.2 Type B complexes

As outlined above, the Type B complexes exhibit limited shared characteristics and are therefore described separately.

The Gorm Chnoc Complex, which is exposed over a ~0.5 x 0.2 km area, is located in the NE of the Central Region, within the Laxford Shear Zone (Figs. 5.1 and 5.2d). Roughly 80 % of the Complex comprises plagioclase-rich mafic rocks, with the remaining 20 % comprising ultramafic rocks that are, in places, layered (Fig. 5.4a). Layering involves metawebsterite and metaolivine-websterite and is comparable to some of the layering observed in the Type A complexes (Section 5.1.1; Fig. 5.4a). The mafic rocks are generally dominated by pyroxene and plagioclase, with centimetre-scale garnet clots occurring rarely (Fig. 5.4b). Although there is some concordance between the layering in the ultramafic rocks, the foliation in the TTG gneiss, and the lithological margins (between the ultramafic and mafic rocks, and between the Complex and TTG), the Gorm Chnoc Complex exhibits examples of discordance between these features (Fig. 5.2d). The Complex is also cross-cut by several mafic-felsic partial melts (Johnson et al. 2012, 2013), and by veins that exploit later, brittle structures (e.g., Fig. 5.4b).

The Loch an Daimh Mor Complex – located in the NW of the Central Region LGC (Fig. 5.1) is a 500 m^2 area of TTG gneiss that contains several irregularly-shaped pods of ultramafic-mafic rocks (Fig. 5.2c). The generally massive ultramafic rocks, which comprise almost exclusively metaperidotite, are high serpentinised (± talc), exhibit grey-brown weathered surfaces and dark grey fresh surfaces (Fig. 5.4c-e). The metaperidotites are variably veined by separate carbonate- and orthopyroxene-rich veins, with the latter more numerous than the former. The orthopyroxene-dominated veins (Fig. 5.4e), which display sharp contacts with the surrounding ultramafic rocks, are 1–40 cm thick and contain centimetre-scale zircon crystals interpreted as associated with Inverian metasomatism (Faithfull et al. 2018). The metagabbro-dominated mafic rocks, which occur in association with volumetrically subordinate intermediate gneiss, are poorly-exposed and locally contain garnet. Unlike the Type A complexes, the foliation in the surrounding TTG gneiss displays distinctive discordance with the lithological contacts on the map-scale (Fig. 5.2c).

As previously described in Chapter 3, the Geodh' nan Sgadan Complex – located in the NW of the Central Region (Fig. 5.1) – is a moderately-dipping, 15 m thick package of mafic rocks (Fig. 3.9). The Complex is underlain and overlain by TTG gneiss, with the gneissosity in the latter parallel to the layering in the former (Fig. 3.9). Ultramafic rocks are notably absent, and the surrounding TTG gneiss contains a relatively large number of centimetre- to metre-scale mafic pods that are rare in the Type A complexes. These pods generally display elongation parallel to the foliation (Fig. 3.10a). Layering in the plagioclase-rich mafic rocks – defined by millimetre-scale variation in the modal abundance of plagioclase and pyroxene – ranges from

well-defined and laterally continuous on a scale of tens of metres to poorly-defined and chaotic (Fig. 3.10c-f). Despite this, layering of some description is almost always present, with garnet restricted to rare, centimetre-scale horizons (Fig. 3.10c).

Figure 5.4: *Field photographs detailing the representative rocks types of the Type B complexes.* ***(a)*** *Layered ultramafic rocks from the Gorm Chnoc Complex.* ***(b)*** *Mafic rocks and cross-cutting felsic veins in the Gorm Chnoc Complex.* ***(c-e)*** *Massive peridotite from the Loch an Daimh Mor Complex. For field photographs of the Geodh' nan Sgadan Complex, see Chapter 3. Hammer length=40 cm. Hammer head width=17cm. Compass-clinometer length=10 cm. Abbreviations: opx=orthopyroxenite.*

5.2 Petrography

A total of 62 polished thin sections (made at Cardiff University) were subject to petrographic assessment as part of this study. For the Type A complexes, 42 thin sections from 7 different complexes (excluding the Ben Strome Complex ultramafic rocks described in Chapter 4) were assessed. For the Type B complexes, 16 thin sections from all 3 complexes were evaluated. A majority of thin sections are of ultramafic samples (n=37), with a smaller subset of thin sections (n=25) of mafic samples. In addition to optical microscopy, 33 out of 62 samples were subject to detailed petrographic assessment by element mapping on an A-SEM (at Cardiff University), with instrumentation and methodology utilised detailed in Appendix A. The location (presented as British National Grid GPS coordinates) and modal mineral proportions of each sample are detailed in Table 5.1 (for ultramafic rocks) and Table 5.2 (for mafic rocks). Where possible, modal mineral proportions were estimated using element maps, with the appropriate methodology described in Appendix A.

5.2.1 Type A complexes

The samples of ultramafic rocks from the Type A complexes (Fig. 5.5a-d) comprise (in modal %): < 19 % olivine; < 32 % serpentine; < 84 % orthopyroxene; < 48 % clinopyroxene; < 100 % amphibole; and < 4 % spinel (Table 5.1), with accessory sulphide minerals (pentlandite, chalcopyrite and pyrrhotite). The mean modal mineral percentages for these ultramafic rocks (summarised in Table 5.1) are generally similar to those for the Ben Strome Complex ultramafic rocks (Table 4.1), although the ultramafic rocks assessed here generally contain less serpentine. Olivine, which generally occurs as small remnants within masses of fine-grained serpentine (± magnetite; Fig. 5.5a), is rarely preserved as millimetre-scale subhedral grains that have been subject to some serpentinisation (Table 5.1; Fig. 5.5b). Clino- and ortho-pyroxene are euhedral to anhedral, 0.5 to 2.8 mm in diameter, and are variably replaced by fine-grained (< 0.2 mm diameter) amphibole (Fig. 5.5c), with orthopyroxene dominant over clinopyroxene (Table 5.1). Amphibolitisation of pyroxene ranges from near-absent (occurring as rare rims on individual pyroxene grains; Fig. 5.5a-c) to near-complete (Fig. 5.5c) within individual thin sections, with such variation observed both within and between individual Type A complexes (Table 5.1). For example, the modal percentage of amphibole in thin sections from the Scouriemore Complex ranges from 7.1 to 99.8 %, while amphibole content ranges from 4.0 to 51.0 % in the Loch Eilean na Craoibhe Moire Complex (Table 5.1). In ultramafic lithologies, pargasitic amphibole also occurs as < 2.1 mm diameter grains that commonly exhibit 120° triple junctions (Fig. 5.5d). Spinel occurs as euhedral to

subhedral grains < 2.5 mm in diameter, while pentlandite, pyrrhotite and chalcopyrite occur rarely, as anhedral-euhedral grains < 0.2 mm in diameter.

Table 5.1: *Location, grid reference and modal mineralogy for each ultramafic sample used in this study. *denotes the presence of millimetre- to centimetre-scale zircons that are not included in the modal mineralogy (see Fig. 5.6 for a photomicrograph of the relevant thin section). For the location and modal mineralogy of ultramafic samples from the Ben Strome Complex, see Table 4.1. Abbreviations: LEC=Loch Eilean na Craoibhe Moire Complex; amf=amphibole; cpx=clinopyroxene; ol=olivine; spn=spinel; srp=serpentine; EM=sample subject to element mapping using an A-SEM at Cardiff University (see Appendix A for details of the instrumentation and methodology used).*

Locality	Sample	Grid ref (NC)	EM?	Modal Mineralogy (%)					
				ol	srp	opx	cpx	amf	spn
Type A complexes (n=28)									
Scouriemore	T2190	N/A	Y	0.0	4.0	7.4	48.1	37.6	2.9
Scouriemore	T2160L	N/A	Y	0.0	20.0	37.5	19.0	21.1	2.4
Scouriemore	T2160U	N/A	Y	0.0	18.9	45.7	26.6	7.1	1.7
Scouriemore	T2110	N/A	Y	0.0	0.0	20.4	22.6	54.7	2.3
Scouriemore	X3	N/A	Y	0.0	0.0	0.0	0.2	99.8	0.0
Scouriemore	Lw16_643B	14230/44184	Y	19.0	0.0	40.5	18.4	21.0	1.0
Scouriemore	Lw16_657	14209/44227	Y	0.0	0.0	28.8	23.8	44.8	2.6
North Scourie Bay	NSB_UMa	N/A		0.0	0.0	75.0	0.0	23.0	2.0
North Scourie Bay	NSB_UMb	N/A		3.5	0.0	31.0	31.0	33.0	1.5
LEC	Lw16_627B	21188/43446		0.0	0.0	39.8	10.0	50.0	0.2
LEC	Lw16_629B	21127/43493	Y	0.0	0.0	42.4	2.9	50.9	3.9
LEC	LW17-E1	21448/43096	Y	0.0	0.0	16.1	33.4	49.9	0.6
LEC	LW17-E2A	21448/43096	Y	0.0	9.3	38.0	6.4	46.4	0.0
LEC	LW17-E2B	21448/43096		4.5	1.0	25.0	45.0	23.0	1.5
LEC	LW17-E2C	21448/43096		15.5	26.0	40.0	12.0	4.0	2.5
LEC	LW17-E3	21448/43096	Y	0.0	19.1	42.8	6.9	31.2	0.0
LEC	LW17-E5	21448/43096	Y	4.0	10.2	48.0	8.3	28.3	1.2
Achmelvich	Lw16-619B	05749/24184	Y	0.0	0.0	0.0	0.0	100.0	0.0
Achmelvich	Lw16-620A	05586/24174	Y	0.0	0.0	0.0	1.7	98.4	0.0
Achmelvich	LW17-Am2	05688/24284	Y	0.0	0.0	4.3	0.0	95.0	0.8
Achiltibuie	Lw16_799A	03048/07951	Y	4.2	4.6	19.0	36.9	34.4	1.0
Achiltibuie	Lw16_799B	03048/07951	Y	2.0	8.1	50.2	7.8	30.9	1.1
Ben Dreavie	LW17-BD1	26738/38805	Y	0.0	0.0	84.3	14.8	0.0	0.9
Ben Dreavie	LW17-BD2	26738/38805	Y	2.5	2.9	51.1	29.1	13.3	1.1
Drumbeg	LW17-Db3b	11067/33060	Y	0.4	32.0	30.8	9.0	26.5	1.4
Drumbeg	LW17-Db8	11255/33061	Y	2.0	18.6	7.9	0.0	70.4	1.2
Drumbeg	LW17-44	11472/33323	Y	0.0	5.2	52.1	13.7	28.7	0.4
Drumbeg	LW17-45A	11455/33353		1.5	0.5	52.0	5.0	39.0	2.0
Min				*0*	*0*	*0*	*0*	*0*	*0*
Max				*19*	*32*	*84*	*48*	*100*	*4*
Mean				*2*	*6*	*33*	*15*	*42*	*1*
Type B complexes (n=9)									
Lochan Daimh Mor	UBCr_P1	N/A	Y	0.3	40.4	56.5	1.2	0.0	1.6
Lochan Daimh Mor	UBCr_P3	N/A	Y	0.0	37.5	42.2	6.7	12.5	1.2
Lochan Daimh Mor	X11A	N/A	Y	0.3	54.2	5.9	0.0	39.6	0.0
Lochan Daimh Mor	X11B	N/A		0.0	100.0	0.0	0.0	0.0	0.0
Lochan Daimh Mor – vein and host rock	UBZr_1a*			0.0	25.0	60.0	5.0	10.0	0.0
Lochan Daimh Mor – vein	LEW014A	15621/41834	Y	0.0	0.0	97.1	0.2	2.7	0.0
Gorm Chnoc	LW17-GC2	21912/44749	Y	0.4	7.0	31.6	6.7	54.0	0.2
Gorm Chnoc	LW17-GC3	21912/44749		1.5	15.0	8.0	18.0	55.0	2.5
Gorm Chnoc	LW17-GC5	21954/44751	Y	4.7	28.1	2.8	0.0	64.4	0.0
Min				*0*	*0*	*0*	*0*	*0*	*0*
Max				*5*	*100*	*97*	*18*	*64*	*3*
Mean				*1*	*34*	*34*	*4*	*26*	*1*

Table 5.2: *Location and modal mineralogy for each mafic sample used in this study. [+]denotes the presence of millimetre-scale chalcopyrite that is not included in the modal mineralogy. Abbreviations: amf=amphibole; cpx=clinopyroxene; fel=feldspar (plagioclase in the Type A complexes; dominantly plagioclase, with subordinate alkali feldspar, in the Type B complexes); gnt=garnet; opx=orthopyroxene; ox=oxides; qtz=quartz; EM=sample subject to element mapping using an A-SEM at Cardiff University (see Appendix A for details of the instrumentation and methodology used).*

				Modal Mineralogy (%)							
Locality	**Sample**	**Grid ref (NC)**	**EM?**	**opx**	**cpx**	**amf**	**fel**	**gnt**	**qtz**	**ox**	**mica**
Type A complexes (n=13)											
Ben Auskaird	LEW004	20926/40272		0.0	0.0	84.0	13.0	0.0	3.0	0.0	0.0
Ben Strome	LEW010	25375/35591		2.0	8.0	71.0	2.0	12.0	0.0	5.0	0.0
Ben Strome	LEW011	25716/36120		16.0	16.0	12.0	13.0	35.0	0.0	8.0	0.0
Ben Strome	LEW012[+]	25553/36005		30.0	60.0	10.0	0.0	0.0	0.0	0.0	0.0
Ben Strome	Lw16_510b	24879/35626		8.0	22.0	11.0	27.0	32.0	0.0	0.0	0.0
Ben Strome	Lw16_Z2a-1	26067/35391		2.0	7.0	46.0	24.5	18.0	0.5	2.0	0.0
Ben Strome	Lw16_Z2a-2	26067/35391		0.0	0.0	65.0	35.0	0.0	0.0	0.0	0.0
Ben Strome	Lw16_Z2b	26067/35391		5.0	30.0	65.0	0.0	0.0	0.0	0.0	0.0
Ben Strome	Lw16_Z13b	26073/35578	Y	0.0	2.7	51.9	45.0	0.0	0.4	0.0	0.0
Ben Strome	Lw16_Z13c	26073/35578	Y	0.0	35.8	39.9	15.4	7.9	1.0	0.0	0.0
Ben Strome	Lw16_Z14a	26073/35585		9.0	48.0	23.0	8.0	12.0	0.0	0.0	0.0
Ben Strome	Lw16_Z14b	26073/35585		0.0	4.8	75.0	20.0	0.0	0.2	0.0	0.0
Ben Strome	Lw16_Z15	26077/35593		0.0	49.0	20.0	18.0	11.0	0.0	2.0	0.0
Min				0	0	10	0	0	0	0	0
Max				30	60	84	45	35	3	8	0
Mean				6	22	44	17	10	0	1	0
Type B complexes (n=7)											
Gorm Chnoc	LW17-GC1	22139/44569		0.0	0.0	85.0	15.0	0.0	0.0	0.0	0.0
Gorm Chnoc	LW17-GC4	22156/44613		0.0	0.0	70.0	30.0	0.0	0.0	0.0	0.0
Geodh' nan Sgadan	LW17-BcT3	14632/41779	Y	11.2	0.0	82.3	6.5	0.0	0.0	0.0	0.0
Geodh' nan Sgadan	LW17-BcT4	14631/41780		5.0	6.0	44.0	45.0	0.0	0.0	0.0	0.0
Geodh' nan Sgadan	LW17-BcT6	14628/41784	Y	0.0	27.9	71.5	0.0	0.0	0.6	0.0	0.0
Geodh' nan Sgadan	LW17-BcT8	14627/41801	Y	0.0	35.4	0.0	64.1	0.0	0.0	0.5	0.0
Geodh' nan Sgadan	LW17-BcT12A	14625/41836		0.0	0.0	20.0	66.0	14.0	0.0	0.0	0.0
Min				0	0	0	0	0	0	0	0
Max				11	35	85	66	14	1	0	0
Mean				2	10	53	32	2	0	0	0

The samples of mafic rocks from the Type A complexes (Fig. 5.5e-f) comprise (in modal %): < 30 % orthopyroxene; < 60 % clinopyroxene; 10–84 % amphibole; < 45 % plagioclase; < 35 % garnet; < 3 % quartz; and < 8 % oxide minerals (magnetite and ilmenite; Table 5.2). Pyroxene is subhedral to anhedral, 0.5 to 2.5 mm in diameter, and (like the ultramafic rocks) variably replaced by fine-grained (< 0.2 mm diameter) amphibole, with clinopyroxene dominant over orthopyroxene. Amphibole also occurs as 0.2 to 1.2 mm diameter grains that commonly display pleochroism and 120° triple junctions. Smaller amphibole grains (generally < 0.5 mm diameter) are sometimes intergrown with similarly sized (< 0.6 mm diameter) plagioclase and occasionally with finer-grained (< 0.1 mm diameter) anhedral quartz. Garnet occurs as millimetre- to centimetre-scale, anhedral to subhedral grains that exhibit significant

retrogression to plagioclase (±amphibole), commonly as rims. Magnetite is the dominant oxide phase, forming subhedral grains < 0.3 mm in diameter. Ilmenite is rare, but where present comprises < 7 modal % (Table 5.2) of individual samples.

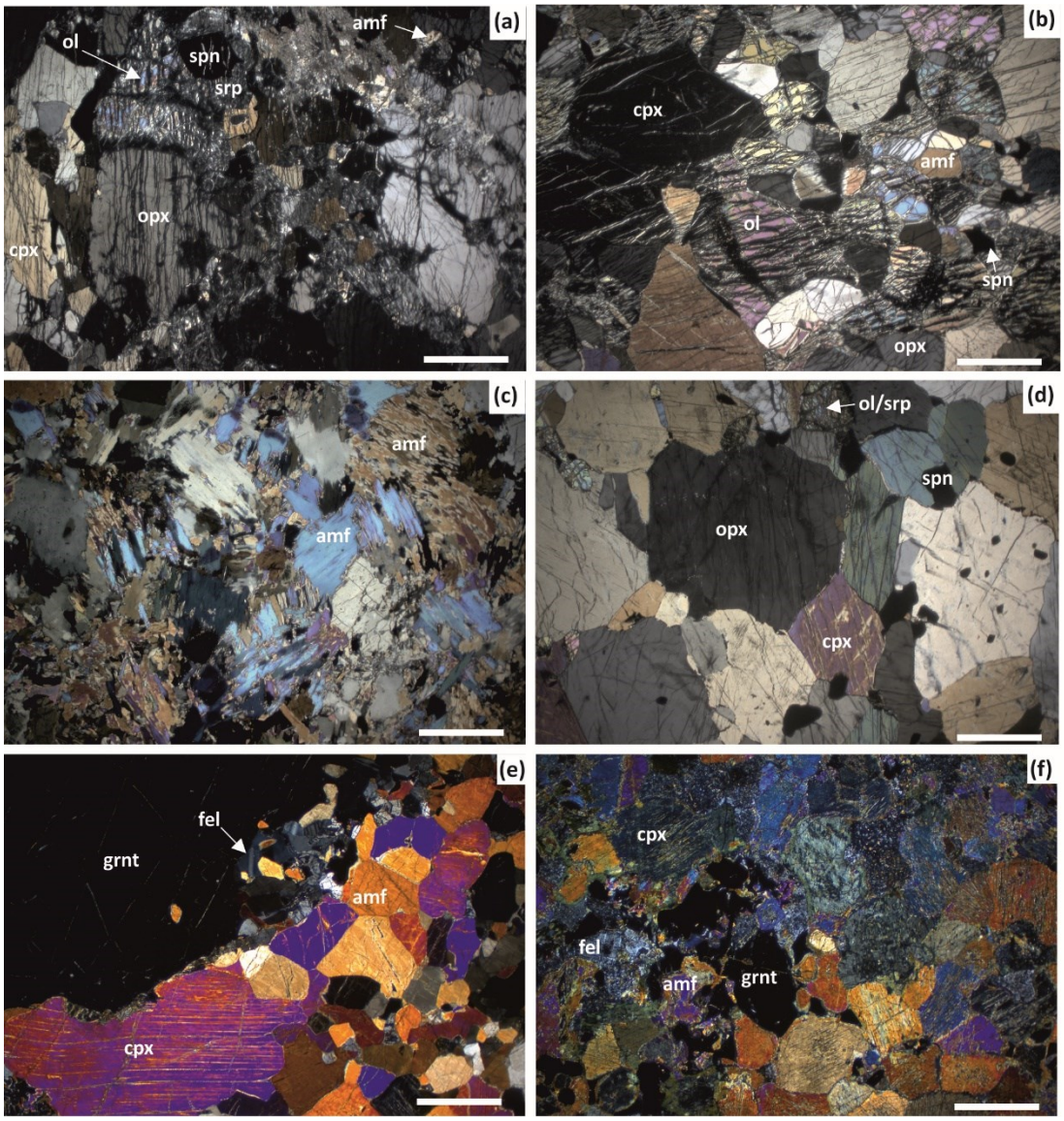

Figure 5.5: *Photomicrographs (in XPL) detailing the petrographic characteristics of the Type A complexes.* ***(a)*** *Metapyroxenite from the Drumbeg Complex (sample LW17-Db3b).* ***(b)*** *Metapyroxenite/metaperidotite from the Loch Eilean na Craoibhe Moire Complex (sample LW17-E2c).* ***(c)*** *Amphibolitised pyroxenite from the Achmelvich Complex (sample Lw16_610B).* ***(d)*** *Metapyroxenite from the Achiltibuie Complex (sample Lw16_799A).* ***(e)*** *Garnet-metagabbro from the Ben Strome Complex (sample Lw16_Z14a).* ***(f)*** *Garnet-metagbabbro from the Ben Strome Complex (sample Lw16_Z15). Abbreviations: amf=amphibole; cpx=clinopyroxene; fel=feldspar; grnt=garnet; ol=olivine; opx=orthopyroxene; serp=serpentine; spn=spinel. White scale bar=1 mm.*

5.2.2 Type B complexes

Excluding those taken from orthopyroxenite veins, the ultramafic samples from the Loch an Daimh Mor Complex (n=4) comprise (in modal %): < 0.3 % olivine; 37.5–100 % serpentine; <

56.5 % orthopyroxene; < 6.7 % clinopyroxene; < 39.6 % amphibole; and < 1.6 % spinel (Table 5.1). In these samples, olivine is largely replaced by fine-grained serpentine (± magnetite), with small remnants of olivine occasionally preserved (Fig. 5.6a). Orthopyroxene is subhedral to anhedral and < 3.2 mm in diameter, while subhedral to anhedral clinopyroxene occurs rarely as < 1.6 mm diameter grains (Fig. 5.6a). Amphibole is subhedral to anhedral and < 2 mm in diameter, while chromite is subhedral to anhedral and < 3.5 mm in diameter. The one sample that is representative only of an orthopyroxenite vein (sample LEW014A; Table 5.1) comprises (in modal %; according to element mapping): 97.1 % orthopyroxene; 0.2 % clinopyroxene; and 2.7 % amphibole. In this sample, orthopyroxene is euhedral to subhedral, 1.0–1.5 mm in diameter and commonly exhibits 120° triple junctions (Fig. 5.6b). Clinopyroxene and amphibole occur rarely as subhedral grains < 1.2 mm in diameter, with < 8 mm diameter zircons hosted by some of the orthopyroxenite veins (Fig. 5.6b). Such veins display sharp contacts with the surrounding peridotite on the thin section-scale, as shown in Figure 5.6b.

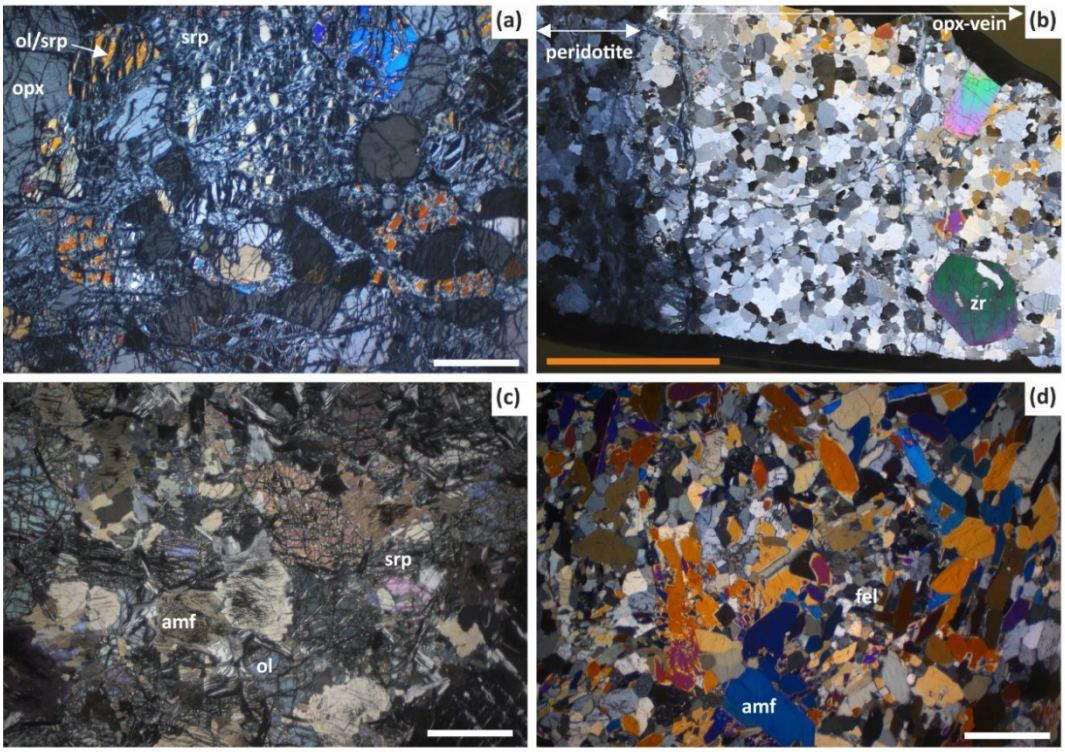

Figure 5.6: *Photomicrographs (in XPL) detailing the petrographic characteristics of the Type B complexes.* ***(a)*** *Metaperidotite from the Loch an Daimh Mor Complex (sample UBCr_P1).* ***(b)*** *Full thin section photo of an orthopyroxenite vein (that extends off the section to the right) cross-cutting metaperidotite, with large zircon crystals (sample UBZr1) from the Loch an Daimh Mor Complex. See Fig. 5.4 for an outcrop scale photograph of a similar orthopyroxene vein cross-cutting metaperidotite.* ***(c)*** *Metapyroxenite from the Gorm Chnoc Complex (sample LW17-GC5).* ***(d)*** *Metagabbro from the Gorm Chnoc Complex (sample LW17-GC1). Abbreviations: amf=amphibole; bi=biotite; cpx=clinopyroxene; fel=feldspar; ol=olivine; opx=orthopyroxene; zr=zircon. White scale bar=1 mm; orange scale bar=1 cm.*

The ultramafic samples from the Gorm Chnoc Complex (n=3) comprise (in modal %): 0.4–4.7 % olivine; 7.0–28.1 % serpentine; 2.8–31.6 % orthopyroxene; < 18 % clinopyroxene; 55–64.4 % amphibole; and < 2.5 % spinel (Table 5.1). Olivine is variably serpentinised, with the majority of grains showing partial serpentinisation that manifest as fine-grained (< 0.2 mm diameter) serpentine and magnetite (Fig. 5.6c). Ortho- and clino-pyroxene, which are generally anhedral and < 1.4 mm in diameter, show variable replacement by fine-grained amphibole, with amphibole also occurring as subhedral to anhedral grains < 2.5 mm in diameter. Magnetite – derived from serpentinisation – occurs as < 0.2 mm diameter grains in association with serpentine, while spinel is green (in PPL), generally subhedral and < 0.5 mm in diameter. The mafic samples from the Gorm Chnoc Complex (n=2) are highly amphibolitised, comprising (in modal %): 70–85 % amphibole; and 15–30 % plagioclase feldspar (Fig. 5.6d; Table 5.2). Amphibole is subhedral to anhedral and ranges from 0.1–2.0 mm in diameter, while feldspar is subhedral to anhedral and < 0.6 mm in diameter (Fig 5.6d).

The mafic samples from the Geodh' nan Sgadan Complex comprise (in modal %): < 11.2 % orthopyroxene; < 35.4 % clinopyroxene; < 82.3 % amphibole; < 66.0 % feldspar (dominantly plagioclase, with subordinate alkali-feldspar); < 14 % garnet; < 0.6 % quartz; and < 0.5 % oxide minerals. As described in Section 3.3.3 (Fig. 3.11), clinopyroxene forms 0.2–0.6 mm diameter, subhedral to euhedral grains that are partially altered to fine-grained amphibole. Feldspar is 0.4–0.6 mm in diameter, generally subhedral and shows occasional 120° triple junctions, and orthopyroxene is subhedral and < 0.3 mm in diameter (Fig. 5.6d).

5.3 Bulk-rock geochemistry

A total of 75 samples were analysed for bulk-rock major, minor, and trace element geochemistry, with 56 samples from Type A complexes and 15 samples from Type B complexes. The majority of the samples analysed are ultramafic (n=46), with a smaller subset of mafic samples (n=29). A total of 54 samples were also analysed for PGE and Au (44 ultramafic samples and 10 mafic samples), with 40 samples from Type A complexes and 10 samples from Type B complexes. Samples were analysed using the methodology and instrumentation described in Appendix A, with Appendix E containing the raw data and details of the analysed duplicates and standards. Throughout the following sections, these data are compared to that of the Ben Strome Complex (Chapters 3 and 4), in order to test (Q2), as outlined in the introduction to this chapter.

5.3.1 Major and minor elements

5.3.1.1 Type A complexes

Excluding the Ben Strome Complex samples (detailed in Chapter 4), the ultramafic rocks from the Type A complexes exhibit relatively tight ranges in their SiO_2 (40.2 to 50.0 wt. %), TiO_2 (0.2 to 0.6 wt. %), MnO (0.1 to 0.2 wt. %), K_2O (< 1.2 wt. %) and Cr_2O_3 (0.1 to 0.7 wt. %) contents, and moderate ranges in their Al_2O_3 (3.4 to 11.3 wt. %), Fe_2O_3 (8.7 to 15.3 wt. %), MgO (17.2 to 39.4 wt. %), CaO (1.4 to 14.2 wt. %) and Na_2O (< 3.6 wt. %). In these rocks, MgO shows a moderate negative correlation with SiO_2, TiO_2, Al_2O_3 and CaO (R^2= 0.4–0.7), a weak negative correlation with K_2O (R^2= 0.1–0.4), and no correlation with Fe_2O_3, MnO, Na_2O and Cr_2O_3 (R^2= < 0.1).

The mafic rocks from the Type A complexes exhibit tight ranges in the MnO (0.1 to 0.3 wt. %), Na_2O (0.7 to 2.7 wt. %), K_2O (< 0.7 wt. %) and Cr_2O_3 (< 0.2 wt. %) contents, and relatively moderate ranges in the SiO_2 (33.6 to 49.4 wt. %), TiO_2 (0.3 to 3.4 wt. %), Al_2O_3 (7.8 to 16.9 wt. %), Fe_2O_3 (9.0 to 27.3 wt. %), MgO (3.5 to 20.7 wt. %), CaO (8.0 to 16.6 wt. %) contents. In these rocks, MgO shows a moderate negative correlation with Cr_2O_3 (R^2=0.4–0.7), a weak negative correlation with TiO_2, Fe_2O_3 and MnO (R^2= 0.1–0.4) and no correlation with SiO_2, Al_2O_3, CaO, Na_2O and K_2O.

Collectively (including both ultramafic and mafic rocks), MgO in the Type A complexes displays a strong negative correlation with Al_2O_3 (R^2= 0.7), a moderate negative correlation with SiO_2, TiO_2, CaO and K_2O (R^2= 0.4–0.7), a weak negative correlation with Fe_2O_3, Na_2O and Cr_2O_3 (R^2= 0.1–0.4), and no correlation with MnO and NiO (R^2= < 0.1). On all major and minor element bivariate plots (Fig. 5.7), the Type A complexes exhibit compositions and trends that overlap significantly with the Ben Strome Complex rocks, with this comparison most prominent on the MgO versus TiO_2, Al_2O_3, CaO, Na_2O and NiO plots (Fig. 5.7).

5.3.1.2 Type B complexes

Unlike the Type A complexes, the Type B complexes do not form one coherent geochemical group on major and minor element bivariate plots (Fig. 5.7), instead forming location-specific clusters. Consequently, the Type B complexes collectively show compositions and trends distinct from the Ben Strome Complex rocks, although there is some overlap with this field on the MgO versus TiO_2, Al_2O_3 and Na_2O plots (Fig. 5.7).

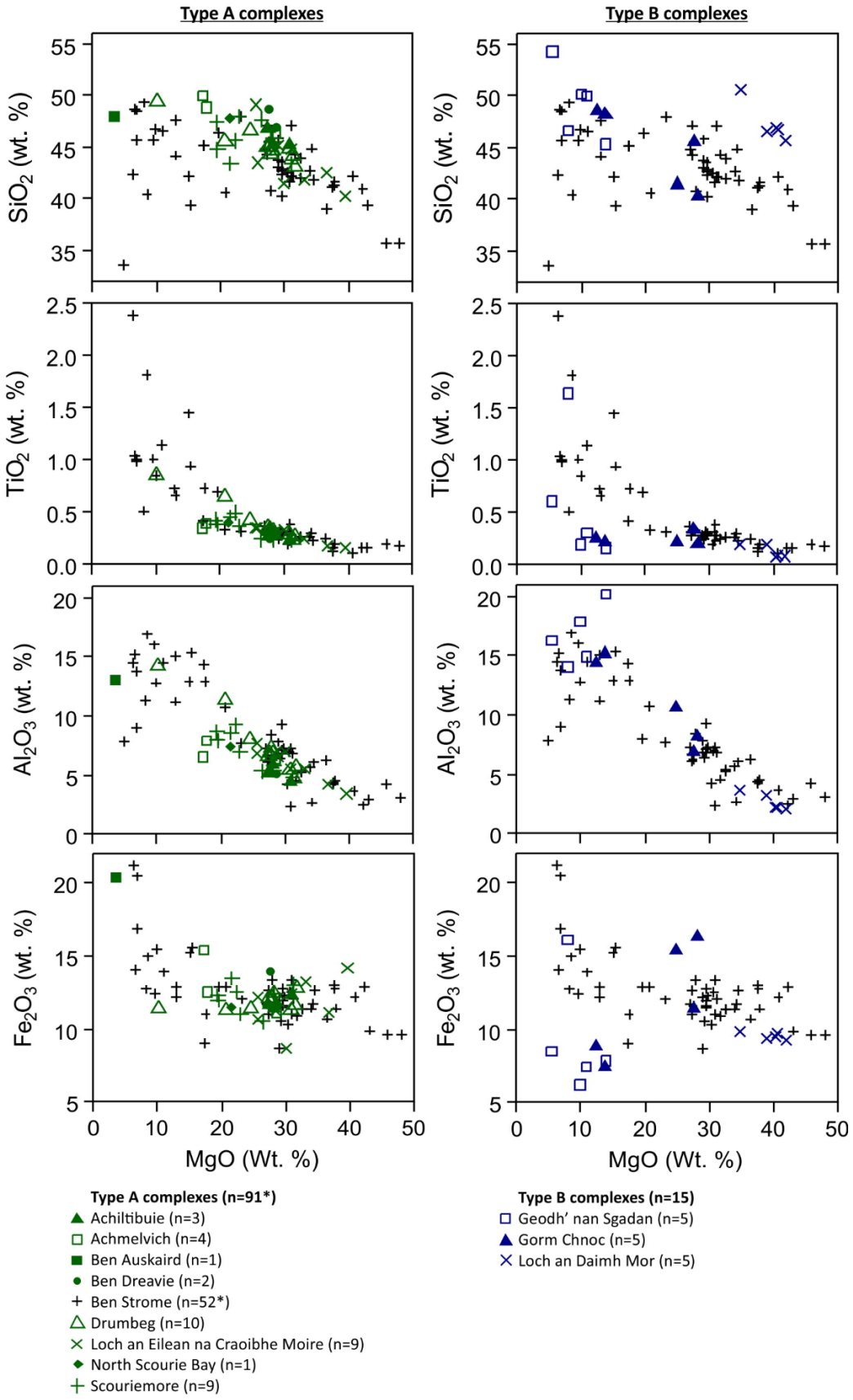

Figure 5.7: *Bivariate plots detailing the anhydrous major and minor element composition of the ultramafic and mafic rocks analysed as part of this study. * includes the 35 ultramafic samples (from the Ben Strome Complex) detailed in Chapter 4. Note: Fe_2O_3=total Fe.*

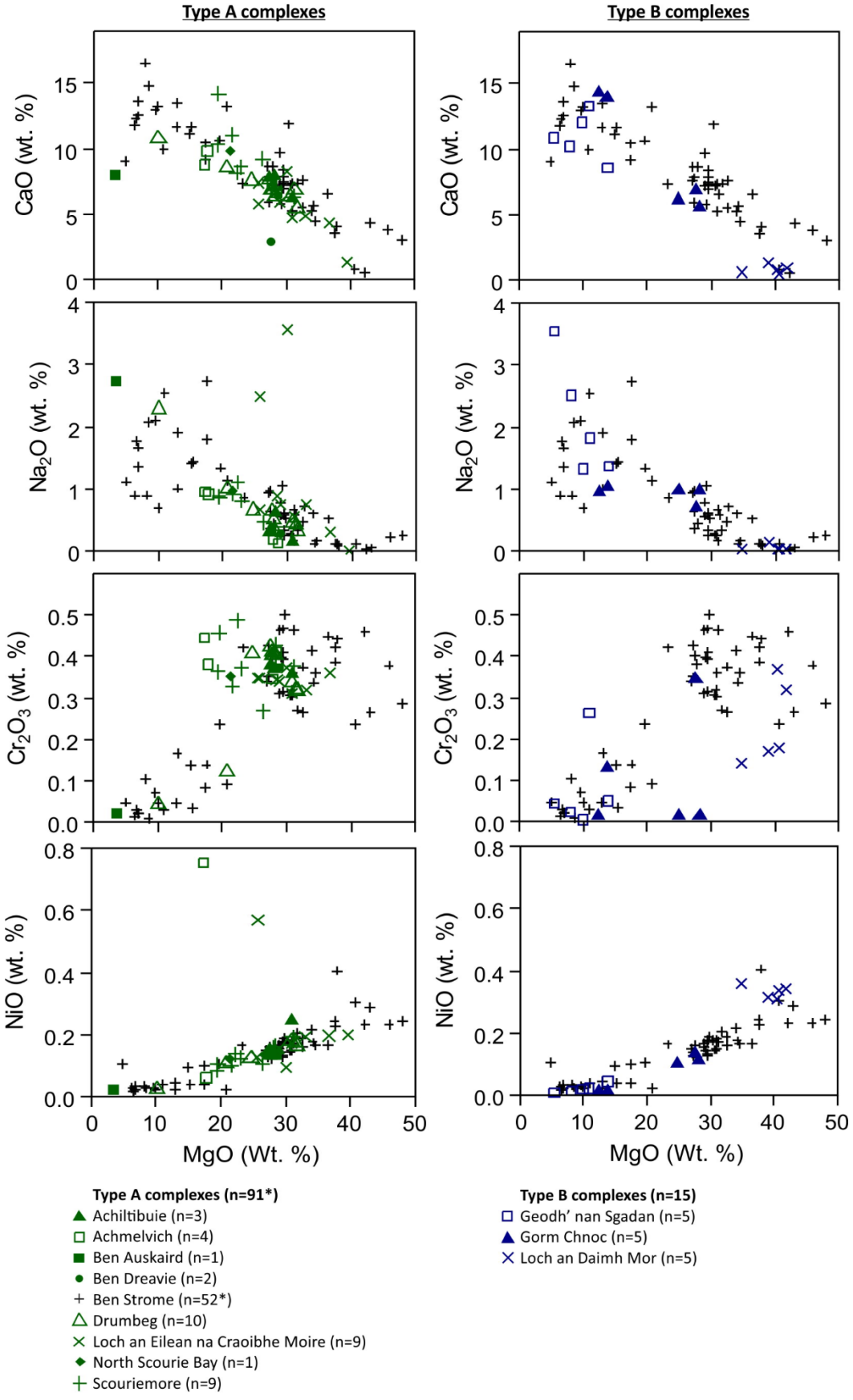

Figure 5.7 (cont.)

The ultramafic rocks from the Loch an Daimh Mor Complex show tight ranges in the TiO_2 (0.1 to 0.2 wt. %), Al_2O_3 (2.1 to 3.7 wt. %), Fe_2O_3 (9.3 to 9.8 wt. %), CaO (< 0.2 wt. %), MgO (34.7 to 41.8 wt. %) and NiO (0.3 to 0.4 wt. %) contents, and moderate ranges in the SiO_2 (45.6 to 50.6 wt. %) and Cr_2O_3 (0.1 to 0.4 wt. %) contents (Fig. 5.7). Relative to the ultramafic rocks for the Type A complexes, these rocks are enriched in MgO, depleted in TiO_2, Al_2O_3 and CaO, and show comparable Fe_2O_3 abundances.

The ultramafic rocks from the Gorm Chnoc Complex show tight ranges in the SiO_2 (40.3 to 45.6 wt. %), TiO_2 (0.2 to 0.3 wt. %), Al_2O_3 (6.8 to 10.7 wt. %), CaO (5.6 to 6.9 wt. %), MgO (24.8 to 28.2 wt. %), Na_2O (0.7 to 1.0 wt. %), Cr_2O_3 (< 0.3 wt. %) and NiO (0.1 to 0.2 wt. %) contents, and a moderate range in the Fe_2O_3 (7.4 to 16.3 wt. %) content. Relative to those for the Type A complexes (Fig. 5.7), these rocks display comparable SiO_2, TiO_2, Al_2O_3, CaO, MgO Na_2O and NiO contents, high Fe_2O_3 contents, and low Cr_2O_3 contents. The mafic rocks from the Gorm Chnoc Complex also show tight ranges in the SiO_2 (48.1 to 48.6 wt. %), TiO_2 (0.2 to 0.3 wt. %), Al_2O_3 (14.4 to 15.2 wt. %), CaO (13.9 to 14.3 wt. %), Fe_2O_3 (7.4 to 8.8 wt. %), Na_2O (1.0 to 1.1 wt. %), Cr_2O_3 (< 0.2 wt. %) and NiO (< 0.1 wt. %) contents. Relative to the mafic rocks for the Type A complexes (Fig. 5.7), these rocks display comparable SiO_2, Al_2O_3, CaO, Na_2O, Cr_2O_3 and NiO contents, and depleted TiO_2 and Fe_2O_3 contents.

The mafic rocks from the Geodh' nan Sgadan Complex show tight ranges in the SiO_2 (45.3 to 54.2 wt. %), TiO_2 (0.2 to 1.6 wt. %), Na_2O (1.3 to 3.5 wt. %), CaO (8.6 to 13.3 wt. %), NiO (< 0.1 wt. %) and Cr_2O_3 (< 0.3 wt. %) contents, and moderate ranges in the Al_2O_3 (14.1 to 20.2 wt. %), Fe_2O_3 (6.2 to 16.1 wt. %) and MgO (5.5 to 13.8 wt. %) contents. Relative to those of the Type A complexes, the mafic rocks of the Geodh' nan Sgadan Complex exhibit high SiO_2 and Al_2O_3 contents, low TiO_2 and Fe_2O_3 contents, and comparable Na_2O, MgO, CaO, NiO and Cr_2O_3 contents (fig. 5.7).

5.3.2 Trace elements

5.3.2.1 Type A complexes

On chondrite-normalised REE plots, the ultramafic rocks from the Type A complexes (Fig. 5.8a-f) generally exhibit flat patterns ($[La/Lu]_N$= 0.4–4.9), with flat to negatively sloping LREE ($[La/Sm]_N$= 0.3–2.9) and generally flat HREE ($[Gd/Lu]_N$= 0.6–1.7). Chondrite-normalised REE abundances range from 1.1 to 35.9, with all complexes showing significant overlap with the field for Ben Strome Complex ultramafic rocks (Fig. 5.8a-f). The analysed ultramafic rocks from the Ben Dreavie Complex (n=2) are the exception to this rule, exhibiting negatively sloping LREE ($[La/Sm]_N$= 6.1–9.7) and flat HREE ($[Gd/Lu]_N$= 1.9; Fig. 5.8d).

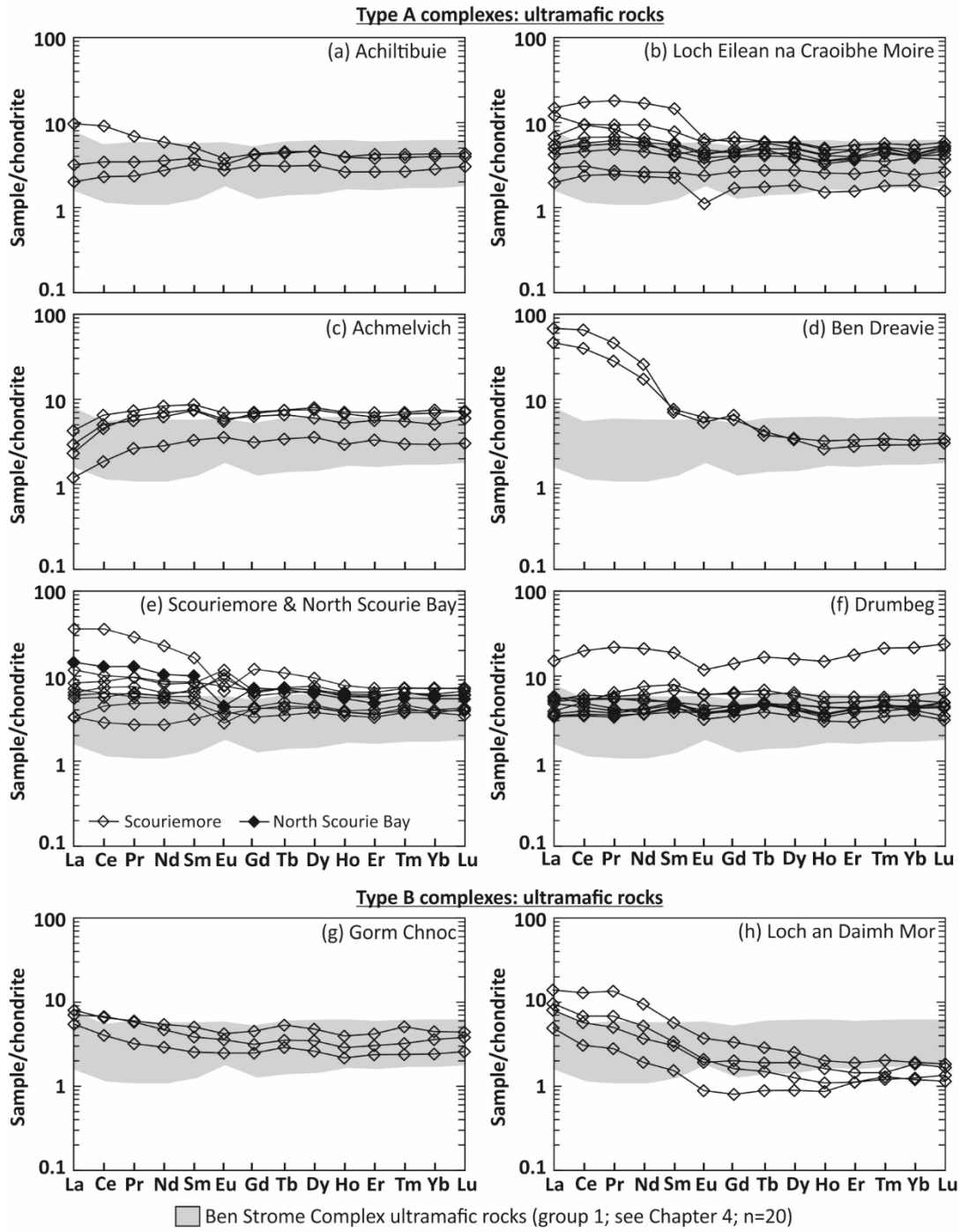

Figure 5.8: *Chondrite-normalised (McDonough and Sun 1995) REE plots for the ultramafic rocks from the Type A and Type B complexes.*

The mafic rocks from the Ben Strome Complex show flat to negatively sloping REE patterns ($[La/Lu]_N$= 0.3–7.2), with the LREE showing mild positive to negative slopes ($[La/Sm]_N$= 0.2–3.1), HREE showing flat to negative slopes ($[Gd/Lu]_N$= 0.8–2.7) and chondrite-normalised abundances ranging from 4.0 to 61.8 (Fig. 5.9a). The other analysed mafic rocks from the Type A complexes show comparable patterns to those from the Ben Strome Complex, but

are relatively enriched in all REE, exhibiting chondrite-normalised abundances ranging from 10.3 to 86.8 (Fig. 5.9b).

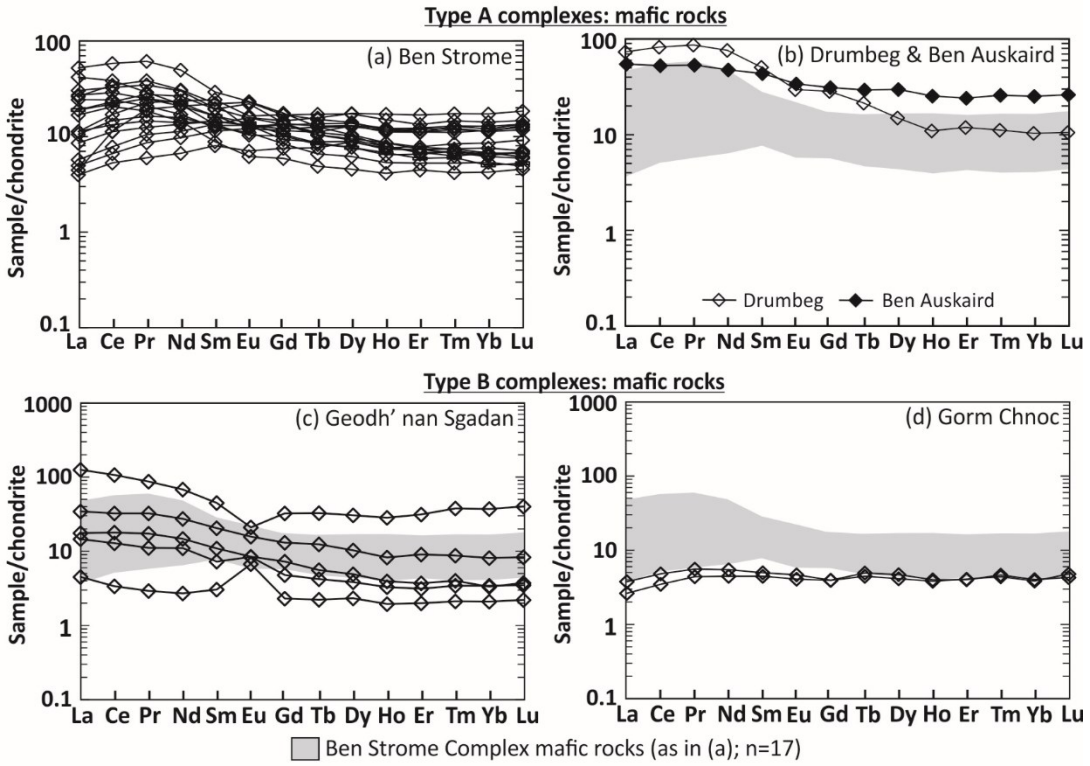

Figure 5.9: *Chondrite-normalised (McDonough and Sun 1995) REE plots for the mafic rocks from the Type A and Type B complexes.*

On primitive mantle-normalised trace element plots, the ultramafic rocks from the Type A complexes (Fig. 5.10a-f) generally exhibit flat patterns ($[Nb/Yb]_N$= 0.4–2.6), with positive Rb, Ba, Th and U anomalies. The ultramafic rocks from the Ben Dreavie Complex display positive La, Ce, Sr and Nd anomalies (or negative HFSE anomalies), while the Achmelvich Complex exhibits generally negative Rb, Ba, Rh and U anomalies, alongside negative Sr anomalies (Fig. 5.10a-f). Despite this variability, the trace element patterns for the Type A complexes consistently show near-complete overlap with the field for the Ben Strome Complex ultramafic rocks (Fig. 5.10a-f).

The mafic rocks from the Ben Strome Complex exhibit varied trace element patterns (Fig. 5.11a), with generally flat patterns ($[Nb/Yb]_N$= 0.3–2.8), some negative Th, U, Zr and Hf anomalies and some positive Rb, Ba, La, Ce and Nd anomalies ($[Ta/La]_N$= 0.1–4.2). One sample, which also exhibits a generally flat normalised trace element pattern (Fig. 5.9e), displays strong positive Nb, Ta and Ti anomalies ($[Ta/La]_N$= 16.3). Although the Nb/Yb ratios for the other analysed mafic rocks from the Type A complexes are comparable to those for the Ben Strome Complex ($[Nb/Yb]_N$= 0.8–2.3), the trace element patterns are highly variable

(Fig. 5.11b). The one analysed mafic sample from the Drumbeg Complex exhibits negative Th, U, Nb, Ta, Zr, Hf and Ti anomalies, and positive Rb, Ba, La, Ce, Sr and Nd anomalies; while the one mafic sample analysed from the Ben Auskaird Complex displays negative Rb and Sr anomalies (Fig. 5.11b).

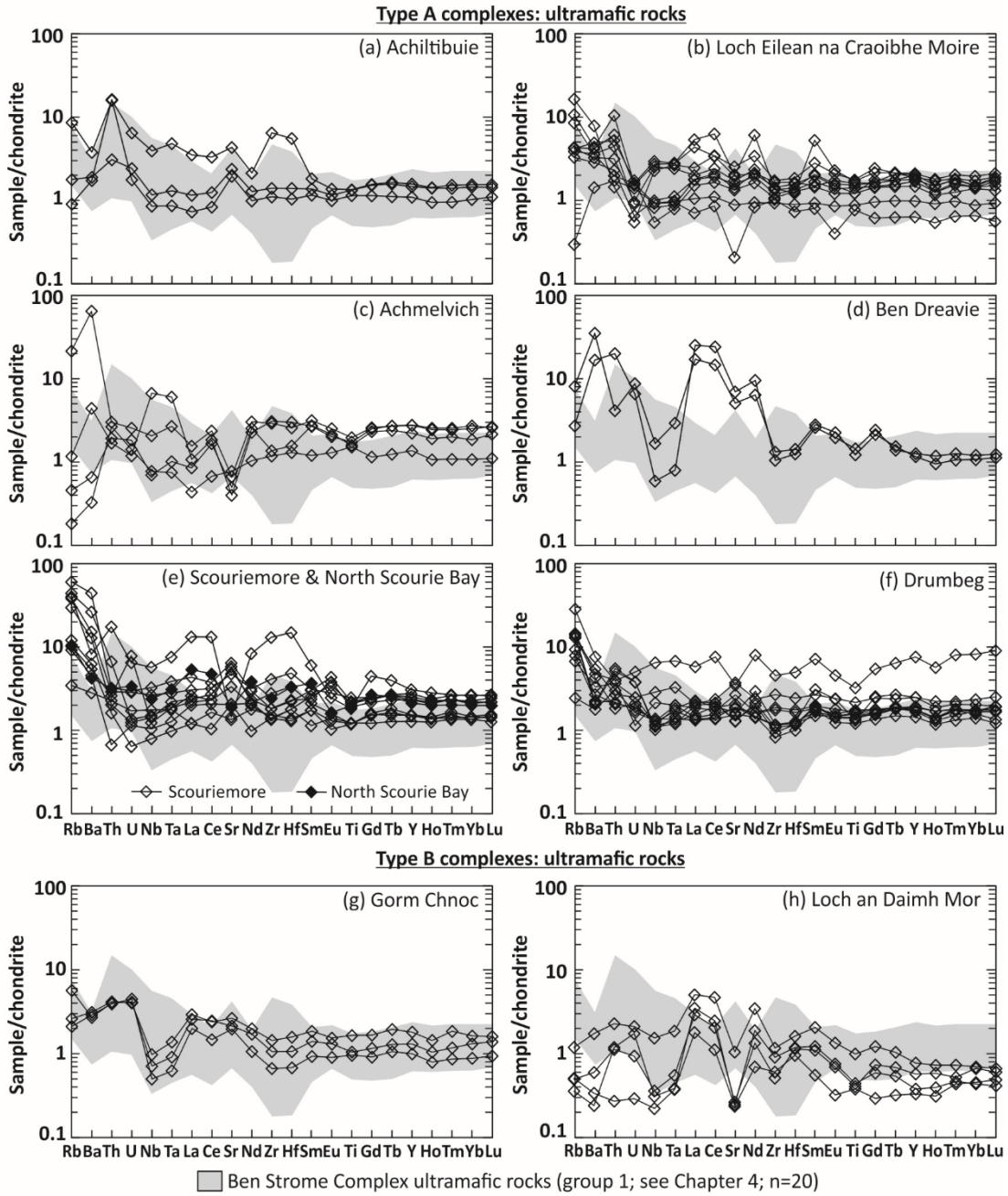

Figure 5.10: *Primitive mantle-normalised (McDonough and Sun 1995) trace element plots for the analysed mafic rocks from the Type A and Type B complexes.*

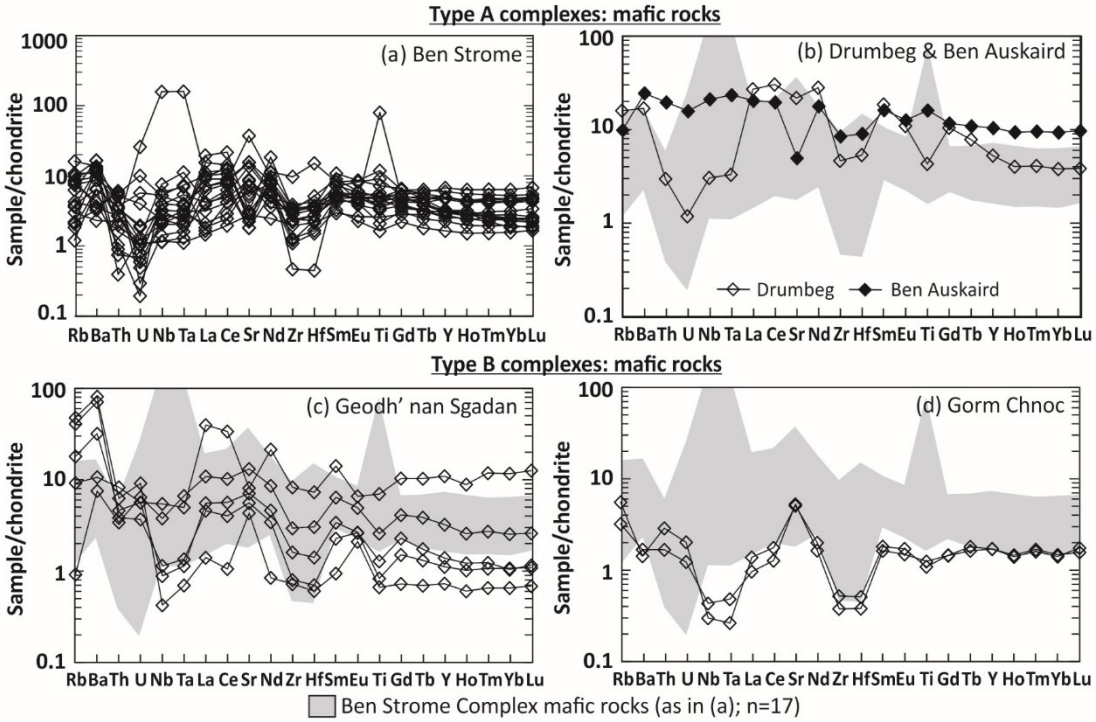

Figure 5.11: *Primitive mantle-normalised (McDonough and Sun 1995) trace element plots for the analysed mafic rocks from the Type A and Type B complexes. Note: scale change in (a).*

5.3.2.2 Type B complexes

On chondrite-normalised REE plots, the ultramafic rocks from the Gorm Chnoc Complex (Fig. 5.8g) display relatively flat patterns ($[La/Lu]_N$= 1.8–2.1), with positively sloping LREE ($[La/Sm]_N$= 1.6–2.1) and flat HREE ($[Gd/Lu]_N$= 0.8–1.0). Exhibiting chondrite-normalised abundances ranging from 2.2 to 8.0, these rocks display significant overlap with the field for Ben Strome Complex ultramafic rocks (Fig. 5.8g). In contrast, the analysed ultramafic rocks from the Loch an Daimh Mor Complex display negatively sloping REE patterns ($[La/Lu]_N$= 3.6–8.4), with negatively sloping LREE ($[La/Sm]_N$= 2.4–3.2) and flat HREE ($[Gd/Lu]_N$= 0.6–1.8). Relative to the field for Ben Strome Complex ultramafic rocks, the Loch an Daimh Mor samples are LREE-rich and HREE-poor, with chondrite-normalised REE abundances ranging from 0.8 to 13.8 (Fig. 5.8h).

The mafic rocks analysed from the Geodh' nan Sgadan Complex (Fig. 5.9c) display chondrite-normalised abundances ranging from 2.0 to 126.2, with this range significantly larger than that displayed by the mafic rocks from the Ben Strome Complex. These rocks exhibit negatively sloping REE patterns ($[La/Lu]_N$= 2.0–4.7), with negatively sloping LREE ($[La/Sm]_N$= 1.5–2.8) and flat HREE ($[Gd/Lu]_N$= 0.8–1.8). The mafic rocks analysed from the Gorm Chnoc Complex (Fig. 5.9d) exhibit positively sloping REE patterns ($[La/Lu]_N$= 0.6–0.9), with positively sloping LREE ($[La/Sm]_N$= 0.6–0.8) and positively sloping HREE ($[Gd/Lu]_N$= 0.8–0.9).

On primitive mantle-normalised plots, the ultramafic rocks from the Gorm Chnoc Complex display flat to positively sloping trace element patterns ($[Nb/Yb]_N$= 0.5–0.6), with positive Rb, Ba, Th, U, La, Ce and Sr anomalies, and negative Nb-Ta anomalies (Fig. 5.10g). These samples, which have primitive mantle-normalised abundances of between 0.5 and 0.7, show complete overlap with the field for the Ben Strome Complex ultramafic rocks (Fig. 5.10g). The ultramafic rocks from the Loch an Daimh Mor Complex exhibit varied trace element patterns, with broadly flat patterns ($[Nb/Yb]_N$= 0.5–2.2), negative Nb, Ta and Sr anomalies, and positive La, Ce and Nd anomalies (Fig. 5.10h). Exhibiting primitive mantle-normalised abundances of between 0.2 and 5.0, the Loch an Daimh Mor Complex ultramafic rocks show some overlap with the field for the Ben Strome Complex ultramafic rocks, but are notably depleted in the most compatible and most incompatible elements relative to this field (Fig. 5.9g).

The mafic rocks from the Geodh' nan Sgadan Complex display varied trace element patterns, with flat to positively sloping patterns, negative Nb, Ta, Zr, Hf and Ti anomalies ($[Ta/La]_N$= 0.1–0.4) and positive Rb, Ba, La, Ce and Nd anomalies (Fig. 5.11c). There is some overlap with the field for Ben Strome Complex mafic rocks, although 3 out of 5 Geodh' nan Sgadan samples are notably depleted in the most compatible elements relative to this field (Fig. 5.11c). The mafic rocks from the Gorm Chnoc Complex show flat compatible element patterns (Sm-Lu), with negative Nb, Ta, Zr and Hf anomalies ($[Ta/La]_N$= 0.2–0.5) and positive Rb, Ba and Sr anomalies (Fig. 5.11d).

5.3.3 Platinum-group elements

5.3.3.1 Type A complexes

On chondrite-normalised PGE plots, the Ben Strome Complex ultramafic rocks (Fig. 5.12a) exhibit generally fractionated PGE patterns ($[Pd/Ir]_N$= 0.4–33.3), with positively sloping IPGE ($[Ru/Os]_N$= 1.4–3.9), negatively to positively sloping PPGE ($[Pd/Rh]_N$= 0.5–5.1), and a mixture of positive and negative Au anomalies. The analysed ultramafic rocks from all other Type A complexes show significant overlap with the field for Ben Strome ultramafic rocks (Fig. 5.12b-f), with broadly fractionated PGE patterns ($[Pd/Ir]_N$= 1.6–25.5), positively sloping IPGE ($[Ru/Os]_N$= 1.1–13.1) and negatively to positively sloping PPGE ($[Pd/Rh]_N$= 0.3–5.6).

The mafic rocks from the Ben Strome Complex have lower IPGE than the ultramafic rocks and display strongly fractionated patterns on chondrite-normalised PGE plots ($[Pd/Ir]_N$= 23.7–46.1), with positively sloping IPGE ($[Ru/Os]_N$= 1.3–4.8), positively sloping PPGE ($[Pd/Rh]_N$= 1.3–4.8) and positive Au anomalies (Fig. 5.12i). The analysed mafic rocks from the Ben Auskaird Complex overlap with the field for Ben Strome Complex mafic rocks (Fig. 5.12j),

with fractionated PGE patterns ($[Pd/Ir]_N$= 15.8–44.4), positively sloping IPGE ($[Ru/Os]_N$= 2.0–2.5) and positively sloping PPGE ($[Pd/Rh]_N$= 1.3–2.5).

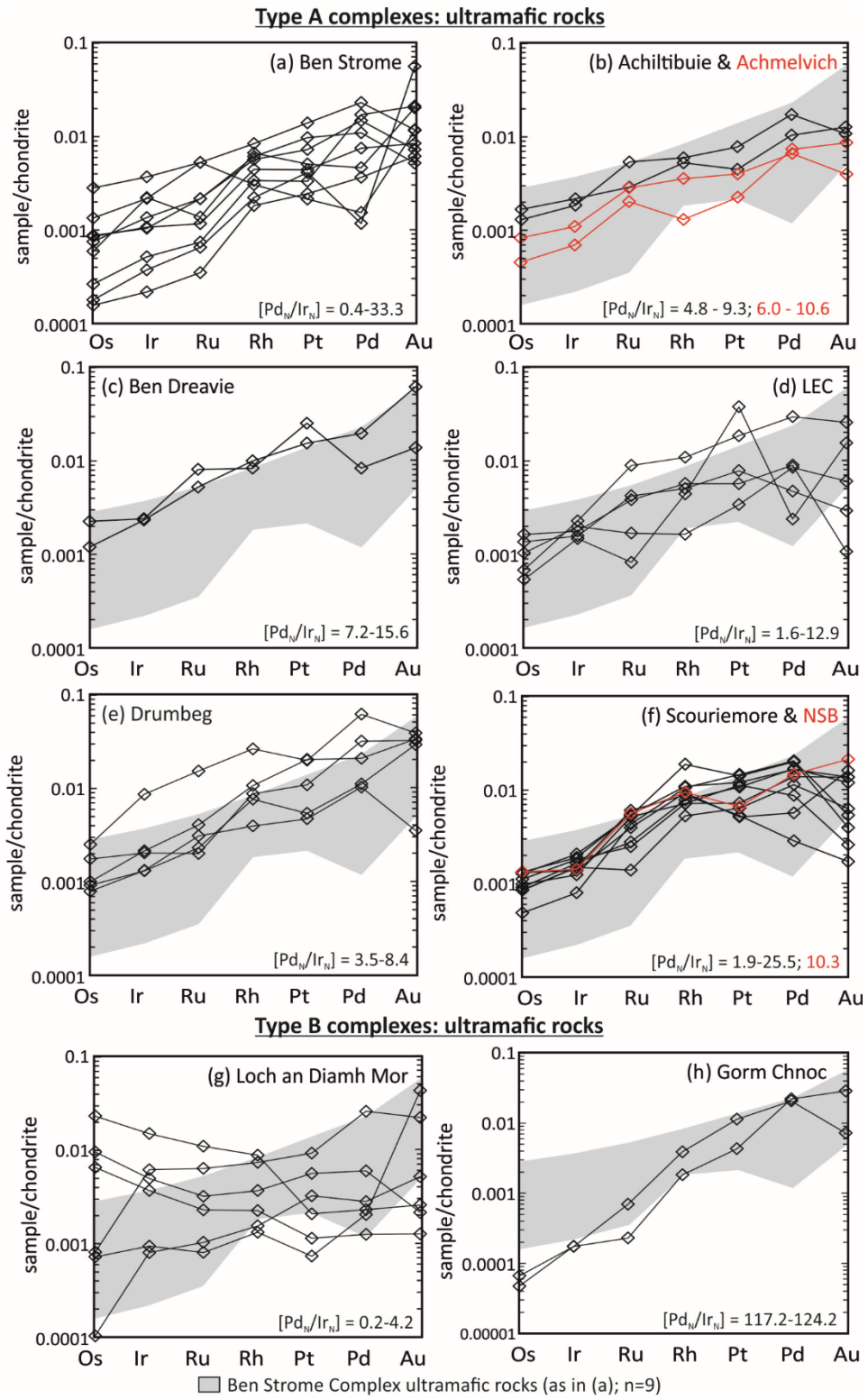

Figure 5.12: *Chondrite-normalised (Lodders 2003) PGE (+Au) plots for the analysed ultramafic and mafic rocks from the LGC. Red colours are used where more than one complex is included on one plot. Abbreviations: LEC= Loch Eilean na Craoibhe Moire Complex.*

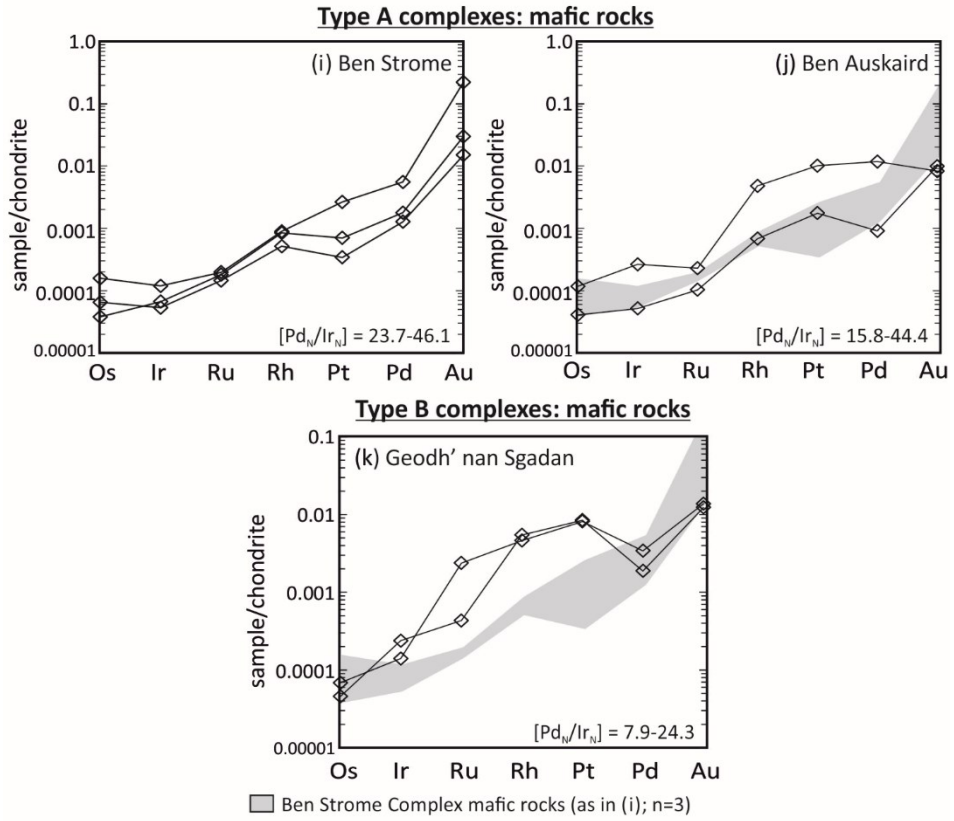

Figure 5.12 (cont.)

5.3.3.2 Type B complexes

On chondrite-normalised PGE plots, the ultramafic rocks from the Loch an Daimh Mor Complex exhibit highly variable PGE patterns (Fig. 5.12g) that can subdivided into two subgroups. One subgroup (n=3) displays flat to negatively sloping PGE patterns ($[Pd/Ir]_N$= 0.2–1.2), negatively sloping IPGE ($[Ru/Os]_N$= 0.3–0.5) and negatively sloping to flat PPGE ($[Pd/Rh]_N$= 0.3–1.6), with these samples containing a significant modal abundance of Cr-spinel (Table 5.1). In contrast, a second subgroup (n=3) displays positively sloping PGE patterns ($[Pd/Ir]_N$= 2.2–4.2), positively sloping to flat IPGE ($[Ru/Os]_N$= 1.1–9.9) and positively sloping to flat PPGE ($[Pd/Rh]_N$= 1.6–3.5), with Cr-spinel absent in these samples (Table 5.1). These patterns are distinct from the consistently fractionated patterns displayed by the Ben Strome Complex ultramafic rocks (Fig. 5.12g). In contrast, the ultramafic rocks from the Gorm Chnoc Complex (Fig. 5.12h) are strongly fractionated ($[Pd/Ir]_N$= 117.2–124.2), with fractionated IPGE ($[Ru/Os]_N$= 4.8–10.4) and fractionated PPGE ($[Pd/Rh]_N$= 5.3–12.0). These rocks display significant overlap with the field for Ben Strome Complex ultramafic rocks in terms of PPGE, but are depleted in IPGE relative to this field (Fig. 5.12h).

The mafic rocks from the Geodh' nan Sgadan Complex (Fig. 5.12k), which exhibit limited overlap with the field for Ben Strome Complex mafic rocks, are also fractionated ($[Pd/Ir]_N$=

7.9–24.3) and display positively sloping IPGE ($[Ru/Os]_N$= 9.5–34.7), but exhibit negatively sloping PPGE ($[Pd/Rh]_N$= 0.3–0.7).

5.4 Spinel mineral chemistry

In total, 701 quantitative chemical analyses were conducted on spinel grains from the studied ultramafic-mafic complexes, with all analyses conducted on ultramafic rocks. Full details of the instrumentation and methodology utilised are included in Appendix A, representative analyses are presented in Table 5.3 (for the Type A complexes) and Table 5.4 (for the Type B complexes), and appendix E contains the full dataset. A total of 572 analyses were conducted on spinel from the Type A complexes, with a further 129 analyses conducted on spinel from the Type B complexes.

5.4.1 Type A complexes

In the ultramafic rocks of the Type A complexes, spinel occurs as subhedral to euhedral grains that are generally 0.1 to 0.5 mm in diameter, with rare millimetre-scale grains also present. As with those recorded from the Ben Strome Complex (see Chapter 3), spinel exhibits pale- to dark-green (in PPL) colours and is most abundant (in terms of modal %) in metapyroxenite samples. In these rocks, individual grains display relatively homogenous compositions (Fig. 5.13a-d).

As summarised in Table 5.3, the composition of spinel (n=572) from the Type A complexes is relatively consistent, with tight ranges in the MgO (0.2 to 1.4 wt. %), Al_2O_3 (0.2 to 3.7 wt. %) and TiO_2 (< 1.9 wt. %) contents, and moderate ranges in the Cr_2O_3 (0.3 to 11.1 wt. %), FeO (31.4 to 42.9 wt. %) and Fe_2O_3 (39.9 to 64.4 wt. %) contents. These compositions show consistent overlap with the magnetite portion of the layered intrusion field (as defined by Barnes and Roeder, 2001) on all bivariate and ternary plots displayed in Figure 5.13(e-h). On the Fe^{2+} number versus Fe^{3+} number plots, there is some overlap with the field for greenschist- to amphibolite-facies magnetite rims, but the Type A spinels are distinct from this field on Fe^{2+} number versus Cr number and Cr-Fe^{3+}-Al plots (Fig. 5.13e-h). There is overlap with the high-grade metamorphic spinel field on the Fe^{2+} number versus Cr number plots, but the spinels are compositionally distinct from this field on the Fe^{2+} number versus Fe^{3+} number plot (Fig. 5.13e-h).

Table 5.3: *Representative analyses of spinel from the Type A complexes. Abbreviations: Ac=Achiltibuie; Am=Achmelvich; BD=Ben Dreavie; LEC=Loch Eilean na Craoibhe Moire; Db=Drumbeg; NSB=North Scourie Bay; Sm=Scouriemore.*

Sample code	Lw16-799A	Lw16-799A	LW17-Am2	LW17-Am2	LW17-BD1	LW17-BD1	Lw16-629B	Lw16-629B	Lw16-Db3b	Lw16-Db3b	Lw16-44	Lw16-44	Lw16-45A	Lw16-45A	NSB-UMB	NSB-UMB	T2_190	T2_190	Lw16-643B	Lw16-643B
Complex	**Ac**	**Ac**	**Am**	**Am**	**BD**	**BD**	**LEC**	**LEC**	**Db**	**Db**	**Db**	**Db**	**Db**	**Db**	**NSB**	**NSB**	**Sm**	**Sm**	**Sm**	**Sm**
SiO_2	0.43	0.41	0.21	0.19	0.24	0.24	0.34	0.28	0.28	0.26	0.34	0.32	0.39	0.39	0.30	0.32	0.34	0.34	0.30	0.30
TiO_2	0.95	1.40	0.08	0.07	0.00	0.00	1.47	1.63	0.35	0.53	0.40	0.45	0.73	0.65	0.98	1.18	1.23	1.22	1.53	1.03
Al_2O_3	1.62	1.23	0.55	0.34	1.40	3.51	1.38	2.68	0.70	1.66	1.19	1.00	0.87	1.00	2.63	2.23	1.13	1.55	1.66	1.36
FeO	38.66	38.57	37.04	36.74	36.04	36.09	37.97	40.05	35.77	36.51	36.40	36.27	37.52	37.08	38.23	37.92	37.07	36.99	38.57	37.83
Fe_2O_3	48.66	50.10	52.57	53.60	51.63	49.85	50.74	42.66	55.45	52.96	53.23	53.30	54.99	54.82	46.25	47.91	51.97	50.95	48.91	51.24
MnO	0.25	0.22	0.10	0.12	0.22	0.22	0.25	0.32	0.14	0.19	0.22	0.25	0.18	0.17	0.27	0.28	0.34	0.37	0.26	0.25
MgO	1.18	1.06	0.23	0.33	0.85	1.41	1.01	1.24	0.66	0.73	0.85	0.83	0.95	0.70	0.86	0.95	0.81	1.03	0.93	0.83
V_2O_3	0.80	0.72	0.73	0.73	0.00	0.00	0.60	0.63	0.67	0.65	0.36	0.37	0.78	0.67	0.62	0.52	0.39	0.44	0.54	0.52
Cr_2O_3	6.62	5.31	6.49	6.12	6.83	6.99	4.78	9.03	4.12	4.82	5.25	5.13	4.34	4.30	7.29	6.21	4.41	4.62	5.79	5.52
NiO	0.95	0.80	0.34	0.31	0.00	0.00	0.98	0.92	0.00	0.00	0.85	0.87	0.94	0.93	0.76	0.83	0.61	0.59	0.78	0.80
Total	100.13	99.81	98.36	98.55	97.19	98.31	99.51	99.46	98.14	98.32	99.08	98.78	101.69	100.69	98.21	98.36	98.31	98.10	99.26	99.69
Cations on the basis of 4 oxygens																				
Si	0.02	0.02	0.01	0.01	0.01	0.01	0.02	0.01	0.01	0.01	0.02	0.02	0.02	0.02	0.01	0.02	0.02	0.02	0.01	0.01
Ti	0.03	0.05	0.00	0.00	0.00	0.00	0.05	0.06	0.01	0.02	0.01	0.02	0.03	0.02	0.03	0.04	0.05	0.04	0.05	0.04
Al	0.07	0.05	0.02	0.02	0.06	0.16	0.06	0.12	0.03	0.07	0.05	0.04	0.04	0.04	0.12	0.10	0.05	0.07	0.07	0.06
Fe^{2+}	1.20	1.21	1.19	1.18	1.16	1.13	1.19	1.24	1.15	1.17	0.01	0.01	0.01	0.01	0.01	0.01	0.01	0.02	0.01	0.01
Fe^{3+}	1.36	1.41	1.52	1.55	1.50	1.41	1.44	1.19	1.61	1.52	1.15	1.16	1.16	1.16	1.21	1.20	1.18	1.18	1.21	1.19
Mn	0.01	0.01	0.00	0.00	0.01	0.01	0.01	0.01	0.01	0.01	1.52	1.53	1.53	1.54	1.32	1.36	1.49	1.46	1.39	1.45
Mg	0.08	0.07	0.02	0.02	0.06	0.10	0.07	0.08	0.05	0.05	0.06	0.06	0.07	0.05	0.06	0.07	0.06	0.07	0.07	0.06
V	0.03	0.03	0.03	0.03	0.00	0.00	0.02	0.02	0.03	0.03	0.01	0.01	0.03	0.03	0.02	0.02	0.02	0.02	0.02	0.02
Cr	0.24	0.20	0.25	0.24	0.26	0.26	0.18	0.33	0.16	0.19	0.20	0.20	0.16	0.16	0.27	0.23	0.17	0.18	0.22	0.21
Ni	0.04	0.03	0.01	0.01	0.00	0.00	0.04	0.03	0.00	0.00	0.03	0.03	0.04	0.04	0.03	0.03	0.02	0.02	0.03	0.03
Total	3.09	3.08	3.07	3.07	3.07	3.08	3.08	3.10	3.06	3.06	3.08	3.08	3.08	3.07	3.09	3.08	3.07	3.08	3.08	3.08
Mg#	3.10	2.77	0.62	0.88	2.27	3.75	2.65	3.35	1.74	1.93	2.23	2.19	2.42	1.80	2.34	2.54	2.15	2.72	2.45	2.18
Cr#	77.43	78.52	91.03	93.93	80.64	62.57	74.60	73.50	83.57	71.22	79.05	81.45	81.07	78.63	69.85	70.05	76.85	71.69	74.57	77.52
Fe^{2+}#	0.94	0.94	0.99	0.98	0.95	0.92	0.94	0.94	0.96	0.96	0.95	0.95	0.95	0.96	0.95	0.95	0.95	0.94	0.95	0.95
Fe^{3+}#	0.81	0.85	0.85	0.86	0.82	0.77	0.86	0.73	0.89	0.85	0.86	0.86	0.88	0.88	0.77	0.80	0.87	0.86	0.83	0.84

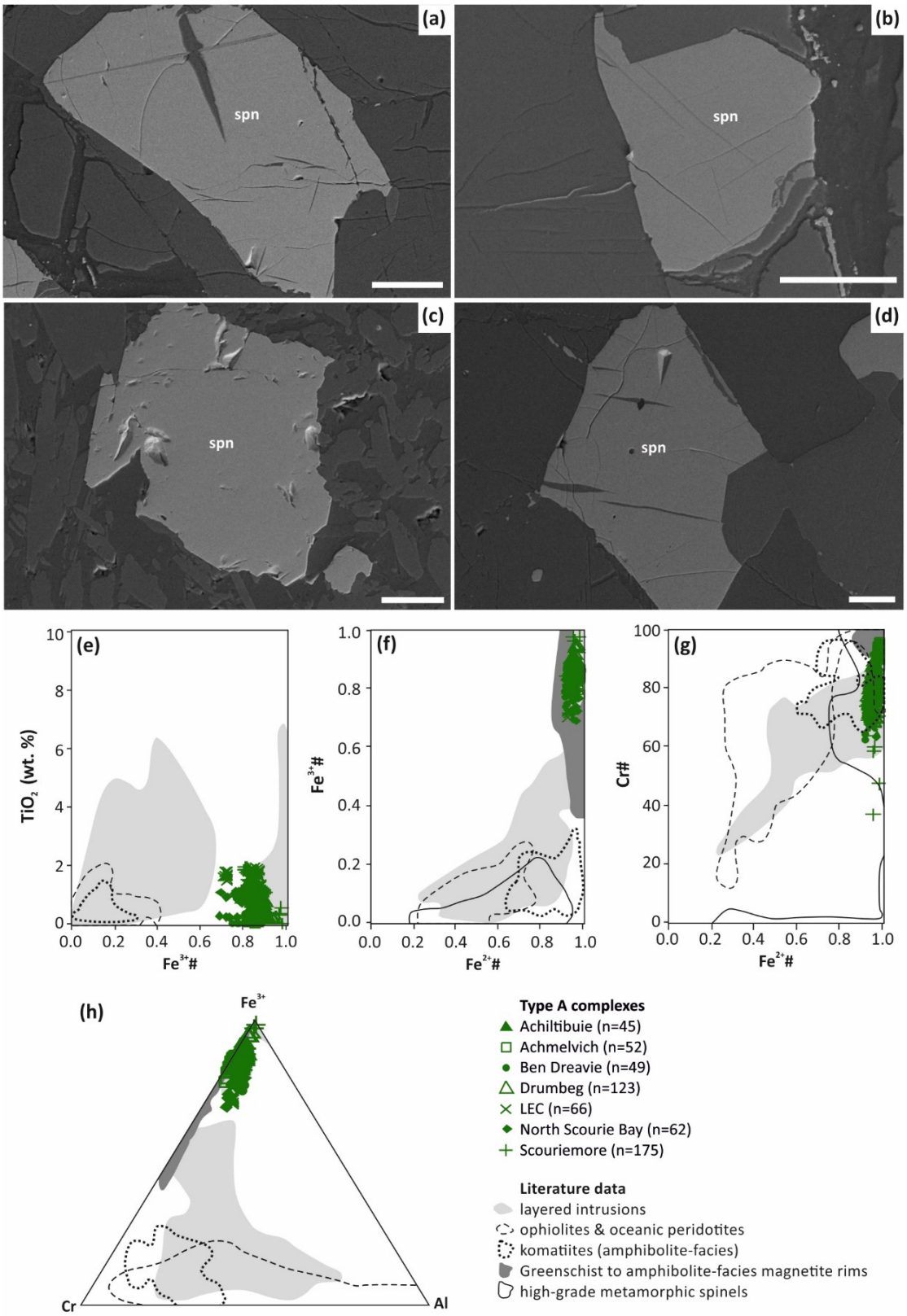

Figure 5.13: *Morphology and composition of spinels from the Type A complex ultramafic rocks.* ***(a-d)*** *SE images detailing the morphology of spinel. White scale bar=50 µm.* ***(e-h)*** *Bivariate and ternary plots detailing the composition of analysed spinel. Fields after: Barnes and Roeder (2001). Abbreviations: spn=spinel; LEC=Loch Eilean na Craoibhe Moire Complex.*

Table 5.4: *Representative analyses of spinel from the Type B complexes. Abbreviations: GC=Gorm Chnoc; LDM=Loch an Daimh Mor.*

	Group B1						Group B2					
Sample	**UBCr_P1**	**LW17-GC2**	**LW17-GC2**	**LW17-GC2**	**UBCr_P3**	**UBCr_P3**	**UBCr_P3**	**UBCr_P1**	**UBCr_P3**	**LW17-GC2**	**LW17-GC2**	**LW17-GC2**
Complex	LDM	GC	GC	GC	LDM	LDM	LDM	LDM	LDM	GC	GC	GC
SiO_2	0.19	0.30	0.30	0.28	0.19	0.21	0.36	0.32	0.75	0.32	0.26	0.28
TiO_2	0.00	0.00	0.00	0.00	0.00	0.00	0.00	0.00	0.00	2.20	0.92	3.10
Al_2O_3	57.19	50.58	52.55	55.19	59.67	59.90	2.72	1.08	1.13	2.70	2.99	3.67
FeO	12.74	23.94	23.05	22.29	14.86	14.58	31.72	32.61	32.51	40.53	38.54	41.50
Fe_2O_3	2.99	2.45	1.82	1.62	1.15	0.98	59.76	58.83	60.43	37.73	40.98	33.10
MnO	0.10	0.25	0.25	0.23	0.14	0.10	0.31	0.32	0.15	0.36	0.26	0.43
MgO	19.08	10.86	11.41	12.10	17.66	17.84	1.19	0.30	0.68	0.91	0.65	1.01
V_2O_3	0.20	0.00	0.00	0.00	0.00	0.00	0.00	0.00	0.00	0.00	0.00	0.00
Cr_2O_3	8.18	10.99	9.41	7.02	6.37	6.24	0.91	2.28	0.69	10.67	10.23	11.94
NiO	0.62	0.00	0.00	0.00	0.00	0.00	0.00	0.00	0.00	0.00	0.00	0.00
Total	101.32	99.36	98.78	98.73	100.05	99.86	96.98	95.73	96.35	95.44	94.82	95.03
	Cations on the basis of 4 oxygens											
Mg	0.74	0.46	0.48	0.50	0.69	0.69	0.09	0.02	0.05	0.06	0.05	0.07
Al	1.74	1.67	1.73	1.79	1.83	1.84	0.12	0.05	0.05	0.12	0.14	0.17
Si	0.01	0.01	0.01	0.01	0.01	0.01	0.02	0.02	0.04	0.02	0.01	0.01
Ti	0.00	0.00	0.00	0.00	0.00	0.00	0.00	0.00	0.00	0.08	0.03	0.11
V	0.00	0.00	0.00	0.00	0.00	0.00	0.00	0.00	0.00	0.00	0.00	0.00
Cr	0.17	0.25	0.21	0.15	0.13	0.13	0.04	0.09	0.03	0.40	0.39	0.43
Mn	0.00	0.01	0.01	0.01	0.00	0.00	0.01	0.01	0.01	0.01	0.01	0.02
Fe^{2+}	0.28	0.56	0.54	0.51	0.32	0.32	1.02	1.08	1.07	1.31	1.26	1.34
Fe^{3+}	0.06	0.05	0.04	0.03	0.02	0.02	1.73	1.76	1.78	1.10	1.20	0.96
Ni	0.01	0.00	0.00	0.00	0.00	0.00	0.00	0.00	0.00	0.00	0.00	0.00
Total	3.01	3.01	3.00	3.00	3.00	3.00	3.04	3.03	3.03	3.10	3.09	3.10
Mg#	69.00	42.75	45.32	47.73	66.52	67.35	3.12	0.80	1.79	2.58	1.84	2.92
Cr#	8.84	12.81	10.79	7.89	6.71	6.55	22.44	64.89	34.65	76.25	73.81	72.20
Fe^{2+}#	0.27	0.55	0.53	0.51	0.32	0.31	0.92	0.98	0.95	0.95	0.96	0.95
Fe^{3+}#	0.03	0.03	0.02	0.02	0.01	0.01	0.92	0.92	0.96	0.68	0.70	0.62

5.4.2 Type B complexes

In the ultramafic rocks of the Type B complexes, spinel occurs as subhedral to anhedral, composite grains that are generally 0.1 to 0.5 mm in diameter (Fig. 5.14a-b), although coarser grains (< 1.2 mm diameter) are present in the Loch an Daimh Mor Complex. As illustrated by the SE images presented in Figure 5.14a-b, spinel in the Type B complexes is commonly altered, with such alteration evident as µm-scale veins, rims and patches. Accordingly, spinel in the Type B complexes is subdivided into group B1 and group B2 varieties, whereby group B1 represents the bulk of individual spinel grains and group B2 represents the altered portions (Fig. 5.14a-b).

As summarised in Table 5.4, the group B1 spinels (n=84) display moderate ranges in the MgO (8.1 to 20.2 wt. %), Al_2O_3 (40.7 to 60.6 wt. %), Cr_2O_3 (5.4 to 18.8 wt. %) and FeO (11.3 to 26.8 wt. %) contents, and tight ranges in the MnO (< 0.3 wt. %) and Fe_2O_3 (< 4.4 wt. %) contents. Relative to those from the Gorm Chnoc Complex, the group B1 spinels from the Loch an Daimh Mor Complex are slightly enriched in MgO and Al_2O_3, and slightly depleted in Cr_2O_3 and FeO (Table 5.4). These compositions show consistent overlap with the ophiolites and oceanic peridotites field on the Fe^{3+} number versus TiO_2, Fe^{2+} number versus Fe^{3+} number and Cr-Fe^{3+}-Al plots, but are distinct from this field on the Fe^{2+} number versus Cr number plot (Fig. 5.14c-f). There is some overlap with the high-grade metamorphic spinels field on the Fe^{2+} number versus Fe^{3+} number plot, but the group B1 spinels are compositionally distinct from this field on all other plots (Fig. 5.14c-f).

As summarised in Table 5.4, the group B2 spinels (n=45) display tight ranges in the MnO (< 0.6 wt. %) contents, moderate ranges in the MgO (0.2 to 7.5 wt. %), Al_2O_3 (< 7.3 wt. %), Cr_2O_3 (< 12.0 wt. %) and FeO (30.6 to 42.4 wt. %) contents, and a broad range in the Fe_2O_3 (32.0 to 65.6 wt. %) content. These compositions show consistent overlap with the field for greenschist- to amphibolite-facies magnetite rims on the Fe^{2+} number versus Fe^{3+} number plot, some overlap with this field on the Cr-Fe^{3+}-Al plot, and no overlap with this field on the Fe^{3+} number versus Cr number plot (Fig. 5.14c-f). These compositions also show some overlap with the high-grade metamorphic spinel field on the Fe^{2+} number versus Cr number plot, but are distinct from this field on the Fe^{2+} number versus Fe^{3+} number plot (Fig. 5.14c-f).

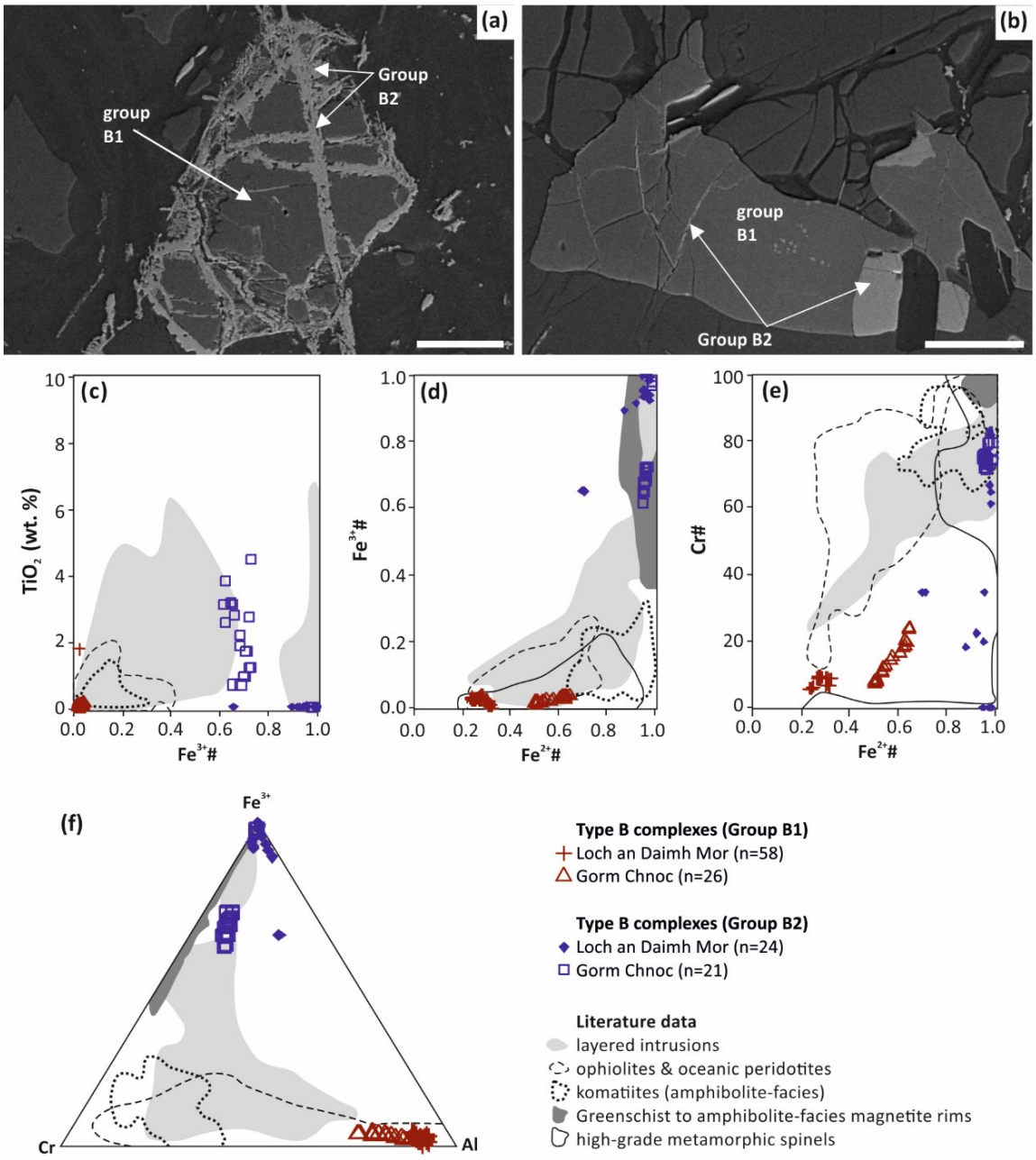

Figure 5.14: *Morphology and composition of spinels from the Type B complex ultramafic rocks.* ***(a-b)*** *SE images detailing the morphology of spinel. White scale bar=50 µm.* ***(c-f)*** *Bivariate and ternary plots detailing the composition of analysed spinel. Subdivision (into B1 and B2 subgroups) as described in the main text. Fields after: Barnes and Roeder (2001). Abbreviations: spn=spinel.*

5.5 Discussion

5.5.1 Multiple suites of ultramafic-mafic magmatism in the LGC?

In Chapter 3, the disparate salient features of the Ben Strome and Geodh' nan Sgadan Complexes were outlined, with the ultramafic-mafic complexes in the mainland LGC interpreted to record multiple temporally and/or petrogenetically distinct suites of Archaean magmatism. This section examines this hypothesis using the more extensive datasets presented in this chapter.

In Section 5.1, the studied ultramafic-mafic complexes are subdivided into Type A and Type B complexes, with the former defined as sharing salient features with the Ben Strome Complex (Chapters 3 and 4) and latter defined as displaying field characteristics that distinguish them from the Ben Strome Complex. The Gorm Chnoc Complex, which could not be easily categorised based on field relationships and mapping, was initially considered a Type B complex. These groupings, including the decision to classify Gorm Chnoc as a Type B complex, are re-assessed here, based on the data presented in Sections 5.2–5.4. Table 5.5 summarises the salient features of the Type A and Type B complexes, with the 3 Type B complexes (Lochan Daimh Mor, Geodh' nan Sgadan and Gorm Chnoc) considered separately due to their variable characteristics.

The Type A complexes display relatively consistent salient field, petrographic, geochemical and mineral chemical features, including (as summarised in Table 5.5): (i) metapyroxenite-dominated ultramafic rocks that are up to 50 m in thickness, display millimetre- to metre-scale layering characteristic of layered intrusions (Fig. 5.3a-d), and can be traced for hundreds of metres along strike (Fig. 5.2a-b); (ii) (garnet)-metagabbro-dominated mafic rocks, which are discretely layered and contain millimetre- to centimetre-scale (often retrogressed) garnet porphyroblasts (Fig. 5.3e-f); (iii) consistent parallelism between the layering in the ultramafic-mafic rocks, foliation in the TTG gneiss and complex margins, irrespective of the predominant structural architecture (Fig. 5.2a-b; see Section 5.5.2.1); (iv) flat chondrite-normalised REE patterns for the ultramafic rocks (Fig. 5.8a-d); (v) flat primitive mantle-normalised trace element plots for the ultramafic rocks (Fig. 5.9a-d); (vi) mild to moderate fractionation of chondrite-normalised PGE patterns (Fig. 5.12a-h); (vii) spinel compositions that consistently overlap with the magnetite portion of the layered intrusion field (Fig. 5.13e-h).

Table 5.5: *Summary of the salient features for the studied Type A and Type B complexes. Abbreviations: amf=amphibole; cpx=clinopyroxene; fel=feldspar; grnt=garnet; opx=orthopyroxene; plg=plagioclase; PM=primitive mantle; qtz=quartz; srp=serpentine; spn=spinel.*

		Type B Complexes		
	Type A complexes	**Gorm Chnoc**	**Geodh' nan Sgadan**	**Loch an Daimh Mor**
Field relationships	- Laterally consistent layering in ultramafic rocks. - Metapyroxenite-dominated ultramafic portions. - Garnet-rich mafic rocks that are cryptically layered. - Consistent parallelism between layering, lithological contacts and TTG gneissosity.	- Rare layering the ultramafic rocks. - Metapyroxenite-dominated ultramafic portions. - Plagioclase-rich mafic rocks that show no evidence of layering. - Garnet is rare in mafic rocks. - Rare discordance between layering and TTG gneissosity.	- Plagioclase-rich mafic rocks that are strongly layered. - Garnet is restricted to rare, centimetre-scale horizons. - Alkali-feldspar occurs rarely.	- Metaperidotite-dominated, massive (rather than layered) ultramafic rocks. - Occurrence as irregularly-shaped pods, rather than laterally continuous bodies. - Significant discordance between the TTG gneissosity and lithological contacts.
Modal mineral abundances (%)	- < 19 ol; < 32 srp; < 84 opx; < 48 cpx; < 100 amf; < 4 spn for ultramafic rocks. - < 30 opx; < 60 cpx; 10–84 amf; < 45 plag; < 35 grnt; < 3 qtz for mafic rocks.	- 1-5 ol; 7–28 srp; 3–32 opx; < 18 cpx; 55–64 amf; < 2.5 spn for ultramafic rocks. - 70–85 amf; 15–30 plag for mafic rocks.	- < 11 opx; < 35 cpx; < 82 amf; < 66 fel for mafic rocks.	< 0.3 ol; 37–100 srp; < 57 opx; < 7 cpx; 40 amf, < 2 spn for ultramafic rocks.
Bulk-rock geochemistry (lithophile elements)	- Flat chondrite-normalised REE patterns for the ultramafic rocks. - Flat PM-normalised trace element patterns for the ultramafic rocks.	- Flat HREE and negatively sloping LREE on chondrite-normalised REE patterns (ultramafic rocks). - Flat PM-norm trace element plots, with negative HFSE anomalies.	- Negatively sloping chondrite-normalised REE patterns. - Flat to positively sloping PM-normalised trace element patterns, with HFSE anomalies.	- Negatively sloping chondrite-normalised REE patterns. - Flat PM-norm trace element patterns, with HFSE anomalies. - Depleted in trace elements relative to Type A complexes.
Bulk-rock geochemistry (PGE patterns)	Weakly-moderately fractionated ($[Pd/Ir]_N$= 0.4–33.3).	Strongly fractionated ($[Pd/Ir]_N$= 117.2–124.2).	Positively sloping IPGE ($[Ru/Os]_N$= 9.5–34.7) and negatively sloping PPGE($[Pd/Rh]_N$= 0.3–0.7).	Variable, with negatively to positively sloping patterns ($[Pd/Ir]_N$= 0.2–4.2).
Spinel mineral chemistry	Consistent overlap with the magnetite portion of the layered intrusion field.	Some overlap with the ophiolites and oceanic peridotites field.	N/A	Some overlap with the ophiolites and oceanic peridotites field.

These consistent salient features, which are shared with the Ben Strome Complex (Chapters 3 and 4; Section 5.3), imply that these occurrences share a common origin, with the specific origin discussed in Section 5.5.2.1. Representing the largest ultramafic-mafic complex in the LGC, the Ben Strome Complex is considered the type locality for Type A complexes.

The field, petrographic, geochemical and mineral chemical characteristics displayed by the Type B complexes (including the Gorm Chnoc Complex) are distinctive from those displayed by the Type A complexes (summarised in Table 5.5), supporting the subdivision suggested in Section 5.1. The Gorm Chnoc Complex is distinguished from the Type A complexes based on (Table 5.5): the rare discordance between the foliation in the TTG gneiss, layering in the ultramafic rocks and lithological contacts (Fig. 5.2d); the predominance of plagioclase-rich mafic rocks (Fig. 5.4b); strongly fractionated chondrite-normalised PGE patterns (Fig. 5.12j); and distinctive spinel compositions (Fig. 5.14c-f). The Geodh' nan Sgadan Complex is distinguished from the Type A complexes based on (Table 5.5): the predominance of plagioclase-rich mafic rocks; restriction of garnet to rare, centimetre-scale layers; negatively sloping chondrite-normalised REE patterns; and distinctive chondrite-normalised PGE patterns (Fig. 5.12k). The Loch an Daimh Mor Complex is distinguished from the Type A complexes based on (Table 5.5): significant discordance between the foliation in the TTG gneiss and lithological contacts (Fig. 5.2c); metaperidotite-dominated, massive (rather than layered) ultramafic rocks (Fig. 5.3c-e); occurrence as irregularly-shaped pods, rather than laterally continuous bodies (Fig. 5.2c); negatively sloping chondrite-normalised REE patterns (Fig. 5.8g); variable, positive to negatively-sloping chondrite-normalised PGE patterns (Fig. 5.12i); and distinctive spinel compositions (Fig. 5.14c-f).

The outlined distinction between Type A and Type B Complexes (summarised in Table 5.5) supports a hypothesis whereby the LGC records multiple temporally and/or petrogenetically distinct suites of Archaean magmatism, as originally proposed in Chapter 3. While the Type A complexes exhibit consistent field, geochemical and mineral chemical features, suggesting that these occurrences share a common origin; the Type B complexes exhibit variable field, geochemical and mineral chemical features, implying that these occurrences may record more than one origin, as discussed in Section 5.5.2.2.

5.5.2 Origin(s) of the ultramafic-mafic rocks in the LGC

5.5.2.1 Type A complexes

In Chapter 3, it was suggested – based on field observations, mapping and spinel mineral chemistry – that the Ben Strome Complex represents a layered intrusion emplaced *into* TTG

gneiss. As the Ben Strome Complex is considered to represent a type locality for the Type A complexes (see Section 5.5.1), a similar interpretation can be invoked for all Type A complexes in the LGC, whereby these occurrences collectively represent a suite of layered intrusions that were emplaced relatively contemporaneously *into* TTG gneiss (Fig. 5.15). In this scenario, complexes that are situated close to one another (e.g., Scouriemore and North Scourie Bay) may represent the dismembered remnants of one common layered intrusion (Fig. 5.15).

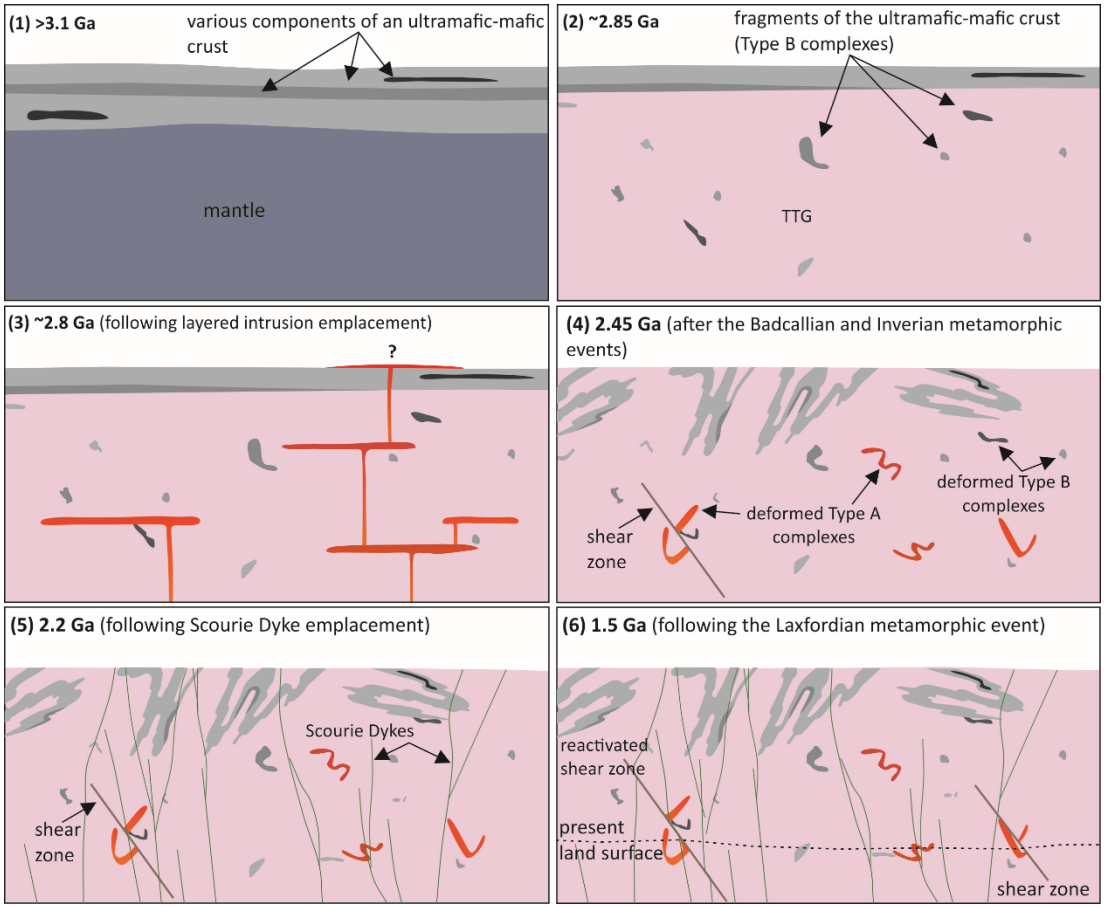

Figure 5.15: *Schematic diagram detailed the proposed evolution of the LGC.*

The data presented in this chapter strengthens the layered intrusion hypothesis (Bowes et al. 1964; Chapter 3). First, the Type A complexes exhibit many field features characteristic of layered intrusions (Namur et al. 2015), such as: gradational contacts between ultramafic and mafic units; gradational contacts between metaperidotite and metapyroxenite layers in the ultramafic portions; gradational variation in modal mineral proportions within individual layers; multiple ultramafic and mafic packages occurring within single, continuous successions (known as "megacyclic units"; Fig. 5.2a); and truncation of layers on the centimetre- to metre-scale (Fig. 5.3b). Second, these complexes collectively display fractionated trends on major element bivariate plots (Fig. 5.7), with MgO displaying

moderate-strong negative correlations with Al_2O_3, SiO_2, TiO_2, CaO and K_2O. Third, these complexes consistently exhibit mild-moderate fractionated chondrite-normalised PGE patterns that are typical of layered intrusions (e.g., Barnes et al. 1985, Gruenewaldt et al. 1989, Maier et al. 1998, Power et al. 2000). Finally, the composition of spinel in the ultramafic rocks from the Type A complexes displays consistent overlap with the magnetite portion of the layered intrusion field established by Barnes and Roeder (2001).

As initially discussed in Chapter 3, the assertion that the Type A complexes were most likely emplaced *into* the TTG gneiss contradicts a widely-held assertion, whereby the majority of ultramafic-mafic rocks in the LGC pre-date the emplacement of the TTG magmas (Rollinson and Windley 1980, Sills 1981, Park et al. 2002). Although this relative age relationship is possible for the Type B complexes (see Section 5.5.2.2), it is considered unlikely for the Type A complexes. The field mapping presented both here (Fig. 5.2a-b) and in Chapter 3 demonstrate that, despite the consistent salient features outlined in Section 5.5.1, the Type A complexes exhibit extremely varied (and seemingly chaotic) map-scale morphologies, with this variability previously used as evidence supporting a hypothesis whereby the ultramafic-mafic complexes pre-date the TTG magmas. However, it is considered here that these varied morphologies are the product of subsequent metamorphism and deformation (Fig. 5.15). The individual map-scale morphologies are considered to reflect the dominant structural regime(s) in a particular portion of crust, as implied by the consistent parallelism between the layering in the ultramafic-mafic rocks, the foliation in the TTG gneiss and all lithological contacts. For example, the Ben Strome Complex (Fig. 3.1) is dominated by Badcallian and Inverian folds, with these structures truncated by Scourie Dykes and a spatially restricted Laxfordian shear zone. In contrast, the Loch Eilean na Craoibhe Moire Complex (Fig. 5.2a), which is located less than 1 km from the southern margin of the Laxford Shear Zone (Goodenough et al. 2010, 2013), is dominated by a NW-SE trend typical of the Inverian and Laxfordian metamorphic events. Here, Badcallian folding appears to have been strongly overprinted, with ultramafic-mafic units truncated by NW-SE-trending Scourie Dykes and NE-SW-trending (Phanerozoic) faults (Fig. 5.2a).

5.5.2.2 Type B complexes

On the map-scale, the Loch an Daimh Mor Complex, which occurs as large pods within the TTG gneiss, displays significant discordance between the foliation in the TTG gneiss and lithological contacts on the map-scale (Fig. 5.2c). These data imply that these ultramafic-mafic rocks pre-date the TTG, as previously suggested for some of the ultramafic-mafic complexes in the LGC (e.g., Sills 1981). This interpretation can also be applied to the Gorm

Chnoc Complex, which also displays discordance (albeit more subtle; Fig. 5.2d) between the foliation in the TTG gneiss and lithological contacts (Fig. 5.3d). Therefore, it is suggested that the Loch an Daimh Mor Complex and Gorm Chnoc Complex represent a pre-TTG ultramafic-mafic crust that was invaded by TTG magmas (Fig. 5.15). The validity of this interpretation for the Geodh' nan Sgadan Complex is unclear, with the relative age relationship between the mafic rocks and surrounding TTG gneiss remaining ambiguous (as outlined in Chapter 3).

The geochemical characteristics of the Type B complexes are varied (see Table 5.5), suggesting that the proposed pre-TTG ultramafic-mafic crust may have comprised several components with different magmatic affinities. On bulk-rock primitive mantle-normalised trace element plots, the Loch an Daimh Mor Complex samples show negative HFSE anomalies (Fig. 5.9h). However, as detailed in Chapter 4, such anomalies are an unreliable proxy for Archaean subduction, particularly in areas (such as the LGC) that have experienced multiple phases of high-grade metamorphism and associated metasomatism. The bulk-rock, chondrite-normalised PGE patterns for the Loch an Daimh Mor Complex, which are generally flat to negatively sloping and exhibit significant depletion of the PPGE (Fig. 5.12i), are comparable to those displayed by the mantle portions of ophiolites (Barnes et al. 1985). This geochemical comparison is also shown by the composition of group B1 spinel grains, which show some (but not consistent) overlap with the established field for ophiolites and oceanic peridotites (Fig. 5.14c-f). However, this comparison is contradicted by the bulk-rock chondrite-normalised REE abundances, which are 1-2 orders of magnitude greater than those for residual mantle rocks (Godard et al. 2000, Paulick et al. 2006, Godard et al. 2008). While it is possible that the Loch an Daimh Mor Complex represents small fragments of Archaean oceanic crust, this interpretation would require a large leap of faith based on the data presented here, particularly given the profound implications for Archaean geodynamic regimes that may be attached to such an interpretation.

On chondrite-normalised REE (Fig. 5.8h) and primitive mantle-normalised trace element plots (Fig. 5.9h), the Gorm Chnoc Complex ultramafic rocks show significant overlap with the field for Ben Strome Complex ultramafic rocks. However, these rocks exhibit extremely fractionated chondrite-normalised PGE patterns (Fig. 5.9j) that are distinct from those of the Type A complexes, with these patterns more consistent with continental and ocean-floor basalts (Barnes et al. 1985). Moreover, the composition of B1 spinel shows some (but not consistent) overlap with the ophiolites and oceanic peridotite field (Fig. 5.14c-f).

To summarise, based on the data presented in this chapter, it is here (tentatively) suggested that the Type B complexes represent an ultramafic-mafic crust that was invaded by TTG (Fig.

5.15). This crust likely comprised several components that formed via various magmatic (and geodynamic) processes, with further research required to establish the precise petrogenetic processes responsible for the formation of these rocks.

5.5.3 Chronological implications for formation of the LGC

Based on the data presented in this chapter, alongside the previously published literature (as described in Chapter 2), the following chronology is proposed for the mainland LGC (Figs. 5.15 and 5.16):

i. Prior to 3.1 Ga, an ultramafic-mafic crust (partially preserved as the Type B complexes) formed via several petrogenetic and/or geodynamic processes.
ii. Between 3.1 and 2.85 Ga, this ultramafic-mafic crust was invaded by TTG magmas, resulting in its fragmentation and inclusion as variably sized complexes within the TTG gneiss.
iii. Between 2.9 and 2.8 Ga, the LGC was intruded by a suite of layered intrusions (preserved as the Type A complexes).
iv. Between 2.8 and 2.7 Ga (during the Badcallian tectonothermal event), the LGC was subject to granulite-facies metamorphism and multiple phases of folding, as demonstrated by the Ben Strome and Drumbeg Complexes (Figs. 3.1 and 5.2b).
v. Between 2.5 and 2.4 Ga (during the Inverian tectonothermal event), the LGC was subject to amphibolites-facies metamorphism and several (NW-SE-trending) shear zones formed, with such shearing possibly dissecting some of the ultramafic-mafic complexes.
vi. Between 2.42 and 2.38 Ga, the Scourie Dykes were emplaced, truncating the ultramafic-mafic complexes and surrounding TTG gneiss.
vii. Between 1.9 and 1.6 Ga (during the Laxfordian tectonothermal event), the LGC was subject to greenschist- to amphibolite-facies metamorphism and shear zones were formed/reactivated, truncating the ultramafic-mafic complexes, as shown by the Ben Strome Complex (Fig. 3.1).
viii. Finally, during the Phanerozoic (< 0.54 Ga), a series of NE-SW-trending faults affected the LGC, as shown by the Loch Eilean na Craoibhe Moire Complex (Fig. 5.2a).

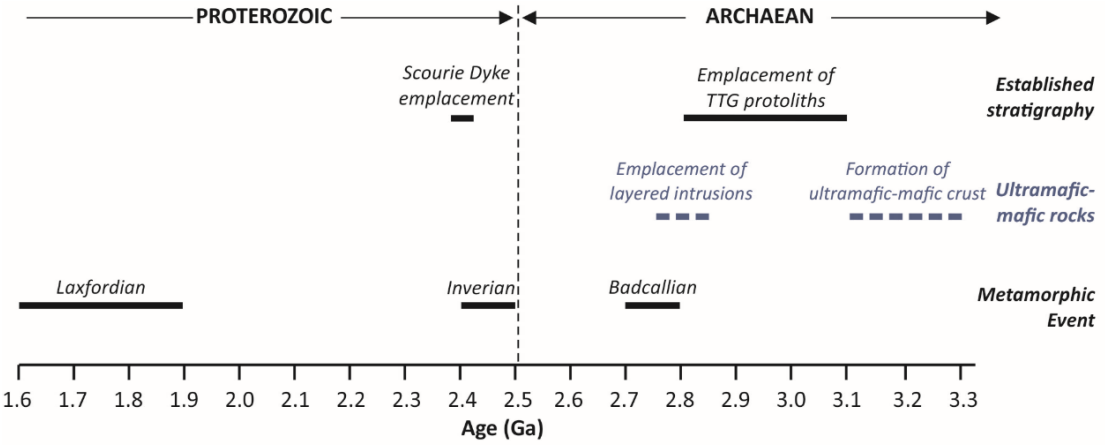

Figure 5.16: *Timeline detailing the established chronology of the mainland LGC, alongside the proposed periods of ultramafic-mafic magmatism, as suggested by the data presented in this chapter.*

5.6 Conclusions and summary

Several research questions were outlined in the introduction to this chapter, with this section providing a response to these questions individually.

> *(Q1) How many suites of temporally and/or petrogenetically distinct phases of ultramafic-mafic magmatism are recorded by the mainland LGC, and what is the relative age relationship between these suites and the TTG?*

A minimum of 2 broad suites of temporally and petrogenetically distinct phases are here identified. The Type B complexes likely preceded the emplacement of the TTG gneiss and may record multiple petrogenetic environments, while the Type A complexes succeeded the emplacement of the TTG gneiss and record a common petrogenetic environment (Figs. 5.15 and 5.16). The map-scale morphologies exhibited by the Type A complexes are considered to reflect the dominant structural regime(s) in a particular portion of crust, rather than their invasion by TTG magmas, as previously suggested.

> *(Q2) How many of the ultramafic-mafic complexes share a common origin with the Ben Strome Complex (Chapters 3 and 4), and are the data for these complexes also consistent with a layered intrusion origin?*

A total of 8 additional ultramafic-mafic complexes in the LGC are here interpreted to share a common origin with the Ben Strome Complex (collectively termed Type A complexes; see Section 5.5.1), with the presented data (for all occurrences) consistent with a layered intrusion origin (see Section 5.5.2.1). Evidence includes: a variety of field features that are characteristic of layered intrusions (Section 5.1.1); major element geochemistry (Section 5.3.1.1); PGE geochemistry (Section 5.3.3.1); and spinel mineral chemistry (Section 5.4.1).

(Q3) What is the origin(s) of any ultramafic-mafic complexes that are not genetically related to the Ben Strome Complex?

Although the specific petrogenetic and geodynamic environment(s) within which the Type B complexes remain elusive, it is here interpreted that these rocks collectively formed an earlier ultramafic-mafic crust that was intruded (and fragmented) *by* TTG magmas. It is possible that these complexes represent fragments of Archaean oceanic crust, but the data presented are insufficient to confidently invoke such an interpretation.

Part Two:

The Johannesburg Dome

Chapter 6

Literature Review: The Kaapvaal Craton

Located in southern Africa (Fig. 6.1), the Kaapvaal Craton is one of the oldest and best preserved fragments of Archaean crust on Earth (Poujol et al. 2003, Poujol 2007). It is sporadically exposed throughout an area that encompasses parts of South Africa, Lesotho, Swaziland, Mozambique and Botswana (Fig. 6.1), and comprises both greenstone belts and granitoid intrusions, with the latter volumetrically dominant over the former (Fig. 6.1). Having formed episodically between 3.7 and 2.5 Ga, the Kaapvaal Craton is largely buried by Neoarchaean to Palaeoproterozoic volcano-sedimentary sequences (Anhaeusser 1973a, Poujol et al. 2003, Robb et al. 2006, Brandl et al. 2006, Poujol 2007), and was intruded by the 2.05 Ga Bushveld Complex (Cawthorn et al. 1981, Yudovskaya et al. 2013). After briefly describing the broad-scale subdivisions of the Kaapvaal Craton and their genetic implications (Section 6.1), this chapter describes the geology of the Johannesburg Dome (Section 6.2) and Barberton Greenstone Belt (Section 6.3; Fig. 6.1), including descriptions of the numerous ultramafic-mafic complexes present in both regions (e.g., Viljoen and Viljoen 1970, Anhaeusser 1977, 1978, 1985, De Wit et al. 1987, Anhaeusser 1992, 2015).

6.1 Terrane and domain-based subdivisions

Based largely on geological mapping and associated geochronology, the Kaapvaal Craton is generally interpreted to have resulted from the amalgamation of several discrete crustal blocks (or "terranes") that assembled (during the Archaean) by processes akin to Phanerozoic style plate tectonics (De Wit et al. 1987, 1992, Kamo and Davis 1994, Poujol et al. 2003, Eglington and Armstrong 2004, Schmitz et al. 2004, Moyen et al. 2006, Kisters et al. 2010, Furnes et al. 2012, 2013). This hypothesis remains disputed (Hamilton 1998, Van Kranendonk, et al. 2014a,b), with the proponents of this model acknowledging that, relative to the Phanerozoic, certain conditions must have been significantly different during any Archaean equivalent of plate tectonics (e.g., heat flow, ocean water depth, magma production rates and the extent of continental recycling; Poujol et al. 2003). Moreover, the precise number of terranes and the position of their boundaries remain unclear (De Wit et al. 1987, 1992, Lowe 1994, Poujol et al. 2003, Eglington and Armstrong 2004, Poujol 2007, Zeh et al. 2013).

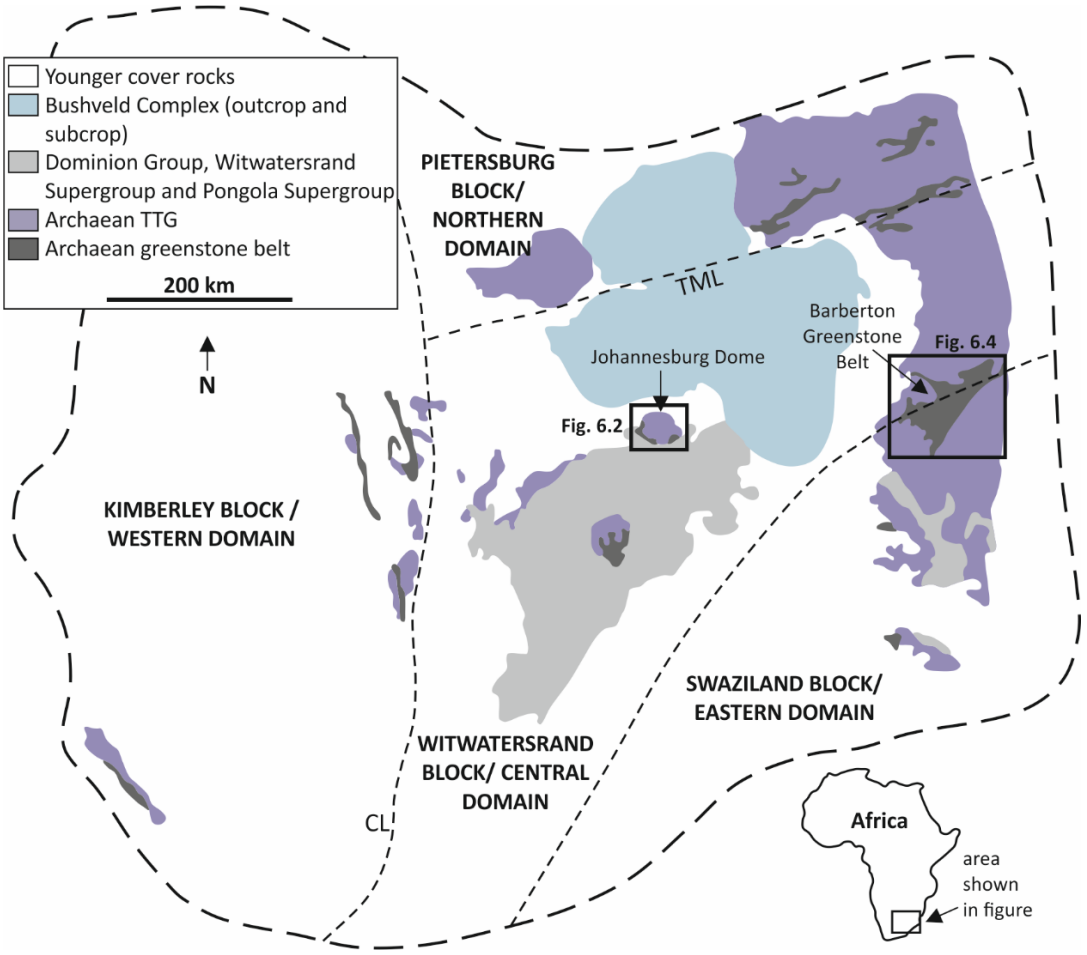

Figure 6.1: *Simplified geological map of the Kaapvaal Craton (redrawn after: Anhaeusser 2006a), including the basic spatial subdivisions proposed by Poujol et al. (2003) and Eglington and Armstrong (2004). Abbreviations; TML=Thambazimbi-Murchison Lineament; CL=Colesburg Lineament.*

Based on the subduction-accretion model, Schmitz et al. (2004) subdivided the Kaapvaal Craton into 3 main blocks that are separated by major lineaments (Fig. 6.1), namely: the Witwatersrand Block (in the E); the Kimberly Block (in the W); and the Pietersburg Block (in the N). The Thambazimbi-Murchison Lineament (TML) separates the Witwatersrand Block from the Pietersburg Block. While the Colesburg Lineament (CL) separates the Witwatersrand Block from the Kimberley Block (Fig. 6.1). Eglington and Armstrong (2004) proposed a similar, terrane-based subdivision, although these authors subdivided the Witwatersrand Block of Schmitz et al. (2004) into the Swaziland Block (in the E) and Witwatersrand Block (in the W; Fig. 6.1). In both scenarios (and other terrane-based subdivisions of the Kaapvaal Craton which invoke subduction-accretion interpretations), the lineaments are interpreted to represent Archaean sutures that mark the collision of originally allochthonous terranes (e.g., De Wit et al. 1992). For example, the CL is interpreted as marking the welding together of the Kimberly and Witwatersrand Blocks at ~2.9 Ga (Schmitz et al. 2004).

In direct opposition to the terrane-based subdivisions, Van Kranendonk et al. (2014a,b) argued that the geochemical and structural characteristics of the Kaapvaal Craton are incompatible with subduction-accretion tectonics. Instead, it is suggested that the proposed terrane boundaries were produced during the "sagduction" of relatively dense greenstone belt(s). According to this model, thick packages of volcano-sedimentary rocks – deposited in a volcanic plateaux setting – buried the granitoid rocks of the Kaapvaal Craton, causing them to partially melt. As a consequence, the relatively dense greenstone belts sank into the partially molten felsic rocks, which were relatively buoyant (Van Kranendonk, et al. 2014b).

To reduce the genetic connotations attached to a specific subdivision, the terms of Poujol et al. (2003) are here utilised. Based purely on descriptive geological and geochronological characteristics, these authors subdivided the Kaapvaal Craton into separate Northern, Central, Eastern and Western Domains (Fig. 6.1).

6.2 The Johannesburg Dome

The Johannesburg Dome is a 700 km^2 basement inlier located between Johannesburg and Pretoria, in the Central Domain of the Kaapvaal Craton (Fig. 6.1; Anhaeusser 1973, Poujol 2007). The Dome, which preserves the best exposures of Archaean basement in the generally poorly-exposed Central Domain, comprises volumetrically dominant TTG gneiss and subordinate ultramafic-mafic rocks (Anhaeusser 1973b, 1977, 1978, 2001, Poujol et al. 2003, Anhaeusser 2006a, 2015). These basement rocks are overlain by the volcano-sedimentary rocks of the Neoarchaean to Neoproterozoic Witwatersrand, Ventersdorp and Transvaal Supergroups (Fig. 6.2), and Phanerozoic rocks of the Karoo Supergroup (Armstrong et al. 1991, Barton et al. 1999, Poujol and Anhaeusser 2001, Poujol et al. 2003).

6.2.1 Stratigraphic framework

The following stratigraphic framework is generally accepted for the Johannesburg Dome and surrounding supracrustal rocks (Fig. 6.3):

(i) Intrusive and/or extrusive ultramafic-mafic magmatism prior to 3.34 Ga (Anhaeusser 1973b, 1977, 1978, 1992, 2015). See Section 6.2.2 for full details.

(ii) Episodic emplacement of TTG magmas between 3.34 and 3.11 Ga (Anhaeusser 1999, Poujol and Anhaeusser 2001, Robb et al. 2006).

(iii) Deposition of the Dominion and Witwatersrand Supergroups between 3.0 and 2.8 Ga (Walraven et al. 1990, Robb and Meyer 1995, Hilliard et al. 1995)

(iv) Deposition of the Ventersdorp Supergroup between 2.7 and 2.5 Ga (Walraven et al. 1990, Van der Westhuizen et al. 1991, Armstrong et al. 1991)

(v) Episodic emplacement of numerous (predominantly mafic) dykes, with varying lithological characteristics and orientations, between 2.7 and 1.3 Ga (Anhaeusser 1973b).

(vi) Deposition of the Transvaal Supergroup between 2.6 Ga and the intrusion of the Bushveld Complex (Walraven et al. 1990), at ~2.05 Ga (Eriksson et al. 2006, Olsson et al. 2011, Coggon et al. 2012, Yudovskaya et al. 2013, Zeh et al. 2015).

The Johannesburg Dome and surrounding supracrustal rocks have experienced several episodes of greenschist- to amphibolite-facies metamorphism during the late-Archaean and Palaeoproterozoic (Anhaeusser 1973b, 1977, Walraven et al. 1990, Brandl et al. 2006). Further to an amphibolite-facies event at ~3.1 Ga, which affected only TTG gneiss and associated ultramafic-mafic rocks, several poorly-constrained greenschist-facies events occurred at 2.7, 2.4 and 2.1 Ga respectively (Armstrong et al. 1991).

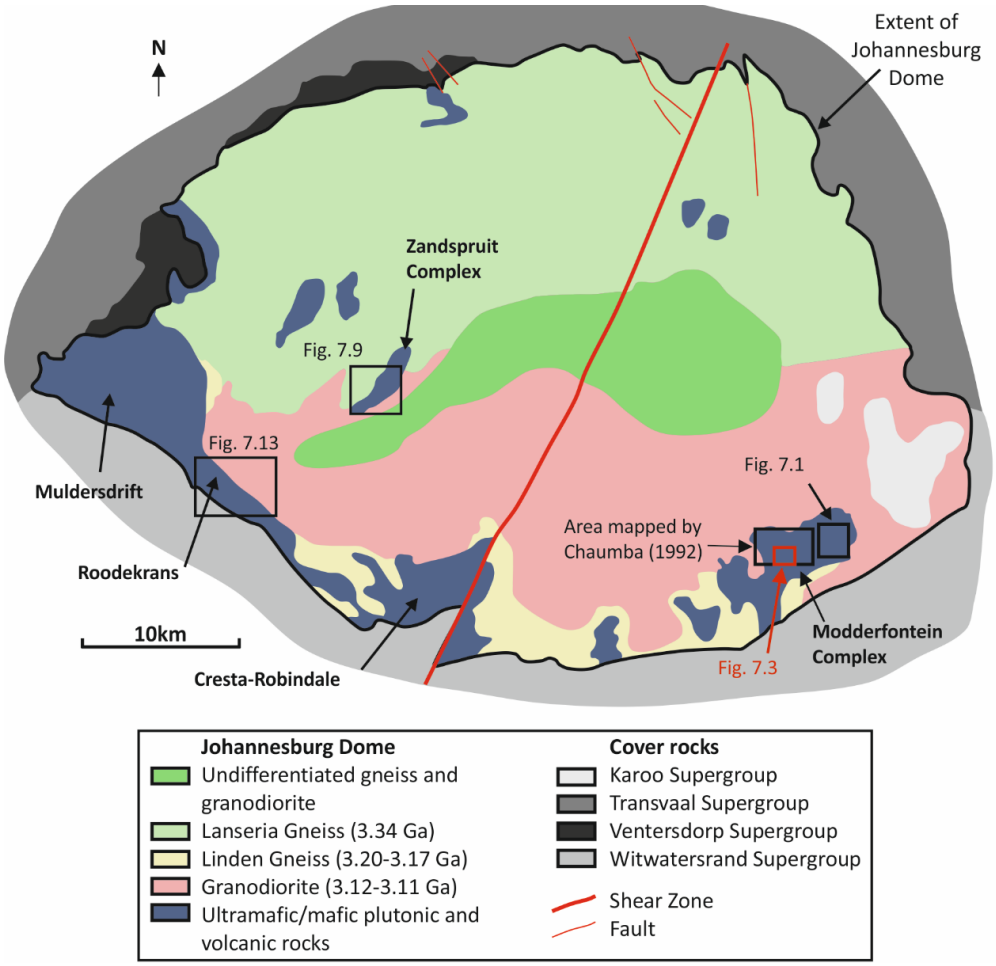

Figure 6.2: *Simplified geological map of the Johannesburg Dome (redrawn after: Poujol and Anhaeusser 2001, Anhaeusser 2006a), including the locations of the ultramafic-mafic complexes studied in Chapters 7-9.*

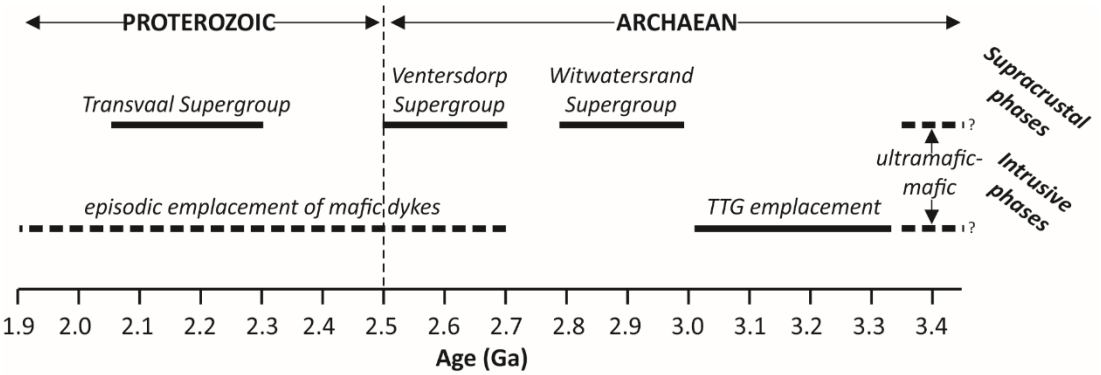

Figure 6.3: *Timeline detailing the established chronology of the Johannesburg Dome and surrounding supracrustal rocks. After: (Anhaeusser 1973b, Walraven et al. 1990, Armstrong et al. 1991, Poujol and Anhaeusser 2001, Poujol et al. 2003, Prevec et al. 2004, Eriksson et al. 2009).*

6.2.1.1 TTG and associated rocks

The Johannesburg Dome comprises mostly TTG gneiss derived from several magmatic events between 3.34 and 3.11 Ga (Fig. 6.3; Anhaeusser 1973, 1999, Poujol and Anhaeusser 2001, Robb et al. 2006). The oldest TTG gneiss in the Johannesburg Dome – the 3.34 Ga Lanseria Gneiss – occupies the northern part of the Dome (Robb and Meyer 1995, Barton et al. 1999, Poujol and Anhaeusser 2001, Robb et al. 2006). These trondhjemitic and tonalitic magmas invaded, fragmented, metamorphosed and migmatised a pre-existing ultramafic-mafic crust that is now manifest as centimetre to kilometre-scale xenoliths and remnants enclosed with the Lanseria Gneiss (Anhaeusser 1973b, 2015). The ultramafic-mafic remnants, which also occur along the southern edge of the Dome and whose ages are only constrained as being older than the TTG gneiss (Anhaeusser 1977, 1978, 1992, 2004, 2006a), are discussed fully in Section 6.2.2.

The 3.20-3.17 Ga hornblende-biotite tonalite (known as the Linden Gneiss; Fig. 6.2) occupies the southern edge of the Johannesburg Dome (Barton et al. 1999, Poujol and Anhaeusser 2001, Robb et al. 2006), while the 3.12-3.11 Ga Bryanston, Honeydew and Victory Park granodiorites dominate the remaining southern portions of the Johannesburg Dome (Poujol and Anhaeusser 2001, Robb et al. 2006). A suite of NW-SE to NE-SW-trending lamproite dykes, which have been metamorphosed to amphibolite-facies (Prevec et al. 2004), are roughly coeval with these granodiorites. All the granitoid rocks on the Dome are cross-cut by numerous pegmatites, which are interpreted as representing the final stages of magmatism (at ~3.0 Ga; Barton et al. 1999, Poujol and Anhaeusser 2001, Robb et al. 2006).

6.2.1.2 Witwatersrand, Ventersdorp and Transvaal Supergroups

Deposited between 3.0 and 2.8 Ga, the Witwatersrand Supergroup overlies the southern margins of the Johannesburg Dome (Robb and Meyer 1995). These volcano-sedimentary rocks, which comprise metamorphosed mudstone, siltstone, sandstone and conglomerate alongside rare mafic volcanic units, strike roughly E-W and display shallow to moderate dips (10 to 45°) that are generally towards the S (Anhaeusser 1973b). The Ventersdorp Supergroup, which was subsequently deposited between 2.7 and 2.5 Ga, is sporadically exposed along the NW margin of the Johannesburg Dome and comprises various felsic and mafic volcanic lithologies (Anhaeusser 1973b, Poujol et al. 2003). The 2.6–2.3 Ga Transvaal Supergroup, which is exposed across the entire northern part of the Johannesburg Dome (Fig. 6.2), is dominated by both carbonate and clastic sedimentary rocks, alongside rare volcanic units (Walraven et al. 1990).

6.2.1.3 Neoarchaean to Palaeoproterozoic dykes

The Johannesburg Dome was episodically intruded by (dominantly mafic) dykes throughout the late Neoarchaean and Palaeoproterozoic (Anhaeusser 1973b, Poujol et al. 2003). Although they have received limited research attention, these dykes display considerable variation in age, orientation, mineralogy and geochemistry, and are commonly poorly-exposed (Anhaeusser 1973b). Some dolerite dykes are equigranular and fine- to medium-grained, while others are porphyritic, with the latter containing plagioclase phenocrysts up to 5 cm in diameter (Anhaeusser 1973b). A younger suite (~1.3 Ga) of composite dykes – known as the Pilanesberg Dykes – comprise both mafic and felsic phases and strike NNW-SSE to NWW-SEE (Gough and Hales 1956, Anhaeusser 1973b).

6.2.2 Ultramafic-mafic complexes

Ultramafic-mafic complexes, which comprise a combination of extrusive (komatiites and high Mg-basalts) and intrusive (peridotite, pyroxenite, dunite and gabbro) ultramafic-mafic rocks, are most prevalent along the southern rim of the Johannesburg Dome (Fig. 6.2), extending from Muldersdrift in the W to Modderfontein in the E (Anhaeusser 1977, 1978, 2006a, 2006b). In addition, smaller xenoliths and remnants are distributed throughout the northern part of the Johannesburg Dome (Fig. 6.2), occurring within the Lanseria Gneiss (Fig. 6.2; Anhaeusser 1992, 2015).

Traditionally, the extrusive rocks were interpreted as representing oceanic plateaux assemblages, with the layered complexes representing contemporaneous intrusions that were emplaced at shallow crustal levels. In this scenario, both the extrusive and intrusive

components were derived from "komatiitic" magmas (i.e., derived from high degrees of partial melting; Viljoen and Viljoen 1970), with the ultramafic-mafic rocks collectively representing fragments of Archaean greenstone belts (and associated intrusions). More recently, Anhaeusser (2006a) suggested that these ultramafic-mafic suites may represent "ophirags" (ophiolite fragments incorporated in continental crust). According to this hypothesis, the ultramafic-mafic complexes located along the southern edge of the Johannesburg Dome may collectively represent an Archaean suture that extends 300 km to the E, correlating with the ultramafic-mafic complexes in the Barberton Greenstone Belt.

The succeeding sections provide brief descriptions of the individual occurrences Muldersdrift, Roodekrans, Zandspruit, Cresta and Modderfontein (Fig. 6.2).

6.2.2.1 Muldersdrift

Located on the western edge of the Johannesburg Dome (Fig. 6.2), the Muldersdrift Complex comprises a combination of extrusive and intrusive ultramafic-mafic rocks, and is constrained as older than the ca. 3.1 Ga, intrusive granodiorites (Anhaeusser 1978, 2006a). The poorly-exposed and highly altered extrusive rocks contain volumetrically dominant mafic pillow lavas and peridotitic komatiites (Anhaeusser 1978, 2006a). Collectively occupying a 10 km^2 area, the (WNW-ESE-trending) intrusive rocks comprise volumetrically dominant ultramafic rocks (dunite, harzburgite and pyroxenite), which form small ridges, alongside volumetrically subordinate metagabbro (Anhaeusser 1978, 2006a). Despite being highly altered to various serpentine-amphibole-chlorite-talc schists, the intrusive ultramafic rocks commonly preserve cumulate textures (Anhaeusser 1978, 2006a). As illustrated by the spatial distribution of the metagabbro units, which act as marker horizons, the Muldersdrift Complex records multiple phases of folding (Anhaeusser 1978).

6.2.2.2 Roodekrans

Located on the SW edge of the Johannesburg Dome (Fig. 6.2), the Roodekrans Complex is a 16 km^2 area of ultramafic-mafic rocks comprising poorly exposed metabasalts and moderately exposed layered ultramafic-mafic rocks (Anhaeusser 1977, 2006a). Although the Complex has not been directly dated, it's age is constrained as being older than the overlying, ca. 2.9 Ga Witwatersrand Supergroup and the intrusive ca. 3.1 Ga granodiorite (Poujol and Anhaeusser 2001, Anhaeusser 2006a). The metabasalts are largely concentrated in the NW of the Complex and display pillow structures, spherulites, amygdales and vesicles in places (Anhaeusser 1977). Mineralogically, these rocks comprise tremolite and actinolite, with small amounts of chlorite, quartz, plagioclase and epidote (Anhaeusser 1977). Towards the contact

with the granodiorite (in the NE), the metabasalts are demonstrably hornfelsed and are often cross-cut by small-scale, anastomosing quartz vein networks (Anhaeusser 1977). The steeply-dipping layered ultramafic-mafic rocks, which are largely concentrated in the SW of the Roodekrans Complex, comprise a combination of massive serpentinites and mafic-ultramafic schists, with all lithologies dipping ~70° towards the SW (Anhaeusser 1977, 2006a). The serpentinites are composed of serpentine, chlorite, talc, magnetite and carbonate phases, while the mafic-ultramafic schists predominantly comprise tremolite, with talc, chlorite and carbonate phases occurring in variable proportions (Anhaeusser 1977, 2006a).

6.2.2.3 Zandspruit

The Zandspruit Complex is a relatively small, 1.5 x 0.25 km area of greenschist- to amphibolite-facies ultramafic-mafic rocks that forms a low, NE-SW-trending ridge in the centre of the Johannesburg Dome, 20 km NW of the Johannesburg city centre (Fig. 6.2; Anhaeusser 1992, 2004, 2006b, 2015). The Complex was intruded and fragmented by the surrounding (3.4–3.1 Ga; Robb et al. 2006) porphyritic granodiorites, with small xenoliths occurring within the granodiorites to the N (Anhaeusser 1992). Following metamorphism and metasomatism, the Zandspruit Complex (and surrounding granodiorite) was intruded by a suite of mafic dykes/sills likely associated with the emplacement of the ca. 2.06 Ga Bushveld Complex (Cawthorn et al. 1981, Anhaeusser 1992, 2015).

The exposed Zandspruit Complex is dominated by intrusive ultramafic lithologies (metaperidotite and metapyroxenite) that dip 20–25° towards the SSE, with minor extrusive phases occurring in places (Anhaeusser 1992, 2015). Metaperidotites, which display prominent internal layering and have distinctive nodular weathered surfaces, comprise serpentinised olivine and variably altered pyroxene, while metapyroxenites form poorly-exposed, negatively weathered layers comprising tremolite and actinolite (representing amphibolitised pyroxene). A 250 x 25 m zone of metasomatised ultramafic rocks occurs on the southern flank of the Zandspruit Complex, to the S of the layered ultramafic rocks (Anhaeusser 2015). These rocks contain a matrix of fine-grained biotite, calcite, sericite and K-feldspar, alongside centimetre-scale K-feldspar clots and K-feldspar megacrysts (Anhaeusser 2015). In the SW of the exposed Zandspruit Complex, a < 100 m diameter, irregularly-shaped area of diorite occurs in association with xenoliths of amphibolite and lithologies containing amphibole, feldspar and quartz. Due to the high density of mafic xenoliths, the diorite is interpreted as recording the assimilation of the ultramafic-mafic Zandspruit Complex by the intruding granodiorite (Anhaeusser, 1992, 2015).

6.2.2.4 Cresta

Located on the southern edge of the Johannesburg Dome (Fig. 6.2), the Cresta Complex occurs in an extremely urbanised area close to the Johannesburg city centre (Anhaeusser 2004, 2006a). Consequently, there are limited exposures and no detailed published account of the Complex, which comprises a suite of ultramafic-mafic rocks that extends roughly 10 km from W to E (Anhaeusser 2006a). The accessible localities exhibit massive serpentinite and schistose amphibolite – both interpreted as representing metamorphosed komatiites – alongside intrusive layered rocks (Anhaeusser 2004, 2006a). Displaying a stratigraphic sequence up to 30 m thick, the layered intrusive rocks comprise serpentinised peridotite and pyroxenite, alongside volumetrically subordinate metagbabbro (Anhaeusser 2006a). The precise age of the Cresta Complex is unknown, but it is older than the ca. 3.2 Ga hornblende-biotite tonalite gneiss that intrudes the Complex (Poujol and Anhaeusser 2001).

6.2.2.5 Modderfontein

Located on the SE edge of the Johannesburg Dome (Fig. 6.2), the Modderfontein Complex is a poorly-exposed and scarcely studied area of ultramafic and mafic rocks that occupies roughly 10 km^2 (Chaumba 1992, Anhaeusser 2004, 2006a). Although the Complex has not been directly dated, its age is constrained as older than the cross-cutting, 3.34–3.20 Ga trondhjemite gneiss on its western side (Poujol and Anhaeusser 2001, Anhaeusser 2004). The Modderfontein Complex comprises massive serpentinite, various serpentinite-talc-chlorite-carbonate schists, amphibolite and highly altered pyroxenites, with steeply-dipping units of serpentinite and amphibolite occurring in the W of the Complex (Chaumba 1992). Interpreted as metamorphosed intrusive rocks, the serpentinites form low ridges, while the amphibolites occupy the intervening lower ground (Chaumba 1992, Anhaeusser 2004).

6.3 The Barberton Greenstone Belt

The Palaeo- to Meso-archaean Barberton Greenstone Belt, which is located in the Eastern Block of the Kaapvaal Craton (in the "Barberton Mountain Land"; Fig. 6.1), is a volcano-sedimentary remnant that is entirely surrounded by TTG and potassic intrusive granitoid rocks (Fig. 6.4; Kamo and Davis 1994, Poujol et al. 2003, Brandl et al. 2006, Robb et al. 2006, Kisters et al. 2010). Occupying a 110 x 50 km area (Fig. 6.4), the ENE/WSW-trending Barberton Greenstone Belt is one of the most intensively studied greenstone belts on Earth, and has contributed to our understanding of both the Archaean Earth and primeval life (De Wit et al. 1987, 1992, Brandl et al. 2006, Van Kranendonk, et al. 2014, Anhaeusser 2014).

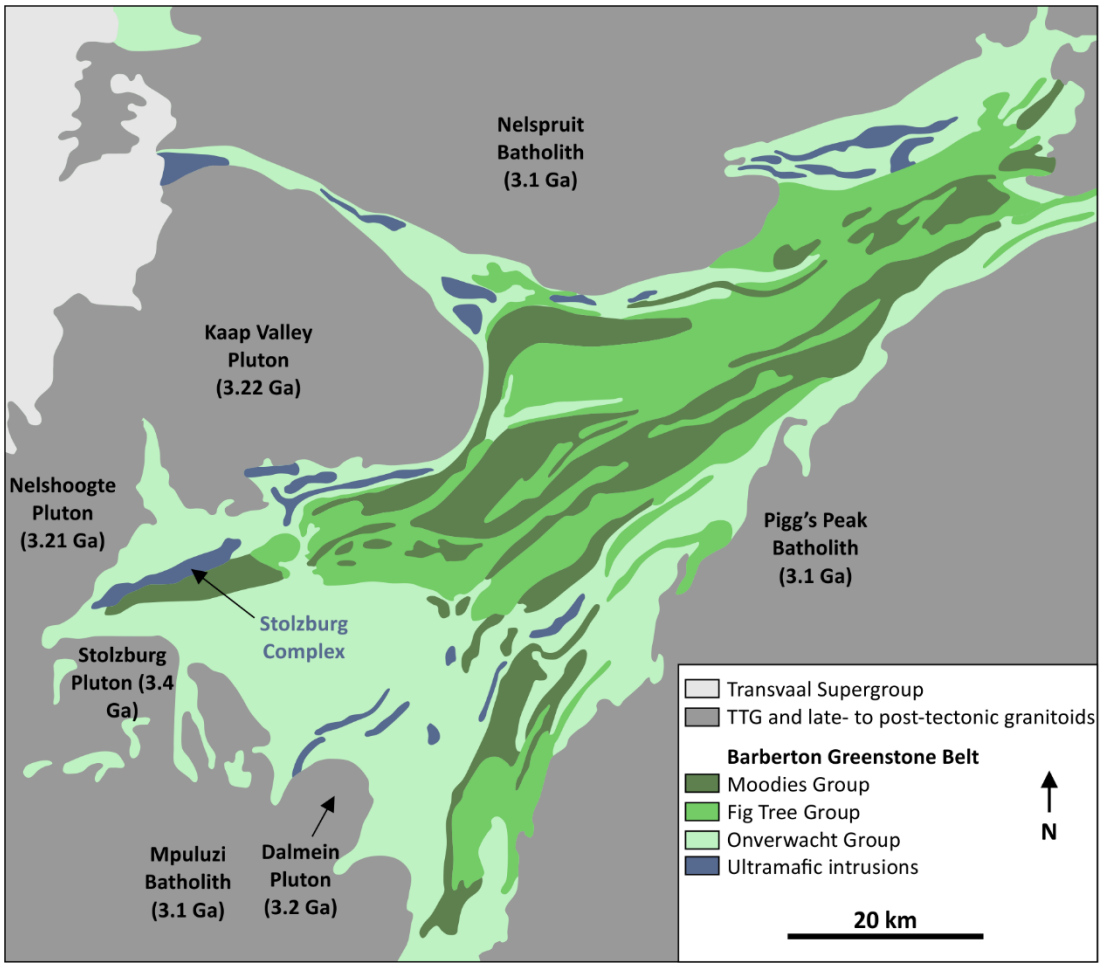

Figure 6.4: *Simplified geological map of the Barberton Greenstone Belt, including the locations of the ultramafic-mafic complexes described in the text. Map location detailed in Figure 6.1. Redrawn after:* (De Ronde and De Wit 1994, Kamo and Davis 1994, Kröner et al. 1996, Brandl et al. 2006, Anhaeusser 2006a).

6.3.1 Stratigraphic and metamorphic chronology

The stratigraphy of the Barberton area is relatively well constrained (Fig. 6.5), with the volcano-sedimentary rocks of the Barberton Greenstone Belt (Barberton Supergroup) deposited between 3.6 and 3.1 Ga (Armstrong et al. 1990, De Ronde and De Wit 1994, Kröner et al. 1996, Dziggel 2002, Poujol et al. 2003, Brandl et al. 2006), and the surrounding TTG and granitoid rocks emplaced episodically between 3.5 and 2.7 Ga (Tegtmeyer and Kröner 1987, Walraven et al. 1990, Poujol et al. 2003, Robb et al. 2006, Kamo and Davis 1994, Poujol 2007). Specific periods of felsic magmatism are dated at 3.55–3.42, 3.26–3.22 and 3.11–3.05 Ga, with more discrete events at 2.98–2.82 and 2.73 Ga (Fig. 6.5; Tegtmeyer and Kröner 1987, Walraven et al. 1990, Kamo and Davis 1994, Poujol et al. 2003, Robb et al. 2006, Poujol 2007). Moreover, several phases of greenschist- to amphibolite-facies metamorphism are recognised in the region, with specific events constrained at 3.45 and 3.23 Ga respectively (Lopez-Martinez et al. 1992, Dziggel 2002, Diener et al. 2005).

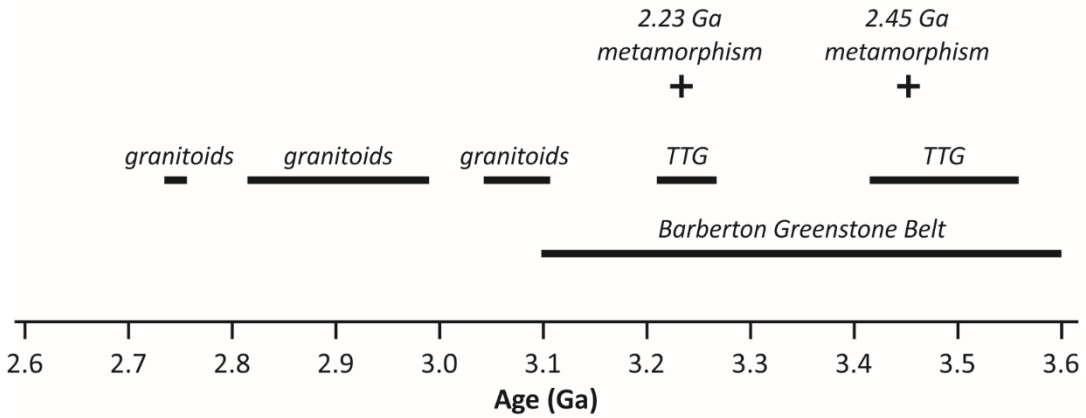

Figure 6.5: *Timeline detailing the established stratigraphic and metamorphic chronology for the Barberton Greenstone Belt and surrounding rocks. After (Lopez-Martinez et al. 1992, Dziggel 2002, Poujol et al. 2003, Diener et al. 2005, Robb et al. 2006).*

6.3.1.1 Barberton Supergroup

The supracrustal rocks of the Barberton Supergroup are subdivided into 3 broad stratigraphic groups (Fig. 6.4), namely (in stratigraphic order): Onverwacht; Fig Tree; and Moonies (Lowe et al. 1985, De Wit et al. 1987, Brandl et al. 2006).

The 3.55–3.30 Ga Onverwacht Group, which largely comprises ultramafic-mafic volcanic rocks and hosts the ultramafic-mafic complexes (Section 6.3.2), comprises (Viljoen and Viljoen 1969a-c, Lowe et al. 1985, Armstrong et al. 1990, Kröner et al. 1996, Brandl et al. 2006, Anhaeusser 2006b, Furnes et al. 2012, 2013): Sandspruit, Theespruit, Komatii, Hooggenoeg, Kromberg and Mendon Formations. The Sandspruit, Theespruit and Komatii Formations are dominated by mafic-ultramafic lavas, while the Hooggenoeg, Kromberg and Mendon Formations contain a combination of ultramafic-mafic and felsic volcanic rocks (Fig. 6.6; Viljoen and Viljoen 1969a-c, Lowe et al. 1985, Armstrong et al. 1990, Kröner et al. 1996, Brandl et al. 2006, Anhaeusser 2006b, Furnes et al. 2012, 2013).

The Sandspruit Formation occurs as isolated xenoliths of ultramafic-mafic rocks within the Theespruit and Stolzburg plutons (Fig. 6.4), SW of the Barberton Greenstone Belt (Brandl et al. 2006). It is dominated by metamorphosed ultramafic-mafic lavas and tuffs, contains units of felsic volcanic rocks and has been metamorphosed to amphibolite-facies (Viljoen and Viljoen 1969a, Dziggel 2002, Diener et al. 2005, Brandl et al. 2006). The Komatii Formation comprises metamorphosed komatiites and basaltic komatiites, with minor mafic lavas and small intrusions also present (Fig. 6.6; Viljoen and Viljoen, 1969a; Brandl et al. 2006). The lower part of the Komatii Formation is dominantly ultramafic, while the upper part is dominantly mafic (Fig. 6.6; Viljoen and Viljoen, 1969; Brandl et al. 2006). The Hooggenoeg Formation comprises mafic lava, felsic lava and chert, with felsic lithologies increasingly

dominant upwards (Fig. 6.6; Viljoen and Viljoen, 1969a-c). The Kromberg Formation comprises ultramafic-mafic lava and mafic tuff, together with rare chert and felsic volcaniclastic rocks, while the Mendon Formation comprises mafic-ultramafic lava and rare chert (Viljoen and Viljoen 1969a-c; Brandl et al. 2006).

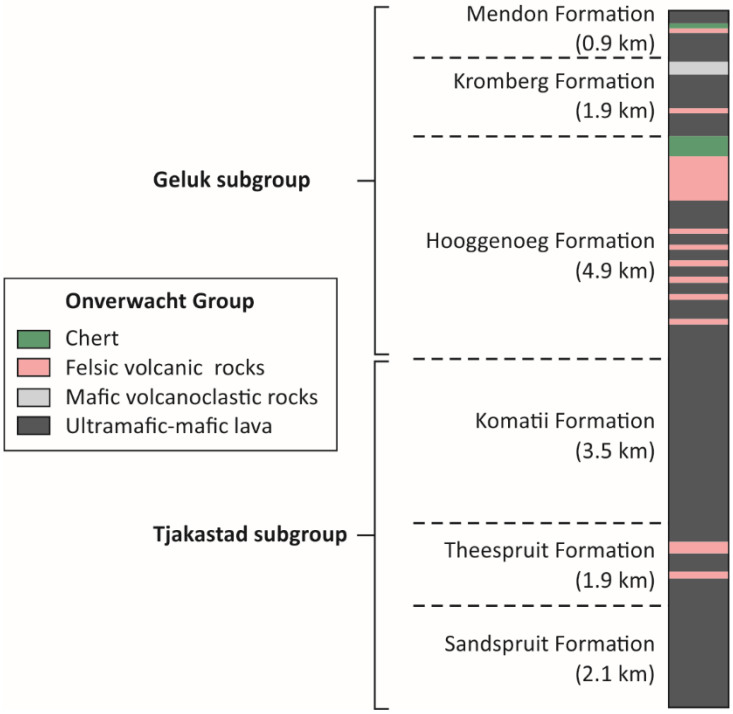

Figure 6.6: *Simplified stratigraphy of the Onverwacht Group, which represents the lowermost group in the Barberton Greenstone Belt (Redrawn after: Viljoen and Viljoen 1969a, Brandl et al. 2006, Anhaeusser 2006a).*

The overlying Fig Tree and Moodies Groups are dominated by sedimentary rocks, with the 3.26–3.23 Ga Fig Tree Group predominantly comprising deep to shallow marine sandstone and shale, with subordinate felsic volcanic rocks and banded iron formations (Brandl et al. 2006). Deeper marine sediments are generally located towards the N, while shallower marine sediments are located towards the S (Brandl et al. 2006). The 3.23 Ga Moodies Group comprises marine and fluvial sandstone and conglomerate, with minor shale and banded iron formations (Brandl et al. 2006).

6.3.1.2 TTG and granitoids

Early felsic magmatism (3.55–3.42 Ga; Fig. 6.5) in the Barberton area is preserved as relatively small (< 6 km diameter) plutons, such as the Stolzburg Pluton, which is located on the SW margin of the Barberton Greenstone Belt (Fig. 6.4; Robb et al. 2006). These plutons commonly contain remnants of the Barberton Greenstone Belt and are largely composed of tonalite and trondhjemite (Anhaeusser and Robb 1981, Robb et al. 2006). Subsequent felsic

magmatism (3.26–3.22 Ga; Fig. 5.5), which is largely concentrated along the W and NW margins of the Barberton Greenstone Belt, includes the Nelshoogte and Kaap Valley plutons (Fig. 6.4; Anhaeusser 1985, Robb et al. 2006). These larger occurrences (< 35 km diameter) are also dominated by TTG gneisses, and contain a number of greenstone belt remnants (Anhaeusser 1985, Robb et al. 2006). The final stages of felsic magmatism in the Barberton region (3.1-2.7 Ga) is concentrated along the N and E margins of the Barberton Greenstone Belt (Robb 1977, 1978, 1979, Robb et al. 2006), with this magmatism post-dating the 3.23 Ga metamorphism (Dziggel 2002, Diener et al. 2005). These occurrences, which include the Nelspruit, Pigg's Peak and Mpuluzi Plutons (Fig. 6.4), are dominated by granodiorite, granite and a syenite-granite (Robb et al. 2006).

6.3.2 Ultramafic-mafic complexes

All of the ultramafic-mafic complexes in the Barberton Greenstone Belt are hosted by the Onverwacht Group, with upwards of 20 occurrences associated with the Tjakastad Subgroup and 5 occurrences associated with the Geluk Subgroup (Fig. 6.4; Viljoen and Viljoen 1970, Anhaeusser 1985, 2006b). Most of the complexes, which were likely emplaced between 3.54 and 3.26 Ga (Lahaye et al. 1995) and are distributed throughout the Onverwacht Group (Fig. 6.4), comprise volumetrically dominant ultramafic lithologies (dunite, orthopyroxenite, websterite and harzburgite) and volumetrically subordinate mafic lithologies (gabbro, gabbronorite and anorthosite; Anhaeusser 1985; 2006b). Relative to intrusive layered ultramafic-mafic complexes globally, those in the Barberton Greenstone Belt are notably Mg-rich, with dunite and harzburgite collectively comprising up to 80 % (Anhaeusser 1985, 2006b). The greenschist- to amphibolite-facies complexes have experienced significant faulting and folding, with tectonism generally attributed to the intrusion of the surrounding granitoids (Viljoen and Viljoen 1970, Anhaeusser 1985, 2006b). Individual occurrences, which are up to 1.5 km thick, often exhibit distinctive magmatic layering and cyclicity, while others are either massive or contain only 1 magmatic cycle (Anhaeusser 1985).

The 1.2 km thick Stolzburg Complex – located in the SW of the Barberton Greenstone Belt (Fig. 6.4) – represents a particularly well-exposed ultramafic-mafic complex that displays characteristic magmatic layering and cyclicity (Fig. 6.7; Viljoen and Viljoen 1970, Anhaeusser 1985, 2006b). The Stolzburg Complex, which is exposed along its 14 km strike length and displays distinctive cumulate textures, contains 3 asbestos deposits and a 20–30 cm thick chromitite layer (Anhaeusser 1985, 2001, 2006a). The lower parts of the Complex are dominated by dunite and orthopyroxenite, with harzburgite, wehrlite, lherzolite, gabbro,

gabbronorite and websterite increasingly common towards the stratigraphic top (Viljoen and Viljoen 1970, Anhaeusser 1985, Rodel 1993, Anhaeusser 2001).

As with the ultramafic-mafic complexes in the Johannesburg Dome, those (comparatively well-exposed and intensively studied) in the Barberton Greenstone Belt, are subject to two opposing hypotheses. Some authors interpret the ultramafic-mafic rocks of the lower Onverwacht Group as oceanic plateaux assemblages (Viljoen and Viljoen 1970) and the layered complexes as contemporaneous intrusions, with both components derived from high-Mg magmas (~28 wt. % MgO; Anhaeusser 1985, 2006b). Others have interpreted the ultramafic-mafic complexes and surrounding supracrustal rocks as representing Archaean ophiolites, or fragments of an Archaean ophiolite (De Wit et al. 1987, 1992).

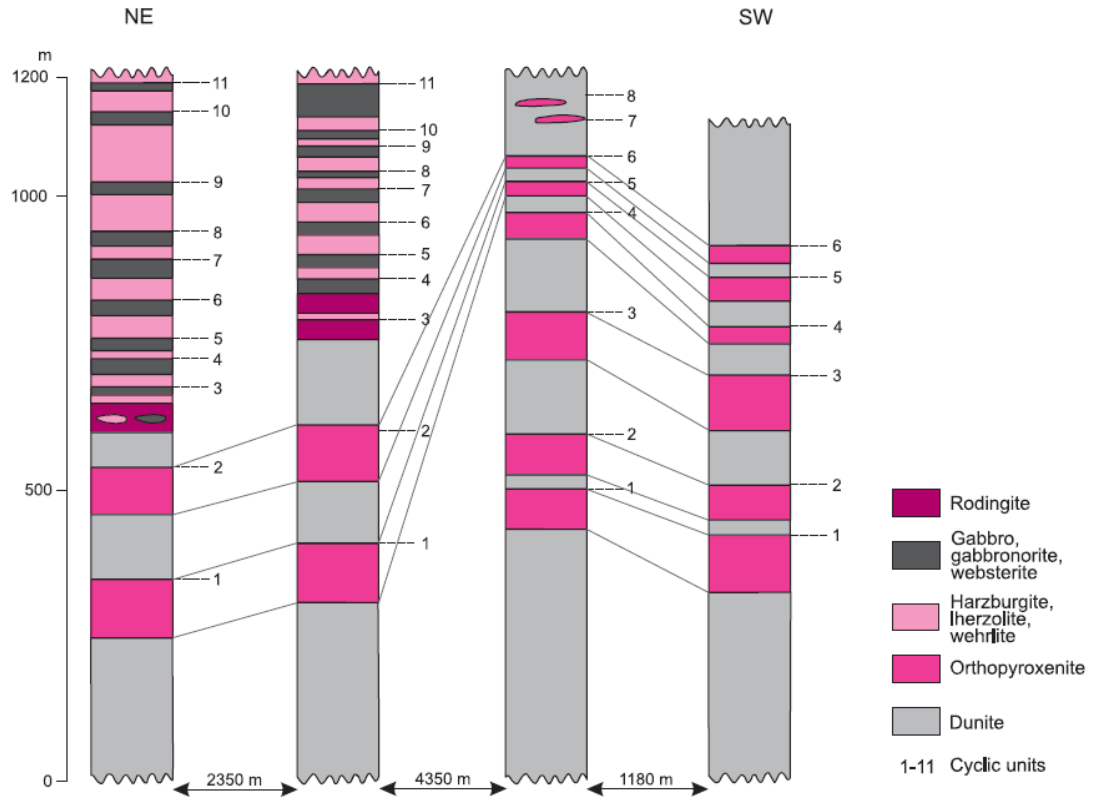

Figure 6.7: *Stratigraphic logs conducted in different parts of the Stolzburg Complex. The numbers refer to individual magmatic cycles (from: Anhaeusser 2006b).*

Chapter 7

Field relationships, petrography and mineral chemistry

Detailed field investigations and associated sampling – carried out in 2016 – focused on the Modderfontein, Zandspruit and Roodekrans Complexes (Fig. 6.3). For descriptions of these complexes according to the previously published literature, see Section 6.2.2. A new geological map for the scarcely studied Modderfontein Complex is presented in Section 7.1.1, while detailed stratigraphic logs of the previously mapped Zandspruit (Anhaeusser 1992, 2015) and Roodekrans (Anhaeusser 1977) Complexes are presented in Sections 7.2.1 and 7.3.1 respectively. During field investigations, which utilised Google Earth basemaps and a Garmin eTrex 10 Handheld GPS, a total of 43 samples were collected from the 3 complexes, with 20 samples collected from the Modderfontein Complex, 12 samples collected from the Zandspruit Complex, and 11 samples collected from the Roodekrans Complex. Sample locations (given in decimal degrees) are included in Appendix F.

All the studied Complexes were also subject to petrographic assessment using polished thin sections made at Cardiff University, with optical microscopy supplemented by element mapping (using the instrumentation and methodology described in Appendix A) in the case of approximately 40 % of samples. Moreover, the composition of spinel from the Modderfontein, Zandspruit and Roodekrans Complexes was also assessed (using the instrumentation and methodology described in Appendix A), with a total of 582 analyses conducted on spinels from 15 thin sections.

7.1 The Modderfontein Complex

This study focuses on a previously un-mapped and un-reported 1 km^2 area in the E of the Modderfontein Complex (Fig. 6.2). The exposure, which is flanked by the R25 road to the N, housing developments to the E and W, and industrial developments to SE and NW (Fig. 7.1), represents the largest remaining exposure of the Modderfontein Complex. Over the preceding 2 decades, significant urban developments (including the Greenstone Shopping Centre) have covered the exposures in the W of the Complex, including those mapped by Chaumba (1992).

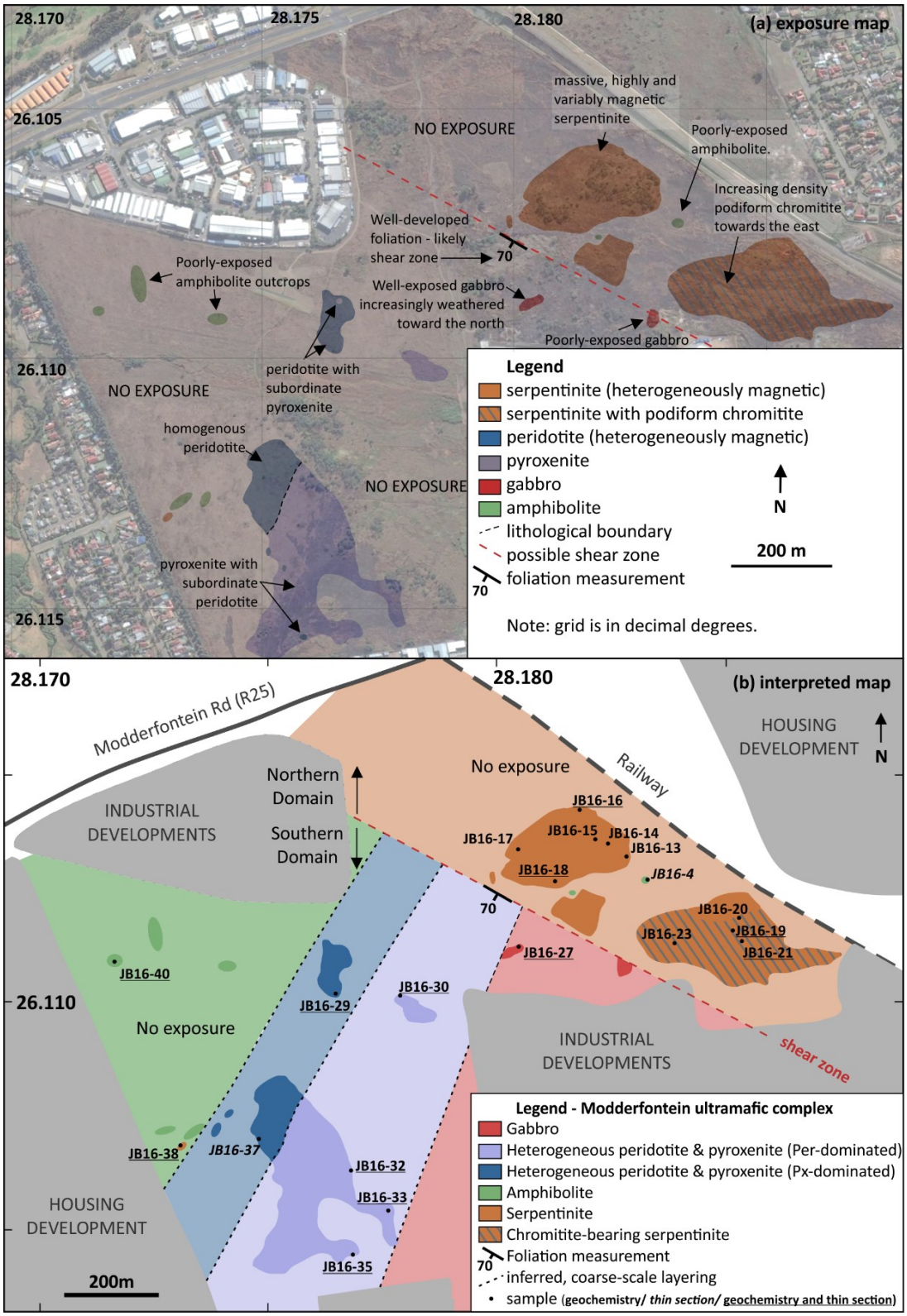

Figure 7.1: (a) *Exposure map of studied portion of the Modderfontein Complex. Satellite imagery from Google Earth (2016).* ***(b)*** *Interpreted geological map of the Modderfontein Complex, detailing sample locations (black dots and associated text) and distribution of exposures (represented by the darker colours). Grid references are in decimal degrees (coordinate system: WGS1984) and geographical features are in grey. Abbreviations: per=peridotite; px=pyroxenite.*

7.1.1 Mapping and field relationships

Separated by a poorly-exposed and steeply-dipping (70° towards the SW) shear zone that strikes roughly NW-SE, the mapped area can be subdivided into two domains that exhibit distinct lithological assemblages (Fig. 7.1). The northern domain is dominated by massive serpentinite, while the southern domain comprises layered (on a scale of tens of metres) peridotite, pyroxenite, amphibolite and gabbro (Fig. 7.1). Ultramafic rocks (serpentinite, peridotite and pyroxenite) generally occur on small hillocks that are better exposed and slightly more vegetated than the surrounding areas (Fig. 7.2a), while amphibolite and gabbro are poorly-exposed and occupy the low ground.

Exposures of massive serpentinite in the NW of the northern domain exhibit distinctly brown weathered surfaces (Fig. 7.2a), with dark fresh surfaces comprising fine-grained serpentine. In the NW of the domain, serpentinites contain fine-grained magnetite that sporadically forms patches < 2 cm in diameter (Fig. 7.2b). The SW of the northern domain contains rare amphibolite enclaves that are irregularly-shaped, have sharp contacts with the host serpentinite and occur on a scale of tens of centimetres (Fig. 7.2c). In the SE of the northern domain (Fig. 7.1), serpentinites contain sporadically distributed and irregularly-shaped chromitite lenses that range from millimetre-scale stringers to centimetre-scale pods (Fig. 7.2d-f). Contacts with the host serpentinite are generally sharp (e.g., Fig. 7.2d), although chromitite is occasionally interspersed with sub-millimetre- to millimetre-scale serpentine patches (e.g., Fig. 7.2f). In the centre of the northern domain, between large exposures of serpentinite (Fig. 7.1), two small (< 60 cm diameter) outcrops of amphibolite occur in poorly-exposed low ground.

The southern domain is dominated by peridotite and pyroxenite, with volumetrically subordinate gabbro and amphibolite in the E and W respectively (Fig. 7.1). The lithological distribution of gabbro, pyroxenite (with subordinate peridotite), peridotite (with subordinate pyroxenite) and amphibolite suggests that this portion of the Modderfontein Complex exhibits NE-SW-trending layering on a scale of tens of metres (Fig. 7.1). The orientation of such layering is supported by satellite imagery (from 2004) and mapping (Chaumba 1992) of an area of the Modderfontein Complex located 2 km W of the current study area (before the area was developed and built upon), which both indicate the presence of NE-SW-trending layering also on a scale of tens of metres (Fig. 7.3). Massive peridotite outcrops are well-exposed and exhibit brown-weathered surfaces, with rare millimetre- to centimetre-scale patches of fine-grained magnetite. The coarse-grained pyroxenites are relatively well-exposed, with millimetre-scale clinopyroxene crystals prominent on the light-brown

weathered surfaces. Amphibolites form poorly-exposed, grey-brown outcrops that display a prominent schistosity and light grey fresh surfaces.

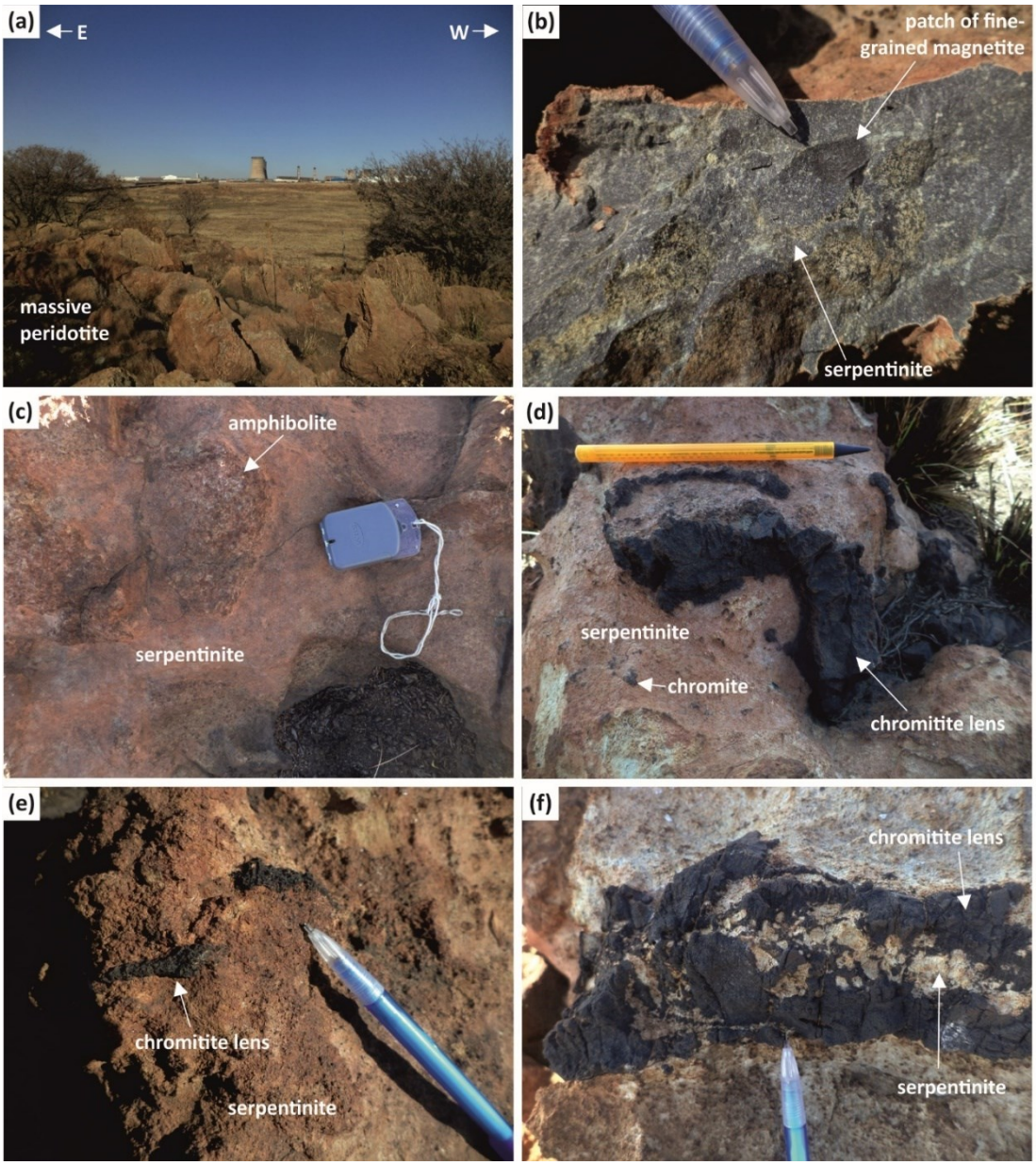

Figure 7.2: *Field photographs from the Modderfontein Complex.* ***(a)*** *Massive peridotite forming a small hillock in the NW of the northern domain.* ***(b)*** *Millimetre-scale patches of fine-grained magnetite in serpentinite from the NW of the northern domain.* ***(c)*** *Decimetre-scale enclave of amphibolite within serpentinite in the SW of the northern domain.* ***(d)*** *Decimetre-scale chromitite lens in the SE of the northern domain. Note sharp contacts with surrounding serpentinite.* ***(e)*** *Millimetre-scale lenses of chromitite in the SE of the northern domain.* ***(f)*** *Irregularly-shaped, centimetre-scale chromitite lens in the SE of the northern domain, exhibiting interspersed chromitite and serpentinite. Pencil length=15 cm; compass length=10 cm.*

Figure 7.3: *Blank* ***(a)*** *and interpreted* ***(b)*** *satellite image for an area now covered by housing developments and the Greenstone Shopping Centre, located 2 km west of the study area (Google Earth 2004). For the satellite image's location relative to the area mapped in Figure 7.1, see Figure 6.2.*

7.1.2 Petrography

In total, 14 samples were subject to petrographic assessment (5 from the northern domain and 9 from the southern domain), with sample locations indicated in Figure 7.1b and included in Appendix F.

Serpentinites (n=4; Fig. 7.4a) comprise (in modal %): > 93 % serpentine and < 7 % tremolite, with accessory magnetite and Cr-spinel. Serpentine grains, which are euhedral to subhedral, elongate and < 0.1 mm long, collectively represent the serpentinised pseudomorphs of olivine and/or orthopyroxene (Fig. 7.4a). Fine-grained (< 0.1 mm diameter) magnetite is sporadically distributed between and within serpentine, and occasionally occurs as rounded amalgamations (as seen on the outcrop scale) < 2 mm in diameter. Rounded, 1.5 mm diameter clusters of tremolite are composed of individual, 0.2 to 0.6 mm long, fibrous grains (Fig. 7.4a).

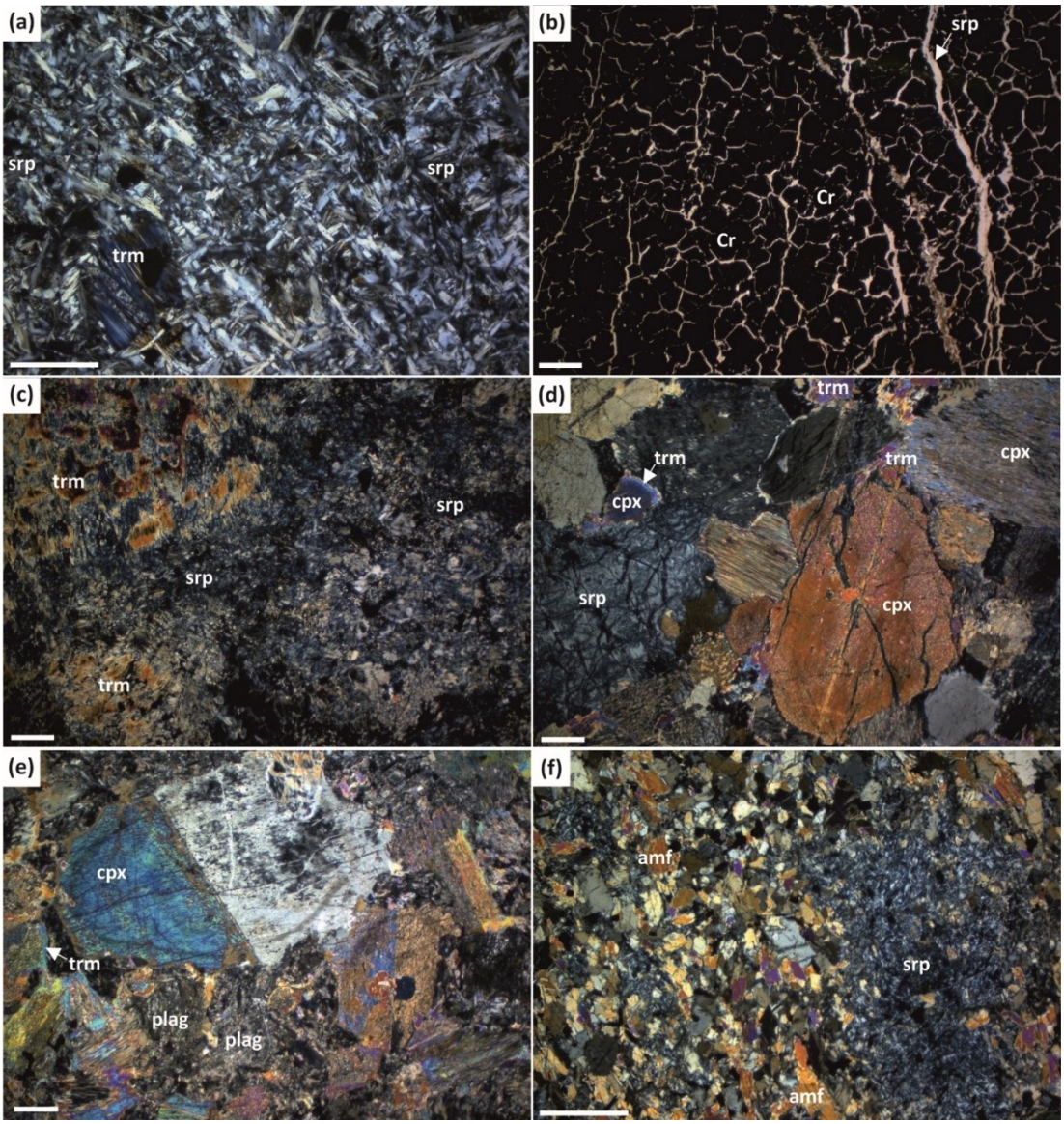

Figure 7.4: *Photomicrographs detailing the petrographic characteristics of the Modderfontein Complex rocks. All photomicrographs were taken using XPL, with the exception of (b), which was taken using PPL.* ***(a)*** *Fine-grained serpentinite containing 500 µm diameter patch of tremolite, from the NW of the northern domain.* ***(b)*** *Podiform chromite from the E of the northern domain.* ***(c)*** *Peridotite from the southern domain, containing serpentine and tremolite.* ***(d)*** *Pyroxenite from the southern domain, comprising coarse-grained clinopyroxene, minor tremolite, and serpentine pseudomorphs of olivine and/or orthopyroxene.* ***(e)*** *Gabbro from the southern domain, comprising clinopyroxene, minor tremolite and interstitial plagioclase.* ***(f)*** *Amphibolite from the W of the southern domain, containing fine-grained amphibole (tremolite and actinolite) and a rare serpentine pseudomorph. Abbreviations: amf=amphibole; Cr=chromite; cpx=clinopyroxene; plag=plagioclase; srp=serpentine; trm=tremolite; white scale bar=500 µm.*

The serpentinite-hosted lenses of chromitite (n=1), which occur in the E of the northern domain (Fig. 7.1), comprise < 0.8 mm diameter, subhedral to euhedral chromite grains (Fig. 7.4b). On the µm-scale, the chromite grains sometimes appear skeletal, comprising parallel blades of chromite that display sharp boundaries with the surrounding silicate material. Such

silicate material also forms the boundaries to individual chromite grains (Fig. 7.4b). The serpentinite-hosted lenses of chromitite also contain several PGM, as described in Section 7.1.2.1.

Peridotites (n=3; Fig. 7.4c), which classify as wehrlite and lherzolite (assuming that serpentine represents serpentinised olivine ± orthopyroxene), comprise (in modal %): 55 to 70 % serpentine, 14 to 35 % tremolite and < 31 % relic clinopyroxene, with accessory Cr-spinel and magnetite. Subhedral to anhedral serpentine is fine-grained (< 0.1 mm diameter), with subhedral clinopyroxene < 4 mm in diameter. Relic clinopyroxene is variably replaced by fine-grained (< 0.1 mm diameter) tremolite that may pseudomorph entire clinopyroxene grains, while fine-grained (< 0.15 mm diameter) magnetite is also associated with serpentine as an accessory phase.

Pyroxenites (n=3; Fig. 7.4d), which classify as olivine-websterite (assuming that serpentine represents serpentinised olivine ± orthopyroxene), comprise (in modal %): 17 to 39 % serpentine, < 2 % amphibole (tremolite and actinolite) and 60 to 81 % (fresh) clinopyroxene, with accessory spinel and magnetite. Large patches of serpentine (< 1 mm diameter), which represent olivine and/or orthopyroxene pseudomorphs, comprise small (< 0.1 mm diameter), subhedral serpentine grains (Fig. 7.4d) and rare, fine-grained (< 0.3 mm diameter) magnetite (Fig. 7.4d). Clinopyroxene is subhedral, occasionally altered to tremolite and < 2 mm in diameter (Fig. 7.4d). Tremolite is randomly distributed within clinopyroxene and forms anhedral grains < 0.2 mm in diameter (Fig. 7.4d).

One gabbro sample (Fig. 7.4e) comprises (in modal %): 77.5 % clinopyroxene, 1.5 % amphibole (tremolite and actinolite) and 21 % sericitized plagioclase feldspar. Large (< 3 mm diameter), subhedral to euhedral clinopyroxene grains exhibit distinctive twinning and limited alteration to tremolite (Fig. 7.4e). These anhedral to subhedral, < 0.15 mm diameter tremolite grains commonly form rims on the clinopyroxene grains (Fig. 7.4e). Plagioclase is generally highly altered (to sericite), with relic subhedral to anhedral grains appearing to be intercumulus to the clinopyroxene (Fig. 7.4e).

Amphibolites (n=2; Fig. 7.4f) comprise (in modal %): > 90 % amphibole and < 10 % serpentine. Amphiboles are generally anhedral to subhedral and < 0.4 mm in diameter, although larger (< 1 mm diameter) pseudomorphs of clinopyroxene are also preserved. Fine-grained (< 0.15 mm diameter), anhedral serpentine is rare, but occasionally forms large (< 2 mm diameter) pseudomorphs of olivine and/or orthopyroxene (Fig. 7.4f).

7.1.2.1 Platinum-group minerals

A total of 20 PGM (summarised in Table 7.1), which range from 0.4 to 4 µm in diameter and are generally subhedral, were identified in the chromitite sample (for which bulk-rock PGE data are shown in Chapter 8). Erlichmanite (OsS_2; n=7), laurite (RuS_2; n=6) and sperrylite ($PtAs_2$; n=3) are the dominant PGM species, with individual occurrences of platarsite (PtAsS), platarsite-hollingworthite (PtAsS-RhAsS), hollingworthite-irarsite (RhAsS-IrAsS) and irarsite (IrAsS; Table 5; Fig. 7.5). The majority of PGM are associated with chromite grains (n=13; Fig. 7.5a-b), with a smaller number associated with silicate-chromite boundaries (n=3) and silicates (n=1; Fig. 7.5c). A further 3 PGM are associated with silicate material located between µm-scale chromite blades (Fig. 7.5d), with some of the chromite-hosted PGM located within chromite blades (Fig. 7.5b).

Table 7.1: *Summary of the platinum-group mineral species and mineralogical associations found in the Modderfontein chromitite (sample JB16-19Cr).*

Mineral	**Chemical Formula**	**Number identified**	**Mineralogical association**				**Grain size (µm)**		
			Silicate-Chromite boundary	Chromite	Silicate blades in chromite	Silicate	Max	Min	Average
Erlichmanite	OsS_2	7	2	5	0	0	4	0.8	2.1
Laurite	RuS_2	6	1	4	1	0	2	0.2	1.0
Sperrylite	$PtAs_2$	3	0	1	1	1	1.0	0.4	0.6
Platarsite	PtAsS	1	0	1	0	0	2.0	2.0	2.0
Platarsite-Hollingworthite	PtAsS-RhAsS	1	0	1	0	0	0.9	0.9	0.9
Hollingworthite-Irarsite	RhAsS IrAsS	1	0	0	1	0	1.0	1.0	1.0
Irarsite	IrAsS	1	0	1	0	0	0.5	0.5	0.5
TOTAL		20	3	13	3	1			

7.1.3 Spinel Mineral Chemistry

Additional to secondary magnetite derived from serpentinisation, spinel is present within the chromitite lenses, serpentinite, pyroxenite and peridotite of the Modderfontein Complex. In chromitite lenses, spinel occurs as 0.2 to 0.5 mm diameter, generally subhedral grains that exhibit altered rims. In pyroxenite, peridotite and serpentinite, spinel is generally subhedral to anhedral and ranges from 0.02 to 0.3 mm in diameter, with some grains displaying altered rims < 0.03 mm thick (Fig. 7.6a-b).

Two-hundred and forty-seven analyses were conducted on spinels from chromitite, serpentine, peridotite and pyroxenite lithologies (Table 7.2), with spinel compositions subdivided into two populations based on Fe^{3+} numbers (calculated as molar $Fe^{3+}/[Cr+Al+Fe^{3+}]$). Group 1 spinels (n=118) display Fe^{3+} numbers of < 0.35, with group 2 (n=129) spinels exhibiting Fe^{3+} numbers of > 0.64 (Table 7.2). Group 1 spinels contain high

abundances of MgO, Al_2O_3, TiO_2, MnO and Cr_2O_3, and low abundances of FeO relative to group 2 spinels (Table 7.2). Group 2 compositions reflect analyses from both spinel cores and altered rims, whereas group 1 spinels were only found from analyses of spinel cores (Fig. 7.6).

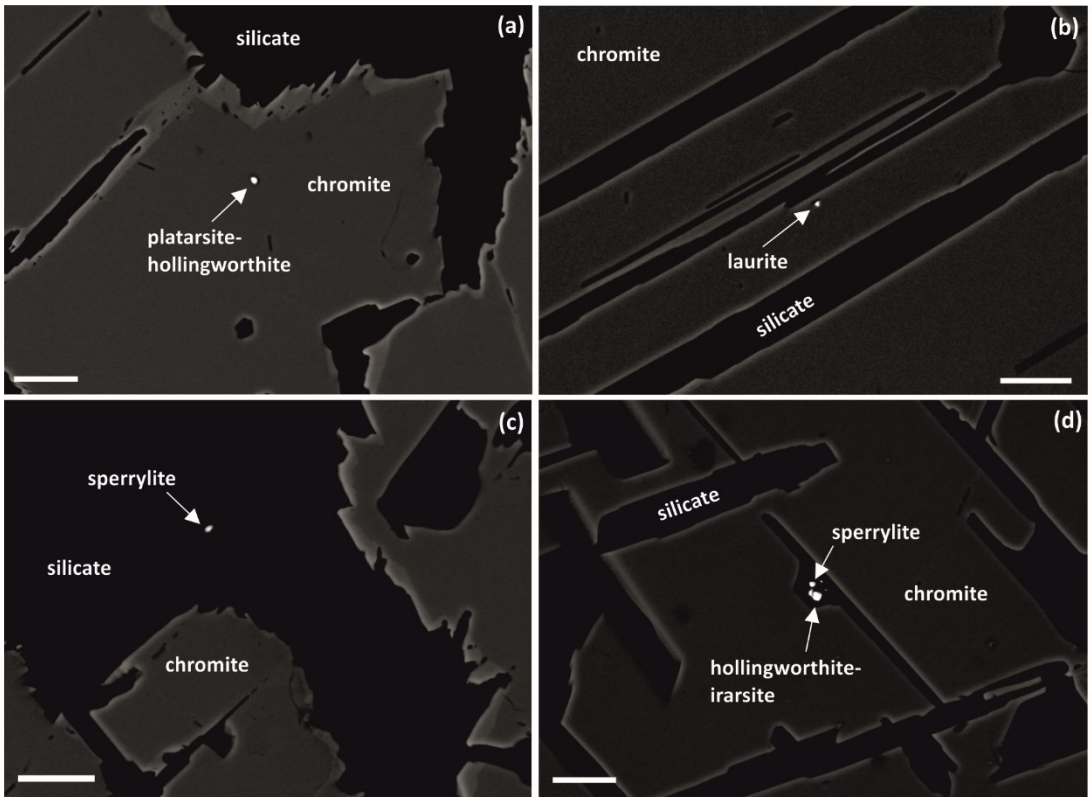

Figure 7.5: *Back-scattered electron images detailing the morphology of representative platinum-group minerals from the Modderfontein chromitite.* ***(a)*** *Chromite-hosted platarsite-hollingworthite grain.* ***(b)*** *Laurite grain hosted by chromite blade.* ***(c)*** *Silicate-hosted (Al-rich serpentine) sperrylite.* ***(d)*** *Separate sperrylite and hollingworthite-irarsite grains hosted by the silicate material (Al-rich serpentine) between a skeletal chromite. White scale bar=10 µm.*

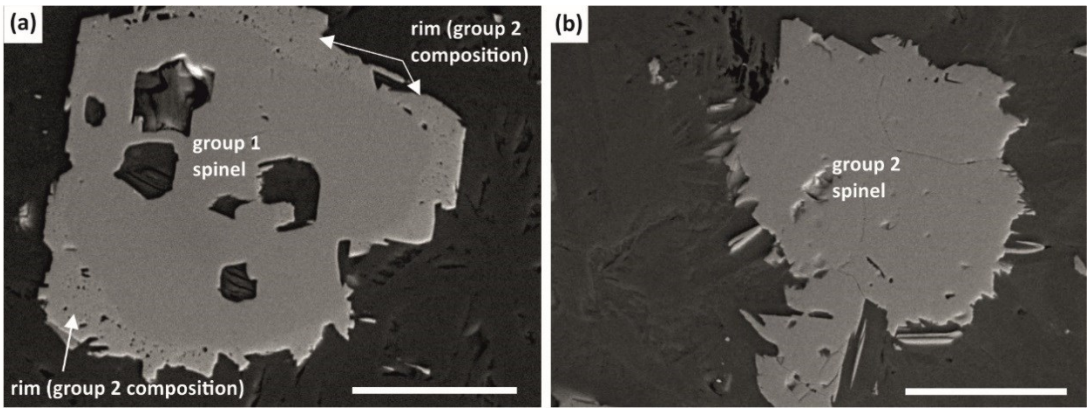

Figure 7.6: *Secondary electron images detailing the morphology of spinel grains from the Modderfontein Complex.* ***(a)*** *120 µm diameter group 1 spinel from the northern domain (sample JB16-16; Fig. 2), with altered rim (of group 2 spinel composition) < 20 µm thick.* ***(b)*** *110 µm diameter group 2 spinel from the southern domain (JB16-33; see Fig. 2). White scale bar=50 µm.*

Table 7.2: *Representative analyses of group 1 and 2 spinel from the Modderfontein Complex. The full dataset is available in Appendix F.*

	group 1 spinel									
Sample	**JB16-19**	**JB16-19**	**JB16-19**	**JB16-19**	**JB16-30**	**JB16-32**	**JB16-32**	**JB16-16**	**JB16-16**	**JB16-16**
Domain	N	N	N	N	S	S	S	N	N	N
Lithology	cr	cr	cr	cr	px	px	px	srp	srp	srp
SiO_2	0.15	0.15	0.15	0.17	0.21	0.24	0.19	0.21	0.21	0.24
TiO_2	2.54	2.29	2.74	2.27	0.20	0.33	0.53	0.08	1.17	1.32
Al_2O_3	1.17	2.49	1.40	1.08	14.66	12.64	7.63	12.91	3.14	1.78
FeO	51.34	52.14	52.57	53.60	25.73	28.21	41.62	30.68	42.29	43.74
Fe_2O_3	0.34	0.39	0.37	0.31	0.17	0.14	0.22	0.15	0.32	0.29
MnO	2.17	1.74	1.73	2.10	0.26	0.37	0.66	0.32	2.44	2.57
MgO	0.68	0.98	1.13	0.61	8.47	6.77	2.72	5.16	1.72	1.56
V_2O_3	0.59	0.39	0.57	0.57	0.24	0.34	0.46	0.20	0.44	0.42
Cr_2O_3	36.69	34.42	34.80	34.70	47.81	49.71	44.12	47.15	43.58	42.81
Total	95.66	95.00	95.45	95.40	97.75	98.75	98.15	96.86	95.31	94.72
Cations on the basis of 4 oxygens										
Si	0.01	0.01	0.01	0.01	0.01	0.01	0.01	0.01	0.01	0.01
Ti	0.08	0.07	0.09	0.07	0.01	0.01	0.01	0.00	0.04	0.04
Al	0.06	0.12	0.07	0.05	0.59	0.51	0.34	0.54	0.15	0.09
Fe^{2+}	1.33	1.33	1.34	1.35	0.69	0.77	1.11	0.85	1.16	1.20
Fe^{3+}	0.30	0.32	0.32	0.35	0.02	0.03	0.13	0.04	0.17	0.20
Mn	0.08	0.06	0.06	0.07	0.01	0.01	0.02	0.01	0.08	0.09
Mg	0.04	0.06	0.07	0.04	0.43	0.35	0.15	0.27	0.10	0.09
V	0.02	0.01	0.02	0.02	0.01	0.01	0.01	0.01	0.01	0.01
Cr	1.20	1.13	1.14	1.15	1.28	1.35	1.30	1.32	1.38	1.38
Total	3.11	3.12	3.12	3.12	3.04	3.03	3.08	3.04	3.09	3.10
Mg#	2.51	3.54	4.03	2.20	37.39	30.30	10.90	23.41	7.17	6.37
Cr#	95.46	90.25	94.35	95.58	68.63	72.51	79.50	71.02	90.31	94.18
Fe^{2+}#	0.97	0.96	0.95	0.97	0.62	0.69	0.88	0.76	0.92	0.93
Fe^{3+}#	0.19	0.20	0.21	0.23	0.01	0.01	0.07	0.02	0.10	0.12

Table 7.2 (cont.):

	group 2 spinel									
Sample	JB16-33	JB16-33	JB16-33	JB16-33	JB16-33	JB16-32	JB16-32	JB16-32	JB16-16	JB16-16
Domain	S	S	S	S	S	S	S	S	N	N
Lithology	per	per	per	per	per	px	px	px	srp	srp
SiO_2	0.26	0.21	0.32	0.28	0.30	0.34	0.21	0.62	0.24	0.28
TiO_2	0.35	0.25	0.15	0.18	0.15	0.10	0.05	0.07	0.00	0.00
Al_2O_3	0.23	0.23	0.09	0.08	0.00	0.00	0.13	0.19	0.00	0.00
FeO	80.86	82.13	82.54	82.67	84.02	88.65	84.82	85.98	84.30	88.32
Fe_2O_3	0.32	0.32	0.34	0.29	0.36	0.00	0.34	0.38	0.00	0.00
MnO	0.39	0.28	0.26	0.30	0.18	0.12	0.21	0.14	0.13	0.09
MgO	0.33	0.27	0.38	0.36	0.35	0.28	0.20	0.27	0.41	0.41
V_2O_3	0.36	0.33	0.21	0.29	0.26	0.00	0.08	0.00	0.00	0.00
Cr_2O_3	9.59	8.27	7.50	7.53	6.83	0.32	5.85	4.09	4.74	1.34
Total	92.67	92.29	91.80	91.98	92.44	89.81	91.89	91.73	89.82	90.45
Cations on the basis of 4 oxygens										
Si	0.01	0.01	0.02	0.01	0.01	0.02	0.01	0.03	0.01	0.01
Ti	0.01	0.01	0.01	0.01	0.01	0.00	0.00	0.00	0.00	0.00
Al	0.01	0.01	0.01	0.00	0.00	0.00	0.01	0.01	0.00	0.00
Fe^{2+}	1.27	1.24	1.22	1.22	1.20	1.04	1.17	1.16	1.14	1.06
Fe^{3+}	1.36	1.44	1.48	1.48	1.53	1.91	1.60	1.64	1.67	1.86
Mn	0.02	0.01	0.01	0.01	0.01	0.01	0.01	0.01	0.01	0.00
Mg	0.02	0.02	0.03	0.03	0.03	0.02	0.01	0.02	0.03	0.03
V	0.01	0.01	0.01	0.01	0.01	0.00	0.00	0.00	0.00	0.00
Cr	0.37	0.32	0.30	0.30	0.27	0.01	0.23	0.16	0.19	0.06
Total	3.10	3.09	3.08	3.08	3.08	3.02	3.07	3.06	3.06	3.03
Mg#	0.91	0.73	1.04	0.99	0.94	0.74	0.54	0.71	1.12	1.09
Cr#	96.59	96.07	98.16	98.53	100.00	100.00	96.74	93.56	100.00	100.00
Fe^{2+}#	0.98	0.98	0.98	0.98	0.98	0.98	0.99	0.98	0.97	0.97
Fe^{3+}#	0.78	0.81	0.83	0.83	0.85	0.99	0.87	0.90	0.90	0.97

Although the composition of the group 1 spinel population is not entirely consistent with any of the established fields of Barnes and Roeder (2001), they plot almost completely within the komatiites field on the Fe^{2+} number versus Fe^{3+} number diagram (Fig. 7.7a) and show significant overlap with this field on the Fe^{2+} number versus Cr number, Fe^{3+} number versus TiO_2 and Cr-Al-Fe^{3+} plots (Fig. 7.7b-d). The group 1 population also overlaps with the greenschist to amphibolite-facies magnetite rims field on the Fe^{2+} number versus Cr number plot, but is compositionally distinct from this field on all other plots (Fig. 7.7a-d). This population is compositionally distinct from the layered intrusion field on the Cr-Al-Fe^{3+} plot (Fig. 7.7d), but shows partial to complete overlap on all other plots (Fig. 7.7a-c), and shows some overlap with the ophiolites field on the Fe^{2+} number versus TiO_2 and Cr-Al-Fe^{3+} plots (Fig. 7.7c-d) despite being compositionally distinct from this field on the Fe^{2+} number versus

Fe^{3+} number and Fe^{2+} number versus Cr number plots (Fig. 7.7a-b). The group 2 spinel population (Fig. 7.7e-g) shows partial to complete overlap with the greenschist to amphibolite-facies magnetite rims field on all plots, indicating that they were derived from secondary processes (see Chapter 9).

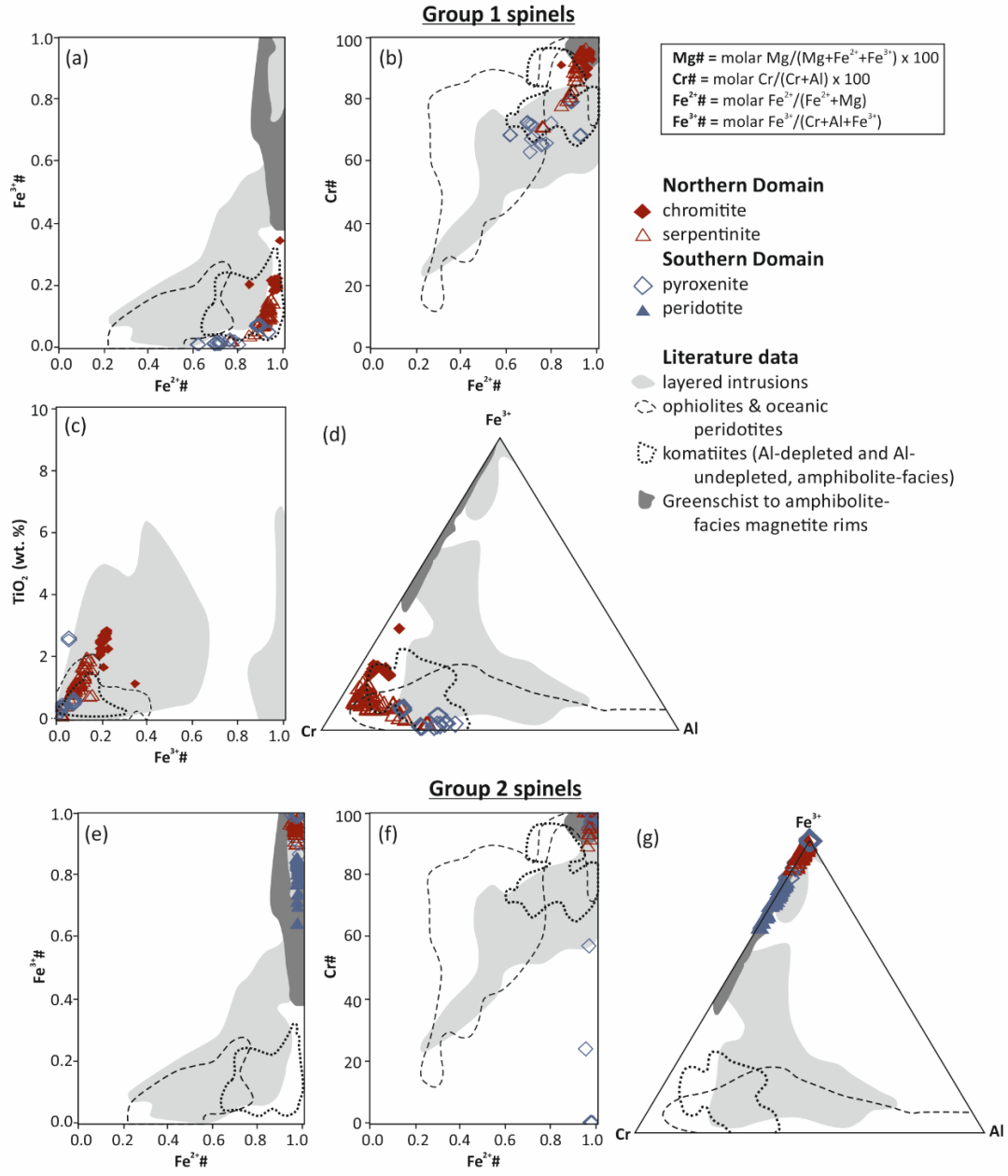

Figure 7.7: *Group 1 and 2 spinel compositions for the northern and southern domains of the Modderfontein Complex. Fields after: Barnes and Roeder (2001). Representative analyses can be found in Table 7.2 and the full dataset is available in Appendix F.*

On the Cr_2O_3 versus Al_2O_3 and Cr_2O_3 versus TiO_2 plots (Fig. 7.8a-b), the composition of group 1 (primary) spinels (from both domains of the Modderfontein Complex) is distinct from those for podiform chromitite, but shows some overlap with the field for stratiform chromitite. On the Al_2O_3 versus TiO_2 plot (Fig.7.8c), the northern domain group 1 spinels generally fall

outside of any established field, with a few analyses plotting within the arc field. In contrast, the southern domain group 1 spinels generally fall within the arc field, but also overlap with the suprasubduction zone peridotite and deep mantle chromitite fields (Fig. 7.8c).

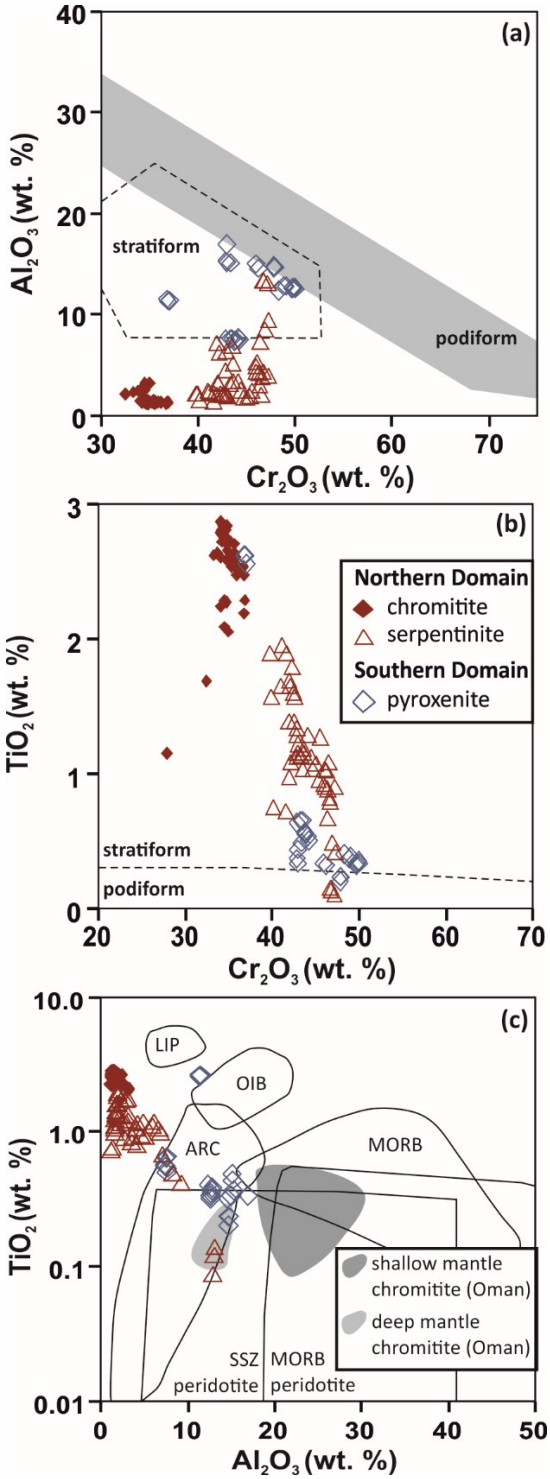

Figure 7.8: *Composition of the Group 1 spinel population (as outlined in text) on various discrimination diagrams.* ***(a)*** *Cr_2O_3 versus Al_2O_3 plot, with fields after Arai et al. (2004).* ***(b)*** *Al_2O_3 versus TiO_2 plots, with fields after Kamenetsky et al. (2001) and Rollinson (2008).* ***(c)*** *Cr_2O_3 versus TiO_2 plot, with fields Arai et al. (2004). Abbreviations: LIP=large igneous province; OIB=ocean island basalt; MORB=mid-ocean ridge basalt; SSZ=suprasubduction zone.*

7.2 The Zandspruit Complex

The logging and associated sampling presented here focuses on the layered ultramafic rocks located in the SE of the Zandspruit Complex (Fig. 7.9). Although housing developments have encroached on N parts of the Complex in recent decades, obscuring some of the field relationships described by Anhaeusser (1992), the layered ultramafic rocks remain untouched and are well-exposed relative to the surrounding ultramafic-mafic rocks.

7.2.1 Logging and field relationships

In accordance with Anhaeusser (2015), the logged section – located in the centre of the exposed layered ultramafic rocks (Fig. 7.9a,b) – is broadly subdivided into metapyroxenite and metaperidotite units (Fig. 7.9c). The metapyroxenite is volumetrically dominant, collectively comprising ~12.5 m of the logged section (stratigraphically), while the metaperidotite is volumetrically subordinate, collectively comprising ~5.5 m (Fig. 7.9c). The contacts between the two units are not exposed, but can generally be constrained to less than 0.3 m. Individual metapyroxenite units range from 0.6 to 8.7 m thick, while individual metaperidotite units are 0.4 to 2.6 m thick (Fig. 7.9c).

The metaperidotites, which are relatively well-exposed and form densely vegetated steeper ground (Fig. 7.10a), are internally layered on the centimetre-scale and display reddish-brown weathered surfaces, with millimetre-scale pyroxene pseudomorphs protruding from the weathered surface (Fig. 7.10b-d). The majority of metaperidotites are strongly magnetic, with rarer, irregularly-shaped pods of non-magnetic metaperidotite also present. These pods are discontinuous along strike and display occasionally sharp, but often cryptic, contacts within the volumetrically dominant magnetic metaperidotite (Fig. 7.10b). There is minimal systematic lithological variation between the two metaperidotite subunits, but rare, millimetre-scale patches of magnetite are prominent on the weathered surfaces of some magnetic metaperidotites (Fig. 7.10e).

The poorly-exposed metapyroxenites, which occur in conjunction with sparsely vegetated flat ground, are massive on the outcrop-scale and display variable amphibolitisation, with millimetre-scale tremolite often prominent on the grey-brown weathered surfaces (Fig. 7.10f). Rare outcrops are blocky and devoid of layering, with individual metapyroxenite units showing thickness variation along strike (Fig. 7.9b).

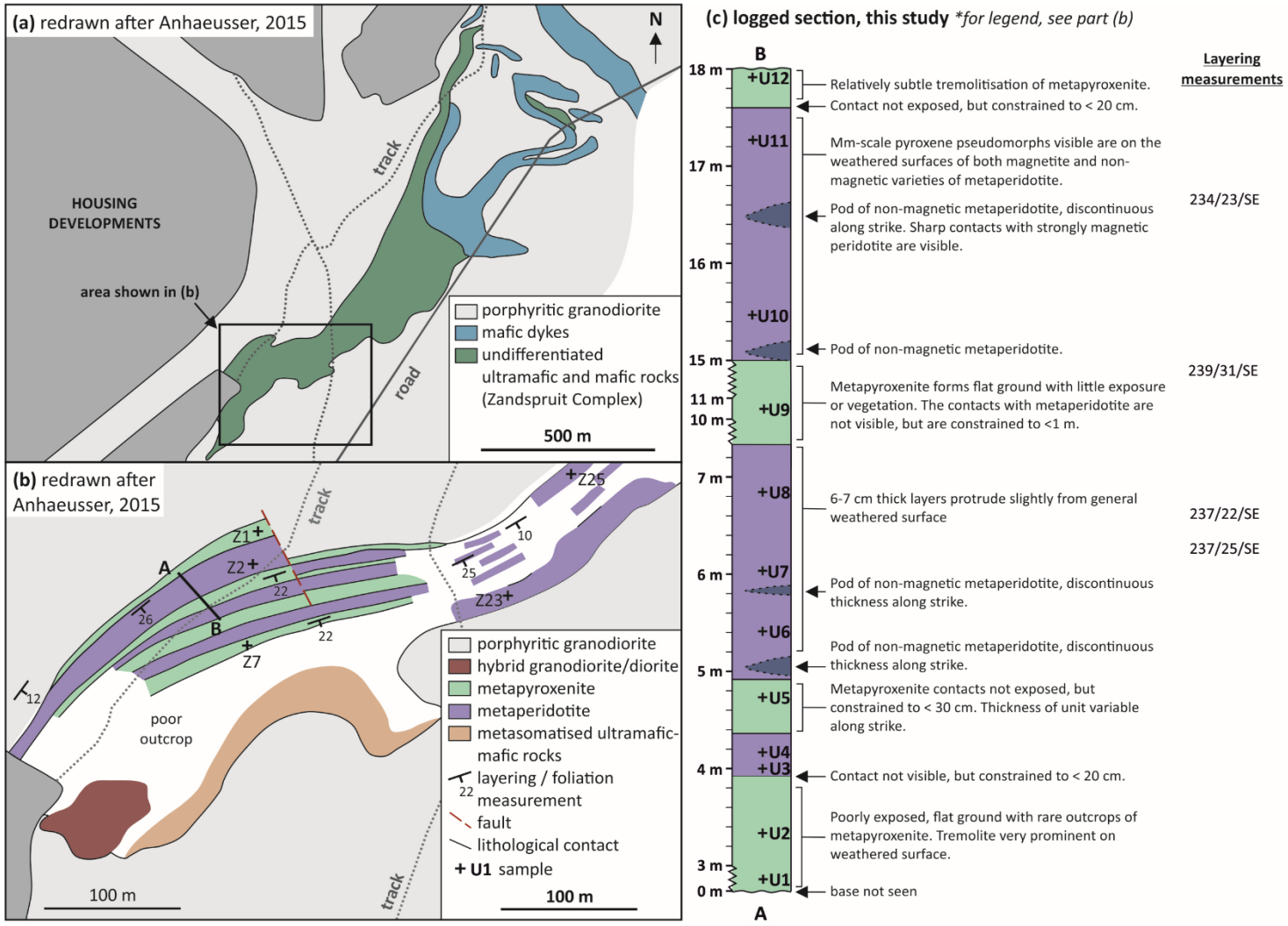

Figure 7.9 (a) *map of the Zandspruit Complex.* ***(b)*** *Small-scale map of the layered ultramafic rocks outlined in (a).* ***(c)*** *Log conducted for this study.*

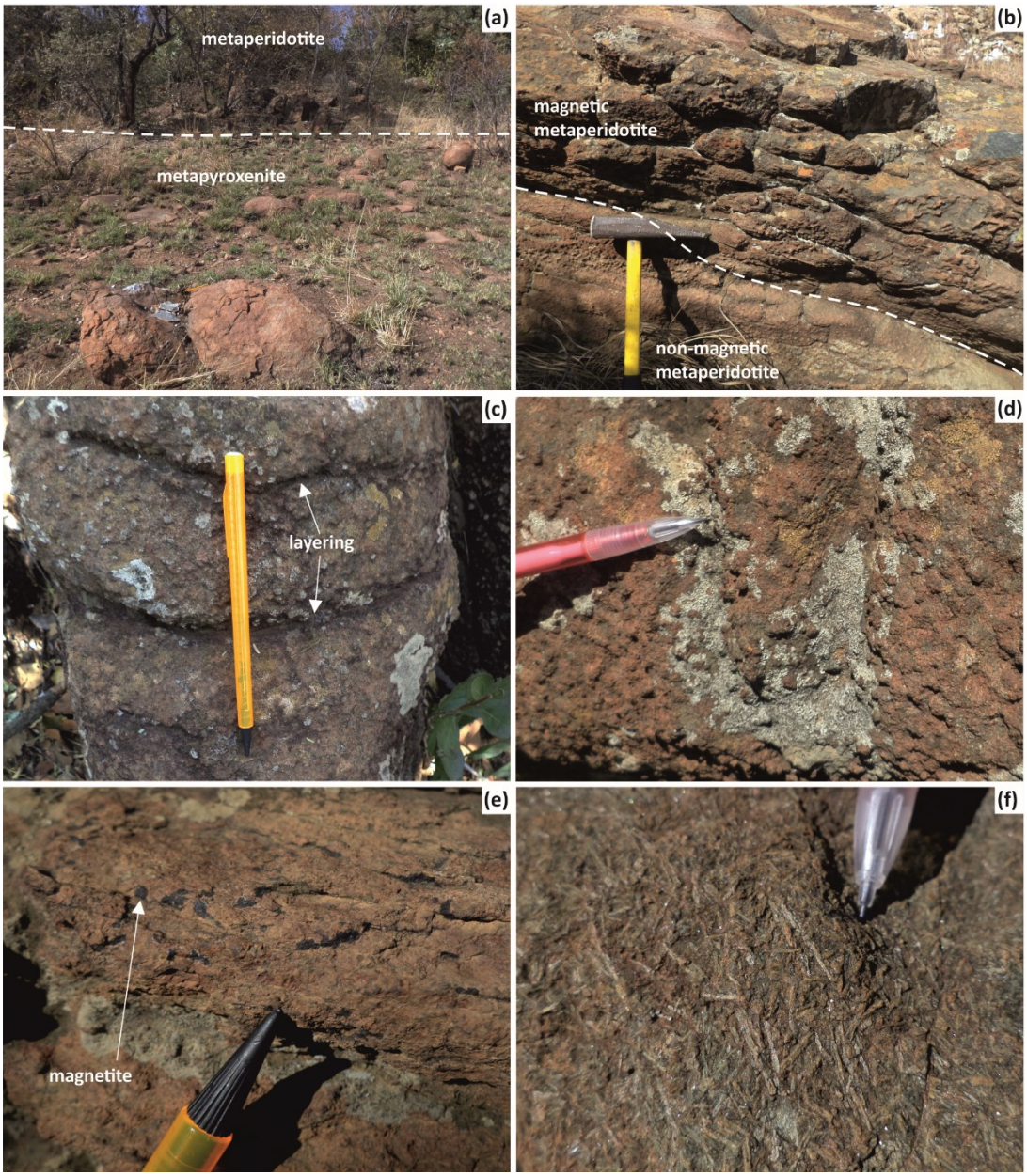

Figure 7.10: *Field photographs detailing representative rock types and field relationships in the Zandspruit Complex.* ***(a)*** *Contact between the metapyroxenite and metaperidotite units.* ***(b)*** *Contact between the strongly magnetic and non-magnetic metaperidotite varieties.* ***(c)*** *Centimetre-scale internal layering within the metaperidotite.* ***(d)*** *Millimetre-scale pyroxene pseudomorphs protruding from the brown metaperidotite weathered surface.* ***(e)*** *Millimetre-scale oxide minerals within the metaperidotite.* ***(f)*** *Elongate tremolite grains characteristic of the metapyroxenite unit.*

7.2.2 Petrography

In total, 7 metaperidotite and 5 petapyroxenite samples (from the logged section outlined in Figure 7.5c) were subject to petrographic assessment.

Metaperidotites (n=7) from the Zandspruit Complex comprise (in modal %): < 2 % orthopyroxene, 44 to 65 % serpentine, chlorite and talc, 34 to 55 % amphibole (tremolite and cummingtonite), and < 0.5 % Cr-spinel. Tremolite is up to 8 mm in diameter, generally forms

subhedral to anhedral, rounded grains, and is partially replaced by fine-grained (< 0.2 mm diameter) cummingtonite (Fig. 7.11a-b). Cummingtonite is localised and sometimes preferentially concentrated along µm-scale, visibly altered fractures. Fine-grained (< 0.4 mm diameter), intergrown serpentine, chlorite and talc form the remainder of the metaperidotites, with individual grains subhedral to anhedral (Fig. 7.11a-b). In most cases, chlorite and talc (collectively) are volumetrically dominant over serpentine.

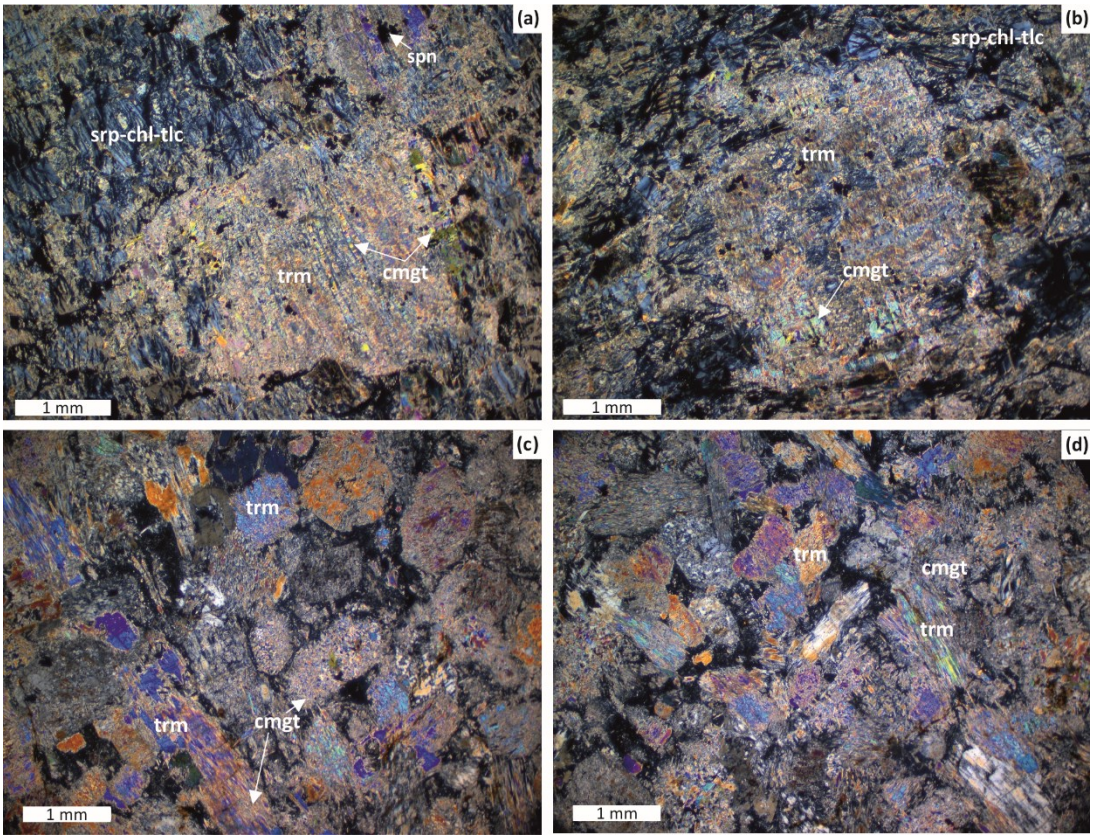

Figure 7.11: *photomicrographs (in XPL) detailing the petrographic characteristics of the metapyroxenites and metaperidotites from the Zandspruit Complex.* ***(a-b)*** *metaperidotite.* ***(c-d)*** *metapyroxenite. Abbreviations: cmgt=cummingtonite; srp-chl-tlc=serpentine, chlorite and talc; spn=spinel; trm=tremolite.*

Metapyroxenites (n=5) from the Zandspruit Complex comprise (in modal %): < 0.2 % orthopyroxene, 80 to 100 % amphibole (tremolite and cummingtonite) and < 20 % intergrown serpentine, chlorite and talc, alongside accessory Cr-spinel. Tremolite forms both elongate and rounded grains, with the former < 10 mm long and the latter generally 0.8 to 1.9 mm in diameter (Fig. 7.11c-d). Both varieties are subhedral to anhedral and show partial replacement by fine-grained (< 0.2 mm) diameter cummingtonite. The majority of metapyroxenites (n=4) comprise nearly 100 % amphibolite (tremolite and cummingtonite), although 20 % of 1 sample – located at the top of the logged section (Fig. 7.11c) – comprises serpentine, chlorite and talc. As with the metaperidotites, the intergrown serpentine,

chlorite and talc form subhedral to anhedral grains that do not exceed 0.4 mm in diameter, with chlorite and talc volumetrically dominant over serpentine.

Presuming that the serpentine, chlorite and talc were derived from metamorphism and alteration of olivine (± orthopyroxene), and that tremolite and cummingtonite were derived from metamorphism and alteration of pyroxene, the Zandspruit ultramafic rocks likely reflect variation in the modal abundances of olivine and pyroxene. Consequently, the protoliths of the metaperidotites were likely lherzolites, and the protoliths to the metapyroxenites were likely olivine-websterites.

7.2.3 Spinel Mineral Chemistry

In the Zandspruit rocks, spinel occurs as < 0.2 mm diameter, euhedral to subhedral grains that occasionally exhibit slightly altered, < 20 μm thick rims. Additional to magnetite derived from serpentinisation, spinel is common in metaperidotite, but rare in metapyroxenite. In total, 162 analyses were conducted on spinel grains, with 147 analyses conducted on spinel in metaperidotite samples and 15 analyses conducted on spinel in metapyroxenite samples. Quantitative major element analysis and imaging were conducted using the instrumentation and methodology described in Appendix A, representative analyses can be found in Table 7.3 and the full dataset is included in Appendix F. Spinel compositions are here subdivided into 2 groups based on Fe^{3+} numbers (calculated as molar $Fe^{3+}/[Cr+Al+Fe^{3+}]$). Group 1 spinels (n=156) have low Fe^{3+} numbers (< 0.25), while group 2 spinels (n=6) have higher Fe^{3+} numbers (> 0.25; Table 7.3). Group 1 spinels, which are exclusively conducted on spinel cores, have high abundances of MgO, Al_2O_3 and Cr_2O_3, and low abundances of FeO relative to Group 2 spinels (Table 7.3), which are exclusively conducted on spinel rims.

The group 1 spinels show partial to complete overlap with the komatiites field (of Barnes and Roeder, 2001) on all plots (Fig. 7.12a-d), although a significant number of analyses plot outside of this field on the Fe^{2+} number versus Fe^{3+} number and Fe^{3+} number versus TiO_2 plots. This population also shows significant overlap with the layered intrusion field on the Fe^{2+} number versus Cr number plot, and partial overlap with this field on the Fe^{3+} number versus TiO_2 and Cr-Fe^{3+}-Al plots (Fig. 7.12a-d). The group 1 spinels show some overlap with the ophiolites field on the Fe^{2+} number versus Cr number, Fe^{3+} number versus TiO_2 and Cr-Fe^{3+}-Al plots, but are distinct from this field on the Fe^{2+} number versus Fe^{3+} number plot (Fig. 7.12a-d). Finally, the group 1 spinels are compositionally distinct from the greenschist- to amphibolite-facies magnetite rims field on all plots (Fig. 7.12a-d). The group 2 spinels, which generally plot outside of any established field, show complete overlap with the greenschist-

to amphibolite-facies magnetite rims field on the Fe^{2+} number versus Cr number plot, and plot just outside of this field on the Fe^{2+} number versus Fe^{3+} number and Cr-Fe^{3+}Al plots (Fig. 7.12e-g).

Table 7.3: *Representative analyses of the group 1 and 2 spinel from the Zandspruit Complex. Analyses are from 7 thin sections (6 metaperidotite and 1 metapyroxenite). Abbreviations: Per=peridotite; Px=pyroxenite.*

	Group 1							
Sample	JB16-U3	JB16-U4	JB16-U5	JB16-U6	JB16-U6	JB16-U7	JB16-U8	JB16-U8
Lithology	Per	Per	Px	Per	Per	Per	Per	Per
MgO	1.48	1.79	1.16	1.28	1.92	1.53	4.15	4.84
Al_2O_3	9.18	10.64	7.78	10.90	9.66	9.56	11.75	11.73
SiO_2	0.30	0.26	0.30	0.30	0.21	0.24	0.32	0.28
TiO_2	1.08	0.17	0.90	0.28	0.18	0.65	0.15	0.13
V_2O_3	0.44	0.46	0.39	0.36	0.26	0.46	0.29	0.28
Cr_2O_3	46.74	47.85	47.87	43.17	49.96	47.50	50.80	51.27
MnO	1.51	1.45	1.59	1.60	1.48	1.54	1.28	1.19
FeO	36.42	35.52	36.99	38.07	34.30	35.30	29.29	28.33
Fe_2O_3	0.19	0.15	0.19	0.15	0.23	0.18	0.22	0.27
Total	97.34	98.28	97.17	96.12	98.20	96.94	98.25	98.32
Cations on the basis of 4 oxygens								
Mg	0.08	0.10	0.06	0.07	0.10	0.08	0.22	0.25
Al	0.40	0.45	0.34	0.48	0.41	0.42	0.49	0.48
Si	0.01	0.01	0.01	0.01	0.01	0.01	0.01	0.01
Ti	0.03	0.00	0.03	0.01	0.01	0.02	0.00	0.00
V	0.01	0.01	0.01	0.01	0.01	0.01	0.01	0.01
Cr	1.36	1.37	1.41	1.27	1.43	1.38	1.41	1.41
Mn	0.05	0.04	0.05	0.05	0.05	0.05	0.04	0.04
Fe^{2+}	1.04	1.00	1.07	1.08	0.98	1.02	0.83	0.80
Fe^{3+}	0.05	0.05	0.06	0.08	0.04	0.05	0.02	0.02
Total	3.05	3.04	3.05	3.06	3.04	3.04	3.02	3.03
Mg#	6.89	8.42	5.43	5.82	9.26	7.30	20.33	23.56
Cr#	77.35	75.11	80.49	72.65	77.63	76.92	74.36	74.56
Fe^{2+}#	0.93	0.91	0.94	0.94	0.90	0.92	0.79	0.76
Fe^{3+}#	0.03	0.03	0.03	0.04	0.02	0.03	0.01	0.01

Table 7.3 (cont.):

	Group 1		Group 2					
Sample	JB16-U10	JB16-U10	JB16-U7	JB16-U7	JB16-U7	JB16-U7	JB16-U7	JB16-U7
Lithology	Per	Per	Per	Per	Per	Per	Per	Per
MgO	2.22	1.38	0.58	0.53	0.58	0.60	0.63	0.58
Al_2O_3	11.49	8.46	0.45	0.64	1.17	0.66	0.83	0.72
SiO_2	0.34	0.28	0.28	0.28	0.28	0.24	0.32	0.30
TiO_2	0.12	0.85	0.52	0.50	0.68	0.53	0.50	0.50
V_2O_3	0.34	0.47	0.31	0.28	0.47	0.18	0.31	0.24
Cr_2O_3	49.97	48.90	30.02	31.12	30.82	32.36	32.56	33.66
MnO	1.15	1.39	1.45	1.42	1.39	1.54	1.61	1.61
FeO	32.46	35.65	60.90	59.47	59.69	57.71	57.08	56.61
Fe_2O_3	0.25	0.18	0.34	0.27	0.24	0.24	0.29	0.22
Total	98.34	97.57	94.85	94.51	95.34	94.06	94.14	94.44
Cations on the basis of 4 oxygens								
Mg	0.12	0.08	0.04	0.03	0.04	0.04	0.04	0.04
Al	0.48	0.37	0.02	0.03	0.06	0.03	0.04	0.04
Si	0.01	0.01	0.01	0.01	0.01	0.01	0.01	0.01
Ti	0.00	0.02	0.02	0.02	0.02	0.02	0.02	0.02
V	0.01	0.01	0.01	0.01	0.02	0.01	0.01	0.01
Cr	1.41	1.42	1.04	1.07	1.05	1.12	1.12	1.15
Mn	0.03	0.04	0.05	0.05	0.05	0.06	0.06	0.06
Fe^{2+}	0.93	1.03	1.38	1.38	1.38	1.37	1.37	1.37
Fe^{3+}	0.02	0.05	0.56	0.53	0.51	0.49	0.47	0.45
Total	3.02	3.04	3.15	3.15	3.15	3.15	3.15	3.15
Mg#	10.99	6.57	1.91	1.78	1.93	2.04	2.17	2.01
Cr#	74.48	79.49	97.80	97.01	94.64	97.04	96.33	96.92
Fe^{2+}#	0.89	0.93	0.97	0.98	0.97	0.97	0.97	0.97
Fe^{3+}#	0.01	0.02	0.35	0.32	0.31	0.30	0.29	0.28

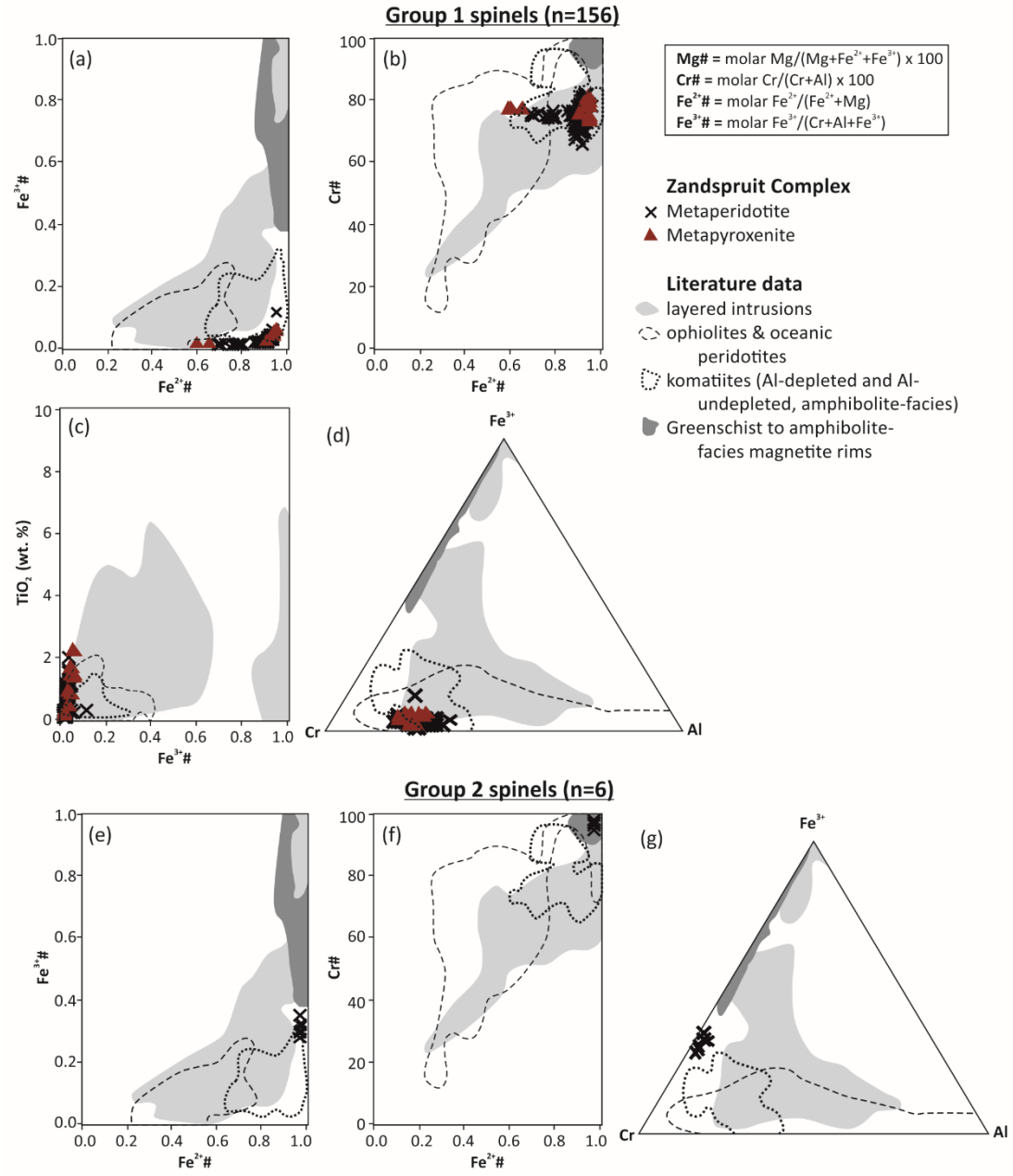

Figure 7.12: *Group 1 and group 2 spinels compositions for the Zandspruit Complex. Fields after: Barnes and Roeder (2001).*

7.3 The Roodekrans Complex

Since the original mapping (conducted by Anhaeusser 1977), exposures of the Roodekrans Complex have been vastly reduced. As shown in Figures 7.13a and 7.14, the majority of the Complex is covered by urban developments at the time of writing, with small exposures remaining in the centre and NW of the originally mapped area (Anhaeusser, 1977). The logging and associated sampling presented here focuses on the 300 m x 450 m area of layered mafic-ultramafic rocks located in the centre of the Roodekrans Complex (Fig. 7.13a-b).

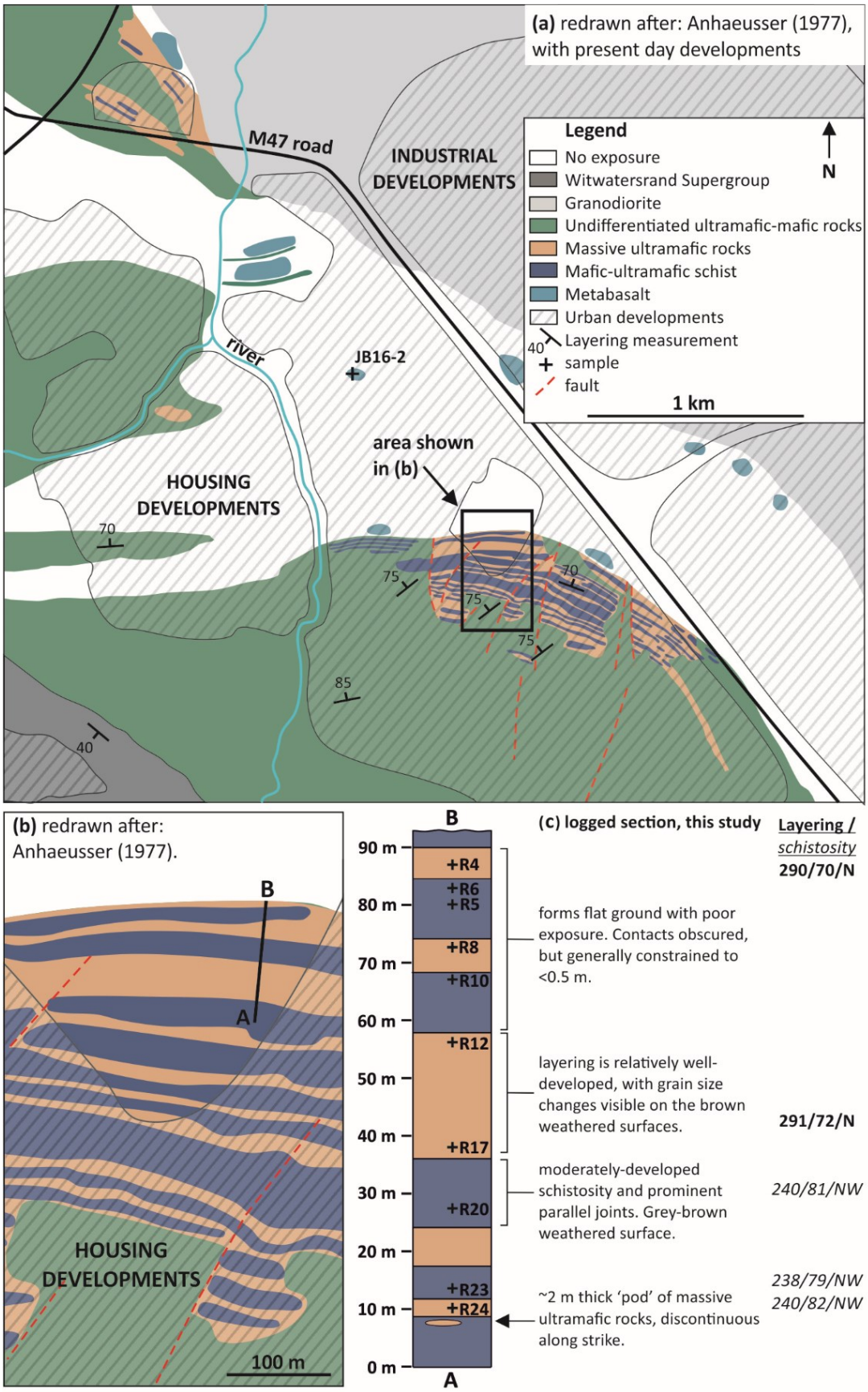

Figure 7.13: (a) *map of the Roodekrans Complex.* ***(b)*** *Small-scale map of the exposed area investigated in this study. Map area marked in (a).* ***(c)*** *Log conducted for this study. Log position labelled on (b).*

Figure 7.14: *Satellite image detailing the extent of urbanisation in the Roodekrans area of the Johannesburg Dome.*

7.3.1 Logging and field relationships

In accordance with Anhaeusser (1977, 2004), the logged section (Fig. 7.13a-b) is here subdivided into two units: massive ultramafic rocks; and mafic-ultramafic schists (Fig. 7.13c). Sharp contacts between the two units are rarely preserved, with the schistosity in the mafic-ultramafic schists terminating against the massive ultramafic rocks where visible. The massive ultramafic rocks form 5 individual packages that range from 3 to 22 m in (stratigraphic) thickness, while the mafic-ultramafic schists form 6 individual packages that range from 3.5 to 12 m in thickness (Fig. 7.13c). In total, the two units occur in roughly equal proportions, with the massive ultramafic rocks and mafic-ultramafic schists comprising 42.5 m and 49.5 of the logged section respectively (Fig. 7.13c). Individual packages of both units display thickness variation along strike, with the entire sequence dipping between 70 and 85° towards the N (Fig. 7.13). In some cases, small, metre-scale pods of massive ultramafic rocks (akin to those that form the "massive ultramafic unit") occur within the mafic-ultramafic schist unit, with these occurrences discontinuous along strike (Fig. 7.13c).

The massive ultramafic rocks, which exhibit distinctly brown weathered surfaces and dark-grey to light-green fresh surfaces, are relatively well-exposed and occasionally form more densely vegetated steeper ground (Fig. 7.15a). The best exposed packages of massive ultramafic rocks (e.g., 35 to 57 m; Fig. 7.13c) preserve centimetre- to decimetre-scale layering defined by distinctive changes in the apparent grain size (Fig. 7.15b). The coarser portions of such packages display a distinctly "nobbled" texture (Fig. 7.15c), with individual "nobbles" likely representing the pseudomorphs of a primary mineral.

The mafic-ultramafic schists, which have grey-brown weathered surfaces, generally form the poorly-exposed low-ground associated with limited vegetation (Fig. 7.15a). This unit displays a characteristic and pervasive steeply dipping schistosity (75 to 82° towards the NW), with joints also forming in the same orientation (Fig. 7.15d). Where pods of massive ultramafic rock occur within the mafic-ultramafic schists, the schistosity is consistently parallel to the contacts between the two rock types.

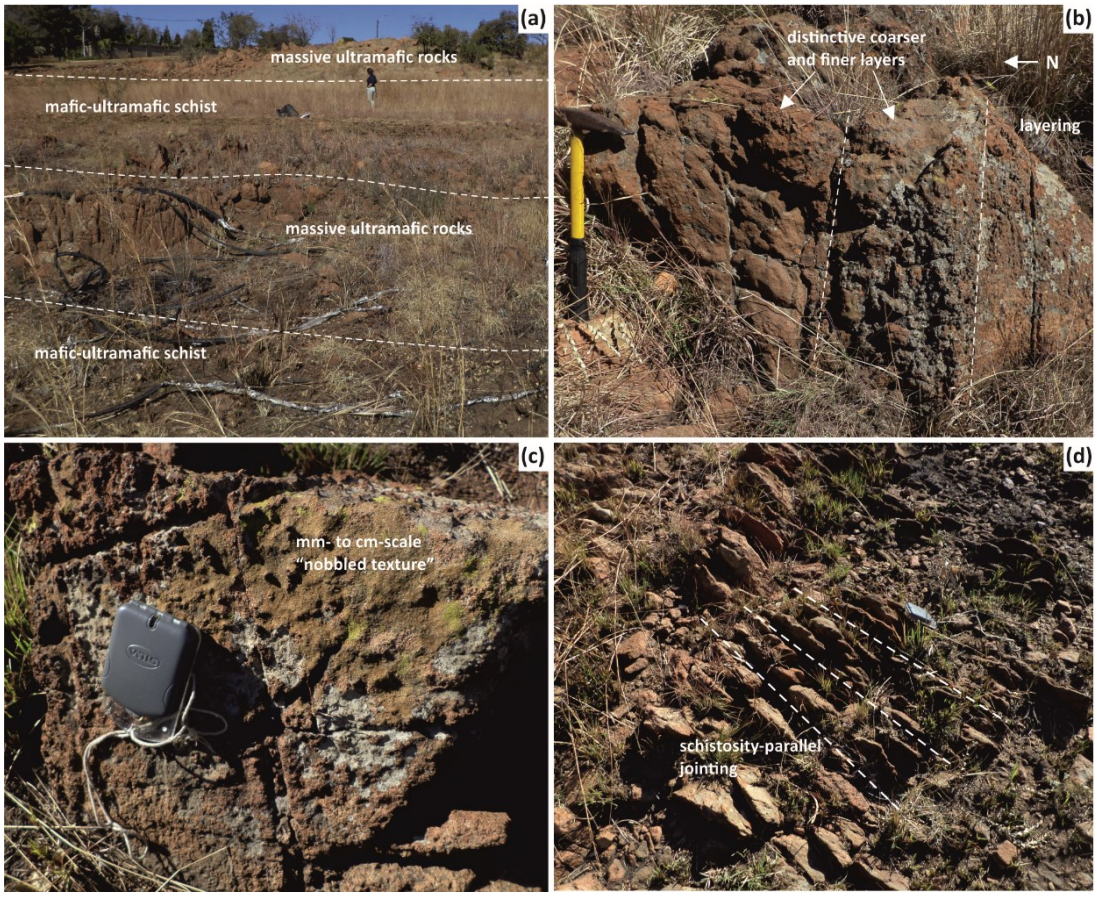

Figure 7.15: *Field photographs detailing the representative rock types in the studied portion of the Roodekrans Complex.* ***(a)*** *Overview of the studied area.* ***(b)*** *Decimetre-scale layering in the massive ultramafic rock unit.* ***(c)*** *Distinctly "nobbled" texture displayed by the massive ultramafic rocks.* ***(d)*** *Schistosity-parallel jointing in the mafic-ultramafic schists.*

7.3.2 Petrography

In total, 3 massive ultramafic samples and 3 mafic-ultramafic schist samples (from the logged section outlined in Figure 7.8c) were subject to petrographic analysis. The massive ultramafic rocks (Fig. 7.16a-c), which classify as amphibolite, metaperidotite and metapyroxenite respectively, display significant variation in modal mineral abundances, comprising (in modal %) < 5 % clinopyroxene, < 80 % amphibole (tremolite and cummingtonite); < 20 % chlorite and talc, and < 2 % spinel. Serpentine commonly occurs as fine-grained (< 0.2 mm diameter) amalgamations that may represent olivine (± orthopyroxene) pseudomorphs (Fig. 7.16a). Clinopyroxene occurs as highly amphibolitised, anhedral relics < 6 mm in diameter, while amphibole occurs as subhedral to anhedral grains < 0.5 mm in diameter (Fig. 7.16b-c). Chlorite and talc occur as < 0.1 mm diameter grains that are largely associated with serpentine. Spinel occurs as rounded grains that are < 0.4 mm in diameter and predominantly associated with serpentine (Fig. 7.16a).

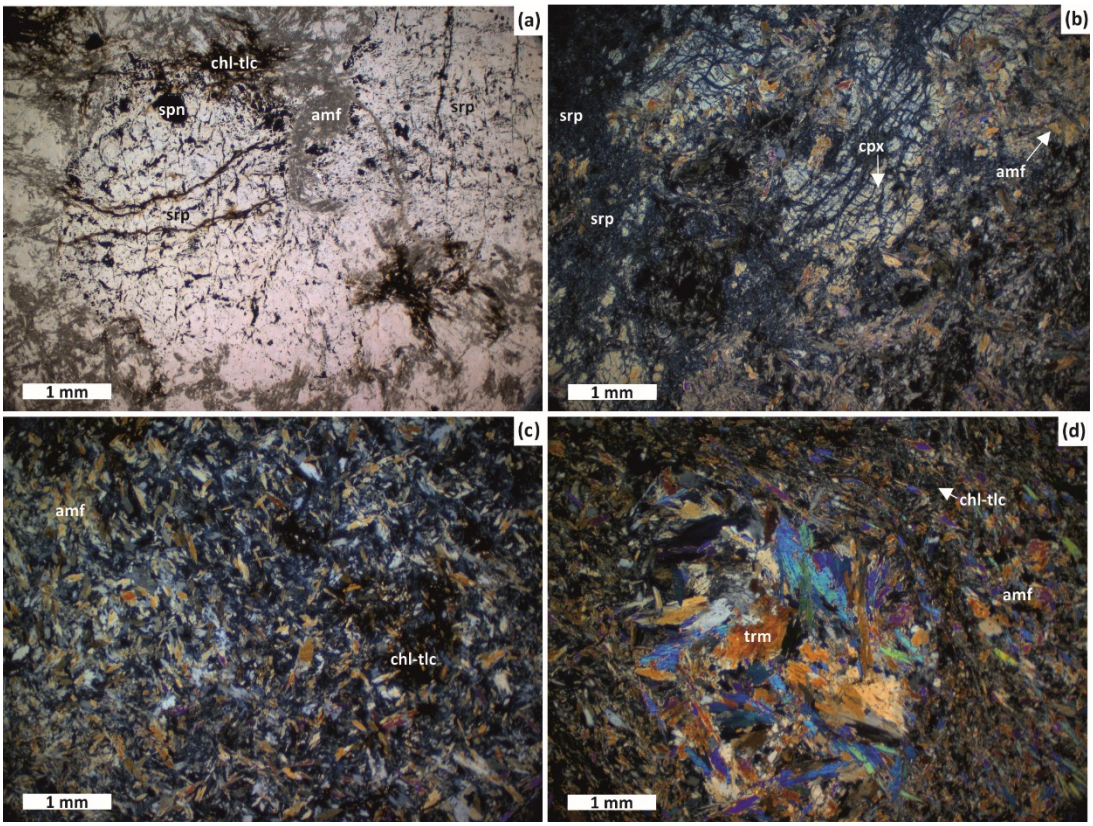

Figure 7.16: *Photomicrographs detailing the representative rocks types of the Roodekrans Complex. All photomicrographs are taken using XPL, with the exception of (a), which is taken using PPL.* ***(a)*** *metaperidodtite (sample JB16-R17) comprising large, rounded areas of serpentine surrounded by amphibole and chlorite-talc.* ***(b)*** *Metapyroxenite (sample JB16-R24) comprising relic clinopyroxene (amphibolitised) surrounded by serpentine and amphibole.* ***(c)*** *Amphibolite (same JB16-R12) comprising µm-scale amphibole and minor chlorite-talc.* ***(d)*** *Amphibolite (sample JB16-R5) comprising tremolite cluster surrounded by finer-grained amphibole and minor chlorite-talc. Abbreviations: amf=amphibole; chl=chlorite; cpx=clinopyroxene; srp=serpentine; spn=spinel; tlc=talc; trm=tremolite.*

The mafic-ultramafic schists (Fig. 7.16d), which all classify as amphibolite, comprise (in modal %) 66 to 92 % amphibole (tremolite and cummingtonite) and < 35 talc and chlorite, with accessory spinel. Amphibole ranges from 1.5 mm diameter, elongate and subhedral tremolite, to 0.1 mm diameter, anhedral cummingtonite. Tremolite, which occasionally forms clusters < 7 mm in diameter (Fig. 7.16d), is also pervasive as finer-grains (< 0.2 mm diameter). Fine-grained (< 0.2 mm diameter) chlorite and talc co-exist as anhedral grains that commonly occur in conjunction with subtle veins.

7.3.3 Spinel Mineral Chemistry

In the Roodekrans rocks, spinel occurs as < 0.3 mm diameter, subhedral to anhedral grains that exhibit variable alteration (Fig. 7.17a-b). Such alteration ranges from little-altered rims (Fig. 7.17a-b) to near-complete alteration of individual grains (Fig. 7.17c-d). Generally, spinels in the mafic-ultramafic schists are visibly more altered than those in the massive ultramafic rocks (Fig. 7.17).

In total, 188 analyses were conducted on spinel grains from both lithologies within the Roodekrans Complex. Quantitative major element analysis and imaging were conducted using the instrumentation and methodology described in Appendix A, representative analyses can be found in Table 7.4, and the full dataset is included in Appendix F. Spinel compositions are here subdivided into 2 groups based on Fe^{3+} numbers (calculated as molar $Fe^{3+}/[Cr+Al+Fe^{3+}]$). Group 1 spinels (n=63) have low Fe^{3+} numbers (< 0.25), while group 2 spinels (n=125) exhibit higher Fe^{3+} numbers (> 0.25; Table 7.4). Group 1 spinels have relatively high abundances of MgO, Al_2O_3 and Cr_2O_3, and relatively low abundances of FeO and Fe_2O_3 (Table 7.5). Group 2 compositions reflect analyses both both spinel cores and altered rims, whereas group 1 spinels were only found from analyses of spinel cores (Fig. 7.17).

The group 1 spinel grains show consistent overlap with the komatiites field (of Barnes and Roeder, 2001) on all plots, although a small cluster of analyses plot outside of this field on the Fe^{2+} number versus Cr number and Cr-Fe^{3+}-Al plots (Fig. 7.18a-d). On the Fe^{2+} number versus Cr number plot (Fig. 7.18b), this small cluster shows overlap with the greenschist to amphibolite-facies magnetite rims, but do not overlap with any field on the Cr-Fe^{3+}-Al ternary plot (Fig. 7.18b,d). The larger cluster of group 1 spinel grains also shows some overlap with the layered intrusion field on the Fe^{2+} number versus Cr number plot (Fig. 7.18b), and with the ophiolite and oceanic peridotite field on the Cr-Fe^{3+}-Al ternary plot (Fig. 7.18d). In contrast, the group 2 spinels (Fig. 7.18e-g) show partial to complete overlap with the

greenschist- to amphibolite-facies rims field on all plots, indicating that they were derived from secondary processes (Chapter 9).

The wealth of mineral chemical data presented for the Modderfontein, Zandspruit and Roodekrans Complexes is summarised in Table 7.5.

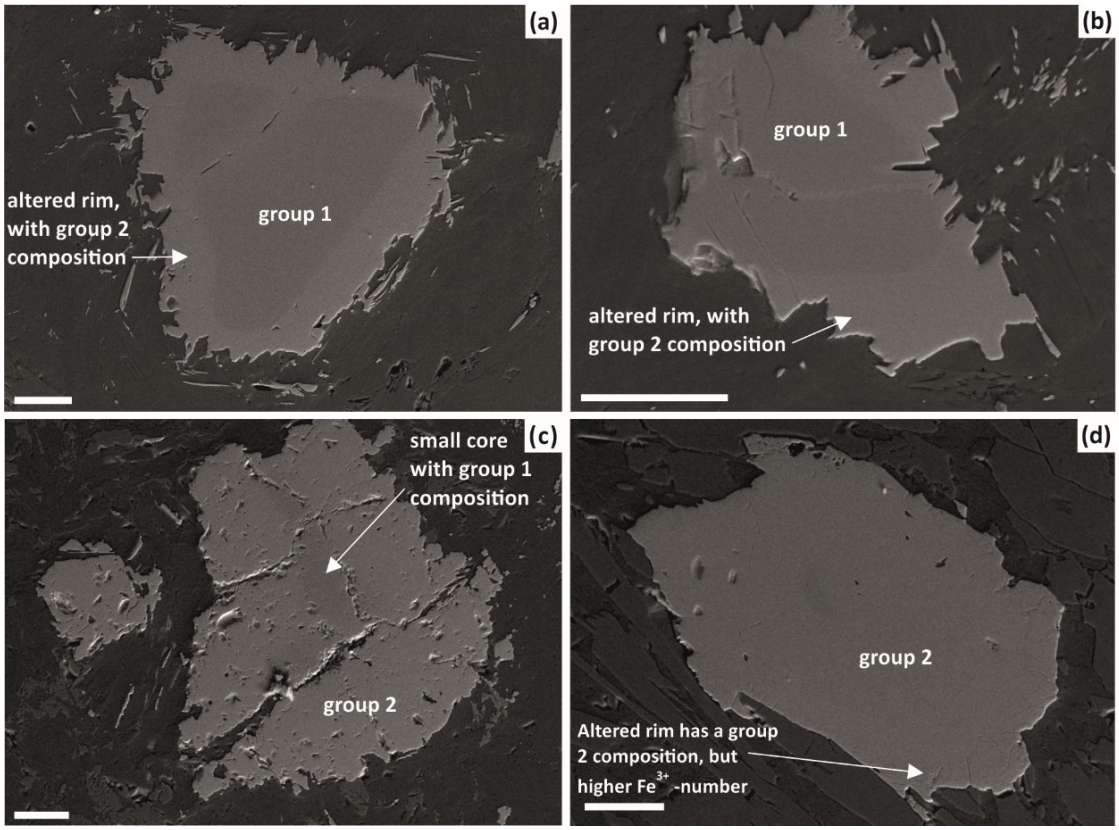

Figure 7.17: *SE images detailing the morphology of spinel grains from the Roodekrans Complex.* ***(a)*** *~160 µm diameter group 1 spinel, with altered rim of group 2 composition (JB16-R24).* ***(b)*** *~100 µm diameter group 1, with altered rim of group 2 composition (JB16-R24).* ***(c)*** *~190 µm diameter group 2 spinel, with small relic of group 1 spinel at its core (JB16-R17).* ***(d)*** *~150 µm diameter group 2 spinel (JB16-R5). White scale bar=50 µm.*

Table 7.4: *Representative analyses of group 1 and 2 spinel from the Roodekrans Complex. Analyses are from 4 thin sections (2 massive ultramafic rock and 2 mafic-ultramafic schist). The full dataset is included In Appendix F. Abbreviations: sch=mafic-ultramafic schist; um=massive ultramafic rock).*

					group 1			
Sample	JB16-R6	JB16-R6	JB16-R17	JB16-R17	JB16-R17	JB16-R24	JB16-R24	JB16-R24
Lithology	sch	sch	um	um	um	um	um	um
MgO	1.56	1.56	3.71	4.01	3.07	3.66	1.48	3.25
Al_2O_3	10.86	10.66	11.43	11.02	10.64	10.98	10.86	11.22
SiO_2	0.32	0.36	0.28	0.24	0.32	0.3	0.32	0.3
TiO_2	0.12	0.12	0.1	0.1	0.13	0.12	0.08	0.13
V_2O_3	0.15	0.2	0.2	0.13	n.d	0.2	0.13	n.d
Cr_2O_3	52	51.68	50.63	50.06	49.66	53.38	52.03	52.43
MnO	1.12	1.12	2.69	2.13	3.11	0.31	0.93	0.5
FeO	31.84	31.99	26.1	26.64	27.16	29.77	32.05	28.65
Fe_2O_3	0.14	0.15	0.13	0.13	1.48	0.09	0.1	0.52
Total	98.11	97.84	95.26	94.45	95.58	98.8	97.98	97
Cations on the basis of 4 oxygens								
Mg	0.08	0.08	0.2	0.22	0.17	0.19	0.08	0.17
Al	0.46	0.45	0.49	0.47	0.45	0.45	0.46	0.47
Si	0.01	0.01	0.01	0.01	0.01	0.01	0.01	0.01
Ti	0	0	n.d	n.d	n.d	n.d	n.d	n.d
V	0	0.01	0.01	n.d	n.d	0.01	n.d	n.d
Cr	1.47	1.47	1.44	1.44	1.43	1.48	1.47	1.47
Mn	0.03	0.03	0.08	0.07	0.1	0.01	0.03	0.02
Fe^{2+}	0.93	0.94	0.77	0.79	0.82	0.85	0.94	0.85
Fe^{3+}	0.01	0.01	0.01	0.02	0.04	0.01	0.01	0.01
Total	3.01	3.02	3.01	3.02	3.02	3.01	3.01	3.01
Mg#	8.07	8.04	20.34	21.33	16.28	18.09	7.63	16.66
Cr#	76.25	76.49	74.82	75.3	76.04	76.54	76.26	75.89
Fe^{2+}#	0.92	0.92	0.79	0.78	0.83	0.82	0.92	0.83
Fe^{3+}#	0.01	0.01	0.01	0.01	0.02	0.01	0.01	0.01

Table 7.4 (cont.)

					group 2			
Sample	JB16-R5	JB16-R5	JB16-R5	JB16-R6	JB16-R17	JB16-R17	JB16-R24	JB16-R24
Lithology	sch	sch	sch	sch	um	um	um	um
MgO	0.28	0.25	0.25	0.25	0.56	0.35	0.45	0.30
Al_2O_3	0.11	0.09	0.02	0.17	0.19	0.17	0.51	0.42
SiO_2	0.30	0.26	0.32	0.32	0.24	0.30	0.19	0.28
TiO_2	0.23	0.17	0.20	0.13	0.35	0.08	1.17	0.82
V_2O_3	0.50	0.46	n.d	0.55	n.d	n.d	n.d	n.d
Cr_2O_3	12.12	7.97	6.83	11.78	19.75	16.24	29.03	23.72
MnO	0.49	0.28	0.27	0.43	2.25	2.16	1.19	1.18
FeO	79.52	82.77	36.45	80.32	40.85	39.71	43.17	42.85
Fe_2O_3	0.33	0.29	51.43	0.32	30.84	35.65	19.74	25.61
Total	93.89	92.54	95.77	94.27	95.02	94.65	95.44	95.17
Cations on the basis of 4 oxygens								
Mg	0.02	0.02	0.02	0.02	0.04	0.03	0.03	0.02
Al	0.01	0.01	n.d	0.01	0.01	0.01	0.02	0.02
Si	0.01	0.01	0.02	0.02	0.01	0.01	0.01	0.01
Ti	0.01	0.01	0.01	0.00	0.01	0.00	0.04	0.03
V	0.02	0.02	n.d	0.02	n.d	n.d	n.d	n.d
Cr	0.46	0.31	0.27	0.44	0.74	0.62	1.02	0.86
Mn	0.02	0.01	0.01	0.02	0.09	0.09	0.04	0.05
Fe^{2+}	1.30	1.23	1.21	1.30	1.34	1.31	1.40	1.40
Fe^{3+}	1.25	1.46	1.53	1.27	0.91	1.06	0.58	0.75
Total	3.11	3.08	3.07	3.11	3.15	3.14	3.14	3.14
Mg#	0.78	0.68	0.68	0.68	1.73	1.05	1.48	0.94
Cr#	98.62	98.26	99.68	97.89	98.83	98.74	97.76	97.82
Fe^{2+}#	0.98	0.99	0.98	0.99	0.97	0.98	0.98	0.99
Fe^{3+}#	0.73	0.82	0.85	0.74	0.55	0.63	0.36	0.46

***Table 7.5**: Summary of the fields overlapped by the group 1 spinel data presented in Figures 7.7 (Modderfontein), 7.12 (Zandspruit) and 7.18 (Roodekrans). A=Fe^{2+} versus Fe^{3+} plot; B=Fe^{2+} versus Cr# plot; C=Fe^{3+} versus TiO_2 plot; D=Al-Cr-Fe^{3+} plot. Green square=complete overlap; Orange square=partial overlap; red square=no overlap; blank square=n/a.*

Field	Komatiite				Layered Int.				Ophiolite				Altered rims			
Plot	A	B	C	D	A	B	C	D	A	B	C	D	A	B	C	D
Modderfontein																
Zandspruit																
Roodekrans																

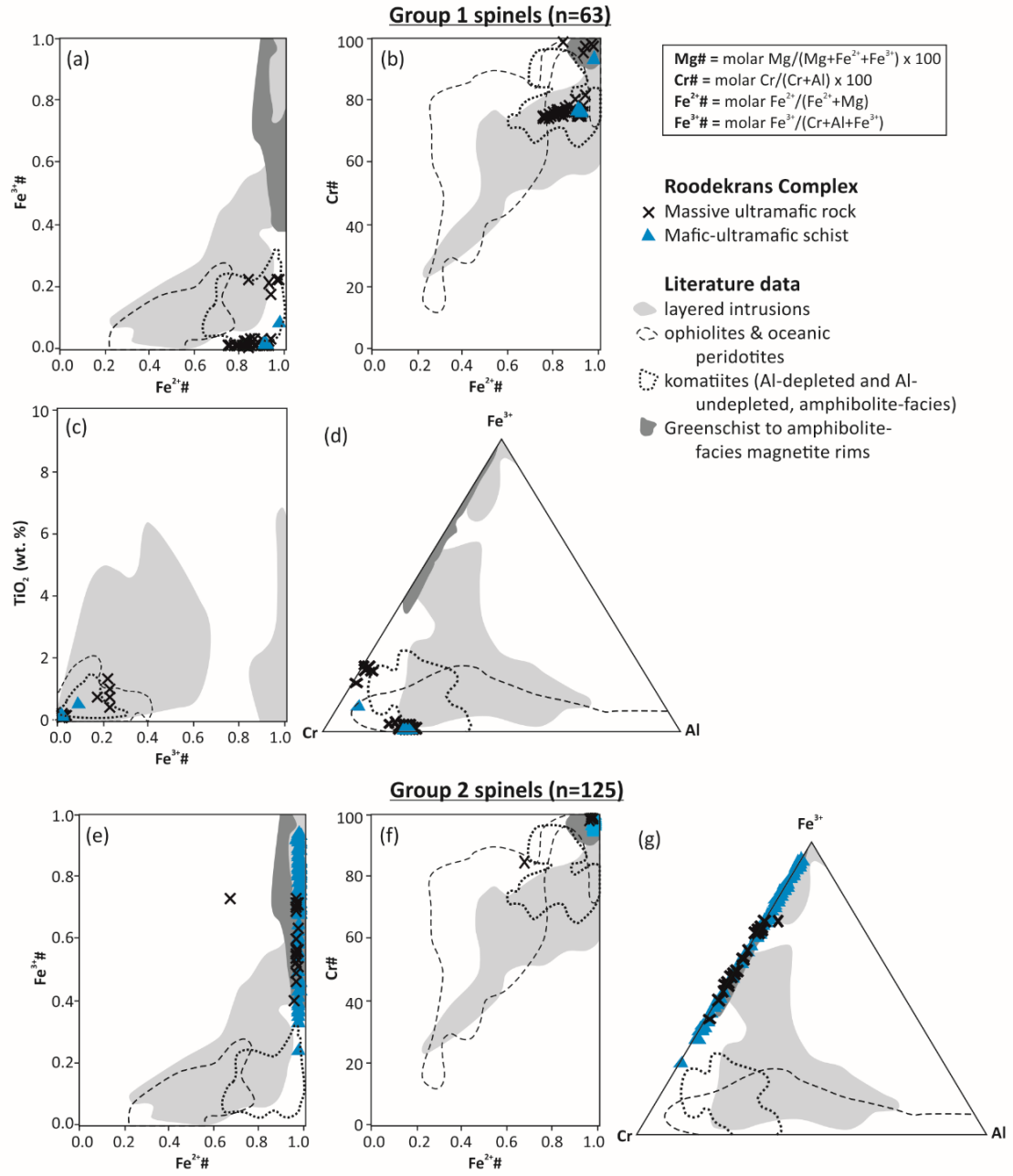

Figure 7.18: *Group 1 and 2 spinel compositions for the Roodekrans Complex. Fields after: Barnes and Roeder (2001).*

Chapter 8

Bulk-rock geochemistry

As outlined in Chapter 6, the ultramafic-mafic complexes of the Johannesburg Dome have previously been interpreted as representing either: Archaean greenstone belt fragments (e.g., Anhaeusser 1977); or ophiolite fragments incorporated into continental crust (Anhaeusser 2006b). The succeeding sections are therefore designed to test these hypotheses, with the studied ultramafic-mafic complexes compared to: extrusive mafic-ultramafic rocks from the Onverwacht Group of the Barberton Greenstone Belt (data from: Brévart et al. 1986, De Wit et al. 1987, Lahaye et al. 1995, Cloete 1999, Blichert-Toft and Arndt 1999, Anhaeusser 2001, Maier 2003, Parman et al. 2003, Chavagnac 2004, Hofmann and Harris 2008, Robins et al. 2010, Thompson Stiegler et al. 2012, Robin-Popieul et al. 2012, Puchtel et al. 2013, Greber et al. 2015); intrusive mafic-ultramafic rocks from the Barberton Greenstone Belt (data from: Viljoen and Viljoen 1969, De Wit et al. 1987, Anhaeusser 2001, Chavagnac 2004, Furnes et al. 2012, Robin-Popieul et al. 2012); and residual mantle rocks from Phanerozoic ophiolites and abyssal peridotites (data from: Godard et al. 2000, Paulick et al. 2006, Godard et al. 2008).

A total of 49 bulk-rock samples from the Modderfontein, Zandspruit and Roodekrans Complexes were analysed for major and trace element geochemistry, with 16 samples analysed for PGE and Au. Samples locations are detailed in Figures 7.1 (Modderfontein), 7.9 (Zandspruit) and 7.13 (Roodekrans), with details of the instrumentation and methodologies utilised for bulk-rock analysis included in Appendix A. The raw (hydrous) data are included in Table 8.1 (Modderfontein), Table 8.2 (Zandspruit) and Table 8.3 (Roodekrans), and the analysed standards and duplicates are included Appendix G.

8.1 Major and minor elements

8.1.1 Modderfontein

With the exception of the two samples that contain significant chromite, the serpentinites of the northern domain (n=10) exhibit relatively restricted ranges in their anhydrous major and minor element compositions (Fig. 8.1; Table 8.1), with tight ranges in SiO_2 (42.9 to 45.3 wt. %), TiO_2 (< 0.1 wt. %), Al_2O_3 (0.9 to 3.5 wt. %), Fe_2O_3 (9.1 to 14.7 wt. %), MgO (38.4 to 43.3 wt. %), CaO (< 1.1 wt. %), NiO (0.3 to 0.4 wt. %) and Cr_2O_3 (0.4 to 0.8 wt. %). Relative to these

serpentinites, the chromitite-bearing serpentinites (n=3; 7.6 to 9.0 wt. % Cr_2O_3) contain less SiO_2 (33.3 to 33.9 wt. %) and MgO (31.0 to 36.3 wt. %), and more TiO_2 (0.2 to 0.4 wt. %), Al_2O_3 (3.1 to 4.2 wt. %) and Fe_2O_3 (18.0 to 21.2 wt. %; Fig. 8.1; Table 8.1). For the northern domain rocks collectively, MgO displays a strong negative correlation (R^2= > 0.7) with TiO_2, Fe_2O_3, MnO, and Cr_2O_3, a moderate negative correlation (R^2= 0.4–0.7) with SiO_2, Al_2O_3 and Na_2O, weak negative correlations (R^2= 0.1–0.4) with K_2O and NiO, and no correlation with CaO.

The greater range of lithologies in the southern domain is reflected by their major and minor element compositions (Fig. 8.1; Table 1), with moderate to broad ranges in SiO_2 (42.3 to 53.0 wt. %), Al_2O_3 (1.8 to 11.8 wt. %), MgO (14.5 to 41.5 wt. %), CaO (1.7 to 11.5 wt. %), Na_2O (0.1 to 0.9 wt. %) and K_2O (< 1.1 wt. %), but tight ranges in TiO_2 (< 0.2 wt. %), Fe_2O_3 (6.9 to 10.6 wt. %), Cr_2O_3 (0.1 to 0.6 wt. %) and NiO (< 0.2 wt. %; Fig. 8.1; Table 8.1). For these rocks, MgO displays strong negative correlations (R^2= > 0.7) with SiO_2, CaO, Na_2O and NiO, moderate negative correlations (R^2= 0.4–0.7) with Fe_2O_3, K_2O and Cr_2O_3, a weak negative correlation (R^2= 0.1–0.4) with Al_2O_3, and no correlation with TiO_2 and MnO.

Collectively, the Modderfontein rocks exhibit compositions and trends comparable to the extrusive mafic-ultramafic rocks from the Barberton Greenstone Belt (Onverwatcht Group) on MgO versus SiO_2, Al_2O_3, CaO, Na_2O, Cr_2O_3 and NiO plots (Fig. 8.1). The Modderfontein rocks also show limited overlap with this field on MgO versus TiO_2 and Fe_2O_3 plots, on which there is also overlap with the intrusive mafic-ultramafic rocks from the Barberton Greenstone Belt (Fig. 8.1). Importantly, the Modderfontein rocks are distinct from those of residual mantle rocks on all plots (Fig. 8.1).

8.1.2 Zandspruit

The metaperidotites of the Zandspruit Complex (n=10) exhibit relatively restricted ranges in their anhydrous major and minor element compositions (Fig. 8.1; Table 8.2), with tight ranges in the SiO_2 (44.3 to 47.1 wt. %), TiO_2 (0.1 to 0.2 wt. %), Al_2O_3 (4.3 to 5.6 wt. %), Fe_2O_3 (10.2 to 12.3 wt. %), MnO (0.1 to 0.2 wt. %) and MgO (31.5 to 36.5 wt. %) contents, and slightly broader ranges in the CaO (1.5 to 4.3 wt. %), Cr_2O_3 (0.7 to 1.6 wt. %) and NiO (0.2 to 0.9 wt. %) contents. In these rocks, MgO displays moderate negative correlations (R^2= 0.4–0.7) with SiO_2, Al_2O_3 and CaO, weak negative correlations (R^2= 0.1–0.4) with Na_2O, K_2O and Cr_2O_3, and no correlation with TiO_2, Fe_2O_3, MnO and NiO.

Table 8.1: *Bulk-rock major and trace element data for the Modderfontein Complex samples. Abbreviations: am=amphibolite; cr=chromitite-bearing serpentinite; gb=gabbro; per=peridotite; px=pyroxenite; srp=serpentinite.*

Sample	JB16-13	JB16-14	JB16-15	JB16-16	JB16-17	JB16-18	JB16-19	JB16-19CR	JB16-20	JB16-21	JB16-22
Domain	N	N	N	N	N	N	N	N	N	N	N
Lithology	srp	srp	srp	srp	srp	srp	srp	cr	srp	srp	srp
Major elements (wt. %)											
SiO_2	39.97	38.57	38.08	39.40	39.98	37.53	40.49	30.77	40.75	39.27	38.36
TiO_2	0.04	0.06	0.08	0.08	0.10	0.06	0.07	0.37	0.08	0.05	0.05
Al_2O_3	1.32	1.44	1.37	2.02	3.05	1.41	1.15	3.89	0.92	0.80	1.05
Fe_2O_3	9.64	10.07	11.00	8.09	8.14	7.48	13.12	19.51	13.87	10.75	9.86
MnO	0.14	0.17	0.14	0.11	0.09	0.08	0.20	0.53	0.18	0.14	0.10
MgO	37.75	37.50	37.72	37.43	35.38	35.51	34.56	28.55	37.25	38.14	38.10
CaO	0.01	0.09	0.05	0.57	0.95	0.07	0.05	0.12	0.13	0.06	0.13
Na_2O	0.02	0.03	0.02	0.01	0.03	0.02	0.03	0.07	0.08	0.03	0.04
K2O	0.02	0.03	0.02	0.03	0.02	0.03	0.02	0.03	0.03	0.01	0.02
P_2O_5	0.01	0.10	0.03	0.06	0.02	0.00	0.01	0.01	0.02	0.03	0.01
Cr_2O_3	0.44	0.63	0.32	0.66	0.67	0.68	0.39	8.32	0.73	0.48	0.45
LOI	11.18	11.58	11.01	12.11	11.80	16.88	11.13	8.39	7.12	10.28	12.21
Trace elements (ppm)											
Sc	4.1	3.2	6.6	6.8	8.2	4.4	3.2	6.3	4.4	3.1	3.6
V	20.1	21.0	23.7	39.4	50.4	29.4	22.3	268.4	37.6	18.9	19.1
Co	130	127	130	111	100	103	133	192	162	134	113
Ni	2922	2807	2706	2366	2031	2696	2632	2177	2726	2292	2867
Cu	3.21	8.50	12.88	4.15	5.16	14.91	27.58	14.29	20.22	12.95	6.6
Zn	53.5	78.00	55.30	58.08	74.43	60.64	80.05	854.3	92.12	83.06	73.9
Ga	2.37	2.74	1.92	2.99	3.04	2.19	2.50	9.15	2.74	1.67	1.4
Ge	0.86	1.07	0.78	0.79	0.74	0.62	1.19	1.35	1.19	0.84	0.6
Rb	0.54	1.74	4.53	1.31	0.74	1.10	1.47	2.09	0.95	0.48	0.2
Sr	2.23	7.00	2.01	20.21	16.52	4.39	5.49	4.96	4.47	2.64	4.9
Y	2.81	2.00	2.73	2.31	2.48	2.63	1.45	1.03	1.56	1.56	2.3
Zr	2.67	21.44	4.67	9.22	4.42	17.08	6.03	4.04	3.65	3.72	2.8
Nb	0.50	0.60	0.63	0.76	0.55	0.68	0.47	0.48	0.51	0.40	0.51
Cs	0.44	1.11	3.64	1.68	1.73	0.58	0.48	0.59	0.33	0.21	0.09
Ba	42.6	47.46	28.53	55.95	154.9	51.44	51.17	31.88	101.52	69.36	29.7
La	1.40	1.34	0.84	1.72	1.63	1.55	0.90	0.61	1.63	1.37	1.21
Ce	2.77	2.68	2.31	3.85	3.72	2.78	1.74	1.54	2.95	3.00	2.33
Pr	0.45	0.30	0.28	0.45	0.43	0.49	0.22	0.18	0.34	0.40	0.28
Nd	1.88	1.31	1.27	1.84	1.81	2.14	0.99	0.86	1.39	1.60	1.20
Sm	0.47	0.33	0.38	0.38	0.42	0.49	0.27	0.20	0.32	0.34	0.28
Eu	0.11	0.09	0.06	0.15	0.08	0.10	0.09	0.06	0.08	0.10	0.10
Gd	0.37	0.28	0.33	0.33	0.37	0.43	0.19	0.17	0.26	0.27	0.24
Tb	0.07	0.04	0.06	0.06	0.06	0.07	0.04	0.03	0.04	0.04	0.04
Dy	0.39	0.29	0.43	0.37	0.43	0.41	0.23	0.19	0.26	0.26	0.31
Ho	0.08	0.06	0.09	0.07	0.08	0.09	0.04	0.04	0.05	0.05	0.06
Er	0.23	0.16	0.27	0.22	0.25	0.26	0.14	0.12	0.15	0.12	0.18
Tm	0.03	0.03	0.04	0.04	0.03	0.04	0.02	0.02	0.02	0.02	0.02
Yb	0.19	0.17	0.26	0.21	0.22	0.22	0.16	0.11	0.12	0.11	0.15
Lu	0.04	0.04	0.05	0.04	0.04	0.04	0.03	0.02	0.02	0.02	0.03
Hf	0.06	0.39	0.14	0.26	0.11	0.41	0.14	0.10	0.08	0.09	0.09
Ta	0.03	0.05	0.06	0.08	0.05	0.06	0.05	0.04	0.04	0.03	0.04
Pb	5.09	4.77	2.50	6.59	7.53	2.92	1.93	4.30	6.26	2.45	0.29
Th	0.59	0.56	0.31	0.39	0.21	0.30	0.19	0.35	0.21	0.18	0.13
U	0.03	0.07	0.03	0.06	0.02	0.04	0.02	0.02	0.05	0.04	0.02

Table 8.1 (cont.)

Sample	JB16-23	JB16-27	JB16-29	JB16-30	JB16-31	JB16-32	JB16-33	JB16-35	JB16-38	JB16-40
Domain	N	S	S	S	S	S	S	S	S	S
Lithology	cr	gb	per	px	per	px	per	px	srp	amf
Major elements (wt. %)										
SiO_2	31.03	51.22	39.49	47.99	41.88	46.76	36.86	46.56	38.31	44.54
TiO_2	0.22	0.10	0.05	0.11	0.07	0.07	0.19	0.08	0.07	0.20
Al_2O_3	2.87	11.39	4.61	2.23	2.69	1.17	3.59	1.69	2.89	5.43
Fe_2O_3	16.45	6.86	7.18	6.64	9.39	7.45	7.48	7.97	9.39	9.52
MnO	0.41	0.14	0.14	0.19	0.18	0.16	0.13	0.13	0.12	0.12
MgO	33.21	13.99	34.70	26.24	33.00	29.25	36.15	30.53	36.30	27.30
CaO	0.21	10.89	2.25	10.94	3.13	8.00	1.89	6.48	1.50	5.74
Na_2O	0.09	0.88	0.13	0.25	0.17	0.21	0.19	0.12	0.07	0.61
K2O	0.04	1.10	0.04	0.03	0.03	0.02	0.03	0.02	0.02	0.07
P_2O_5	0.01	0.01	0.01	0.01	0.02	0.02	0.02	0.01	0.00	0.02
Cr_2O_3	6.96	0.13	0.34	0.35	0.45	0.32	0.50	0.45	0.28	0.33
LOI	9.24	2.99	10.64	4.51	8.56	5.78	13.56	5.98	11.77	5.56
Trace elements (ppm)										
Sc	7.8	25.3	15.2	34.8	19.2	27.5	7.3	30.2	12.8	21.5
V	134.4	80.2	55.1	86.0	55.1	71.8	54.1	70.7	52.2	104.7
Co	233	49	82	69	97	84	105	87	91	86
Ni	2675	275	1472	748	1197	787	1107	1292	1800	1316
Cu	25.9	48.99	6.95	8.71	13.35	25.81	36.35	11.33	6.05	14.48
Zn	409.5	44.98	64.83	43.82	76.50	35.40	57.91	70.58	61.09	117.34
Ga	6.1	6.90	3.02	2.75	2.35	1.79	4.95	2.04	2.36	5.06
Ge	0.9	0.88	0.65	1.01	0.88	0.95	0.78	0.90	0.78	1.04
Rb	1.2	82.16	0.69	2.50	1.52	0.70	1.35	1.76	0.52	1.46
Sr	3.8	188.13	10.83	16.32	10.89	10.00	14.90	9.26	10.26	26.75
Y	1.4	3.94	3.21	4.99	3.33	2.49	5.75	2.51	2.30	5.09
Zr	2.7	3.84	1.89	4.15	2.16	2.43	17.09	3.49	5.89	9.85
Nb	0.31	0.34	0.22	0.28	0.21	0.29	1.29	0.24	0.36	0.52
Cs	0.20	5.15	1.76	1.51	1.22	1.27	1.05	0.54	1.28	0.29
Ba	22.6	143.76	32.51	61.40	94.15	28.66	34.21	37.21	84.65	46.31
La	0.45	1.10	0.52	1.31	1.44	0.67	1.68	0.97	0.58	1.00
Ce	1.15	2.10	1.25	2.78	2.05	1.68	4.25	2.48	1.19	2.01
Pr	0.13	0.31	0.11	0.44	0.34	0.18	0.56	0.31	0.11	0.35
Nd	0.58	1.48	0.44	1.82	1.36	0.97	2.60	1.32	0.53	1.61
Sm	0.19	0.46	0.13	0.63	0.36	0.31	0.76	0.37	0.19	0.52
Eu	0.07	0.22	0.05	0.21	0.08	0.12	0.25	0.12	0.07	0.19
Gd	0.17	0.45	0.19	0.69	0.47	0.32	0.79	0.39	0.20	0.65
Tb	0.03	0.08	0.05	0.12	0.08	0.06	0.14	0.07	0.04	0.12
Dy	0.20	0.62	0.37	0.82	0.52	0.38	0.90	0.47	0.32	0.85
Ho	0.04	0.13	0.09	0.16	0.11	0.08	0.17	0.09	0.06	0.18
Er	0.15	0.38	0.34	0.48	0.34	0.24	0.54	0.28	0.23	0.57
Tm	0.02	0.06	0.06	0.07	0.05	0.04	0.08	0.03	0.03	0.08
Yb	0.15	0.39	0.38	0.45	0.28	0.20	0.50	0.23	0.24	0.52
Lu	0.03	0.06	0.07	0.07	0.04	0.04	0.08	0.04	0.04	0.08
Hf	0.07	0.12	0.05	0.13	0.08	0.07	0.48	0.11	0.16	0.26
Ta	0.02	0.03	0.02	0.02	0.02	0.02	0.12	0.02	0.02	0.04
Pb	1.66	2.58	5.66	1.13	2.11	8.90	4.68	0.73	0.37	4.40
Th	0.13	0.10	0.05	0.07	0.04	0.05	0.41	0.12	0.04	0.09
U	0.01	0.01	0.01	0.01	0.01	0.02	0.06	0.02	0.01	0.01

Table 8.2: *Bulk-rock major and trace element data for the analysed ultramafic samples from the Zandspruit Complex. Abbreviations: Px=metapyroxenite; Per=metaperidotite.*

Sample	JB16-U1	JB16-U2	JB16-U3	JB16-U4	JB16-U5	JB16-U6	JB16-U7	JB16-U8	JB16-U9	JB16-U10	JB16-U11	JB16-U12
Lithology	Px	Px	Per	Per	Px	Per	Per	Per	Px	Per	Per	Px
Major elements (wt. %)												
SiO_2	46.79	46.77	43.13	40.30	45.70	42.30	41.55	39.92	48.59	43.74	41.25	40.59
TiO_2	0.17	0.18	0.12	0.15	0.14	0.11	0.12	0.11	0.14	0.12	0.10	0.11
Al_2O_3	6.70	6.49	4.73	4.98	5.46	4.44	4.51	4.12	5.74	4.73	3.98	4.25
Fe_2O_3	9.67	9.18	9.71	11.02	9.75	9.26	9.75	9.65	8.75	10.04	9.84	9.62
MnO	0.16	0.18	0.16	0.15	0.15	0.19	0.16	0.15	0.19	0.21	0.18	0.15
MgO	23.60	25.27	29.60	28.77	28.14	29.78	31.10	31.71	24.46	30.29	33.27	31.38
CaO	5.08	6.56	3.49	2.86	3.54	3.29	3.16	3.19	6.94	2.09	1.66	3.60
Na_2O	0.10	0.12	0.08	0.07	0.07	0.08	0.08	0.11	0.28	0.13	0.03	0.06
K_2O	0.03	0.03	0.03	0.02	0.03	0.03	0.03	0.02	0.03	0.03	0.03	0.03
P_2O_5	0.03	0.02	0.02	0.00	0.02	0.01	0.02	0.01	0.02	0.02	0.01	0.01
Cr_2O_3	0.97	1.00	1.49	1.47	1.50	1.46	1.43	1.18	0.65	1.55	1.26	1.12
LOI	5.71	5.39	8.45	8.30	6.69	8.08	8.62	9.26	4.76	8.37	8.84	8.56
Total	99.02	101.19	101.01	98.09	101.19	99.02	100.51	99.42	100.54	101.32	100.46	99.48
Trace elements (ppm)												
Sc	23.28	23.69	17.35	16.16	19.74	16.33	16.32	15.41	22.88	16.72	15.14	15.95
V	112.06	112.85	88.24	82.42	100.65	82.40	82.23	74.67	98.26	84.25	75.25	78.26
Co	91.43	89.87	103.04	6524.40	126.29	109.97	110.31	109.05	87.73	120.51	94.08	104.51
Ni	1109.1	929.7	1347.9	6729.1	1747.3	1988.2	1782.6	1439.4	887.6	1911.8	1620.6	1289.7
Cu	21.89	8.47	62.57	3112.58	47.19	15.20	27.27	124.26	27.83	20.69	9.05	39.14
Zn	167.36	79.26	107.89	138.49	107.09	97.00	121.24	87.42	23.22	150.60	112.78	98.74
Ga	6.55	6.38	4.60	5.96	5.77	4.95	4.81	4.68	5.84	5.11	4.09	4.94
Rb	2.18	0.89	3.09	3.16	3.85	3.57	3.60	2.25	0.89	5.40	2.81	3.20
Sr	15.58	10.31	13.85	7.52	6.36	10.39	8.25	25.25	11.85	9.71	8.48	26.39
Y	9.25	8.12	4.89	9.09	7.59	7.26	6.30	4.99	10.45	6.38	7.60	5.32
Zr	27.07	17.46	10.08	19.55	14.59	11.19	25.40	10.49	14.41	12.20	9.90	10.52
Nb	2.03	0.88	0.64	2.02	1.02	0.80	1.43	0.57	0.72	0.80	0.74	0.56
Cs	0.36	0.22	1.06	0.54	0.81	0.68	0.96	0.97	0.16	0.89	0.86	1.23
Ba	163.34	27.59	51.81	71.91	34.62	59.15	32.01	264.98	28.90	69.63	101.20	18.90
La	14.24	6.27	2.19	17.37	4.33	9.59	3.38	1.88	14.02	4.54	4.59	1.86
Ce	7.00	6.43	4.13	4.75	6.29	5.51	4.63	3.61	14.25	9.13	3.41	3.91
Pr	1.95	1.03	0.43	1.81	0.91	1.33	0.61	0.42	1.81	0.81	0.87	0.43
Nd	6.88	3.71	1.64	6.31	3.23	4.36	2.24	1.65	6.03	2.96	3.08	1.73
Sm	1.34	0.84	0.39	1.11	0.79	0.84	0.51	0.40	1.13	0.57	0.63	0.46
Eu	0.23	0.18	0.20	0.30	0.18	0.25	0.23	0.22	0.25	0.16	0.19	0.18
Gd	1.34	0.98	0.50	1.41	0.91	0.99	0.67	0.54	1.39	0.69	0.79	0.60
Tb	0.21	0.16	0.10	0.22	0.18	0.18	0.13	0.10	0.22	0.13	0.13	0.11
Dy	1.40	1.18	0.70	1.46	1.21	1.21	0.90	0.68	1.53	0.92	0.86	0.77
Ho	0.28	0.23	0.14	0.28	0.25	0.24	0.19	0.15	0.28	0.18	0.19	0.16
Er	0.78	0.71	0.46	0.82	0.75	0.74	0.57	0.46	0.89	0.54	0.55	0.48
Tm	0.13	0.12	0.08	0.14	0.13	0.13	0.09	0.08	0.14	0.10	0.09	0.08
Yb	0.89	0.80	0.52	0.94	0.90	0.88	0.64	0.52	0.88	0.62	0.56	0.54
Lu	0.13	0.12	0.09	0.15	0.13	0.13	0.10	0.08	0.13	0.09	0.08	0.09
Hf	0.56	0.42	0.27	0.47	0.37	0.25	0.59	0.26	0.36	0.31	0.22	0.23
Ta	0.10	0.06	0.04	0.12	0.05	0.04	0.05	0.04	0.05	0.05	0.04	0.04
Pb	0.73	1.56	2.64	2.88	1.11	4.76	2.97	2.84	0.74	2.72	1.99	3.19
Th	1.15	0.67	0.50	0.49	0.44	0.40	0.42	0.37	0.39	0.41	0.32	0.34
U	0.12	0.12	0.09	0.08	0.07	0.08	0.08	0.09	0.09	0.10	0.08	0.09

Table 8.3: *Bulk-rock major and trace element data for the analysed Roodekrans Complex samples. Abbreviations: PL=pillow lava; um=massive ultramafic rock; sch=mafic-ultramafic schist.*

Sample	JB16-2	JB16-R4	JB16-R8	JB16-R12	JB16-R17	JB16-R5	JB16-R6	JB16-R10	JB16-R20	JB16-R23	JB16-R24
Lithology	PL	um	um	um	um	sch	sch	sch	sch	sch	um
Major elements (wt. %)											
SiO_2	50.54	39.39	47.58	42.04	40.90	46.61	47.83	50.56	46.55	47.31	44.20
TiO_2	0.36	0.08	0.15	0.10	0.06	0.13	0.14	0.12	0.16	0.16	0.13
Al_2O_3	16.12	3.27	5.45	4.51	2.36	5.85	5.44	4.80	7.01	6.44	5.11
Fe_2O_3	8.34	8.53	8.60	10.47	6.58	9.17	8.17	6.29	8.87	8.14	7.65
MnO	0.19	0.13	0.29	0.16	0.18	0.24	0.26	0.11	0.18	0.09	0.15
MgO	5.86	35.77	26.40	29.23	36.72	24.38	26.11	28.15	24.15	28.47	31.61
CaO	16.98	1.09	6.55	6.45	2.66	8.17	8.25	4.69	6.74	2.09	2.78
Na_2O	1.03	0.05	0.12	0.07	0.04	0.07	0.04	0.07	0.14	0.02	0.03
K_2O	0.07	0.01	0.03	0.02	0.01	0.01	0.01	0.01	0.02	0.00	0.00
P_2O_5	0.04	0.02	0.01	0.00	0.01	0.01	0.01	0.00	0.00	0.01	0.01
Cr_2O_3	0.06	0.30	0.37	0.43	0.41	0.38	0.41	0.34	0.60	0.35	0.42
LOI	0.63	10.93	5.48	5.51	10.16	4.50	4.64	5.59	5.49	6.86	8.01
Total	100.22	99.58	101.02	99.00	100.08	99.52	101.30	100.75	99.92	99.94	100.10
Trace elements (ppm)											
Sc	41.23	13.98	20.72	14.79	10.59	21.20	21.23	16.79	23.59	21.43	19.25
V	187.16	55.92	90.55	62.60	44.57	91.07	87.61	70.44	97.20	89.22	88.49
Co	37.98	98.97	139.42	11694	119.57	120.49	95.16	63.28	77.14	92.48	106.87
Ni	152.5	1753.0	2539.5	6351.3	2205.1	1108.5	1337.8	961.9	914.0	1530.0	1712.4
Cu	33.19	5.47	48.57	1379.49	65.46	24.81	12.88	89.89	21.89	15.14	2.35
Zn	69.17	94.94	49.93	85.31	59.04	50.60	60.99	39.53	35.57	35.97	75.17
Ga	13.76	3.45	4.79	4.61	2.36	4.82	4.85	5.10	4.61	5.31	4.61
Rb	0.82	0.76	1.63	0.43	0.49	0.21	0.24	n.d.	0.01	n.d.	0.55
Sr	121.47	11.26	24.43	25.71	6.90	16.46	9.62	10.01	6.90	6.18	15.54
Y	15.87	4.66	6.02	6.77	3.45	8.93	5.45	2.51	4.39	3.50	5.03
Zr	33.35	6.50	7.83	5.20	2.72	6.30	42.93	7.94	7.26	9.56	7.33
Nb	2.06	0.68	0.42	0.60	0.46	0.40	0.97	0.34	0.45	0.36	0.43
Cs	0.50	0.19	0.08	0.14	0.46	0.07	0.04	0.01	0.02	0.04	0.29
Ba	20.28	182.96	236.22	78.99	100.47	107.92	138.71	19.73	13.84	14.31	108.28
La	1.03	8.59	3.99	4.82	1.69	12.29	0.81	0.26	0.32	0.26	4.14
Ce	2.28	3.99	15.67	1.68	1.39	9.07	3.45	1.36	0.98	0.85	2.84
Pr	0.37	1.19	0.86	0.89	0.27	2.35	0.24	0.10	0.15	0.11	0.49
Nd	1.92	4.30	3.33	3.61	1.18	8.50	1.19	0.52	0.81	0.52	1.82
Sm	0.73	0.74	0.72	0.74	0.23	1.57	0.38	0.19	0.29	0.24	0.43
Eu	0.36	0.15	0.16	0.15	0.15	0.40	0.17	0.04	0.09	0.05	0.14
Gd	1.19	0.79	0.75	0.86	0.36	1.46	0.51	0.23	0.38	0.32	0.49
Tb	0.26	0.12	0.14	0.15	0.06	0.24	0.11	0.05	0.09	0.07	0.09
Dy	2.02	0.76	0.93	1.05	0.43	1.48	0.81	0.34	0.65	0.56	0.69
Ho	0.46	0.15	0.19	0.21	0.10	0.29	0.15	0.08	0.14	0.11	0.14
Er	1.48	0.43	0.59	0.62	0.29	0.80	0.52	0.24	0.41	0.35	0.47
Tm	0.27	0.07	0.11	0.10	0.05	0.14	0.09	0.04	0.07	0.06	0.08
Yb	1.76	0.50	0.75	0.65	0.33	0.96	0.60	0.30	0.52	0.43	0.50
Lu	0.30	0.07	0.12	0.11	0.06	0.15	0.11	0.06	0.09	0.07	0.09
Hf	0.86	0.13	0.17	0.11	0.05	0.13	0.81	0.14	0.18	0.23	0.18
Ta	0.11	0.03	0.03	0.04	0.02	0.02	0.05	0.03	0.02	0.02	0.02
Pb	1.73	2.25	0.65	2.48	0.78	0.59	0.42	0.29	0.26	0.66	1.15
Th	0.20	0.17	0.11	0.12	0.10	0.14	0.18	0.11	0.11	0.10	2.33
U	0.02	0.06	0.03	0.06	0.04	0.03	0.02	0.02	0.02	0.02	0.01

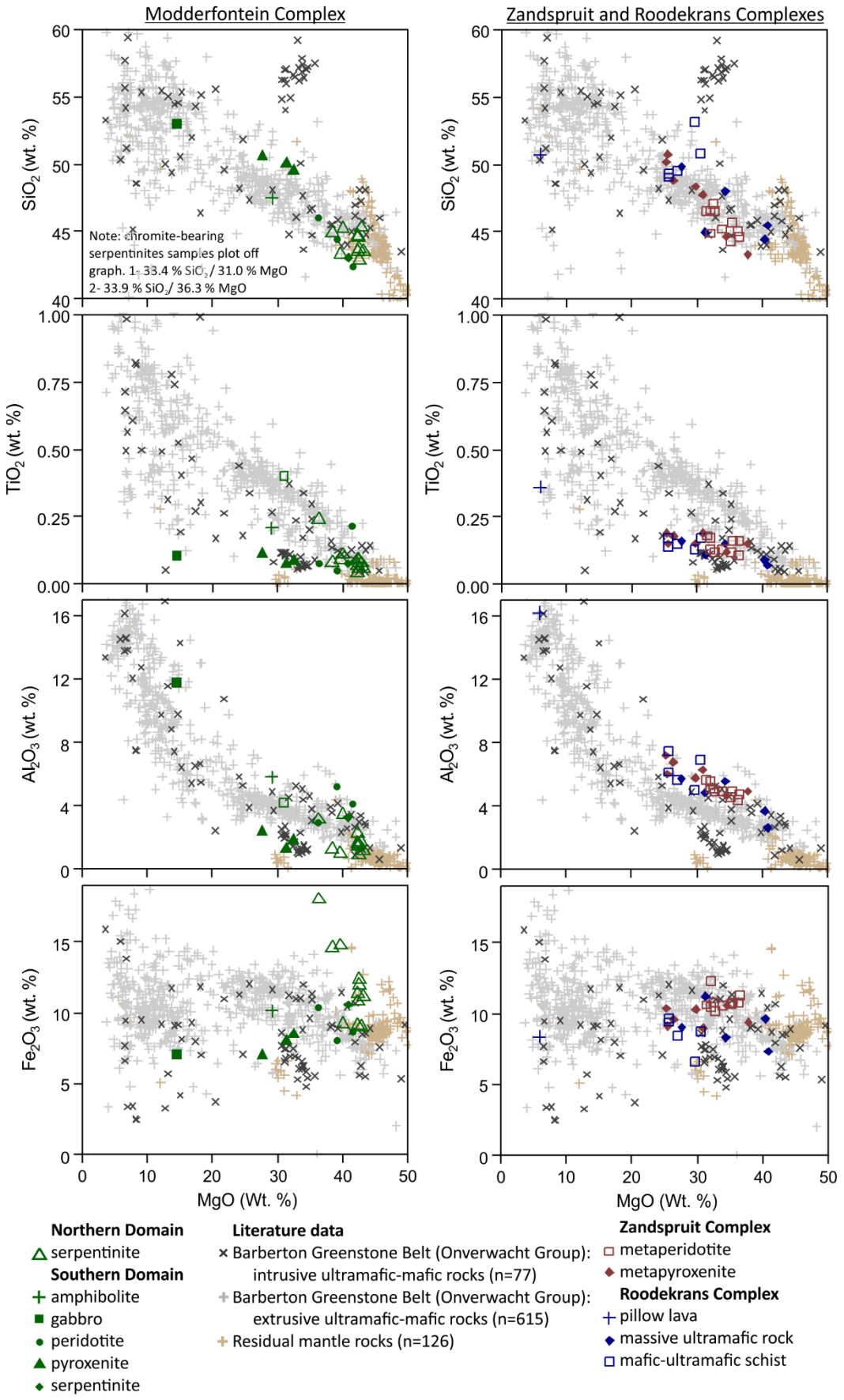

Figure 8.1: *Anhydrous major and minor element bivariate plots for the Modderfontein, Zandspruit and Roodekrans Complexes. For references to the literature data, see main text.*

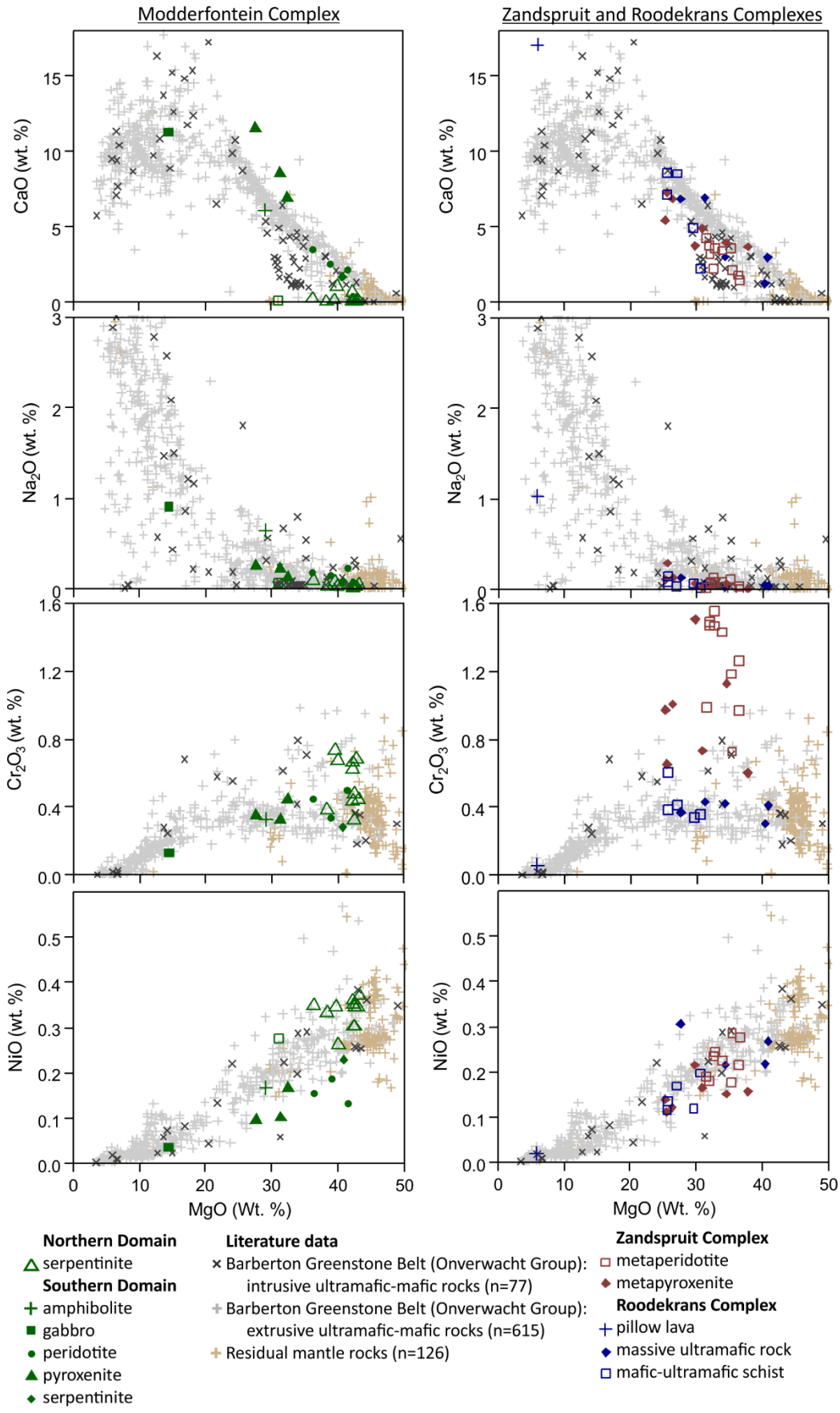

Figure 8.1 (cont.)

The metapyroxenites of the Zandspruit Complex (n=7) exhibit broader ranges in their anhydrous major and minor element compositions (Fig. 8.1; Table 8.2), with moderate ranges in the SiO_2 (43.3 to 50.7 wt. %), Al_2O_3 (4.7 to 7.2 wt. %), MgO (25.3 to 37.8 wt. %), CaO (3.7 to 7.3 wt. %) and Cr_2O_3 (0.6 to 1.5 wt. %) contents, and relatively restricted ranges in the TiO_2 (0.1 to 0.2 wt. %), Fe_2O_3 (9.0 to 10.6 wt. %), MnO (0.1 to 0.2 wt. %) and NiO (0.1 to 0.2 wt. %) contents. In these rocks, MgO exhibits strong negative correlations (R^2= > 0.7) with SiO_2, Al_2O_3 and MnO, moderate negative correlations (R^2= 0.4–0.7) with CaO and Na_2O, weak negative correlations (R^2= 0.1–0.4) with TiO_2, K_2O and NiO, and no correlation with Fe_2O_3 and Cr_2O_3.

Collectively, the Zandspruit rocks exhibit compositions and trends comparable to the extrusive mafic-ultramafic rocks from the Barberton Greenstone Belt (Onverwacht Group) on MgO versus SiO_2, Al_2O_3, Fe_2O_3, CaO, Na_2O and NiO plots (Fig. 8.1). The Zandspruit rocks, which show significant enrichment of Cr_2O_3 relative to the extrusive mafic-ultramafic rocks from the Barberton Greenstone Belt, also show some overlap with this field on the MgO versus TiO_2 plot (Fig. 8.1). The Zandspruit rocks also show significant overlap with the intrusive mafic-ultramafic rocks from the Barberton Greenstone Belt on MgO versus TiO_2, CaO and NiO plots, and are distinct from the residual mantle rocks on all plots (Fig. 8.1).

8.1.3 Roodekrans

The massive ultramafic rocks (n=5) exhibit moderate ranges in their anhydrous major and minor element compositions (Fig. 8.1; Table 8.3), with tight ranges in the TiO_2 (0.1 to 0.2 wt. %) and Cr_2O_3 (0.3 to 0.4 wt. %) contents, and moderate ranges in the MgO (27.6 to 40.8 wt. %), SiO_2 (44.4 to 49.8 wt. %), Al_2O_3 (2.6 to 5.7 wt. %), Fe_2O_3 (7.3 to 11.2 wt. %), CaO (1.2 to 6.9 wt. %) and NiO (0.2 to 0.8 wt. %) contents. In these rocks, MgO displays a strong negative correlation (R^2= > 0.7) with Al_2O_3 and CaO, moderate negative correlations (R^2= 0.4–0.7) with SiO_2, TiO_2, MnO and Na_2O, and weak negative correlations (R^2= 0.1–0.4) with Fe_2O_3, Cr_2O_3 and NiO.

The mafic-ultramafic schists (n=5) exhibit relatively tight ranges in their anhydrous major and minor element compositions (Fig. 8.1; Table 8.3), with tight ranges in the MgO (25.6 to 30.6 wt. %), SiO_2 (49.1 to 53.1 wt. %), TiO_2 (0.1 to 0.2 wt. %), Al_2O_3 (5.1 to 7.4 wt. %), Fe_2O_3 (6.6 to 9.7 wt. %) and NiO (0.2 to 0.7 wt. %) contents, and slightly broader ranges in the CaO (2.2 to 8.6 wt. %) and Cr_2O_3 (0.3 to 0.6 wt. %) contents. In these rocks, MgO displays strong negative correlations (R^2= > 0.7) with CaO, moderate negative correlations (R^2= 0.4–0.7) with SiO_2, Fe_2O_3, MnO, Na_2O, K_2O and Cr_2O_3, a weak negative correlation (R^2= 0.1–0.4) with NiO, and no correlation with TiO_2 and Al_2O_3.

Collectively, the Roodekrans rocks exhibit compositions and trends comparable to the extrusive mafic-ultramafic rocks of the Barberton Greenstone Belt (Onverwacht Group; Fig. 8.1). Such trends are most notable on the MgO versus SiO_2, Al_2O_3, CaO, Cr_2O_3 and NiO plots, with some overlap on the MgO versus Fe_2O_3 plot (Fig. 8.1). The Roodekrans rocks also show some overlap with the intrusive mafic-ultramafic rocks from the Barberton Greenstone Belt on MgO versus TiO_2 and CaO plots, but are distinct from the residual mantle field on all plots (Fig. 8.1).

8.2 Lithophile trace elements: bivariate plots

The succeeding subsections are primarily utilised to establish the degree of element mobility (Chapter 9), with the method utilised detailed in Figure 8.2 (developed after: Cann 1970).

8.2.1 Modderfontein

Except for Hf, the northern domain rocks display poor correlations between Zr and almost all immobile elements (R^2= < 0.32), and no correlation between Zr and mobile elements (R^2= < 0.10; Fig. 8.2). In contrast, the southern domain rocks generally exhibit strong correlations between Zr and Nb, Ti, Ta, Hf and Th (Fig. 8.2; R^2= > 0.77), moderate correlations between Zr and Y, Yb and Ho (R^2= 0.41–0.50), and no correlation between Zr and Al_2O_3 (Fig. 8.2; R^2= 0.01). These rocks exhibit weak to moderate correlations with the LREE (R^2= 0.29–0.51), and no correlation between Zr and other mobile elements (Fig. 8.2; R^2= < 0.06).

On most Zr versus immobile element plots (except Th), the Modderfontein rocks display compositions and trends comparable to those of the extrusive mafic-ultramafic rocks from the Barberton Greenstone Belt (Onverwacht Group; Fig. 8.2). The Modderfontein rocks are generally enriched in mobile elements relative to this field, although there is some overlap on the Zr versus Nd, Rb and Cs plots (Fig. 8.2). In contrast, the Modderfontein rocks show compositions and trends distinct from residual mantle rocks on all Zr versus trace element plots (Fig. 8.2).

8.2.2 Zandspruit

The Zandspruit Complex metaperidotites display weak positive correlations (R^2= 0.1–0.4) between Zr and most immobile elements (Nb, Ta, Y, Th, Ho and Yb), no correlation (R^2= < 0.1) between Zr and TiO_2 and Al_2O_3, and a strong positive correlation (R^2= 0.8) between Zr and Hf (Fig. 8.3). In terms of elements generally considered mobile, Zr displays weak positive correlations with the LREE, and no correlation (R^2= < 0.1) with Ba, Rb and Cs (Fig. 8.3).

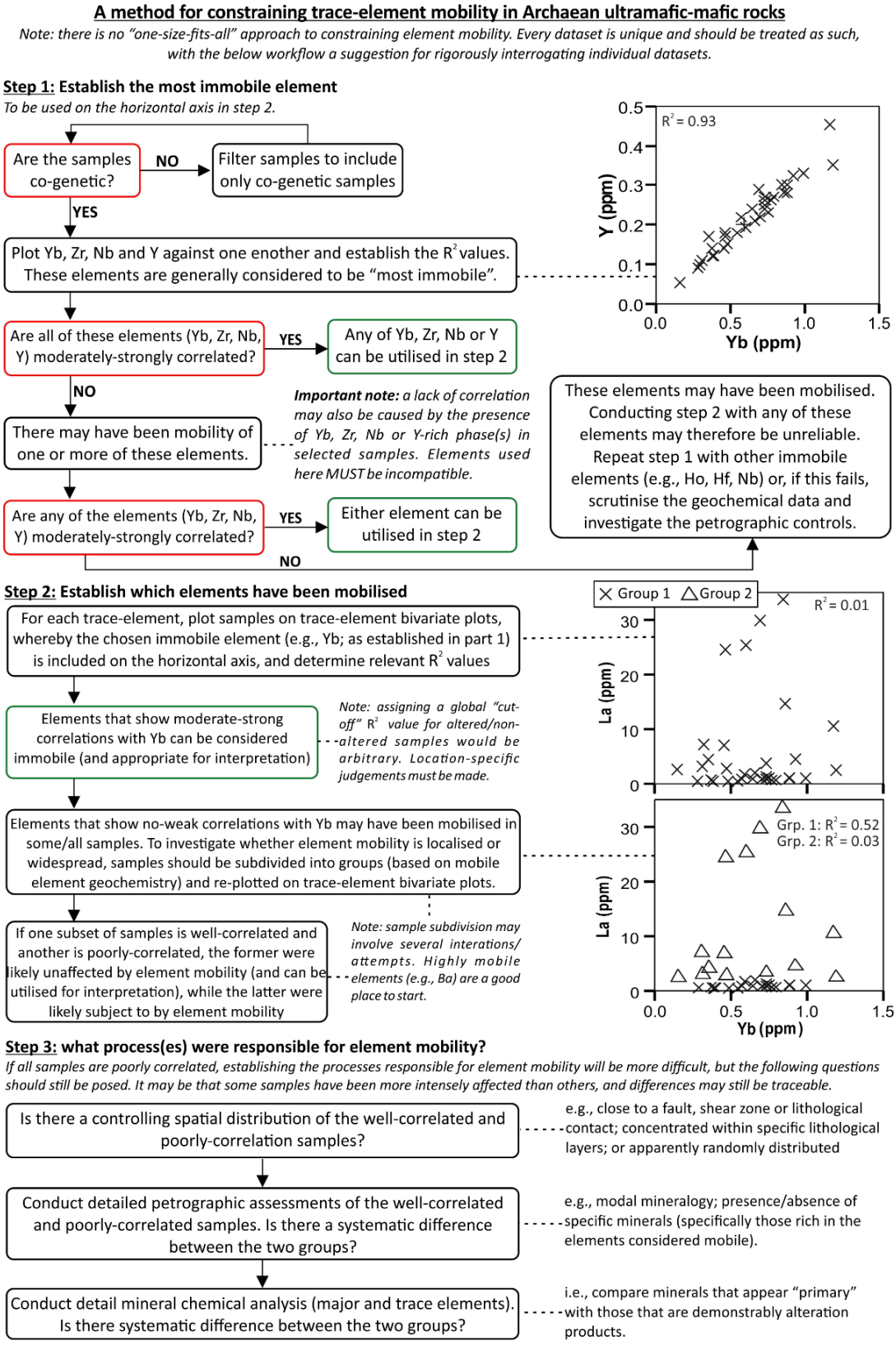

Figure 8.2: *Broad workflow detailing a method for constraining element mobility in Archaean ultramafic-mafic rocks.*

The Zandspruit Complex metapyroxenites display moderate positive correlations (R^2= 0.4–0.7) between Zr and most immobile elements (Al_2O_3, Ta, Y, Yb and Ho), strong positive

correlations (R^2= > 0.7) between Zr and Hf and Th, and weak positive correlations (R^2= 0.1–0.4) between Zr and Nb and TiO_2 (Fig. 8.3). In terms of elements generally considered mobile, Zr has a strong positive correlation with Ba, moderate positive correlations with the LREE, a weak correlation with Cs, and no correlation with Rb (Fig. 8.3).

On most Zr versus immobile element plots, the Zandspruit ultramafic rocks are collectively comparable to the extrusive ultramafic-mafic rocks from the Barberton Greenstone Belt (Fig. 8.3). The Zandspruit ultramafic rocks are also comparable to these data on some Zr versus mobile element plots (e.g., Cs and Nd), but are relatively enriched in mobile elements (Fig. 8.3). On all Zr versus trace element plots, the Zandspruit rocks exhibit compositions distinct from those for residual mantle rocks (Fig. 8.3).

8.2.3 Roodekrans

The massive ultramafic rocks display a wide-range of correlations between Zr and elements generally considered immobile (Fig. 8.3), with TiO_2, Al_2O_3 and Hf displaying strong positive correlations with Zr (R^2= > 0.7), Yb showing moderate positive correlations with Zr (R^2= 0.4–0.7), Y, Th and Ho exhibiting weak positive correlations with Zr (R^2= 0.1–0.4), and Nb and Ta displaying no correlation with Zr (Fig. 8.3). Moreover, the massive ultramafic rocks consistently exhibit moderately positive correlations between Zr and elements generally considered mobile (e.g., Ba, Rb, La, Nd and Cs; Fig. 8.3).

The mafic-ultramafic schists also display a wide-range of correlations between Zr and elements generally considered immobile (Fig. 8.3), with Nb, Ta, Hf and Th displaying strong positive correlations with Zr (R^2= > 0.7), Al_2O_3 showing a weak positive correlation with Zr (R^2= 0.1–0.4), and TiO_2, Y, Yb and Ho exhibiting no correlation with Zr. Moreover, the mafic-ultramafic schists exhibit variable correlations between Zr and elements generally considered mobile (Fig. 8.3), with Ba and Rb showing moderate positive correlations with Zr (R^2= 0.4–0.7), and La, Nd and Cs exhibiting no correlation with Zr.

On most Zr versus immobile element plots, the Roodekrans rocks (including the 1 pillow lava sample) collectively display compositions and trends similar to those shown by the extrusive rocks in the Barberton Greenstone Belt (Fig. 8.3), although there is a notable distinction on the Zr versus Al_2O_3 plot. In contrast, the Roodekrans Complex rocks exhibit compositions and trends that are either enriched or depleted in mobile elements relative to the Barberton Greenstone Belt extrusive rocks (Fig. 8.3). Similarly, the Roodekrans Complex rocks are comparable to those of the Modderfontein Complex on Zr versus immobile element plots, while these rocks show some overlap on the Zr versus mobile element plots (Fig. 8.3). On all

Zr versus trace element plots, the Roodekrans rocks are compositionally distinct from the field for residual mantle rocks (Fig. 8.3).

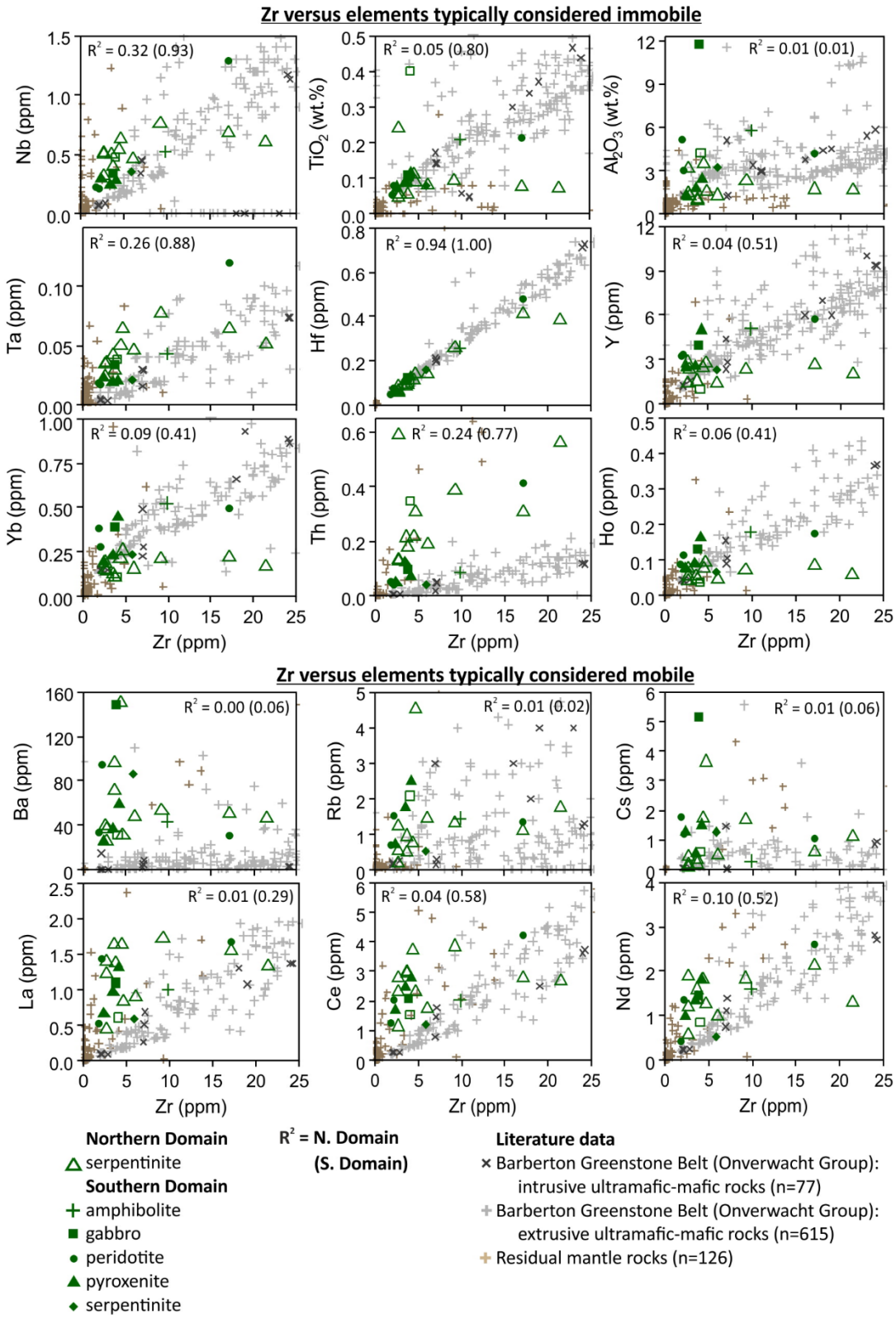

Figure 8.3: *Trace element bivariate plots for the Modderfontein Complex. For references to the literature data, see main text.*

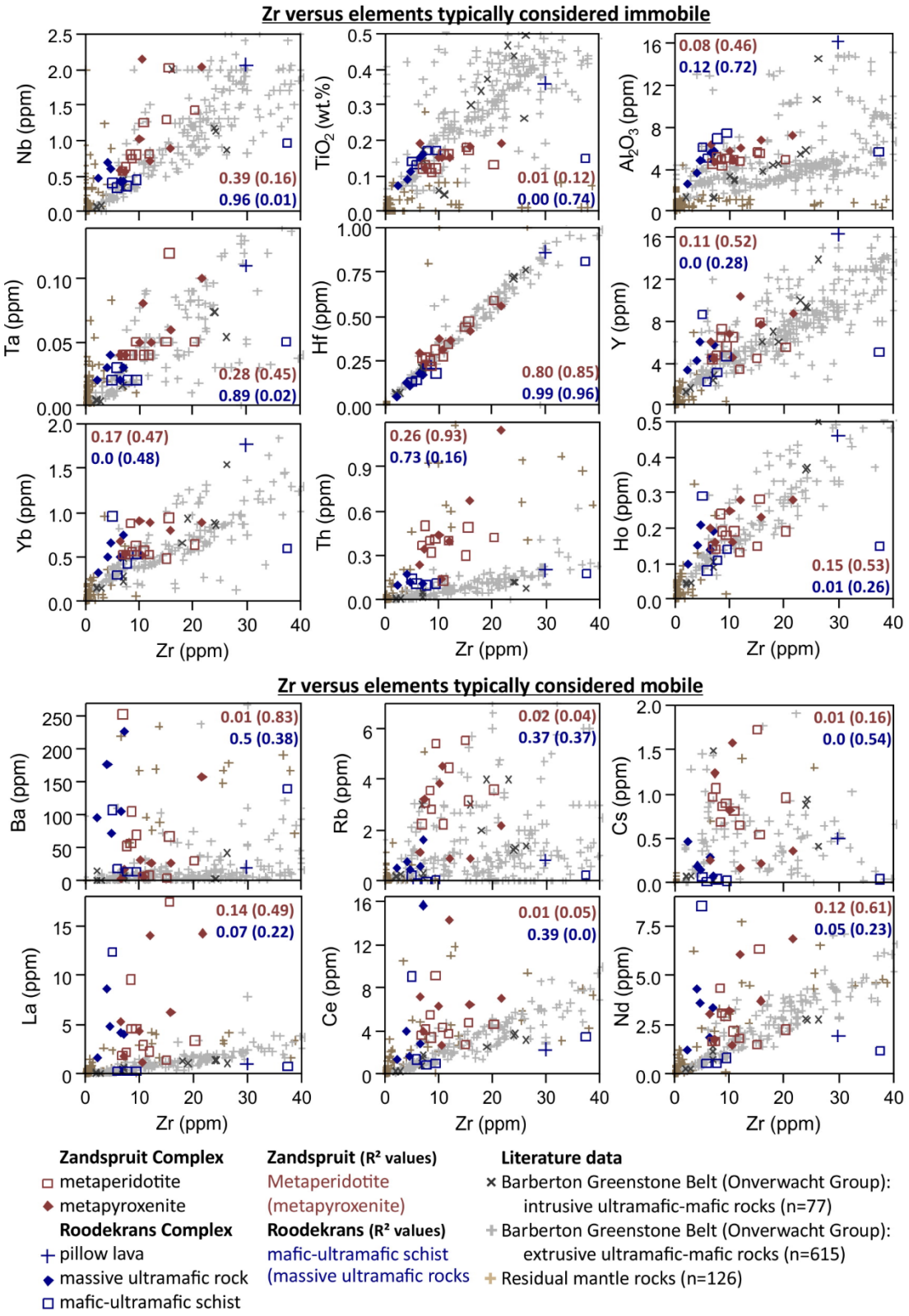

Figure 8.4: *Trace element bivariate plots for the Zandspruit and Roodekrans Complexes. For references to the literature data, see main text.*

8.3 Lithophile trace elements: normalised plots

8.3.1 Modderfontein

On chondrite-normalised REE plots (Fig. 8.4a), the northern domain serpentinites exhibit flat HREE patterns ($[Gd/Lu]_N$= 0.7–1.6) and negatively sloping LREE patterns ($[La/Sm]_N$= 1.4–3.2; $[La/Lu]_N$= 2.1–5.3), with chondrite-normalised REE abundances ranging from 0.7 to 7.3. On the primitive mantle-normalised trace element plots (Fig. 8.4b), these rocks display negatively sloping patterns ($[Th/Yb]_N$= 4.9–18.2). Within this broad pattern, the incompatible elements show negative slopes ($[Th/Eu]_N$= 2.5–11.2) and the compatible elements display relatively flat patterns ($[Eu/Yb]_N$= 0.7–2.7), with the broad pattern punctuated by mild negative Nb-Ta-Zr-Hf-Ti anomalies, negative Sr anomalies and positive Ba anomalies. The northern domain chromitite-bearing serpentinites display REE and trace element patterns broadly comparable to the serpentinites (Fig. 8.4a-b). The only major difference is on trace element plots, with chromitites displaying positive Ti anomalies (reflecting the increased spinel content) and serpentinites showing negative Ti anomalies (Fig. 8.4b).

The southern domain rocks display generally flat REE patterns ($[La/Lu]_N$= 0.8-3.5), with flat HREE patterns ($[Gd/Lu]_N$= 0.6–1.3), gently sloping LREE patterns ($[La/Sm]_N$= 1.3–2.4) and chondrite-normalised REE abundances ranging from 0.9 to 7.1 (Fig. 8.4c,e). On primitive mantle-normalised trace element plots (Fig. 8.4d,f), these rocks exhibit generally flat patterns ($[Th/Yb]_N$= 0.7–4.6) that are punctuated by negative Nb-Ta-Zr-Hf-Ti anomalies, negative Sr anomalies and positive Ba anomalies (Fig. 8.4d,f). The one gabbro sample analysed is comparable to the other southern domain rocks, but displays a positive Sr anomaly and significant enrichment in Rb (Fig. 8.4f).

The chondrite-normalised REE and primitive mantle-normalised trace element compositions of the Modderfontein rocks (both in the northern and southern domains) show significant overlap with the field for Barberton komatiites and are distinct from the field for residual mantle rocks (Fig. 8.4).

8.3.2 Zandspruit

On chondrite-normalised REE plots, the Zandspruit Complex metaperidotites display negatively sloping patterns ($[La/Lu]_N$= 2.3–12.4), with negatively sloping LREE ($[La/Sm]_N$= 2.4–9.8), flat HREE ($[Gd/Lu]_N$= 0.6–1.2), and chondrite-normalised abundances between 2.1 and 73.3 (Fig. 8.5a). The metapyroxenites also exhibit negatively sloping REE patterns ($[La/Lu]_N$= 2.3–11.4), with negatively sloping LREE ($[La/Sm]_N$= 1.9–7.7), flat HREE ([Gd/Lu]= 0.6–1.3), and normalised abundances ranging from 2.2 to 60.1 (Fig. 8.5b). Both

metaperidotite and metapyroxenite lithologies show near-complete overlap with the field for Barberton komatiites on normalised REE plots (Fig. 8.5a-b).

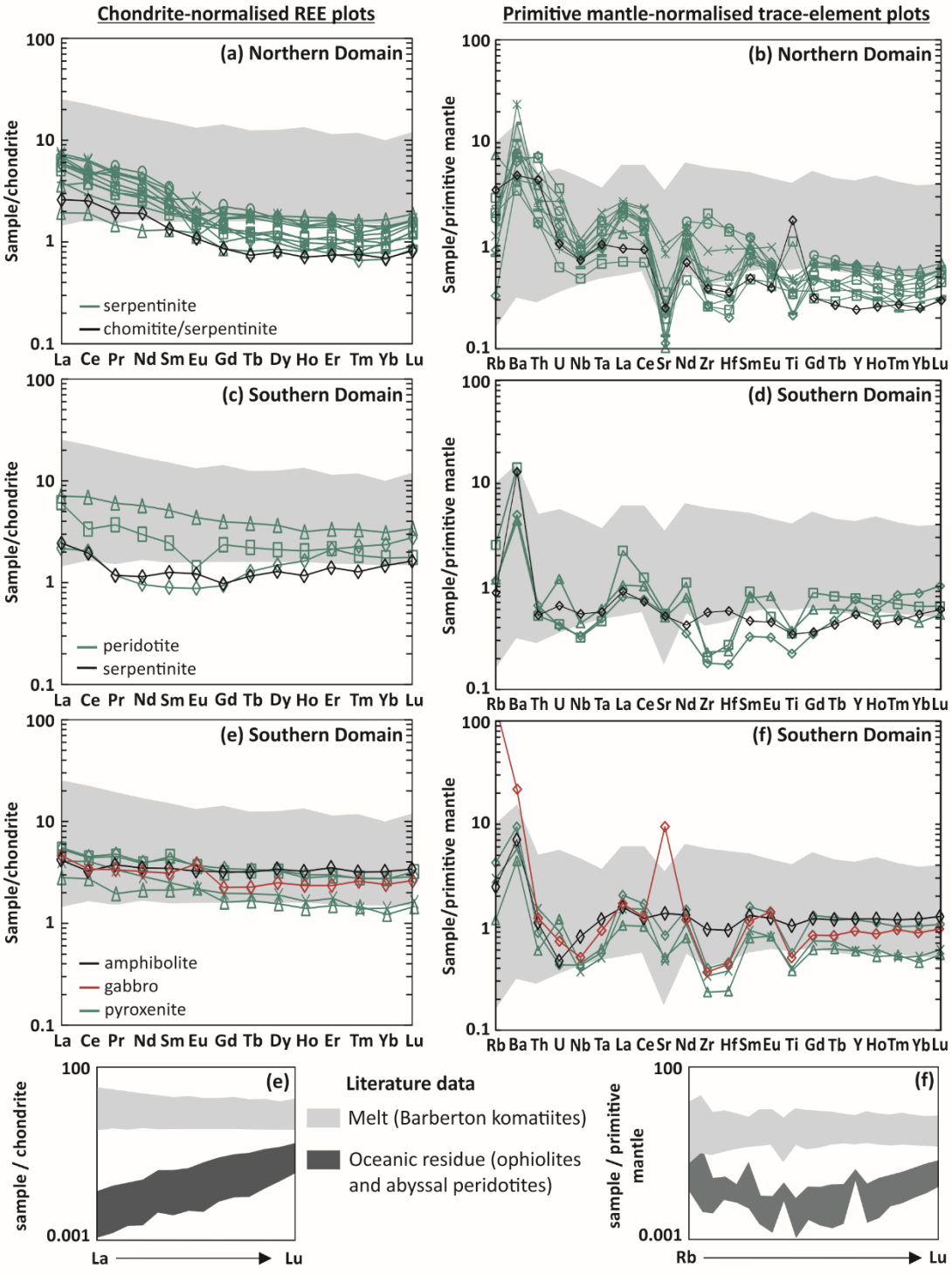

Figure 8.5: *Chondrite-normalised REE and primitive mantle-normalised (McDonough and Sun 1995) trace element plots for the Modderfontein Complex rocks. Note: "Barberton komatiites" refers to rocks specifically referred to as "komatiites", rather than the full mafic-ultramafic dataset shown in Fig. 8.1.*

On primitive mantle-normalised trace element plots, the metaperidotites display negatively sloping incompatible elements ($[Th/Sm]_N$= 1.4–6.6) and relatively flat compatible element

patterns ($[Zr/Lu]_N$= 0.4–1.7), with normalised abundances ranging from 0.4 to 40.2 (Fig. 8.5c). On these plots, metaperidotites show some negative Ba, Th, Nb, Ta, Sr, Zr and Ti anomalies, and some positive Ba, La, Ce and Nd anomalies (Fig. 8.5c). The metapyroxenites display more consistent trace element patterns, with negatively sloping compatible elements ($[Th/Sm]_N$= 1.9–4.4), flat incompatible elements ($[Zr/Lu]_N$= 1.3–5.4), and normalised abundances ranging from 0.3 to 24.8 (Fig. 8.5d). On these plots, metapyroxenites show consistent negative Nb, Ta, Sr and Ti anomalies, and positive La, Ce and Nd anomalies (Fig. 8.5d). Both metaperidotite and metapyroxenite lithologies show near-complete overlap with the field for Barberton komatiites on these normalised trace element plots (Fig. 8.5c-d).

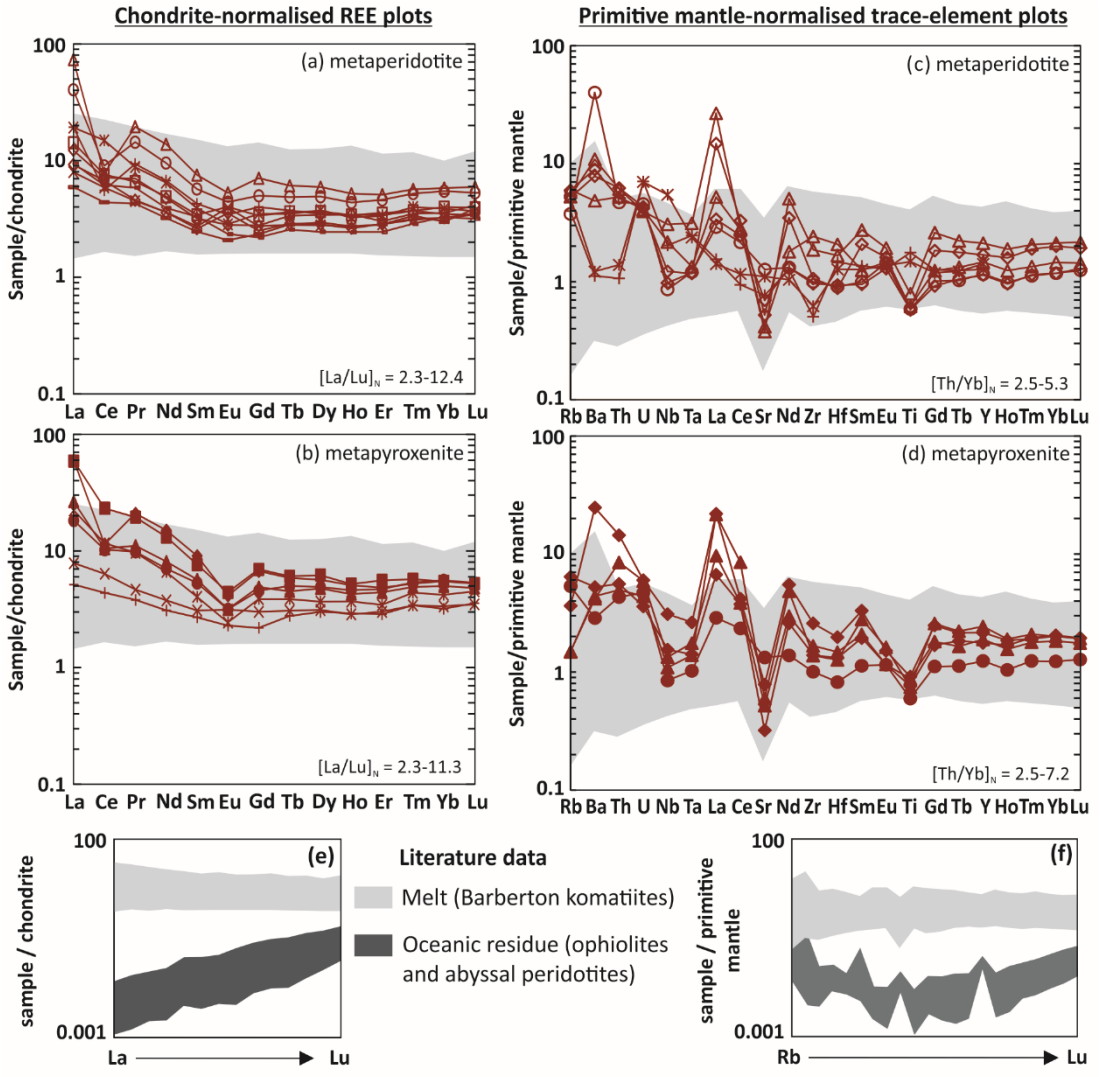

Figure 8.6: *Chondrite-normalised REE and primitive mantle-normalised (McDonough and Sun 1995) trace element plots for the Zandspruit Complex ultramafic rocks. Note: "Barberton komatiites" refers to rocks specifically referred to as "komatiites", rather than the full mafic-ultramafic dataset shown in Fig. 8.1.*

8.3.3 Roodekrans

On chondrite-normalised REE plots, the massive ultramafic rocks exhibit negatively sloping patterns ($[La/Lu]_N$= 2.8–12.4), with negatively sloping LREE ($[La/Sm]_N$= 3.4–7.2), flat HREE ($[Gd/Lu]_N$= 0.7–1.4) and normalised REE abundances ranging from 1.5 to 36.2 (Fig. 8.6a). Some samples display negative Eu anomalies, while 1 shows a positive Eu anomaly (Fig. 8.6a). In contrast, the mafic-ultramafic schists generally exhibit positively sloping REE patterns ($[La/Lu]_N$= 0.4–0.8), with 1 sample displaying a negatively sloping pattern ($[La/Lu]_N$= 8.3) accompanied by a negative Ce anomaly (Fig. 8.6b). The 1 pillow lava sample analysed exhibits a REE pattern comparable to those of the mafic-ultramafic schists, with positively sloping patterns ($[La/Lu]_N$= 0.4; Fig. 8.6b). All 3 lithologies largely overlap with the field for Barberton komatiites (Fig. 8.6a-b).

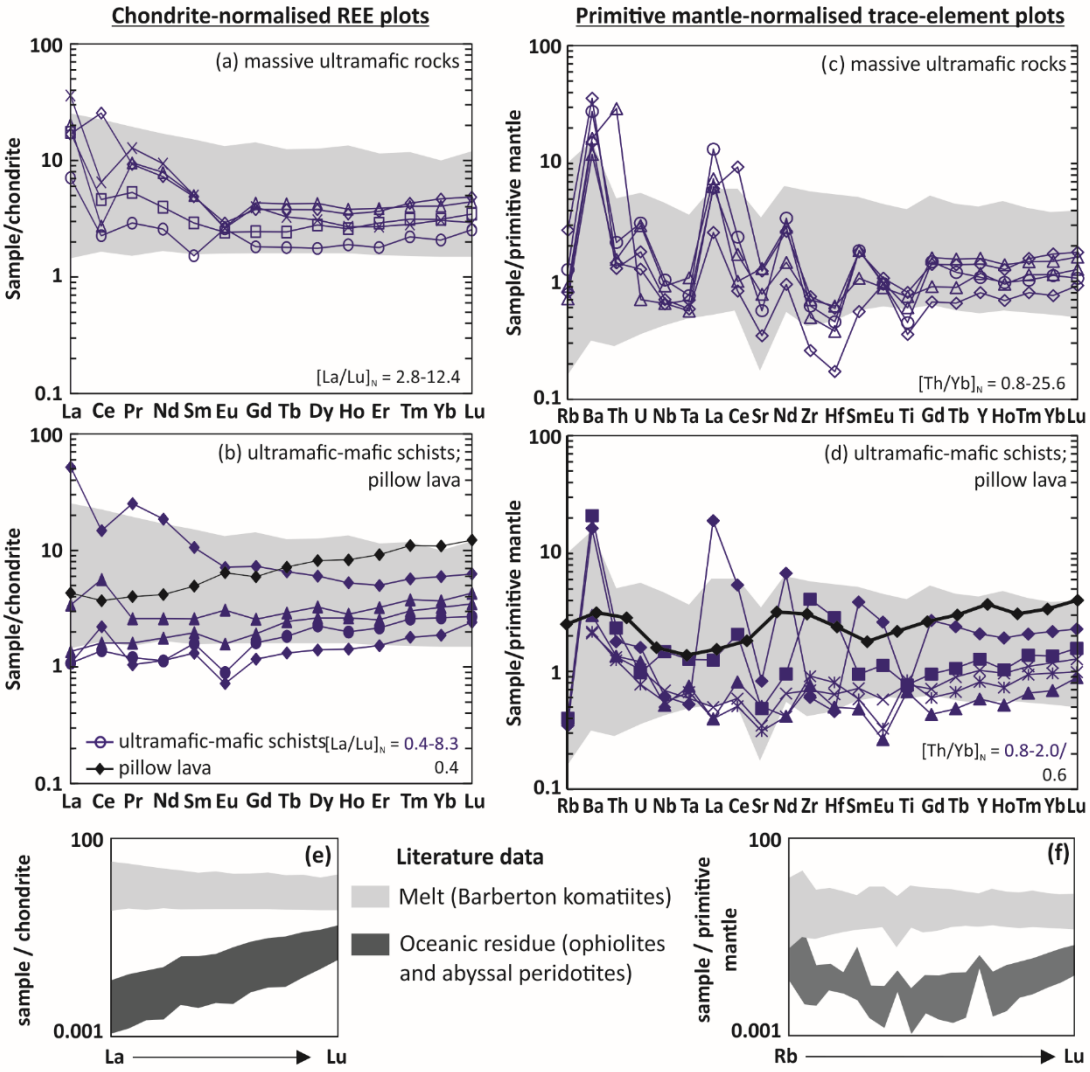

Figure 8.7: *Chondrite-normalised REE and primitive mantle-normalised (McDonough and Sun 1995) trace element plots for the Roodekrans Complex rocks. Note: "Barberton komatiites" refers to rocks specifically referred to as "komatiites", rather than the full mafic-ultramafic dataset shown in Fig. 8.1.*

On primitive mantle-normalised plots, the massive ultramafic rocks display largely flat patterns ($[Th/Yb]_N$= 0.8–1.6, except 1 sample), with pronounced positive Ba, La, Ce, Nd and Sm anomalies and negative Nb, Ta, Sr, Zr, Hf and Ti anomalies (Fig. 8.6c). The mafic-ultramafic schists exhibit more consistent flat patterns ($[Th/Yb]_N$= 0.8–2.0), with rare positive Ba, La, Ce, Nd and Sm anomalies. Similarly, the trace element pattern displayed by the 1 pillow lava sample exhibits a broad negatively sloping ($[Th/Yb]_N$= 0.6). As with the REE plots, all 3 lithologies largely overlap with the field for Barberton komatiites on the primitive mantle-normalised trace element plots (Fig. 8.6a-b).

8.4 Platinum-group elements

8.4.1 Modderfontein

Northern domain serpentinites (n=3) display mildly fractionated patterns ($[Pd/Ir]_N$= 1.7–5.0), with flat PPGE patterns ($[Pd/Rh]_N$= 0.5–4.0; Fig. 8.7a), positive Ru anomalies and positive Au anomalies (Fig. 8.7a). Relative to these serpentinites, the analysed chromitite-bearing serpentinite (n=1; Cr_2O_3= 9.0 wt. %) is enriched in all PGE except Pd by 1-2 orders of magnitude (Fig. 8.7b). The normalised pattern for this sample is comparatively flat from Ir to Pt ($[Pt/Ir]_N$ = 1.8), with significant depletion in Pd and Au (Fig. 8.7b). By contrast, the southern domain pyroxenite and peridotite consistently exhibit distinctly fractionated patterns ($[Pd/Ir]_N$= 8.3–77.7), with positively sloping IPGE ($[Ru/Os]_N$= 6.5–11.1), flat to mildly fractionated PPGE ($[Pd/Rh]_N$= 0.6–4.5) and negative Au anomalies (Fig. 8.7c-d). Excluding the chromitite-bearing serpentinite sample, the Modderfontein samples show a moderate correlation between Pt and Pd (R^2= 0.5). However, when the chromitite-bearing serpentinite is included, the Modderfontein samples show no correlation between Pt and Pd (R^2= 0.1). Relative to the komatiite and residual mantle fields (Fig. 8.7a-d), the northern domain PGE patterns are comparable, while the southern domain PGE patterns are IPGE-poor.

8.4.2 Zandspruit

Metaperidotites (n=2) display moderately fractionated patterns ($[Pd/Ir]_N$= 6.1–7.4) that show flat PPGE (+Ru) patterns ($[Pd/Ru]_N$= 1.1–1.3) and fractionated IPGE (-Ru) patterns ($[Ru/Os]_N$= 6.5–6.7; Fig. 8.7e). Metapyroxenites also display moderately fractionated patterns ($[Pd/Ir]_N$= 8.4), with flat PPGE (+Ru) ($[Pd/Ru]_N$= 1.6) and fractionated IPGE (-Ru) ($[Ru/Os]_N$= 6.9; Fig. 8.7f). Both metaperidotites and metapyroxenites show some overlap with the field for Barberton komatiites, although the Zandspruit Complex rocks are generally PPGE-rich and IPGE-poor relative to this field (Fig. 8.7). Pt and Pd are well correlated in the Zandspruit Complex ultramafic rocks collectively (R^2= 0.86).

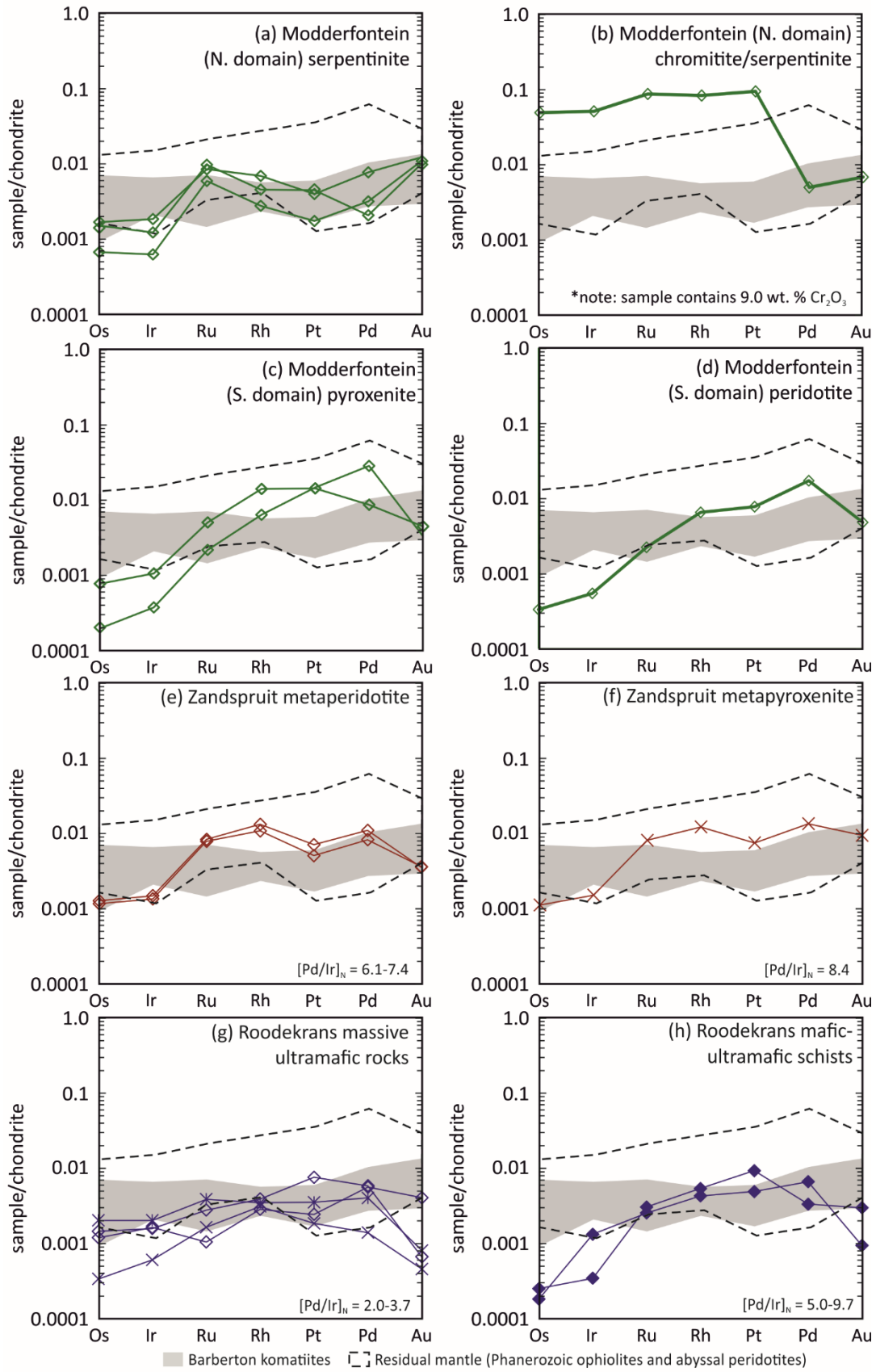

Figure 8.8: *Chondrite-normalised (Lodders 2003) PGE plots for the Modderfontein (a-d), Zandspruit (e-f) and Roodekrans (g-h) Complexes. Barberton komatiites data from: Maier et al. 2003, Puchtel et al. 2014. Residual mantle data from: Luguet et al. 2003, Hanghòj et al. 2010.*

8.4.3 Roodekrans

The massive ultramafic rocks (n=4) display mildly fractionated chondrite-normalised PGE patterns ($[Pd/Ir]_N$= 2.0–3.7) accompanied by negative Au anomalies, with this pattern showing significant overlap with the field for Barberton komatiites (Fig. 8.7g). In contrast, the mafic-ultramafic schists exhibit mildly to moderately fractionated PGE patterns ($[Pd/Ir]_N$= 5.0–9.7; Fig. 8.7h), with positively sloping IPGE ($[Ru/Os]_N$= 12.1–13.9) and flat PPGE [$[Pd/Rh]_N$= 0.6–1.6; Fig. 5.9h). These patterns show some overlap with the field for Barberton komatiites (in terms of PPGE), but are depleted in the IPGE and Au relative to this field (Fig. 8.7).

8.5 Summary

The wealth of bulk-rock geochemical data presented for the Modderfontein, Zandspruit and Roodekrans Complexes is summarised in Table 8.4.

Table 8.4: *Summary of the bulk-rock geochemical characteristics displayed by the Modderfontein, Zandspruit and Roodekrans Complexes. Abbreviations: BK=Barberton komatiites; OR=oceanic residue; PM=primitive mantle.*

	Modderfontein	**Zandspruit**	**Roodekrans**
Chondrite-normalised REE plot	• 0.7 to 7.3 x chondrite • Near-complete overlap with BK field • No overlap with OR field • Flat HREE and negatively sloping LREE.	• 2.2 to 73.3 x chondrite • Near-complete overlap with BK field • No overlap with OR field • Flat HREE and negatively sloping LREE	• 1.5 to 36.2 x chondrite • Near-complete overlap with BK field • No overlap with OR field • Flat to negatively sloping LREE and positively sloping to flat HREE.
PM-normalised trace element plot	• Negatively sloping to flat pattern, punctuated by negative HFSE and Sr anomalies and positive Ba anomalies • Significant overlap with BK field • No overlap with OR field	• Flat to negatively sloping patterns, punctuated by HFSE anomalies and positive LREE anomalies • Near-complete overlap with BK field • No overlap with OR field	• Broadly flat patterns, with some negative HFSE/positive LREE anomalies • Near-complete overlap with BK field • No overlap with OR field
Chondrite-normalised PGE plot	• Significant/some overlap with BK field • Significant overlap with OR field • Flat to positively sloping patterns	• Significant overlap with BK field • Near-complete overlap with OR field • Mild positively sloping patterns	• Significant overlap with BK field • Some overlap with OR field • Flat to positively sloping patterns

Chapter 9

Discussion: ultramafic-mafic complexes in the Johannesburg Dome

The ultramafic-mafic complexes of the Johannesburg Dome have experienced a protracted metamorphic and magmatic history that has resulted in greenschist- to amphibolite-facies mineral assemblages and extensive (and sometimes complete) serpentinisation. The former is illustrated by the replacement of tremolite – itself a product of pyroxene alteration – by cummingtonite at Zandspruit (Fig. 7.11). In addition to the multiple phases of greenschist- to amphibolite-facies metamorphism, the ultramafic-mafic rocks of the Johannesburg Dome were invaded by TTG magmas between 3.3 and 3.1 Ga (Chapter 6), with all of these processes commonly associated with metasomatism of varying styles (e.g., Barton and Ilchik 1991, Lahaye et al. 1995, Yardley 2013, Anhaeusser 2015). The degree of element mobility experienced by the Modderfontein, Zandspruit and Roodekrans Complexes is therefore assessed in Section 9.1, in order to avoid over-interpretation of the geochemical data in Section 9.2, which focuses on constraining the origin of the ultramafic-mafic complexes in the Johannesburg Dome. Section 9.3 focuses on establishing the specific petrogenetic environments represented by the individual ultramafic-mafic complexes, within the context of the discussion presented in Sections 9.1 and 9.2.

9.1 Effects of element mobility and metamorphism

Bulk-rock lithophile element mobility is discussed in Section 9.1.1, while Sections 9.1.2 and 9.1.3 focus on bulk-rock PGE mobility and spinel alteration respectively. Section 9.1.2 also includes a discussion of the PGM recorded in the Modderfontein Complex chromitite (described in Section 7.1.2.1).

9.1.1 Lithophile element mobility

9.1.1.1 Modderfontein

As indicated by the lack of correlation between Zr and the fluid mobile elements (e.g., Ba, Rb, Cs; Fig. 8.2), these elements experienced significant mobility in both domains of the Modderfontein Complex – a common effect of serpentinisation (Deschamps et al. 2013). The bivariate plots of Figure 8.2 also hint at mobility of the LREE and some elements considered immobile in many geological settings, such as Yb, Ho, Y, Al and Ti. While this effect is extremely pronounced in the northern domain, it is negligible in the southern domain, as

highlighted by the respective correlations between Zr and these elements (and LREE) for the two domains (Fig. 8.2). This apparent element mobility (which is most prominent in the northern domain of the Modderfontein Complex) may be the product of melt/rock interaction prior to the serpentinisation, as suggested by Deschamps et al. (2013). In this scenario however, LREE mobility by melt/rock interaction must have either exclusively operated in the northern domain or been inefficient in the southern domain (to explain the disparate apparent mobilities in the northern and southern domains), which appears unlikely. Moreover, mapping of the Modderfontein Complex records no evidence of the gradational zonation typically produced by such melt-rock interaction (e.g., Zhou et al. 1996).

Alternatively, the apparent geochemical discrepancy between the two domains of the Modderfontein Complex may be controlled by modal abundances of alteration minerals, which in turn reflect the modal abundance of primary olivine (± orthopyroxene). Comprising > 92 modal % serpentine, the originally high proportions of olivine (± orthopyroxene) in the northern domain rocks would amplify the chemical effects of alteration (including) serpentinisation. In contrast, the lower modal abundance of olivine (± orthopyroxene) in the southern domain rocks would supress the chemical effects of serpentinisation, leading to a less pronounced apparent mobility of the aforementioned elements (Fig. 9.1). This interpretation is consistent with the evidence for the mobility of Ba, Sr and Cs, which is a common chemical effect associated with serpentinisation (Deschamps et al. 2013); but may initially appear at odds with the notable depletion in Sr displayed by all-but-one of the Modderfontein samples (Fig. 8.4), as serpentinisation is commonly associated with Sr-rich fluids that often generate bulk-rock Sr enrichment (Deschamps et al. 2013). Despite this caveat, the hydrothermal alteration hypothesis is considered to be much more likely than the melt/rock interaction hypothesis (Fig. 9.1).

9.1.1.2 Zandspruit

In the Zandspruit rocks, Zr exhibits poor correlations with the fluid mobile elements (e.g., Ba, Rb and Cs), LREE and some elements generally considered immobile, such as Ti, Al, Y, Yb and Nb (Fig. 8.3), demonstrating that these rocks have experienced significant lithophile element mobility. As with the Modderfontein Complex, such mobility may be attributed to hydrothermal alteration (including serpentinisation), with the modal abundance of serpentine within individual ultramafic samples controlling the apparent element mobility. This hypothesis is supported by the relative mobility of these elements in metaperidotite sample and metapyroxenite samples, with serpentine comprising 44–65 modal % of metaperidotite samples compared with < 20 modal % serpentine in metapyroxenite samples

(Section 7.2.2). This hypothesis is also supported by the spatial distribution of metaperidotite and metapyroxenite units (and samples; Fig. 7.9), which exist as alternating, metre-scale layers, and by the mobility of Ba, Sr and Cs, which, as discussed above, are commonly mobilised during serpentinisation (Deschamps et al. 2013). Given the spatial relationship between Modderfontein and Zandspruit, which are separated by over 25 km (Fig. 6.2), this implies that the geochemical effects of hydrothermal alteration were widespread throughout the ultramafic-mafic rocks of the Johannesburg Dome.

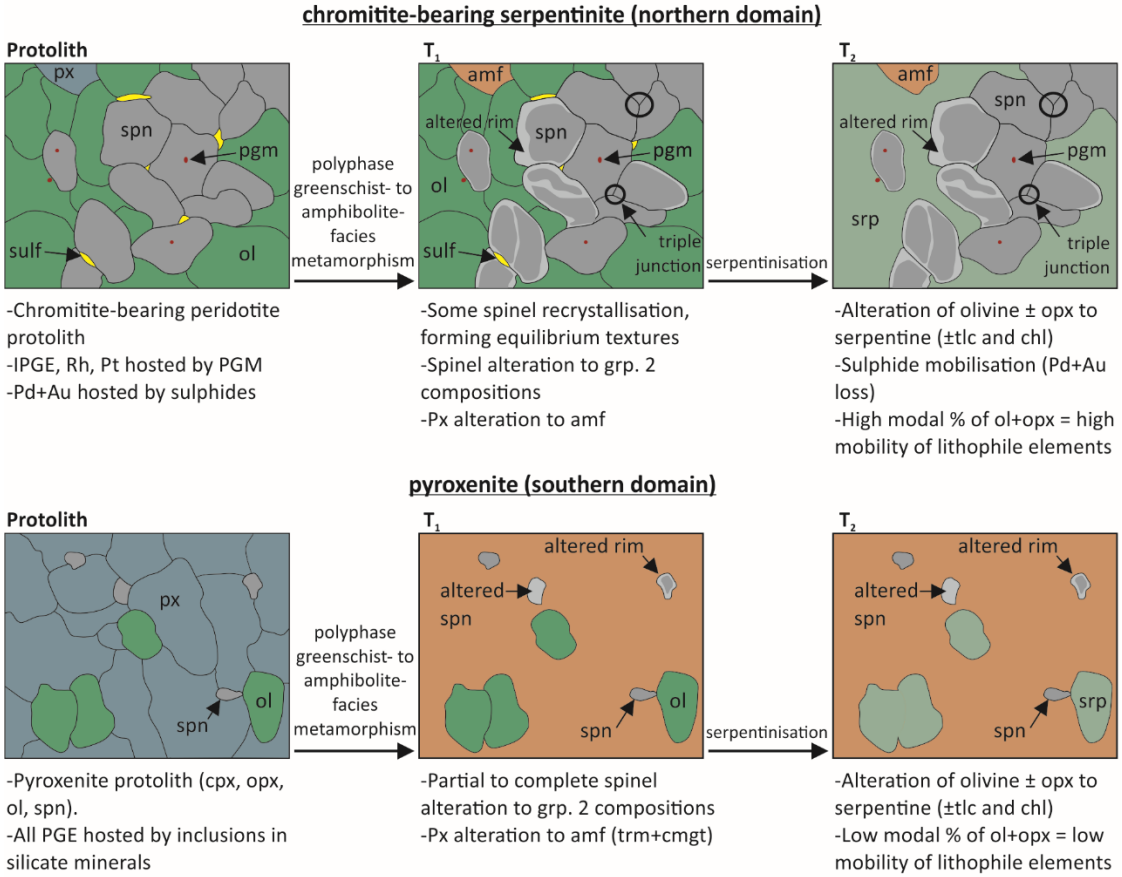

Figure 9.1: *Schematic diagrams summarising the microscopic petrographic and geochemical effects of greenschist- to amphibolite-facies metamorphism and serpentinisation on the primary Modderfontein rocks. Abbreviations: amf=amphibole; chl=chlorite; cmgt=cummingtonite; cpx=clinopyroxene; ol=olivine; PGM=platinum-group mineral; px=pyroxenite; spn=spinel; srp=serpentine; sulph=base-metal sulphide; trm=tremolite.*

9.1.1.3 Roodekrans

Relative to the Modderfontein and Zandspruit Complexes, the lithophile element mobility shown by the Roodekrans Complex is more difficult to constrain. Here, there is no systematic relationship between R^2 values and lithology, with Zr in the massive ultramafic rocks poorly correlated with Ti, Al, Y, Yb, Ho, Cs, Rb, La and Nd, but moderately to strongly correlated with Nb, Ta, Hf, Th and Ba (Fig. 8.3). In contrast, Zr in the mafic-ultramafic schists is poorly

correlated with Nb, Ta, Y, Ho, Ba, Rb, La, Ce and Nd, but moderately to strongly correlated with Ti, Al, Hf, Yb and Cs. Given the possible petrogenesis of the Roodekrans Complex (see Section 9.3.3 for details), it is possible that the mafic-ultramafic schists experienced a metasomatic episode prior to the emplacement of the massive ultramafic rocks. However, these R^2 values are the product of a small sample set (5 massive ultramafic rocks and 5 mafic-ultramafic schists) and, as care must be taken not to over-interpret these data, this is suggested only as a possibility. Irrespective of the precise processes involved, it is evident that the Roodekrans rocks (like those from the Modderfontein and Zandspruit Complexes) have been subject to at least one phase of metasomatism during a protracted magmatic and metamorphic history that includes multiple phases of greenschist- to amphibolite-facies metamorphism.

9.1.2 PGE mobility and PGM

The moderate to strong positive correlation between Pt and Pd in most samples from the Modderfontein (R^2= 0.5), Zandspruit (R^2= 0.8) and Roodekrans (R^2= 0.4) Complexes suggests that these elements were relatively immobile in the majority of the ultramafic rocks in the Johannesburg Dome. In the Modderfontein chromitite sample however, Os, Ir, Ru, Rh and Pt concentrations are an order of magnitude higher than the Pd concentration (Fig. 8.7), with its inclusion with the Modderfontein samples significantly reducing the correlation between Pt and Pd (R^2= 0.1). This suggests that this sample either: (i) experienced considerable depletion of Pd during secondary processes; or (ii) experienced considerable enrichment of Os, Ir, Ru, Rh and Pt (but not Pd) through either magmatic or hydrothermal processes.

Of the 20 PGM identified in the chromitite sample, 13 are sulphides and 7 are As-bearing phases. Arsenic-bearing PGM species can be the product of either secondary or high temperature processes (e.g., Gauthier et al. 1990; Prichard et al. 1994). The Os and Ru sulphides (erlichmanite and laurite, respectively) on the other hand are nearly always magmatic and, coupled with the absence of any IPGE alloys, are most consistent with relatively high fS_2 conditions and sulphide saturation during formation of the chromitite (Brenan and Andrews 2001, Holwell and McDonald 2007). The close spatial association between sulphide and arsenide-sulpharsenide PGM suggests that many of the latter have either primary or (at least) late-magmatic origin(s) analogous to the high temperature arsenide PGM recorded in settings such as the Great Dyke (Coghill and Wilson 1993), Lavatrafo Complex, Madagascar (McDonald 2008) and Sudbury, Canada (Dare et al. 2010). Once formed, these PGM often remain stable during serpentinisation and supergene

alteration and may effectively fix the IPGE (+ Rh and Pt) budgets of the rocks even at very high degrees of alteration (Mcdonald et al. 1999, Suárez et al. 2010, Smith et al. 2014).

In sulphide-bearing chromitites, Pd may be accommodated in both PGM and via solid solution in pentlandite (Holwell and McDonald 2007, Godel et al. 2007, Osbahr et al. 2013, Junge et al. 2014). Removal of sulphides during alteration, and pentlandite in particular, may potentially liberate significant amounts of Pd, particularly where semi-metals ligands (to form secondary Pd-PGM) are absent (Holwell et al. 2017). Consequently, it is considered most likely that Pd was preferentially mobilised (and removed) from former (interstitial) sulphides in the chromitite-bearing serpentinite sample during a secondary process(es). As with the lithophile element mobility outlined in Section 9.1.1, it is possible that such Pd mobility is associated with the hydrothermal alteration (including serpentinisation) of the Modderfontein Complex, with this suggestion supported by research conducted by Barnes and Liu (2012). These authors suggest that Pd is more soluble than Pt in sulphide mineral phases during hydrothermal alteration, and that it will be more readily mobilised as a result. Moreover, these authors suggest that such mobility can be achieved by relatively low-temperature (~300 °C) hydrothermal fluids (Barnes and Liu 2012), further supporting the hypothesis that Pd was mobilised by hydrothermal fluids associated with serpentinisation.

This selective Pd mobility – whereby Pd is immobile in the majority of the ultramafic-mafic rocks, but mobile in the chromitite – can likely be attributed to the different mineral phases hosting the PGE in the respective lithologies. In the majority of the ultramafic rocks in the Johannesburg Dome, the PGE are probably hosted by nanometre-scale PGM inclusions in silicate minerals, whereas these elements are demonstrably hosted by PGM sulphide mineral phases (and a primary base metal sulphide assemblage that is now absent) in the chromitite. This hypothesis – whereby the differential mobility of Pd is a function of different primary sulphide assemblages (Fig. 9.1) – is again supported the work by Barnes and Liu (2012), who described Pt and Pd as well correlated in S-poor environments, where the PGE are largely hosted by silicate phases.

9.1.3 Spinel Mineral Chemistry

In all 3 of the studied ultramafic-mafic complexes, spinel grains are subdivided into two compositionally distinct groups, with group 1 spinels enriched in TiO_2, Al_2O_3, MnO, MgO and Cr_2O_3, and depleted in FeO relative to the group 2 spinels.

The group 2 spinel compositions show almost complete overlap with the greenschist- to amphibolite-facies rims field on all plots (Figs. 7.7, 7.12 and 7.18; Barnes and Roeder, 2001),

demonstrating that they were derived from secondary processes. These altered (group 2) spinel compositions most commonly occur as rims on group 1 spinels (e.g., Figs. 7.6 and 7.16) suggesting that they were derived from alteration of primary (group 1) spinel. This alteration led to decreases in the TiO_2, Al_2O_3, MnO, MgO and Cr_2O_3 contents, and increases in the FeO contents of the group 1 spinels. In addition, some group 1 spinels have been completely altered to group 2 compositions (e.g., Figs. 7.6 and 7.17; Fig. 9.1). In contrast, the group 1 spinels, which commonly form spinel cores, are geochemically distinct from the field for greenschist- to amphibolite-facies recrystallised rims, recording compositions that are interpreted to be most close to primary and that show significant overlap with the komatiite and layered intrusion fields (Figs. 7.7, 7.12 and 7.18). It should be noted however, that the group 1 spinels may have experienced some enrichment in the most immobile elements (e.g., Cr and Ti) as a result of the alteration to group 2 compositions, with this process potentially generating some of the observed geochemical scatter within the group 1 compositions.

As spinels are used as a petrogenetic indicator in rocks of various ages (Wood 1990, Barnes and Roeder 2001), including in regions that have experienced multiple phases of amphibolite- to granulite-facies metamorphism (e.g., Kusky and Jianghai 2010, Szilas et al. 2014, 2015), these data demonstrate that a rigorous assessment of spinel texture and composition should be undertaken prior to invoking any such interpretation. Despite the partial- to complete-alteration of spinel grains and significant element mobility identified using the bulk-rock data described above, the Modderfontein, Zandspruit and Roodekrans Complexes record spinel compositions that are interpreted as close to primary and that can therefore be utilised to aid petrogenetic interpretations. Consequently, although caution is advised, spinel is potentially an important tool for petrogenetic interpretations in areas that have experienced significant metamorphism, alteration and associated element mobility, such as the Johannesburg Dome.

Further to the work of Anhaeusser (2015), who suggested that a suite of elements had been mobilised at Zandspruit, the preceding subsections outline the extensive evidence for element mobility (including elements generally considered immobile) experienced by the ultramafic-mafic complexes in the Johannesburg Dome. This outlines the requirement for rigorous petrographic and geochemical assessments (on a case-by-case basis) prior to applying geochemical-based geodynamic interpretations to Archaean rocks, as demonstrated by several previous authors (Collerson and Kamber 1999, Condie 2003, 2005, Babechuk and Kamber 2011). In the case of the ultramafic-mafic complexes studied here,

multiple phases of greenschist- to amphibolite-facies metamorphism led to (Fig. 9.1): the alteration of spinel compositions to those with higher abundances of FeO, and lower abundances of TiO_2, Al_2O_3, MnO, MgO and Cr_2O_3; the amphibolitisation of clinopyroxene to tremolite and subsequently cummingtonite; and, in the case of the Modderfontein chromite, recrystallisation of chromite grains. The subsequent hydrothermal alteration of the ultramafic-mafic rocks is here interpreted to have had a more profound effect on the bulk-rock geochemistry, resulting in (Fig. 9.1): significant mobility of lithophile elements, including selected elements generally considered immobile; and some removal of Pd and Au from the chromitite-bearing serpentinite at Modderfontein. Importantly, the data indicate that the modal % of olivine in the primary Modderfontein and Zandspruit rocks exercises a degree of control on lithophile element mobility, while the mobility of Pd is controlled by the degree to which it is hosted in PGM or BMS. Moreover, the effects of hydrothermal alteration on bulk-rock geochemistry appear widespread across the Johannesburg Dome, having had similar effects on the geochemistry of the Modderfontein and Zandspruit (± Roodekrans) Complexes, which are located more than 25 km apart.

9.2 Origin of the ultramafic-mafic complexes

As outlined in Chapter 6, the ultramafic-mafic complexes of the Johannesburg Dome have been collectively interpreted as representing either: fragment(s) of an Archaean ophiolite(s) (e.g., Anhaeusser 2006); or the intrusive and/or extrusive remnants of Archaean greenstone belts (Anhaeusser 1977). The succeeding discussion evaluates the various merits of the two previously proposed hypotheses for the Modderfontein, Zandspruit and Roodekrans Complexes in the context of the data presented in Chapter 7 and 8, and with the evidence for element mobility outlined above.

9.2.1 Ophiolite fragment(s)

The distinctive presence of chromitite lenses, which occur in association with the northern domain serpentinites at Modderfontein, may be interpreted (based on field observations alone) as podiform chromitites, with this interpretation suggestive of an ophiolitic origin for the ultramafic-mafic complexes in the Johannesburg Dome. In this scenario, the Modderfontein Complex would represent residual upper mantle, where podiform chromitites commonly form in association with dunite melt channels through peridotite (Arai and Yurimoto 1994, Arai and Miura 2015, 2016), while the Zandspruit and Roodekrans Complexes would represent other portions of the potential ophiolite. This interpretation is supported by *some* aspects of the PGM mineralogy from the Modderfontein chromitite (as

detailed in Section 7.1.2.1), with 14 of the 20 PGM identified being IPGE-rich species (e.g., erlichmanite, laurite and irarsite; Table 7.1; Fig. 7.5). This assemblage is consistent with podiform chromitites in Phanerozoic ophiolites, which are generally dominated by IPGE-PGM (González-Jiménez et al. 2009), although PPGE-rich PGM species are prominent in some examples (Tarkian and Prichard 1987, Prichard and Lord 1990, Prichard et al. 1994, Ahmed and Arai 2003). Moreover, laurite-erlichmanite (solid-solution series) is the most common PGM in the Modderfontein Complex chromitite, which is also consistent with Phanerozoic ophiolites generally (Stribrny et al. 2000, Ahmed and Arai 2003, González-Jiménez et al. 2009). However, this hypothesis is inconsistent with other aspects of the PGM and PGE geochemistry recorded by the Modderfontein Complex. First, although laurite-erlichmanite (solid-solution series) are the most common PGM, ophiolites characteristically also contain IPGE alloys that are entirely absent in the Modderfontein chromitite (Ahmed and Arai 2003, González-Jiménez et al. 2009). As outlined in Section 7.1.2, it is unlikely that the Modderfontein chromitite originally contained primary magmatic IPGE alloys that were subsequently mobilised. Second, the bulk-rock PGE pattern for the Modderfontein chromitite (Fig. 8.7) was originally positively fractionated, with Rh and Pt enriched over the IPGE (Section 8.4.1), whereas those for ophiolitic chromite generally exhibit IPGE-rich/PPGE-poor patterns with negative slopes (Barnes et al. 1985). Third, as described in Section 9.1.2, the PGM species are consistent with sulphur-saturation and relatively high fS_2 conditions, with this extremely rare in ophiolites.

The ophiolite hypothesis is also inconsistent with the major and trace element geochemical characteristics of the ultramafic-mafic complexes in the Johannesburg Dome (including those of the Modderfontein chromitite lenses), which are distinct from the established geochemical characteristics of ophiolitic rocks. First, the composition of the group 1 chromite within the Modderfontein chromitite lenses are distinct from the chromitite with Phanerozoic podiform chromitites (Fig. 7.8). Relative to these Phanerozoic examples, the Modderfontein Complex chromitite lenses are systematically depleted in Cr_2O_3 and Al_2O_3, and enriched in TiO_2 (Fig. 7.8). Second, primary (group 1) spinel (see Section 9.1.3) from all other lithologies in the Modderfontein, Zandspruit and Roodekrans Complexes exhibits compositions that are consistently compositionally distinct from the established field (Barnes and Roeder 2001) for ophiolites and oceanic peridotites (Figs. 7.7, 7.12, 7.18; Table 7.5). Third, the trace element abundances displayed by the Modderfontein, Zandspruit and Roodekrans Complexes are at least 2 orders of magnitude greater than those for oceanic mantle residue (Figs. 8.2–8.6), with no evidence for systematic enrichment of all trace

elements by secondary processes (Section 9.1.1). The geochemical distinction between the ultramafic-mafic complexes of the Johannesburg Dome and the established field for ophiolitic rocks is well-illustrated on both bivariate (Figs. 8.2–8.3) and normalised (Figs. 8.4–8.6) plots. Fourth, the composition of the ultramafic-mafic complexes are distinct from those of Phanerozoic ophiolites and abyssal peridotites on major element bivariate plots. Relative to these rocks, the Modderfontein, Zandspruit and Roodekrans Complexes are depleted in MgO and NiO, and enriched in SiO_2, TiO_2, Al_2O_3, Fe_2O_3, CaO and Cr_2O_3 (Fig. 8.1).

In summary, the petrographic and geochemical evidence presented in Chapters 7 and 8 demonstrate that the ultramafic-mafic complexes in the Johannesburg Dome are unlikely to represent fragment(s) of an Archaean ophiolite(s), as proposed by Anhaeusser (2006a).

9.2.2 Greenstone belt remnants

The geochemical characteristics of the Modderfontein, Zandspruit and Roodekrans rocks are more suggestive of a greenstone belt-related origin for the ultramafic-mafic rocks in the Johannesburg Dome. First, the bulk-rock major element compositions and trends are comparable to those shown by the extrusive ultramafic-mafic rocks from the Barberton Greenstone Belt (Onverwacht Group), with all 3 complexes showing near-complete overlap with this field on MgO versus SiO_2, Al_2O_3, Fe_2O_3, CaO and NiO plots (Fig. 8.1). Moreover, the Modderfontein and Roodekrans Complexes show near-complete overlap with this field on the MgO versus Cr_2O_3 and TiO_2 plots (Fig. 8.1). Second, the trace element compositions of the Modderfontein, Zandsprtuit and Roodekrans Complexes also show significant overlap with the extrusive ultramafic-mafic rocks from the Barberton Greenstone Belt, with all 3 complexes showing compositions and trends comparable to this field on the majority of Zr versus (generally) immobile element plots (Figs. 8.2–8.3). This is reinforced by normalised plots, which demonstrate that all 3 complexes show significant or complete overlap with the field for the Komatii Formation (Chapter 6) komatiites (Figs. 8.4–8.6). The affiliation between the Johannesburg and Barberton rocks on such plots is strongest for elements that have experienced limited mobility (e.g., Hf and Nb) and weakest for elements that have experienced significant mobility (e.g., Ba; Section 9.1.1; Figs. 8.2–8.3). Third, the chemistry of group 1 (primary; see Section 9.1.3) spinel grains from all 3 of the studied complexes display consistent overlap with the previously established (Barnes and Roeder 2001) field for komatiites (Figs. 7.7, 7.12 and 7.18; Table 7.5). However, this interpretation is questioned slightly by the fractionated, rather than flat, chondrite-normalised PGE patterns exhibited by the Modderfontein and Zandspruit Complexes (Fig. 8.7). Although these PGE patterns are distinct from the field for Komatii Formation komatiites, they show significant overlap with

this field and, as described in Section 7.3, likely result from the specific petrogenetic environment(s) represented by the two Complexes (Fig. 9.2). Consequently, it is considered likely that the ultramafic-mafic complexes in the Johannesburg Dome represent various intrusive and extrusive greenstone belt remnants, with the individual Complexes derived from a similar magma(s).

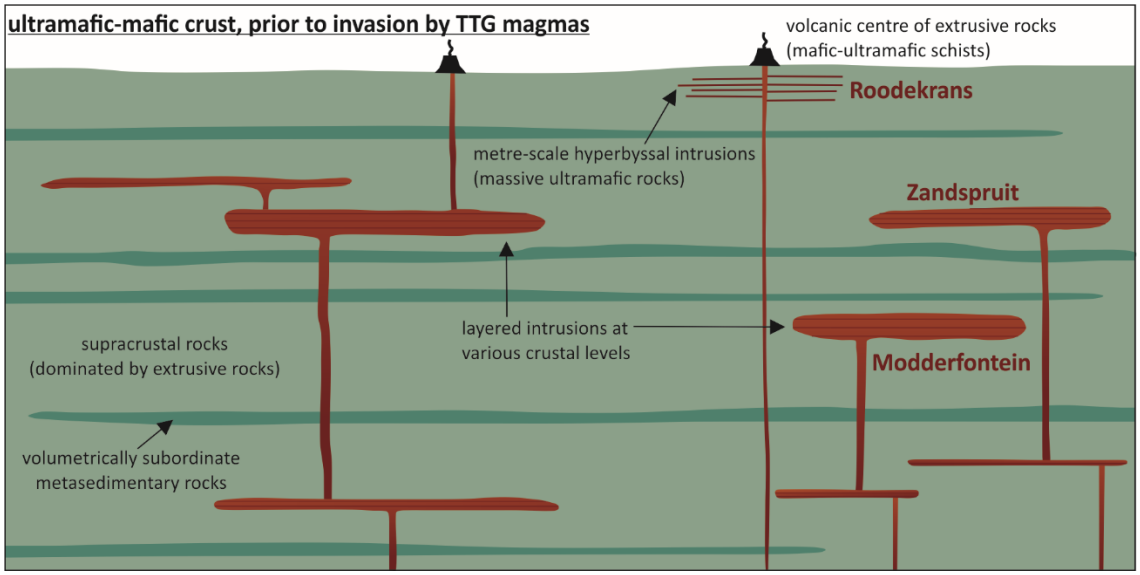

Figure 9.2: *Schematic diagram summarising the envisaged geodynamic environment within which the ultramafic-mafic complexes of the Johannesburg Dome formed, including individual petrogenetic interpretations for the Modderfontein, Zandspruit and Roodekrans Complexes.*

9.3 Petrogenesis

While the Modderfontein, Zandspruit and Roodekrans Complexes share many characteristics, the 3 occurrences exhibit some unique field, petrographic and geochemical features that can likely be attributed to subtly different petrogenetic environments (within a common extrusive-intrusive greenstone belt succession; see Section 9.2.2). The succeeding paragraphs discuss the potential petrogenetic environments represented by the Modderfontein, Zandpsruit and Roodekrans Complexes, with a summary diagram provided in Figure 9.2. However, given the degree of element mobility experienced by the ultramafic-mafic rocks of the Johannesburg Dome (Section 9.1), over-interpretation of the geochemical data is avoided and the individual hypotheses should be treated as suggestions. Moreover, the rapid (and ongoing) urban expansion between Johannesburg and Pretoria over the preceding decades has greatly reduced exposures of ultramafic-mafic rocks in the Johannesburg Dome (see Figs. 7.12 and 7.13 for details). The studied complexes therefore represent a small fraction of the ultramafic-mafic rocks in the Johannesburg Dome, and may

not be wholly representative. These caveats should be considered throughout the succeeding sections, which make suggestions on the basis of the data presented in this thesis.

9.3.1 Modderfontein

For the Modderfontein Complex, the coarse grain size of the un-serpentinised lithologies and presence of layering on a scale of tens of metres (Fig. 7.2) is suggestive of a layered intrusion origin for the Modderfontein Complex, with this interpretation supported by several petrographic and geochemical characteristics. First, 100 % of the PGM identified from the Modderfontein Complex chromitite are either PGM sulphides or PGM arsenides, with PGM in layered intrusions generally hosted by either PGM bismuthides, sulphides or arsenides (Stribrny et al. 2000). Second, a significant part of the Pd budget in layered intrusions is hosted by base-metal sulphides such as pentlandite, rather than PGM (Godel et al. 2007, Holwell and McDonald 2007, Osbahr et al. 2013, Junge et al. 2014). Third, the chondrite-normalised PGE patterns for the Modderfontein Complex are generally mildly to moderated fractionated, which is characteristic of layered intrusions (Barnes et al. 1985). However, this hypothesis is questioned slightly by the absence of any obvious layering in the northern domain of the Complex (Fig. 7.1), and the composition of spinel, which only shows partial overlap with the stratiform chromitite field on the Cr_2O_3 versus Al_2O_3 plot (Fig. 7.8). Despite these inconsistencies, it is considered that the Modderfontein Complex most likely represents an intrusive complex, whereby the ultramafic-mafic rocks represent metamorphosed and altered cumulates (Fig. 9.2).

9.3.2 Zandspruit

Similarly, the coarse size of pseudomorphed pyroxene and olivine in the metapyroxenites of the Zandspruit Complex (Fig. 7.11) are suggestive of an intrusive origin, with this hypothesis supported by several field and geochemical features. First, as shown by previous mapping (Fig. 7.9b) and new logging (Fig. 7.9c), the Zandspruit Complex exhibits metre-scale layering characteristic of layered intrusions (Namur et al. 2015). Second, the chondrite-normalised PGE patterns are mildly fractionated, and third, the composition of group 1 (see Section 9.1.3) spinel grains show considerable overlap with the established layered intrusion field (Barnes and Roeder 2001; Fig. 7.7). Consequently, it is considered likely that the Zandspruit Complex represents an intrusive complex, whereby the ultramafic rocks represent metamorphosed and altered cumulates (Fig. 9.2).

9.3.3 Roodekrans

For the Roodekrans Complex, the mafic-ultramafic schists likely represent extrusive rocks, as initially proposed by Anhaeusser (1977). First, there is no evidence of coarser grains having been pseudomorphed by alteration minerals (e.g., tremolite, cummingtonite, serpentine, talc and chlorite; Fig. 7.16), as is evident at Modderfontein and Zandspruit Complexes (Figs. 7.4 and 7.11). Second, the chondrite-normalised REE and primitive mantle-normalised trace element patterns for the mafic-ultramafic schist and analysed pillow lava sample are consistently parallel, with the relative depletion of the former indicating that they represent relatively primitive melts, when compared to the pillow lava. While the origin of the massive ultramafic rocks is more cryptic, it is possible that these rocks represent hypabyssal intrusions that were emplaced *into* the surrounding extrusive rocks at relatively shallow crustal levels (Fig. 9.2), as originally suggested by Anhaeusser (1977). This interpretation is supported by the normalised trace element patterns for the massive ultramafic rocks, which are distinctive from the mafic-ultramafic schists (with which they are spatially associated) but comparable to the Zandspruit ultramafic rocks (Figs. 8.5–8.6). It is therefore probable that the Roodekrans Complex collectively represents mafic-ultramafic rocks formed at extremely shallow crustal levels, with the rocks preserved being a combination of supracrustal volcanic rocks and hypabyssal intrusions (Fig. 9.2).

Part Three:

Synthesis

Chapter 10

Synthesis

This thesis focuses on ultramafic-mafic complexes in the LGC and Johannesburg Dome, combining detailed field investigations with petrography, lithophile element bulk-rock geochemistry, PGE bulk-rock geochemistry, silicate mineral chemistry and spinel mineral chemistry. In order to expand on the largely craton-specific objectives tackled in Parts One and Two, this chapter engages with the broader Archaean geodynamics debate by focusing on the following aims, as outlined in Chapter 1:

a) Critically evaluate geochemical proxies that may be used to interpret ultramafic rocks in Archaean cratons.

b) Investigate the origin of the ultramafic-mafic complexes in the North Atlantic and Kaapvaal Cratons.

c) Assess any implications for Archaean geodynamic regimes.

d) Evaluate the possibility that ultramafic-mafic complexes represent a primary source of placer PGM.

The following sections will directly address these aims by drawing together the findings from the two parts of this thesis, with Section 10.1 addressing aim (a), Section 10.2 addressing aim (b), Section 10.3 addressing aim (c), and Section 10.4 addressing aim (d). These sections refer back to relevant material from Parts One and Two, and illustrate key points by re-presenting and combining important data.

10.1 Geochemical proxies for interpreting ultramafic rocks in Archaean cratons

10.1.1 Lithophile element bulk-rock geochemistry

Lithophile element bulk-rock geochemistry is a traditional method for investigating the origin and magmatic affinity of igneous rocks, including those of Archaean age (e.g., Pearce and Cann 1973, Floyd and Winchester 1975, Winchester and Floyd 1976, 1977, Floyd and Winchester 1978, Wood et al. 1979, Shervais 1982, Pearce and Peate 1995, Pearce 1996, Hastie et al. 2007, Pearce 2008, Agrawal et al. 2008, Polat et al. 2009, 2011, Verma and Verma 2013, Furnes et al. 2015, Polat et al. 2016, Verma et al. 2017). Principally, such investigations

utilise normalised plots and/or discrimination diagrams to aid interpretation, with the succeeding sections exploring the effectiveness of these methods individually.

10.1.1.1 Normalised plots

Chondrite-normalised REE and primitive mantle-normalised trace element plots are commonly used to visualise trace element data, with elements ordered according to compatibility (Rollinson 1993). The normalised abundances and patterns illustrated by such plots can be used to aid petrogenetic/geodynamic interpretations of igneous rocks (e.g., Klemme et al. 2005), including those of Archaean age (e.g., O'Neil et al. 2011, Yellappa et al. 2012, 2014, Wang et al. 2015, Guo et al. 2017). For example, negative Eu anomalies are commonly attributed to the removal of feldspar during fractional crystallisation, while the extreme depletion of HREE relative to LREE may indicate the presence of garnet in the melt source region (Eby 1992, Rollinson 1993).

In Chapter 9, normalised plots are utilised to test two end-member (and relatively broad) hypotheses, with the ultramafic-mafic complexes in the Johannesburg Dome previously interpreted as representing either: fragment(s) of an Archaean ophiolite(s) (Anhaeusser 2006b); or the intrusive/extrusive remnants of Archaean greenstone belts (Anhaeusser 1977). Such plots (Fig. 8.4–8.6) demonstrate that the normalised trace element abundances shown by the Modderfontein, Zandspruit and Roodekrans Complexes are at least 2 orders of magnitude greater than those for oceanic mantle residue preserved in Phanerozoic ophiolites. Instead, the data show significant overlap with the field for Komatii Formation komatiites (from the Barberton Greenstone Belt; Fig. 6.1), implying that the Archaean greenstone belt hypothesis is the more likely of the two previously proposed. This assertion is further supported by major element bulk-rock geochemistry, spinel mineral chemistry and field relationships, with the greenstone belt hypothesis favoured as a result.

Chapter 4 investigates the validity of using HFSE anomalies (on normalised trace element plots) to fingerprint subduction-related magmatism in the Archaean Eon, as has been applied to some Archaean ultramafic-mafic intrusive and/or extrusive rocks (Manya 2004, Ordóñez-Calderón et al. 2009, Yellappa et al. 2012, 2014, Wang et al. 2015, Guo et al. 2017). In the case of the Ben Strome ultramafic rocks, the HFSE anomalies were most likely generated by LREE enrichment during metasomatism associated with amphibolitisation, rather than reflecting a signature inherited from subduction-related magmatism (see Fig. 4.14 and associated text for a comprehensive summary). This hypothesis is reached by placing the studied bulk-rock samples within the context provided by detailed mapping (Chapter 3) and

petrography, and by combining these data with major and trace element mineral chemistry. Crucial to this investigation was the characterisation of element mobility, which was conducted using the method detailed in Figure 8.2 (developed after: Cann 1970).

The trace elements included on normalised plots are variably mobile, with adjacent elements displaying differing mobilities within individual scenarios (Fig. 10.1) due to the ordering of elements along the x axis. For example, in the Ben Strome Complex ultramafic rocks (Chapter 4), La, which is highly mobile in the group 2 and 3 samples, is located next to Ta, which was relatively immobile in the same rocks, resulting in the observed apparent negative HFSE anomalies (Fig. 4.14; Fig. 10.1a). Moreover, the suite of elements mobilised is specific to the metasomatic and metamorphic history of individual ultramafic-mafic complexes. Element mobility may be either restricted to the most mobile elements (e.g., K, Ba), or extended to a suite of elements typically considered immobile (e.g., LREE and MREE), but which are demonstrably mobile (e.g., Chapters 4 and 9). Consequently, trace element patterns may reflect the local/regional metamorphic and metasomatic history of a portion of Archaean crust, rather than any primary magmatic processes, rendering inter-craton comparisons unreliable. HFSE anomalies alone are therefore considered an unreliable proxy for Archaean subduction, with the very nature of normalised plots ensuring that trace element patterns are highly susceptible to the effects of element mobility.

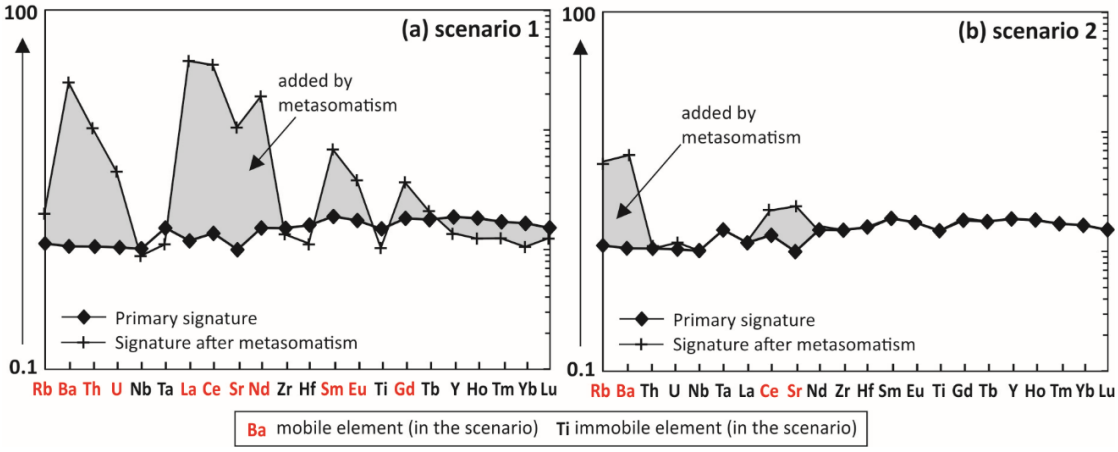

Figure 10.1: *Primitive mantle-normalised trace element plots for a hypothetical ultramafic rock subject to two metasomatic episodes that mobilised different suites of elements. In scenario 1, whereby a large suite of elements is mobilised, distinctive negative HFSE anomalies are generated. Scenario 2, where a small suite of elements (those typically considered mobile) is mobilised, a broadly flat pattern is preserved.*

To illustrate this point, Figure 10.1 presents two hypothetical scenarios, whereby an ultramafic rock with an initially flat trace element pattern is subject to different metasomatic and metamorphic histories, mobilising different suites of elements. In scenario 1, a large suite

of elements are mobilised, resulting in apparent negative HFSE anomalies as elements immediately adjacent the HFSE are increased without commensurate changes in the HFSE (Fig. 10.1). In scenario 2, mobility is restricted to elements typically considered mobile, with a smaller suite of elements mobilised and the broadly flat pattern largely preserved. Archaean ultramafic rocks (irrespective of whether they are intrusive or extrusive) may therefore owe their trace element patterns (at least in-part) to the specific metasomatic and metamorphic conditions experienced by the Archaean crust within which they are located. Such differences, which will be most pronounced on the craton-scale, may also implicate intra-craton comparisons, as hydrothermal alteration and associated metasomatism may be restricted to localised structures, such as shear zones, faults or lithological contacts. When considered in isolation, trace element patterns on normalised plots are here considered a poor proxy for interpreting the origin and geodynamic significance of Archaean ultramafic rocks. However, such patterns may be useful from a primary magmatic point-of-view, providing detailed field-based, petrographic and mineral chemical studies are first used to constrain the likelihood and extent of regional-scale element mobility (see Chapter 4).

10.1.1.2 Discrimination diagrams

Discrimination diagrams – whereby trace element ratios (e.g., Nb/Th) are plotted on bivariate and ternary plots – are routinely used to fingerprint Phanerozoic magmatic processes and geotectonic environments (e.g., Pearce and Cann 1973, Hastie et al. 2007, Pearce 2008 and references therein), with some authors extending their use to the Archaean (Polat et al. 2009, 2011, Szilas et al. 2013, Furnes et al. 2015, Polat et al. 2016, Chandan-Kumar and Ugarkar 2017). These diagrams, which were originally developed using well-constrained Phanerozoic samples, generally utilise volcanic rocks and discard elements generally considered mobile (e.g., K and Ba), instead focusing on elements considered to be the most immobile (e.g., Zr, Hf, Nb, Ta, Y, Ti, Cr, the REE, Th, Ga and Sc; Hastie et al. 2007 and references therein). However, as discussed above (Section 10.1.1.1), some of these elements can be mobilised during metamorphism (above greenschist-facies) and/or by specific hydrothermal fluids (e.g., Hynes 1980, McCulloch and Gamble 1991, Lahaye et al. 1995, Pearce 1996, Hill et al. 2000, Hastie et al. 2007, Honour et al. 2018). For example, Lahaye et al. (1995) identify REE mobility in komatiites from the Barberton and Abitibi Greenstone Belts following interaction with CO_2-rich fluids.

Polat et al. (2011, 2016) utilised a range of trace element ratios to compare Archaean ultramafic-mafic rocks from Greenland with Phanerozoic arc rocks, including a chondrite-normalised La/Sm versus Gd/Yb plot (Fig. 10.2a) and a La/Nb versus Th/Nb plot (Fig. 10.2b).

Based on the significant overlap with the Phanerozoic arc rocks (Fig. 10.2a-b), the studied Archaean rocks were interpreted as the product(s) of subduction-related magmatism directly comparable to modern analogues. However, as shown in Chapter 4, some of the elements incorporated into these trace element ratios (e.g., La and Gd) may be mobilised under some conditions (Lahaye et al. 1995, Hill et al. 2000, Polat and Hofmann 2003, Polat et al. 2003), severely reducing the confidence with which such plots can be used to compare rock from different Eons. While Phanerozoic arc rocks are unlikely to have experienced extensive metasomatism, those in Archaean cratons have generally been subject to multiple phases of high-grade (amphibolite- and granulite-facies) metamorphism and associated metasomatism. To illustrate this point, Figure 10.2(c-d) compares group 1 ultramafic rocks from the Ben Strome Complex (where La, Sm, Gd and Th were relatively immobile; Chapter 4) with the group 2 and 3 samples, which have been variably enriched in La, Sm, Gd and Th. In both examples (Fig. 10.2c-d), the group 1 samples form tight clusters, while the group 2 and 3 samples exhibit large ranges in their La/Sm, Gd/Yb, La/Nb and Th/Nb ratios. If all of the Ben Strome ultramafic rocks had been subject to the same metasomatism (and therefore all of the Ben Strome rocks displayed group 2 and 3 compositions), these plots would provide an unrealistic image of the primary trace element geochemistry of the Ben Strome rocks, rendering comparisons to relatively unaltered Phanerozoic rocks unreliable.

The Nb/Yb versus Th/Yb plot – developed by Pearce (2008) to fingerprint oceanic basalts and ultimately distinguish them from non-oceanic basalts – has been applied to Archaean rocks by several authors (e.g., Polat et al. 2009, 2011, Szilas et al. 2013, Furnes et al. 2015, Polat et al. 2016, Chandan-Kumar and Ugarkar 2017). Many authors use the position of samples above the MORB-OIB array (Fig. 10.3) as evidence supporting a subduction-related magmatic origin for the studied rocks. However, as shown in Chapter 4, Th is capable of being mobilised by hydrothermal fluids during amphibolitisation. To illustrate the effect that Th enrichment may have on the position of samples on the Nb/Yb versus Th/Yb plot, Figure 10.2 compares group 1 ultramafic rocks from the Ben Strome Complex with the group 2 and 3 samples, which experienced Th enrichment by secondary processes.

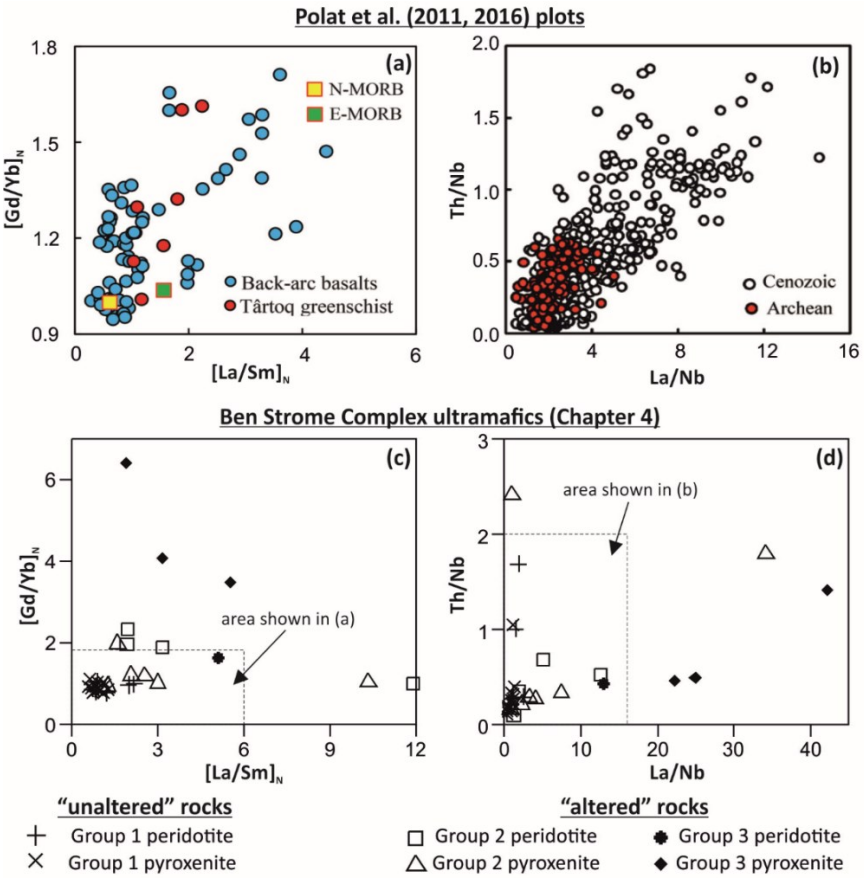

Figure 10.2: (a-b) *Selected trace element bivariate plots used to interpret the magmatic affinity of Archaean mafic (predominantly extrusive) rocks from Tartoq, Greenland (Polat et al. 2011, 2016), including a comparison to modern back-arc basalts.* ***(c-d)*** *Equivalent plots for the Ben Strome Complex ultramafic rocks, as in Chapter 4. Note: all plots normalised using values of* McDonough and Sun (1995).

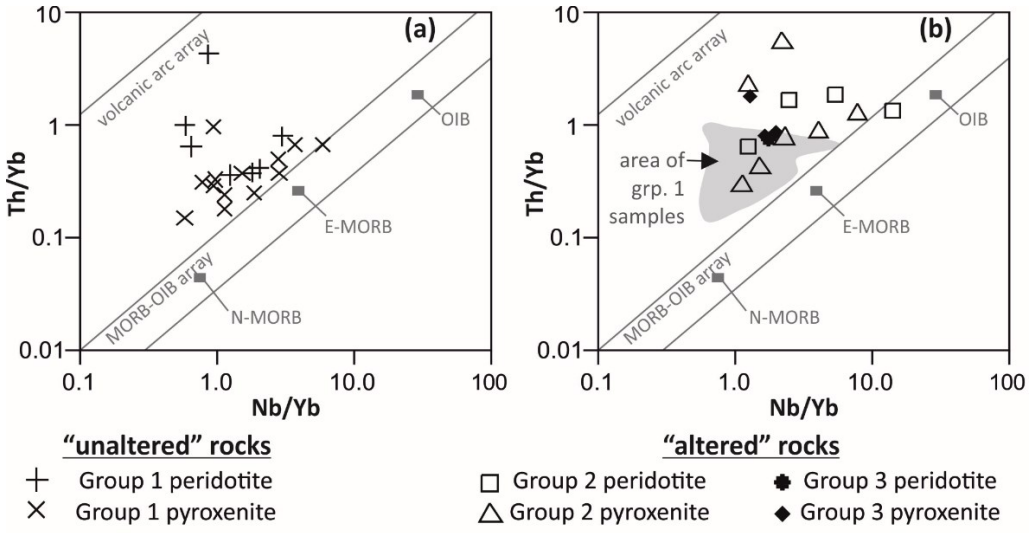

Figure 10.3: *Nb/Yb versus Th/Yb plot, including the established fields often used to interpret Archaean volcanic rocks (e.g., Pearce 2008 and references therein).* ***(a)*** *Group 1 (relatively unaltered) ultramafic rocks from the Ben Strome Complex.* ***(b)*** *Group 2 and 3 ultramafic rocks from the Ben Strome Complex, which have experienced significant mobility of some elements (e.g., LREE and Th) typically considered immobile. Note: the shaded area in part (b) omits the high Th/Yb outlier.*

Irrespective of the issues associated with element mobility outlined above, the uncritical application of discrimination diagrams to Archaean rocks may be subject to greater uncertainty than many authors appreciate or are willing to admit. Such diagrams are based upon modern-style plate tectonics, with individual geodynamic environments extremely well-constrained by the access to modern analogues. However, the application of such plots to the Archaean – an Eon within which the geodynamic regime(s) and associated processes are highly uncertain (see Chapter 1) – is fraught with uncertainty. While it is possible that the geodynamic processes that operated 4.0–2.5 Ga were comparable to those observed on Earth today, it is highly unlikely that the geochemical effects of the equivalent Archaean processes exactly mirror those well-constrained in the Phanerozoic. This secular geochemical and geodynamic evolution is supported by the temporal distribution of komatiites throughout the geological record (concentred largely within the Archaean Eon; Storey et al. 1991; Kerr et al. 1996), and by the reported secular geochemical evolution of the Earth (Smithies et al. 2018, Moyen and Laurent 2018, Halla 2018, Johnson et al. 2019; see Section 1.1.2).

10.1.2 PGE bulk-rock geochemistry

The PGE budget of a melt is ultimately controlled by: (a) the degree of mantle melting (Lorand et al. 2008); (b) various magmatic and petrogenetic processes, such as crustal contamination, fractional crystallisation and sulphur saturation (e.g., Singh et al. 2016); and (c) the nature (e.g., mineralogy of PGE hosts and prior melt extraction) of the mantle source (e.g., Rehkämper et al. 1999, Lorand et al. 2013). PGE geochemistry can therefore be utilised to interpret the geodynamic and petrogenetic history recorded by magmatic rocks, including those of Archaean age (Barnes et al. 1985, Barnes 1990, McDonald and Viljoen 2006, Ismail et al. 2014, Najafzadeh and Ahmadipour 2014, Saha et al. 2015, Singh et al. 2016). For example, low degrees of partial melting produces high Pd/Ir ratios in the melt (with the IPGE-rich sulphides retained in the restite), while higher degrees of partial melting (> 20 %) consumes the IPGE-rich sulphides (and alloys) and generates lower Pd/Ir ratios (Alard et al. 2000, Lorand et al. 2008). Importantly, this process is considered responsible for the characteristically IPGE-rich/PPGE-poor nature of residual mantle rocks (Barnes et al. 1985). Fingerprinting such processes using PGE, and ultimately distinguishing between ultramafic-mafic rocks with different geodynamic and petrogenetic affinities, is principally achieved using normalised plots (Naldrett et al. 1979, Barnes et al. 1985, Rollinson 1993) and bivariate plots (e.g., Barnes 1990).

Chondrite-normalised PGE plots, whereby the PGE (and Au) are plotted in order of decreasing melting point (Naldrett et al. 1979, Rollinson 1993), are particularly useful for visualising the degree of PGE fractionation (expressed as $[Pd/Ir]_N$ or PPGE/IPGE), with Barnes et al. (1985) attempting to characterise the PGE patterns for a range of petrogenetic/geodynamic environments (e.g., layered intrusions, ophiolites and komatiites). In Chapter 5, such plots (alongside field and spinel geochemical evidence) aid the distinction between two groups of ultramafic-mafic complex, with one interpreted to represent layered intrusions (the Type A complexes) and another interpreted to represent a pre-TTG ultramafic-mafic crust (the Type B complexes). While the Type A complexes show consistent mild-moderate fractionated PGE patterns, those displayed by the Type B complexes are more variable, with a variety of IPGE-rich, flat and strongly fractionated PGE patterns (Fig. 5.10). In Chapter 9, normalised plots aid the testing of the ophiolite and greenstone belt hypotheses (as described in Section 10.1.1.1), with the fractionated PGE patterns shown by the Modderfontein Complex silicate rocks and chromitite inconsistent with residual mantle rocks from Phanerozoic chromitites (Barnes et al. 1985).

Another method for interpreting PGE data is the use of bivariate plots as discrimination diagrams (Barnes et al. 1988, Barnes 1990). In a well-cited study, Barnes et al. (1988) established a series of geodynamic/petrogenetic fields (e.g., layered intrusions, ophiolites) based on Pd/Ir and Ni/Cu ratios, with several authors applying this method to Archaean ultramafic-mafic rocks (Najafzadeh and Ahmadipour 2014, Saha et al. 2015, Singh et al. 2016). Although Pd/Ir ratios are certainly useful (providing appropriate caution is applied; as described above), Cu is highly susceptible to hydrothermal alteration and is highly mobile in Archaean ultramafic-mafic rocks (e.g., Feng et al. 1993). The Ni/Cu ratio may therefore be controlled by the degree of Cu mobility (enrichment or depletion), with this proxy considered unreliable when applied to Archaean rocks that have been subject to multiple phases of high-grade metamorphism and associated metasomatism.

Moreover, while the IPGE (+Rh) are considered relatively immobile during hydrothermal alteration, Pd, Pt and Au can all be mobilised to different degrees (Watkinson and Ohnenstetter 1992, McDonald et al. 1995, 1999, Baker et al. 2001, Peregoedova et al. 2006, Wang et al. 2008, Said et al. 2011, Barnes and Liu 2012), with the degree of element mobility controlled by the solubility of these elements and the nature of the host phase(s) experiencing alteration (Singh et al. 2016). The latter control – whereby PGE mobility is controlled by the host phase(s) – is reinforced by the data presented from the Modderfontein Complex (in Chapters 7-9; see Section 9.1.2). In the majority of the Modderfontein Complex

rocks, the PGE, which are hosted by silicate mineral phases, are immobile. In the chromite-bearing serpentinites (located in the northern part of the Modderfontein Complex; Fig. 7.1) however, the PGE display different mineralogical hosts and associations. While Os, Ir, Ru, Rh and Pt are hosted by nano-scale PGM in sulphides (and are therefore immobile), Pd was likely hosted by sulphide mineral phases (especially pentlandite; Watkinson and Ohnenstetter 1992, Xue et al. 2016), with the nature of this host phase rendering Pd mobile in these rocks when the rocks are altered and the BMS destroyed. Consequently, while extremely useful in a majority of cases, Pd/Ir ratios may also be unreliable as a petrogenetic indicator in some scenarios, particularly where the studied rocks were originally sulphide-rich (Barnes and Liu 2012). Consequently, the confident application of such discrimination diagrams, which were developed principally as petrogenetic and exploration tools, to Archaean rocks is difficult to reconcile.

10.1.3 Spinel mineral chemistry

For over half a century, spinel has been used as a 'petrogenetic indicator' (Irvine 1965, 1967, 1977, Barnes and Roeder 2001, Kamenetsky et al. 2001, Arai et al. 2011, Dönmez et al. 2014, Ahmed and Surour 2016), with occasional application to Archaean ultramafic rocks (e.g., Kusky and Jianghai 2010, Szilas et al. 2014, 2015). This group of minerals are particularly useful as they crystalise from ultramafic-mafic magmas over a broad of conditions (Barnes and Roeder 2001), exhibit a wide-range of solid solution (O'Neil and Wall 1987, Mattioli and Wood 1988, Wood 1990), and are considered resistant to alteration relative to other high-temperatures igneous minerals (e.g., olivine; Burkhard 1993, Barnes and Roeder 2001). To further develop the petrogenetic usefulness of spinel, Barnes and Roeder (2001) utilised a large dataset of mineral chemical analyses (n=26,000) from well-constrained geological and geodynamic environments to develop a series of compositional fields based on data density plots. These authors developed Fe^{2+} number (calculated as: $Fe^{2+}/[Mg+Fe^{2+}]$), Fe^{3+} number (calculated as: molar $Fe^{3+}/[Cr+Al+Fe^{3+}]$), Mg number (calculated as: molar $Mg/[Mg+Fe^{2+}+Fe^{3+}]$) and Cr number (calculated as: molar $Cr/[Cr+Al] \times 100$) proxies, and plotted the data on various bivariate and ternary plots (Barnes and Roeder 2001). Compositional fields for a range of geotectonic environments (e.g., layered intrusions, ophiolites and oceanic peridotites, and komatiites) were established, alongside fields for high-grade metamorphic spinels and those affected by greenschist- to amphibolite-facies metamorphism (Barnes and Roeder 2001).

As demonstrated throughout this thesis, the plots developed by Barnes and Roeder (2001) can be applied to Archaean ultramafic rocks, aiding petrogenetic interpretations. In Chapter

3, spinel mineral chemistry supports an interpretation (drawn up based initially on field evidence) whereby the Ben Strome Complex represents a deformed layered intrusion (Section 3.4.2), showing consistent overlap with this field on bivariate and ternary plots (Fig. 3.8). In Chapter 5, spinel mineral chemistry aids the identification of 2 temporally and/or petrogenetically distinct suites of mafic-ultramafic magmatism in the Lewisian Gneiss Complex. In Chapter 9, spinel mineral chemistry facilitates the testing of two end-member hypothesis (as described in Section 10.1.1.1), supporting a likely greenstone belt origin for the ultramafic-mafic complexes in the Johannesburg Dome.

In all of the examples described above, the studied ultramafic rocks experienced multiple phases of high-grade metamorphism and associated metasomatism. Consequently, the spinel is commonly altered, with this alteration manifesting as veins, rims and, occasionally, replacement of entire grains (Figs. 7.7, 7.12 and 7.18). The hydrothermal alteration of spinel is, however, a manageable limitation, with its effects constrained through a combination of detailed petrography (by BSE and SE imaging) and mineral analysis. As detailed in Figure 10.4, the composition of demonstrably altered portions (veins, rims etc.) were first identified and imaged, before a comprehensive suite of spinel grains were analysed. Establishing both the primary and alteration components (of spinel grains) is of paramount importance when utilising this geochemical proxy, as assuming that altered and recrystallised spinels were representative of primary magmatic compositions would lead to a profoundly different geotectonic interpretation (see the group 2 (altered) compositions in Figures 7.7, 7.12 and 7.18 for details; Fig. 10.4).

The resilience of spinel under these conditions, and ability for primary magmatic compositions to be carefully unpicked, demonstrates that it is a relatively robust geochemical proxy that can be successfully utilised when studying Archaean ultramafic rocks. Despite this, the range of demonstrably altered compositions identified as part of this study (from both the LGC and Johannesburg Dome) is broader than those previously established (Fig. 10.5). This demonstrates that the field for altered spinels – as established by Barnes and Roeder (2001) using a relatively limited dataset from 4 papers (which is a function of previous authors being reluctant to publish altered spinel data) – could be expanded to improve its effectiveness (Fig. 10.5). Providing the primary and alteration components of spinel are rigorously investigated (see Fig. 10.4), this potential expansion of the secondary spinel fields does not hinder interpretations using the plots established by Barnes and Roeder (2001).

A basic workflow for constraining spinel chemistry

1. Conduct a detailed petrographic assessment (modal mineralogy; degree/style of alteration etc.) of every thin section containing spinel.

For each thin section...

2. Identify and analyse the demonstrably altered components (i.e., rims/veins) of composite spinels thoroughly. *This process will provide an end-member for known altered compositions.*

3. Image and analyse all spinel grains, ensuring that the location of each analysis within spinel grains is recorded. *This will aid subsequent interpretations and resolve ambiguous compositions.*

Subsequently

4. Plot analyses on bivariate and ternary diagrams. separating demonstrably altered portions from spinel cores. *Any spinel cores that consistently plot with the altered compositions can be re-categorised as grains that have been completely altered.*

Some questions to consider during interpretation:

- Are the altered compositions consistent between thin sections, lithologies etc.?

- Are the "primary" compositions consistent between thin sections, lithologies etc.?

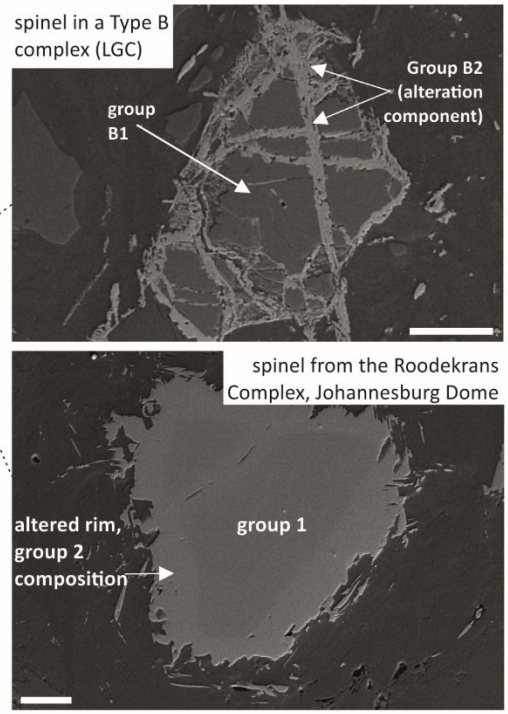

Figure 10.4: *Broad workflow detailing a method for constraining primary and altered spinel compositions. Note: alteration of spinel is variably prominent, as demonstrated by the two SE images (right).*

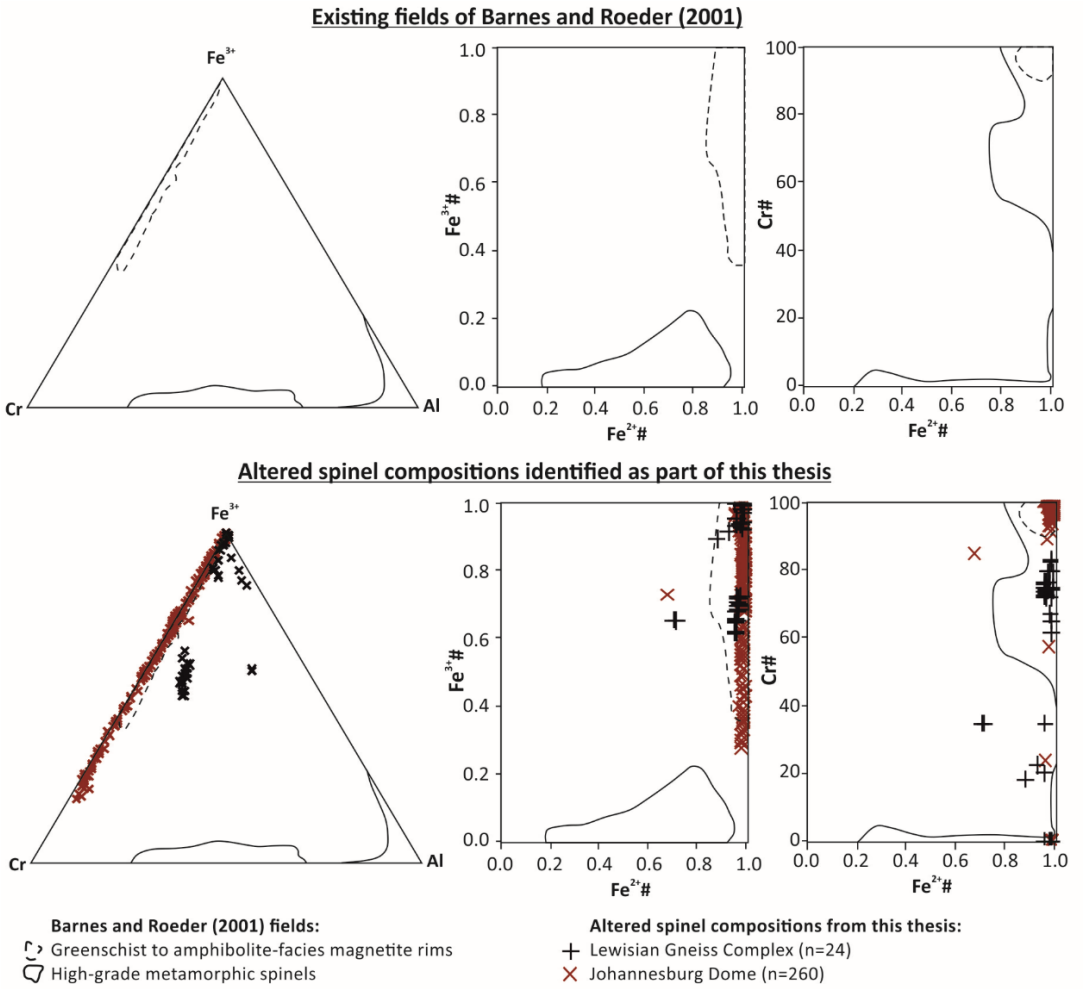

Figure 10.5: *Bivariate and ternary plots (Barnes and Roeder 2001) detailing the range of altered spinel compositions identified as part of this study, alongside the fields for altered spinels previously established.*

10.2 Origin of the studied ultramafic-mafic complexes

This thesis establishes the likely origin(s) of ultramafic-mafic complexes in the North Atlantic and Kaapvaal Cratons, namely: the > 3.3 Ga ultramafic-mafic complexes in the Johannesburg Dome; the > 3.1 Ga Type B complexes in the LGC; and the ca. 2.8 Ga Type A complexes in the LGC (Fig. 10.6). In the absence of reliable geochronological data for the ultramafic-mafic rocks themselves, the cited ages are based upon a combination of field relationships and geochronological data for demonstrably younger lithologies (e.g., cross-cutting TTG ages in the Johannesburg Dome) and/or events (e.g., pervasive granulite-facies metamorphism in the LGC). The > 3.3 Ga ultramafic-mafic complexes are interpreted as the intrusive/extrusive remnants of an Archaean greenstone belt(s). The Modderfontein and Zandspruit Complex are considered to preserve intrusive complexes, while the Roodekrans Complex likely represents a combination of formerly supracrustal and hypabyssal rocks (Fig. 9.2). In the LGC, the > 3.1 Ga Type B complexes are interpreted as an early ultramafic-mafic crust that was

invaded by 3.1–2.8 Ga TTG magmas (Figs. 5.5 and 10.6). This crust likely comprised several components that formed via various magmatic (and geodynamic) processes, with further research required to establish the precise petrogenetic processes responsible. The ca. 2.8 Ga Type A complexes in the LGC, which includes the 7 km^2 Ben Strome Complex, are interpreted as layered intrusions emplaced *into* TTG (Chapters 3 and 5; Fig. 5.15).

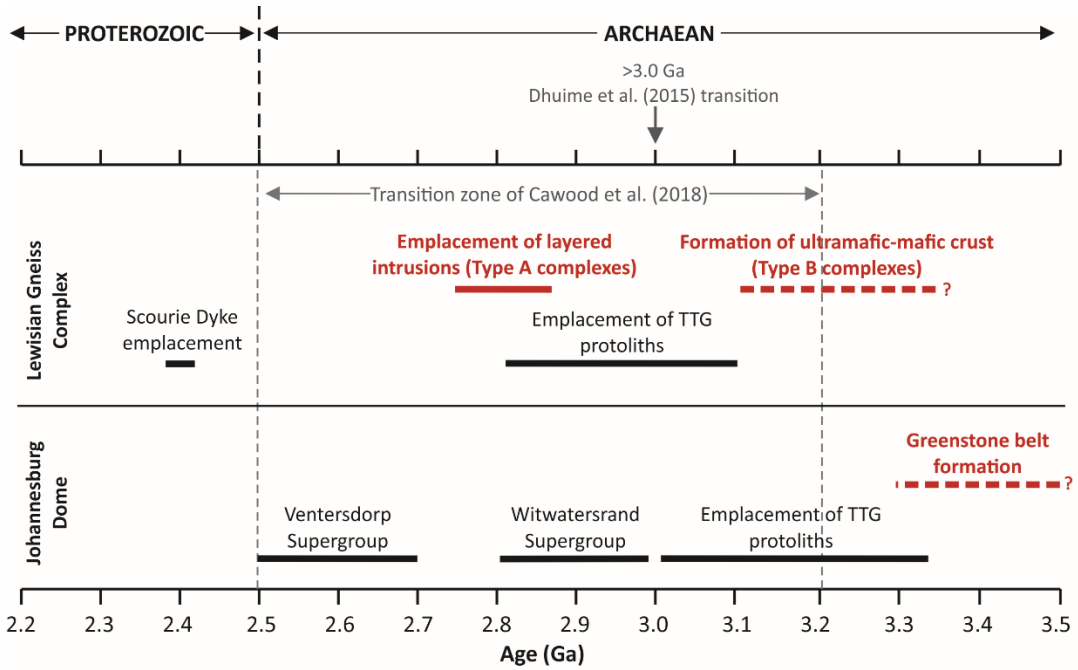

Figure 10.6: *Early Archaean–early Palaeoproterozoic timeline detailing the temporal distribution of the ultramafic-mafic magmatism studied as part of this thesis, alongside other significant events in the LGC and Johannesburg Dome. Dashed lines=limited age constraints.*

The relative success of establishing the origin of the studied ultramafic-mafic complexes, which have often experienced multiple phases of metamorphism, metasomatism and deformation, is owed to the integrated approach undertaken. Rigorous fieldwork, which involved mapping, logging and structural assessment, provides the crucial context upon which detailed petrography, bulk-rock geochemistry and mineral chemistry is considered. In addition to the investigation focusing on the origin of HFSE anomalies in the Ben Strome Complex (see Chapter 4 or Section 10.1.1 for a detailed summary), the effectiveness of this integrated approach is well illustrated in Chapter 9, when considering the origin of the > 3.3 Ga ultramafic-mafic complexes in the Johannesburg Dome. Detailed mapping of the Modderfontein Complex identified coarse layering (on a scale of tens of metres) not observed on the outcrop-scale. When combined with bulk-rock geochemistry and spinel chemistry, this mapping supports an intrusive greenstone belt origin for the ultramafic-mafic complexes in the Johannesburg Dome, opposing a previously proposed ophiolite fragment

hypothesis (Anhaeusser 2006b) that would have profound implications for Archaean geodynamic regime interpretations.

Despite being under-utilised in geological investigations today, the power of geological mapping and associated structural geology as a tool for examining the origin of ultramafic-mafic complexes is further demonstrated in Part One of this thesis. In previous studies, the varied (and seemingly chaotic) morphologies of the Type A complexes informed a widely-held assertion whereby the majority of these occurrences pre-date the emplacement of TTG magmas (e.g., Rollinson and Windley 1980, Sills 1981). However, detailed mapping and accompanying structural geology presented for the Ben Strome, Drumbeg and Loch Eilean na Craoibhe Moire Complexes (Chapters 3 and 5) indicate that these varied morphologies can be attributed to subsequent deformation. This assertion, which was supported by various geochemical data (e.g., spinel mineral chemistry and PGE bulk-rock geochemistry) and represents a significant re-evaluation of the fundamental age relationships in the LGC, has implications for the origin of this suite of complexes, which are here interpreted as layered intrusions emplaced *into* TTG (see Chapters 3 and 5).

10.3 Implications for Archaean geodynamic regimes

As this thesis focuses on a relatively small number of ultramafic-mafic complexes in 2 cratons, the data presented should not be over-interpreted. However, it is possible to revisit the Archaean geodynamics debate summarised in Chapter 1.

As summarised in Chapter 1, many authors suggest that modern-style plate tectonics (defined in Chapter 1; Fig. 1.1) has operated since > 3.6 Ga (De Wit et al. 1987, 1992, De Wit 1998, Komiya et al. 1999, Nutman et al. 2002, Friend et al. 2002, Furnes et al. 2007a, Dilek and Polat 2008, Hopkins et al. 2008, Shirey et al. 2008, Furnes et al. 2009, Hopkins et al. 2010, Hastie et al. 2010, Friend and Nutman 2010, Korenaga 2013, Arndt 2013, Nutman et al. 2013, Turner et al. 2014, Hastie et al. 2016, Keller and Schoene 2018, Khanna et al. 2018). The most controversial evidence cited in favour of this geodynamic regime having operated throughout the Archaean is the proposed existence of early-mid Archaean ophiolites (De Wit et al. 1987, Hart et al. 1990, Furnes et al. 2007b, Dilek and Polat 2008, Furnes et al. 2009, Grosch and Slama 2017). As the formation of oceanic crust and its preservation as ophiolites is a characteristic feature of modern-style plate tectonics, it is reasonable to expect that early Archaean ophiolites would be preserved if this geodynamic regime has indeed predominated since ~4.0 Ga (Hopkins et al. 2008, Hastie et al. 2016, Keller and Schoene 2018).

Chapters 7–9, which examine the origin of various ultramafic-mafic complexes in the Johannesburg Dome, contradicts a previously proposed hypothesis whereby these occurrences represent fragments of an Archaean ophiolite (Anhaeusser 2006b). This is further to similar investigations in the Greenlandic portion of the NAC (Szilas et al. 2015, 2018), where ultramafic rocks previously interpreted as fragments of residual mantle are re-interpreted as representing metamorphosed cumulates. While the contradiction of individual ophiolite interpretations is not necessarily of great significance to the Archaean geodynamics discussion, a complete absence of such rocks from the early Archaean record would be significant (Kamber 2015). The ongoing contradiction of such hypotheses (e.g., Szilas et al. 2015, 2018; Chapters 3, 5 and 9) therefore raises questions as to the validity of a > 3.6 Ga onset for modern-style plate tectonics. It is the author's opinion that, until early Archaean ophiolites (including residual mantle rocks) are unequivocally shown to exist, it is difficult to envisage modern-style plate tectonics having operated since > 3.6 Ga.

Alternatively, several authors have proposed a major change in Earth's geodynamic regime between 3.2 and 2.5 Ga (e.g., Cawood et al. 2018), with secular changes displayed by various geological and geochemical proxies (e.g., Brown and Johnson 2018, Halla 2018, Smithies et al. 2018, Moyen and Laurent 2018, Johnson et al. 2019; see Section 1.1.2). For example, Dhuime et al. (2015) interpreted a marked increase in the Rb/Sr ratios of juvenile crust (globally) at ~3.0 Ga as representing the onset of modern-style plate tectonics. The temporal distribution of the studied ultramafic-mafic complexes (Fig. 1.6) offers the chance to examine whether this proposed geodynamic evolution is recorded by the data presented here. Spanning > 0.5 Ga, the > 3.1 Ga Type B complexes from the LGC and > 3.3 Ga ultramafic-mafic complexes from the Johannesburg Dome pre-date the proposed ~3.0 Ga transition, while the ~2.8 Ga Type A complexes from the LGC post-date this transition (Fig. 10.6). These 3 groups are compared on bulk-rock bivariate plots in Figure 10.7 (using elements consistently considered relatively immobile in both cratons), whereby a more compatible element is included on the x axis and more incompatible element is included on the y axis. These data are also compared to the 3.6–3.3 Ga extrusive ultramafic-mafic rocks in the Barberton Greenstone Belt.

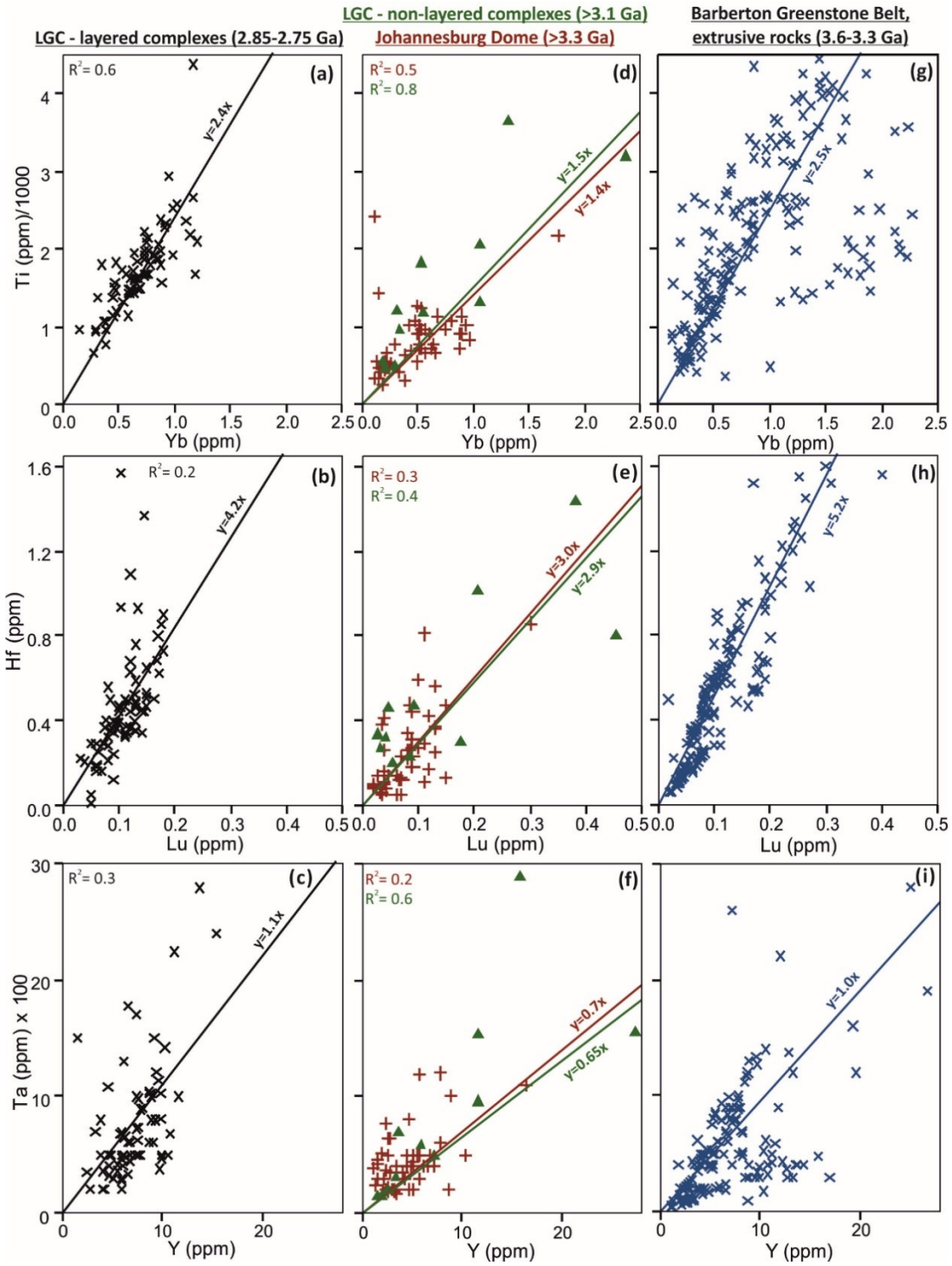

Figure 10.7: *Bivariate plots summarising the bulk-rock geochemical data for the 3 periods of ultramafic-mafic magmatism studied in this thesis, alongside a comparison to the ultramafic-mafic magmatism preserved in the Barberton Greenstone Belt.* ***(a-c)*** *~2.8 Ga Type A complexes from the LGC (n=72).* ***(d-f)*** *> 3.1 Ga Type B complexes from the LGC (n=13) and > 3.3 Ga ultramafic-mafic complexes from the Johannesburg Dome (n=39).* ***(g-i)*** *3.6–3.3 Ga extrusive ultramafic-mafic rocks from the Barberton Greenstone Belt (references as in Chapter 8). Note: an intercept of 0 is assumed for all linear regressions; for visualisation purposes, 2 data points are clipped from plots d-f.*

On all plots (Yb versus Ti; Lu versus Hf; and Y versus Ta), the 2.8 Ga Type A complexes evolve along a steeper gradient than the > 3.1 Ga Type B complexes and > 3.3 Ga ultramafic-mafic complexes (Fig. 10.7a-f), demonstrating that the 2.8 Ga complexes record higher Ti/Yb, Hf/Lu and Ta/Y ratios than the > 3.1 and > 3.3 Ga complexes. Considered in isolation, these data may be used to support a major geochemical evolution at ca. 3.0 (Dhuime et al. 2015), whereby a significant change in the predominant geodynamic regimes – combined with differing style(s) and/or degree of partial melting in the source region – may have been responsible for an increase in the Ti/Yb, Hf/Lu and Ta/Y ratios of juvenile ultramafic-mafic crust (Fig. 10.7a-f). However, the trends shown by the 3.6–3.3 Ga extrusive rocks in the Barberton Greenstone Belt are comparable to those of the ca. 2.8 Ga Type A complexes in the LGC (Fig. 10.7g-i), contradicting the ca. 3.0 Ga geochemical evolution hypothesis. Rather than recording a predominant geodynamic regime, the trends shown by the various ultramafic-mafic suites (Fig. 10.7) are likely controlled by a combination of processes, including: degree of partial melting; presence/absence of specific mineral phases in the source region (e.g., rutile); nature and/or degree of crustal contamination; various petrogenetic processes; and the K^D values of individual minerals. Therefore, instead of representing a major shift in the Earth's geodynamic regime, these data record multiple combinations of these processes were operating both before and after 3.0 Ga. Whilst not contradicting a major change in the Earth's geodynamic regime between 3.2 and 2.5 Ga, this insight reinforces the requirement to constrain the variety of processes that contribute to the bulk-rock budget of ultramafic-mafic rocks prior to invoking broad-scale geodynamic interpretations.

Irrespective of when modern-style plate tectonics commenced, the data presented in Chapter 4 offer an important geodynamic insight. These findings question some previous interpretations of Archaean ultramafic-mafic magmatism as being associated with subduction-related magmatism, particularly where bulk-rock HFSE anomalies are cited as sole or primary evidence. As in the case of the Ben Strome Complex, it is possible that some of these anomalies were generated by discrete secondary processes, rather than primary, subduction-related processes (Klemme et al. 2005). While it is entirely plausible that subduction-related magmatism contributed to crustal growth during the Archaean, erroneous use of HFSE anomalies may have led to an overestimation of its prevalence during this Eon. This assertion may have implications for regional palaeogeographic reconstructions of Archaean terranes, as subduction-related interpretations of ultramafic-mafic complexes may be used to inform regional-scale assumptions regarding craton accretion and assembly.

10.4 Ultramafic-mafic complexes: a potential source of placer PGM?

The late Archaean Witwatersrand Basin – host to the largest Au deposit on Earth – also contains associated PGE mineralisation, most notably in the form of Os-Ir-Ru alloys that were recovered along with Au (Wagner 1929, Feather 1976, Robb and Meyer 1995, Schaefer et al. 2010). Traditionally, two end-member models were proposed for the origin of the Witwatersrand Basin Au mineralisation, namely: detrital/placer (Feather 1976, Kirk et al. 2001, 2002); and hydrothermal (Phillips 1987, Barnicoat et al. 1997, Jolley et al. 2004). More recently, a relative consensus has been built around a hybrid modified placer model, whereby Au (and to a lesser extent, PGE) were re-mobilised after a primarily detrital origin (Robb and Meyer 1995, Schaefer et al. 2010). The primary source of the Au and associated PGE alloys is more ambiguous, with several authors considering an Archaean greenstone terrane(s) a likely candidate (Viljoen et al. 1970, Feather 1976, Sinjeng 1987, Schaefer et al. 2010). Although the ultramafic-mafic complexes do not represent a viable source of the Au (see the consistent negative Au anomalies on PGE plots for details; Fig. 8.7), this section considers whether the chromite-hosted PGE present in the Modderfontein Complex (Section 7.1.2.1) might be an example of a primary PGM source for the Witwatersrand Basin.

The PGM found in the Witwatersrand Basin are generally Ir, Os and Ru alloys, with Os and Ir alloys most common (Feather 1976, Sinjeng 1987). Sulphide minerals (e.g., erlichmanite and laurite) are extremely rare, occurring as inclusions in the alloys, while sperrylite (PtAs) generally occurs as 0.5–50 μm diameter (altered) rims on the alloys (Feather 1976, Sinjeng 1987). Similarly, sulpharsenides, such as iarsite (IrAsS) and hollingworthite (RhAsS), are rarely present, but are reported to occur as localised alteration products on the alloys (Feather 1976). In contrast, the PGM assemblage recorded by the Modderfontein chromitite is dominated by erlichmanite (OsS_2; n=7) and laurite (RuS_2; n=6) (Section 7.1.2.1; Table 7.1), which represent Os and Ir sulphides respectively. While this PGM assemblage is distinctive from that of the Witwatersrand Basin (Feather 1976, Sinjeng 1987), it is theoretically possible for Modderfontein-type chromitite to be (at least in-part) a source of PGM in the Witwatersrand Basin. This scenario would require:

i. Significant S mobility during hydrothermal alteration of the primary IPGE-sulphide assemblage prior to erosion, generating secondary Ir, Os and Ru alloys and Pt-bearing alloys or arsenides in the host rock.
ii. Exposure of the ultramafic-mafic rocks at the Archaean land surface, and subsequent erosion of the PGM-rich material.

iii. Following deposition, the Pt-bearing PGM were partially altered/dissolved to produce Pt-rich fluids, and Pt was re-precipitation to generate the observed sperrylite rims on the Os-Ir-Ru alloys.

Geochronological data published by Schaefer et al. (2010) constrains step (i) further. These authors report a distribution of Re-Os ages with the majority in the window of 3.2–3.0 Ga for osmiridium, which are significantly younger than both the > 3.4 Ga ultramafic-mafic rocks in the Barberton Greenstone Belt and the Johannesburg Dome. For the outlined scenario to be valid, step (i) must have occurred between 3.2 and 3.0 Ga. While not impossible, an Ockham's Razor approach suggests that this scenario is unlikely, with this assertion strengthened by the published compositions of detrital spinels from the Witwatersrand Basin (von Rahden et al. 1991). Relative to those from the ultramafic-mafic complexes of the Johannesburg Dome (Chapter 7), those from the Witwatersrand Basin are consistently Cr_2O_3 and MgO-rich, and FeO-poor (von Rahden et al. 1991).

To summarise, based on the different PGM mineralogy, likely ages and the compositions of associated spinels, it is considered unlikely that Modderfontein-type chromitite represents a viable source for the PGM in the Witwatersrand Basin. As a result, the source of such PGM in the Witwatersrand Basin remains ambiguous. The data published here indicates that intrusive complexes in the Johannesburg Dome are an unlikely source, with the geochronological data published by Schaefer et al. (2010) reducing the probability that any of the ultramafic rocks in the Barberton Greenstone Belt or Johannesburg Dome represent credible possibilities. These data indicate that PGM may have been eroded from 3.2–3.0 Ga ultramafic rocks (Schaefer et al. 2010), although such material is not currently exposed in the immediate hinterland of the Witwatersrand Basin.

10.5 Final statement

This thesis demonstrates that investigations of Archaean ultramafic-mafic complexes can provide crucial information relating to the magmatic evolution of Archaean crust on the regional-scale. For example, in the Lewisian Gneiss Complex, the studied complexes, which were previously assumed to record a single origin, represent two phases of Archaean ultramafic-mafic magmatism separated by ~0.5 Ga, with the first interpreted as an early ultramafic-mafic crust and second as layered intrusions that were emplaced into TTG. In both the North Atlantic and Kaapvaal Cratons, the studied ultramafic-mafic complexes have experienced multiple phases of (often high-grade) metamorphism, metasomatism and associated element mobility. Confidently constraining such element mobility, which is specific to individual portions of Archaean crust, is of critical importance prior to applying

geochemical proxies to Archaean ultramafic rocks. For example, HFSE anomalies – a geochemical proxy commonly used to fingerprint subduction-related magmatism – is one example of a geochemical proxy shown here to be particularly susceptible to element mobility. In this case, the role of subduction as a geodynamic process during the Archaean may be currently overestimated. Element mobility can, however, be constrained using the integrated approach utilised throughout this thesis, whereby detailed petrography, bulk-rock geochemistry and mineral chemistry are considered using the context provided by rigorous field geology. Providing appropriate care is taken to constrain element mobility, ultramafic-mafic complexes globally could provide crucial information pertaining to the Archaean geodynamics debate. Key to this discussion is the interpretation of some ultramafic-mafic complexes as representing Archaean ophiolites. If unequivocally shown to exist, Archaean ophiolites would provide strong evidence in favour of modern-style plate tectonics having operated. However, one such proposal – previously proposed for the ultramafic-mafic complexes in the Johannesburg Dome – is contradicted by the data presented in this thesis. When combined with similar opposition to other proposed occurrences globally, this raises questions as to the validity of a > 3.6 Ga onset for modern-style plate tectonics.

Bibliography

Abbott, D., Drury, R., and Smith, W.H.F. (1994) 'Flat to Steep Transition in Subduction Style'. *Geology* 22 (10), 937–940

Agrawal, S., Guevara, M., and Verma, S.P. (2008) 'Tectonic Discrimination of Basic and Ultrabasic Volcanic Rocks through Log-Transformed Ratios of Immobile Trace Elements'. *International Geology Review* 50 (12), 1057–1079

Ahmed, A.H. and Arai, S. (2003) 'Platinum-Group Minerals in Podiform Chromitites of the Oman Ophiolite'. *Canadian Mineralogist* 41 (3), 597–616

Ahmed, A.H. and Surour, A.A. (2016) 'Fluid-Related Modifications of Cr-Spinel and Olivine from Ophiolitic Peridotites by Contact Metamorphism of Granitic Intrusions in the Ablah Area, Saudi Arabia'. *Journal of Asian Earth Sciences* 122 (November), 58–79

Alard, O., Griffin, W.L., Lorand, J.-P., Jackson, S.E., and O'Reilly, S.Y. (2000) 'Non-Chondritic Distribution of the Highly Siderophile Elements in Mantle Sulphides.' *Nature* 407, 891–894

Andersen, T., Whitehouse, M.J., and Burke, E.A.J. (1997) 'Fluid Inclusions in Scourian Granulites from the Lewisian Complex of NW Scotland: Evidence for CO2-Rich Fluid in Late Archaean High-Grade Metamorphism'. *Lithos* 40 (2–4), 93–104

Anhaeusser, C.R. (1973a) 'The Evolution of the Early Precambrian Crust of Southern Africa'. *Phil. Trans. R. Soc. Lond.* 273, 359–388

Anhaeusser, C.R. (1973b) 'The Geology and Geochemistry of the Archaean Granites and Gneisses of the Johannesburg-Petoria Dome'. *Special Publication of the Geological Society of South Africa* 3, 361–385

Anhaeusser, C.R. (1977) 'Geological and Geochemical Investigations of the Roodekrans Ultramafic Complex and Surrounding Archaean Volcanic Rocks, Krugersdorp District'. *Transactions of the Geological Society of South Africa* 80, 17–28

Anhaeusser, C.R. (1978) 'The Geology and Geochemistry of the Muldersdrif Ultramafic Complex, Krugersdorp District'. *Trans. Geol. Soc. S. Afr.* 81, 193–203

Anhaeusser, C.R. (1985) 'Archaean Layered Ultramafic Complexes in the Barberton Mountain Land, South Africa'. *Special Paper for the Geological Association of Canada*

28, 281–320

Anhaeusser, C.R. (1992) 'Archaean Granite-Greenstone Relationships on the Farm Zandspruit 191-IQ , North Riding Area , Johannesburg Dome'. *South African Journal of Geology* 95 (3/4), 94–101

Anhaeusser, C.R. (1999) 'Archaean Crustal Evolution of the Central Kaapval Craton, South Africa: Evidence from the Johannesburg Dome'. *South African Journal of Geology* 102 (4), 303–322

Anhaeusser, C.R. (2001) 'The Anatomy of an Extrusive-Intrusive Archaean Mafic-Ultramafic Sequence: The Nelshoogte Schist Belt and Stolzburg Layered Ultramafic Complex, Barberton Greenstone Belt, South Africa'. *South African Journal of Geology* 104 (2), 167–204

Anhaeusser, C.R. (2004) 'Palaeoarchaean to Mesoproterozoic (c. 3500 - 1000 Ma) Ultramafic and Mafic Intrusions of the Kaapvaal Craton and Neighbouring Metamorphic Belts: A Review'. *Econ. Geol. Res. Unit, Univ. Witwatersrand, Johannesburg* 384

Anhaeusser, C.R. (2006a) 'Mafic and Ultramafic Intrusions of the Kaapvaal Craton'. *The Geology of South Africa* 95–134

Anhaeusser, C.R. (2006b) 'A Reevaluation of Archean Intracratonic Terrane Boundaries on the Kaapvaal Craton, South Africa: Collisional Suture Zones?' *Geological Society of America, Special Paper* 405, 193–210

Anhaeusser, C.R. (2014) 'Archaean Greenstone Belts and Associated Granitic Rocks - A Review'. *Journal of African Earth Sciences* 100, 684–732

Anhaeusser, C.R. (2015) 'Metasomatized and Hybrid Rocks Associated with a Palaeoarchaean Layered Ultramafic Intrusion on the Johannesburg Dome, South Africa'. *Journal of African Earth Sciences* 102, 203–217

Anhaeusser, C.R. and Robb, L.J. (1981) 'Magmatic Cycles and the Evolution of the Archaean Granitic Crust in the Eastern Transvaal and Swaziland'. *Special Paper of the Geological Society* 7, 457–467

Arai, S. and Miura, M. (2015) 'Podiform Chromitites Do Form beneath Mid-Ocean Ridges'. *Lithos* 232, 143–149

Arai, S. and Miura, M. (2016) 'Formation and Modification of Chromitites in the Mantle'. *Lithos* 264, 277–295

Arai, S., Okamura, H., Kadoshima, K., Tanaka, C., Suzuki, K., Ishimaru, S., and Sciences, E. (2011) 'Chemical Characteristics of Chromian Spinel in Plutonic Rocks: Implications for Deep Magma Processes and Discrimination of Tectonic Setting'. *Island Arc* 20 (1), 125–137

Arai, S., Uesugi, J., and Ahmed, A.H. (2004) 'Upper Crustal Podiform Chromitite from the Northern Oman Ophiolite as the Stratigraphically Shallowest Chromitite in Ophiolite and Its Implication for Cr Concentration'. *Contributions to Mineralogy and Petrology* 147, 145–154

Arai, S. and Yurimoto, H. (1994) 'Podiform Chromitites of the Tari-Misaka Ultramarie Complex, Southwestern Japan, as Mantle-Melt Interaction Products'. *Economic Geology* 89, 1279–1288

Armstrong, R.A., Compston, W., Retief, E.A., Williams, I.S., and Welke, H.J. (1991) 'Zircon Ion Microprobe Studies Bearing on the Age and Evolution of the Witwatersrand Triad'. *Precambrian Research* 53 (3–4), 243–266

Armstrong, R.A., Compston, W., de Wit, M.J., and Williams, I.S. (1990) 'The Stratigraphy of the 3.5-3.2 Ga Barberton Greenstone Belt Revisited: A Single Zircon Ion Microprobe Study'. *Earth and Planetary Science Letters* 101 (1), 90–106

Arndt, N. (1999) 'Why Was Flood Volcanism on Submerged Continental Platforms so Common in the Precambrian?' *Precambrian Research* 97 (3–4), 155–164

Arndt, N.T. (2013) 'Formation and Evolution of the Continental Crust'. *Geochemical Perspectives* 2 (3), 405–533

Attfield, P. (1987) 'The Structural History of the Canisp Shear Zone'. *Geological Society, London, Special Publications* 27 (1), 165–173

Babechuk, M.G. and Kamber, B.S. (2011) 'An Estimate of 1.9 Ga Mantle Depletion Using the High-Field-Strength Elements and Nd–Pb Isotopes of Ocean Floor Basalts, Flin Flon Belt, Canada'. *Precambrian Research* 189 (1–2), 114–139

Babechuk, M.G., Kamber, B.S., Greig, A., Canil, D., and Kodolányi, J. (2010) 'The Behaviour of Tungsten during Mantle Melting Revisited with Implications for Planetary

Differentiation Time Scales'. *Geochimica et Cosmochimica Acta* 74 (4), 1448–1470

Bagas, L., Kolb, J., Fiorentini, M.L., Thebaud, N., Owen, J., Rennick, S., and Stensgaard, B.M. (2016) 'On the Processes That Formed Archaean Ni-Cu Sulfide Mineralisation in the Deep Continental Crust, Thrym Complex, Southeastern Greenland'. *Precambrian Research* 277, 68–86

Baker, D.R., Barnes, S.J., Simon, G., and Bernier, F. (2001) 'Fluid Transport of Sulfur and Metals between Sulfide Melt and Basaltic Melt'. *Canadian Mineralogist* 39 (2), 537–546

Bamford, D., Nunn, K., Proedehl, C., and Jacob, B. (1978) 'Crustal Studies of Northern Britain'. *Royal Astronomical Society* 54, 43–60

Barnes, S.-J., Boyd, R., Korneliussen, A., Nilsson, L.-P., Often, M., Pedersen, R.B., and Robins, B. (1988) 'The Use of Mantle Normalization and Metal Ratios in Discriminating between the Effects of Partial Melting, Crystal Fractionation and Sulphide Segregation on Platinum-Group Elements, Gold, Nickel and Copper: Examples from Norway'. in *Geo-Platinum 87*. ed. by Prichard, H.M., Potts, P.J., Bowles, J.F.W., and Cribb, S.J. Dordrecht: Springer Netherlands, 113–143

Barnes, S. (1990) 'The Use of Metal Ratios in Prospecting for Platinum- Group Element Deposits in Mafic and Ultramafic Intrusions'. *Journal Geochemical Exploration* 37, 91–99

Barnes, S.J. and Liu, W. (2012) 'Pt and Pd Mobility in Hydrothermal Fluids: Evidence from Komatiites and from Thermodynamic Modelling'. *Ore Geology Reviews* 44, 49–58

Barnes, S.J., Naldrett, A.J., and Gorton, M.P. (1985) 'The Origin of the Fractionation of Platinum-Group Elements in Terrestrial Magmas'. *Chemical Geology* 53 (3–4), 303–323

Barnes, S.J. and Roeder, P.L. (2001) 'The Range of Spinel Compositions in Terrestrial Mafic and Ultramafic Rocks'. *Journal of Petrology* 42 (12), 2279–2302

Barnicoat, A.C. (1983) 'Metamorphism of the Scourian Complex, NW Scotland'. *Journal of Metamorphic Geology* 1, 163–182

Barnicoat, A.C., Henderson, I.H.C., Knipe, R.J., Yardley, B.W.D., Napier, R.W., Fox, N.P.C., Kenyon, A.K., Muntingh, D.J., Strydom, D., Winkler, K.S., Lawrence, S.R., and Cornford, C. (1997) 'Hydrothermal Gold Mineralization in the Witwatersrand Basin'. *Nature* 386,

820–824

Barnicoat, A.C. and O'Hara, M.J. (1978) 'High-Temperature Pyroxenes from an Ironstone at Scourie, Sutherland'. *Mineralogical Magazine* 43, 371–375

Barooah, B.C. and Bowes, D.R. (2009) 'Multi-Episodic Modification of High-Grade Terrane near Scourie and Its Significance in Elucidating the History of the Lewisian Complex'. *Scottish Journal of Geology* 45 (1), 19–41

Barton, J.M., Barton, E.S., and Kröner, A. (1999) 'Age and Isotopic Evidence for the Origin of the Archaean Granitoid Intrusives of the Johannesburg Dome, South Africa'. *Journal of African Earth Sciences* 28 (3), 693–702

Barton, M.D. and Ilchik, R.P. (1991) 'Metasomatism'. in *Contact Metamorphism, Vol. 26. Mineralogical Society of America*. ed. by Kerrick, D.M. 321–350

Barton, P.J. (1992) *LISPB Revisited: A New Look under the Caledonides of Northern*. 371–391

Beach, A. (1973) 'The Mineralogy of High Temperature Shear Zones at Scourie, N.W. Scotland'. *Journal of Petrology* 14 (January), 231–248

Beach, A. (1974) 'Amphibolitization of Scourian Granulites'. *Scottish Journal of Geology* 10 (i), 35–43

Beach, A., Coward, M.P., and Graham, R.H. (1974) 'An Interpretation of the Structural Evolution of the Laxford Front, North-West Scotland'. *Scottish Journal of Geology* 9 (4), 297–308

Beach, A. and Tarney, J. (1978) 'Major and Trace Element Patterns Established during Retrogressive Metamorphism of Granulite-Facies Gneisses, NW Scotland'. *Precambrian Research* 7, 325–348

Bédard, J.H. (2013) 'How Many Arcs Can Dance on the Head of a Plume? A "comment" on: A Critical Assessment of Neoarchean "Plume Only" Geodynamics: Evidence from the Superior Province, by Derek Wyman, Precambrian Research, 2012'. *Precambrian Research* 229, 189–197

Bédard, J.H. (2018) 'Stagnant Lids and Mantle Overturns: Implications for Archaean Tectonics, Magma Genesis, Crustal Growth, Mantle Evolution, and the Start of Plate Tectonics'. *Geoscience Frontiers* 9 (1), 19–49

Bédard, J.H., Brouillette, P., Madore, L., and Berclaz, A. (2003) 'Archaean Cratonization and Deformation in the Northern Superior Province, Canada: An Evaluation of Plate Tectonic versus Vertical Tectonic Models'. *Precambrian Research* 127 (1–3), 61–87

Bédard, J.H., Harris, L.B., and Thurston, P.C. (2013) 'The Hunting of the SnArc'. *Precambrian Research* 229, 20–48

BGS (2011) *[Shapefile Geospatial Data]. Scale 1:250000, Tile: NC. Updated April 2011, Version 4, British Geological Survey, UK. Using: EDINA Geology Digimap Service, Http://Edina.Ac.Uk/Digimap. Downloaded: Feb. 2016*.

Bleeker, W. (2002) 'Archaean Tectonics: A Review, with Illustrations from the Slave Craton'. *Geological Society, London, Special Publications* 199 (1), 151–181

Blichert-Toft, J. and Arndt, N.T. (1999) 'Hf Isotope Compositions of Komatiites'. *Earth and Planetary Science Letters* 171 (3), 439–451

Bowes, D.R., Park, R.G., and Wright, A.E. (1964) 'Layered Intrusive Rocks in the Lewisian of the North-West Highlands of Scotland'. *Quarterly Journal of the Geological Society* 120 (1–4), 153

Bowes, D.R., Wright, A.E., and Park, R.G. (1966) 'Origin of Ultrabasic and Basic Masses in Lewisian'. *Geological Magazine* 103 (3), 280-

Bradley, D.C. (2008) 'Passive Margins through Earth History'. *Earth-Science Reviews* 91 (1–4), 1–26

Brandl, G., Cloete, M., and Anhaeusser, C.R. (2006) 'Archaean Greenstone Belts'. *Geology of South Africa* (3), 9–25

Brenan, J.M. and Andrews, D. (2001) 'Higher-Temperature Stability of Laurite and Ru-Os-Lr Alloy and Their Role in PGE Fractionation in Mafic Magmas'. *Canadian Mineralogist* 39 (2), 341–360

Brévart, O., Dupré, B., and Allègre, C.J. (1986) 'Lead-Lead Age of Komatiitic Lavas and Limitations on the Structure and Evolution of the Precambrian Mantle'. *Earth and Planetary Science Letters* 77 (3–4), 293–302

Brown, M. (2006) 'Duality of Thermal Regimes Is the Distinctive Characteristics of Plate Tectonics since the Neoarchean'. *Geology* 34 (11), 961–964

Brown, M. (2008) 'Characteristic Thermal Regimes of Plate Tectonics and Their Metamorphic Imprint throughout Earth History: When Did Earth First Adopt a Plate Tectonic Mode of Behavior?' *The Geological Society of America, Special Paper* 440, 97–113

Brown, M. and Johnson, T.E. (2018) 'Secular Change in Metamorphism and the Onset of Global Plate Tectonics'. *American Mineralogist* 103 (2), 181–196

Burkhard, D.J.M. (1993) 'Accessory Chromium Spinels: Their Coexistence and Alteration in Serpentinites'. *Geochimica et Cosmochimica Acta* 57 (6), 1297–1306

Burton, K.W., Capmas, F., Birck, J.L., Allegre, C.J., and Cohen, A.S. (2000) 'Resolving Crystallisation Ages of Archean Mafic-Ultramafic Rocks Using the Re-Os Isotope System'. *Earth and Planetary Science Letters* 179, 453–467

Burton, K.W., Cohen, A.S., O'Nions, R.K., and O'Hara, M.J. (1994) 'Archaean Crustal Development in the Lewisian Complex of Northwest Scotland'. *Nature* 370 (552–555)

Cann, J.R. (1970) 'Rb, Sr, Y, Zr and Nb in Some Ocean Floor Basaltic Rocks'. *Earth and Planetary Science Letters* 10 (1), 7–11

Cartwright, I., Fitches, W.R., O'Hara, M.J., Barnicoat, A.C., and O'Hara, S. (1985) 'Archaean Supracrustal Rocks from the Lewisian near Stoer, Sutherland'. *Scottish Journal of …* 21 (2), 187–196

Cawood, P.A. and Hawkesworth, C.J. (2015) 'Temporal Relations between Mineral Deposits and Global Tectonic Cycles'. *Geological Society, London, Special Publications* 393 (1), 9–21

Cawood, P.A., Hawkesworth, C.J., Pisarevsky, S.A., Dhuime, B., Capitanio, F.A., and Nebel, O. (2018) 'Geological Archive of the Onset of Plate Tectonics'. *Philosophical Transactions. Series A, Mathematical, Physical, and Engineering Sciences* 376 (2132)

Cawood, P.A., Kröner, A., and Pisarevsky, S.A. (2006) 'Precambrian Plate Tectonics: Criteria and Evidence'. *GSA Today* 16 (7)

Cawthorn, R.G., Davies, G., Clubley-Armstrong, A., and McCarthy, T.S. (1981) 'Sills Associated with the Bushveld Complex, South Africa: An Estimate of the Parental Magma Composition'. *Lithos* 14 (1), 1–16

Chandan-Kumar, B. and Ugarkar, A.G. (2017) 'Geochemistry of Mafic–ultramafic Magmatism in the Western Ghats Belt (Kudremukh Greenstone Belt), Western Dharwar Craton, India: Implications for Mantle Sources and Geodynamic Setting'. *International Geology Review* 59 (12), 1507–1531

Chapman, H.J. (1979) '2,390 Myr Rb-Sr Whole-Rock for the Scourie Dykes of North-West Scotland'. *Nature* 277, 642–643

Chaumba, J.B. (1992) *The Geology and Geochemistry of Part of the Edenvale Granite-Greenstone Terrane, Johannesburg-Pretoria Granite Dome (BSc (Hons) Thesis)*. Univ. Witwatersrand, Johannesburg

Chavagnac, V. (2004) 'A Geochemical and Nd Isotopic Study of Barberton Komatiites (South Africa): Implication for the Archean Mantle'. *Lithos* 75 (3–4), 253–281

Chen, J. (1992) 'Oceanic Crustal Thickness versus Spreading Rate'. *Geophysical Research Letters* 19 (8), 753–756

Cloete, M. (1999) 'Aspects of Volcanism and Metamorphism of the Onverwacht Group Lavas in the South-Western Portion of the Barberton Greenstone Belt'. *Memoirs of the Geological Survey of South Africa* 84, 232

Coggon, J.A., Nowell, G.M., Pearson, D.G., Oberthür, T., Lorand, J.P., Melcher, F., and Parman, S.W. (2012) 'The 190Pt- 186Os Decay System Applied to Dating Platinum-Group Element Mineralization of the Bushveld Complex, South Africa'. *Chemical Geology* 302–303, 48–60

Coghill, B.M. and Wilson, A.H. (1993) 'Platinum-Group Minerals in the Selukwe Subchamber, Great Dyke, Zimbabwe - Implications for Pge Collection Mechanisms and Post-Formational Redistribution'. *Mineralogical Magazine* 57 (389), 613–633

Cohen, A.S., O'Nions, R.K., and O'Hara, M.J. (1991) 'Chronology and Mechanism of Depletion in Lewisian Granulites'. *Contributions to Mineralogy and Petrology* 106, 142–153

Collerson, K.D. and Kamber, B.S. (1999) 'Evolution of the Continents and the Atmosphere Inferred from Th-U-Nb Systematics of the Depleted Mantle'. *Science* 283 (5407), 1519–1522

Condie, K.C. (1993) *Plate Tectonics & Crustal Evolution*. 3rd editio. Oxford, UK: Pergamon

Press

Condie, K.C. (2003) 'Incompatible Element Ratios in Oceanic Basalts and Komatiites: Tracking Deep Mantle Sources and Continental Growth Rates with Time'. *Geochemistry, Geophysics, Geosystems* 4 (1), 1–28

Condie, K.C. (2005) 'TTGs and Adakites: Are They Both Slab Melts?' *Lithos* 80 (1–4 SPEC. ISS.), 33–44

Condie, K.C. (2018) 'A Planet in Transition: The Onset of Plate Tectonics on Earth between 3 and 2 Ga?' *Geoscience Frontiers* 9 (1), 51–60

Condie, K.C. and Kröner, A. (2008) 'When Did Plate Tectonics Begin? Evidence from the Geological Record'. in *When Did Plate Tectonics Begin on Planet Earth?*. ed. by Condie, Kent, C. and Pease, V. Geological Society of America Special Paper 440, 281–294

Condie, K.C. and O'Neill, C. (2010) 'The Archean-Proterozoic Boundary: 500 My of Tectonic Transition in Earth History'. *American Journal of Science* 310 (9), 775–790

Corazzato, C., Francalanci, L., Menna, M., Petrone, C.M., and Renzulli, A. (2008) 'What Controls Sheet Intrusion in Volcanoes? Structure and Petrology of the Stromboli Sheet Complex , Italy'. *Journal of Volcanology and Geothermal Research* 173, 26–54

Corfu, F. (1998) 'U-Pb Zircon Systematics at Gruinard Bay, Northwest Scotland : Implications for the Early Orogenic Evolution of the Lewisian Complex'. *Contributions to Mineralogy and Petrology* 133, 329–345

Corfu, F., Heaman, L.M., and Rogers, G. (1994) 'Polymetamorphic Evolution of the Lewisian Complex, NW Scotland, as Recorded by U-Pb Isotopic Compositions of Zircon, Titanite and Rutile'. *Contributions to Mineralogy and Petrology* 117 (3), 215–228

Crowley, Q.G., Key, R., and Noble, S.R. (2015) 'High-Precision U–Pb Dating of Complex Zircon from the Lewisian Gneiss Complex of Scotland Using an Incremental CA-ID-TIMS Approach'. *Gondwana Research* 27 (4), 1381–1391

Dare, S.A.S., Barnes, S.J., and Prichard, H.M. (2010) 'The Distribution of Platinum Group Elements (PGE) and Other Chalcophile Elements among Sulfides from the Creighton Ni-Cu-PGE Sulfide Deposit, Sudbury, Canada, and the Origin of Palladium in Pentlandite'. *Mineralium Deposita* 45 (8), 765–793

Davaille, A., Smrekar, S.E., and Tomlinson, S. (2017) 'Experimental and Observational Evidence for Plume-Induced Subduction on Venus'. *Nature Geoscience* 10 (5), 349–355

Davies, F.B. (1974) 'A Layered Basic Complex in the Lewisian, South of Loch Laxford, Sutherland'. *Journal of the Geological Society* 130, 279–284

Davies, J.H.F.L. and Heaman, L.M. (2014) 'New U-Pb Baddeleyite and Zircon Ages for the Scourie Dyke Swarm: A Long-Lived Large Igneous Province with Implications for the Paleoproterozoic Evolution of NW Scotland'. *Precambrian Research* 249, 180–198

Debaille, V., Neill, C.O., Brandon, A.D., Haenecour, P., Yin, Q., Mattielli, N., and Treiman, A.H. (2013) 'Stagnant-Lid Tectonics in Early Earth Revealed by 142Nd in Late Archean Rocks'. *Earth and Planetary Science Letters* 373, 83–92

Deschamps, F., Godard, M., Guillot, S., Hattori, K., Deschamps, F., Godard, M., Guillot, S., and Hattori, K. (2013) 'Geochemistry of Subduction Zone Serpentinites: A Review'. *Lithos* 178 (March), 96–127

Dhuime, B., Hawkesworth, C.J., Delavault, H., and Cawood, P.A. (2018) 'Rates of Generation and Destruction of the Continental Crust: Implications for Continental Growth'. *Philosophical Transactions. Series A, Mathematical, Physical, and Engineering Sciences* 376 (2132)

Dhuime, B., Wuestefeld, A., and Hawkesworth, C.J. (2015) 'Emergence of Modern Continental Crust about 3 Billion Years Ago'. *Nature Geoscience* 8 (July), 552–555

Diener, J.F.A., Stevens, G., Kisters, A.F.M., and Poujol, M. (2005) 'Metamorphism and Exhumation of the Basal Parts of the Barberton Greenstone Belt, South Africa: Constraining the Rates of Mesoarchaean Tectonism'. *Precambrian Research* 143 (1–4), 87–112

Dilek, Y. and Polat, A. (2008) 'Suprasubduction Zone Ophiolites and Archean Tectonics'. *Geology* 36 (5), 431–432

Dönmez, C., Keskin, S., Günay, K., Çolakoğlu, A.O., Çiftçi, Y., Uysal, I., Türkel, A., and Yildirim, N. (2014) 'Chromite and PGE Geochemistry of the Elekdağ Ophiolite (Kastamonu, Northern Turkey): Implications for Deep Magmatic Processes in a Supra-Subduction Zone Setting'. *Ore Geology Reviews* 57, 216–228

Droop, G.T.R. (1987) 'A General Equation for Estimating Fe3+ Concentrations in

Ferromagnesian Silicates and Oxides from Microprobe Analyses, Using Stoichiometric Criteria'. *Mineralogical Magazine* 51 (361), 431–435

Ducea, M.N., Saleeby, J.B., and Bergantz, G. (2015) 'The Architecture, Chemistry, and Evolution of Continental Magmatic Arcs'. *Annual Review of Earth and Planetary Sciences* 43 (1), 299–331

Dziggel, A. (2002) *The Petrogenesis of 'Lower' Onverwacht Group Clastic Metasediments and Related Metavolcanic Rocks in the Southern Part of the Barberton Mountain Land, South Africa*. University of the Witwatersrand, Johannesburg

Eby, G.N. (1992) 'Chemical Subdivision of the A-Type Granitoids: Petrogenetic and Tectonic Implications'. *Geology* 20 (7), 641–644

Eglington, B.M. and Armstrong, R.A. (2004) 'The Kaapvaal Craton and Adjacent Orogens, Southern Africa: A Geochronological Database and Overview of the Geological Development of the Craton'. *South African Journal of Geology* 107 (1–2), 13–32

Eriksson, P.G., Altermann, W., and Hartzer, F.J. (2006) 'The Tansvaal Supergroup and Its Precursors'. in *The Geology of South Africa*. 237–260

Eriksson, P.G., Banerjee, S., Nelson, D.R., Rigby, M.J., Catuneanu, O., Sarkar, S., Roberts, R.J., Ruban, D., Mtimkulu, M.N., and Sunder Raju, P. V. (2009) 'A Kaapvaal Craton Debate: Nucleus of an Early Small Supercontinent or Affected by an Enhanced Accretion Event?' *Gondwana Research* 15 (3–4), 354–372

Evans, C.R. (1965) 'Geochronology of the Lewisian Basement near Lochinver, Sutherland'. *Nature* 207, 54–56

Evans, C.R. and Lambert, R.S.J. (1974) 'The Lewisian of Lochinver, Sutherland; the Type Area for the Inverian Metamorphism'. *Journal of the Geological Society* 130 (2), 125–150

Evans, C.R. and Tarney, J. (1964) 'Isotopic Ages of Assynt Dykes'. *Nature* 201, 464–466

Faithfull, J.W., Dempster, T.J., MacDonald, J.M., and Reilly, M. (2018) 'Metasomatism and the Crystallization of Zircon Megacrysts in Archaean Peridotites from the Lewisian Complex, NW Scotland'. *Contributions to Mineralogy and Petrology* 173 (12), 99

Feather, C.E. (1976) 'Mineralogy of Platinum-Group Minerals in the Witwatersrand, South Africa'. *Economic Geology* 71, 1399–1428

Feisel, Y., White, R.W., Palin, R.M., and Johnson, T.E. (2018) 'New Constraints on Granulite Facies Metamorphism and Melt Production in the Lewisian Complex, Northwest Scotland'. *Journal of Metamorphic Geology* 36 (March), 799–819

Feng, F., Fan, J., and Kerrich, R. (1993) 'Noble Metal Abundances and Characteristics of Six Granitic Magma Series, Archean Abitibi Belt, Pontiac Subprovince: Relationships to Metallogeny and Overprinting of Mesothermal Gold Deposits'. *Economic Geology* 88 (6), 1376–1401

Floyd, P.A. and Winchester, J.A. (1975) 'Magma Type and Tectonic Setting Discrimination Using Immobile Elements'. *Earth and Planetary Science Letters* 27, 211–218

Floyd, P.A. and Winchester, J.A. (1978) 'Identification and Discrimination of Altered and Metamorphosed Volcanic Rocks Using Immobile Elements'. *Chemical Geology* 21, 291–306

Forsyth, D. and Uyeda, S. (1975) 'On the Relative Importance of the Driving Forces of Plate Motion'. *Geophys. J. R. Atr. Soc.* 43, 163–200

Fowler, A.C. (1996) 'A Mechanism for Episodic Subduction on Venus'. *Journal of Geophysical Research E: Planets* 101 (E2), 4755–4763

Friend, C.R.L. and Kinny, P.D. (1995) 'New Evidence for the Protolith Ages of Lewisian Granulites, Northwest Scotland'. *Geology* 23, 1027–1030

Friend, C.R.L. and Kinny, P.D. (2001) 'A Reappraisal of the Lewisian Gneiss Complex: Geochronological Evidence for Its Tectonic Assembly from Disparate Terranes in the Proterozoic'. *Contributions to Mineralogy and Petrology* 142 (2), 198–218

Friend, C.R.L. and Nutman, A.P. (2010) 'Eoarchean Ophiolites? New Evidence for the Debate on the Isua Supracrustal Belt, Southern West Greenland'. *American Journal of Science* 310, 826–861

Friend, L., Bennett, C., Nutman, P., Friend, C.R.L., Bennett, V.C., and Nutman, A.P. (2002) 'Abyssal Peridotites >3,800 Ma from Southern West Greenland: Field Relationships, Petrography, Geochronology, Whole-Rock and Mineral Chemistry of Dunite and Harzburgite Inclusions in the Itsaq Gneiss Complex'. *Contributions to Mineralogy and Petrology* 143 (1), 71–92

Furnes, H., Dilek, Y., and de Wit, M. (2015) 'Precambrian Greenstone Sequences Represent

Different Ophiolite Types'. *Gondwana Research* 27 (2), 649–685

Furnes, H., Robins, B., and De Wit, M.J. (2012) 'Geochemistry and Petrology of Lavas in the Upper Onverwacht Suite, Barberton Mountain Land, South Africa'. *South African Journal of Geology* 115 (2), 171–210

Furnes, H., Rosing, M., Dilek, Y., and de Wit, M. (2009) 'Isua Supracrustal Belt (Greenland)-A Vestige of a 3.8 Ga Suprasubduction Zone Ophiolite, and the Implications for Archean Geology'. *Lithos* 113 (1–2), 115–132

Furnes, H., de Wit, M., and Robins, B. (2013) 'A Review of New Interpretations of the Tectonostratigraphy, Geochemistry and Evolution of the Onverwacht Suite, Barberton Greenstone Belt, South Africa'. *Gondwana Research* 23 (2), 403–428

Furnes, H., de Wit, M., Staudigel, H., Rosing, M., and Muehlenbachs, K. (2007a) 'A Vestige of Earth's Oldest Ophiolite'. *Science* 315 (5819), 1704–1707

Furnes, H., de Wit, M., Staudigel, H., Rosing, M., and Muehlenbachs, K. (2007b) 'Response to Comments on "A Vestige of Earth's Oldest Ophiolite"'. *Science* 318 (5851), 746e–746e

Gauthier, M., Corrivaux, L., Trottier, L.J., and Bortholomew, I.D. (1990) 'Chromitites Platiniferes Des Complexes Ophiolitiques de l'Estrie - Beauce, Appalaches Du Sud Du Quebec'. *Mineralium Deposita* 25 (169–178)

Godard, M., Jousselin, D., and Bodinier, J. (2000) 'Relationships between Geochemistry and Structure beneath a Palaeo-Spreading Centre: A Study of the Mantle Section in the Oman Ophiolite'. *Earth and Planetary Science Letters* 180, 133–148

Godard, M., Lagabrielle, Y., Alard, O., and Harvey, J. (2008) 'Geochemistry of the Highly Depleted Peridotites Drilled at ODP Sites 1272 and 1274 (Fifteen-Twenty Fracture Zone, Mid-Atlantic Ridge): Implications for Mantle Dynamics beneath a Slow Spreading Ridge'. *Earth and Planetary Science Letters* 267, 410–425

Godel, B., Barnes, S.J., and Maier, W.D. (2007) 'Platinum-Group Elements in Sulphide Minerals, Platinum-Group Minerals, and Whole-Rocks of the Merensky Reef (Bushveld Complex, South Africa): Implications for the Formation of the Reef'. *Journal of Petrology* 48 (8), 1569–1604

González-Jiménez, J.M., Gervilla, F., Proenza, J.A., Augé, T., and Kerestedjian, T. (2009)

'Distribution of Platinum-Group Minerals in Ophiolitic Chromitites'. *Applied Earth Science: IMM Transactions Section B* 118 (3), 101–110

Goodenough, K.M., Crowley, Q.G., Krabbendam, M., and Parry, S.F. (2013) 'New U-Pb Age Constraints for the Laxford Shear Zone, NW Scotland: Evidence Fortectono-Magmatic Processes Associated with the Formation of a Paleoproterozoic Supercontinent'. *Precambrian Research* 232, 1–19

Goodenough, K.M. and Krabbendam, M. (2011) *A Geological Excursion Guide to the North-West Highlands of Scotland*. Edinburgh Geological Society

Goodenough, K.M., Park, R.G., Krabbendam, M., Myers, J.S., Wheeler, J., Loughlin, S.C., Crowley, Q.G., Friend, C.R.L., Beach, A., Kinny, P.D., and Graham, R.H. (2010) 'The Laxford Shear Zone: An End-Archaean Terrane Boundary?' *Geological Society, London, Special Publications* 335 (1), 103–120

Google Earth (2004) *Greenstone Hill. 26°07'14.34"S, 28°09'05.75"E. Accessed: 1st June 2016*.

Google Earth (2016) *Greenstone Hill. 26°07'14.34"S, 28°09'05.75"E. Accessed 1st June 2016*.

Gough, D.I. and Hales, A.L. (1956) 'A Study of the Palaeomagnetism of the Pilanesberg Dykes'. *Geophysical Journal International* 7, 196–213

Govindaraju, K. (1994) 'Compilation of Working Values and Samples Description for 383 Geostandards'. *Geostandards Newsletter* 18 (1–158)

Greber, N.D., Puchtel, I.S., Nägler, T.F., and Mezger, K. (2015) 'Komatiites Constrain Molybdenum Isotope Composition of the Earth's Mantle'. *Earth and Planetary Science Letters* 421, 129–138

Grosch, E.G. and Slama, J. (2017) 'Evidence for 3.3-Billion-Year-Old Oceanic Crust in the Barberton Greenstone Belt, South Africa'. *Geology* 45 (7), 1–4

Gruenewaldt, G. Von, Hulbert, L.J., and Naldrett, A.J. (1989) 'Contrasting Platinum-Group Element Concentration Patterns in Cumulates of the Bushveld Complex'. *Mineralium Deposita* 229, 219–229

Guice, G.L., McDonald, I., Hughes, H., Schlatter, D., Goodenough, K., MacDonald, J., and Faithfull, J. (2018a) 'Assessing the Validity of Negative High Field Strength-Element

Anomalies as a Proxy for Archaean Subduction: Evidence from the Ben Strome Complex, NW Scotland'. *Geosciences* 8 (9), 338

Guice, G.L., Mcdonald, I., Hughes, H.S.R., and Anhaeusser, C.R. (2019) 'An Evaluation of Element Mobility in the Modderfontein Ultramafic Complex, Johannesburg: Origin as an Archaean Ophiolite Fragment or Greenstone Belt Remnant?' *Lithos* [online] 332–333, 99–119. available from <https://doi.org/10.1016/j.lithos.2019.02.013>

Guice, G.L., McDonald, I., Hughes, H.S.R., MacDonald, J.M., Blenkinsop, T.G., Goodenough, K.M., Faithfull, J.W., and Gooday, R.J. (2018b) 'Re-Evaluating Ambiguous Age Relationships in Archean Cratons: Implications for the Origin of Ultramafic-Mafic Complexes in the Lewisian Gneiss Complex'. *Precambrian Research* 311, 136–156

Guo, R., Liu, S., Bai, X., and Wang, W. (2017) 'A Neoarchean Subduction Recorded by the Eastern Hebei Precambrian Basement, North China Craton: Geochemical Fingerprints from Metavolcanic Rocks of the Saheqiao-Shangying-Qinglong Supracrustal Belt'. *Journal of Asian Earth Sciences* 135, 347–369

Halla, J. (2018) 'Highlights on Geochemical Changes in Archaean Granitoids and Their Implications for Early Earth Geodynamics'. *Geosciences* 8 (9), 353

Hamilton, W.B. (1998) 'Archean Magmatism and Deformation Were Not Products of Plate Tectonics'. *Precambrian Research* 91 (1–2), 143–179

Hamilton, W.B. (2003) 'An Alternative Earth'. *GSA Today* 13 (11), 4–12

Hamilton, W.B. (2007) 'Earth's First Two Billion Years — The Era of Internally Mobile Crust'. *The Geological Society of America, Memoir* 200, 233–296

Hamilton, W.B. (2011) 'Plate Tectonics Began in Neoproterozoic Time, and Plumes from Deep Mantle Have Never Operated'. *Lithos* 123, 1–20

Hanghòj, K., Kelemen, P.B., Hassler, D., Godard, M., Hanghøj, K., Kelemen, P.B., Hassler, D., and Godard, M. (2010) 'Composition and Genesis of Depleted Mantle Peridotites from the Wadi Tayin Massif, Oman Ophiolite; Major and Trace Element Geochemistry, and Os Isotope and PGE Systematics'. *Journal of Petrology* 51 (1–2), 201–227

Harper, G.D. (1986) 'Dismembered Archean Ophiolite in the Southeastern Wind River'. *Dept. Geological Sciences, State University of New York* 47–49

Hart, R.J., Andreoli, M.A.G., Smith, C.B., Otter, M.L., and Durrheim, R. (1990) 'Ultramafic Rocks in the Centre of the Vredefort Structure (South Africa): Possible Exposure of the Upper Mantle ?' *Chemical Geology* 83, 233–248

Hastie, A.R., Fitton, J.G., Bromiley, G.D., Butler, I.B., and Odling, N.W.A. (2016) 'The Origin of Earth's First Continents and the Onset of Plate Tectonics'. *Geology* (10), 855–858

Hastie, A.R., Kerr, A.C., McDonald, I., Mitchell, S.F., Pearce, J.A., Wolstencroft, M., and Millar, I.L. (2010) 'Do Cenozoic Analogues Support a Plate Tectonic Origin for Earth's Earliest Continental Crust?' *Geology* 38 (6), 495–498

Hastie, A.R., Kerr, A.C., Pearce, J.A., and Mitchell, S.F. (2007) 'Classification of Altered Volcanic Island Arc Rocks Using Immobile Trace Elements: Development of the Th-Co Discrimination Diagram'. *Journal of Petrology* 48 (12), 2341–2357

Heaman, L.M. and Tarney, J. (1989) 'U–Pb Baddeleyite Ages for the Scourie Dyke Swarm, Scotland – Evidence for 2 Distinct Intrusion Events'. *Nature* 340, 705–708

Hill, I.G., Worden, R.H., and Meighan, I.G. (2000) 'Yttrium: The Immobility-Mobility Transition during Basaltic Weathering'. *Geology* 28 (10), 923–926

Hilliard, P., S., M., and McCourt, S. (1995) 'Bedding-Parallel Simple Shear Deformation in the West Rand Group Rocks on Northcliff Promontory, Johannesburg, South Africa - Insight into the Late Archaean Evolution of the Kaapvaal Craton'. *South African Journal of Geology* 98 (4), 349–355

Hoatson, D.M. and Sun, S.S. (2002) 'Archean Layered Mafic-Ultramafic Intrusions in the West Pilbara Craton, Western Australia: A Synthesis of Some of the Oldest Orthomagmatic Mineralizing Systems in the World'. *Economic Geology* 97 (4), 847–872

Hoffmann, J.E., Münker, C., Polat, A., König, S., Mezger, K., and Rosing, M.T. (2010) 'Highly Depleted Hadean Mantle Reservoirs in the Sources of Early Archean Arc-like Rocks, Isua Supracrustal Belt, Southern West Greenland'. *Geochimica et Cosmochimica Acta* 74 (24), 7236–7260

Hofmann, A. and Harris, C. (2008) 'Silica Alteration Zones in the Barberton Greenstone Belt: A Window into Subseafloor Processes 3.5-3.3 Ga Ago'. *Chemical Geology* 257 (3–4), 224–242

Holwell, D.A. and McDonald, I. (2007) 'Distribution of Platinum-Group Elements in the Platreef at Overysel, Northern Bushveld Complex: A Combined PGM and LA-ICP-MS Study'. *Contributions to Mineralogy and Petrology* 154 (2), 171–190

Holwell, D.A., Mitchell, C.L., Howe, G.A., Evans, D.M., Ward, L.A., and Friedman, R. (2017) 'The Munali Ni Sulfide Deposit , Southern Zambia : A Multi-Stage , Megabreccia'. *Ore Geology Reviews*

Honour, V.C., Goodenough, K.M., Shaw, R.A., Gabudianu, I., and Hirtopanu, P. (2018) 'REE Mineralisation within the Ditrău Alkaline Complex, Romania: Interplay of Magmatic and Hydrothermal Processes'. *Lithos* 314–315, 360–381

Hopkins, M., Harrison, T.M., and Manning, C.E. (2008) 'Low Heat Flow Inferred from >4 Gyr Zircons Suggests Hadean Plate Boundary Interactions'. *Nature* 456 (November), 493–496

Hopkins, M.D., Harrison, T.M., and Manning, C.E. (2010) 'Constraints on Hadean Geodynamics from Mineral Inclusions in >4Ga Zircons'. *Earth and Planetary Science Letters* 298 (3–4), 367–376

Huber, H., Koeberl, C., McDonald, I., and Reimold, W.U. (2001) 'Geochemistry and Petrology of Witwatersrand and Dwyka Diamictites from South Africa: Search for an Extraterrestrial Component'. *Geochimica et Cosmochimica Acta* 65 (12), 2007–2016

Hughes, H.S.R., McDonald, I., and Kerr, A.C. (2014) 'Platinum-Group Element Signatures in the North Atlantic Igneous Province: Implications for Mantle Controls on Metal Budgets during Continental Breakup'. *Lithos* 233, 89–110

Hynes, A. (1980) 'Carbonitization and Mobility of Ti, Y and Zr in Ascot Formation Metabasalts, S.E. Quebec'. *Contributions to Mineralogy and Petrology* 75 (1), 79–87

Irvine, T.N. (1965) 'Chromian Spinel as a Petrogenetic Indicator. Part I. Theory.' *Canadian Journal of Earth Science* 2, 648–672

Irvine, T.N. (1967) 'Chromian Spinel as a Petrogenetic Indicator, Part 2. Petrologic Applications'. *Canadian Journal of Earth Science* 4, 71–103

Irvine, T.N. (1977) 'Origin of Chromitite Layers in the Muskox Intrusion and Other Stratiform Intrusions: A New Interpretation'. *Geology* 5, 273–277

Irvine, T.N. (1982) 'Terminology for Layered Intrusions'. *Journal of Petrology* 23 (2), 127–162

Isacks, B., Oliver, J., and Sykes, L.R. (1968) 'Seismology and the New Global Tectonics'. *Journal of Geophysical Research* 73, 5855–5899

Ismail, S.A., Kettanah, Y.A., Chalabi, S.N., Ahmed, A.H., and Arai, S. (2014) 'Petrogenesis and PGE Distribution in the Al- and Cr-Rich Chromitites of the Qalander Ophiolite, Northeastern Iraq: Implications for the Tectonic Environment of the Iraqi Zagros Suture Zone'. *Lithos* 202–203, 21–36

Ivanic, T.J., Nebel, O., Brett, J., and Murdie, R.E. (2017) 'The Windimurra Igneous Complex: An Archean Bushveld?' *Geological Society, London, Special Publications* 453, SP453.1

Ivanic, T.J., Wingate, M.T.D., Kirkland, C.L., and Kranendonk, M.J. Van (2010) 'Age and Significance of Voluminous Mafic – Ultramafic Magmatic Events in the Murchison Domain , Yilgarn Craton Age and Significance of Voluminous Mafic – Ultramafic Magmatic Events in the Murchison Domain , Yilgarn'. *Australian Journal of Earth Sciences* 57 (5), 597–614

Johnson, T.E., Brown, M., Gardiner, N.J., Kirkland, C.L., and Smithies, R.H. (2017) 'Earth's First Stable Continents Did Not Form by Subduction'. *Nature* 543, 239

Johnson, T.E., Brown, M., Goodenough, K.M., Clark, C., Kinny, P.D., and White, R.W. (2016) 'Subduction or Sagduction? Ambiguity in Constraining the Origin of Ultramafic – Mafic Bodies in the Archean Crust of NW Scotland'. *Precambrian Research* 283, 89–105

Johnson, T.E., Fischer, S., and White, R.W. (2013) 'Field and Petrographic Evidence for Partial Melting of TTG Gneisses from the Central Region of the Mainland Lewisian Complex, NW Scotland'. *Journal of the Geological Society* 170 (2), 319–326

Johnson, T.E., Fischer, S., White, R.W., Brown, M., and Rollinson, H.R. (2012) 'Archaean Intracrustal Differentiation from Partial Melting of Metagabbro-Field and Geochemical Evidence from the Central Region of the Lewisian Complex, NW Scotland'. *Journal of Petrology* 53 (10), 2115–2138

Johnson, T.E., Hartley, S., Guice, G.L., and Goodenough, K.M. (2018) 'Granulites & Granulites 2018: Assynt Field Guide'. *Granulites & Granulites Conference*

Johnson, T.E., Kirkland, C.L., Gardiner, N.J., Brown, M., Smithies, R.H., and Santosh, M.

(2019) 'Secular Change in TTG Compositions: Implications for the Evolution of Archaean Geodynamics'. *Earth and Planetary Science Letters* 505, 65–75

Johnson, T.E. and White, R.W. (2011) 'Phase Equilibrium Constraints on Conditions of Granulite-Facies Metamorphism at Scourie, NW Scotland'. *Journal of the Geological Society* 168 (1), 147–158

Jolley, S.J., Freeman, S.R., Barnicoat, A.C., Phillips, G.M., Knipe, R.J., and Pather, A. (2004) 'Structural Controls on Witwatersrand Gold Mineralisation'. *Journal of Structural Geology* 26, 1067–1086

Josey, I.K. and Shaw, N.D. (1974) 'Discussion of a Layered Basic Complex in the Lewisian'. *Journal of the Geological Society* 130, 595–597

Junge, M., Wirth, R., Oberthür, T., Melcher, F., and Schreiber, A. (2014) 'Mineralogical Siting of Platinum-Group Elements in Pentlandite from the Bushveld Complex, South Africa'. *Mineralium Deposita* 50 (1), 41–54

Kamber, B.S. (2015) 'The Evolving Nature of Terrestrial Crust from the Hadean, through the Archaean, into the Proterozoic'. *Precambrian Research* 258, 48–82

Kamenetsky, V.S., Crawford, A.J., and Meffre, S. (2001) 'Factors Controlling Chemistry of Magmatic Spinel : An Empirical Study of Associated Olivine, Cr-Spinel and Melt Inclusions from Primitive Rocks'. *Journal of Petrology* 42 (4), 655–671

Kamo, S.L. and Davis, D.W. (1994) 'Reassessment of Archean Crustal Development in the Barberton Mountain Land, South Africa, Based on U-Pb Dating'. *Tectonics* 13 (1), 167–192

Kearey, P., Klepeis, K.A., and Vine, F.J. (2009) *Global Tectonics*. 3rd editio. Wiley-Blackwell

Keller, B. and Schoene, B. (2018) 'Plate Tectonics and Continental Basaltic Geochemistry throughout Earth History'. *Earth and Planetary Science Letters* 481, 290–304

Kerr, A., Marriner, G., Arndt, N., Tarney, J., Nivia, A., Saunders, A., and Duncan, R. (1996) 'The Petrogenesis of Gorgona Komatiites, Picrites and Basalts New Field, Petrographic and Geochemical Constraints.' *Lithos* 37, 245–260

Khanna, T.C., Sesha Sai, V.V., Jaffri, S.H., Krishna, A.K., and Korakoppa, M.M. (2018) 'Boninites in the ~3.3 Ga Holenarsipur Greenstone Belt, Western Dharwar Craton,

India'. *Geosciences* 8 (7), 248

Kinny, P., Friend, C., and Love, G. (2005) 'Proposal for a Terrane-Based Nomenclature for the Lewisian Gneiss Complex of NW Scotland'. *Journal of the Geological Society* 162, 175–186

Kinny, P.D. and Friend, C.R.L. (1997) 'U-Pb Isotopic Evidence for the Accretion of Different Crustal Blocks to Form the Lewisian Complex of Northwest Scotland'. *Contributions to Mineralogy and Petrology* 129 (4), 326–340

Kirk, J., Ruiz, J., Chesley, J., Titley, S., and Walshie, J. (2001) 'A Detrital Model for the Origin of Gold and Sulfides in the Witwatersrand Basin Based on Re-Os Isotopes'. *Geochimica et Cosmochimica Acta* 65 (13), 2149–2159

Kirk, J., Ruiz, J., Chesley, J., Walshe, J., and England, G. (2002) *A Major Archean , Gold- and Crust-Forming Event in the Kaapvaal Craton , South Africa*. 297 (September), 1856–1859

Kisters, A.F.M., Belcher, R.W., Poujol, M., and Dziggel, A. (2010) 'Continental Growth and Convergence-Related Arc Plutonism in the Mesoarchaean: Evidence from the Barberton Granitoid-Greenstone Terrain, South Africa'. *Precambrian Research* 178 (1–4), 15–26

Kisters, A.F.M. and Szilas, K. (2012) 'Geology of an Archaean Accretionary Complex – The Structural Record of Burial and Return Flow in the Tartoq Group of South West Greenland'. *Precambrian Research* 220–221 (November), 107–122

Klemme, S., Prowatke, S., Hametner, K., and Gunther, D. (2005) 'Partitioning of Trace Elements between Rutile and Silicate Melts: Implications for Subduction Zones'. *Geochimica et Cosmochimica Acta* 69 (9), 2361–2371

Kolb, J., Bagas, L., and Fiorentini, M.L. (2015) 'Metallogeny of the North Atlantic Craton in Greenland'. *Mineralogical Magazine* 78 (4), 813–853

Kolb, J., Thrane, K., and Bagas, L. (2013) 'Field Relationship of High-Grade Neo- to Mesoarchaean Rocks of South-East Greenland: Tectonometamorphic and Magmatic Evolution'. *Gondwana Research* 23 (2), 471–492

Komiya, T., Maruyama, S., Masuda, T., Nohda, S., Hayashi, M., and Okamoto, K. (1999) 'Plate Tectonics at 3.8-3.7 Ga: Field Evidence from the Isua Accretionary Complex,

Southern West Greenland'. *The Journal of Geology* 107, 515–554

Kontinen, A. (1987) 'An Early Proterozoic Ophiolite - the Jormua Mafic-Ultramafic Complex, Northeastern Finland'. *Precambrian Research* 35, 313–341

Korenaga, J. (2013) 'Initiation and Evolution of Plate Tectonics on Earth: Theories and Observations'. *Annual Review of Earth and Planetary Sciences* 41 (1), 117–151

Van Kranendonk, M.J. and Cassidy, K. (2003) 'Comment and Reply An Alternative Earth, Warren B. Hamilton'. *GSA Today* 13 (11), 4–12

Van Kranendonk, M.J., Collins, W.J., Hickman, A., and Pawley, M.J. (2004) 'Critical Tests of Vertical vs. Horizontal Tectonic Models for the Archaean East Pilbara Granite-Greenstone Terrane, Pilbara Craton, Western Australia'. *Precambrian Research* 131 (3–4), 173–211

Van Kranendonk, M.J., Hugh Smithies, R., Hickman, A.H., and Champion, D.C. (2007) 'Review: Secular Tectonic Evolution of Archean Continental Crust: Interplay between Horizontal and Vertical Processes in the Formation of the Pilbara Craton, Australia'. *Terra Nova* 19 (1), 1–38

Van Kranendonk, M. J, Kröner, A., Hoffmann, J.E., Nagel, T., and Anhaeusser, C.R. (2014) 'Just Another Drip : Re-Analysis of a Proposed Mesoarchean Suture from the Barberton Mountain Land, South Africa'. *Precambrian Research* 254, 19–35

Van Kranendonk, M. J., Smithies, R.H., Griffin, W.L., Huston, D.L., Hickman, A.H., Champion, D.C., Anhaeusser, C.R., and Pirajno, F. (2014) 'Making It Thick: A Volcanic Plateau Origin of Palaeoarchean Continental Lithosphere of the Pilbara and Kaapvaal Cratons'. *Geological Society, London, Special Publications* 389 (1), 83–111

Kröner, A., Hegner, E., Wendt, J.I., and Byerly, G.R. (1996) 'The Oldest Part of the Barberton Granitoid-Greenstone Terrain, South Africa: Evidence for Crust Formation between 3.5 and 3.7 Ga'. *Precambrian Research* 78 (1–3), 105–124

Kusky, T.M. (2012) 'The Neoarchean Ophiolite in the North China Craton : Early Precambrian Plate Tectonics and Scientific Debate'. *Journal of Earth Science* 23 (3), 277–284

Kusky, T.M. and Jianghai, L. (2010) 'Origin and Emplacement of Archean Ophiolites of the Central Orogenic Belt , North China Craton'. *Journal of Earth Science* 21 (5), 744–781

Kusky, T.M., Li, J., and Tucker, R.D. (2001) 'The Archean Dongwanzi Oceanic Crust and Mantle'. *Science* 292 (May), 1142–1146

Kusky, T.M. and Li, J.H. (2008) 'Note on the Paper by Guochun Zhao , Simon A . Wilde , Sanzhong Li , Min Sun , Matthew L . Grant and Xuping Li , 2007 , " U – Pb Zircon Age Constraints on the Dongwanzi Ultramafic – Mafic Body , North China, Confirm It Is Not an Archean Ophiolite "'. *Earth and Planetary Science Letters* 273, 227–230

Kusky, T.M., Zhi, X., Li, J., Xia, Q., Raharimahefa, T., and Huang, X. (2007) 'Chondritic Osmium Isotopic Composition of Archean Ophiolitic Mantle, North China Craton'. *Gondwana Research* 12, 67–76

Lahaye, Y., Arndt, N., Byerly, G., Chauvel, C., Fourcade, S., and Gruau, G. (1995) 'The Influence of Alteration on the Trace-Element and Nd Isotopic Compositions of Komatiites'. *Chemical Geology* 126, 43–64

Landi, P., Francalanci, L., Pompilio, M., Rosi, M., and Corsaro, R.A. (2006) 'The December 2002 – July 2003 Effusive Event at Stromboli Volcano , Italy : Insights into the Shallow Plumbing System by Petrochemical Studies'. *Journal of Volcanology and Geothermal Research* 155 (July 2003), 263–284

Lee, J.H. and Byrne, R.H. (1993) 'Complexation of Trivalent Rare Earth Elements (Ce, Eu, Gd, Tb, Yb) by Carbonate Ions'. *Geochemica et Cosmochimica Acta* 57, 295–302

Lodders, K. (2003) 'Solar System Abundances and Condensation Temperatures of the Elements'. *The Astrophysical Journal* 591 (2), 1220–1247

Lopez-Martinez, M., York, D., and Hanes, J.A. (1992) 'A 40Ar/ 39Ar Geochronological Study of Komatiites and Komatiitic Basalts from the Lower Onverwacht Volcanics : Barberton Mountain Land, South Africa'. *Precambrian Research* 57, 91–119

Lorand, J., Luguet, A., and Alard, O. (2008) 'Platinum-Group Elements: A New Set of Key Tracers for the Earth's Interior'. *Elements* 4 (Aug. 2008), 247–252

Lorand, J., Luguet, A., and Alard, O. (2013) 'Platinum-Group Element Systematics and Petrogenetic Processing of the Continental Upper Mantle: A Review'. *Lithos* 164–167, 2–21

Love, G.J., Friend, C.R.L., and Kinny, P.D. (2010) 'Palaeoproterozoic Terrane Assembly in the Lewisian Gneiss Complex on the Scottish Mainland, South of Gruinard Bay: SHRIMP U-

Pb Zircon Evidence'. *Precambrian Research* 183 (1), 89–111

Love, G.J., Kinny, P.D., and Friend, C.R.L. (2004) 'Timing of Magmatism and Metamorphism in the Gruinard Bay Area of the Lewisian Gneiss Complex: Comparisons with the Assynt Terrane and Implications for Terrane Accretion'. *Contributions to Mineralogy and Petrology* 146 (5), 620–636

Lowe, D.R. (1994) 'Accretionary History of the Archean Barberton Greenstone Belt (3.55-3.22 Ga), Southern Africa'. *Geology* 22 (12), 1099–1102

Lowe, D.R., Byerly, G.R., Ransom, B.L., and Nocita, B.W. (1985) 'Stratigraphic and Sedimentological Evidence Bearing on Structural Repetition in Early Archean Rocks of the Barberton Greenstone Belt, South Africa'. *Precambrian Research* 27 (1–3), 165–186

Luguet, A., Lorand, J.-P., and Seyler, M. (2003) 'Sulfide Petrology and Highly Siderophile Element Geochemistry of Abyssal Peridotites: A Coupled Study of Samples from the Kane Fracture Zone (45° W 23°20N , MARK Area , Atlantic Ocean)'. *Geochemica et Cosmochimica Acta* 67 (8), 1553–1570

MacDonald, J.M., Goodenough, K.M., Wheeler, J., Crowley, Q., Harley, S.L., Mariani, E., and Tatham, D. (2015) 'Temperature-Time Evolution of the Assynt Terrane of the Lewisian Gneiss Complex of Northwest Scotland from Zircon U-Pb Dating and Ti Thermometry'. *Precambrian Research* 260, 55–75

MacDonald, J.M., Magee, C., and Goodenough, K.M. (2017) 'Dykes as Physical Buffers to Metamorphic Overprinting: An Example from the Archaean – Palaeoproterozoic Lewisian Gneiss Complex of NW Scotland'. *Scottish Journal of Geology* 53 (2), 41–52

MacDonald, J.M., Wheeler, J., Harley, S.L., Mariani, E., Goodenough, K.M., Crowley, Q., and Tatham, D. (2013) 'Lattice Distortion in a Zircon Population and Its Effects on Trace Element Mobility and U-Th-Pb Isotope Systematics: Examples from the Lewisian Gneiss Complex, Northwest Scotland'. *Contributions to Mineralogy and Petrology* 166 (1), 21–41

Maier, W.D. (2003) 'The Concentration of the Platinum-Group Elements in South African Komatiites: Implications for Mantle Sources, Melting Regime and PGE Fractionation during Crystallization'. *Journal of Petrology* 44 (10), 1787–1804

Maier, W.D., Barnes, S.-J., and de Waal, S.A. (1998) 'Exploration for Magmatic Ni-Cu-PGE Sulphide Deposits: A Review of Recent Advances in the Use of Geochemical Tools, and Their Applications to Some South African Ores'. *South African Journal of Geology* 101 (3), 237–253

Maier, W.D., Barnes, S.J., Gartz, V., and Andrews, G. (2003) 'Pt-Pd Reefs in Magnetitites of the Stella Layered Intrusion, South Africa: A World of New Exploration Opportunities for Platinum Group Elements'. *Geology* 31 (10), 885–888

Manikyamba, C. and Kerrich, R. (2011) 'Geochemistry of Alkaline Basalts and Associated High-Mg Basalts from the 2.7 Ga Penakacherla Terrane, Dharwar Craton, India: An Archean Depleted Mantle-OIB Array'. *Precambrian Research* 188 (1–4), 104–122

Manya, S. (2004) 'Geochemistry and Petrogenesis of Volcanic Rocks of the Neoarchaean Sukumaland Greenstone Belt , Northwestern Tanzania'. *Journal of African Earth Sciences* 40, 269–279

Mason, A.J. (2016) 'The Palaeoproterozoic Anatomy of the Lewisian Complex, NW Scotland: Evidence for Two "Laxfordian" Tectonothermal Cycles'. *Journal of the Geological Society* 173 (1), 153–169

Mattioli, G.S. and Wood, B.J. (1988) 'Magnetite Activities across the MgAl2O4-Fe3O4 Spinel Join, with Application to Thermobarometric Estimates of Upper Mantle Oxygen Fugacity'. *Contributions to Mineralogy and Petrology* 98 (2), 148–162

McCall, G.J.H. (2003) 'A Critique of the Analogy between Archaean and Phanerozoic Tectonics Based on Regional Mapping of the Mesozoic-Cenozoic Plate Convergent Zone in the Makran, Iran'. *Precambrian Research* 127 (1–3), 5–17

McCulloch, M.T. and Gamble, J.A. (1991) 'Geochemical and Geodynamical Constraints on Subduction Zone Magmatism'. *Earth and Planetary Science Letters* 102 (3–4), 358–374

McDonald, I. (2008) 'Platinum-Group Element and Sulphide Mineralogy in Ultramafic Complexes at Western Andriamena, Madagascar'. *Applied Earth Science* 117 (1), 1–10

McDonald, I., Ohnenstetter, D., Rowe, J.P., Tredoux, M., Pattrick, R.A.D., and Vaughan, D.J. (1999) 'Platinum Precipitation in the Waterberg Deposit, Naboomspruit, South Africa'. *South African Journal of Geology* 102 (3), 184–191

Mcdonald, I., Ohnenstetter, D., and Vaughan, D.J. (1999) 'Palladium Oxides in Ultramafic

Complexes near Lavatrafo,Western Andriamena, Madagascar'. *Mineralogical Magazine* 63 (3), 345–352

McDonald, I., Vaughan, D.J., and Tredoux, M. (1995) 'Platinum Mineralization in Quartz Veins near Naboomspruit, Central Transvaal'. *South African Journal of Geology* 98 (2), 168–175

McDonald, I. and Viljoen, K.S. (2006) 'Platinum-Group Element Geochemistry of Mantle Eclogites: A Reconnaissance Study of Xenoliths from the Orapa Kimberlite, Botswana'. *Applied Earth Science* 115 (3), 81–93

McDonough, W.F. and Sun, S. s. (1995) 'The Composition of the Earth'. *Chemical Geology* 120 (3–4), 223–253

Metrich, N., Bertagnini, A., Landi, P., and Rosi, M. (2001) 'Crystallization Driven by Decompression and Water Loss at Stromboli Volcano (Aeolian Islands, Italy)'. *Journal of Petrology* 42 (8), 1471–1490

Metrich, N., Bertagnini, A., Landi, P., Rosi, M., and Belhadj, O. (2005) 'Triggering Mechanism at the Origin of Paroxysms at Stromboli (Aeolian Archipelago, Italy): The 5 April 2003 Eruption'. *Geophysical Research Letters* 32 (April 2003), 3–6

Moyen, J.-F. (2011) 'The Composite Archaean Grey Gneisses: Petrological Significance, and Evidence for a Non-Unique Tectonic Setting for Archaean Crustal Growth'. *Lithos* 123 (1–4), 21–36

Moyen, J. and Laurent, O. (2018) 'Archaean Tectonic Systems : A View from Igneous Rocks'. *Lithos* 302–303, 99–125

Moyen, J.F., Stevens, G., and Kisters, A. (2006) 'Record of Mid-Archaean Subduction from Metamorphism in the Barberton Terrain, South Africa'. *Nature* 442 (7102), 559–562

Myers, J.S. (1985) *Stratigraphy and Structure of the Fiskenæsset Complex, Southern West Greenland*. Geol. Survey Greenland. 150, 72 pp.

Najafzadeh, A.R. and Ahmadipour, H. (2014) 'Using Platinum-Group Elements and Au Geochemistry to Constrain the Genesis of Podiform Chromitites and Associated Peridotites from the Soghan Mafic-Ultramafic Complex, Kerman, Southeastern Iran'. *Ore Geology Reviews* 60, 60–75

Nakamura, N. (1974) 'Determination of REE, Ba, Fe, Na and K in Carbonaceous and Ordinary Chondrites'. *Geochemica et Cosmochimica Acta* 38, 757–775

Naldrett, A.J., Hoffman, E.L., Green, A.H., Chou, C., and Naldrett, S.R. (1979) 'The Composition of Ni-Sulfide Ores, with Particular Reference to Their Content of PGE and Au'. *Canadian Mineralogist* 17, 403–415

Namur, O., Abily, B., Boudreau, A.E., Blanchette, F., Bush, J.W.M., Ceulenneer, G., Charlier, B., Donaldson, C.H., Duchesne, J.-C., Higgins, M.D., Morata, D., Neilsen, T.F.D., O'Driscoll, B., Pang, K.N., Peacock, T., Spandler, C.J., Toramaru, A., and Veksler, I. V. (2015) 'Igneous Layering in Basaltic Magma Chambers'. in *Layered Intrusions*.

Nilsson, M.K.M. and Hamilton, M.A. (2016) *New U-Pb Ages for Mafic Dykes of SE Greenland*. 90 (July), 81–82

Nutman, A.P., Bennett, V.C., Friend, C.R.L., Hidaka, H., Yi, K., and Lee, S.R. (2013) 'The Itsaq Gneiss Complex of Greenland: Episodic 3900 to 3660 Ma Juvenile Crust Formation and Recycling in the 3660 to 3600 Ma Isukasian Orogeny'. *American Journal of Science* 313, 877–911

Nutman, A.P., Friend, C.R.L., and Bennett, V.C. (2002) 'Evidence for 3650-3600 Ma Assembly of the Northern End of the Itsaq Gneiss Complex, Greenland: Implication for Early Archaean Tectonics'. *Tectonics* 21 (1), 5-1-5–28

O'Hara, M.J. (1961) 'Zoned Ultrabasic and Basic Gneiss Masses in the Early Lewisian Metamorphic Complex at Scourie, Sutherland'. *Journal of Petrology* 2 (2), 248–276

O'Neil, G.S.C. and Wall, V.J. (1987) 'The Olivine-Orthopyroxene-Spinel Oxygen Geobarometer, the Nickel Precipitation Curve, and the Oxygen Fugacity of the Earth's Upper Mantle'. *Journal of Petrology* 28, 1169–1191

O'Neil, J., Francis, D., and Carlson, R.W. (2011) 'Implications of the Nuvvuagittuq Greenstone Belt for the Formation of Earth's Early Crust'. *Journal of Petrology* 52 (5), 985–1009

Olsson, J.R., Söderlund, U., Hamilton, M.A., Klausen, M.B., and Helffrich, G.R. (2011) 'A Late Archaean Radiating Dyke Swarm as Possible Clue to the Origin of the Bushveld Complex'. *Nature Geoscience* 4, 865

Ordóñez-calderón, J.C., Polat, A., Fryer, B.J., Appel, P.W.U., Gool, J.A.M. Van, Dilek, Y., and

Gagnon, J.E. (2009) 'Geochemistry and Geodynamic Origin of the Mesoarchean Ujarassuit and Ivisaartoq Greenstone Belts , SW Greenland'. *Lithos* 113 (1–2), 133–157

Osbahr, I., Klemd, R., Oberthür, T., Brätz, H., and Schouwstra, R. (2013) 'Platinum-Group Element Distribution in Base-Metal Sulfides of the Merensky Reef from the Eastern and Western Bushveld Complex, South Africa'. *Mineralium Deposita* 48 (2), 211–232

Ottley, C.J., Pearson, D.G., and Irvine, G.J. (2003) 'A Routine Method for the Dissolution of Geological Samples for the Analysis of REE and Trace Elements via ICP-MS.' in *Plasma Source Mass Spectrometry: Applications and Emerging Technologies*. 221–230

Park, R.G. (1970) 'Observations on Lewisian Chronology'. *Scottish Journal of Geology* 6 (4), 379–399

Park, R.G. (2005) 'The Lewisian Terrane Model: A Review'. *Scottish Journal of Geology* 41 (2), 105–118

Park, R.G., Stewart, A.D., and Wright, A.E. (2002) 'The Hebridean Terrane'. in *The Geology of Scotland*.

Park, R.G. and Tarney, J. (1987) 'The Lewisian Complex: A Typical Precambrian High-Grade Terrain?' *Geological Society, London, Special Publications* 27 (1), 13–25

Parman, S.W., Shimizu, N., Grove, T.L., and Dann, J.C. (2003) 'Constraints on the Pre-Metamorphic Trace Element Composition of Barberton Komatiites from Ion Probe Analyses of Preserved Clinopyroxene'. *Contributions to Mineralogy and Petrology* 144 (4), 383–396

Paulick, H., Bach, W., Godard, M., Hoog, J.C.M. De, Suhr, G., and Harvey, J. (2006) 'Geochemistry of Abyssal Peridotites (Mid-Atlantic Ridge , 15°20'N, ODP Leg 209): Implications for Fluid/Rock Interaction in Slow Spreading Environments'. *Chemical Geology* 234, 179–210

Peach, B.N., Horne, J., Gunn, A.G., and Clough, C.T. (1907) 'The Geological Structure of the North-West Highlands'. in *Memoir of the Geological Survey of Great Britain*.

Pearce, J.A. (1996) 'A Users Guide to Basalt Discrimination Diagrams'. *Trace Element Geochemistry of Volcanic Rocks: Applications for Massive Sulphide Exploration. Geological Association of Canada, Short Course Notes* 12, 79–113

Pearce, J.A. (2008) 'Geochemical Fingerprinting of Oceanic Basalts with Applications to Ophiolite Classification and the Search for Archean Oceanic Crust'. *Lithos* 100 (1–4), 14–48

Pearce, J.A. (2014) 'Geochemical Fingerprinting of the Earth's Oldest Rocks'. *Geology* 42 (2), 175–176

Pearce, J.A. and Cann, J.R. (1973) 'Tectonic Setting of Basic Volcanic Rocks Determined Using Trace Element Analyses'. *Earth and Planetary Science Letters* 19, 290–300

Pearce, J.A. and Peate, D.W. (1995) 'Tectonic Implications of the Composition of Volcanic Arc Magmas.' *Annual Review of Earth and Planetary Sciences* 23, 251–285

Peltonen, P., Kontinen, A., and Huhma, H. (1996) 'Petrology and Geochemistry of Metabasalts from the 1.95 Ga Jormua'. *Journal of Petrology* 37 (6), 1359–1383

Peregoedova, A., Barnes, S.J., and Baker, D.R. (2006) 'An Experimental Study of Mass Transfer of Platinum-Group Elements, Gold, Nickel and Copper in Sulfur-Dominated Vapor at Magmatic Temperatures'. *Chemical Geology* 235 (1–2), 59–75

Phillips, G.N. (1987) 'Metamorphism of the Witwatersrand Gold Fields: Conditions during Peak Metamorphism'. *Journal of Metamorphic Geology* 5 (3), 307–322

Philpotts, A.R. and Ague, J.J. (2009) *Principles of Igneous and Metamorphic Petrology*. Cambridge University Press

Piskorz, D., Elkins-Tanton, L.T., and Smrekar, S.E. (2014) 'Coronae Formation on Venus via Extension and Lithospheric Instability'. *Journal of Geophysical Research: Planets* 119 (12), 2568–2582

Polat, A., Appel, P.W.U., Fryer, B., Windley, B., Frei, R., Samson, I.M., and Huang, H. (2009) 'Trace Element Systematics of the Neoarchean Fiskenaesset Anorthosite Complex and Associated Meta-Volcanic Rocks, SW Greenland: Evidence for a Magmatic Arc Origin'. *Precambrian Research* 175 (1–4), 87–115

Polat, A., Appel, P.W.U., and Fryer, B.J. (2011) 'An Overview of the Geochemistry of Eoarchean to Mesoarchean Ultramafic to Mafic Volcanic Rocks, SW Greenland: Implications for Mantle Depletion and Petrogenetic Processes at Subduction Zones in the Early Earth'. *Gondwana Research* 20 (2–3), 255–283

Polat, A., Frei, R., Appel, P.W.U., Dilek, Y., Fryer, B., Ordóñez-Calderón, J.C., and Yang, Z. (2008) 'The Origin and Compositions of Mesoarchean Oceanic Crust: Evidence from the 3075 Ma Ivisaartoq Greenstone Belt, SW Greenland'. *Lithos* 100 (1–4), 293–321

Polat, A. and Hofmann, A.W. (2003) 'Alteration and Geochemical Patterns in the 3.7 – 3.8 Ga Isua Greenstone Belt , West Greenland'. *Precambrian Research* 126, 197–218

Polat, A., Hofmann, A.W., Munker, C., Regelous, M., and Appel, P.W.U. (2003) 'Contrasting Geochemical Patterns in the 3.7–3.8 Ga Pillow Basalt Cores and Rims , Isua Greenstone Belt, Southwest Greenland: Implications for Postmagmatic Alteration Processes'. *Geochemica et Cosmochimica Acta* 67 (3), 441–457

Polat, A., Kokfelt, T., Burke, K.C., Kusky, T.M., Bradley, D.C., Dziggel, A., Kolb, J., William, P., Polat, A., Kokfelt, T., Burke, K.C., Kusky, T.M., Bradley, D.C., and Dziggel, A. (2016) 'Lithological, Structural, and Geochemical Characteristics of Mesoarchean TâRtoq Greenstone Belt, Southern West Greenland, and the Chugach – Prince William Accretionary Complex, Southern Alaska: Evidence for Uniformitarian Plate-Tectonic Processes'. *Canadian Journal of Earth Science* 1371 (May), 1336–1371

Poujol, M. (2007) 'Chapter 5.1 An Overview of the Pre-Mesoarchean Rocks of the Kaapvaal Craton, South Africa'. *Developments in Precambrian Geology* 15, 453–463

Poujol, M. and Anhaeusser, C.R. (2001) 'The Johannesburg Dome, South Africa: New Single Zircon U-Pb Isotopic Evidence for Early Archaean Granite-Greenstone Development within the Central Kaapvaal Craton'. *Precambrian Research* 108 (1–2), 139–157

Poujol, M., Robb, L.J., Anhaeusser, C.R., and Gericke, B. (2003) 'A Review of the Geochronological Constraints on the Evolution of the Kaapvaal Craton, South Africa'. *Precambrian Research* 127 (1–3), 181–213

Powell, W., Zhang, M., Reilly, S.Y.O., and Tiepolo, M. (2004) 'Mantle Amphibole Trace-Element and Isotopic Signatures Trace Multiple Metasomatic Episodes in Lithospheric Mantle, Western Victoria, Australia'. *Lithos* 75, 141–171

Power, M.R., Pirrie, D., Andersen, J.C., and Butcher, A.R. (2000) 'Stratigraphic Distribution of Platinum-Group Minerals in the Eastern Layered Series, Rum, Scotland'. *Mineralium Deposita* 35 (8), 762–775

Prevec, S.A., Poujol, M., Craton, K., Africa, S., Prevec, S.A., Anhaeusser, C.R., and Poujol, M.

(2004) ‘Evidence for Archaean Lamprophyre from the Kaapvaal Craton, South Africa’. *South African Journal of Science* 100 (August 2015), 549–555

Prichard, H.M., Ixer, R.A., Lord, R.A., Maynard, J., and Williams, N. (1994) ‘Assemblages of Platinum-Group Minerals and Sulfides in Silicate Lithologies and Chromite-Rich Rocks within the Shetland Ophiolite’. *Canadian Mineralogist* 32 (2), 271–294

Prichard, H.M. and Lord, R.A. (1990) ‘Platinum and Palladium in the Troodos Ophiolite Complex, Cyprus’. *Canadian Mineralogist* 28, 607–617

Pronin, A.A. and Stofan, E.R. (1990) ‘Coronae on Venus: Morphology, Classification, and Distribution’. *Icarus* 87 (2), 452–474

Puchtel, I.S., Blichert-Toft, J., Touboul, M., Walker, R.J., Byerly, G.R., Nisbet, E.G., and Anhaeusser, C.R. (2013) ‘Insights into Early Earth from Barberton Komatiites: Evidence from Lithophile Isotope and Trace Element Systematics’. *Geochimica et Cosmochimica Acta* 108, 63–90

Puchtel, I.S., Walker, R.J., Touboul, M., Nisbet, E.G., and Byerly, G.R. (2014) ‘Insights into Early Earth from the Pt-Re-Os Isotope and Highly Siderophile Element Abundance Systematics of Barberton Komatiites’. *Geochimica et Cosmochimica Acta* 125, 394–413

von Rahden, H.V.R., de Nooy, C.D., Tucker, R.F., and Adlington-Corfield, A. (1991) ‘The Composition of Chromite from the Aandenk Formation, Witwatersrand, and Its Relation to the Composition of the Source Rocks’. *International Congress on Applied Mineralogy* 2, 64

Reagan, M., Ishizuka, O., Stern, R.J., Kelley, K.A., Ohara, Y., Blichert-Toft, J., Bloomer, S.H., Cash, J., Fryer, P., Hanan, B.B., and Hickey-Vargas, R. (2010) ‘Fore-Arc Basalts and Subduction Initiation in the Izu-Bonin-Mariana System’. *Geochemistry, Geophysics, Geosystems* 11 (3), 1–17

Rehkämper, M., Halliday, a N., Fitton, J.G., Lee, D.C., Wieneke, M., and Arndt, N.T. (1999) ‘Ir, Ru, Pt, and Pd in Basalts and Komatiites: New Constraints for the Geochemical Behavior of the Platinum-Group Elements in the Mantle’. *Geochimica et Cosmochimica Acta* 63 (22), 3915–3934

Reimink, J.R., Davies, J.H.F.L., Chacko, T., Stern, R.A., Heaman, L.M., Sarkar, C., Schaltegger, U., Creaser, R.A., and Pearson, D.G. (2016) ‘No Evidence for Hadean Continental Crust

within Earth's Oldest Evolved Rock Unit'. *Nature Geoscience* 9 (1), 777–780

Renzulli, A., Moro, S. Del, Menna, M., Landi, P., and Piermattei, M. (2009) 'Transient Processes in Stromboli ' s Shallow Basaltic System Inferred from Dolerite and Magmatic Breccia Blocks Erupted during the 5 April 2003 Paroxysm'. *Bulletin of Volcanology* 71 (April 2003), 795–813

Robb, L.J. (1977) *The Geology and Geochemisty of the Archaean Granite-Greenstone Terrane between Nelspruit and Bushbuckridge, Eastern Transvaal*. University of the Witwatersrand

Robb, L.J. (1978) 'General Geological Description of the Archaean Granitic Terrane between Nelspruit and Bushbuckridge, Eastern Transvaal'. *Trans. Geol. Soc. S. Afr.* 81, 331–338

Robb, L.J. (1979) 'The Distribution of Granitophile Elements in Archaean Granites of the Eastern Transvaal, and Their Bearing on Geomorphological and Geological Features of the Area'. *Trans. Geol. Soc. S. Afr.* 82, 169–171

Robb, L.J., Brandl, G., and Poujol, M. (2006) 'Archaean Granitoid Intrusions'. in *Geology of South Africa*. 57–94

Robb, L.J. and Meyer, F.M. (1995) 'The Witwatersrand Basin, South Africa: Geological Framework and Mineralization Processes'. *Ore Geology Reviews* 10, 67–94

Robin-Popieul, C.C.M., Arndt, N.T., Chauvel, C., Byerly, G.R., Sobolev, A. V., and Wilson, A. (2012) 'A New Model for Barberton Komatiites: Deep Critical Melting with High Melt Retention'. *Journal of Petrology* 53 (11), 2191–2229

Robins, B., Sandstå, N.R., Furnes, H., and de Wit, M. (2010) 'Flow Banding in Basaltic Pillow Lavas from the Early Archean Hooggenoeg Formation, Barberton Greenstone Belt, South Africa'. *Bulletin of Volcanology* 72 (5), 579–592

Rodel, J.E. (1993) *The Petrography and Geochemistry of the Stolzburg and Rosentuin Layered Ultramafic Complexes, Barberton Mountain Land, Eastern Transvaal*. University of the Witwatersrand

Rolland, Y., Cox, S., Boullier, A., Pennacchioni, G., and Mancktelow, N. (2003) 'Rare Earth and Trace Element Mobility in Mid-Crustal Shear Zones : Insights from the Mont Blanc Massif (Western Alps)'. *Earth and Planetary Science Letters* 214, 203–219

Rollinson, H. (2008) 'The Geochemistry of Mantle Chromitites from the Northern Part of the Oman Ophiolite : Inferred Parental Melt Compositions'. *Contributions to Mineralogy and Petrology* 156, 273–288

Rollinson, H. (2012) 'Geochemical Constraints on the Composition of Archaean Lower Continental Crust: Partial Melting in the Lewisian Granulites'. *Earth and Planetary Science Letters* 351–352, 1–12

Rollinson, H. and Gravestock, P. (2012) 'The Trace Element Geochemistry of Clinopyroxenes from Pyroxenites in the Lewisian of NW Scotland: Insights into Light Rare Earth Element Mobility during Granulite Facies Metamorphism'. *Contributions to Mineralogy and Petrology* 163 (2), 319–335

Rollinson, H.R. (1987) 'Early Basic Magmatism in the Evolution of Archaean High-Grade Gneiss Terrains : An Example from the Lewisian of NW Scotland'. *Mineralogical Magazine* 51 (September), 345–355

Rollinson, H.R. (1993) *Using Geochemical Data: Evaulation, Presentation, Interpretation*. Pearson Education Limited

Rollinson, H.R. and Windley, B.F. (1980) 'An Archaean Granulite-Grade Tonalite-Trondhjemite-Granite Suite from Scourie, NW Scotland: Geochemistry and Origin'. *Contributions to Mineralogy and Petrology* 72 (3), 265–281

De Ronde, C.E.J. and De Wit, M.J. (1994) 'Tectonic History of the Barberton Greenstone Belt, South Africa: 490 Million Years of Archaean Evolution'. *Tectonics* 13 (13), 983–1005

Rozel, A.B., Golabek, G.J., Jain, C., Tackley, P.J., and Gerya, T. (2017) 'Continental Crust Formation on Early Earth Controlled by Intrusive Magmatism'. *Nature* 545, 332–335

Rudnick, R.L., Mcdonough, W.F., and Chappell, B.W. (1993) 'Carbonatite Metasomatism in the Northern Tanzanian Mantle : Petrographic and Geochemical Characteristics'. *Earth and Planetary Science Letters* 114, 463–475

Saha, A., Manikyamba, C., Santosh, M., Ganguly, S., Khelen, A.C., and Subramanyam, K.S. V (2015) 'Platinum Group Elements (PGE) Geochemistry of Komatiites and Boninites from Dharwar Craton, India: Implications for Mantle Melting Processes'. *Journal of Asian Earth Sciences* 105, 300–319

Said, N., Kerrich, R., Maier, W.D., and McCuaig, C. (2011) 'Behaviour of Ni-PGE-Au-Cu in Mafic-Ultramafic Volcanic Suites of the 2.7Ga Kambalda Sequence, Kalgoorlie Terrane, Yilgarn Craton'. *Geochimica et Cosmochimica Acta* 75 (10), 2882–2910

Saji, N.S., Larsen, K., Wielandt, D., Schiller, M., Costa, M.M., Whitehouse, M.J., Rosing, M.T., and Bizzarro, M. (2018) *Hadean Geodynamics Inferred from Time-Varying in the Early Earth Rock Record 142 Nd / 144 Nd*. 43–48

Saunders, A. and Tarney, J. (1991) 'Back-Arc Basins'. in *Oceanic Basalts*.

Schaefer, B.F., Pearson, D.G., Rogers, N.W., and Barnicoat, A.C. (2010) 'Re–Os Isotope and PGE Constraints on the Timing and Origin of Gold Mineralisation in the Witwatersrand Basin'. *Chemical Geology* 276 (1–2), 88–94

Schmitz, M.D., Bowring, S.A., de Wit, M.J., and Gartz, V. (2004) 'Subduction and Terrane Collision Stabilize the Western Kaapvaal Craton Tectosphere 2.9 Billion Years Ago'. *Earth and Planetary Science Letters* 222 (2), 363–376

Searle, R. (2013) *Mid-Ocean Ridges*. Cambridge University Press

Sheraton, J.W., Skinner, A.C., and Tarney, J. (1973) 'The Geochemistry of the Scourian Gneisses of the Assynt District'. in *The Early Precambrian Rocks of Scotland and Related Rocks of Greenland*. University of Keele, 13–30

Shervais, J.W. (1982) 'Ti-V Plots and the Petrogrenesis of Modern and Ophiolitic Lavas'. *Earth and Planetary Science Letters* 59, 101–118

Shirey, S.B., Kamber, B.S., Whitehouse, M.J., Mueller, P.A., and Basu, A.R. (2008) 'A Review of the Isotopic and Trace Element Evidence for Mantle and Crustal Processes in the Hadean and Archean: Implications for the Onset of Plate Tectonic Subduction'. in *When Did Plate Tectonics Begin on Planet Earth?*. ed. by Condie, Kent, C. and Pease, V. Geological Society of America Special Paper 440

Sills, J.D. (1981) *Geochemical Studies of the Lewisian Complex of the Western Assynt Region, NW Scotland. (PhD Thesis)*. University of Leicester

Sills, J.D. (1982) 'The Retrogression of Ultramafic Granulites from the Scourian of NW Scotland'. *Mineralogical Magazine* 46 (338), 55–61

Sills, J.D., Savage, D., Watson, J. V., and Windley, B.F. (1982) 'Layered Ultramafic-Gabbro

Bodies in the Lewisian of Northwest Scotland: Geochemistry and Petrogenesis'. *Earth and Planetary Science Letters* 58 (3), 345–360

Singh, M.R., Manikyamba, C., Ray, J., Ganguly, S., Santosh, M., Saha, A., Rambabu, S., and Sawant, S.S. (2016) 'Major, Trace and Platinum Group Element (PGE) Geochemistry of Archean Iron Ore Group and Proterozoic Malangtoli Metavolcanic Rocks of Singhbhum Craton, Eastern India: Inferences on Mantle Melting and Sulphur Saturation History'. *Ore Geology Reviews* 72, 1263–1289

Sinjeng, P.P. (1987) *Mineralogy and Genesis of Zoned Platinum Mineral Grains from the Leslie and Bracken Gold Mines, Witwatersrand, South Africa*. University College Cardiff

Smart, K.A., Tappe, S., Stern, R.A., Webb, S.J., and Ashwal, L.D. (2016) 'Early Archaean Tectonics and Mantle Redox Recorded in Witwatersrand Diamonds'. *Nature Geoscience* (January), 1–6

Smith, J.W., Holwell, D.A., and McDonald, I. (2014) 'Precious and Base Metal Geochemistry and Mineralogy of the Grasvally Norite–Pyroxenite–Anorthosite (GNPA) Member, Northern Bushveld Complex, South Africa: Implications for a Multistage Emplacement'. *Mineralium Deposita* 49 (6), 667–692

Smith, M.P., Henderson, P., and Campbell, L.S. (2000) 'Fractionation of the REE during Hydrothermal Processes : Constraints from the Bayan Obo Fe-REE-Nb Deposit, Inner Mongolia, China.' *Geochimica et Cosmochimica Acta* 64 (18), 3141–3160

Smithies, R.H., Champion, D.C., and Cassidy, K.F. (2003) 'Formation of Earth's Early Archaean Continental Crust'. *Precambrian Research* 127 (1–3), 89–101

Smithies, R.H., Ivanic, T.J., Lowrey, J.R., Morris, P.A., Barnes, S.J., Wyche, S., and Lu, Y. (2018) 'Two Distinct Origins for Archean Greenstone Belts'. *Earth and Planetary Science Letters* 487, 106–116

Stern, R.J. (2005) 'Evidence from Ophiolites, Blueschists, and Ultrahigh-Pressure Metamorphic Terranes That the Modern Episode of Subduction Tectonics Began in Neoproterozoic'. *Geology* 33 (7), 557–560

Stern, R.J. (2008) 'Modern-Style Plate Tectonics Began in Neoproterozoic Time: An Alternative Interpretation of Earth's Tectonic History'. *Special Publication of the Geological Society of America* 440, 265–280

Stern, R.J. (2016) 'Is Plate Tectonics Needed to Evolve Technological Species on Exoplanets?' *Geoscience Frontiers* 7 (4), 573–580

Stofan, E.R., Bindschadler, D.L., Head, J.W., and Parmentier, E.M. (1991) 'Corona Structures on Venus: Models of Origin'. *Journal of Geophysical Research* 96 (E4), 20933

Storey, M., Mahoney, J.J., Kroenke, L.W., and Saunders, A.D. (1991) 'Are Oceanic Plateaus Sites of Komatiite Formation?' *Geology* 19 (4), 376–379

Stribrny, B., Wellmer, F.-W., Burgath, K.-P., Oberthür, T., Tarkian, M., and Pfeiffer, T. (2000) 'Unconventional PGE Occurrences and PGE Mineralization in the Great Dyke: Metallogenic and Economic Aspects'. *Mineralium Deposita* 35 (2–3), 260–280

Suárez, S., Prichard, H.M., Velasco, F., Fisher, P.C., and McDonald, I. (2010) 'Alteration of Platinum-Group Minerals and Dispersion of Platinum-Group Elements during Progressive Weathering of the Aguablanca Ni-Cu Deposit, SW Spain'. *Mineralium Deposita* 45 (4), 331–350

Sun, S. -s. and McDonough, W.F. (1989) 'Chemical and Isotopic Systematics of Oceanic Basalts: Implications for Mantle Composition and Processes'. *Geological Society, London, Special Publications* 42 (1), 313–345

Sutton, J. and Watson, J.V. (1951) 'The Pre-Torridonian Metamorphic History of the Loch Torridon and Scourie Areas in the Northwest Highland, and Its Bearing on the Chronological Classification of the Lewisian'. *Quarterly Journal of the Geological Society* 106, 241–307

Szilas, K., van Hinsberg, V., Mcdonald, I., Næraa, T., Rollinson, H., Adetunji, J., Bird, D., Hinsberg, V. Van, Mcdonald, I., Næraa, T., Rollinson, H., Adetunji, J., and Bird, D. (2018) 'Highly Refractory Archaean Peridotite Cumulates: Petrology and Geochemistry of the Seqi Ultramafic Complex, SW Greenland'. *Geoscience Frontiers* 9 (3), 689–714

Szilas, K., Van Hinsberg, V.J., Creaser, R.A., Kisters, A.F.M.M., Hinsberg, V. Van, and Kisters, A.F.M.M. (2014) 'The Geochemical Composition of Serpentinites in the Mesoarchaean Tartoq Group, SW Greenland: Harzburgitic Cumulates or Melt-Modified Mantle?' *Lithos* 198–199 (1), 103–116

Szilas, K., Hinsberg, V.J. Van, Kisters, A.F.M., Hoffmann, J.E., Windley, B.F., Kokfelt, T.F., Scherstén, A., Frei, R., Rosing, M.T., and Münker, C. (2013) 'Remnants of Arc-Related

Mesoarchaean Oceanic Crust in the Tartoq Group of SW Greenland'. *Gondwana Research* 23 (2), 436–451

Szilas, K., Kelemen, P.B., and Bernstein, S. (2015) 'Peridotite Enclaves Hosted by Mesoarchaean TTG-Suite Orthogneisses in the Fiskefjord Region of Southern West Greenland'. *GeoResJ* 7, 22–34

Tang, M., Chen, K., and Rudnick, R.L. (2016) 'Archean Upper Crust Transition from Mafic to Felsic Marks the Onset of Plate Tectonics'. *Science* 351 (6271), 372–275

Tarkian, M. and Prichard, H.M. (1987) 'Irarsite-Hollingworthite Solid-Solution Series and Other Associated Ru-, Os-, Ir-, and Rh-Bearing PGM's from the Shetland Ophiolite Complex'. *Mineralium Deposita* 22 (3), 178–184

Tarney, J. and Weaver, B.L. (1987) 'Mineralogy, Petrology and Geochemistry of the Scourie Dykes: Petrogenesis and Crystallization Processes in Dykes Intruded at Depth'. *Geological Society, London, Special Publications* 27 (1), 217–233

Teall, J.J.H. (1885) 'The Metamorphosis of Dolerite into Hornblende-Schist'. *Quarterly Journal of the Geological Society* 41

Tegtmeyer, A.R. and Kröner, A. (1987) 'U-Pb Zircon Ages Bearing on the Nature of Early Archaean Greenstone Belt Evolution, Baberton Mountain Land, South Africa'. *Precambrian Research* 36, 1–20

Thompson Stiegler, M., Cooper, M., Byerly, G.R., and Lowe, D.R. (2012) 'Geochemistry and Petrology of Komatiites of the Pioneer Ultramafic Complex of the 3.3Ga Weltevreden Formation, Barberton Greenstone Belt, South Africa'. *Precambrian Research* 212–213, 1–12

Timms, N.E., Kinny, P.D., and Reddy, S.M. (2006) 'Enhanced Diffusion of Uranium and Thorium Linked to Crystal Plasticity in Zircon.' *Geochemical Transactions* 7, doi:10.1186/1467-4866-7-10

Turner, S., Rushmer, T., Reagan, M., and Moyen, J.F. (2014) 'Heading down Early on? Start of Subduction on Earth'. *Geology* 42 (2), 139–142

Verma, S.K., Oliveira, E.P., Silva, P.M., Moreno, J.A., and Amaral, W.S. (2017) 'Geochemistry of Komatiites and Basalts from the Rio Das Velhas and Pitangui Greenstone Belts, São Francisco Craton, Brazil: Implications for the Origin, Evolution, and Tectonic Setting'.

Lithos 284–285, 560–577

Verma, S.K. and Verma, S.P. (2013) 'Identification of Archaean Plate Tectonic Processes from Multidimensional Discrimination Diagrams and Probability Calculations'. *International Geology Review* 55 (2), 225–248

Vezzoli, L., Renzulli, A., and Menna, M. (2014) 'Growth after Collapse: The Volcanic and Magmatic History of the Neostromboli Lava Cone (Island of Stromboli, Italy)'. *Bulletin of Volcanology* 76

Viljoen, M.J. and Viljoen, R.P. (1969a) 'An Introduction Tot the Geology of the Barberton Granuite-Greenstone Terrane'. *Special Publication of the Geological Society of South Africa* 2, 9–28

Viljoen, M.J. and Viljoen, R.P. (1969b) 'The Geology and Geochemistry of the Lower Ultramafic Unit of the Onverwacht Group and a Proposed New Class of Igneous Rocks'. *Special Publication of the Geological Society of South Africa* 2, 55–86

Viljoen, M.J. and Viljoen, R.P. (1969c) 'Evidence for the Existence of a Mobile Extrusive Peridotitic Magma from the Kamoti Formation of the Onverwacht Group'. *Special Publication of the Geological Society of South Africa* 2, 87–112

Viljoen, R.P., Saager, R., and Viljoen, M.J. (1970) 'Some Thoughts on the Origin and Processes Responsible for the Concentration of Gold in the Early Precambrian of Southern-Africa'. *Mineralium Deposita* 5 (2), 164–180

Viljoen, R.P. and Viljoen, M.J. (1969) 'The Geological and Geochemical Significance of the Upper Formations of the Onverwacht Group'. *Special Publication of the Geological Society of South Africa* 2, 113–152

Viljoen, R.P. and Viljoen, M.J. (1970) 'The Geology and Geochemistry of the Layered Ultramafic Bodies of the Kaapmuiden Area, Barberton Mountain Land'. *The Geological Society of South Africa, Special Publication* 1

Wagner, P.A. (1929) *The Platinum Deposits and Mines of South Africa*.

Walraven, F., Armstrong, R.A., and Kruger, F.J. (1990) 'A Chronostratigraphic Framework for the North-Central Kaapvaal Craton, the Bushveld Complex and the Vredefort Structure'. *Tectonophysics* 171 (1–4), 23–48

Wang, C.Y., Prichard, H.M., Zhou, M.F., and Fisher, P.C. (2008) 'Platinum-Group Minerals from the Jinbaoshan Pd-Pt Deposit, SW China: Evidence for Magmatic Origin and Hydrothermal Alteration'. *Mineralium Deposita* 43 (7), 791–803

Wang, D., Guo, J., Huang, G., and Scheltens, M. (2015) 'The Neoarchean Ultramafic-Mafic Complex in the Yinshan Block, North China Craton: Magmatic Monitor of Development of Archean Lithospheric Mantle'. *Precambrian Research* 270, 80–99

Wang, X., Peng, P., Wang, C., and Yang, S. (2015) 'Petrogenesis of the 2115 Ma Haicheng Mafic Sills from the Eastern North China Craton: Implications for an Intra-Continental Rifting'. *Gondwana Research* 39, 347–364

Warren, J.M. (2016) 'Global Variations in Abyssal Peridotite Compositions'. *Lithos* 248–251, 193–219

Watkinson, D.H. and Ohnenstetter, D. (1992) 'Hydrothermal Origin of Platium-Group Mineralization in the Two Duck Lake Intrusion, Colwell Complex, Northwestern Ontario'. *Canadian Mineralogist* 30, 121–136

Weaver, B.L. and Tarney, J. (1981) 'The Scourie Dyke Suite: Petrogenesis and Geochemical Nature of the Proterozoic Sub-Continental Mantle'. *Contributions to Mineralogy and Petrology* 78, 175–188

Van der Westhuizen, W.A., De Bruiyn, H., and Meintjes, P.G. (1991) 'The Ventersdorp Supergroup: An Overview'. *Journal of African Earth Sciences* 13 (1), 83–105

Wheeler, J. (2007) 'A Major High-Strain Zone in the Lewisian Complex in the Loch Torridon Area, NW Scotland: Insights into Deep Crustal Deformation'. *Geological Society, London, Special Publications* 272 (1), 27–45

Wheeler, J., Park, R.G., Rollinson, H.R., and Beach, A. (2010) 'The Lewisian Complex: Insights into Deep Crustal Evolution'. *Geological Society, London, Special Publications* 335 (1), 51–79

Whitehouse, M.J. (1989) 'Sm-Nd Evidence for Diachronous Crustal Accretion in the Lewisian Complex of Northwest Scotland'. *Tectonophysics* 161 (3–4), 245–256

Whitehouse, M.J. and Fedo, C.M. (2003) 'Deformation Features and Critical Field Relationships of Early Archaean Rocks , Akilia , Southwest Greenland'. *Precambrian Research* 126, 259–271

Whitehouse, M.J. and Kemp, A.I.S. (2010) 'On the Difficulty of Assigning Crustal Residence, Magmatic Protolith and Metamorphic Ages to Lewisian Granulites: Constraints from Combined in Situ U-Pb and Lu-Hf Isotopes'. *Geological Society, London, Special Publications* 335 (1), 81–101

Williams-Jones, A.E., Migdisov, A.A., and Samson, I.M. (2012) 'Of the Rare Earth Elements – a Tale of " Ceria " and " Yttria "'. *Elements* 8, 355–360

Winchester, J.A. and Floyd, P.A. (1976) 'Geochemical Magma Type Discrimination: Application to Altered and Metamorphosed Basic Igneous Rocks'. *Earth and Planetary Science Letters* 28, 459–469

Winchester, J.A. and Floyd, P.A. (1977) 'Geochemical Discrimination of Different Magma Series and Their Differentiation Products Using Immobile Elements'. *Chemical Geology* 20, 325–343

De Wit, M.J. (1998) 'On Archean Granites, Greenstones, Cratons and Tectonics: Does the Evidence Demand a Verdict?' *Precambrian Research* 91 (1–2), 181–226

De Wit, M.J., Hart, R.A., and Hart, R.J. (1987) 'The Jamestown Ophiolite Complex, Barberton Mountain Belt: A Section through 3.5 Ga Oceanic Crust'. *Journal of African Earth Sciences* 6 (5), 681–730

De Wit, M.J., De Ronde, C.E.J., Tredoux, M., Roering, C., Hart, R.J., Armstrong, R.A., Green, R.W.E., Peberdy, E., and Hart, R.A. (1992) 'Formation of an Archaean Continent'. *Nature* 357 (6379), 553–562

Wood, B.J. (1990) 'An Experimental Test of the Spinel Peridotite Oxygen Barometer'. *Journal of Geophysical Research* 95 (B10), 15845–15851

Wood, D.A., Joron, J.L., and Treuil, M. (1979) 'Re-Appraisal of the Use of Trace Elements to Classify and Discriminate between Magma Series Erupted in Different Tectonic Settings'. *Earth and Planetary Science Letters* 45, 326–336

Wood, S.A. (1990) 'The Aqueous Geochemistry of the Rare-Earth Elements and Yttrium'. *Chemical Geology* 82, 159–186

Xue, S., Qin, K., Li, C., Tang, D., Mao, Y., Qi, L., and Ripley, E.M. (2016) 'Geochronological, Petrological, and Geochemical Constraints on Ni-Cu Sulfide Mineralization in the Poyi Ultramafic-Troctolitic Intrusion in the Northeast Rim of the Tarim Craton, Western

China'. *Economic Geology* 111, 1465–1484

Yardley, B.W.D. (2013) 'The Chemical Composition of Metasomatic Fluids in the Crust'. in *Metasomatism and the Chemical Transformation of Rock: The Role of Fluids in Terrestrial and Extraterrestrial Processes*. Springer, London, 17–51

Yaxley, G.M., Crawford, A.J., and Green, D.H. (1991) 'Evidence for Carbonatite Metasomatism in Spinel Peridotite Xenoliths from Western Victoria , Australia'. *Earth and Planetary Science Letters* 107, 305–317

Yaxley, G.M., Green, D.H., and Kamenetsky, V. (1998) 'Carbonatite Metasomatism in the Southeastern Australian Lithosphere'. *Journal of Petrology* 39 (11), 1917–1930

Yellappa, T., Santosh, M., Chetty, T.R.K., Kwon, S., Park, C., Nagesh, P., Mohanty, D.P., and Venkatasivappa, V. (2012) 'A Neoarchean Dismembered Ophiolite Complex from Southern India: Geochemical and Geochronological Constraints on Its Suprasubduction Origin'. *Gondwana Research* 21 (1), 246–265

Yellappa, T., Venkatasivappa, V., Koizumi, T., Chetty, T.R.K., Santosh, M., and Tsunogae, T. (2014) 'Journal of Asian Earth Sciences The Mafic – Ultramafic Complex of Aniyapuram , Cauvery Suture Zone , Southern India : Petrological and Geochemical Constraints for Neoarchean Suprasubduction Zone Tectonics'. *Journal of Asian Earth Sciences* 95, 81–98

Yudovskaya, M., Kinnaird, J., Naldrett, A.J., Rodionov, N., Antonov, A., Simakin, S., and Kuzmin, D. (2013) 'Trace-Element Study and Age Dating of Zircon from Chromitites of the Bushveld Complex (South Africa)'. *Mineralogy and Petrology* 107 (6), 915–942

Zeh, A., Jaguin, J., Poujol, M., Boulvais, P., Block, S., and Paquette, J.L. (2013) 'Juvenile Crust Formation in the Northeastern Kaapvaal Craton at 2.97Ga-Implications for Archean Terrane Accretion, and the Source of the Pietersburg Gold'. *Precambrian Research* 233, 20–43

Zeh, A., Ovtcharova, M., Wilson, A.H., and Schaltegger, U. (2015) 'The Bushveld Complex Was Emplaced and Cooled in Less than One Million Years - Results of Zirconology, and Geotectonic Implications'. *Earth and Planetary Science Letters* 418, 103–114

Zhao, G., Wilde, S.A., Li, S., Sun, M., Grant, M.L., and Li, X. (2007) 'U – Pb Zircon Age Constraints on the Dongwanzi Ultramafic – Mafic Body, North China , Confirm It Is Not

an Archean Ophiolite'. *Earth and Planetary Science Letters* 255, 85–93

Zhao, G., Wilde, S.A., Li, S., Sun, M., Grant, M.L., and Li, X. (2008) 'Response to Note on " U – Pb Zircon Age Constraints on the Dongwanzi Ultramafic – Mafic Body , North China, Confirm It Is Not an Archean Ophiolite " by Kusky and Li'. *Earth and Planetary Science Letters* 273, 231–234

Zhou, M.F., Robinson, P.T., Malpas, J., and Li, Z. (1996) 'Podiform Chromitites in the Luobusa Ophiolite (SouthernTibet) :Implications for Melt-Rock Interaction and Chromite Segregation in the Upper Mantle'. *Journal of Petrology* 37 (1), 3–21

Zirkler, A., Johnson, T.E., White, R.W., and Zack, T. (2012) 'Polymetamorphism in the Mainland Lewisian Complex, NW Scotland - Phase Equilibria and Geochronological Constraints from the Cnoc an t'Sidhean Suite'. *Journal of Metamorphic Geology* 30 (8), 865–885

List of Appendices

Appendix A – Analytical methodology and instrumentation

Appendix B – A field excursion guide to the Ben Strome Complex

Electronic appendices specific to Part One:

Appendix C – Supplementary material specific to Chapter 3 (sample locations and spinel mineral chemistry, as 1 x excel files)

Appendix D – Supplementary material specific to Chapter 4 (lithophile element bulk-rock geochemistry, major element mineral chemistry and trace element mineral chemistry, as 3 x excel files)

Appendix E – Supplementary material specific to Chapter 5 (lithophile element bulk-rock geochemistry, PGE bulk-rock geochemistry and spinel mineral chemistry, as 2 x excel files)

Electronic appendices specific to Part Two:

Appendix F – Supplementary material specific to Chapter 7 (sample locations and spinel mineral chemistry, as 1 x excel files)

Appendix G – Supplementary material specific to Chapter 8 (lithophile element bulk-rock geochemistry and PGE bulk-rock geochemistry)

Other electronic appendices:

Appendix H – Pdf copy of this thesis

Appendix A

Analytical methodology and instrumentation

A.1 Bulk-rock geochemistry

All analysed samples were crushed and ground to a fine powder using the rock preparation facilities at Cardiff University (School of Earth and Ocean Sciences). Weathered surfaces were removed using a diamond-bladed rock saw, before samples were crushed (to a coarse grit) using a Mn-steel jaw-crusher and ground (to a fine powder) using an agate ball mill. Powdered samples were then ignited (at ~900°C) for 2 hours, with LOI determined gravimetrically, using the following equation:

$$LOI\ (wt.\%) = \frac{mass\ of\ original\ rock\ powder - mass\ of\ ignited\ powder}{mass\ of\ original\ rock\ powder} \times 100$$

A.1.1 Lithophile elements

In preparation for lithophile element analysis by ICP-OES and ICP-MS, a sample mass of 0.1 g was accurately weight and mixed with 0.6 g of Claisse 50:50 Li metaborate flux in a Claisse BIS! Pt-Rh crucible (see McDonald and Viljoen 2006 for full details). Approximately 0.5 mL of a Li iodide solution was added as a non-wetting agent, before the mixture was fused over a propane burner on a Claisse FLUXY (automated) fusion system. The mixture was subsequently poured into a Teflon beaker containing 50 ml of 4 % HNO_3, where it was dissolved using a magnetic stirrer. Following dissolution of all glass fragments, the solution was spiked with 1 mL of a 100 ppm Rh spike solution (for use an as internal standard) and made up to 100 mL with 18.2 MΩ deionised water (McDonald and Viljoen 2006). Samples were subsequently analysed (by Dr Iain McDonald, Cardiff University) for major and trace elements using ICP-OES and ICP-MS respectively.

Standard reference materials and blanks were prepared and analysed using the methodology and instrumentation described above, with the sample material omitted for the blanks. Accuracy was constrained by analysis of the following international reference materials (Govindaraju 1994, Ottley et al. 2003, Babechuk et al. 2010): BIR-1, JA2, JB1b, JB3, JG1A, JG3, JP1, MRG1, NIM-G, NIM-N, NIM-P, SDO1, GP13. Analytical results for the analysed standards can be found in Appendix D, Appendix E and Appendix G. Precision was constrained by duplicate analyses of ~10 % of samples and by conducting repeat analyses of standards in different sample batches (see Appendix D, Appendix E and Appendix G for details).

A.1.2 Platinum-group elements and Au

For PGE (Os, Ir, Ru, Rh, Pt and Pd) and Au analysis, samples were prepared by Ni sulphide fire assay and Te co-precipitation (fully described in: Huber et al. 2001, McDonald and Viljoen 2006). Typically, 10 g of sample material (as ground rock powder; method described above) is mixed with: 5 g of silica, 6 g of Na-carbonate, 12 g of borax, 0.9 g of Sulphur and 1.1 g of carbonyl-purified Ni. Reagents were thoroughly mixed before samples were transferred to fire-clay crucibles before being fired at 1050°C for 90 minutes. Buttons were dissolved using concentrated HCl, with co-precipitation achieved using Te and $SnSl_2$. The filtered residues were digested using 3 ml of concentrated HNO_3 and 4 ml of concentrated HCl in sealed 15 ml Saville screw-top Teflon vials. After the residue had dissolved, the liquid contents were transferred to 50 ml volumetric flasks, spiked with a 2.5 ppm Tl spike (for use as an internal standard) and made up to 50 ml with 18.2 MΩ deionised water. Solutions were then analysed for PGE and Au (by Dr Iain McDonald) using an ICP-MS system at Cardiff University.

Standard reference materials and blanks were prepared and analysed using the methodology and instrumentation described above, with the sample material omitted for the blanks, for which a 10 g Si mass was used. Accuracy was constrained by analysis of the following international reference materials: TDB1, WPR1, WMG1, Wits1, WPR1 and SARM64. Analytical results for the analysed standards can be found in Appendix E and Appendix G. Precision was constrained by conducting duplicate analyses of ~10 % of samples, and by conducting repeat analyses of standards in different sample batches (see Appendix E and Appendix G).

A.2 Element mapping

Detailed petrographic assessment by element mapping used a Zeiss Sigma HD Field Emission Gun A-SEM equipped with two Oxford Instruments 150 mm^2 Energy Dispersive X-ray Spectrometry (EDS) detectors at the School of Earth and Ocean Sciences, Cardiff University. Operating conditions were set at 20 kV and aperture size to 120 µm, with a nominal beam current of 4 nA and working distance of 8.9 mm. Using Aztec software, maps were acquired at 100 to 150× magnifications, with resulting pixel sizes ranging from 10 to 22 µm, depending on the resolution of acquired spectral images. A process time of 1 µs was used in conjunction with a pixel dwell time of 3000–6000 µs. Element maps were then background correlated and element overlaps deconvolved using Aztec software, before modal mineralogy was calculated from relative element concentrations using the analyse phases algorithm in Aztec. Boundary tolerance and grouping level were set at 2 and 1 respectively, with any unassigned pixels (typically < 5 %) discarded from the modal mineralogy.

A.3 Major element mineral chemistry

Major element mineral chemistry was conducted using the A-SEM described in Section A.2. Operating conditions were set at 20 kV, with aperture size set to 60 µm and working distance of 8.9 mm. Analytical drift checks were carried out every 20 minutes using a Co reference standard, with a suite of standards from ASTIMEX and Smithsonian used to calibrate the EDS analyser. Table A.1 details the standards (and their certified values) that were used to perform instrument calibrations. Using standard reference materials from the same suppliers, secondary standard checks were performed regularly during data collection, with such checks performed on minerals not used for instrument calibration. Table A.2 includes a series of secondary standard checks performed on Cr-diopside and Cr-spinel during two separate A-SEM sessions. The raw data were recalculated to element oxide percentages, with Fe^{2+} and Fe^{3+} calculated using the stoichiometric method of Droop (1987).

Table A.1: *Standard reference materials used to calibrate the EDS analyser and perform secondary standard checks.*

Mineral	Locality	O	Si	Ti	Al	Fe	Mn	Mg	Ca	Na	K	Cr	C
Astimex standard block													
Albite	Amelia, Virginia	49.03	32.14		10.46				0.16	8.66	0.14		
Almandine	New York State	42.11	18.30	0.04	12.02	18.56	0.43	6.12	2.86				
Calcite	Iceland Spar	47.97							40.24				11.97
Cr-diopside	Batbjerg,	44.07	25.67	0.06	0.16	1.00		10.69	17.63	0.30		0.38	
Chromite	New South Wales	35.20	0.06	0.07	12.47	10.04		10.12				31.08	
Diopside	Wakefield, Quebec	44.18	25.87		0.33	0.65		10.71	17.72	0.30			
Dolomite	New York	51.97				0.11		13.06	21.72				13.01
Magnetite	unknown	27.53	0.01			71.88	0.18						
Olivine	mantle nodule	44.09	19.45			5.64		30.74					
Plagioclase	Sonora, Mexico	46.79	24.83		15.54	0.27		0.06	8.53	3.24	0.20		
Pyrope	Bohemia	44.38	19.37	0.30	11.42	6.81	0.24	12.27	3.11			1.14	
Smithsonian standard block													
Chromite	N/A	32.71			5.25	10.14	0.09	9.17				41.40	
Fayalite	N/A	31.10	13.66	0.02		52.51	1.66						
Hornblende	Kakanui	42.73	18.87	2.83	7.89	5.49	0.07	7.72	7.36	1.93	1.70		
Hornblende	Arenal	43.07	19.38	0.85	8.19	8.92	0.12	8.59	8.25	1.42	0.17		
Magnetite	N/A	27.02		0.16		70.68		0.05				0.25	

Table A.2: *Secondary standard checks for Cr-diopside (top) and Cr-spinel (bottom) performed during major element mineral analysis, including precision calculations.*

Standard: Cr-diopside (Astimex)

Date	Time		O	Mg	Si	Ca	Cr	Fe
		certified values	***44.07***	***10.69***	***25.67***	***17.63***	***0.38***	***1.00***
02/12/2017	8.30 AM	standard check 1a	44.10	10.60	25.77	17.54	0.28	1.05
02/12/2017	8.30 AM	standard check 1b	44.04	10.56	25.70	17.46	0.38	1.06
02/12/2017	8.30 AM	standard check 1c	44.07	10.59	25.72	17.54	0.35	1.09
02/12/2017	2.00 PM	standard check 2a	44.08	10.56	25.71	17.46	0.42	1.08
02/12/2017	2.00 PM	standard check 2b	44.19	10.63	25.75	17.45	0.43	1.06
02/12/2017	2.00 PM	standard check 2c	44.06	10.59	25.69	17.44	0.39	1.09
02/12/2017	5.30 PM	standard check 3a	43.83	10.65	25.59	17.37	0.26	1.05
02/12/2017	5.30 PM	standard check 3b	43.90	10.61	25.56	17.36	0.38	1.09
02/12/2017	5.30 PM	standard check 3c	43.82	10.53	25.55	17.34	0.43	1.12
			Precision, as calculated using the above standard checks					
		mean	44.01	10.59	25.67	17.44	0.37	1.08
		st dev	0.13	0.04	0.08	0.07	0.06	0.02
		% RSD	0.29	0.35	0.32	0.42	16.84	2.18

Standard: Cr-spinel (Astimex)

Date	Time		O	Mg	Al	Cr	Fe
		certified values	***35.20***	***10.12***	***12.47***	***31.08***	***10.04***
05/07/2017	7.50 PM	standard check 1a	36.09	10.34	12.68	31.98	10.08
05/07/2017	7.50 PM	standard check 1b	36.11	10.17	12.74	32.12	10.05
05/07/2017	7.50 PM	standard check 1c	36.25	10.43	12.7	32.11	10.15
06/07/2017	8.20 AM	standard check 2a	36.05	10.38	12.66	31.9	10.1
06/07/2017	8.20 AM	standard check 2b	36.15	10.45	12.71	31.93	10.13
06/07/2017	8.20 AM	standard check 2c	36.13	10.4	12.72	31.86	10.11
06/07/2017	11.00 AM	standard check 3a	35.76	10.27	12.5	31.78	10.05
06/07/2017	11.00 AM	standard check 3b	35.78	10.34	12.49	31.55	9.98
06/07/2017	1.40 PM	standard check 4a	35.69	10.27	12.52	31.58	9.94
06/07/2017	1.40 PM	standard check 4b	35.71	10.27	12.54	31.62	9.97
			Precision, as calculated using the above standard checks				
		mean	35.97	10.33	12.63	31.84	10.06
		st dev	0.21	0.09	0.10	0.21	0.07
		%RSD	0.59	0.84	0.80	0.65	0.71

A.4 Trace element mineral chemistry

Trace element mineral chemistry was carried out on silicate and carbonate minerals using a New Wave Research UP213 UB laser system and attached Thermo X Series 2 ICP-MS at Cardiff University. Line analyses were used, with a minimum line length of 300 µm and beam diameter of 80 µm. Samples were analysed using an acquisition time of between 90 and 410 seconds, with a 20 second gas blank and 10 second wash out. Calibration of the ICP-MS was accomplished using a series of USGS basalt glass standards, with standard BCR analysed as a secondary standard to check the accuracy (see Table A.3 for details). For silicate mineral phases, Si concentrations (as determined using the A-SEM method described above) were

used as an internal standard, with Ca concentrations used as an internal standard for carbonate mineral phases. The suite of isotopes analysed were as follows: ^{23}Na, ^{25}Mg, ^{29}Si, ^{39}K, ^{44}Ca, ^{47}Ti, ^{51}V, ^{52}Cr, ^{55}Mn, ^{60}Ni, ^{71}Ga, ^{85}Rb, ^{88}Sr, ^{89}Y, ^{90}Zr, ^{93}Nb, ^{133}Cs, ^{137}Ba, ^{139}La, ^{140}Ce, ^{141}Pr, ^{146}Nd, ^{147}Sm, ^{153}Eu, ^{157}Gd, ^{159}Tb, ^{163}Dy, ^{165}Ho, ^{166}Er, ^{169}Tm, ^{172}Yb, ^{175}Lu, ^{178}Hf, ^{181}Ta, ^{208}Pb, ^{232}Th and ^{238}U. Blank correction, drift correction and conversion of ICP-MS output data (as counts/s) to concentrations (wt. % or µg/g) were all undertaken using the Thermo plasmalab software.

Table A.3: *Analysis of standard reference material BCR, including precision calculations.*

Run number		1	2	3	4	certified values	Mean	st dev	% RSD
23Na2O	wt%	3.13	3.33	3.269	3.413	3.27	3.29	0.12	3.64
25MgO	wt%	3.59	3.86	1.6	2.355	3.48	2.85	1.06	37.21
39K2O	wt%	1.65	1.74	1.689	1.681	1.69	1.69	0.04	2.16
47Ti	ppm	11670	12980	11700	13480	13010.00	12457.50	915.15	7.35
51V	ppm	410.80	457.10	414.2	490.6	425.00	443.18	37.99	8.57
52Cr	ppm	16.22	17.50	21.04	20	17.00	18.69	2.22	11.87
55Mn	ppm	1436	1603	1139	1645	1463.00	1455.75	229.65	15.78
60Ni	ppm	23.24	20.58	22.36	26.74	12.70	23.23	2.59	11.14
71Ga	ppm	22.00	24.92	24.75	25.85	24.00	24.38	1.66	6.80
85Rb	ppm	48.39	53.54	50.05	51.82	51.00	50.95	2.22	4.36
88Sr	ppm	275.50	318.10	309.4	334.3	321.00	309.33	24.80	8.02
89Y	ppm	24.24	27.70	32.5	30.96	31.00	28.85	3.67	12.71
90Zr	ppm	127.50	145.00	177.7	168.3	167.00	154.63	22.71	14.69
93Nb	ppm	9.74	11.17	11.84	11.14	10.90	10.97	0.88	8.03
133Cs	ppm	0.94	1.00	1.144	1.052	0.96	1.03	0.09	8.55
137Ba	ppm	599.40	678.00	645.1	641.7	641.00	641.05	32.23	5.03
139La	ppm	21.61	24.56	25.15	24.72	25.00	24.01	1.62	6.74
140Ce	ppm	47.67	53.26	51.48	52.17	52.00	51.15	2.43	4.75
141Pr	ppm	5.62	6.27	6.444	6.093	6.30	6.11	0.35	5.77
146Nd	ppm	25.38	28.62	28.3	25.72	27.00	27.01	1.69	6.26
147Sm	ppm	5.94	6.67	6.326	6.298	6.30	6.31	0.30	4.71
153Eu	ppm	1.84	1.99	1.942	1.87	1.91	1.91	0.07	3.55
157Gd	ppm	6.03	6.88	6.701	6.277	6.50	6.47	0.39	6.00
159Tb	ppm	0.87	1.02	0.998	0.899	0.95	0.95	0.07	7.60
163Dy	ppm	5.61	6.29	6.1	5.848	6.00	5.96	0.30	4.98
165Ho	ppm	1.14	1.23	1.255	1.113	1.20	1.18	0.07	5.76
166Er	ppm	3.13	3.44	3.362	3.095	3.30	3.25	0.17	5.23
169Tm	ppm	0.40	0.50	0.455	0.482	0.46	0.46	0.04	9.35
172Yb	ppm	3.07	3.28	3.248	3.074	3.20	3.17	0.11	3.55
175Lu	ppm	0.44	0.49	0.484	0.443	0.47	0.46	0.03	5.42
178Hf	ppm	3.30	3.78	4.876	4.408	4.50	4.09	0.69	16.95
181Ta	ppm	0.50	0.54	0.643	0.59	0.63	0.57	0.06	11.00
208Pb	ppm	10.34	9.86	7.335	12.68	10.90	10.05	2.19	21.80
232Th	ppm	5.11	5.68	5.511	5.495	5.50	5.45	0.24	4.45
238U	ppm	1.65	1.74	1.735	1.685	1.70	1.70	0.05	2.69

Appendix B

A field excursion guide to the Ben Strome Complex

This appendix was originally written as a subsection in the following (unpublished) fieldguide:

Tim Johnson, Simon Harley, George Guice, Kathryn Goodenough. Assynt fieldguide. *Granulites and granulites 2018 conference* (July 6th – 10th 2018), Ullapool, UK.

Author contributions and declarations:

G.L.G. wrote the entire contents of the Ben Strome Complex excursion, including figures, and led 2 fieldtrips to Ben Strome as part of the Granulite and granulites 2018 conference. T.E.J. provided minor edits to the text.Some contents of the fieldguide are largely adapted from Guice et al. (2018), *Precambrian Research* (Chapter 3 – this thesis).

Purpose: To study the layered ultramafic–mafic complex between Ben Strome and Loch an Leathaid Bhuain.

Maps: Ordnance Survey (OS) 1:50 000 Landranger sheet 9 Cape Wrath; 1:25 000 Explorer sheet 445 Foinaven/Arkle/Kylesku/Scourie. British Geological Survey (BGS): 1:50 000 Sheet 107, Glencoul.

Terrain: This excursion involves a long walk (~12 km) that is mostly along gravel tracks. Localities 1–3 are all located close to the lower track with easy access (Fig. B.1). Localities 4–7 involve traversing rough, undulating, heathery and locally boggy ground, with some steep, rocky and vegetated slopes. Note: the walk to locality 7 (through localities 5 and 6) is continuously uphill, with a total ascent of ~200 m.

Time: The excursion should occupy a full day.

Access: The field area is part of the Grosvenor Estate. There are generally no access problems, but it is advisable to contact the Grosvenor Estate during the Autumn (deer stalking season).

Directions and parking: When travelling from Ullapool, take the A837 towards Lochinver. At Loch Assynt, turn right onto the A838 towards Kylesku/Scourie/Durness. Drive through Unapool and Kylesku, before driving over the spectacular Kylesku Bridge. After the Kylesku Bridge, take the first right you encounter (a paved road). Immediately on your right, there is a small parking area, as marked on the 1:25 000 OS map (NC 2180 3458).

Geological Background

Fabulously exposed over some 7 km^2, the Ben Strome Complex is the largest ultramafic–mafic complex in the mainland Lewisian Gneiss Complex. It is composed of ~70 % heterogeneous mafic rocks (metagabbro, garnet-metagabbro, garnet-amphibolite and amphibole) and ~30 % layered ultramafic rocks (predominantly metapyroxenite, with subordinate metaperidotite). A major E–W trending Laxfordian shear zone cross-cuts the complex, subdividing it into the Maldie (southern) and Leathaid (northern) domains (Fig. B.1). In the Maldie Domain, the Ben Strome Complex forms an open synform, with two distinct packages of ultramafic rocks separated by a thick package of mafic rocks. In the Leathaid Domain, the Ben Strome Complex forms a series of tight to isoclinal re-folded folds (Fig. B.1). The Ben Strome Complex has recently been interpreted as a deformed layered intrusion that was emplaced into the TTG gneiss prior to the Badcallian metamorphic event (Chapter 3).

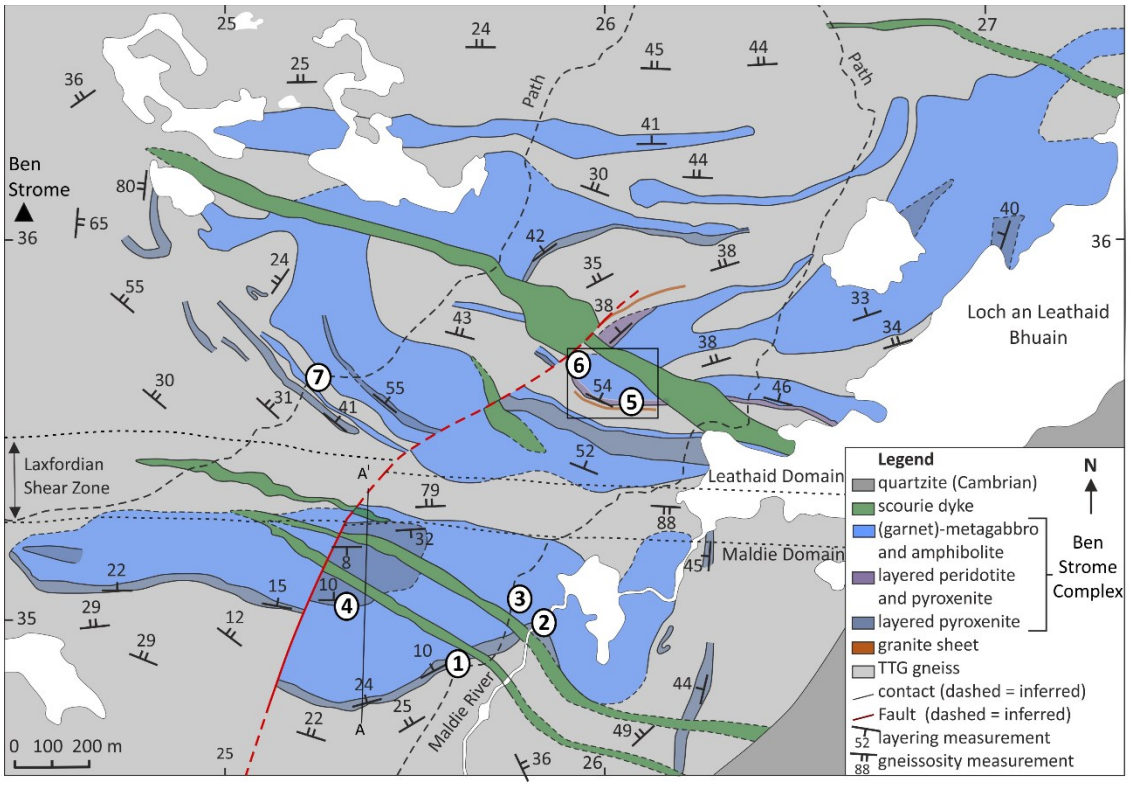

Figure B.1: *Geological map of the Ben Strome Complex (After: Guice et al. 2018, Precambrian Research/Chapter 3: this thesis) showing the location of localities B.1–B.7. The black rectangle shows the detailed map shown in Fig. B.4b.*

Locality 1. Contact between TTG gneiss and ultramafic rocks [NC 2564 3489]

Turn right (E) out of the car park and walk along the track for 3 km, keeping on the northern edge of Loch Gleann Dubh. Before reaching the Maldie River, turn left and follow the track uphill (NC 2470 3415) towards Loch an Leathaid Bhuin. Continue along this track for ~ 2 km

to reach locality 1. On the walk from the car park to locality 1, you will pass several good exposures (on the N shore of Loch Gleann Dubh), where features typical of the central region Lewisian Gneiss Complex can be observed. A shallowly- to moderately-dipping gneissosity, typical of the Badcallian gneisses, is well preserved, alongside rare Scourie Dykes and Laxfordian shear zones.

This locality (Fig. B.2a) is one of few well-exposed contacts between TTG gneiss and layered ultramafic rocks. The shallowly-dipping Badcallian gneissosity in the TTG gneiss is parallel to both the layering in the ultramafic rocks and the lithological contacts, a feature that is consistent throughout the complex, irrespective of latter folding. Heterogeneous mafic rocks are also exposed above the ultramafic rocks (Fig. B.2a). Slickensides and recrystallised quartz in the underlying TTG gneiss indicate that the ultramafic–TTG contact is tectonic. The ultramafic rocks exposed here are metapyroxenites (i.e., metamorphosed olivine-websterite and websterite). Continue NE along the track for ~100 m. Leave the track where it takes a relatively sharp turn towards the north, and continue walking E/NE towards the Maldie River to some small waterfalls.

Locality 2. Contact between ultramafic and mafic rocks [NC 2584 3401]

The area around the waterfalls exposes a contact between the ultramafic and mafic portions of the Ben Strome Complex (Fig. B.2b). The contact is irregular and gradational over ~30 cm, in which metapyroxenites grade into a garnetiferous metagabbro. A variety of mafic rocks occupy the higher ground on the E side of the Maldie River. Further downstream, a Scourie Dyke occupies the contact between the ultramafic rocks and TTG gneiss. Return back to the track and continue walking N for almost 100 m.

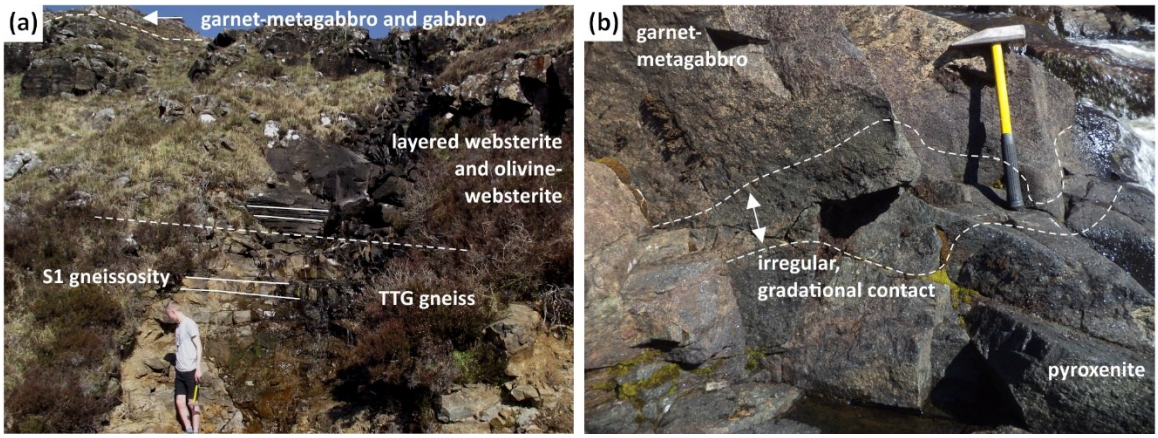

Figure B.2: (a) *Contact between TTG gneiss and overlying ultramafic-mafic rocks are locality 1.* ***(b)*** *Contact between the ultramafic and mafic units of the Ben Strome Complex at locality 2. After: Guice et al. (2018), Precambrian Research/Chapter 3 of this thesis.*

Locality 3. Partial melting of metabasic rocks [NC 2577 3503]

On the right-hand side of the track, before it turns sharply to the NE, are a series of outcrops preserving clear evidence for partial melting. Plagioclase- and clinopyroxene-rich leucosomes, which are restricted to the mafic portions of the Ben Strome Complex, generally occur on a centimetre- to metre-scale. They exhibit irregular morphologies and have sharp contacts with the surrounding residual mafic host rocks (Fig. B.3a). Return to the track and continue N/NE towards Loch an Leathaid Bhuain.

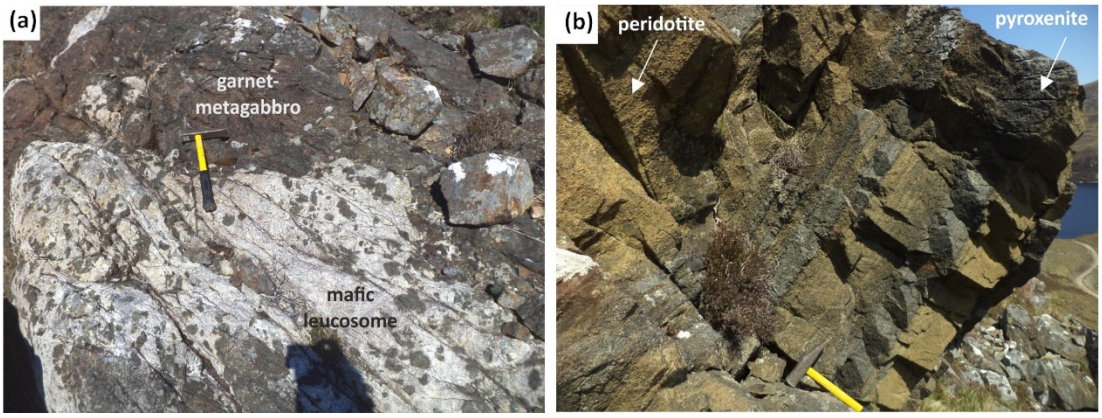

Figure B.3: (a) *Evidence for partial melting of the mafic rocks during the Badcallian metamorphic event, locality 3.* ***(b)*** *Spectacularly layered ultramafic rocks at locality 6.*

Locality 4. Maldie Domain overview (optional extra) [NC 2533 3503]

Walk west from locality 3 (over rough terrain) for ~400 m, heading towards the southern edge of the NE/SW trending cliff in the distance. The cliff represents a post-Laxfordian, dextral fault that juxtaposes shallow-dipping ultramafic rocks in the E and mafic rocks in the W (Fig. B.1). Looking N from locality 4, the broad structure of the Maldie Domain can be observed (Fig. B.4). The layered ultramafic rocks to the N – along with the underlying mafic-ultramafic rocks and TTG gneiss to the S – form an open synform. The layered ultramafic rocks (dominantly metapyroxenite, with subordinate metaperidotite) are truncated by two NW/SE trending Scourie Dykes, which are sub-vertical and therefore show limited offset either side of the fault (in the W).

Return to the track the way you came and continue towards the N.

Locality 5. Layered ultramafic rocks – Ben Strome or Bushveld Complex? [NC 2608 3489]

The Laxfordian shear zone is exposed in exposures on the left of the track [NC 2533 3503] as it begins to ascend. A variety of mafic to felsic lithologies within the shear zone exhibit a steeply-dipping foliation typical of the Laxfordian (e.g., Goodenough et al. 2010, 2013).

Continue along the track until you reach a small hut. Turn left off the track and ascend towards locality 5.

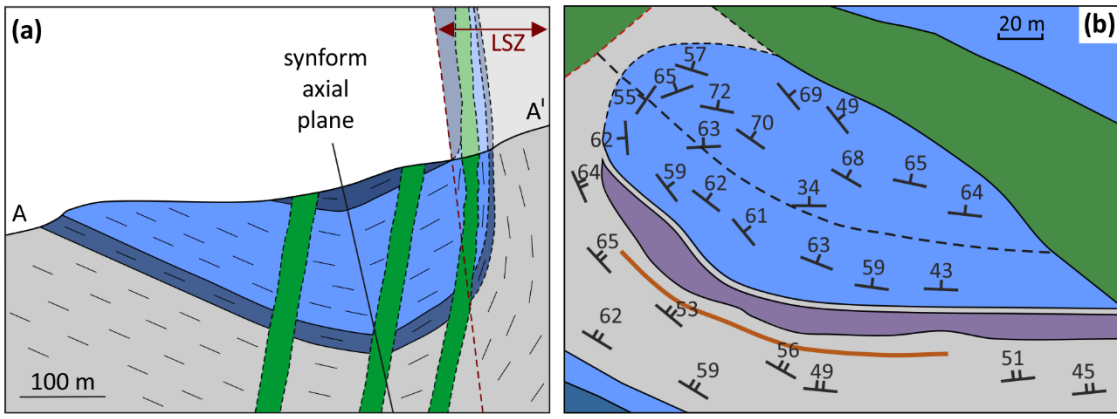

Figure B.4: (a) *Cross-section detailing the structure of the Maldie Domain. Line of section as shown in Fig. B.1.* ***(b)*** *Small-scale map of the area shown in Fig. B.1. Legend as in Figure B.1.*

This locality is best viewed in the afternoon, when the sun is in the west. The rocks comprise layered ultramafic rocks that dip at ~60° towards the N, and are arguably more spectacular than any of the layered ultramafic rocks exposed within the LGC. The rocks consist of layers of brownish metaperidotite and grey/green metapyroxenite (Fig. B.3b) containing fresh orthopyroxene, clinopyroxene, hornblende and spinel with (partially serpentinised) olivine. The contact between layers may be sharp or more diffuse. Individual layers commonly exhibit a gradational variation in the mineral proportions, notably within the uppermost pyroxenite layer), on a millimetre- to metre-scale. Some truncation of the layering is evident (Fig. B.3b).

Heterogeneous mafic rocks above the ultramafic rocks contain abundant garnet. Below (~20–30 m to the south of) the layered ultramafic rocks is a thick granite sheet (Fig. B.1). This sheet can be traced along strike for several hundred metres, and it is also exposed on the northern side of the large Scourie Dyke. This sheet may represent one of the main conduits into and through which melt derived from the TTG gneisses and mafic rocks migrated (Johnson et al. 2013, Johnson et al. 2012). Follow the distinctive unit of layered ultramafic rocks along strike (towards the west) until the ground levels off at locality 6.

Locality 6. Folded mafic rocks [NC 2593 3565]

The mafic rocks in this area form a re-folded isoclinal fold (Fig. B.4b) and preserve subtle remnants of primary layering in places. To the NE, the folded mafic rocks are cross-cut by the large, central Scourie Dyke (Fig. B.1) that, along with the Ben Strome Complex, is disected by a large post-Laxfordian fault (see locality 4). From here walk northwest (uphill) towards the upper track marked on Fig. B.1.

Locality 7. Pegmatoidal amphibolite [NC 2529 3564]

Once you reach the track, walk SW until you reach a series of large cliffs on your right-hand side. You may be able to see a phone mast on the top of the cliffs. At this locality a succession of mafic, ultramafic and felsic rocks are exposed (Fig. B.1), including some pegmatoidal amphibolite containing amphibole crystals up to 6 cm in diameter. Follow the upper track southwest for 4 km until you reach the main road. Turn left onto the main road and take the first left. The car park is on your right-hand side.